

**SEISMIC ANALYSIS AND ASSESSMENT OF HISTORIC
UNREINFORCED MASONRY STRUCTURES**

RYAN MANUEL VALADAO

**A THESIS SUBMITTED TO THE FACULTY OF GRADUATE
STUDIES IN PARTIAL FULFILLMENT OF THE DEGREE
REQUIREMENTS FOR THE DEGREE OF MASTER OF
APPLIED SCIENCE**

**GRADUATE PROGRAM IN CIVIL ENGINEERING
YORK UNIVERSITY
TORONTO, ONTARIO**

OCTOBER 2021

© Ryan Manuel Valadao, 2021

Abstract

This thesis is targeted towards understanding the behaviour of unreinforced masonry structures (URM) under lateral loads that simulate earthquake effects, as well what aspects of their composition affects their behaviour. To understand the composition of masonry and its mechanical properties, a series of parametric studies were conducted studying several critical factors involved in the makeup of a masonry specimen. This includes the brick arrangement, global mortar joint thickness and the individual material strengths. From these studies it was found that the brick arrangement and the global mortar joint thickness have a significant influence on the computed mechanical properties. In addition, studies were conducted on the effectiveness of empirical equations at estimating the mechanical properties of masonry. The outcomes of the investigation indicated that empirical equations when used with conventional masonry can successfully estimate the mechanical properties of masonry. The final aspect of this thesis was three-dimensional finite element modelling of a 1/2 scale URM structure that had been tested on a shake table test. The purpose of those models was to evaluate the applicability of the calibrated empirical estimates of the mechanical response of masonry in reproducing and estimating the lateral load behaviour of a complete structural system. To this end, the fundamental dynamic properties of the URM structure and the lateral response resulting from simulated seismic loads were compared with the experimental evidence. It was found that both objectives were successfully completed and that numerical modelling techniques can accurately assess the dynamic properties and lateral load behaviour of a URM structure. The methodology presented included application of a horizontal gravitational field to reproduce inertia forces generated in buildings with spatial distribution of both stiffness and mass, such as older masonry structures that lack stiff diaphragms at floor levels thereby exhibiting a truly 3-D dynamic response. The assessment procedure applied depends on the pushover-type analysis that was conducted using the gravitational field in the direction of the considered ground motion. Comparison of the identified locations and intensity of damage against the experimental results is used as proof test of the proposed seismic assessment methodology.

This thesis is dedicated to the memory of my uncle, Pupu.

Acknowledgements

I want to express my deepest gratitude to my Supervisor Dr. Stavroula Pantazopoulou, for her constant guidance and support throughout completing this Thesis. Being her student has made me a better professional and provided me with invaluable lessons which I will cherish. I am eternally grateful for the opportunity to work with her.

I also want to express my thanks to Dr. John Gales, for being a part of my journey and for providing me with beneficial feedback every step of the way.

I am incredibly grateful for the opportunity to have spent 6 years in the Department of Civil Engineering at Lassonde School of Engineering completing a BEng degree and my Master's degree. Special thanks goes to Ms. Sindy Mahal for all her help throughout my graduate studies, your dedication to students is remarkable.

To my good friend Konstantinos Tsiotsias, sincere appreciation for all the assistance throughout my numerical work. He was always there for anything I needed, and I am eternally grateful for that.

Special thanks to all my friends and colleagues who were there for me throughout the entirety of my graduate studies: Jordan, Farah, Syed, and Arham.

To my family, I am indebted for always supporting me throughout all my academic endeavours. Their constant belief in me has been crucial to my success and has inspired me to strive further. I truly would not have succeeded in all my accomplishments without them.

Finally, to my partner Hannah, thank you for inspiring me to be the best version of myself. You have supported me every step of the way and I would not have reached this point in my academic career without you.

Table of Contents

Abstract	ii
Dedication	iii
Acknowledgements	iv
Table of Contents	v
List of Figures	xi
List of Tables	xxv
Chapter 1 - Introduction	1
1.0 Introduction	2
1.1 Knowledge Gaps	2
1.2 Summary of Methodology	3
1.3 Organization of the Thesis	5
1.3.1 Chapter 1	6
1.3.2 Chapter 2	6
1.3.3 Chapter 3	6
1.3.4 Chapter 4	7
1.3.5 Chapter 5	7
1.3.6 Chapter 6	7
1.3.7 Chapter 7	7
1.3.8 Chapter 8	7
1.3.9 Conclusion	8
Chapter 2 – State of the Art & Literature Review	9
2.0 Background of Unreinforced Masonry Structures	10
2.1 Modelling Techniques	14
2.1.1 Equivalent Frame Analysis	15
2.1.2 Finite Element Analysis	16
2.1.3 Discrete Element Modelling	17
2.1.4 Shell Type Finite Element Analysis	17
2.2 Physical Test Models	18

2.2.1 <i>A full-scale shaking table test on a two-story stone masonry building – Guido Magenes, Andrea Penna, and Alessandro Galasco, and, Shaking Table Test of a Strengthened Full-Scale Stone Masonry Building with Flexible Diaphragms – Magenes, G., Penna, A., Senaldi, I. E., Rota, M., and Galasco, A.</i>	18
2.2.2 <i>Seismic Performance of an unreinforced masonry building: An experimental investigation – Jitendra K. Bothara, Rajesh P. Dhakal, and John B. Mander.....</i>	21
2.2.3 <i>Shaking Table Tests on Two Multi-Leaf Stone Masonry Buildings – Mazzon, N., Valluzzi, M., Aoki, T., Garbin, E., De Canio, G., Ranieri, N., and Modena, C. ..</i>	24
2.2.4 <i>Shaking Table Tests on 24 Simple Masonry Buildings – Benedetti, P., Carydis, P., and Pezzoli, P.....</i>	25
2.2.5 <i>Seismic Assessment of a Lab-Tested Two-Story Unreinforced Masonry Dutch House – Esposito, R., Messali, F., Ravenshorst, G. J. P., Roel Schipper, H., and Rots, J. G.....</i>	26
2.2.6 <i>NIKER Project</i>	28

Chapter 3 – Introduction to Studied NIKER Experiment and Preliminary Modelling in SAP 2000	29
3.0 Introduction.....	30
3.1 Model Dimensions	30
3.2 Material Properties.....	31
3.2.1 Masonry	31
3.2.2 Timber.....	31
3.3 Model Elements	32
3.3.1 Finite Element Mesh.....	34
3.3.2 Floor to Wall Spring Connections	35
3.3.3 Additional Mass	36
3.4 Applied Earthquake	38
3.5 Period Correlation Analyses	41
3.5.1 Model 1: Direct Connection.....	41
3.5.2 Model 2: Spring Connection.....	42
3.5.3 Model 3: No Floor System.....	44

3.6 Conclusion	45
Chapter 4 – Numerical Modelling of Masonry Wall Elements in ATENA 3D	46
4.0 Introduction.....	47
4.1 Wall Element Designs & Dimensions	48
4.2 Material Properties.....	52
4.3 Direct Compression and Pushover Models.....	54
4.3.1 Methodology (Direct Compression)	55
4.3.2 Macro-elements.....	55
4.3.3 Contacts.....	56
4.3.4 Finite Element Mesh	57
4.3.5 Load Cases	58
4.3.5.1 Supports	59
4.3.5.2 Prescribed Deformation	60
4.4 Monitoring Points	60
4.5 Analysis Steps.....	61
4.6 Pushover Models.....	62
4.6.1 Methodology	62
4.6.1.1 Macroelements	62
4.6.1.2 Supports	63
4.6.1.3 Prescribed Deformation	64
4.6.1.4 Forces	64
4.6.1.5 Monitoring Points	65
4.6.1.6 Analysis Steps.....	65
4.7 Alternate Material Properties Models.....	66
4.8 Alternate Loading Conditions.....	66
4.9 Collection of Analysis Cases	67
Chapter 5 – Results of the Direct Compression Study on URM Wallettes	71
5.0 Introduction.....	72
5.1 Review of Specimens.....	72

5.2 Review of Loading Conditions	73
5.3 SYM Results	73
5.4 EQS Results	77
5.5 RAN Results	81
5.6 STONE Results	85
5.7 Conclusions	87
 Chapter 6 – Results of the Pushover Study on Wallete Specimens	89
6.0 Introduction	90
6.1 Review of Loading Conditions	90
6.2 SYM Results	91
6.2.1 SYMJ5	91
6.2.2 SYMJ10	94
6.2.3 SYMJ20	99
6.2.4 SYM Summary	102
6.3 EQS Results	103
6.3.1 EQSJ5	103
6.3.2 EQSJ10	107
6.3.3 EQSJ20	111
6.3.4 EQS Summary	114
6.4 RAN Results	115
6.4.1 RANJ5	115
6.4.2 RANJ10	119
6.4.3 RANJ20	123
6.4.4 RAN Summary	126
6.5 STONE Results	127
6.5.1 STONE Summary	131
6.6 Conclusions	132
 Chapter 7 – Parametric Studies and Empirical Comparisons	135
7.0 Introduction	136

7.1 Empirical Equations.....	136
7.2 Review of Compressive Strength Panels	139
7.3 Material Strength Combinations	139
7.4 SYM Results	140
7.4.1 SYM Overview	146
7.5 EQS Results	147
7.5.1 EQS Overview	154
7.6 RAN Results	154
7.6.1 RAN Overview	161
7.7 STONE Results.....	162
7.7.1 STONE Overview	165
7.8 Lateral Stiffness and Effective Modulus of Elasticity	166
7.9 Conclusions.....	168
 Chapter 8 – SAP2000 Modelling of NIKER Project Specimen	 173
8.0 Introduction.....	174
8.1 Model Modifications.....	174
8.1.1 Masonry Mechanical Properties	174
8.1.2 Base Spring Connections	176
8.2 Results/Analysis.....	177
8.2.1 Modal Analysis	178
8.2.2 Gravitational Analysis	182
8.2.3 Time History Analysis	185
8.2.4 Spectral Analysis	187
8.2.5 Pushover Analysis.....	189
8.3 Conclusion	193
 Chapter 9 – Conclusion	 195
9.0 Findings.....	196
9.1 Next Steps	198

References	199
Appendices	203
Appendix A – Lateral response of masonry wallettes	203
Appendix B – Axial response of masonry wallettes	282

List of Figures

Figure 2-1: [A] The First Toronto Post Office (Simon Pulviser, 2005), [B] Beardmore Building (Bob Krawczyk, n.d.).....	10
Figure 2-2: University College, University of Toronto (Jon Bilous, n.d.).....	11
Figure 2-3: City of Pompeii (Alec & Marlene Hartill, n.d.).....	12
Figure 2-4: Idealization of a masonry structure using the equivalent frame method (Lagomarsino et al., 2013)	15
Figure 2-5: Design of constructed specimen (Magenes et al., 2010).....	19
Figure 2-6: Design of physical specimen (Bothara et al., 2010).	21
Figure 2-7: Physical specimen on shake table (Bothara et al., 2010).	22
Figure 2-8: Fragility curve (Bothara et al., 2010).	23
Figure 2-9: Physical specimen tested on a shake table (Mazzon et al., 2009).....	24
Figure 2-10: Stone masonry structure designed at LEE in Greece (Benedetti et al., 1996).	25
Figure 2-11: Stone masonry specimens built at ISMES in Italy (Benedetti et al., 1996).	26
Figure 2-12: Specifications of physical specimen (Esposito et al., 2019)	27
Figure 2-13: [A] Design and specifications, [B] Physical specimen (Vintzileou et al., 2015).....	28
Figure 3-1: Model Dimensions and tested physical model (Vintzileou et al., 2015).	30
Figure 3-2: Overall Model (Extruded)	33
Figure 3-3: Overall Model (Extruded)	33
Figure 3-4: (Left) Discretized Front Wall, (Right) Discretized Back Wall	34
Figure 3-5: (Left) Discretized Left Wall, (Right) Discretized Right Wall	34
Figure 3-6: Spring SAP2000 Model – idealization of a typical timber joist	35
Figure 3-7: Timber joist anchorage.....	36
Figure 3-8: UX Accelogramme (ITSAK, 2021).	39
Figure 3-9: UY Accelogramme (ITSAK, 2021).	39
Figure 3-10: Kalamata Earthquake Response Spectrum (UX) (ITSAK, 2021).....	40
Figure 3-11: Kalamata Earthquake Response Spectrum (UX) (ITSAK, 2021).....	40
Figure 3-12: Direct Connection Diagram	42
Figure 3-13: (Left) In-Plane Modal Analysis (Direct Connection), (Right) Out-of-Plane Modal Analysis (Direct Connection)	42
Figure 3-14: Spring Connection Diagram.....	43

Figure 3-15: (Left) In-Plane Modal Analysis (Spring Connection), (Right) Out-of-Plane Modal Analysis (Spring Connection).....	43
Figure 3-16: (Left) In-Plane Modal Analysis (Floorless), (Right) Out-of-Plane Modal Analysis (Floorless)	44
Figure 4-1: Initial assumed brick and specimen dimensions.	48
Figure 4-2: Block and joint patterns in the wallettes.	49
Figure 4-3: Collection of nine wallette specimens.	50
Figure 4-4:[A] STONE design. [B] Stone masonry example (Schiavi et al., 2019).....	52
Figure 4-5: Stress - Strain relationship (Masonry Bricks)	53
Figure 4-6: Stress - Strain relationship (Mortar).....	53
Figure 4-7: Macro-elements for EQS (10 mm Joints)	55
Figure 4-8:[A] Adjusted model with no partial contacts, [B] Original model with partial contacts	56
Figure 4-9: Finite element mesh of SYM model with 20 mm joints.	57
Figure 4-10: [A] EQS - 10 mm Joints, [B] RAN - 10 mm Joints. [C] SYM - 10 mm Joints	58
Figure 4-11: Axes of symmetry	59
Figure 4-12: [A] X-Axis supports along plane 1-4-5-8, [B] Y-Axis supports along plane 3-4-7-8, [C] Z-Axis supports along plane 5-6-7-8.....	60
Figure 4-13: Monitoring Points EQS (10 mm Joints).....	61
Figure 4-14: Steel plate applied for pushover analyses.	62
Figure 4-15: Supports for pushover specimens.	63
Figure 4-16: Axial overbearing stress.....	64
Figure 4-17: Pushover Monitoring Points.....	65
Figure 5-1: Wallette designs.	72
Figure 5-2: SYM specimens.	73
Figure 5-3: [A] Deformed-shape SYMJ5 ($\epsilon = 0.00372$ mm/mm), [B] Deformed-shape SYMJ10 ($\epsilon = 0.0042$ mm/mm), [C] Deformed-shape SYMJ20 ($\epsilon = 0.00743$ mm/mm).....	74
Figure 5-4: Summary of compression behaviour for SYM specimens.....	75
Figure 5-5: Summary of compression behaviour for SYM specimens (MOE 5%-33% Method)	76
Figure 5-6: Relationship between Mortar Joint Thickness and Compressive Strength (SYM). ..	76
Figure 5-7: EQS Specimens.....	77

Figure 5-8: [A] Deformed-shape EQSJ5 ($\epsilon = 0.00485$ mm/mm), [B] Deformed-shape EQSJ10 ($\epsilon = 0.00485$ mm/mm), [C] Deformed-shape EQSJ20 ($\epsilon = 0.00582$ mm/mm)	78
Figure 5-9: Summary of compression behaviour for EQS specimens.....	79
Figure 5-10: Summary of compression behaviour for EQS specimens (MOE 5%-33% Method).....	80
Figure 5-11: Relationship between Mortar Joint Thickness and Compressive Strength (EQS)...	80
Figure 5-12: RAN Specimens.....	81
Figure 5-13: [A] Deformed-shape RANJ5 ($\epsilon = 0.00323$ mm/mm), [B] Deformed-shape RANJ10 ($\epsilon = 0.00269$ mm/mm), [C] Deformed-shape RANJ20 ($\epsilon = 0.00269$ mm/mm)	82
Figure 5-14: Summary of compression behaviour for RAN specimens.....	83
Figure 5-15: Summary of compression behaviour for SYM specimens (MOE 5%-33% Method)	84
Figure 5-16: Relationship between Mortar Joint Thickness and Compressive Strength (RAN)..	84
Figure 5-17: Stone Specimen.....	85
Figure 5-18: STONE, [A] Deformed-shape ($\epsilon = 0.000462$ mm/mm), [B] Deformed-shape ($\epsilon = 0.00138$ mm/mm), [C] Deformed-shape ($\epsilon = 0.00277$ mm/mm)	86
Figure 5-19: Stress - Strain diagram of STONE.....	86
Figure 5-20: Stress - Strain diagram of STONE (5%-33% Secant Method)	87
Figure 5-21: Comparing the compressive behaviour of each design.....	88
Figure 6-1: [A] Failure state SYMJ5 (0.05 MPa), [B] Failure state SYMJ5 (0.1 MPa), [C] Failure state SYMJ5 (0.2 MPa), [D] Failure state SYMJ5 (0.3 MPa), [E] Failure state SYMJ5 (0.4 MPa)	91
Figure 6-2: SYMJ5 Pushover Curves Tests 1-5	92
Figure 6-3: [A] Failure state SYMJ5 (1.79 MPa), [B] Failure state SYMJ5 (4.47 MPa), [C] Failure state SYMJ5 (7.15 MPa).....	93
Figure 6-4: SYMJ5 Pushover Curves Tests 6-8	94
Figure 6-5: [A] Failure state SYMJ10 (0.05 MPa), [B] Failure state SYMJ10 (0.1 MPa), [C] Failure state SYMJ10 (0.2 MPa), [D] Failure state SYMJ10 (0.3 MPa), [E] Failure state SYMJ10 (0.4 MPa).....	95
Figure 6-6: SYMJ10 Pushover Curves Tests 1-5	96
Figure 6-7: [A] Failure state SYMJ10 (1.79 MPa), [B] Failure state SYMJ10 (4.47 MPa), [C] Failure state SYMJ10 (7.15 MPa)	97

Figure 6-8: SYMJ10 Pushover Curves Tests 6-8	97
Figure 6-9: [A] Failure state SYMJ20 (0.05 MPa), [B] Failure state SYMJ20 (0.1 MPa), [C] Failure state SYMJ20 (0.2 MPa), [D] Failure state SYMJ20 (0.3 MPa), [E] Failure state SYMJ20 (0.4 MPa)	99
Figure 6-10: SYMJ20 Pushover Curves Tests 1-5	100
Figure 6-11: [A] Failure state SYMJ20 (1.79 MPa), [B] Failure state SYMJ20 (4.47 MPa), [C] Failure state SYMJ20 (7.15 MPa)	101
Figure 6-12: SYMJ20 Pushover Curves Tests 6-8	101
Figure 6-13: Summary of SYM Results (Pushover)	102
Figure 6-14: [A] Failure state EQSJ5 (0.05 MPa), [B] Failure state EQSJ5 (0.1 MPa), [C] Failure state EQSJ5 (0.2 MPa), [D] Failure state EQSJ5 (0.3 MPa), [E] Failure state EQSJ5 (0.4 MPa)	104
Figure 6-15: EQSJ5 Pushover Curves Tests 1-5	105
Figure 6-16: [A] Failure state EQSJ5 (1.79 MPa), [B] Failure state EQSJ5 (4.47 MPa), [C] Failure state EQSJ5 (7.15 MPa)	106
Figure 6-17: EQSJ5 Pushover Curves Tests 6-8	106
Figure 6-18: [A] Failure state EQSJ10 (0.05 MPa), [B] Failure state EQSJ10 (0.1 MPa), [C] Failure state EQSJ10 (0.2 MPa), [D] Failure state EQSJ10 (0.3 MPa), [E] Failure state EQSJ10 (0.4 MPa)	107
Figure 6-19: EQSJ10 Pushover Curves Tests 1-5	108
Figure 6-20: [A] Failure state EQSJ10 (1.79 MPa), [B] Failure state EQSJ10 (4.47 MPa), [C] Failure state EQSJ10 (7.15 MPa)	109
Figure 6-21: EQSJ10 Pushover Curves Tests 6-8	109
Figure 6-22: [A] Failure state EQSJ20 (0.05 MPa), [B] Failure state EQSJ20 (0.1 MPa), [C] Failure state EQSJ20 (0.2 MPa), [D] Failure state EQSJ20 (0.3 MPa), [E] Failure state EQSJ20 (0.4 MPa)	111
Figure 6-23: EQSJ20 Pushover Curves Tests 1-5	112
Figure 6-24: [A] Failure state EQSJ20 (1.79 MPa), [B] Failure state EQSJ20 (4.47 MPa), [C] Failure state EQSJ20 (7.15 MPa)	113
Figure 6-25: EQSJ20 Pushover Curves Tests 6-8	113
Figure 6-26: Summary of EQS Results (Pushover)	114

Figure 6-27: [A] Failure state RANJ5 (0.05 MPa), [B] Failure state RANJ5 (0.1 MPa), [C] Failure state RANJ5 (0.2 MPa), [D] Failure state RANJ5 (0.3 MPa), [E] Failure state RANJ5 (0.4 MPa)	116
Figure 6-28: RANJ5 Pushover Curves Tests 1-5.....	117
Figure 6-29: [A] Failure state RANJ5 (1.79 MPa), [B] Failure state RANJ5 (4.47 MPa), [C] Failure state RANJ5 (7.15 MPa).....	118
Figure 6-30: RANJ5 Pushover Curves Tests 6-8.....	118
Figure 6-31: [A] Failure state RANJ10 (0.05 MPa), [B] Failure state RANJ10 (0.1 MPa), [C] Failure state RANJ10 (0.2 MPa), [D] Failure state RANJ10 (0.3 MPa), [E] Failure state RANJ10 (0.4 MPa)	120
Figure 6-32: RANJ10 Pushover Curves Tests 1-5.....	121
Figure 6-33: [A] Failure state RANJ10 (1.79 MPa), [B] Failure state RANJ10 (4.47 MPa), [C] Failure state RANJ10 (7.15 MPa)	121
Figure 6-34: RANJ10 Pushover Curves Tests 6-8.....	122
Figure 6-35: [A] Failure state RANJ20 (0.05 MPa), [B] Failure state RANJ20 (0.1 MPa), [C] Failure state RANJ20 (0.2 MPa), [D] Failure state RANJ20 (0.3 MPa), [E] Failure state RANJ20 (0.4 MPa)	123
Figure 6-36: RANJ20 Pushover Curves Tests 1-5.....	124
Figure 6-37: [A] Failure state RANJ20 (1.79 MPa), [B] Failure state RANJ20 (4.47 MPa), [C] Failure state RANJ20 (7.15 MPa)	125
Figure 6-38: RANJ20 Pushover Curves Tests 6-8.....	125
Figure 6-39: Summary of RAN Results (Pushover)	126
Figure 6-40: [A] Failure state STONE (0.05 MPa), [B] Failure state STONE (0.1 MPa), [C] Failure state STONE (0.2 MPa), [D] Failure state STONE (0.3 MPa), [E] Failure state STONE (0.4 MPa)	128
Figure 6-41: STONE Pushover Curves Tests 1-5.....	129
Figure 6-42: [A] Failure state STONE (1.79 MPa), [B] Failure state STONE (4.47 MPa), [C] Failure state STONE (7.15 MPa).....	130
Figure 6-43: STONE Pushover Curves Tests 6-8.....	131
Figure 6-44: Summary of STONE Results (Pushover).....	132
Figure 6-45: Collection of Interaction Diagrams (All Designs)	133

Figure 7-1: Wallette Panel Designs.	139
Figure 7-2: [LEFT] SYMJ5 $f_{bc} = 30$ MPa, [MIDDLE] SYMJ5 $f_{bc} = 50$ MPa, [RIGHT] SYMJ5 $f_{bc} = 100$ MPa.....	140
Figure 7-3: SYMJ5 ATENA vs Theoretical Equations (Varying Brick Compressive Strength)	141
Figure 7-4: [LEFT] SYMJ5 $f_{mc} = 1.0$ MPa, [MIDDLE] SYMJ5 $f_{mc} = 2.3$ MPa, [RIGHT] SYMJ5 $f_{mc} = 4.6$ MPa.....	141
Figure 7-5: SYMJ5 ATENA vs Theoretical Equations (Varying Mortar Compressive Strength)	142
Figure 7-6: [LEFT] SYMJ10 $f_{bc} = 30$ MPa, [MIDDLE] SYMJ10 $f_{bc} = 50$ MPa, [RIGHT] SYMJ10 $f_{bc} = 100$ MPa.....	142
Figure 7-7: SYMJ10 ATENA vs Theoretical Equations (Varying Brick Compressive Strength)	143
Figure 7-8: [LEFT] SYMJ10 $f_{mc} = 1.0$ MPa, [MIDDLE] SYMJ10 $f_{mc} = 2.3$ MPa, [RIGHT] SYMJ10 $f_{mc} = 4.6$ MPa.....	143
Figure 7-9: SYMJ10 ATENA vs Theoretical Equations (Varying Mortar Compressive Strength)	144
Figure 7-10: [LEFT] SYMJ20 $f_{bc} = 30$ MPa, [MIDDLE] SYMJ20 $f_{bc} = 50$ MPa, [RIGHT] SYMJ20 $f_{bc} = 100$ MPa.....	144
Figure 7-11: SYMJ20 ATENA vs Theoretical Equations (Varying Brick Compressive Strength)	145
Figure 7-12: [LEFT] SYMJ20 $f_{mc} = 1.0$ MPa, [MIDDLE] SYMJ20 $f_{mc} = 2.3$ MPa, [RIGHT] SYMJ20 $f_{mc} = 4.6$ MPa.....	145
Figure 7-13: SYMJ20 ATENA vs Theoretical Equations (Varying Mortar Compressive Strength)	146
Figure 7-14: [LEFT] EQSJ5 $f_{bc} = 30$ MPa, [MIDDLE] EQSJ5 $f_{bc} = 50$ MPa, [RIGHT] EQSJ5 $f_{bc} = 100$ MPa.....	148
Figure 7-15: EQSJ5 ATENA vs Theoretical Equations (Varying Brick Compressive Strength)	148
Figure 7-16: [LEFT] EQSJ5 $f_{mc} = 1.0$ MPa, [MIDDLE] EQSJ5 $f_{mc} = 2.3$ MPa, [RIGHT] EQSJ5 $f_{mc} = 4.6$ MPa.....	149

Figure 7-17: EQSJ5 ATENA vs Theoretical Equations (Varying Mortar Compressive Strength)	149
Figure 7-18: [LEFT] EQSJ10 $f_{bc} = 30$ MPa, [MIDDLE] EQSJ10 $f_{bc} = 50$ MPa, [RIGHT] EQSJ10 $f_{bc} = 100$ MPa	150
Figure 7-19: EQSJ10 ATENA vs Theoretical Equations (Varying Brick Compressive Strength)	150
Figure 7-20: [LEFT] EQSJ10 $f_{mc} = 1.0$ MPa, [MIDDLE] EQSJ10 $f_{mc} = 2.3$ MPa, [RIGHT] EQSJ10 $f_{mc} = 4.6$ MPa	151
Figure 7-21: EQSJ10 ATENA vs Theoretical Equations (Varying Mortar Compressive Strength)	151
Figure 7-22: [LEFT] EQSJ20 $f_{bc} = 30$ MPa, [MIDDLE] EQSJ20 $f_{bc} = 50$ MPa, [RIGHT] EQSJ20 $f_{bc} = 100$ MPa	152
Figure 7-23: EQSJ20 ATENA vs Theoretical Equations (Varying Brick Compressive Strength)	152
Figure 7-24: [LEFT] EQSJ20 $f_{mc} = 1.0$ MPa, [MIDDLE] EQSJ20 $f_{mc} = 2.3$ MPa, [RIGHT] EQSJ20 $f_{mc} = 4.6$ MPa	153
Figure 7-25: EQSJ20 ATENA vs Theoretical Equations (Varying Mortar Compressive Strength)	153
Figure 7-26: [LEFT] RANJ5 $f_{bc} = 30$ MPa, [MIDDLE] RANJ5 $f_{bc} = 50$ MPa, [RIGHT] RANJ5 $f_{bc} = 100$ MPa	155
Figure 7-27: RANJ5 ATENA vs Theoretical Equations (Varying Brick Compressive Strength)	156
Figure 7-28: [LEFT] RANJ5 $f_{mc} = 1.0$ MPa, [MIDDLE] RANJ5 $f_{mc} = 2.3$ MPa, [RIGHT] RANJ5 $f_{mc} = 4.6$ MPa	156
Figure 7-29: RANJ5 ATENA vs Theoretical Equations (Varying Mortar Compressive Strength)	157
Figure 7-30: [LEFT] RANJ10 $f_{bc} = 30$ MPa, [MIDDLE] RANJ10 $f_{bc} = 50$ MPa, [RIGHT] RANJ10 $f_{bc} = 100$ MPa	157
Figure 7-31: RANJ10 ATENA vs Theoretical Equations (Varying Brick Compressive Strength)	158

Figure 7-32: [LEFT] RANJ10 $f_{mc} = 1.0$ MPa, [MIDDLE] RANJ10 $f_{mc} = 2.3$ MPa, [RIGHT] RANJ10 $f_{mc} = 4.6$ MPa.....	158
Figure 7-33: RANJ10 ATENA vs Theoretical Equations (Varying Mortar Compressive Strength)	159
Figure 7-34: [LEFT] RANJ20 $f_{bc} = 30$ MPa, [MIDDLE] RANJ20 $f_{bc} = 50$ MPa, [RIGHT] RANJ20 $f_{bc} = 100$ MPa.....	159
Figure 7-35: RANJ20 ATENA vs Theoretical Equations (Varying Brick Compressive Strength)	160
Figure 7-36: [LEFT] RANJ20 $f_{mc} = 1.0$ MPa, [MIDDLE] RANJ20 $f_{mc} = 2.3$ MPa, [RIGHT] RANJ20 $f_{mc} = 4.6$ MPa.....	160
Figure 7-37: RANJ20 ATENA vs Theoretical Equations (Varying Mortar Compressive Strength)	161
Figure 7-38: [LEFT] STONE $f_{bc} = 30$ MPa, [MIDDLE] STONE $f_{bc} = 50$ MPa, [RIGHT] STONE $f_{bc} = 100$ MPa.....	163
Figure 7-39: STONE ATENA vs Theoretical Equations (Varying Brick Compressive Strength)	163
Figure 7-40: [LEFT] STONE $f_{mc} = 1.0$ MPa, [MIDDLE] STONE $f_{mc} = 2.3$ MPa, [RIGHT] STONE $f_{mc} = 4.6$ MPa.....	164
Figure 7-41: STONE ATENA vs Theoretical Equations (Varying Mortar Compressive Strength)	164
Figure 7-42: Characteristic Values from Lateral Pushover Curve.....	166
Figure 7-43: Percentage Error of Empirical Equations. [A] SYMJ5, [B] SYMJ10, [C] SYMJ20	169
Figure 7-44: Percentage Error of Empirical Equations. [A] EQSJ5, [B] EQSJ10, [C] EQSJ20	171
Figure 8-1: PO-STONE-OB0.1 Pushover Curve for SAP 2000 Calibration.....	175
Figure 8-2: Non-Linear Stress-Strain Relationship of Utilized Masonry	176
Figure 8-3: Mode 1 (UY).....	179
Figure 8-4: Mode 2 (UX).....	180
Figure 8-5: Mass participation vs mode type.....	181
Figure 8-6: Mass participation by the inclusion of modes.....	182
Figure 8-7: Gravitational Analysis (UX)	183

Figure 8-8: Gravitational Analysis (UY)	184
Figure 8-9: Normalized Mode Shapes vs Normalized Gravitational Shapes	185
Figure 8-10: Deformed Shape 90% Kalamata UY	186
Figure 8-11: Deformed Shape 90% Kalamata UX	186
Figure 8-12: Deformed Shape 90% Response Spectrum UY	187
Figure 8-13: Deformed Shape 90% Response Spectrum UX	187
Figure 8-14: Normalized Mode Shapes vs Normalized Gravitational Shapes	188
Figure 8-15: Darwin-Pecknold effective uniaxial stress-strain curve.....	189
Figure 8-16: Deformed Shape Pushover UY	190
Figure 8-17: Pushover Curve UY	191
Figure 8-18: Deformed Shape Pushover UX	192
Figure 8-19: Pushover Curve UX	193
Figure A-1: PO-SYMJ5-OB0.05 Response [A] 0.1% Drift, [B] 0.2% Drift, [C] 0.5% Drift, [D] 1% Drift.....	203
Figure A-2: PO-SYMJ5-OB0.1 Response [A] 0.1% Drift, [B] 0.2% Drift, [C] 0.5% Drift, [D] 1% Drift.....	204
Figure A-3: PO-SYMJ5-OB0.2 Response [A] 0.1% Drift, [B] 0.2% Drift, [C] 0.5% Drift, [D] 1% Drift.....	205
Figure A-4: PO-SYMJ5-OB0.3 Response [A] 0.1% Drift, [B] 0.2% Drift, [C] 0.5% Drift, [D] 1% Drift.....	206
Figure A-5: PO-SYMJ5-OB0.4 Response [A] 0.1% Drift, [B] 0.2% Drift, [C] 0.5% Drift, [D] 1% Drift.....	207
Figure A-6: PO-SYMJ5-OB1.79 Response [A] 0.092% Drift, [B] 0.23% Drift, [C] 0.51% Drift, [D] 0.83% Drift.....	208
Figure A-7: PO-SYMJ5-OB4.47 Response [A] 0.092% Drift, [B] 0.18% Drift, [C] 0.51% Drift, [D] 0.92% Drift.....	209
Figure A-8: PO-SYMJ5-OB7.15 Response [A] 0.092% Drift, [B] 0.18% Drift, [C] 0.51% Drift, [D] 0.92% Drift.....	210
Figure A-9: PO-SYMJ10-OB0.05 Response [A] 0.1% Drift, [B] 0.2% Drift, [C] 0.5% Drift, [D] 0.74% Drift	211

Figure A-10: PO-SYMJ10-OB0.1 Response [A] 0.1% Drift, [B] 0.2% Drift, [C] 0.5% Drift, [D] 0.81% Drift	212
Figure A-11: PO-SYMJ10-OB0.2 Response [A] 0.1% Drift, [B] 0.2% Drift, [C] 0.5% Drift, [D] 0.94% Drift	213
Figure A-12: PO-SYMJ10-OB0.3 Response [A] 0.1% Drift, [B] 0.2% Drift, [C] 0.5% Drift, [D] 1% Drift	214
Figure A-13: PO-SYMJ10-OB0.4 Response [A] 0.1% Drift, [B] 0.2% Drift, [C] 0.5% Drift, [D] 1% Drift	215
Figure A-14: PO-SYMJ10-OB1.79 Response [A] 0.231% Drift, [B] 0.415% Drift, [C] 0.922% Drift.....	216
Figure A-15: PO-SYMJ10-OB4.47 Response [A] 0.092% Drift, [B] 0.23% Drift, [C] 0.55% Drift	217
Figure A-16: PO-SYMJ10-OB7.15 Response [A] 0.092% Drift, [B] 0.23% Drift, [C] 0.369% Drift	218
Figure A-17: PO-SYMJ20-OB0.05 Response [A] 0.1% Drift, [B] 0.2% Drift, [C] 0.5% Drift, [D] 1% Drift	219
Figure A-18: PO-SYMJ20-OB0.1 Response [A] 0.1% Drift, [B] 0.2% Drift, [C] 0.5% Drift, [D] 1% Drift	220
Figure A-19: PO-SYMJ20-OB0.2 Response [A] 0.1% Drift, [B] 0.2% Drift, [C] 0.5% Drift, [D] 1% Drift	221
Figure A-20: PO-SYMJ20-OB0.3 Response [A] 0.1% Drift, [B] 0.2% Drift, [C] 0.5% Drift, [D] 1% Drift	222
Figure A-21: PO-SYMJ20-OB0.4 Response [A] 0.1% Drift, [B] 0.2% Drift, [C] 0.5% Drift, [D] 1% Drift	223
Figure A-22: PO-SYMJ20-OB1.79 Response [A] 0.092% Drift, [B] 0.23% Drift, [C] 0.415% Drift	224
Figure A-23: PO-SYMJ20-OB4.47 Response [A] 0.092% Drift, [B] 0.231% Drift, [C] 0.431% Drift.....	225
Figure A-24: PO-SYMJ20-OB7.15 Response [A] 0.092% Drift, [B] 0.23% Drift, [C] 0.322% Drift	226

Figure A-25: PO-EQSJ5-OB0.05 Response [A] 0.1% Drift, [B] 0.2% Drift, [C] 0.5% Drift, [D] 1% Drift	227
Figure A-26: PO-EQSJ5-OB0.1 Response [A] 0.1% Drift, [B] 0.2% Drift, [C] 0.5% Drift, [D] 1% Drift.....	228
Figure A-27: PO-EQSJ5-OB0.2 Response [A] 0.1% Drift, [B] 0.2% Drift, [C] 0.5% Drift, [D] 1% Drift.....	229
Figure A-28: PO-EQSJ5-OB0.3 Response [A] 0.1% Drift, [B] 0.2% Drift, [C] 0.5% Drift, [D] 1% Drift.....	230
Figure A-29: PO-EQSJ5-OB0.4 Response [A] 0.1% Drift, [B] 0.2% Drift, [C] 0.5% Drift, [D] 1% Drift.....	231
Figure A-30: PO-EQSJ5-OB1.79 Response [A] 0.092% Drift, [B] 0.184% Drift, [C] 0.508% Drift, [D] 0.831% Drift.....	232
Figure A-31: PO-EQSJ5-OB4.47 Response [A] 0.092% Drift, [B] 0.184% Drift, [C] 0.507% Drift, [D] 0.784% Drift.....	233
Figure A-32: PO-EQSJ5-OB7.15 Response [A] 0.092% Drift, [B] 0.184% Drift, [C] 0.507% Drift, [D] 0.646% Drift.....	234
Figure A-33: PO-EQSJ10-OB0.05 Response [A] 0.1% Drift, [B] 0.2% Drift, [C] 0.5% Drift, [D] 0.87% Drift	235
Figure A-34: PO-EQSJ10-OB0.1 Response [A] 0.1% Drift, [B] 0.2% Drift, [C] 0.5% Drift, [D] 0.78% Drift	236
Figure A-35: PO-EQSJ10-OB0.2 Response [A] 0.1% Drift, [B] 0.2% Drift, [C] 0.5% Drift, [D] 1% Drift	237
Figure A-36: PO-EQSJ10-OB0.3 Response [A] 0.1% Drift, [B] 0.2% Drift, [C] 0.5% Drift, [D] 1% Drift	238
Figure A-37: PO-EQSJ10-OB0.4 Response [A] 0.1% Drift, [B] 0.2% Drift, [C] 0.39% Drift .	239
Figure A-38: PO-EQSJ10-OB1.79 Response [A] 0.092% Drift, [B] 0.184% Drift, [C] 0.461% Drift.....	240
Figure A-39: PO-EQSJ10-OB4.47 Response [A] 0.092% Drift, [B] 0.184% Drift, [C] 0.507% Drift, [D] 0.554% Drift.....	241
Figure A-40: PO-EQSJ10-OB7.15 Response [A] 0.092% Drift, [B] 0.184% Drift, [C] 0.507% Drift.....	242

Figure A-41: PO-EQSJ20-OB0.05 Response [A] 0.1% Drift, [B] 0.2% Drift, [C] 0.5% Drift, [D] 1% Drift	243
Figure A-42: PO-EQSJ20-OB0.1 Response [A] 0.1% Drift, [B] 0.2% Drift, [C] 0.5% Drift, [D] 1% Drift	244
Figure A-43: PO-EQSJ20-OB0.2 Response [A] 0.1% Drift, [B] 0.2% Drift, [C] 0.5% Drift, [D] 1% Drift	245
Figure A-44: PO-EQSJ20-OB0.3 Response [A] 0.1% Drift, [B] 0.2% Drift, [C] 0.5% Drift, [D] 1% Drift	246
Figure A-45: PO-EQSJ20-OB0.4 Response [A] 0.1% Drift, [B] 0.2% Drift, [C] 0.5% Drift, [D] 1% Drift	247
Figure A-46: PO-EQSJ20-OB1.79 Response [A] 0.092% Drift, [B] 0.184% Drift, [C] 0.369% Drift.....	248
Figure A-47: PO-EQSJ20-OB4.47 Response [A] 0.092% Drift, [B] 0.184% Drift, [C] 0.507% Drift, [D] 0.646% Drift.....	249
Figure A-48: PO-EQSJ20-OB7.15 Response [A] 0.092% Drift, [B] 0.184% Drift, [C] 0.507% Drift, [D] 0.738% Drift.....	250
Figure A-49: PO-RANJ5-OB0.05 Response [A] 0.1% Drift, [B] 0.2% Drift, [C] 0.48% Drift.	251
Figure A-50: PO-RANJ5-OB0.1 Response [A] 0.1% Drift, [B] 0.2% Drift, [C] 0.45% Drift... ..	252
Figure A-51: PO-RANJ5-OB0.2 Response [A] 0.1% Drift, [B] 0.2% Drift	253
Figure A-52: PO-RANJ5-OB0.3 Response [A] 0.1% Drift	253
Figure A-53: PO-RANJ5-OB0.4 Response [A] 0.1% Drift	254
Figure A-54: PO-RANJ5-OB1.79 Response [A] 0.092% Drift, [B] 0.184% Drift, [C] 0.231% Drift	255
Figure A-55: PO-RANJ5-OB4.47 Response [A] 0.092% Drift, [B] 0.184% Drift, [C] 0.277% Drift	256
Figure A-56: PO-RANJ5-OB7.15 Response [A] 0.092% Drift, [B] 0.184% Drift, [C] 0.276% Drift	257
Figure A-57: PO-RANJ10-OB0.05 Response [A] 0.1% Drift, [B] 0.2% Drift, [C] 0.5% Drift, [D] 0.71% Drift	258
Figure A-58: PO-RANJ10-OB0.1 Response [A] 0.1% Drift, [B] 0.2% Drift, [C] 0.5% Drift, [D] 0.81% Drift	259

Figure A-59: PO-RANJ10-OB0.2 Response [A] 0.1% Drift, [B] 0.2% Drift, [C] 0.45% Drift.	260
Figure A-60: PO-RANJ10-OB0.3 Response [A] 0.1% Drift, [B] 0.2% Drift, [C] 0.35% Drift.	261
Figure A-61: PO-RANJ10-OB0.4 Response [A] 0.1% Drift, [B] 0.2% Drift, [C] 0.29% Drift.	262
Figure A-62: PO-RANJ10-OB1.79 Response [A] 0.092% Drift, [B] 0.184% Drift, [C] 0.415% Drift.....	263
Figure A-63: PO-RANJ10-OB4.47 Response [A] 0.092% Drift, [B] 0.184% Drift, [C] 0.415% Drift.....	264
Figure A-64: PO-RANJ10-OB7.15 Response [A] 0.0921% Drift, [B] 0.184% Drift, [C] 0.507% Drift, [D] 0.646% Drift	265
Figure A-65: PO-RANJ20-OB0.05 Response [A] 0.1% Drift, [B] 0.2% Drift, [C] 0.5% Drift, [D] 0.87% Drift	266
Figure A-66: PO-RANJ20-OB0.1 Response [A] 0.1% Drift, [B] 0.2% Drift, [C] 0.5% Drift, [D] 0.78% Drift	267
Figure A-67: PO-RANJ20-OB0.2 Response [A] 0.1% Drift, [B] 0.2% Drift, [C] 0.5% Drift, [D] 0.65% Drift	268
Figure A-68: PO-RANJ20-OB0.3 Response [A] 0.1% Drift, [B] 0.2% Drift, [C] 0.36% Drift.	269
Figure A-69: PO-RANJ20-OB0.4 Response [A] 0.1% Drift, [B] 0.2% Drift, [C] 0.36% Drift.	270
Figure A-70: PO-RANJ20-OB1.79 Response [A] 0.092% Drift, [B] 0.184% Drift, [C] 0.415% Drift.....	271
Figure A-71: PO-RANJ20-OB4.47 Response [A] 0.091% Drift, [B] 0.184% Drift, [C] 0.507% Drift, [D] 0.553% Drift.....	272
Figure A-72: PO-RANJ20-OB7.15 Response [A] 0.101% Drift, [B] 0.205% Drift, [C] 0.436% Drift.....	273
Figure A-73: PO-STONE-OB0.05 Response [A] 0.0925% Drift, [B] 0.185% Drift, [C] 0.277% Drift.....	274
Figure A-74: PO-STONE-OB0.1 Response [A] 0.0925% Drift, [B] 0.185% Drift	275
Figure A-75: PO-STONE-OB0.2 Response [A] 0.0928% Drift, [B] 0.185% Drift, [C] 0.324% Drift	276
Figure A-76: PO-STONE-OB0.3 Response [A] 0.0929% Drift, [B] 0.231% Drift	277
Figure A-77: PO-STONE-OB0.4 Response [A] 0.0932% Drift, [B] 0.232% Drift	278

Figure A-78: PO-STONE-OB1.79 Response [A] 0.096% Drift, [B] 0.189% Drift, [C] 0.327% Drift	279
Figure A-79: PO-STONE-OB4.47 Response [A] 0.102% Drift, [B] 0.194% Drift, [C] 0.379% Drift	280
Figure A-80: PO-STONE-OB7.15 Response [A] 0.107% Drift, [B] 0.199% Drift, [C] 0.384% Drift	281
Figure B-1: SYMJ5, [A] Deformed Shape & Cracks ($\epsilon = 0.00124$ mm/mm), [B] Deformed Shape & Cracks ($\epsilon = 0.00248$ mm/mm), [C] Deformed Shape & Cracks ($\epsilon = 0.00372$ mm/mm)	282
Figure B-2: SYMJ10, [A] Deformed-shape ($\epsilon = 0.00162$ mm/mm), [B] Deformed-shape ($\epsilon = 0.00355$ mm/mm), [C] Deformed-shape ($\epsilon = 0.0042$ mm/mm)	282
Figure B-3: SYMJ20, [A] Deformed-shape ($\epsilon = 0.00124$ mm/mm), [B] Deformed-shape ($\epsilon = 0.00495$ mm/mm), [C] Deformed-shape ($\epsilon = 0.00743$ mm/mm)	283
Figure B-4: EQSJ5, [A] Deformed-shape ($\epsilon = 0.000969$ mm/mm), [B] Deformed-shape ($\epsilon = 0.00388$ mm/mm), [C] Deformed-shape ($\epsilon = 0.00485$ mm/mm)	283
Figure B-5: EQSJ10, [A] Deformed-shape ($\epsilon = 0.000969$ mm/mm), [B] Deformed-shape ($\epsilon = 0.00388$ mm/mm), [C] Deformed-shape ($\epsilon = 0.00485$ mm/mm)	284
Figure B-6: EQSJ20, [A] Deformed-shape ($\epsilon = 0.000969$ mm/mm), [B] Deformed-shape ($\epsilon = 0.00485$ mm/mm), [C] Deformed-shape ($\epsilon = 0.00582$ mm/mm)	284
Figure B-7: RANJ5, [A] Deformed-shape ($\epsilon = 0.000808$ mm/mm), [B] Deformed-shape ($\epsilon = 0.00242$ mm/mm), [C] Deformed-shape ($\epsilon = 0.00323$ mm/mm)	285
Figure B-8: RANJ10, [A] Deformed-shape ($\epsilon = 0.000538$ mm/mm), [B] Deformed-shape ($\epsilon = 0.00215$ mm/mm), [C] Deformed-shape ($\epsilon = 0.00269$ mm/mm)	285
Figure B-9: RANJ20, [A] Deformed-shape ($\epsilon = 0.000538$ mm/mm), [B] Deformed-shape ($\epsilon = 0.00108$ mm/mm), [C] Deformed-shape ($\epsilon = 0.00269$ mm/mm)	286
Figure B-10: STONE, [A] Deformed-shape ($\epsilon = 0.000462$ mm/mm), [B] Deformed-shape ($\epsilon = 0.00138$ mm/mm), [C] Deformed-shape ($\epsilon = 0.00277$ mm/mm)	286

List of Tables

Table 3-1: Chosen material properties for Masonry (Vintzileou et al., 2015).....	31
Table 3-2: Chosen material properties for Timber (Karapitta et al., 2012), (Engineering ToolBox, 2004.)	32
Table 3-3: Summary of applied joint forces	37
Table 4-1: % Bricks and Mortar	51
Table 4-2: Sample of material property input in ATENA.	54
Table 4-3: Strength combinations.....	66
Table 4-4: Summary of ATENA 3D Wallette Investigation models.....	68
Table 6-1: Summary of overbearing stress and values and suppressed conditions.	90
Table 7-1: Combinations of Material Strengths.....	139
Table 7-2: Summary of Lateral Stiffness and Modulus of Elasticity Results.....	167
Table 8-1: Chosen material properties for Masonry (Karapitta et al., 2012).....	174

Chapter 1

Introduction

1.0 Introduction

Long before the proliferation of concrete, houses were made of various forms of masonry – either clay, stone or various types of manufactured blocks. These structures comprised mostly unreinforced, double or triple-wythe construction with floor and roof diaphragms resting, or loosely embedded but not monolithically connected to the structure. Today, many of these structures are deemed traditional or heritage construction and because they mostly abound in the older or historical urban cores or many towns, their maintenance and preservation is related to bigger objectives, such as projecting the historical past, and defining the ambiance of the place where they exist (Campbell, 2003).

The materials of choice in unreinforced masonry (URM) construction were often a combination of masonry and timber for the walls and floor systems respectively (Pantazopoulou, 2013). One important aspect missing from these structures is a diaphragm action at each of the floor levels which causes a high level of unpredictability when determining the behaviour of the structure to earthquakes. Recent earthquakes in various parts of the globe where there is a large stock of URM construction, have caused dramatic losses to URM heritage and have underscored the vulnerability of these structures to seismic action (see Amatrice Earthquake 2016, Nepal 2015, L'Aquila 2012, Christchurch N.Z. 2011, Kroatia 2020, etc.).

Due to the complexity of the material behavior under mechanical loads, and the uncertainties inherent to modelling the structural system of a masonry building there are limited options in the current state of the art (software-wise) to assess the performance limit state and to quantify with confidence the capacity to resist the seismic hazard of the region. The current focus of the industry is to utilize modelling techniques to define a procedure which could be as general as needed to allow assessment of the multitude of URM structural types and materials considered. This work is the focus of the project at hand.

1.1 Knowledge Gaps

This research study explores a critical knowledge gap in the field of seismic assessment of URM structures – the uncertainty regarding the dynamic nonlinear behaviour of URM structures during a seismic event. This unpredictability is owing to (a) the spatial distribution of the mass and stiffness, and (b) frequent lack of diaphragm action at the floor levels and roof. Both of these aspects characterize heritage masonry structures and differentiate their behaviour from that of

modern reinforced concrete buildings. Lack of diaphragm action means that the walls of the structure move independently without indeterminacy and paths for load redistribution (Pantazopoulou, 2013). A significant part of the mass is distributed height wise in the masonry walls rather than in the floor and roof levels, which render the un-tied masonry walls vulnerable to out of plane action owing to the large lateral inertia forces they develop due to their large mass, whereas their resistance to out of plane flexural action is negligible, being only supported by the precompression affected by the overbearing vertical loads since there is no reinforcement available (Pantazopoulou, 2013). Due to the complexity of the behaviour of URM structures owing to the strong material nonlinearity, and the uncertainties which arise when attempting to model a URM structure numerically, there is a shortage of methods which can be used to assess the seismic response of these structures. Masonry walls are continuous shells – with nonlinearity in behavior both under in-plane and out-of-plane action. The complexity of this constitutive behavior of the material renders convergence under reversed cyclic loading a very difficult task; only few monotonic nonlinear simulations have been published in the literature so far when considering this detailed representation. Thus, the objective of the present study was to explore this gap in knowledge. In order to do so, the study prioritized developing and proof-testing a detailed procedure which can be used to model a URM structure. An essential step is calibration of the developed procedures with test evidence and acceptance criteria from some of the prevalent governing assessment codes. This procedure and the overall findings of the research program provide the basis for the future development of Canadian provisions for assessment of URM construction with particular emphasis on heritage and historical structures in some of the older parts of the Canadian cities.

1.2 Summary of Methodology

The research involved a detailed numerical investigation of a URM building model tested on a shake table as well as an array of simulated URM wallettes, using various modelling tools. The first stage of the numerical campaign was an investigation conducted on a scaled URM structural model which was part of a European multi-Institutional experimental program (NIKER project see (Karatzetzu et al., 2014, Karapitta et al., 2012, Vintzileou et al., 2015, Adami et al., 2012)). A series of computer models have been developed using SAP2000 where different properties and connectivity details of the structural system were analyzed while assessing the

model under a 90% scaled version of the 1986 Kalamata earthquake which occurred in South Peloponnese, Greece (Laube, 1987). The stages of this work involved developing the interfacial contact models of the URM structure (timber to masonry connections) using properly calibrated spring and gap-elements, to account for the compliance between the floor system and the walls which is characteristic of the URM structure.

In light of this need for effective stiffness estimates that would be appropriate for lateral load analysis, a parametric study was conducted to model a series of simple masonry wallettes using a nonlinear finite element platform (ATENA 3D v5). The objective of this study was to assess the contribution of strength from the masonry bricks and the mortar which would help determine an effective modulus of elasticity and failure criteria that can be used for lateral load analysis of URM structures such as the NIKER model. Over 100 model variants were created based on three unique brick arrangements. These arrangements are, symmetrically stacked (SYM), equally staggered like what is seen in modern industrial brick construction (EQS), a random arrangement of stone blocks (RAN), and a historically inspired stone arrangement (STONE). The stone arrangement utilizes no systematic geometry when deciding the size and placement of each brick and is meant to be a representation of what is commonly seen in historic URM structures. In addition to the arrangement, the effects of changing the thickness and strength of the mortar joints were also investigated. The SYM, RAN and EQS arrangements were built into three unique models where the thickness of the mortar joints was a study variable. These combinations of arrangements and joint thicknesses created a total of 10 unique geometric designs which have been tested under various loading combinations. Thus, each model was studied under direct compression as well as to increasing lateral pushover loads, in order to determine what effects the magnitude of overbearing compressive stress has on the lateral resistance of the specimen. The goal of this extensive study was first to define a methodology for nonlinear modelling of masonry, and to compute crucial properties such as the effective modulus of elasticity and strength and failure of masonry when considered as a composite material. The effective modulus of elasticity, compressive and composite shear strength and associated deformation capacities have been compared to the estimates of empirical equations provided by various codes such as the Eurocode 8-III (2005) and the ASCE-SEI 41 (2017) Codes for computing the acceptance criteria for masonry. An additional goal of this study was to define which parameters in the design and construction of a masonry specimen such as the ratio of mortar to bricks and the ratio of the

respective mechanical properties as well as the overall arrangement of the brick layout have the greatest impact on the overall performance.

In developing this first stage of the analytical study it became quickly evident that it was practically impossible to capture the measured dynamic properties of the buildings without significantly modifying the mechanical properties of masonry from the reported values that were based on conventional material tests. The reason for that is that different mechanisms of resistance (friction along bed joints and diagonal tension cracking of the weak mortar joints) control the lateral behaviour than those characterized by the masonry compressive strength that is measured from standard compression testing. Thus it was found that alternative, calibrated estimates for stiffness and lateral strength would be needed, having probably significantly lower values than those obtained from Code expressions.

The last part of the numerical investigation aimed to proof test the calibrated relations derived from the parametric investigation, through matching of the dynamic characteristics of the NIKER structure with the reported experimental results. An added objective was to proof-test a practical methodology for seismic assessment of structures that lack a strong diaphragm action, by conducting a gravitational analysis whereby the gravitational field is acting in the direction of the earthquake (here assumed to be the principal axes of the building plan); obtained concentrations of deformation demand which identify the area of damage in the buildings are correlated with measured lateral deformation profiles. Important conclusions regarding the applicability of the approach in the practical analysis software used (SAP 2000) were extracted, as part of the feedback for the development of pertinent seismic assessment procedures for masonry structures in Canada.

1.3 Organization of the Thesis

The research program discussed aids in fulfilling a severe need of methodologies and knowledge surrounding URM assessment. URM structures make up a large portion of the housing stock in many European countries and in Canada. For example, in Italy approximately 62.2% of the housing stock are URM structures (Crespi et al., 2019). In Canada, practically all brick construction, whether veneer or massive, was unreinforced up until the sixties. This risk in Canada is only reduced by the low seismicity of many of its urban centers, but the inherent vulnerability of this form of construction is also prevalent in regions of higher seismicity such as Montreal and Vancouver.

1.3.1 Chapter 1

Chapter 1 provides an overview of this research. It goes into details on the motivations behind conducting the work discussing the many complexities and uncertainties regarding URM structures causing the knowledge gaps this work is intended to fill. The chapter also provides a summary of the methodology followed to complete the research work. It goes into details on the various numerical analyses conducted and the reasoning and outcomes behind each of them.

1.3.2 Chapter 2

In Chapter 2, a detailed state of the art and literature review is presented. In this review, details regarding the mechanical behaviour of masonry and URM structures are discussed, specifically the implications of flexible diaphragms. The review also presents details regarding available numerical modelling techniques such as finite element modelling and elastic finite element modelling using software such as SAP 2000.

The second half of the review presents a collection of literature on past experiments conducted on physical specimens as well as modelling techniques which could be used to model those specimens. Collecting physical specimens was the main priority of this review as they were needed to form a database of baseline data which could be referred to. By collecting a series of well documented projects, an abundance of data exists which can be used to calibrate any tested modelling techniques.

1.3.3 Chapter 3

In Chapter 3, the preliminary models of the elastic finite element modelling done on the NIKER project in SAP 2000 is presented. The chapter discusses the various aspects pertaining to the models such as the mechanical material properties, the model elements, and the additional mass. The purpose of the work is to understand how to model the specimen correctly so that the dynamic properties of the structure correlate with the referenced physical results.

The chapter then discusses details regarding three preliminary models that incorporate different methods for representing the floor systems. The purpose of the models was to determine the optimal way to model the floor systems and determine if additional modifications are needed to achieve the desired dynamic properties.

1.3.4 Chapter 4

Chapter 4 presents the preliminary details regarding the series of finite element models of masonry wallettes created. The chapter focuses the aspects involved with creating the models such as the macro-elements, material properties, boundary conditions, and loading conditions. The outlines and details regarding the compression and pushover tests are discussed at the end of the chapter.

1.3.5 Chapter 5

This chapter focuses primarily on the results of the compression tests run on the collection of finite element models of masonry wallettes. The chapter presents the results from each of the four wallette designs and draws conclusions on the failure states and resultant compressive strengths from the specimens and determines the optimal specimen design and conditions.

1.3.6 Chapter 6

Chapter 6 focuses on the results of the pushover tests run on the collection of finite element models of masonry wallettes. The chapter presents the results from each of the four wallette designs and draws conclusions on the failure states and resultant shear strengths from the specimens and determines the optimal specimen design and conditions. The chapter also discusses the comparison of effective modulus of elasticity attained through modelling the slope of the elastic portion of the pushover results in SAP with the values provided an empirical equation.

1.3.7 Chapter 7

In Chapter 7, a detailed investigation on the implications of varying the strengths of masonry bricks and mortar is presented. In the chapter a total of five strength combinations are considered for each of the masonry wallettes which are then tested under compression. The resultant compressive strengths and modulus of elasticity values are then compared with the values provided by a variety of empirical equations.

1.3.8 Chapter 8

Chapter 8 presents the final stage of the modelling done on the NIKER specimen in SAP 2000. In this chapter modifications are discussed which were done following the results of the

wallette modelling. Then, a series of linear and non-linear analyses that were conducted and are presented and the results and conclusions are discussed.

1.3.9 Conclusion

The final chapter of this thesis is a conclusion which discusses a summary of the findings following all of the numerical analyses conducted. In addition, the chapter discusses next steps in the research topic which can be explored following the conclusion of this research work.

Chapter 2

State of the Art & Literature Review

2.0 Background of Unreinforced Masonry Structures

During the past two centuries, societies around the globe have been faced with a steep task of supplying housing and facilities for a rapidly increasing population. Structures were constructed using readily available materials and construction methods drawn from past experiences tracing a continuous evolution from antiquity, where unreinforced masonry has been the principal method of choice (Karantoni et al., 2016). Depending on the availability of material, the practices of the masons and the disposable budget, older unreinforced masonry structures may comprise stone, fired brick, or adobe; the usual mode of construction consisted of massive vertical walls with thickness decreasing in the upper floors; masonry structures of that period seldom exceeded four to five floors, having vaulted basements or lower floors and timber floors and roof in the upper stories. The vast majority of residential masonry buildings, however, were mostly one or two floors, comprising timber floor and roof diaphragms (see Figure 2-1) (Karantoni et al., 2016).



Figure 2-1: [A] *The First Toronto Post Office* (Simon Pulfiser, 2005), [B] *Beardmore Building* (Bob Krawczyk, n.d.)

Unreinforced Masonry was displaced by concrete in the early and mid 20th century however many structures still exist from these former times; several of this contrast the modern architecture of bold steel and glass high-rises and are considered a part of the ambiance and defining the identity of the urban center where they belong (see Figure 2-2) (Karantoni et al., 2016).



Figure 2-2: University College, University of Toronto (Jon Bilous, n.d.)

Monumental URM structures that are still in use today, are now defined as heritage structures and are protected by international treaties for heritage preservation (e.g., World Heritage Convention, UNESCO, Paris 1972). There are several aspects to a structure that could classify it as heritage. This includes the original materials or decorations within a structure, or the architectural design, the methods of construction used to build it which are considered historic in the present-day era, the uniqueness and importance of the building, its relationship to milestone historical events of the nation or society or township, as well as its past use (Pantazopoulou, 2013). In the present, heritage structures make up a large portion of the built environment in some core urban areas of the oldest Canadian cities (Montreal, Quebec, Ottawa, Toronto) and it is widely prevalent in several parts of the US (e.g., Boston) and Europe (throughout). Not every URM structure is a heritage structure, however, most heritage structures constructed prior to the 1950's are URM structures. In Canada, recent editions of the National Building Code of Canada (NBCC) have banned load bearing unreinforced masonry from being used in areas where the peak ground acceleration exceeds 0.08g (Bruneau, 1994). This means that no new URM structures can be constructed in the majority of Canada, except in the case of non-load bearing components such as veneers and infills. However, the existing URM structures that survive from the past serve as an important evidence of past technological evolutions of humankind and testify the cultural developments within our societies. Today, several restrictions and guidelines are in place surrounding restoration and retrofitting of heritage structures, with the purpose of preserving the

heritage information (materials, methods of construction, aesthetics, architectural synthesis), and the ambiance of the structures and the communities where they exist. Under these restrictions no irreversible alterations can be made to any aspects of a structure which are now considered heritage (UN Educational, 1977). Unfortunately, heritage structures have suffered damage over their lifespan caused by ageing, exposure to the natural elements and disasters. It has now become a priority of many communities around the world to preserve heritage structures so they can be in use and an important preserved testimony of our past for generations to come.

The primary makeup of the heritage structures involves a combination of masonry and either iron or timber; iron was used in important edifices after the first industrial revolution and many of the Canadian state or finance buildings constructed in the mid-1800's were built in this manner (Pardalopoulos & Pantazopoulou, 2017). On the contrary, most residential URM buildings were constructed using timber in the role of lacing, framing, as well as in the function of flexible diaphragms at roofs and floors (Karantoni et al., 2016). Stone masonry was either rubble (undressed) or Ashlar (dressed); the former was used in low-cost housing whereas the latter in important construction (e.g., the Parliament Building comprises the latter type of masonry); fired clay bricks were used where industrial brick production was possible and it abounds from ancient times (e.g., Pompeii, Italy) till today (see Figure 2-3) (Pardalopoulos et al., 2019).

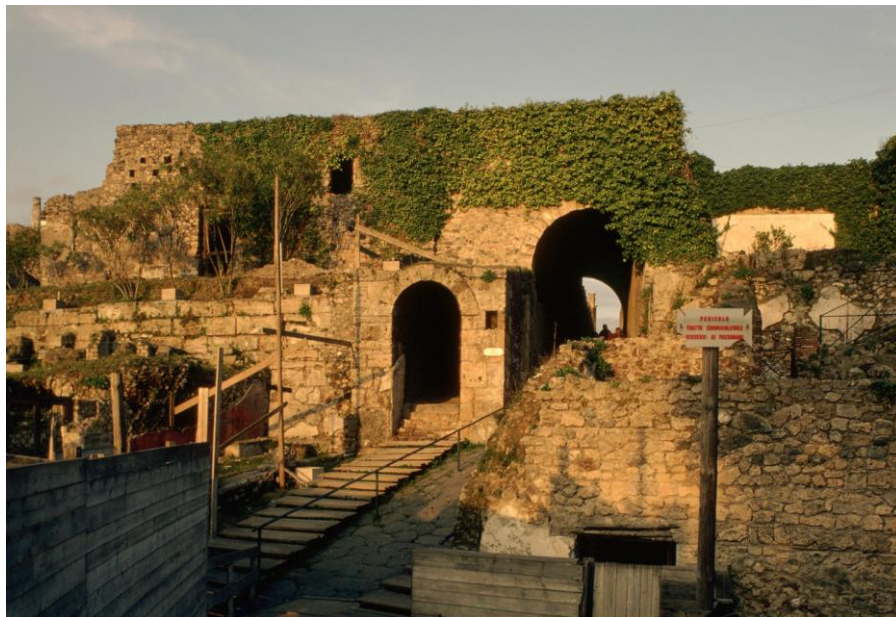


Figure 2-3: City of Pompeii (Alec & Marlene Hartill, n.d.)

Masonry may generally be classified as a composite material formed by laying masonry blocks or units (stone, clay or other materials) with mortar which serves as a binding agent.

Masonry as a composite exhibits an extremely complex mechanical behavior under stress and it is challenging to analyze with classical continuum mechanics due to its variability in quality and strength which varies greatly from structure to structure and also throughout generations, making masonry's capacity and performance a difficult task to estimate (Lourenco, 2015).

The present research study focuses on the seismic response of heritage type unreinforced masonry (URM) construction, i.e., construction that is characterized by flexible diaphragms. It is well known based on reconnaissance studies that URM structures are extremely vulnerable to earthquake events due to their structural behavior leading to severe damage and collapse caused by several characteristic failure sources. The main source of problems in URM construction which has drawn concern in research and past investigations is the absence of any kinematic restraint on the lateral displacement of the vertical components of the structural system which would, in usual frames, be affected by stiff diaphragms. Diaphragms mainly provided by the planar action of floors and roofing systems connect the surrounding load bearing masonry walls and force them to attract and therefore resist a share of the lateral load according with their translational stiffness (Hendry et al., 2004). In modern structures they are also the main source of mass mobilized by inertia forces, which has important effects on the share of total mass participating in each mode of vibration, with the first translational modes engaging more than 70% of the total mass; in turn, this simplifies their analysis by allowing consideration of only few modes in estimating their dynamic response. With flexible diaphragms, the larger part of the structural mass is distributed spatially throughout the walls, whereas the induced inertia forces are also spatially distributed rather than lumped and the contribution of the floor or roofing systems is relatively low (Pantazopoulou, 2013). The lack of rigid diaphragms is caused by the use of thin and flexible timber planks for flooring and roofing supported on on-directional timber girders that are partially fixed in the ends through embedment in the perimeter walls. Furthermore, in parts of the Mediterranean floor to wall ties were often neglected completely during construction leading to flexible diaphragms throughout the building stock (Tomazevic, 1999). Without restraint effected by the floor diaphragms the structural interlocking the walls is vulnerable, with the walls detaching at the corners and deflect in out of plane action under the effect of inertia pressures that during seismic events can lead to severe damage and total failure (Vlachakis et al., 2020).

Primary modes of failure involve in-plane and out-of-plane response depending on the orientation of the wall relative to the lateral load action. These can be mitigated by stiffening the

horizontal diaphragms and by improving their anchorage to the vertical walls. Therefore, when attempting to retrofit a URM structure the first evaluation criterion is the state of the diaphragms (Bruneau, 1994). If insufficient interlocking exists and the walls are likely to detach from each other during an earthquake, then improving the rigidity of the diaphragms becomes the priority.

Overall, the behaviour and performance of masonry as a material is difficult to quantify due to the variability in performance caused by several factors. This includes the variability in the material quality based on the chosen bricks and mortar, the unpredictable load paths due to the shapes of the materials and their placement within the masonry walls, and natural degradation owing to aggressive deteriorating mechanisms during the material's useful life (e.g. freeze thaw cycles, salt crystallization, joint mortar crumbling and delamination). Typically, the mortar used in historic construction is weaker and does not meet the required strength of modern codes (Reitherman & Perry, 2009). The complexities of masonry as a material and as load bearing elements in URM structures render the analytical modelling and assessment a challenging task. Difficulties are found when making assumptions about the connectivity of the components, their structural function, and in terms of assigning properties to reproduce the constitutive behavior of masonry. After exploring through various sources of literature regarding the overall behaviour of unreinforced masonry, the main finding was that field is marked by a great degree of empiricism and uncertainty. For this reason, this work was focused on the representation and study of the composite behaviour of masonry under stress representing seismic response and on how to implement and properly model these aspects of the response in URM structural analysis for lateral loads simulating ground excitation.

2.1 Modelling Techniques

Due to the complexity of URM structures, developing and testing modelling techniques which can be used to assess the vulnerability of a URM structure has been a priority of the scientific community in seismic assessment of masonry (See, Tomazevic, 1999, Lagomarsino et al., 2013, Mendes & Lourenco, 2010). Several tools are currently available which are very effective for reinforced concrete (RC) and steel structures. Unfortunately, these tools are not easily extendable to URM on account of important simplifying idealizations that users take for granted in RC and are not obvious in URM girders that are partially fixed in the ends through embedment in the perimeter walls. For example, the typical beam/column element which is the staple of

nonlinear structural modeling of RC frames must be endowed with Moment-Rotation Response backbone curves that have been based on extensive experimentation and analysis of RC beams and columns (Lagomarsino et al., 2013). There is no such well established literature for RM and even more so for URM where there is no reinforcement to enable ductility in the post-elastic response. This reduces the versatility of these programs in modeling URM structures in the nonlinear range. This portion of the state of the art will explore various tools being used in the industry today to assess URM structures and will comment on the effectiveness and limitations of each.

2.1.1 Equivalent Frame Analysis

Equivalent frame analysis is a simplified approach in which the masonry walls are idealized into two main types of elements which are defined as piers and spandrels, both of which are modelled using beam/column elements (see for example, Eurocode 8-III (2022 draft version) and ASCE/SEI 41 (2017)). The ease in borrowing software originally developed for RC frames and using in it to model masonry structures has made this approach very popular among practitioners. One example of a dedicated software that transfers the frame analysis technology from RC to masonry buildings is the program TREMURI which was developed at the University of Genoa (Lagomarsino et al., 2013). TREMURI idealizes the masonry walls as deformable elements where the damage in the structure is likely to occur. The vertical portions of the walls which are parallel to vertical openings are defined as piers, while the horizontal portions are defined as spandrels. The piers and spandrels are connected using rigid zones which are areas within the structure which do not typically suffer damage during an earthquake (Lagomarsino et al., 2013). An overview of how a structure is idealized using the equivalent frame method are shown in Figure 2-4 below.

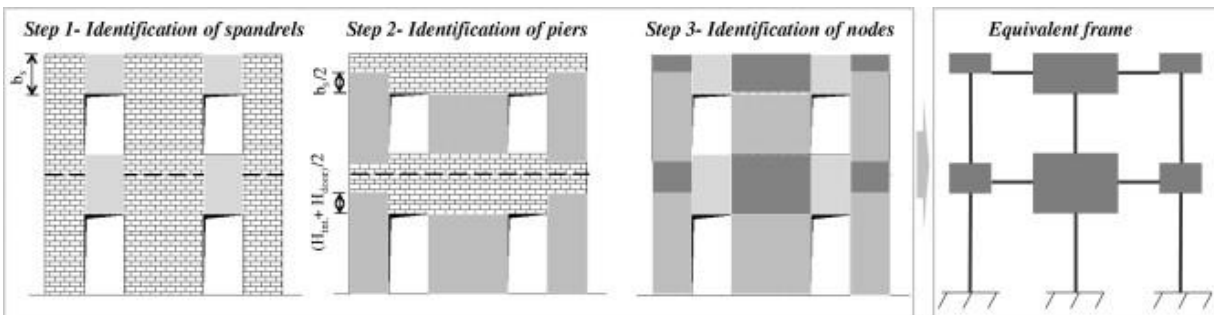


Figure 2-4: Idealization of a masonry structure using the equivalent frame method (Lagomarsino et al., 2013)

The TREMURI software uses the equivalent frame and idealizes it as one of two cases and is up to the engineer to decide. The first case is SSWP which assumes that the piers will fail prior to the spandrels. The other is WSSP which assumes that the spandrels have negligible strength and stiffness meaning that the main source of strength comes from the strong piers (Lagomarsino et al., 2013). Currently in design codes such as the Italian Building Code the WSSP idealization is recommended and is the most simplified method of analysis, however, the SSWP idealization is prohibited for multi-story masonry structures (Lagomarsino et al., 2013).

TREMURI provides a simplified approach for in-plane analyses however, one main limitation exists. The limitation is that the software models the piers and spandrels as 2D elements and therefore no out-of-plane degrees of freedom exist throughout the length of the elements (Lagomarsino et al., 2013). This makes the software unable to assess out-of-plane failure mechanisms. The out-of-plane response is neglected in the software since the in-plane behaviour governs the performance of a URM structure (Simões et al., 2013). Overall, TREMURI and the equivalent frame method is a useful and simplified method which should be considered when tasked with computing the in-plane response of a URM building under an earthquake, and therefore the underlying assumption is that the building contains stiff diaphragms to secure the walls against out of plane independent action spanning several floors.

2.1.2 Finite Element Analysis

Finite element modelling (FEM) can be used as an effective tool to model masonry and analyze its mechanical behaviour. When using an appropriate FEM software such as ATENA 3D which was primarily used throughout this thesis, the first step is to decide how the masonry material will be defined. Since masonry is a composite material made of bricks and mortar, that means both materials must be either directly modelled as a homogeneous medium or explicitly accounted for. The two main approaches available are defined as micro-models or macro-models (Giordano et al., 2002). In the micro-model models the geometry of both the masonry units and the mortar joints are described in detail using solid finite elements, where a separate constitutive model is considered for each material (explicit modeling). In the macro-model the material is treated as homogenous and is equipped with a constitutive model which accounts for composite mechanical properties accounting implicitly for the contribution of masonry units and mortar joints (Giordano et al., 2002). The main drawback of the micro-model approach is that the computational

power needed rapidly increases as the size of the model increases on account of the increase in the number of joints, contact surfaces and discretized elements (Giordano et al., 2002). Therefore, the micro-model should only be used when doing small scale analyses such as a wallette study in order to comprehend the response and extract from it homogenized composite properties that would be subsequently used to model complete structural systems. In this thesis micro-modelling was done on a series of masonry wallettes and FEM modelling served as a valuable tool to analyze the mechanical behaviour of masonry.

2.1.3 Discrete Element Modelling

Discrete element modelling (DEM) is a numerical method which is similar to the explicit FEM model. The main difference is that the elements modelled are blocks which can be defined as either rigid or deformable. The blocks interact with each other using elasto-plastic contacts to develop forces along the contacts (Giordano et al., 2002). Once a contact is broken, the respective blocks are free to form new contacts with different blocks, and this allows the analyses to reproduce in a detailed manner the failure mechanisms. The main limitation from this type of analysis is that the performance of the analysis is reduced when deformable blocks are considered (Giordano et al., 2002). Overall, this analysis method provides some advantages as it can reproduce the dynamic characteristics of the failure process, however, a main limitation does exist. Typically deformable blocks perform poorly, therefore DEM modelling is not accurate analyzing stress states (Giordano et al., 2002). Therefore, the limitation should be considered when choosing the appropriate method to model a structure or specimen.

2.1.4 Shell Type Finite Element Analysis

This approach utilizes common and simplistic software available in the industry such as SAP2000 (CSi Inc. 2021), which considers homogenized, nonlinear material properties without distinguishing for masonry unit or mortar joint. Using this approach, three-dimensional models of a structure can be created which can be tested in-plane and out-of-plane under a variety of loading conditions. These models can be used to compute approximate load paths and anticipated damage within a structure, and can also be used to assess the effectiveness of retrofitting techniques (Pantazopoulou, 2013). This form of analysis was crucial throughout this thesis and will be revisited in later chapters.

2.2 Physical Test Models

As this thesis is prioritized around numerical modelling and assessment of URM structures, the main objective of this state of the art and literature review was to gain insights regarding the response that would be reproduced numerically, by reviewing reported observation of the behavior of URM structures, preferably obtained under well controlled, traceable conditions of loading. To this end, relevant laboratory experiments conducted on URM structures and reported in detail were reviewed, with particular emphasis to tests carried out under dynamic excitation on shake tables. Through this collection, it was the objective to test and calibrate the proposed modelling procedures of the numerical study. The following section of this review will present a series of laboratory experiments drawn from the literature. An introduction the test set-up and loading conditions will be provided before summarizing the results and conclusions of the experiment. The goal is to not only have a collection of relevant tests for benchmarking of the analytical procedures, but to also develop a thorough understanding of the observations found and the failure patterns commonly occurring in the actual dynamic response of URM structures.

2.2.1 *A full-scale shaking table test on a two-story stone masonry building* – Guido Magenes, Andrea Penna, and Alessandro Galasco, and, *Shaking Table Test of a Strengthened Full-Scale Stone Masonry Building with Flexible Diaphragms* – Magenes, G., Penna, A., Senaldi, I. E., Rota, M., and Galasco, A.

This test series was conducted at the EUCENTRE at the University of Pavia and involved a collection of 3 stone masonry structures with each having been strengthened to a different degree. The focus on the referenced reports was on the non-retrofitted structure and therefore considered a URM structure (Magenes et al., 2010). When designing the structure, the researchers were constrained by the size of the shake table, as well as the payload of the table (< 100 tons). After developing a nearly full scale model design as depicted in Figure 2-5 below, the specimen was built outside the lab before being transferred inside to be placed and tested on a shake table (Magenes et al., 2010).

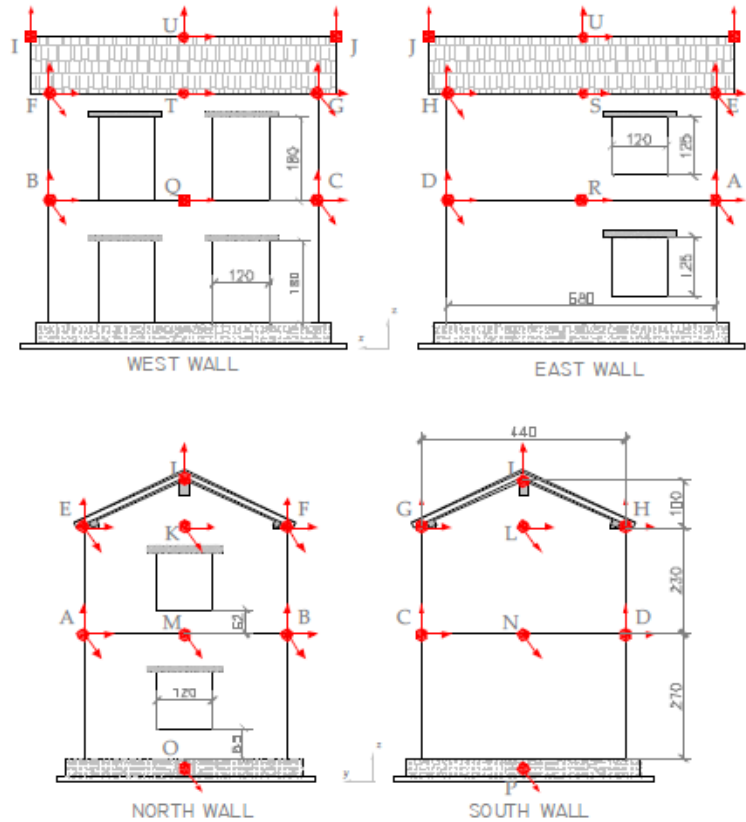


Figure 2-5: Design of constructed specimen (Magenes et al., 2010).

The specimen was constructed with double leaf masonry having a wall thickness equal to 32 cm. The leaves of masonry were joined together and filled with a combination of rubble, comprising small stones and mortar (Magenes et al., 2010). To determine the mechanical material properties of the masonry, a series of compression tests were done on small specimens which concluded that the compressive strength was 3.3 MPa having a modulus of elasticity of 2550 MPa (Magenes et al., 2010). The floor and roof systems were built from timber and were designed to form flexible diaphragms with the walls to represent the unreinforced conditions which are the reference condition in this experiment.

To prepare the specimen for analyses, an additional 3.2 tons of mass were applied throughout the floor levels to correct the scale of the specimen. In addition, the structure was fixed to the shake table using clamps to ensure no sliding occurred (Magenes et al., 2010). To analyze the specimen, the seismic data from the 1979 Montenegro earthquake was used (Magenes et al., 2010). The seismic excitations were scaled, and trials were done with different PGA (peak ground accelerations) of 0.05g, 0.10g, 0.20g, 0.30g, 0.40g (Magenes et al., 2010).

During the analyses each of the PGA values were applied in increasing order to the structure. It was found that the structure reached the near collapse performance limit at a PGA of 0.30g. Failure occurred on the top corner of the north wall which began to overturn out-of-plane, the roof supports also slid once the north wall began to translate (Magenes et al., 2010). Finally, the south wall began to overturn as it was connected to the north wall. After conducting the 0.4g test, the test was repeated with the steel rods engaged to help create rigid diaphragm conditions. It was found that the specimen was able to resist the failure mechanisms which were previously experienced, and some small microcracks which were previously opened began to close (Magenes et al., 2010).

Overall, this experiment outlined the importance of rigid diaphragms within a masonry specimen. The steel tie rods utilized were able to improve the diaphragm conditions and successfully improved the performance of the specimen. In comparison, the specimen which was strengthened could withstand an increased level of shaking which was up to 84% higher than the un-strengthened model (Magenes et al., 2014).

2.2.2 Seismic Performance of an unreinforced masonry building: An experimental investigation – Jitendra K. Bothara, Rajesh P. Dhakal, and John B. Mander

This project involved constructing a half scale unreinforced masonry structure which was inspired by what was common practice in the 20th century New Zealand. The scale was set to 1/2 scale due to space constraints within the lab. The final dimensions and design as shown in Figure 2-6 had a footprint of 2.8 m by 1.92 m and an overall height of 3.295 m which included the story heights as well as the pitched roof (Bothara et al., 2010).

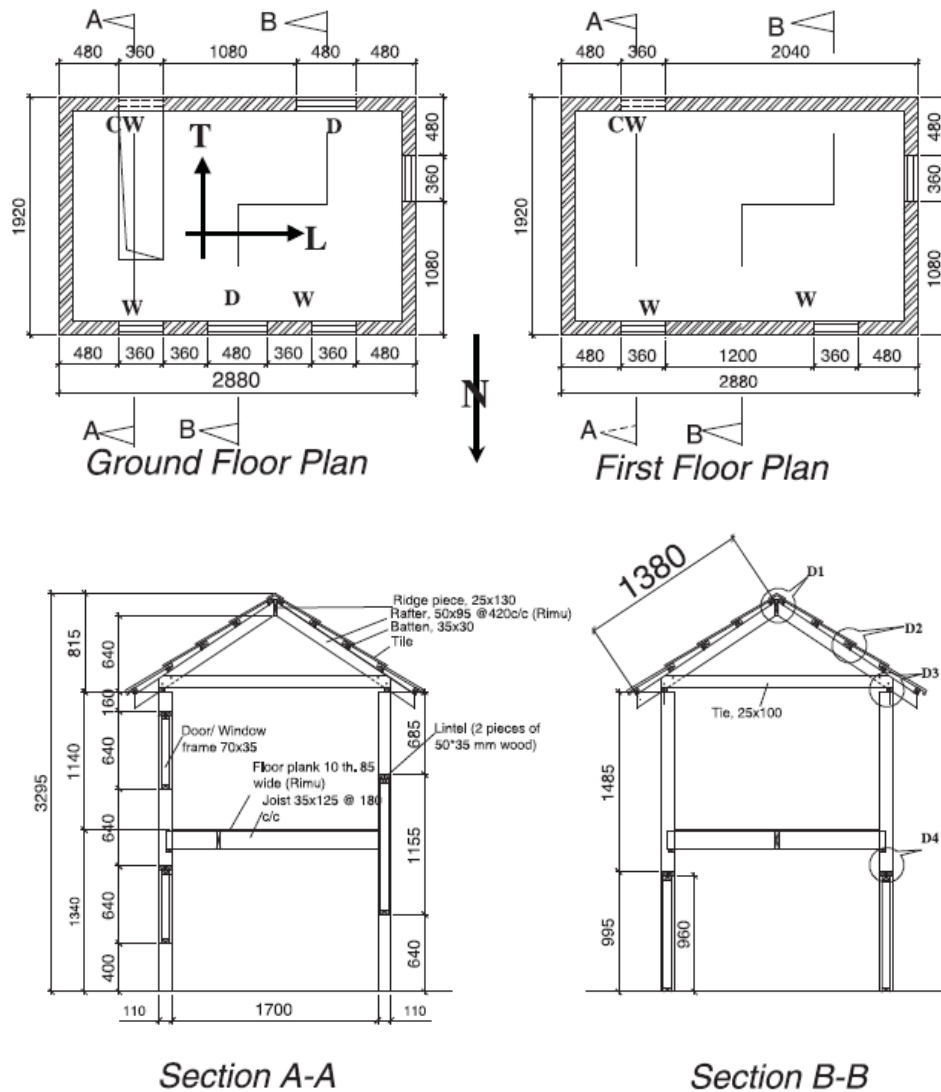


Figure 2-6: Design of physical specimen (Bothara et al., 2010).

The masonry walls were constructed of model solid clay bricks, as single leaf walls with a mortar joint thickness of 12 mm throughout. The strength properties of the masonry included the

compressive strength which was estimated experimentally as 16.2 MPa and a modulus of elasticity equal to 6100 MPa (Bothara et al., 2010). To meet the scaling requirements a total of 4.2 tons of additional mass was applied to the structure along the walls and floor levels, and an additional 2 tons was applied to the timber pitched roof. To roof was overdesigned in order to support the additional mass applied on top (Bothara et al., 2010). The physical specimen is shown in Figure 2-7 below placed on a shake table for dynamic testing.



Figure 2-7: Physical specimen on shake table (Bothara et al., 2010).

The specimen was tested under several earthquake records of increasing intensity, acting either along the longitudinal or the transverse principal axes of the plan. From the tests it was found that the damage sustained varied depending on the direction of application of the ground motion record. For walls oriented parallel to the line of action of the earthquake, (in-plane loading), damage was more likely to occur in an area that would be susceptible to higher shear stress values, like the bottom story. For walls oriented normal to the seismic action, out-of-plane bending occurred, the damage was dependent on the intensity of inertia pressure acting normal to the wall, and was more severe in areas of higher acceleration such as the top story (Bothara et al., 2010).

In addition, fragility curves were proposed which could be used to predict the level of damage which would be expected in a given region of known site characteristics and distance from

the epicenter, during an earthquake (Fig. 2-5). The three performance limit states included in the figure are identified depending on the intensity of damage starting from green which represents no damage (immediate occupancy of the structure). The second damage limit state is marked in yellow, representing moderate damage, which corresponds to a repairable damage level. The next limit state is identified by orange color, representing extensive damage – which means that the structure is damaged beyond repair but has not reached the state of collapse. The final limit state is marked in red which stands for total collapse (Bothara et al., 2010). These curves have been calibrated using expected peak ground accelerations causing allowable drift limits for each level of damage (performance criteria). These limits have been calibrated into fragility curves like the one shown in Figure 2-8 below. DBE stands for design-base earthquake, whereas MCE corresponds to the maximum credible earthquake event for a given hazard, calculated from Probabilistic Seismic Hazard assessment tools given the local seismicity of the region of interest.

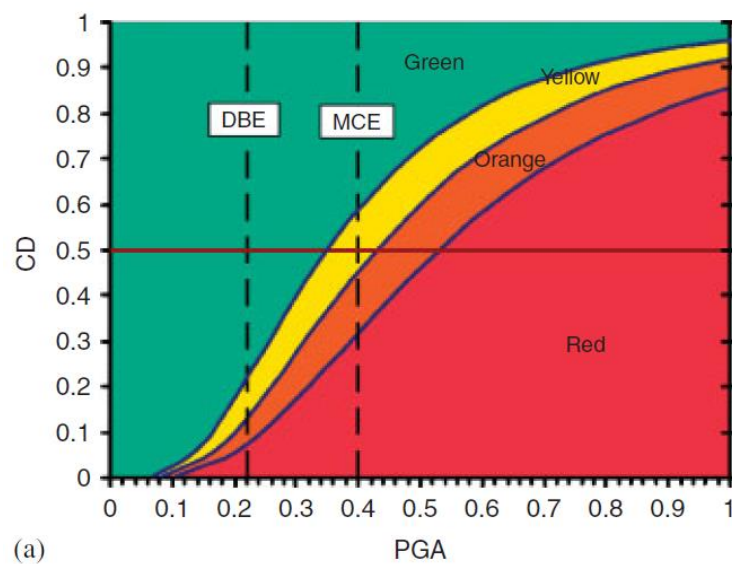


Figure 2-8: Fragility curve (Bothara et al., 2010).

Using the fragility curve above, a vertical line can be drawn at the value of expected peak ground acceleration from a design earthquake. Using that vertical line, the portions of the line which fall into each of the four states represents the percentage of the building stock which will reach each of the damage states (Bothara et al., 2010).

Overall, this project served as a demonstrative case study for performance based seismic assessment of URM buildings. The proposed fragility curves were intended to be used for rapid

assessment given the seismic hazard in a region and can also provide insights on the level of retrofit required in the area.

2.2.3 Shaking Table Tests on Two Multi-Leaf Stone Masonry Buildings – Mazzon, N., Valluzzi, M., Aoki, T., Garbin, E., De Canio, G., Ranieri, N., and Modena, C.

This project involved two stone masonry structures. The first structure was un-strengthened therefore representing unreinforced masonry conditions. The second was strengthened using a hydraulic injection consisting of a lime base (Mazzon et al., 2009). The two structures shown in Figure 2-9 had a footprint of 2.40 m by 2.8 m and had an overall height of 3.60 m (Mazzon et al., 2009).



Figure 2-9: Physical specimen tested on a shake table (Mazzon et al., 2009).

After running the various ground motions, it was found that the unreinforced model could only withstand a peak ground acceleration of 0.45g while the strengthened model could support a peak ground acceleration of 0.7g (Mazzon et al., 2009). Overall, it was found that the lime-based injection provided numerous benefits. It was found that the injection can reduce issues such as separation of masonry layers specifically in the out-of-plane direction. It was also found that the injection did not alter any of the dynamic characteristics such as the modal response (Mazzon et al., 2009). Therefore, it was concluded that lime-based injections can effectively improve the

performance of a URM structure while not causing drastic changes to its mechanics. In terms of its application on heritage URM structures, it would have to meet the defined restrictions including reversibility.

2.2.4 Shaking Table Tests on 24 Simple Masonry Buildings – Benedetti, P., Carydis, P., and Pezzoli, P.

This project was an extensive effort undertaken by the ISMES facilities in Italy and the LEE facilities in Greece. This project incorporated 24 ½ scaled masonry structures which were subjected to a total of 119 tests conducted on a shake table (Benedetti et al., 1996).

The structures designed and built in each of the two countries followed different principles. The 6 specimens build at the LEE facilities in Greece had arched window openings with the wall thickness equal to 45 cm as shown in Figure 2-10 below (Benedetti et al., 1996). The specimens were also constructed with poor quality mortar to represent the existing building stock in the area.



Figure 2-10: Stone masonry structure designed at LEE in Greece (Benedetti et al., 1996).

In Italy, the structures were constructed with poor practices to match what was common in that area, specifically poor connection of the adjoining masonry walls (Benedetti et al., 1996). The specimens also followed different design procedures then what was done in Greece. This can be observed by the lack of arches in the openings in Figure 2-11 below, but also the use of different masonry types (stone masonry in the former, vs fired clay brick in the latter).



Figure 2-11: Stone masonry specimens built at ISMES in Italy (Benedetti et al., 1996).

Throughout the shake table tests, strengthening techniques were applied to the structures to strengthen them and assess the effectiveness of the retrofitting measure. Overall, it was revealed that simple retrofit techniques such as crack sealing caused significant increases to the lateral resistance (Benedetti et al., 1996). Furthermore, the study emphasized that a major aspect involved in structural performance is the original construction quality. It was found that damaged structures which were built using high quality procedures could withstand severe earthquakes without collapse (Benedetti et al., 1996). Finally, securing the diaphragms using methods such as steel ties proved to be extremely effective at improving the performance of a URM structure as shown in the aforementioned experiments and therefore, preventing collapse (Benedetti et al., 1996).

2.2.5 Seismic Assessment of a Lab-Tested Two-Story Unreinforced Masonry Dutch House –

Esposito, R., Messali, F., Ravenshorst, G. J. P., Roel Schipper, H., and Rots, J. G.

This project involved the design and assessment of a Dutch-style house, common after the 1980s. The full-scale two-story structure was constructed under a length restraint of 5.4 m imparted by the lab capabilities as shown in Figure 2-12 below.

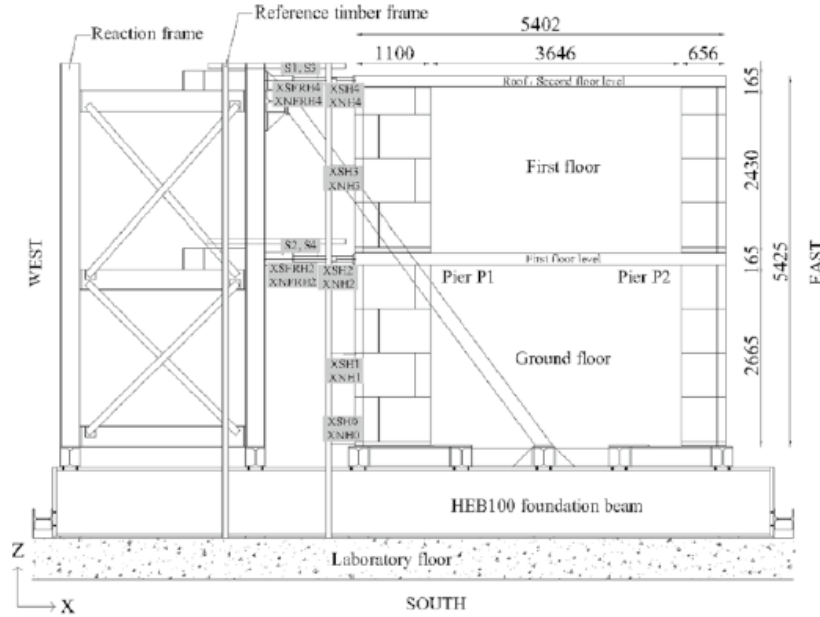


Figure 2-12: Specifications of physical specimen (Esposito et al., 2019)

To replicate the idea of large window openings, piers were used on the façades (Esposito et al., 2019). The materials utilized consisted of 100 mm and 120 mm thick masonry for the façade and transverse walls respectively. In addition, cement-based mortar was used throughout with 2 mm head joints and 3 mm bed joints. The floors were designed with an increased thickness to add weight to the structure which would be taken as additional mass (Esposito et al., 2019). Finally, steel ties were used along every bed joint at the connection of the piers to the transverse walls to reinforce the connection between the adjoining walls.

The structure was tested using a quasi-static cyclic analysis and the amplitude was increased in a step-wise scheme until collapse (Esposito et al., 2019). After the results were acquired, a numerical modelling competition was run where participants had to model the structure and analyze it without having access to the experimental results. This allowed for a collection of unique analysis methods to be tested and it was determined from the result of the competition that by applying several different modelling methods it is possible to build confidence in the validity of the numerical results (Esposito et al., 2019).

Overall, this project has offered insights regarding the capabilities of numerical modelling and the potential of producing well validated results. This is an important finding as this thesis project is aimed at analyzing this very capability.

2.2.6 NIKER Project

The NIKER project was considered as a benchmark case in the present thesis, since it was used as the baseline of the entire numerical investigation in order to test the modelling methodology. This project was conducted at the Technical University of Athens and consisted of two ½ scaled masonry specimens (Karatzetzou et al., 2014). Both specimens were two-story high, but the first specimen was unreinforced masonry whereas the other was timber laced. The specimens were built of three-leaf masonry comprising limestone and mortar in the outer wythes, and a filler material in the center. The filler was rubble consisting of small brick fragments and grout. Timber sections were used to build the floor sections which were partially fixed to the masonry walls to represent typical unreinforced masonry construction. The specimens had a footprint of 3.65 m by 2.30 m and had a height of 3.2 m as shown in Figure 2-13 below (Karapitta et al., 2012).

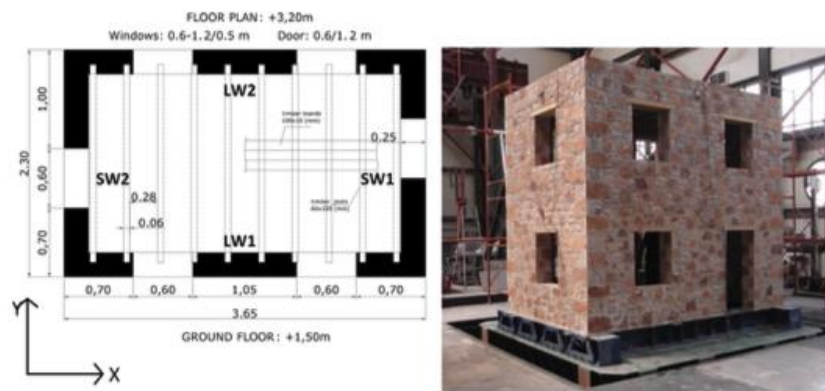


Figure 2-13: [A] Design and specifications, [B] Physical specimen (Vintzileou et al., 2015).

The specimens were tested under scaled versions of the 1986 Kalamata earthquake and the 1980 Irpina earthquake. After concluding the original tests, the URM specimen was strengthened using grout and steel tie connections to strengthen the diaphragms of the structure (Vintzileou et al., 2015). After strengthening it was concluded that the structure could support significantly increased excitations prior to failure (Adami et al., 2012). Overall, this project among others proves that the transition from flexible to rigid diaphragms causes a significant improvement to the overall performance of a URM specimen.

This project will be discussed in detail in Chapter 3 to provide information on the project and detail how it will be used during the numerical sections of this thesis.

Chapter 3

Introduction to Studied NIKER Experiment and Preliminary Modelling in SAP 2000

3.0 Introduction

The following chapter discusses the numerical model developed to represent the physical specimen analyzed during the referenced NIKER project. The numerical model was developed in SAP2000 (CSI Inc.) using the same dimensions, material properties and loading conditions as the original physical specimen. Throughout this chapter details regarding the methodology taken to develop the model will be discussed, and the results of the preliminary series of analyses conducted will be presented.

3.1 Model Dimensions

The SAP2000 model of the NIKER project was designed using the dimensions shown in Figure 3-1. The model spans 3.65 m along the X-axis and 2.30 m along the Y-axis. Furthermore, the story height was 1.6m (total model height of 3.2 m). The windows were located throughout each of the 4 walls, with dimensions of 0.6 m wide by 0.7 m tall (Vintzileou et al., 2015). Additionally, 0.6 m wide by 1.2 m tall doorway was located on one of the long sides in the lower floor. Masonry wall thickness was 0.25 m throughout the entire structure (Vintzileou et al., 2015).

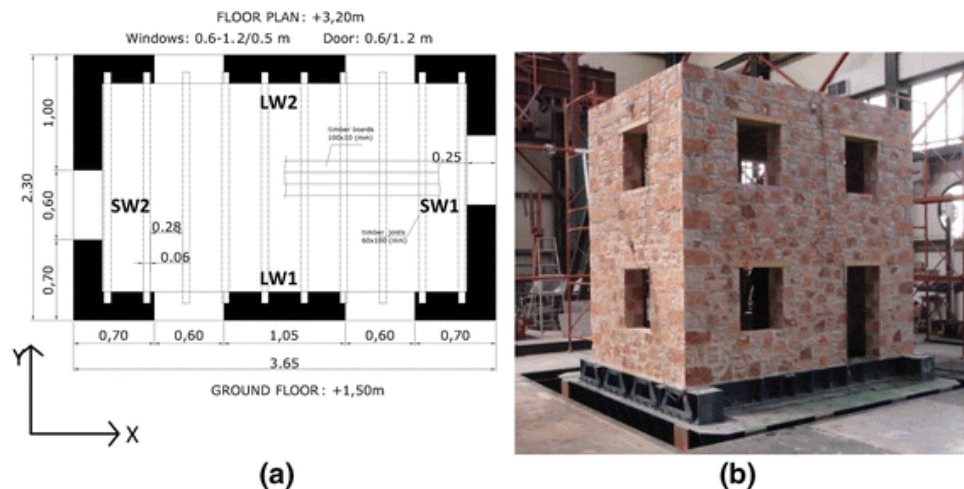


Figure 3-1: Model Dimensions and tested physical model (Vintzileou et al., 2015).

Additional elements in the structural system were, the timber floor system and roof. This comprised timber floor joists, 0.06 m wide, 0.1 m deep and spanning a total of 2.30 m along the y-axis (short plan dimension). The joists supported a system of timber floor planks, 0.1 m wide, by 0.01 m deep, covering the entire floor area, spanning 3.65 m along the X-axis (Vintzileou et al., 2015).

3.2 Material Properties

Two primary materials were used to model the NIKER specimen, i.e., homogenized composite masonry and timber. Custom materials with respective material properties were created in SAP2000 for both material types.

3.2.1 Masonry

Values for the material properties entered in the series of SAP2000 models were derived from the experimental report of the reference project, as summarized in Table 3-1 below.

Table 3-1: Chosen material properties for Masonry (Vintzileou et al., 2015).

Weight	18.63 kN/m ³
Modulus of Elasticity	840 MPa
Compressive Strength	4.33 MPa
Poisson's Ratio	0.2
Shear Modulus	350 MPa

3.2.2 Timber

Like masonry, custom material properties were used for timber to define a custom material in SAP2000. As the properties of timber can vary significantly, many of the properties were chosen in accordance with past experiments. However, the density of timber was chosen based on the properties of spruce. The property values input in the computer model for timber are listed in Table 3-2 below.

Table 3-2: Chosen material properties for Timber (Karapitta et al., 2012), (Engineering ToolBox, 2004.)

Density	4.413 kN/m ³
Modulus of Elasticity	10 GPa
Poisson's Ratio	0.3
Shear Modulus	3.85 GPa

All timber components (i.e., timber floor joists and floor planks) were modelled using the above.

3.3 Model Elements

For building the model, consideration was given to the choices of elements that could be used in the idealization. Options for the masonry walls included shells, or solid elements. However, to be able to model material nonlinearity and brittleness while maintaining the robustness of the algorithm, and enabling the out-of-plane flexural action where this occurs, shells with an applied thickness of 0.25m were used to represent the masonry walls. When defining the shell elements, two different types were considered, i.e., for linear elastic analyses thick shells were used as they account for transverse shear deformations (Computers & Structures, 2017), whereas for non-linear analyses, non-linear layered shells were used, discretized in 10 layers of equal thickness to formulate the 250 mm thick masonry walls.

Much of the difficulty encountered when selecting elements pertained to the timber floor system. To represent the planks and floor joists in monolithic connection frame elements were used, having been assigned a composite T-type of section; an alternative approach considered used a combination of frame elements for the floor joists and shells for the floor planks. After modelling both options in SAP, the combination of shells and frames was selected as the shells allowed for discretization of the floor that could provide a better representation of the distributed floor weight. However, this approach lacked in robustness causing numerical problems, and for this reason the former alternative was chosen, by combining tributary width of planks and joists in a single frame element. Overall, the model contains masonry walls on all four sides, as well as 20 joists along the Y-axis 10 of which are on each floor level as shown in Figure 3-2 below. The layout of the defined timber frame elements is shown in Figure 3-3 below.

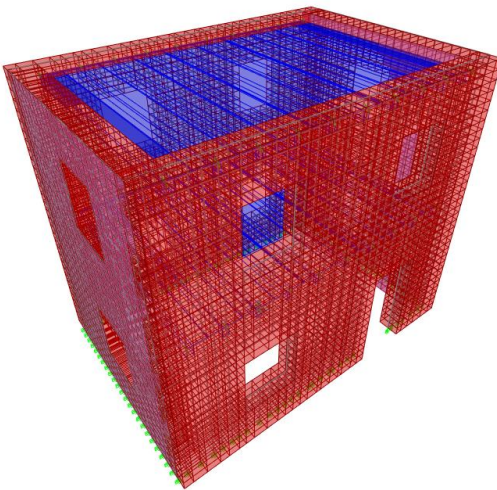


Figure 3-2: Overall Model (Extruded)



Figure 3-3: Overall Model (Extruded)

3.3.1 Finite Element Mesh

In order to improve the accuracy of the results, as well as visualize the change in deflection over the height of the structure, the finite element mesh was defined so as to avoid having distorted elements, by adhering to an aspect ratio not exceeding 2:1. In light of this, an element size of about 0.1m x 0.1m was selected with an overall thickness of 0.25m being the thickness of the walls, however, adjustments were made along the midspan and along the windows of the front and back walls to allow the floor joists to be entered at the correct locations and spacing. The selected dimension allowed the windows and doors to be inserted efficiently while ensuring that full elements surrounded each window and door opening. Overall, the chosen mesh allowed for sufficient independent elements to be created which allowed for a high degree of numerical robustness in the computed results.

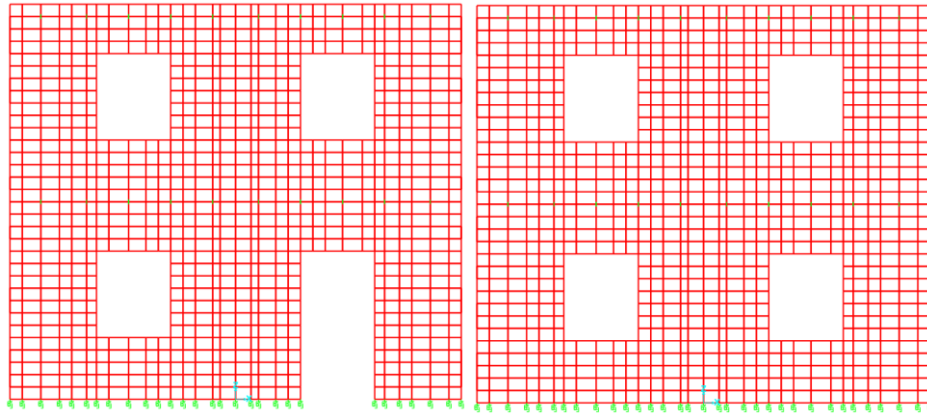


Figure 3-4: (Left) Discretized Front Wall, (Right) Discretized Back Wall

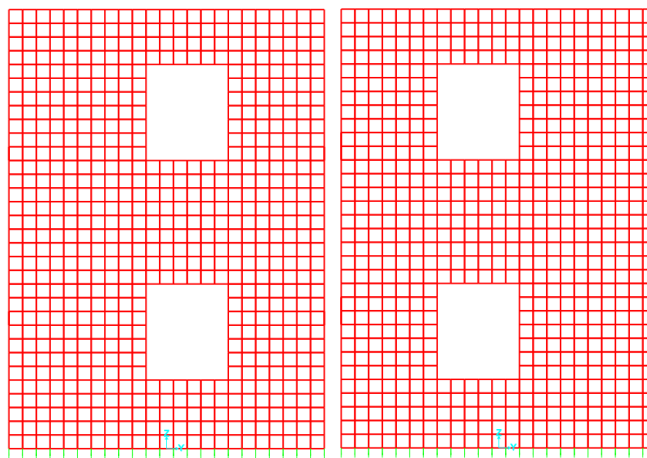


Figure 3-5: (Left) Discretized Left Wall, (Right) Discretized Right Wall

Figures 3-4 and 3-5 above present the layout of both the windows and door openings, and the wall discretization in the plane of their action.

3.3.2 Floor to Wall Spring Connections

Spring connections were used to model the relatively compliant anchorage of timber joists into the masonry walls. Preliminary modelling using direct connection between the floor joists and walls, led to increased in-plane stiffness of the diaphragms. Springs were designed to fix the connection between the frames and walls in all directions except axially. By allowing axial freedom, relative slip is enabled between joists and masonry: note that this behavior is actually non symmetrical: a timber joist that pushes in the wall encounters greater resistance from the exterior wythe of the wall, than when pulling away from the wall where the only mechanism of force transfer is bond along the contact surface between timber and the surrounding masonry. . Details on how this connection was designed and implemented are given below.

The spring connection was designed in a separate SAP 2000 model of a single timber joists to ensure that the parameters could be selected and implemented with reference to the anchorage conditions. The ends of the joist are connected to the end supports by interpolation linear two-jointed links as depicted in Figure 3-6 below.

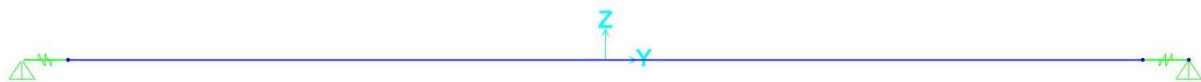


Figure 3-6: Spring SAP2000 Model – idealization of a typical timber joist

Each link has 6 degrees of freedom at each end, translations along the X, Y and Z axes and rotations along each of the respective axes. Of those all degrees of freedom were fixed to, except for the axial translation, U1. Instead, a finite stiffness value was associated with the link stiffness along U1.

To enforce a true spring behaviour, a translational stiffness was calculated using an anchorage model for the embedment length of 180mm, as depicted in Figure 3-7, where the joist force F is transferred by longitudinal bond stresses developing on the contact perimeter: The total stiffness applied to degree of freedom U1 was computed as $k_{\text{pull}} = 6.0 \times 10^5 \text{ kN/m}$ as shown below:

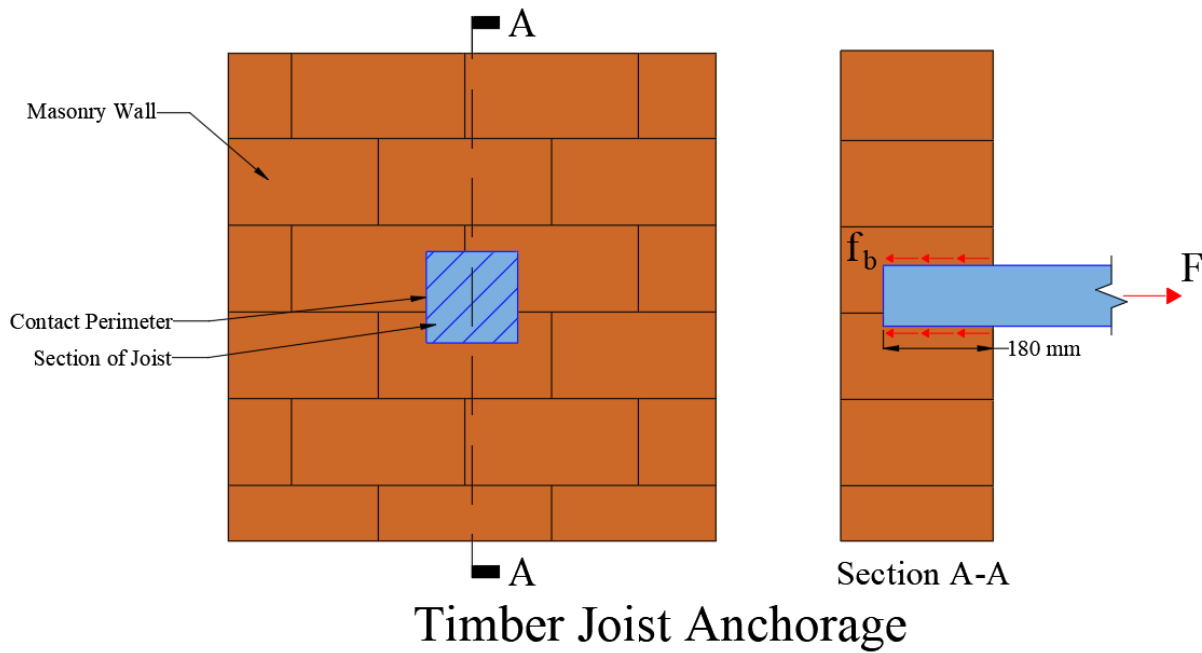


Figure 3-7: Timber joist anchorage.

$$f_b = 0.5 \text{ MPa}$$

$$F = f_b \times P = (0.5 \text{ MPa}) \times (180 \text{ mm}) \times ((2 \times 100 \text{ mm}) + (2 \times 60 \text{ mm})) = 28 \text{ kN},$$

where P is the perimeter of the joist cross section

$$f_w = (28,000 \text{ N}) / (100 \text{ mm} \times 60 \text{ mm}) = 4.67 \text{ MPa} \text{ is the axial timber stress}$$

$$\epsilon = (4.67 \text{ MPa}) / (10,000 \text{ MPa}) = 0.000467 \text{ is the axial strain of the joist}$$

$$\Delta = (0.000467) \times (180 \text{ mm} / 2) = 0.04203 \text{ mm is the elongation (slip) over the anchorage length}$$

$$k_{\text{pull}} = (28,000 \text{ N}) / (4.2 \times 10^{-5} \text{ m}) = \mathbf{6.0 \times 10^5 \text{ kN/m (pullout stiffness)}}$$

With the spring fully designed, it was then applied to all the joists of the structure. Joints were created at a 0.01 m offset from each joint on the wall where a link was to be located. Frame elements were drawn connecting each set of arbitrary points and the properties of the links were specified using the boundary conditions and stiffness coefficient as described above.

3.3.3 Additional Mass

The final component required to prepare the model of the structure was representing lumped and distributed mass. It is noted that during the tests, additional masses were placed at the levels of the timber diaphragms to compensate for the non-proportional reduction of the mass with

scaling of the size of the structure. During the shake table test, the studied specimen was scaled down to a ratio of 1:2 to allow the specimen to fit the capabilities of the test facility. For scaling of length units in half, i.e., $SF=1/2$, it is noted that volume and therefore the weight (which is a force) of the structure is reduced by a factor of SF^3 . But for constant mass density and material strength, forces are supposed to be scaled down by a factor SF^2 in order to cause stress magnitudes that are comparable to the full model. It is therefore evident that external weights need to be added to compensate for the lack of the self-weight of the model. Therefore, to ensure that both the mass and dimensions are scaled to a ratio of 1:2, a total of 7.5 tons were applied to the model. The lower level received a total of 4.5 tons, whereas the upper level received 3 tons (Karapitta, Mouzakis, Adami, & Vintzileou, 2012). These masses were placed on the floor diaphragms bearing on the joists; in the model, forces were transferred to the supports of the joists, and applied as joint forces to the nodes on the masonry walls. The total joint forces were computed as a function of the tributary area of each frame. Therefore, the total mass was divided over the entire area of the floor and applied proportionally to each end of the timber floor joists on the masonry walls. The applied joint forces were equal for Models 1 and 2, however, for Model 3 the forces were increased to account for the absent timber elements. The summary of the applied joint forces can be found in Table 3-3 below.

Table 3-3: Summary of applied joint forces

Frame Element	Joint Force (kN) (Per End)			
	Models 1 & 2		Model 3	
	Top Floor	Bottom Floor	Top Floor	Bottom Floor
Edge (Left)	0.550	0.825	0.591	0.866
Edge (Right)	0.550	0.825	0.591	0.866
Intermediate	1.700	2.55	1.745	2.595
Center	1.850	2.775	1.896	2.821
Total	30	45	30.883	45.883

Joint forces were entered as negative numbers (pointing in the negative direction of the Z axis). In total 30.0 kN was applied to the top floor, and 45.0 kN was applied to the bottom floor for a total of 75.0 kN. In Model 3 additional forces were applied to account for the weight of the timber floors which were removed. The added loads along with the self-weight of the structure equaled a total weight of 229.262 kN.

3.4 Applied Earthquake

An appropriate earthquake was selected to represent a scenario relevant for areas with a high density of unreinforced masonry structures such as Italy and Greece. The selected earthquake was the 1986 Kalamata earthquake (Mouzakis et al., 2012). A Magnitude 6.2 on the Richter scale earthquake shook the city of Kalamata, Greece and its surrounding area on September 13th, 1986; an aftershock occurred again on September 15th, 1986 this time measuring 5.6 on the Richter scale (Laube, 1987). The combination of seismic events caused a severe level of destruction in the area as well as numerous cases of injuries and death. Due to the devastation caused by these seismic events, it was deemed that their respective seismic records would be analysed in the studied and current experiments. The provided accelerograms recorded the variation of ground acceleration in both the N-S and E-W directions for a duration of 20s. To stay consistent with past experiments, the time and acceleration values were scaled before being applied to the structure. The acceleration values were reduced by 10% to equal 90% of the original values while the time was scaled down by dividing each recorded time stamp value by the square root of the scale factor which was equal to 2. The accelogramme for the UX direction was used to analyze in-plane action along the x-axis of the structure, whereas the UY direction was used to analyze out-of-plane action along the y-axis of the structure. Graphs of the accelogrammes are shown in Figures 3-8 and 3-9 below.

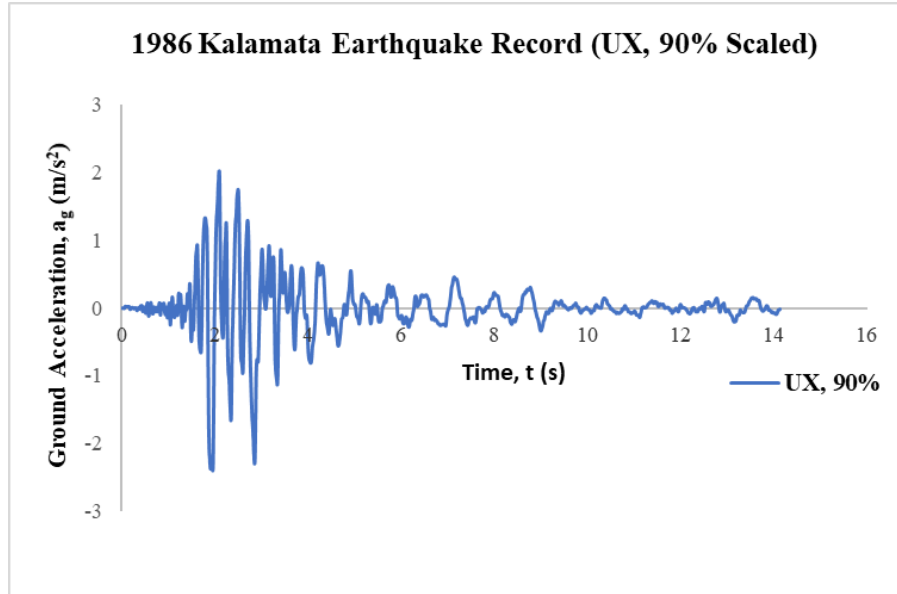


Figure 3-8: UX Accelogramme (ITSAK, 2021).

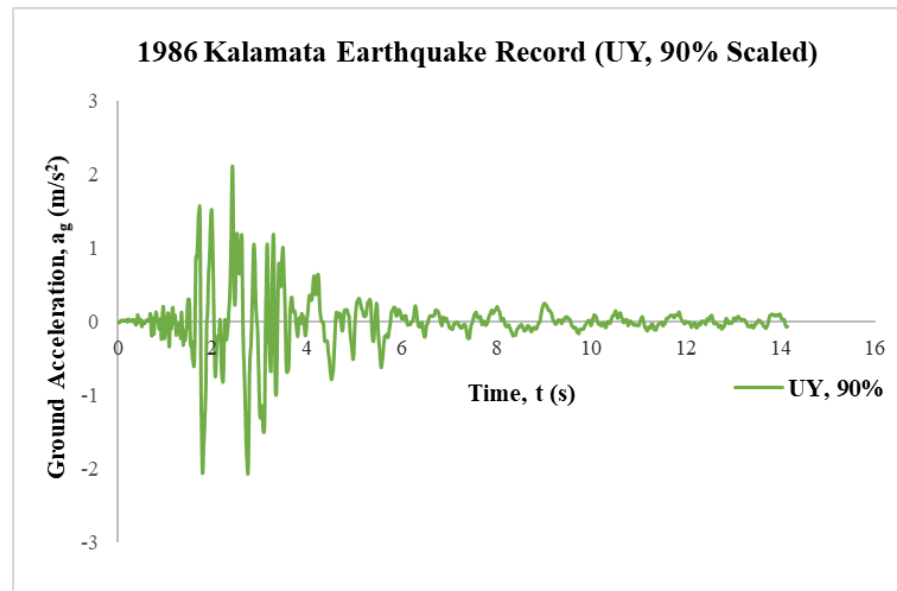


Figure 3-9: UY Accelogramme (ITSAK, 2021).

As shown above, the ground acceleration was at its highest severity from approximately 1.7s to 3.8s, after which the acceleration decreased and remained at a lower severity until completion. The majority of the damage caused during these events commenced during the severe region of accelerations, and the damage then propagated further during the later stages of the earthquake.

In addition to the time history accelogrammes, the scaled response spectrums were also considered from the 1986 Kalamata Earthquake and are presented in Figures 3-10 and 3-11 below.

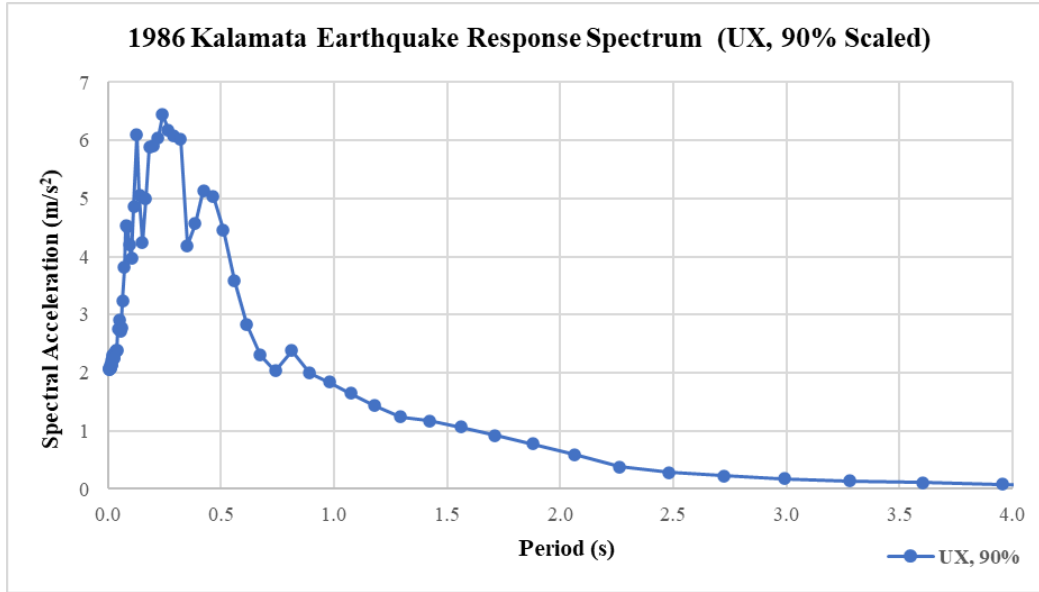


Figure 3-10: Kalamata Earthquake Response Spectrum (UX) (ITSAK, 2021).

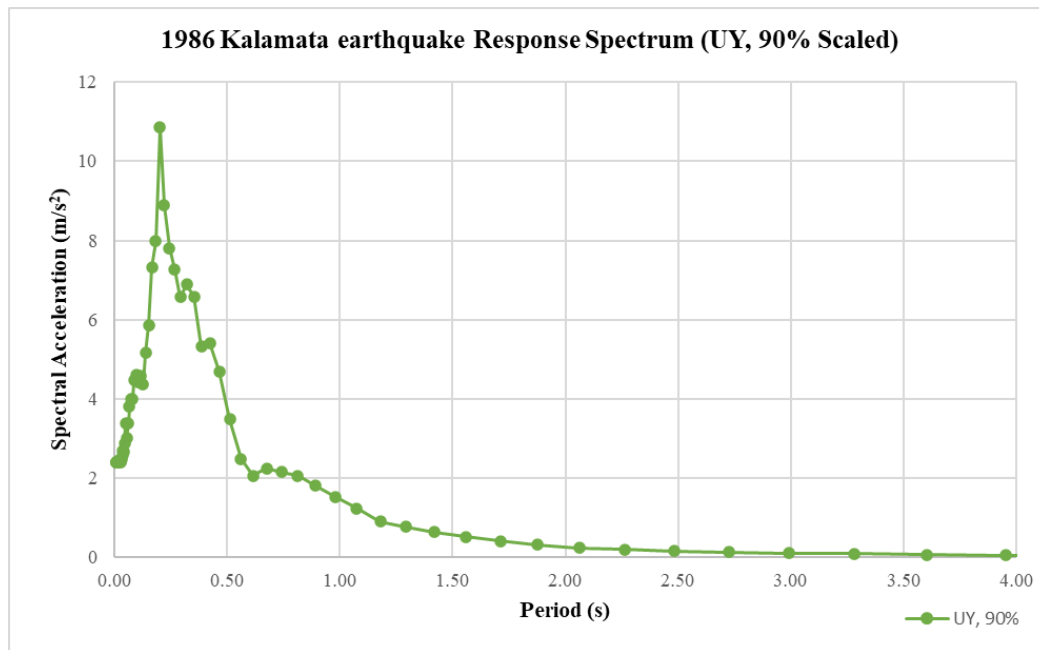


Figure 3-11: Kalamata Earthquake Response Spectrum (UY) (ITSAK, 2021).

The records from the 1986 Kalamata Earthquake were used to run non-linear analyses on the NIKER structure developed in SAP. Both records were used to conduct non-linear time history analyses as well as non-linear spectral analyses in both the in-plane and out-of-plane directions. The resulting shapes at failure were collected and compared. To incorporate the four records into SAP, custom time history and response spectrum functions were created by importing the values from each record into the function definition menu as a text document. The four records were

applied to the structure in their appropriate direction, and the results of these tests will be discussed below.

3.5 Period Correlation Analyses

The first stage of the finite element modelling conducted in SAP 2000 involved matching the fundamental periods of the numerical model which the referenced physical experiment. During the physical experiment, it was reported that the specimen had a period of 0.238s in the out-of-plane direction (UY) and 0.165s in the in-plane direction (Vintzileou et al., 2015). Therefore, the objective of the numerical analyses was to replicate those fundamental periods through model modifications including the implementation of spring connections allowed for flexible diaphragms within the model.

The methodology included a parametric study where the period was recorded as the composition of the model was altered. Throughout the study four main modifications were made to the model. These included modelling the connections between the timber floor joists and masonry walls as direct fixed connections, spring connections, and lastly removing the floor system entirely and adding additional mass to the structure which represented the absent floor systems. The results of those analyses will be discussed below.

The main analysis run during this study was a modal analysis. Modal analysis is a typical procedure conducted to define the fundamental periods and shapes of a structure. When running a modal analysis, the software excites a portion of the total mass laterally. In the case of unreinforced masonry structures, modal analyses become quite complex due to the amount of degrees of freedom, therefore requiring a significant quantity of modes to be considered in order to excite an acceptable quantity of mass in the lateral directions (Pantazopoulou, 2013).

3.5.1 Model 1: Direct Connection

The first model considered in the parametric study was the direct connection model. This model utilizes direct connections between the timber floor joists and masonry walls as shown in Figure 3-12 below. Under these conditions, the model does not consider the reduced stiffness in the axial direction of the timber joists resulting in flexible diaphragms.

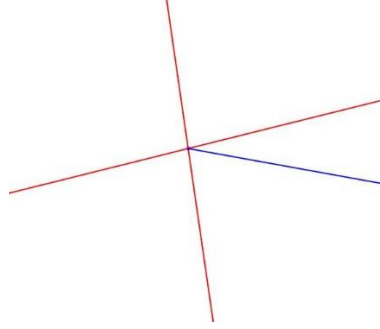


Figure 3-12: Direct Connection Diagram

The model was run under modal conditions as shown in Figure 3-13 below. The main output of interest from analyzing the structure under modal conditions was the fundamental periods. As shown in Figure 3-13 below, the structure followed the expected distribution in both the in-plane and out-of-plane directions and experienced a period of 0.1138s and 0.1675s in those respective directions.

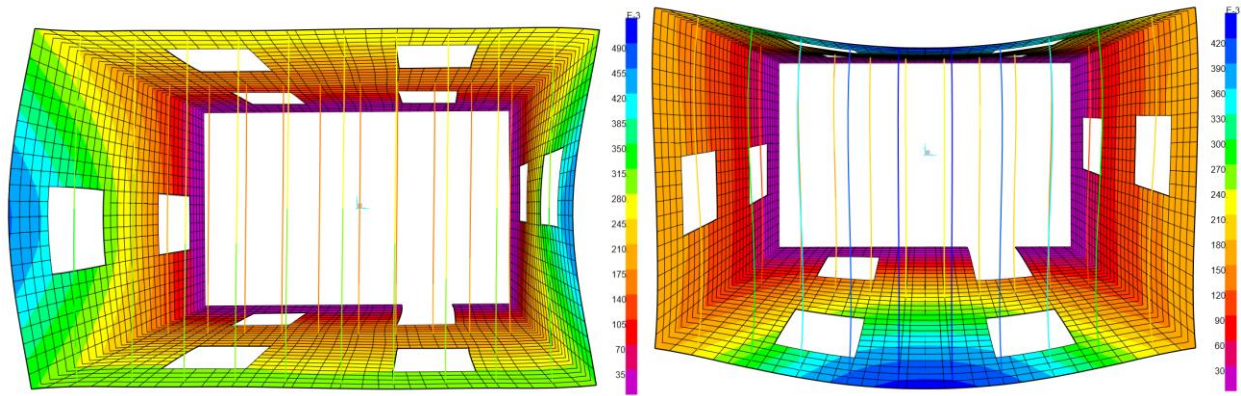


Figure 3-13: (Left) In-Plane Modal Analysis (Direct Connection), (Right) Out-of-Plane Modal Analysis (Direct Connection)

While the distribution of displacements under modal conditions is correct as the maximum displacement is located at the top-centre portion of each wall, the period provided from this analysis is lower than what is expected from referenced results.

From this model it was concluded that the specimen is excessively stiff in the out-of-plane direction due to the direct connections between the timber joists and the masonry walls. Therefore, the spring connections were introduced which will be discussed below.

3.5.2 Model 2: Spring Connection

The second model analyzed in this the parametric study included the spring connections described above to connect the timber frame elements to the masonry walls. A visualization of this

connection is shown in Figure 3-14 below. This model utilized a total of 40 additional arbitrary joints to connect the timber frames to the masonry walls through two joint links. This model was designed to incorporate the flexible diaphragms from the un-strengthened physical specimen which was examined during the NIKER project. This model achieves that through the spring connections which provide axial freedom to the timber floor systems.

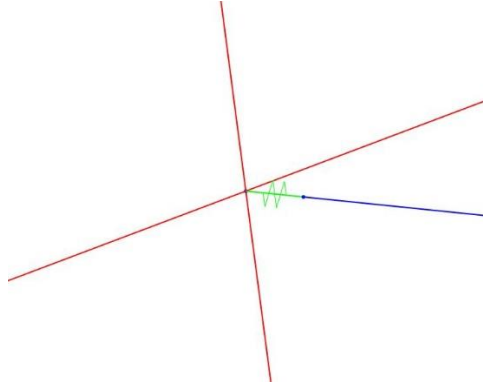


Figure 3-14: Spring Connection Diagram

The model was run under modal conditions similar to Model 1 as shown in Figure 3-15 below. As shown in Figure 3-15 below, the structure also followed the expected distribution in both the in-plane and out-of-plane directions and experienced a period of 0.1138 s and 0.1671s in those respective directions.

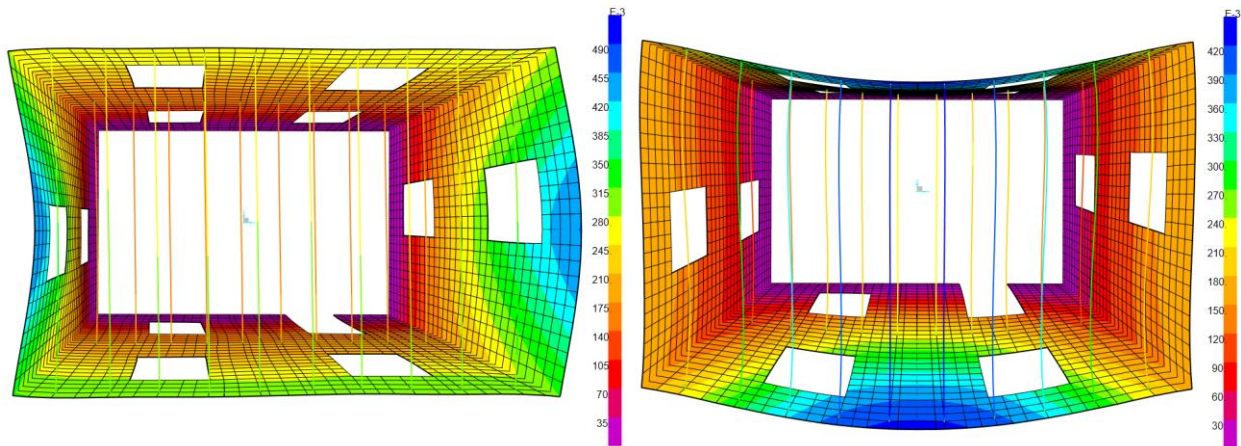


Figure 3-15: (Left) In-Plane Modal Analysis (Spring Connection), (Right) Out-of-Plane Modal Analysis (Spring Connection)

Similar as the results of Model 1, the analysis of Model 2 under modal conditions also provides the expected displacement distributions. However, the implementation of spring connections did not increase the fundamental periods to the desired values from referenced literature. Furthermore, the fundamental periods experienced by Models 1 and 2 were similar and

differed by a very small margin. This indicates that the spring connections did not correct the fundamental periods and signifies that the errors are a source of other issues in the models.

3.5.3 Model 3: No Floor System

The final model analyzed in this parametric study did not utilize any elements to represent the timber floor system. Instead, the mass contributions from the timber floor elements were computed and applied as lumped mass to the joints on the masonry walls where the timber elements would originally be connected to directly or through springs as discussed in Models 1 and 2. The applied masses also includes the respective portions of the additional 7.5 tons applied to the structure as described in Table 3-3 above. The model was run under modal conditions as shown in Figure 3-16 below. As shown below, the structure also followed the expected distribution in both the in-plane and out-of-plane directions and experienced a period of 0.115s and 0.220s in those respective directions.

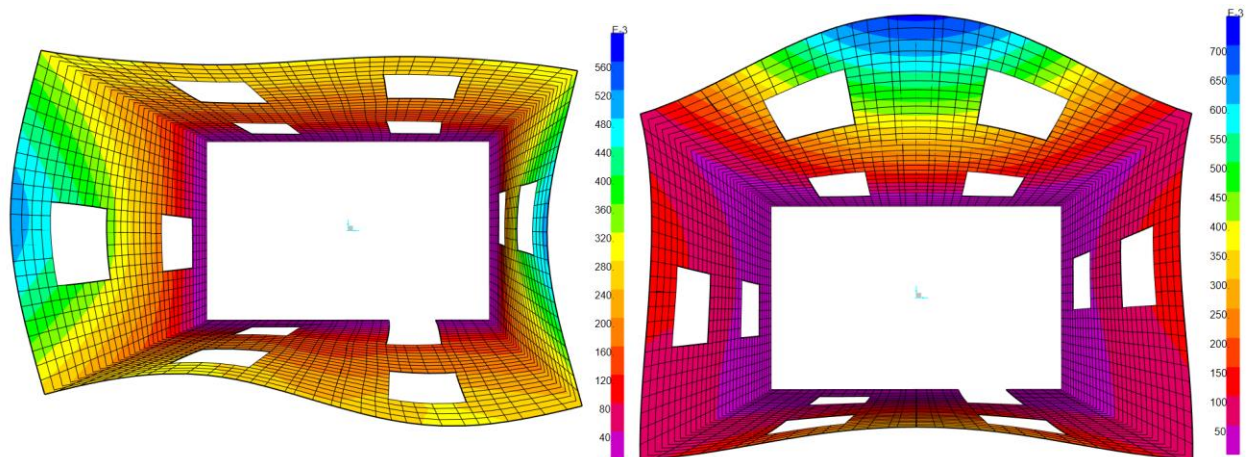


Figure 3-16: (Left) In-Plane Modal Analysis (Floorless), (Right) Out-of-Plane Modal Analysis (Floorless)

While the distributions meet expectations based on the unreinforced conditions, the periods are still incorrect and significantly lower than the desired values. However, the period in both the in-plane and out-of-plane directions did increase compared to the two previous results in Models 1 and 2. This proved that additional issues existed elsewhere since the structure no longer obtained the provided stiffness from a floor system but still had undesirable periods.

3.6 Conclusion

After concluding the preliminary analyses in SAP 2000, it was concluded that the cause of the underestimated fundamental periods lies within the defined material properties for the masonry material, leading to an overestimated stiffness. It was concluded that the modulus of elasticity considered was too high and needed to be reduced to a more realistic value. It was decided that the conditions in Model 2 would be used as the spring connections between the timber joists and masonry walls provided the best representation of flexible diaphragms.

To correct the modulus of elasticity and therefore the fundamental periods in the model, a thorough investigation was required on the material properties of masonry in order to compute a rational value. The details regarding the conducted studies on the mechanical properties of masonry will be discussed throughout Chapters 4 – 7. Finally, the outcomes and modifications to the SAP2000 model of the NIKER structure, as a result of the mechanical properties investigation will be discussed in Chapter 8.

Chapter 4

Numerical Modelling of Masonry Wall Elements in ATENA 3D

4.0 Introduction

Analysis of unreinforced masonry structures, particularly older non-engineered construction, is hampered by uncertainty in many aspects such as material properties and interactions between materials, actual geometry of voids and contacts, boundary restraints etc., all of which may contribute to limiting the reliability of the computed results. Understanding these factors is an essential step towards completing a relevant and valid analysis of the structural behavior. For example, in idealizing masonry as a continuum - such as in a finite element model that considers masonry as a homogenized composite, it is required to specify proper values for the key properties of masonry (e.g. moduli, stress-strain response curve, failure stresses, etc.) that impact critically the calculated response. Describing the homogenized constitutive properties of masonry is a poorly understood area – the actual behavior is very much affected by the layout of joints and blocks, the individual strength and stiffness of the constituent materials, and the joint thickness. Both joint mortar and masonry blocks exhibit nonlinear response in compression but are brittle in tension – therefore the composite material properties need be determined with reference to the magnitude of the anticipated deformation.

In an effort to quantify parametrically the equivalent homogenized properties for masonry which can be used in global response modeling of complete structural systems, a detailed computational campaign is undertaken in the following four chapters. The scope was motivated by the need to define pertinent material properties in modeling the NIKER structure; however, the study has been expanded to be more general, including standard types of industrial masonry forms (with rectangular bricks) such as would be found in heritage construction in urban N.A. cities. Combinations of masonry bricks and mortar having different mechanical properties are considered so as to compute an effective modulus of elasticity, compressive strength, and shear strength for the composite masonry material and the variation of these parameters with increasing deformation. Additional parameters of the investigation include mortar joint thickness, masonry brick size and arrangement, intrinsic material strengths and various loading conditions. The computed results will be compared to the empirical equations previously discussed to determine the optimal equations for estimating representative homogenized URM masonry properties for analysis of complete structural systems. The first chapter of this section will focus primarily on the steps taken to develop the series of models using advanced nonlinear finite element modeling in the software platform ATENA 3D (Cervenka & Cervenka, 2017).

4.1 Wall Element Designs & Dimensions

A series of wall-elements referred to for brevity as “wallettes” were modelled. These were formulated using details from the NIKER project and were designed in conformance with specimen size recommended in CSA D.3.2.2 for material characterization, which calls for a minimum of four courses of masonry bricks and a height to thickness ratio greater than 2 for any solid clay unit or concrete brick prism (CSA, 2010). The masonry walls used in the NIKER project were 250 mm thick double-wythe walls where each layer of masonry was approximately 83.3 mm thick in the scaled model (Vintzileou et al., 2015). In the present study mechanical properties are examined for in-plane wall actions (i.e., plane stress conditions); in this state of stress wall thickness is only a multiplier and therefore the thickness of the wallettes matched the experiment, however scaling up to different wall thicknesses is straightforward. To select the overall dimensions an initial brick size of 200 mm x 100 mm x 83.3 mm was assumed as shown in Figure 4-1 below. To conform with CSA masonry prism standards a total of 6 – 2 brick courses were used. Finally, an initial joint thickness of 10 mm was assumed throughout creating an overall height of 650 mm and a width of 410 mm also shown in Figure 4-1. This makes for a height to thickness ratio of approximately 7.80 which meets the CSA standards. These specimen dimensions were used for all the wallettes analyzed in this study.

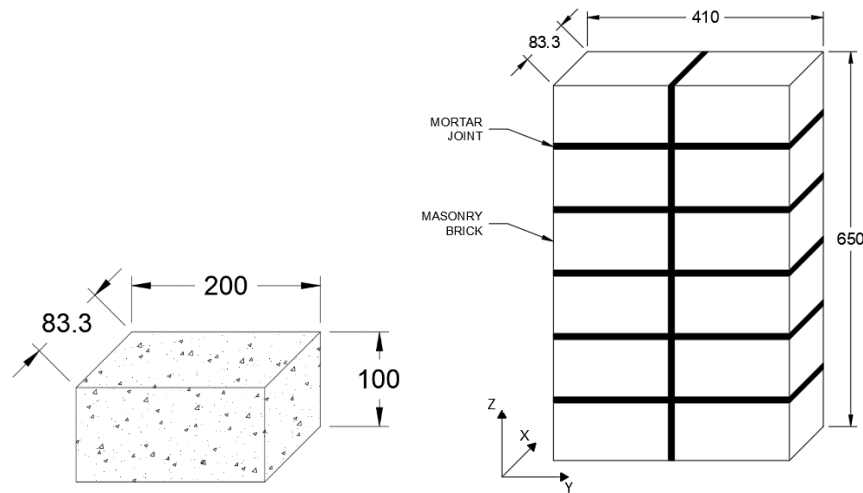


Figure 4-1: Initial assumed brick and specimen dimensions.

To conduct the parametric sensitivity analyses, a total of three basic geometric patterns were created. These patterns included a symmetrical 6 – 2 course wallette denoted as SYM. The purpose of the SYM design was to create a simplified baseline model which was effective at verifying the behaviour during the various tests. Next, an equally staggered model denoted as EQS

was created to represent what is typically found in urban heritage masonry construction. Finally, a random design was created denoted as RAN. The RAN model was created to replicate typical practice used for historic URM structures which lacked patterns and principles for choosing a brick arrangement. To begin the analyses, all three designs were created with 10 mm mortar joints throughout as shown in Figure 4-2.

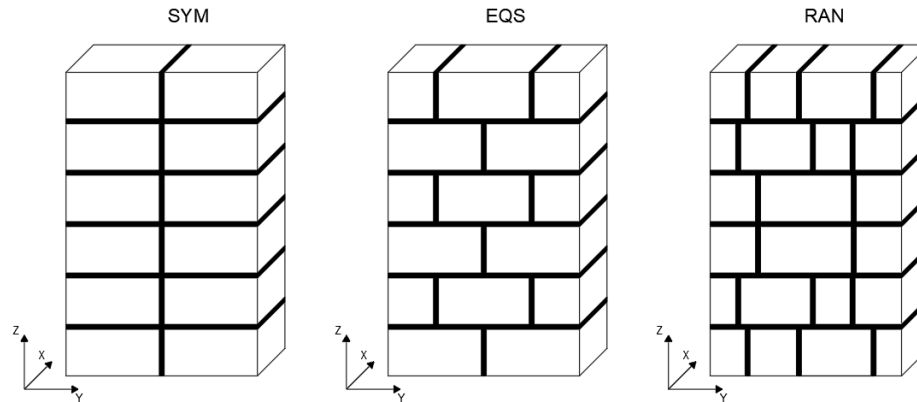


Figure 4-2: Block and joint patterns in the wallettes.

Each of these three patterns are unique and are expected to behave differently under both compression and lateral loading. Significant differences are found in terms of strength and deformation capacity and in the dominant crack paths that are created during failure according with the arrangement of the head joints.

The SYM model is what would be referred to as stack-bond masonry, with aligned head joints height-wise creating a plane of weakness that extends along the entire height of the specimen. Under later loading, the head joints are at risk of forming a sliding plane (a vertical shear crack) since the strength contribution of the mortar is generally lower than the contribution of the masonry bricks. Therefore, this would cause the specimen to crack and divide in half along the head joint. For these reasons, the stack-bond pattern of the SYM model is not common in practice and is not expected to exceed the other two patterns in terms of performance.

The EQS model is the running-bond type of masonry, arranged so that each head joint is centered over the block unit below. This maximizes the horizontal distance between head joints in successive courses throughout the specimen. Under compression this arrangement ensures maximum engagement and cooperation between units minimizing the risk of formation of major vertical fissures through head joints until large levels of deformation. It is expected that the EQS

pattern will have the best performance of the three options on account of the optimal arrangement of the head joints.

The RAN arrangement shares similar disadvantages as the SYM model. As shown in Figure 4-2 above, the head joints are arranged nearly linear along the height of the specimen on both the left and right edge. Like the SYM design, this creates a large risk that severe cracking will occur along these joints that will weaken the specimen.

The other important parameter considered in the parametric investigation is the area ratio of brick and bed and head mortar joint in their facade. Since the masonry bricks have a significantly higher compressive strength than the mortar, models with a higher percent area of bricks are expected to attain higher strength from among the various models. To study this, a total of three unique models were created for each of the three designs by varying the bed and head joint thickness. The mortar thicknesses considered were 5 mm, 10 mm, and 20 mm. Thus, a total of 9 unique wallette variations were assembled to be analyzed as shown in Figure 4-3 below.

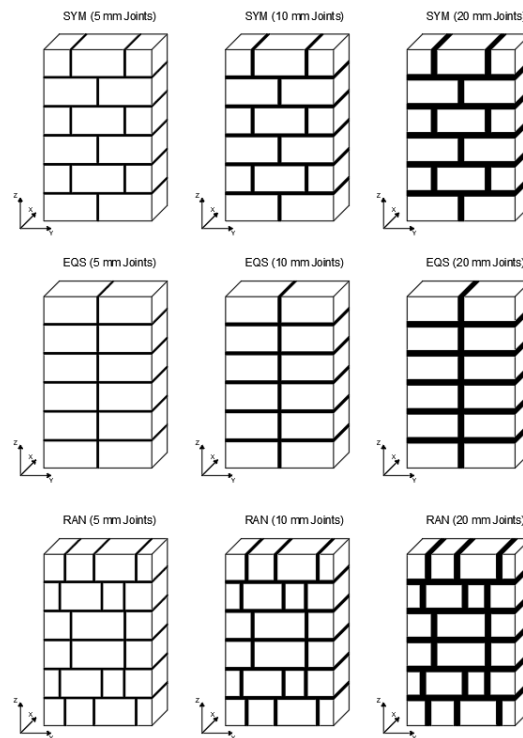


Figure 4-3: Collection of nine wallette specimens.

Each of the specimens contain different proportions (calculated with reference to the façade surface area) of bricks and mortar as shown in Table 4-1 below. Altering the joint area fraction

throughout these nine specimens provides the necessary data to quantify the impact of the weaker material (joint mortar) on the composite properties of the wall.

The modelling procedure used resembles that of discrete element models although it is conducted in the framework of Finite Element analysis. Therefore, the actual components are described exactly and are not homogenized; instead, results of the composite behavior are used to derive the homogenized equivalent properties.

Table 4-1: % Bricks and Mortar

Joints	Design					
	SYM		EQS		RAN	
	Brick	Mortar	Brick	Mortar	Brick	Mortar
5 mm	93%	7%	94%	6%	93%	7%
10 mm	90%	10%	88%	12%	86%	14%
20 mm	83%	17%	76%	24%	74%	26%

As shown in Table 4-1, increasing the mortar thickness reduces the area ratio of bricks in the specimen by approximately 0.6% per 1 mm increase. The three different joint thickness are considered for studying the behavior under both axial and lateral loads, providing further insight regarding potential effects on crack patterns and crack severity.

In addition to the three regular brick patterns considered, a fourth pattern was defined, referred to here on as STONE, to replicate historic masonry construction such as that tested in the NIKER structure. The design of STONE is similar to RAN; however, RAN uses bricks while STONE uses uneven stones to make up the specimen. The use of stones means that there are no apparent courses of bricks and bed joints, but instead various sizes of stones are used to create an unsymmetrical and unpredictable specimen as shown in Figure 4-4 below.

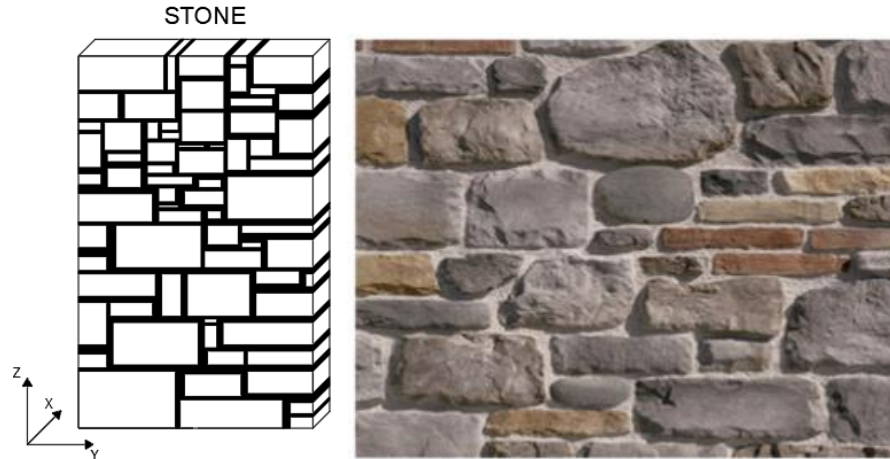


Figure 4-4:[A] STONE design. [B] Stone masonry example (Schiavi et al., 2019)

Another difference between STONE and the other three patterns is that the mortar joints differ in thickness throughout. Therefore, for this pattern only one specimen will be tested under compressive and lateral loads increasing the total count of specimens to ten.

4.2 Material Properties

Throughout preliminary analysis of the ten model specimens the properties of the masonry bricks and mortar were kept constant. However, in later stages of this investigation more analysis cases were considered in which the material properties were varied from their reference values. To account for the nonlinearity in compression and brittleness in tension of the constituent materials, the model properties were entered into ATENA using the routine intended for concrete with proper modifications to account for either masonry unit or mortar. Reference values were obtained from both the NIKER project and manual computation. For example, for the STONE model, the compressive strength utilized for the masonry bricks and mortar was 100 MPa and 4.6 MPa respectively which was adopted and used in the ATENA 3D analyses (Vintzileou et al., 2015). Also from the NIKER project, the specific weight utilized was 2.68 Mgr/m^3 for the masonry bricks and 1.76 Mgr/m^3 for the mortar. The first computed property was the tensile strength which was assumed to be 10% of the compressive strength, estimated as 10% of the respective compressive strength. Finally, the modulus of elasticity for each material were computed by plotting their individual stress – strain curves in compression assuming a Hognestad type parabola. After plotting the curves, a secant was plotted through the origin and the point which represents 40% of

the maximum compressive strength in order to define the engineering value of the modulus of elasticity for each constituent material as shown in Figures 4-5 and 4-6 below.

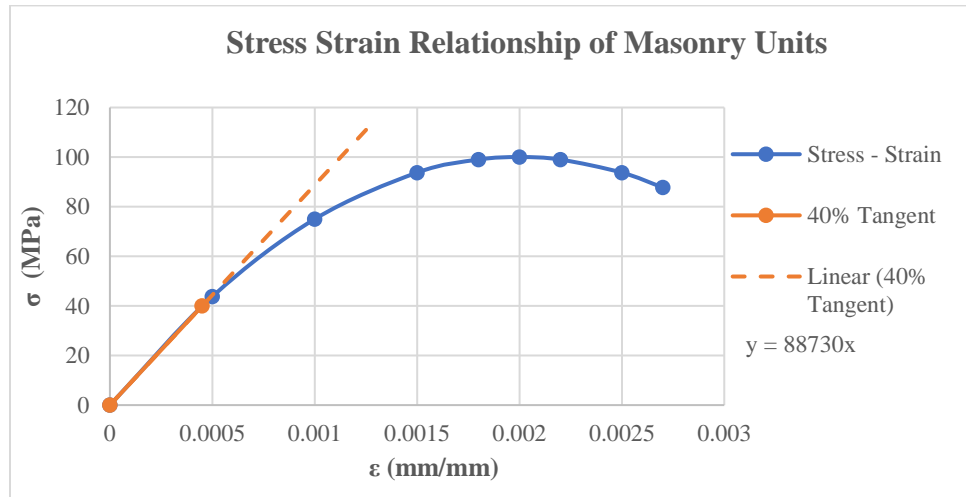


Figure 4-5: Stress - Strain relationship (Masonry Bricks)

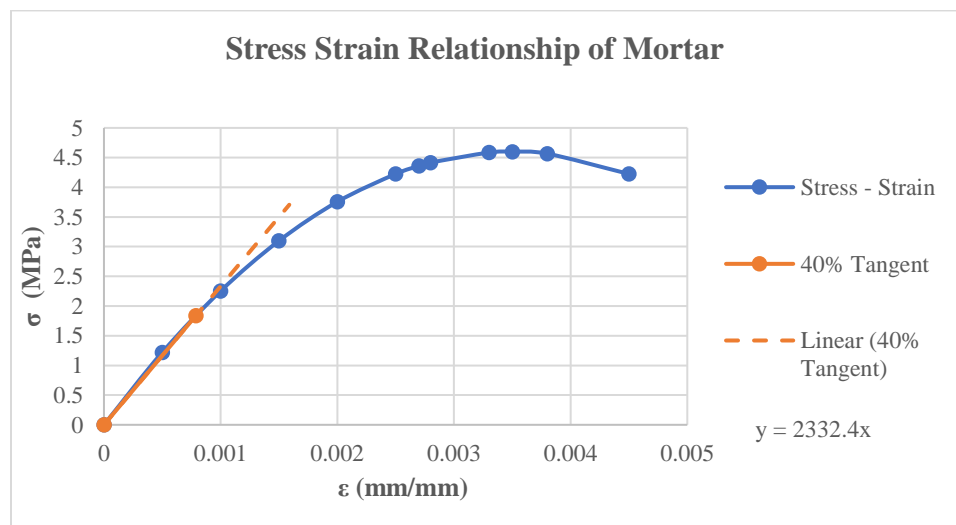


Figure 4-6: Stress - Strain relationship (Mortar)

In addition to masonry bricks and mortar, 550 MPa steel was also used for loading hardware in simulating uniaxial compression and pushover of the wallettes. An overview of the material properties used for this investigation can be found in Table 4-2 below.

Table 4-2: Sample of material property input in ATENA.

Properties	Material		Properties	Steel
	Masonry Bricks	Mortar		
Modulus of Elasticity, E (MPa)	88,730	2332.4	Modulus of Elasticity, E (MPa)	200,000
Compressive Strength, f_c (MPa)	100	4.6	Yield Strength, σ_y (MPa)	550
Tensile Strength, f_t (MPa)	10	0.46	Poisson's Ratio, μ	0.3
Poisson's Ratio, μ	0.2	0.2	Specific Weight, ρ (kN/m ³)	78.5
Specific Weight, ρ (kN/m ³)	26.29 (2.68 Mgr/m ³)	17.27 (1.76 Mgr/m ³)		

4.3 Direct Compression and Pushover Models

Two loading conditions were considered to conduct numerous parametric sensitivity analyses. The first loading condition studied was direct monotonically increasing compression. All ten specimens were subjected to prescribed axial deformation increments until failure. The overall load – displacement results were measured along the top face of each specimen to compute the compressive strength of the wallette. In addition, lateral expansion was measured at mid-height to determine the dilative behavior of masonry under direct compression. The second set of experiments were a series of pushover analyses conducted on each of the ten specimens. The pushover analysis involved applying an overbearing compressive stress onto the top face of the wallette to load it axially, then following with a prescribed lateral deformation which increases gradually pushing the wall until failure. The goal of this set of analyses was to determine the shear strength of the wallettes (useful for analysis under lateral loads such as earthquake) and how the strength is affected by factors such as joint thickness, brick arrangement and overbearing stress. The methodology for the pushover experiments mirrored what was done for the direct compression models. Where necessary for convergence, adjustments were made to the boundary conditions and load application.

4.3.1 Methodology (Direct Compression)

Modelling of the wallette specimens in ATENA was conducted in a manner that is representative of the mechanical tests under compression used in experimental studies in order to derive the uniaxial stress-strain response of the composite.

4.3.2 Macro-elements

Eight noded solid elements were used throughout the simulation. Each brick was discretized into a macroelement, comprising identical solid sub-elements as depicted in Figure 4-7. To accurately define this element, each design was initially drafted in AutoCAD with complete dimensions. Mortar was divided into two portions, bed joints and head joints. Separate macro-elements were created for each portion of the mortar joints which surround one brick. This includes elements for the bed joints on the above and below the brick, head joints on the left and right of the brick and a square element which is created at the intersection of the head joint and the bed joint as shown in Figure 4-7 below. For a wallette specimen like the one shown below in Figure 4-7, a typical brick element contains 50 macro-elements, and the entire mesh contains 10,480 elements. These values vary depending on the design and the selected density of the mesh.

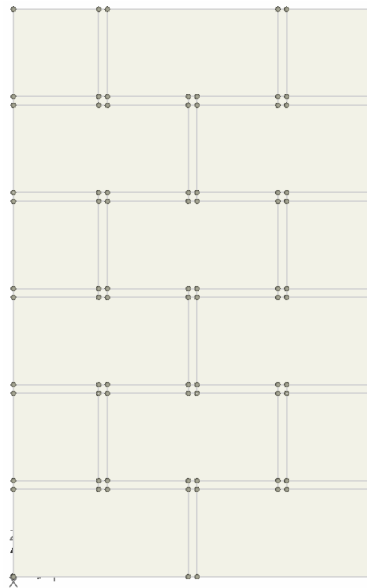


Figure 4-7: Macro-elements for EQS (10 mm Joints)

4.3.3 Contacts

In the model, contacts are defined as the surface which is common to two or more macro-elements. In ATENA 3D two main contact types are available, i.e., partial and full. Full contact means that the surfaces of the two elements which form the contact do not connect with any other surface and share fully the degrees of freedom of common joints. Partial contact means that one or both surfaces which form the contact are also in contact with an additional surface (to model inadequate interaction, such as sliding between surfaces otherwise in contact). When the wallette models were originally developed in ATENA, the EQS and RAN specimens had partial contacts throughout since the bricks are not vertically aligned like the SYM design. This caused stability and convergence issues when running the analyses and provided unrealistic behaviours. To correct this, any element which formed a partial contact was divided into strips as shown in Figure 4-8.

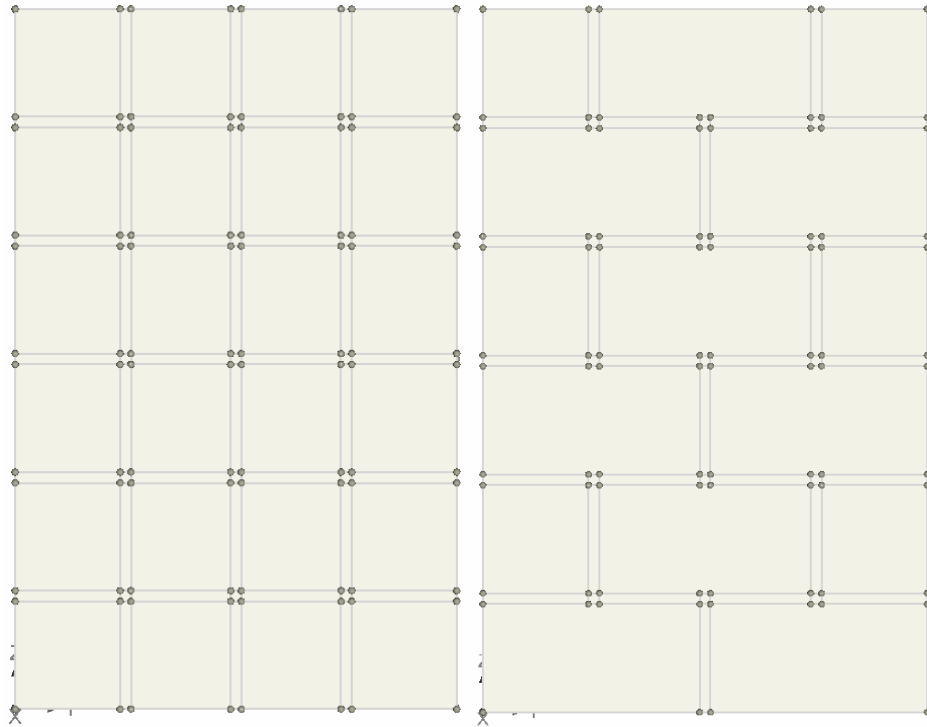


Figure 4-8:[A] Adjusted model with no partial contacts, [B] Original model with partial contacts

4.3.4 Finite Element Mesh

For the direct compression models two mesh sizes were selected to represent the masonry bricks and the mortar. Primarily, an element size of 0.0200 m was used to discretize the masonry bricks whereas elements of 0.0050 m size were used in discretizing the mortar joints as shown in Figure 4-9 below.

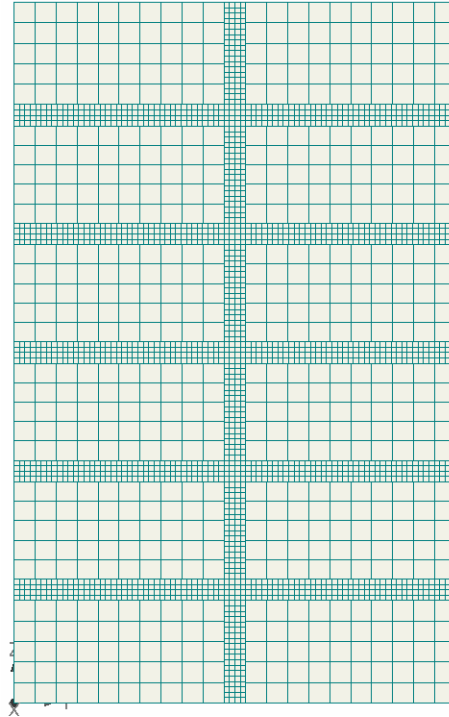


Figure 4-9: Finite element mesh of SYM model with 20 mm joints.

The smaller mesh was used for the mortar joints since the macro-elements have a total small area. A smaller mesh is needed to discretize the mortar joint elements into sufficient sub-elements otherwise the accuracy of the results will be reduced. ATENA 3D provides two main mesh types, brick and tetrahedral. The brick type mesh was used for all models studied in this investigation. The brick type mesh was chosen as it allows for a more accurate calculation of the total load being applied on the top surface using tributary areas. For some of the wall specimens, the mesh magnitude was reduced due to the thickness of the element strips needed to fulfill the full contact conditions. This was primarily seen in the RAN and EQS model sets where the length of overlap between brick courses can be small depending on the joint thickness and therefore requires a thin strip to create a full contact. The finite mesh for each of the three designs with 10 mm joints and the STONE design are shown in Figure 4-10 below.

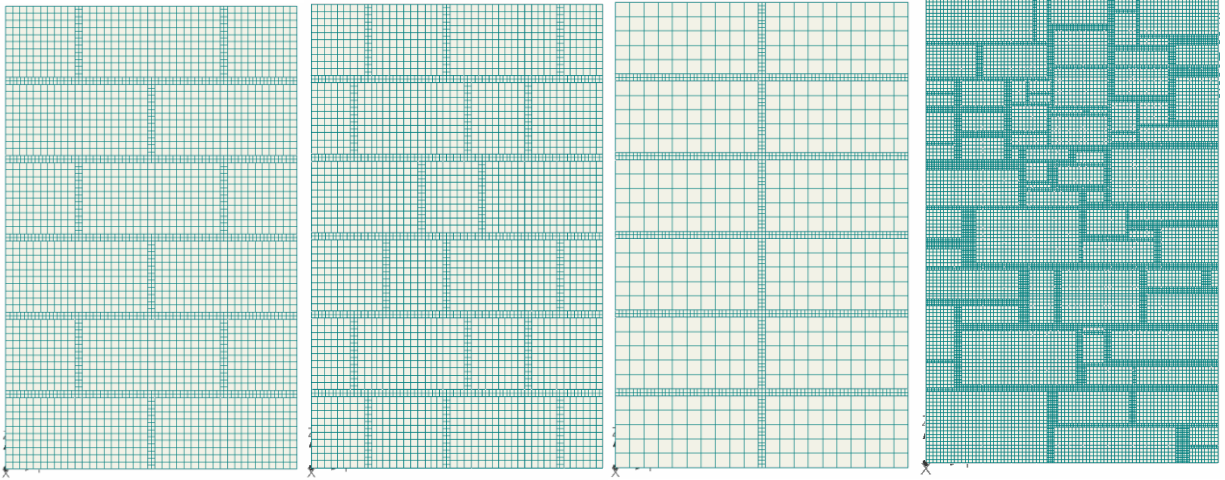


Figure 4-10: [A] EQS - 10 mm Joints, [B] RAN - 10 mm Joints, [C] SYM - 10 mm Joints

As shown above, the discretization of macro-elements into strips was only necessary in the RAN, EQS, and STONE designs. This means that smaller mesh sizes were required for the bricks since they were divided into strips some of which were the same thickness as the mortar joints. The SYM design could support a larger mesh size since no partial contacts existed as the bricks were all aligned both horizontally and vertically.

4.3.5 Load Cases

In ATENA 3D load cases are used to define any conditions being applied to the model including loads, deformations and boundary conditions. For the direct compression models a total of two load cases were used, supports and prescribed deformations. The supports load case is used to apply all boundary conditions onto the models such as fixing surfaces along an axis of symmetry. Prescribed deformation is used to apply a deformation to an element. This can be enforced onto a joint, surface or line. These two load cases were sufficient to conduct the compression analysis however an additional load case was required for the pushover analyses.

4.3.5.1 Supports

In the direct compression models supports were used to fix the base of the structure at the planes of symmetry along the XZ and YZ planes as shown in Figure 4-11. All other nodes were restrained from displacement in the Z-direction, but lateral expansion was allowed to occur in the YZ plane.

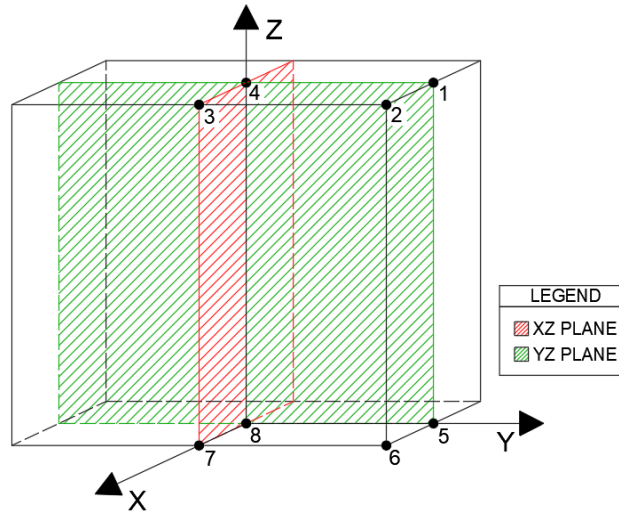


Figure 4-11: Axes of symmetry

As mentioned previously, one quarter of the wall was modelled which is defined within joints 1 – 8 in Figure 4-11 above. This creates an axis of symmetry on the plane 3 – 4 – 7 – 8 where no translation is permitted along the y-axis. There also exists an axis of symmetry on the plane 1 – 4 – 5 – 8 where no translation is permitted along the x-axis. To enforce these conditions surface y-axis fixities were applied to every macro-element surface along the plane 3 – 4 – 7 – 8, and x-axis fixities were applied to every surface along the plane 1 – 4 – 5 – 8. Finally, the base was fixed along the z-axis which lies on plane 5 – 6 – 7 – 8. The applied boundary conditions are shown in Figure 4-12 below which references the planes described in Figure 4-11.

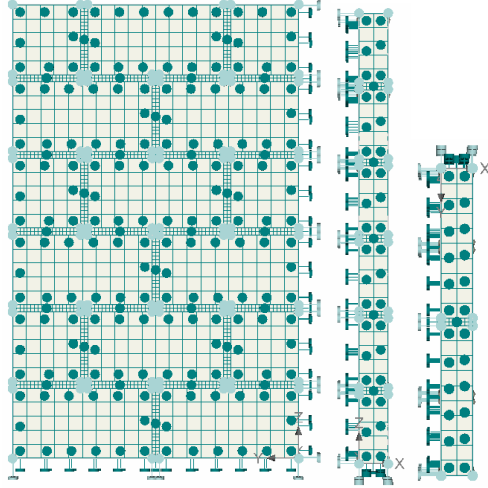


Figure 4-12: [A] X-Axis supports along plane 1-4-5-8, [B] Y-Axis supports along plane 3-4-7-8, [C] Z-Axis supports along plane 5-6-7-8.

4.3.5.2 Prescribed Deformation

Load cases in the direct compression models were also used to create prescribed displacement on the top surface of the wallettes, to translate the surface by the specified amount to failure. In this case the model runs until the structure can no longer support any further displacement which, in the context of the present study is interpreted as failure accompanied with a significant loss of resistance. For the direct compression models a prescribed displacement of 35 mm in the -Z direction was applied to all the surfaces on the top face of the wallettes. The total displacement applied to the structure in each step of the analysis is dependent on the step multiplier which will be discussed below.

4.4 Monitoring Points

Predefined monitoring points are used to measure a result of interest such as displacements at a specific point on any macro-element. As mentioned previously, the main purpose of the direct compression models was to compute the equivalent compressive and tensile resistance curve of masonry from the contributions of the constituent elements using detailed discrete element modeling. Therefore, a load – displacement curve was plotted for each wallette and then converted to a stress – strain plot from where the strengths and stiffness could be obtained. To achieve this, monitoring points were used at all four corners on the top surface of each brick located in the top course of the wallette. At each of these locations a monitoring point was placed to measure the displacements along the z-axis, and another to measure the reactions along the z-axis. To compute

the lateral dilation a monitoring point was placed at the mid-height of the structure to measure the displacements along the y-axis. The quantity of monitoring points differed in each design as each have different quantities of bricks in the top course. The monitoring points for the EQS design are shown in Figure 4-13 below.

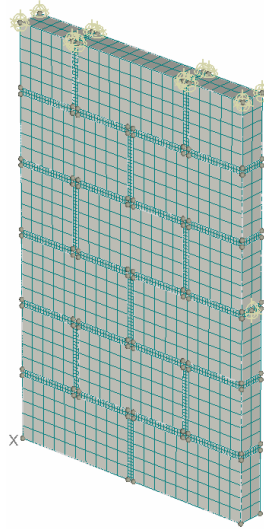


Figure 4-13: Monitoring Points EQS (10 mm Joints)

Data was collected from each monitoring point at each step in the analysis to form the entire load – displacement curves which were then used to compute the stress – strain response of the specimens. Additional monitoring points were required for the pushover analysis.

4.5 Analysis Steps

Analysis steps were used to break down the entire experiment into smaller load increments where a predefined portion of the prescribed deformation and forces are applied in each increment until the analysis is complete. For the direct compression analyses both the supports and prescribed deformation cases were applied in all steps. The second component in creating the analysis steps is to define a solution algorithm. Standard Newton-Raphson was used for solution of the incremental equations of equilibrium.

4.6 Pushover Models

The purpose of the pushover analyses was to assess the lateral resistance with increasing lateral drift ratio (horizontal displacement at the top divided by the wall height) and the effect of the pattern of brick arrangement and mortar joint thickness on this property. The shear strength of the wallettes was obtained from peak resistance. A critical parameter of study in this regard was the overbearing axial load, since in URM construction strength is owing to the frictional resistance generated at the weakest planes of sliding contributed to by overbearing pressure.

4.6.1 Methodology

The procedure followed to create the pushover models was similar to that used in the compression models. Modelling differences where they exist, are discussed in the following section.

4.6.1.1 Macroelements

The compression model was used as the basis for developing the pushover models. A small steel plate was added to the top of the XZ plane at the area where the prescribed deformation was applied as shown in Figure 4-14.

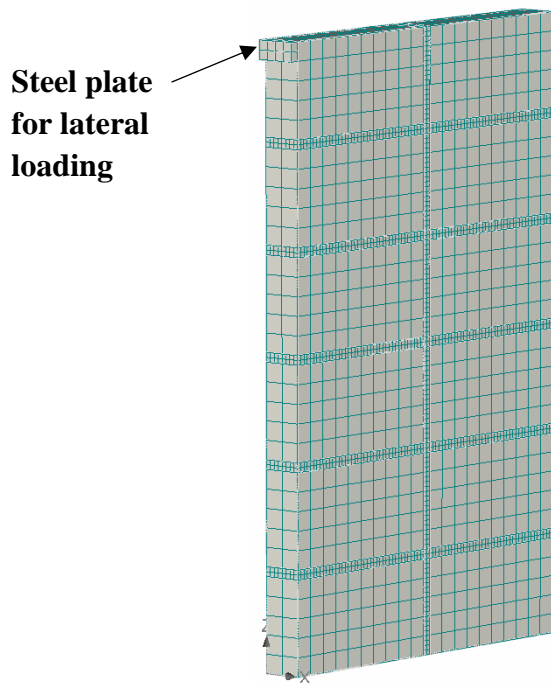


Figure 4-14: Steel plate applied for pushover analyses.

This plate was added to all the pushover specimens to distribute the prescribed deformation across the entire thickness to ensure that the entire wallette would deform laterally and to avoid localized rupture of the brick unit at the upper corner near the point of application of the displacement.

4.6.1.2 Supports

With reference to the compression specimens, the wallettes were restrained along two axes of symmetry, i.e., along the intersection of the XZ and the YZ planes. For pushover analyses, the restraint along the YZ plane of symmetry is eliminated, whereas the base of the specimens was fixed from translating in the Y direction to suppress sliding while the wallette deforms under the lateral displacement; this was needed as it was observed that the entire specimen was sliding if unrestrained, without bending. The final support conditions for the pushover specimens are shown in Figure 4-15 below.

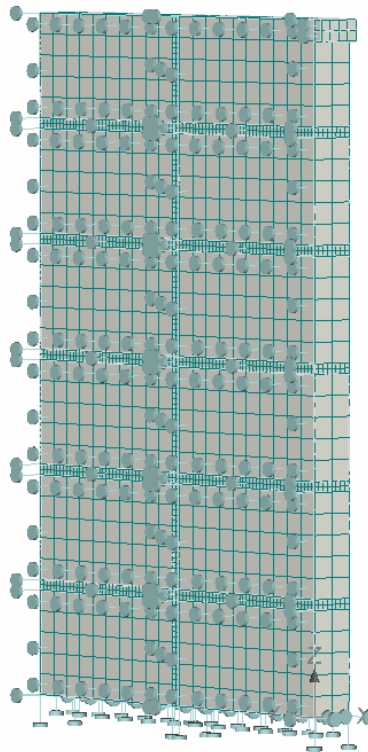


Figure 4-15: Supports for pushover specimens.

4.6.1.3 Prescribed Deformation

The pushover specimens were all subjected to prescribed horizontal displacements controlled at the top to push the wallettes laterally. A total of 3 mm of prescribed deformation was applied at the centre of the steel plate which was added to the pushover specimens. The prescribed deformation was applied in small increments in throughout a series of analysis steps. The total of 3 mm of prescribed displacement was sufficient to bring the wallettes to failure.

4.6.1.4 Forces

When conducting lateral pushover analysis, apart from the lateral displacement axial overbearing stress is required since this is the only mechanism of shear resistance to URM. In this investigation, the overbearing stress was applied using forces on the top surface of each specimen as shown in Figure 4-16.

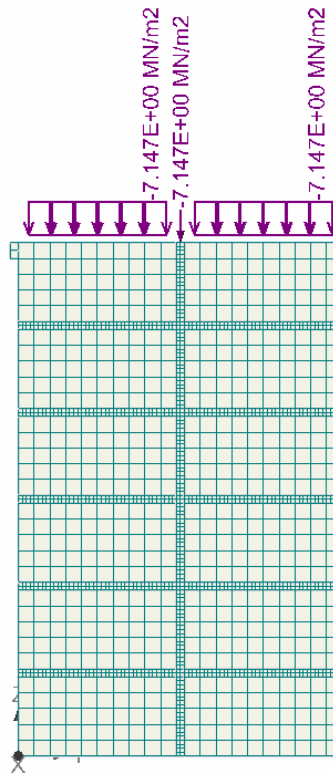


Figure 4-16: Axial overbearing stress.

To assess the effects that the overbearing stress has on the shear strength, 8 different values for axial overbearing stress as follows: 0.05 MPa, 0.1 MPa, 0.2 MPa, 0.3 MPa, and 0.4 MPa, 1.79 MPa, 4.47 MPa and 7.15 MPa.

4.6.1.5 Monitoring Points

Two additional monitoring points were used in the pushover analysis at the centre of the steel plate where the prescribed displacement was applied. The two monitoring points included one to measure the induced reactions at the centre of the steel plate along the Y-axis, and one to measure the lateral displacements at the centre of the plate as shown in Figure 4-17.

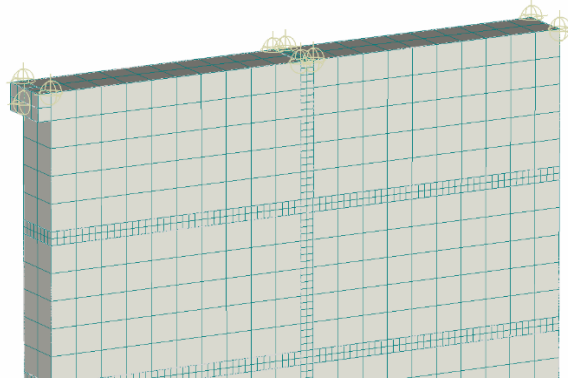


Figure 4-17: Pushover Monitoring Points.

4.6.1.6 Analysis Steps

The pushover specimens utilized very similar analysis steps as the compression specimens. The main point to consider is that the overbearing stress must be completely applied prior to the lateral deformations. This is to ensure the specimens have developed the lateral strength provided by the overbearing stress once the prescribed deformation is applied. To achieve this, one additional step was added in the beginning of the analyses which applies the support conditions and forces to the specimens. This additional step uses a multiplier of 1.0 to ensure the axial load is completely applied in the first step. From step 2 until failure, the analyses steps follow with a predefined step multiplier of 0.1.

4.7 Alternate Material Properties Models

The main purpose of this extensive investigation is to fill knowledge gaps regarding the behaviour of masonry. One of the areas of interest is the effects of altering the strengths of the bricks and mortar that make up a masonry specimen. Altering the strengths of each material provides insight on how much each material contributes to the total strength of masonry. To assess this, each of the 10 wallette designs were tested under a variety of strength confirmations as listed in Table 4-3 below.

Table 4-3: Strength combinations.

Combination	Masonry Bricks		Mortar	
	Compressive Strength (MPa)	Tensile Strength (MPa)	Compressive Strength (MPa)	Tensile Strength (MPa)
A	100	10	4.6	0.46
B	50	5	4.6	0.46
C	30	3	4.6	0.46
D	100	10	2.3	0.23
E	100	10	1.0	0.10

The strength combinations displayed above were applied to each of the ten models and tested under axial compression. The expectation is that each of the 5 combinations will develop different compressive strengths when applied to each design.

4.8 Alternate Loading Conditions

Loading conditions were also varied to quantify the effects on lateral strength caused by the overbearing stress. To assess this, a total of eight unique values of axial overbearing stress were applied to the specimens in the pushover analyses. These values were divided into two categories, where one was an overall value ranging from 0.05 MPa, 0.1 MPa, 0.2 MPa, 0.3 MPa, and 0.4 MPa. The other category was defined as a ratio of the theoretical compressive strength of the wall. The theoretical strength was calculated as 17.87 MPa. The ratios considered were $0.1f_{wc}$, $0.2f_{wc}$, and $0.3f_{wc}$ which equated axial overbearing stresses of 1.79 MPa, 4.47 MPa and 7.15 MPa respectively.

4.9 Collection of Analysis Cases

The planning done throughout this extensive investigation allowed for sufficient analyses to be conducted under a variety of conditions to fill several knowledge gaps. These gaps revolve around the behaviour of masonry and the uncertainty regarding its behaviour. To fill these gaps a series of alterations were made to the three primary brick patterns in order to create additional specimens which test the effects of various changes to the specimen designs. Changes include joint thickness, brick arrangement, material strengths, and overbearing stress. The alterations made to the properties of each specimen created a series of additional models to be tested. A summary of all the analyses done in ATENA 3D are shown in Table 4-4 below.

Table 4-4: Summary of ATENA 3D Wallette Investigation models.

Test Number.	Design	Test Type	Joint Thickness	Material Strength Combination	Overbearing Stress (MPa)
1	SYM	Compression	5	A	N/A
2	SYM	Compression	5	B	N/A
3	SYM	Compression	5	C	N/A
4	SYM	Compression	5	D	N/A
5	SYM	Compression	5	E	N/A
6	SYM	Compression	10	A	N/A
7	SYM	Compression	10	B	N/A
8	SYM	Compression	10	C	N/A
9	SYM	Compression	10	D	N/A
10	SYM	Compression	10	E	N/A
11	SYM	Compression	20	A	N/A
12	SYM	Compression	20	B	N/A
13	SYM	Compression	20	C	N/A
14	SYM	Compression	20	D	N/A
15	SYM	Compression	20	E	N/A
16	SYM	Pushover	5	A	0.05
17	SYM	Pushover	5	A	0.1
18	SYM	Pushover	5	A	0.2
19	SYM	Pushover	5	A	0.3
20	SYM	Pushover	5	A	0.4
21	SYM	Pushover	5	A	1.79
22	SYM	Pushover	5	A	4.47
23	SYM	Pushover	5	A	7.15
24	SYM	Pushover	10	A	0.05
25	SYM	Pushover	10	A	0.1
26	SYM	Pushover	10	A	0.2
27	SYM	Pushover	10	A	0.3
28	SYM	Pushover	10	A	0.4
29	SYM	Pushover	10	A	1.79
30	SYM	Pushover	10	A	4.47
31	SYM	Pushover	10	A	7.15
32	SYM	Pushover	20	A	0.05
33	SYM	Pushover	20	A	0.1
34	SYM	Pushover	20	A	0.2
35	SYM	Pushover	20	A	0.3
36	SYM	Pushover	20	A	0.4
37	SYM	Pushover	20	A	1.79
38	SYM	Pushover	20	A	4.47
39	SYM	Pushover	20	A	7.15

Test Number.	Design	Test Type	Joint Thickness	Material Strength Combination	Overbearing Stress (MPa)
40	EQS	Compression	5	A	N/A
41	EQS	Compression	5	B	N/A
42	EQS	Compression	5	C	N/A
43	EQS	Compression	5	D	N/A
44	EQS	Compression	5	E	N/A
45	EQS	Compression	10	A	N/A
46	EQS	Compression	10	B	N/A
47	EQS	Compression	10	C	N/A
48	EQS	Compression	10	D	N/A
49	EQS	Compression	10	E	N/A
50	EQS	Compression	20	A	N/A
51	EQS	Compression	20	B	N/A
52	EQS	Compression	20	C	N/A
53	EQS	Compression	20	D	N/A
54	EQS	Compression	20	E	N/A
55	EQS	Pushover	5	A	0.05
56	EQS	Pushover	5	A	0.1
57	EQS	Pushover	5	A	0.2
58	EQS	Pushover	5	A	0.3
59	EQS	Pushover	5	A	0.4
60	EQS	Pushover	5	A	1.79
61	EQS	Pushover	5	A	4.47
62	EQS	Pushover	5	A	7.15
63	EQS	Pushover	10	A	0.05
64	EQS	Pushover	10	A	0.1
65	EQS	Pushover	10	A	0.2
66	EQS	Pushover	10	A	0.3
67	EQS	Pushover	10	A	0.4
68	EQS	Pushover	10	A	1.79
69	EQS	Pushover	10	A	4.47
70	EQS	Pushover	10	A	7.15
71	EQS	Pushover	20	A	0.05
72	EQS	Pushover	20	A	0.1
73	EQS	Pushover	20	A	0.2
74	EQS	Pushover	20	A	0.3
75	EQS	Pushover	20	A	0.4
76	EQS	Pushover	20	A	1.79
77	EQS	Pushover	20	A	4.47
78	EQS	Pushover	20	A	7.15

Test Number.	Design	Test Type	Joint Thickness	Material Strength Combination	Overbearing Stress (MPa)
79	RAN	Compression	5	A	N/A
80	RAN	Compression	5	B	N/A
81	RAN	Compression	5	C	N/A
82	RAN	Compression	5	D	N/A
83	RAN	Compression	5	E	N/A
84	RAN	Compression	10	A	N/A
85	RAN	Compression	10	B	N/A
86	RAN	Compression	10	C	N/A
87	RAN	Compression	10	D	N/A
88	RAN	Compression	10	E	N/A
89	RAN	Compression	20	A	N/A
90	RAN	Compression	20	B	N/A
91	RAN	Compression	20	C	N/A
92	RAN	Compression	20	D	N/A
93	RAN	Compression	20	E	N/A
94	RAN	Pushover	5	A	0.05
95	RAN	Pushover	5	A	0.1
96	RAN	Pushover	5	A	0.2
97	RAN	Pushover	5	A	0.3
98	RAN	Pushover	5	A	0.4
99	RAN	Pushover	5	A	1.79
100	RAN	Pushover	5	A	4.47
101	RAN	Pushover	5	A	7.15
102	RAN	Pushover	10	A	0.05
103	RAN	Pushover	10	A	0.1
104	RAN	Pushover	10	A	0.2
105	RAN	Pushover	10	A	0.3
106	RAN	Pushover	10	A	0.4
107	RAN	Pushover	10	A	1.79
108	RAN	Pushover	10	A	4.47
109	RAN	Pushover	10	A	7.15
110	RAN	Pushover	20	A	0.05
111	RAN	Pushover	20	A	0.1
112	RAN	Pushover	20	A	0.2
113	RAN	Pushover	20	A	0.3
114	RAN	Pushover	20	A	0.4
115	RAN	Pushover	20	A	1.79
116	RAN	Pushover	20	A	4.47
117	RAN	Pushover	20	A	7.15

The results of the investigation will be discussed in detail in the following chapters focussing on compression (Chapter 5) and pushover results (Chapter 6). Predictive expressions for stiffness and strength will be calibrated with the computational results in Chapter 7.

Chapter 5

Results of the Direct Compression Study on URM Wallettes

5.0 Introduction

This chapter will discuss the results of direct compression simulated tests that were conducted on 10 unique wallette specimens developed in ATENA 3D. The main purpose of these models is to illustrate through their differences, how the construction pattern and mortar to brick ratio in the wall affect the equivalent homogenized stress – strain response of masonry in uniaxial compression. Another purpose is to produce adequate volume of numerical results in order to calibrate the design equations provided by various design codes around the world. Through this correlation consistently derived, deformation and geometry dependent effective homogenized material properties will be extracted for seismic assessment of complete URM structural systems. A benefit of this work is that it may enable understanding of the constitutive behavior of masonry, supplement gaps in the laboratory test databases and illustrate the mechanistic behavior of masonry at advanced levels of deformation.

5.1 Review of Specimens

The direct compression component of this finite element investigation includes all 10 of the specimen patterns developed in Chapter 4 as shown in Figure 5-1 below.

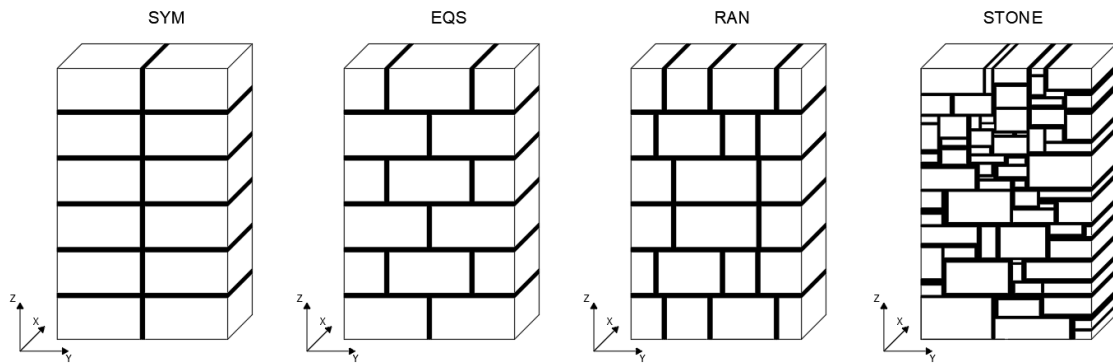


Figure 5-1: Wallette designs.

The nomenclature used to define the parametric variations of the specimens is as follows: design name – J – mortar joint thickness in mm. For example, the name SYMJ10 is used to represent the stack-bond specimen with a global mortar joint thickness of 10 mm. This nomenclature will be used when referring to all 10 of the wallette specimens. For the pushover analyses the nomenclature will be modified and will include -OB- and the applied overbearing stress to the end of the original name.

5.2 Review of Loading Conditions

The collection of 10 analyses which will be discussed are all direct compression tests. The top surface of each specimen has been assigned a prescribed deformation of 35 mm in the negative Z direction. This quantity of displacement is sufficient to compress the specimens until failure and will be utilized throughout the investigation.

5.3 SYM Results

Figure 5-2 depicts the variations of the stacked bond wallettes obtained by varying the joint thickness.

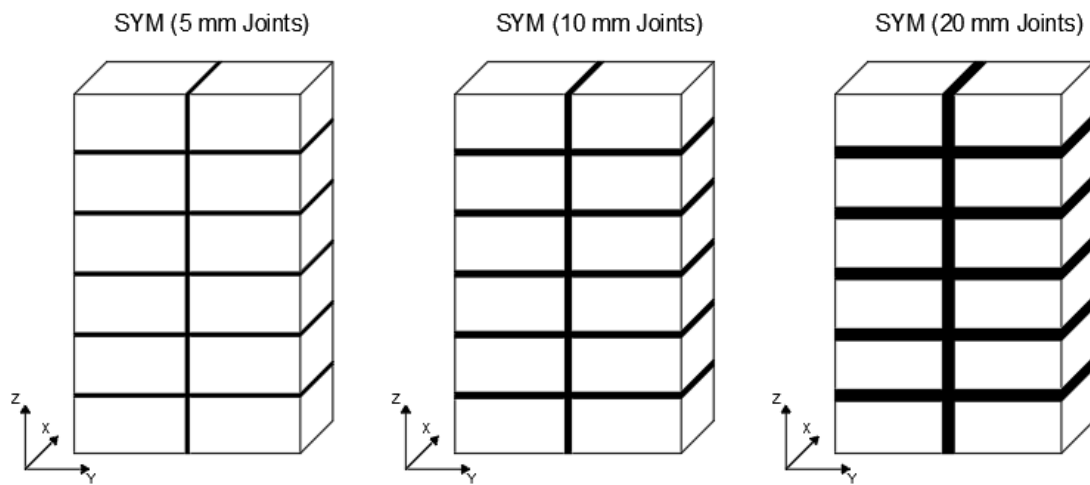


Figure 5-2: SYM specimens.

After conducting the compression analyses on the trio of SYM specimens, the results answered the questions regarding the effects of altering the global mortar joint thickness. As was discussed, the main difference between the three specimens was the mortar joint thickness and since the exterior dimensions of the specimens were held constant, the varying joint thicknesses affected the ratios between masonry bricks to mortar in each specimen. Figure 5-3 below presents the failure states for each of the three SYM specimens. The progression of failure for all three specimens can be found in Appendix B.

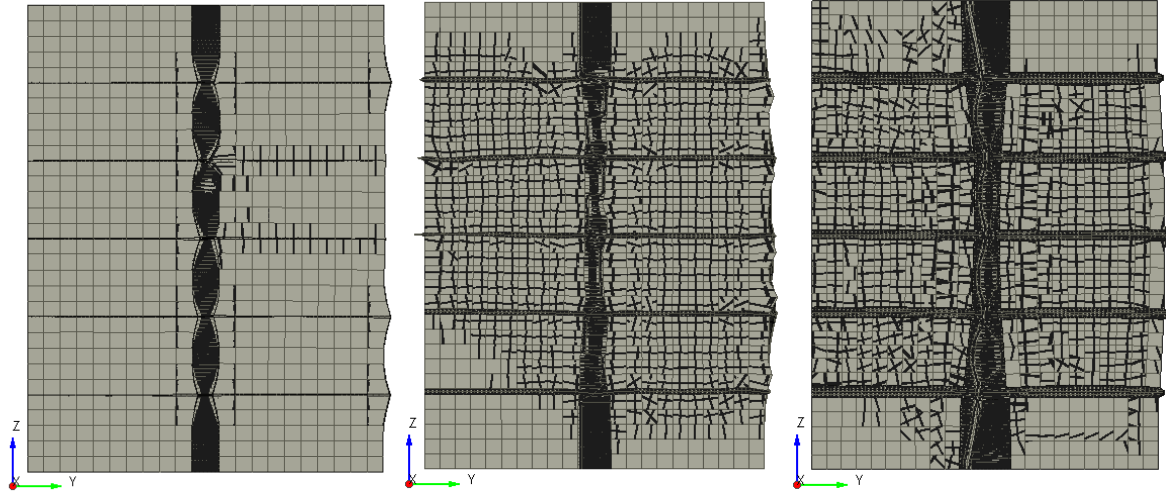


Figure 5-3: [A] Deformed-shape SYMJ5 ($\epsilon = 0.00372 \text{ mm/mm}$), [B] Deformed-shape SYMJ10 ($\epsilon = 0.0042 \text{ mm/mm}$), [C] Deformed-shape SYMJ20 ($\epsilon = 0.00743 \text{ mm/mm}$)

The failure states shown above present the condition of the wallette specimens at failure. At failure it was observed that the mortar bed joints had failed and were completely crushed by the surrounding masonry units. Furthermore, the head mortar joints cracked and propagated height wise throughout the specimens causing a division between the two columns of bricks. Finally, the commencement of bulging along the right edge was observed. The bulging occurred along the right edge because that surface of the specimen does not lie on an axis of symmetry unlike the left edge. Overall, the level of damage suffered varies throughout each of the three specimens and the level of damage increased as the mortar joints thickness increased. The computed stress – strain diagrams are shown in Figure 5-4.

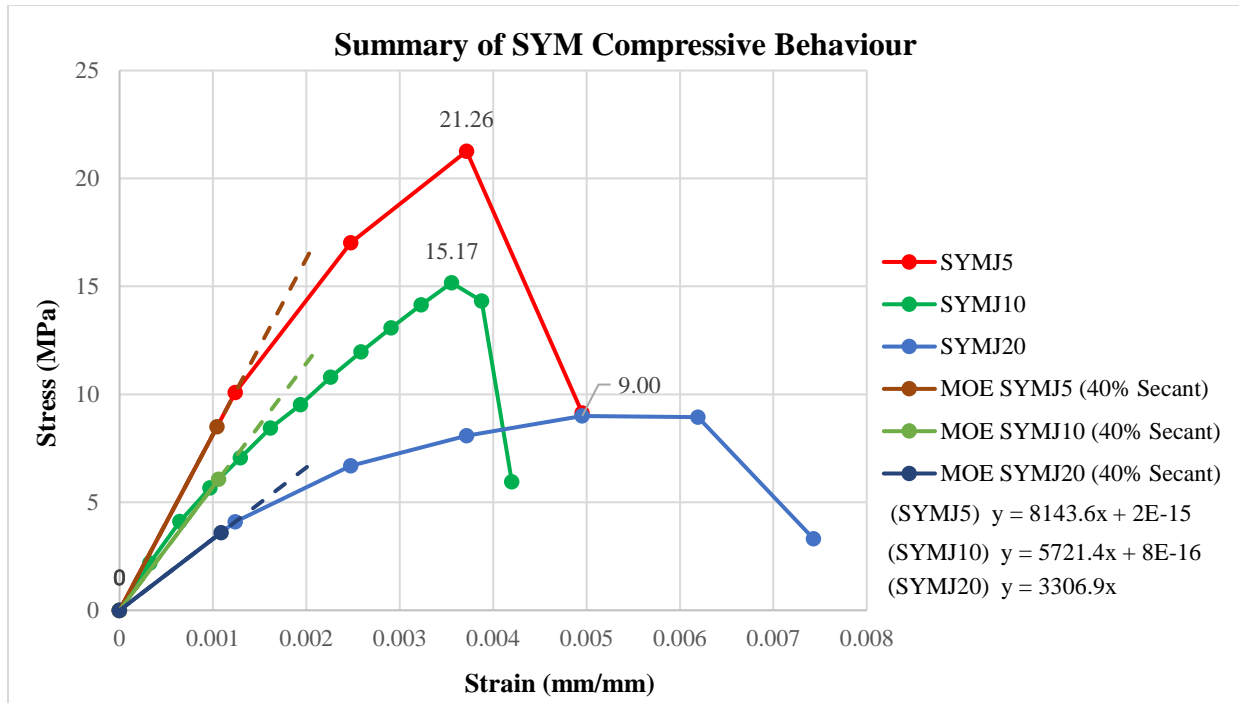


Figure 5-4: Summary of compression behaviour for SYM specimens.

When comparing the three specimens under compression, the results follow what was expected based on the design of the specimen. As shown in Figure 5-4, SYMJ5 has the highest compressive strength of 21.26 MPa, followed by SYMJ10 with a compressive strength of 15.17 MPa and finally SYMJ20 with a compressive strength of 9.00 MPa. The total loss of compressive strength starting from SYMJ5 was a 28.36% deduction when increasing the mortar joints from 5 mm to 10 mm which corresponds to a 3% increase in mortar area. The compressive strength is further reduced by 40.67% when increasing the joint thicknesses from 10 mm to 20 mm which is a percent increase in area of 7%. What this data determines is that each 1 mm increase in the global mortar joint thickness reduces the compressive strength as shown in Figure 5-6 below.

The modulus of elasticity was calculated for each of the three specimens by computed the slope of a secant between 0% and 40% of the peak compressive strength as shown above in Figure 5-4. The resulting values were 8143.6 MPa for SYMJ5, 5721.4 MPa for SYMJ10 and 3306.9 MPa for SYMJ20. The modulus of elasticity was also computed using a second method recommended by CSA D.4.6 which is to take the slope of the secant between points 5% and 33% of the compressive strength as shown in Figure 5-5 below (CSA, 2010).

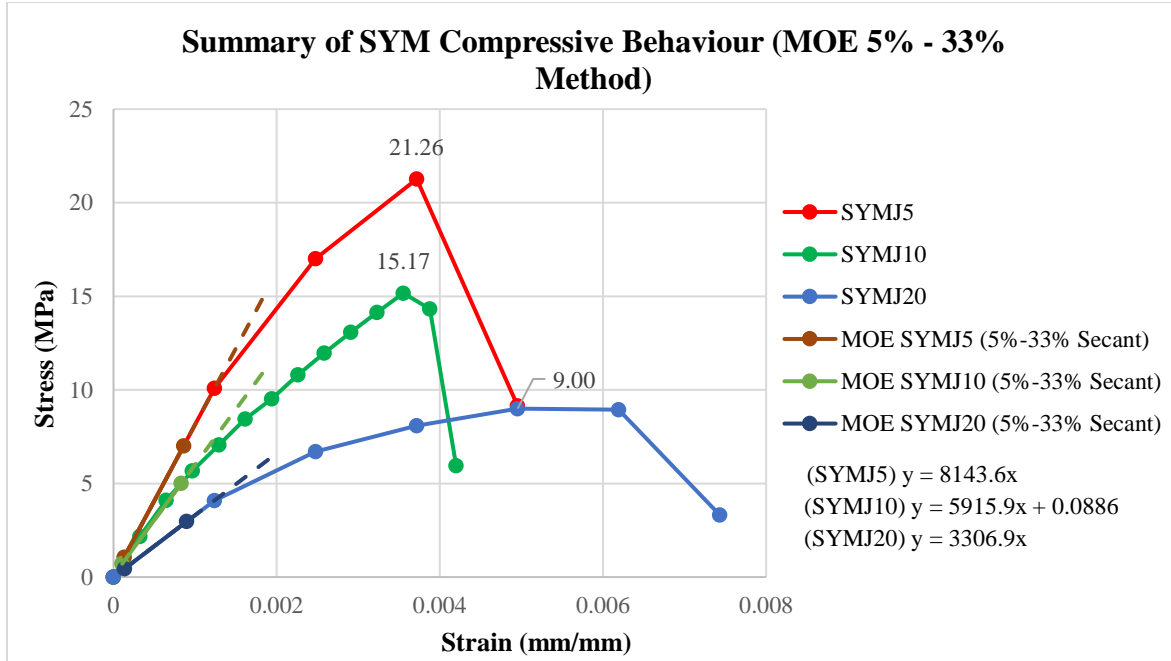


Figure 5-5: Summary of compression behaviour for SYM specimens (MOE 5%-33% Method)

Using the second method, the computed values for the modulus of elasticity were 8143.6 MPa for SYMJ5, 5915.9 MPa for SYMJ10 and 3306.9 MPa for SYMJ20. For the purpose of seismic assessment, the values were reduced by 50%.

Figure 5-6 below presents the relationship between the global mortar joint thickness and the compressive strength of the specimen.

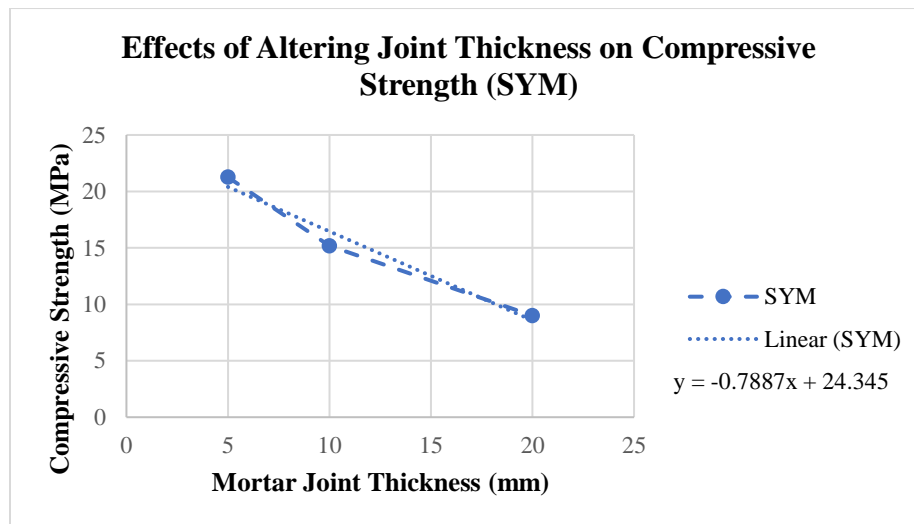


Figure 5-6: Relationship between Mortar Joint Thickness and Compressive Strength (SYM).

Figure 5-6 above presents the relationship between the global mortar joint thickness and the compressive strength of the specimen. The relationship was plotted for the three SYM

specimens and a linear relationship was assumed to define a trendline for the data. Using the trendline equation $y = -0.7887x + 24.345$, each 1 mm increase in the global mortar joint thickness causes approximately a 0.7887 MPa or 3.86% reduction in compressive strength. Although the performance improved as the mortar joint thickness decreased, the results should not be interpreted as it is more beneficial to reduce the thickness even further than 5 mm, as the thicknesses would begin to fall outside of the minimum values for many of the design codes.

5.4 EQS Results

The second set of specimens analyzed was the equivalently staggered (EQS) set. The EQS design utilizes an arrangement which is common to modern day brick construction, which has each head mortar joint above and below the center of a masonry brick as shown in Figure 5-7 below.

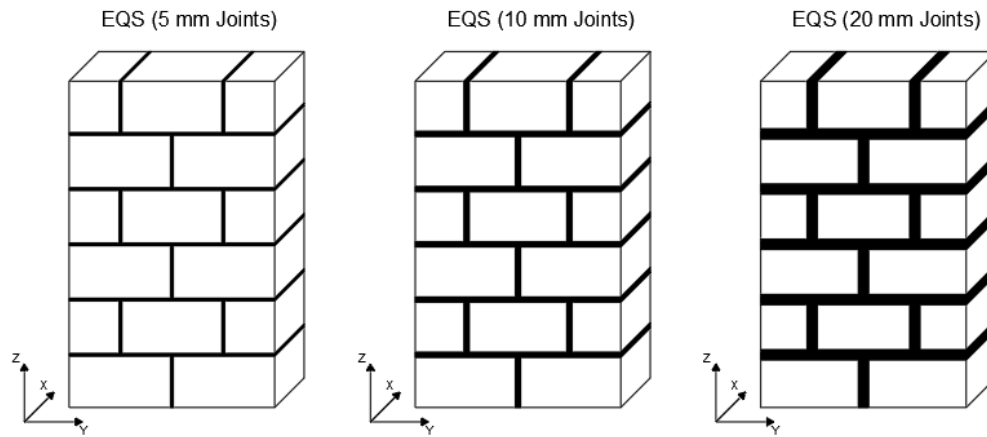


Figure 5-7: EQS Specimens.

The EQS design was tested using 5 mm, 10 mm, and 20 mm joints as was done in the SYM portion of the investigation. The conclusion of the EQS analyses brought answers to the speculation regarding trends within the behaviour of the group of specimens. Figure 5-8 below presents the failure states for each of the three SYM specimens. The progression of failure for all three specimens can be found in Appendix B.

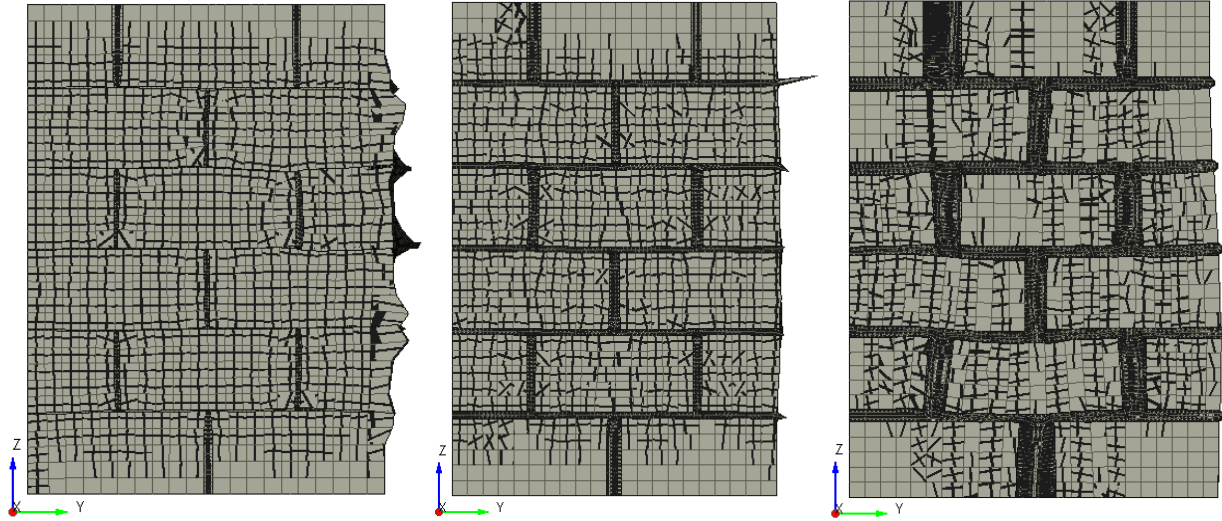


Figure 5-8: [A] Deformed-shape EQSJ5 ($\epsilon = 0.00485$ mm/mm), [B] Deformed-shape EQSJ10 ($\epsilon = 0.00485$ mm/mm), [C] Deformed-shape EQSJ20 ($\epsilon = 0.00582$ mm/mm)

The Figure above presents the state of each of the three specimens at failure. The main observations are that the masonry bricks located on the courses with two full bricks were completely severed at the center which is where the head joints lie above and below specifically in the EQSJ20 model. These cracks occurred since the mortar has a lower compressive strength. Therefore, the prescribed deformation causes the mortar joints to displace more than the bricks, causing significant stress to the center of the bricks which lie below a head joint along the line of the two head joints in the top course of the specimen. It was originally expected that the EQS specimens with lower global joint thicknesses would have a higher compressive strength than the specimens with thicker mortar joints. As shown in Figure 5-9 below, the speculation was true and EQS5 did have the highest compressive strength of the three specimens.

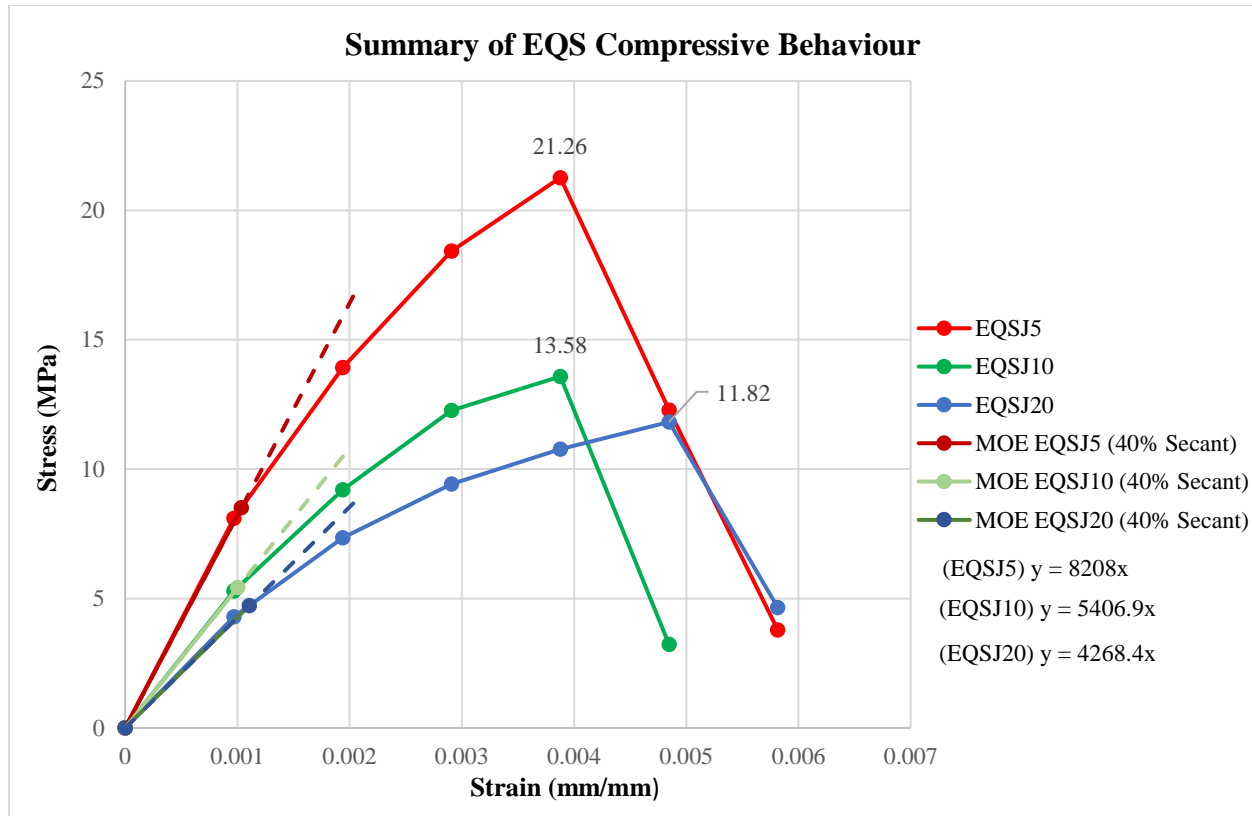


Figure 5-9: Summary of compression behaviour for EQS specimens.

As shown above, EQSJ5 performed the best under compression with a strength of 21.26 MPa. The thicker jointed specimens did not perform as well with EQSJ10 having a compressive strength of 13.58 MPa and EQSJ20 with 11.82 MPa. Overall, increasing the mortar thickness did affect the outcome of the analysis. Increasing the global joint thickness from 5 mm to 10 mm decreased the observed compressive strength by 36.12%. The compressive strength was further reduced when increasing the global joint thickness from 10 mm to 20 mm, which caused a strength decrease of 12.96%.

The modulus of elasticity was also computed for each of the three specimens first using the slope of the secant through 0% and 40% of the peak compressive strength of each specimen. The resultant values were 8208 MPa for EQSJ5, 5406.9 MPa for EQSJ10, and 4268.4 MPa for EQSJ20. The modulus of elasticity was also computed using the 5%-33% method as shown in Figure 5-10 below.

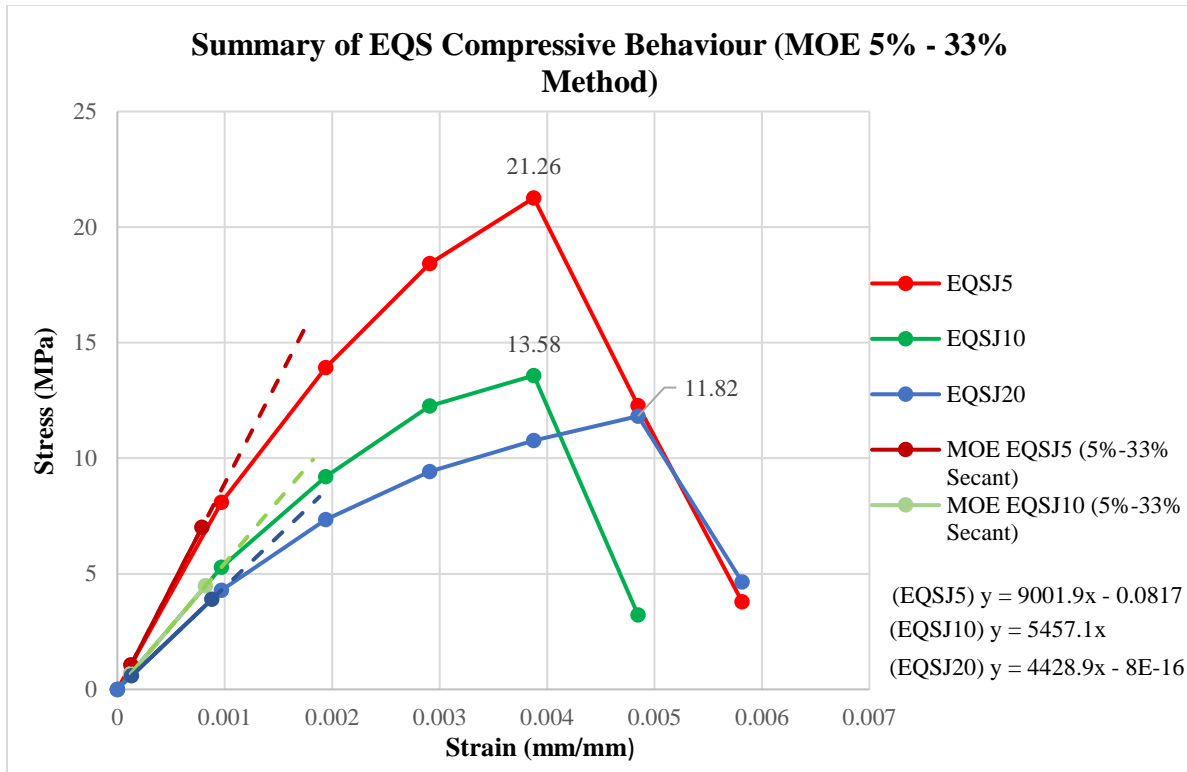


Figure 5-10: Summary of compression behaviour for EQS specimens (MOE 5%-33% Method)

As shown above, the modulus of elasticity was also computed for each specimen using the second method. The resultant values were 9001.9 MPa for EQSJ5, 5457.1 MPa for EQSJ10, and 4428.9 MPa for EQSJ20. The values differed from the first method since the secants are being drawn between different points therefore causing the slope to change. Figure 5-11 below presents the relationship between the mortar joints thickness and the decreasing compressive strength.

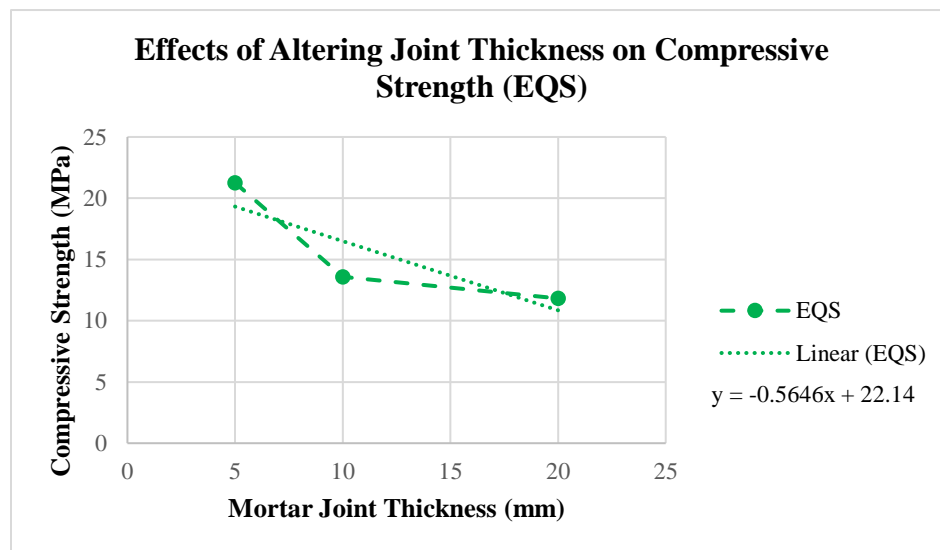


Figure 5-11: Relationship between Mortar Joint Thickness and Compressive Strength (EQS).

Figure 5-11 presents the relationship between the mortar joints thickness and the decreasing compressive strength. To compute intermediate values a linear relationship was assumed to produce the trendline formula $y = -0.5646x + 22.14$. Using said formula, it was determined that each 1 mm increase in the global mortar joint thickness caused approximately a 0.5646 MPa or 2.92% decrease in the compressive strength of the specimen. This trend is for the assumed linear relationship assigned for the data set. It should be noted that the rate that the compressive strength decreased was significantly higher from 5 mm to 10 mm then from 10 mm to 20 mm.

5.5 RAN Results

The final set of specimens analyzed of the three original designs was the RAN group. The RAN design as mentioned utilizes no set pattern or arrangement and places the bricks as random as possible within the specimen as shown in Figure 5-12 below.

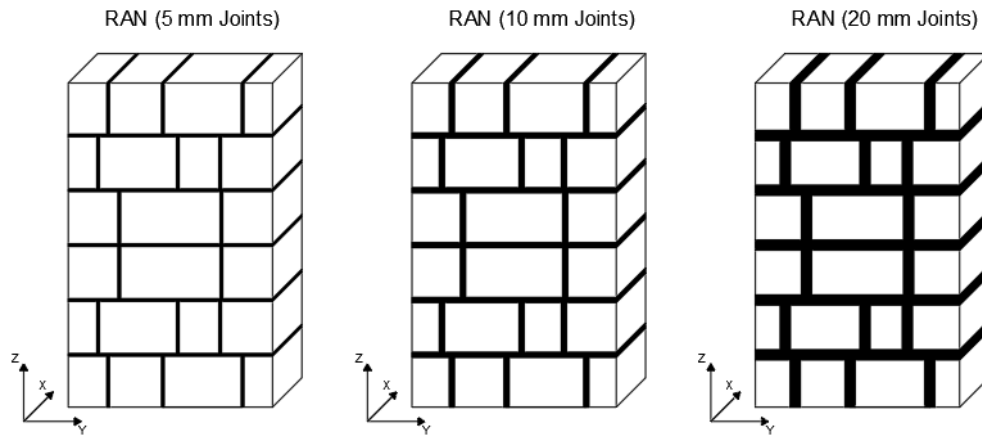


Figure 5-12: RAN Specimens.

This design is more aligned to common historic practices and promotes unpredictable load patterns and distribution unlike the SYM and EQS specimens. The only portion of the design that is not random is the height of the courses which were held constant throughout. On average each of the three RAN specimens contains a higher percentage of mortar than the EQS and SYM specimens at each of the three mortar thicknesses. Given the unpredictable load patterns and high quantities of mortar, it is expected that the RAN specimens will have lower compressive strengths than the other two designs. The failure states of the three RAN specimens are shown in Figure 5-13 below. The progression of failure for all three specimens can be found in Appendix B.

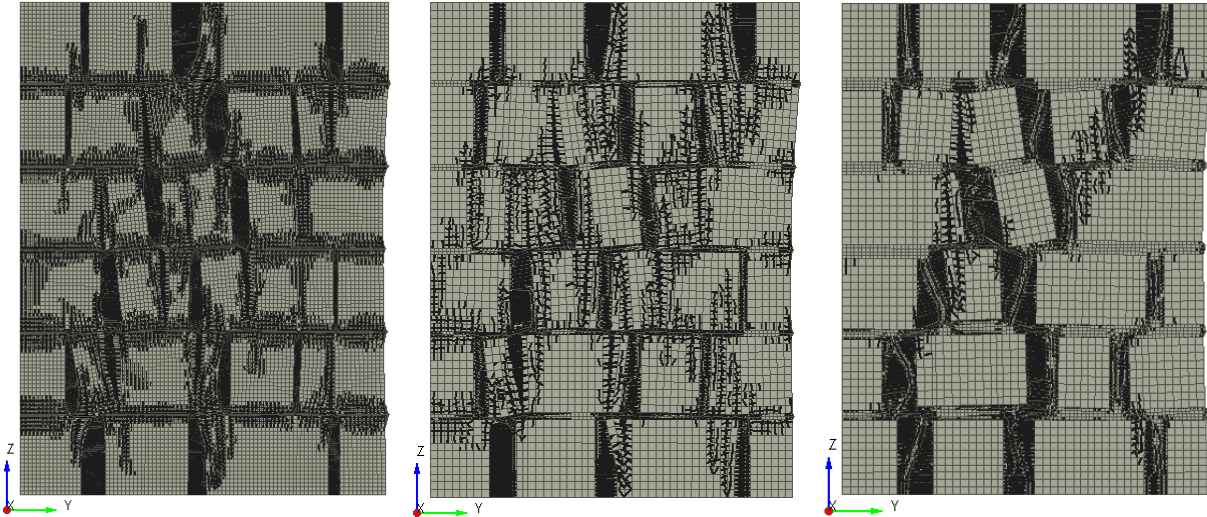


Figure 5-13: [A] Deformed-shape RANJ5 ($\varepsilon = 0.00323$ mm/mm), [B] Deformed-shape RANJ10 ($\varepsilon = 0.00269$ mm/mm), [C] Deformed-shape RANJ20 ($\varepsilon = 0.00269$ mm/mm)

At the end of the analysis severe opening occurred along the head joints, however, less damage was observed throughout the masonry bricks as the mortar joints thickness increased. The bricks experience less damage due to the large quantity of mortar within the specimen. Since the mortar is significantly weaker than the masonry bricks, it undergoes the greater part of the deformation throughout the specimen therefore causing the mortar to experience increased levels of damage.

The results of the RAN analyses showed two different trends than what was observed with the EQS and SYM results. The first difference was the relationship between the mortar joints thickness and the compressive strength. In the previous two designs the compressive strength decreased as the mortar joints thickness increased, however, as shown in Figure 5-14 this did not occur in the RAN analyses.

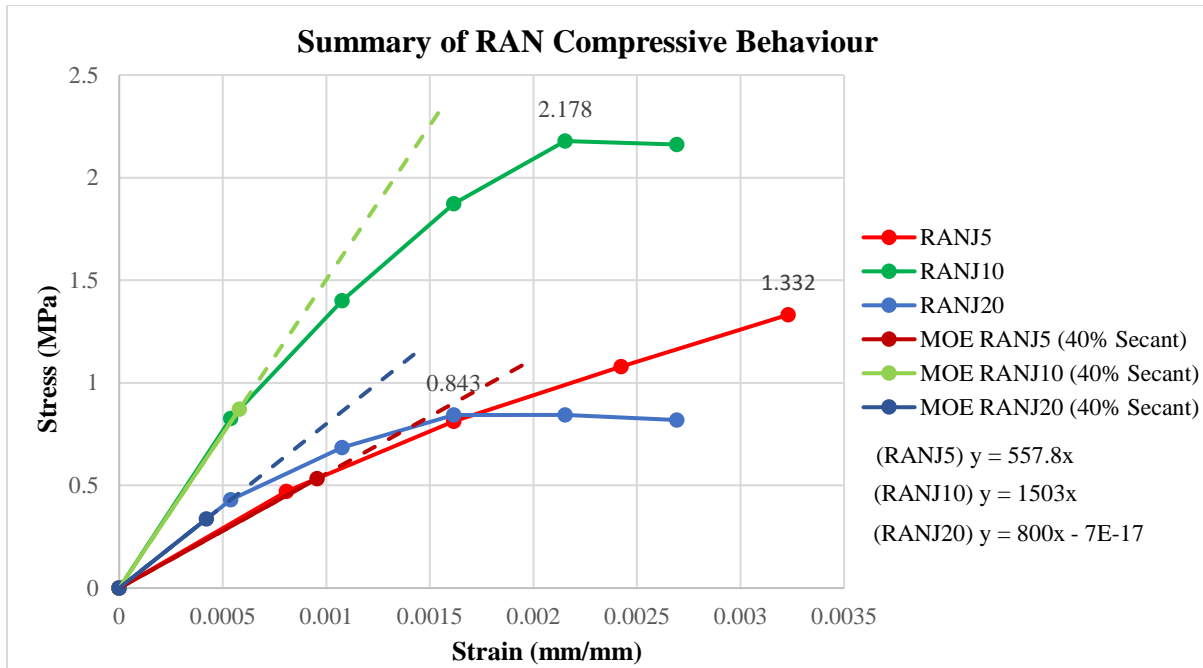


Figure 5-14: Summary of compression behaviour for RAN specimens.

The strongest of the three RAN specimens in compression was RANJ10 which had a compressive strength of 2.178 MPa, then followed by RANJ5 which had a compressive strength of 1.332 MPa, and finally RANJ20 which had a compressive strength of 0.843 MPa. The ordering in performance differs and instead of decreasing, the compressive strength initially increases by 63.91% when increasing the mortar joints thickness from 5 mm to 10 mm. The compressive strength then decreases by 62.48% when increasing the mortar joints thickness from 10 mm to 20 mm.

The modulus of elasticity was also computed for the RAN specimens. Using the 40% secant method the resulting values were 557.8 MPa for RANJ5, 1503 MPa for RANJ10, and 800 MPa for RANJ20. The values were also computed using the 5%-33% method as shown in Figure 5-15 below.

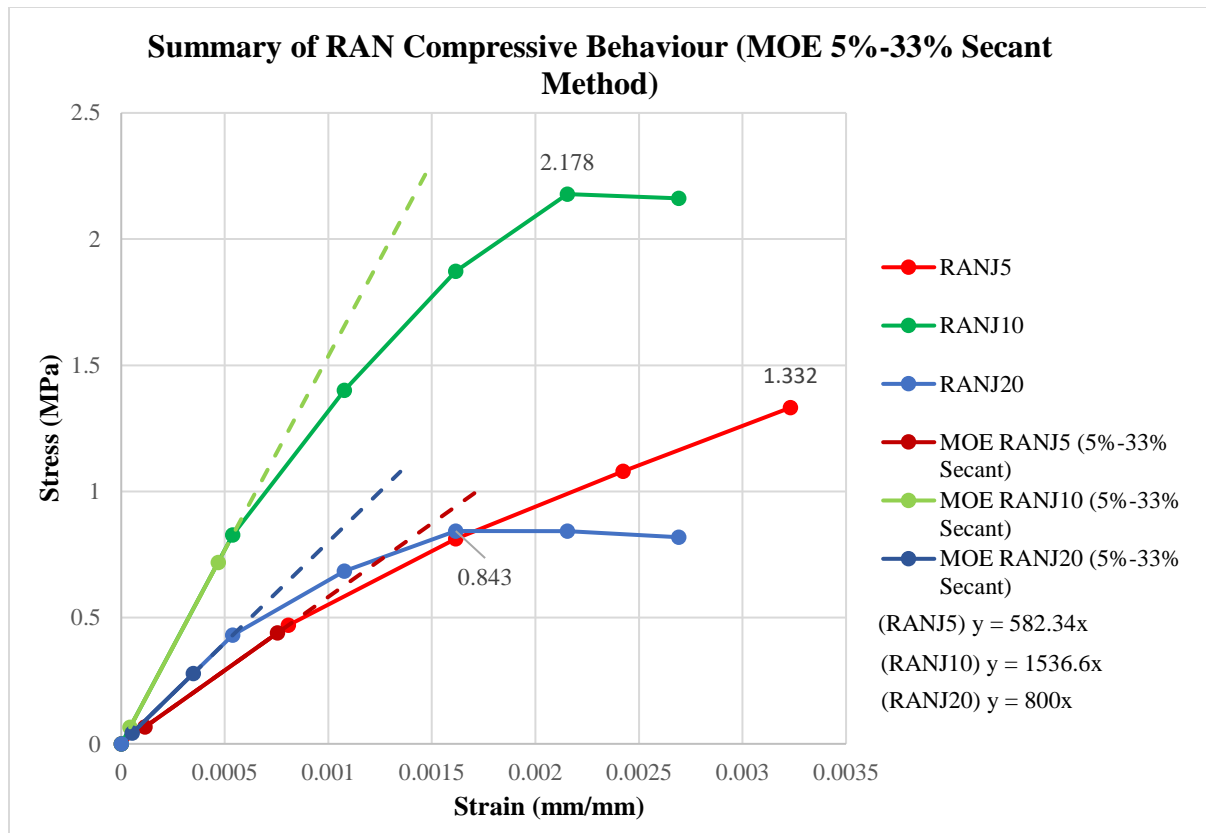


Figure 5-15: Summary of compression behaviour for SYM specimens (MOE 5%-33% Method)

Using the 5%-33% secant method, the resulting values for the modulus of elasticity were 582.34 MPa for RANJ5, 1536.6 MPa for RANJ10, and 800 MPa for RANJ20.

Figure 5-16 below represents the effects altering the mortar joints thickness had on the peak compressive strength.

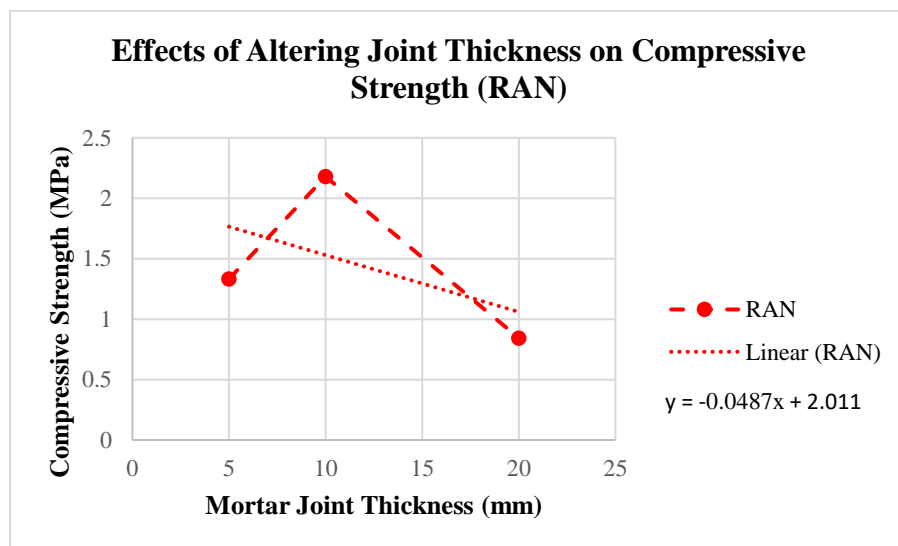


Figure 5-16: Relationship between Mortar Joint Thickness and Compressive Strength (RAN).

As shown in Figure 5-16, there is an increase in strength proceeded by a decrease as the mortar joints reach a thickness of 20 mm. Assuming a linear relationship along the data set, the overall trend of the strength remains decreasing as the mortar joints thickness increases. Using the formula $y = -0.0487x + 2.011$ from Figure 5-16, it is estimated that each 1 mm increase in joint thickness causes a 0.0487 MPa or 2.76% decrease in compressive strength.

5.6 STONE Results

The final compression analysis conducted in using the discussed loading conditions was on the stone design. The stone design utilizes a historic design approach where the sizes of the bricks vary both horizontally and vertically as shown in Figure 5-17 below.

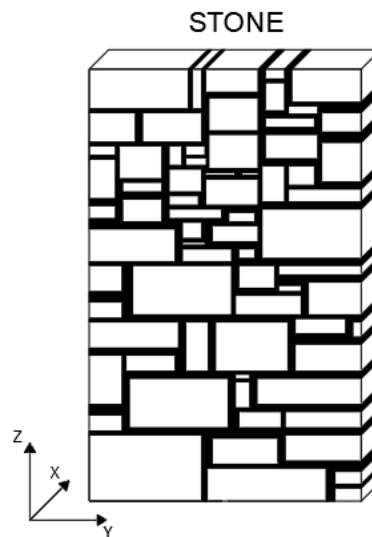


Figure 5-17: Stone Specimen

In addition to the varying brick sizes, the mortar joint thicknesses also vary throughout. This creates for complex load paths which could lead to significant cracking and a low compressive strength due to the arrangement of the mortar joints. The progression of the behaviour and the computed stress – strain diagram are shown in Figures 5-18 and 5-19 below.

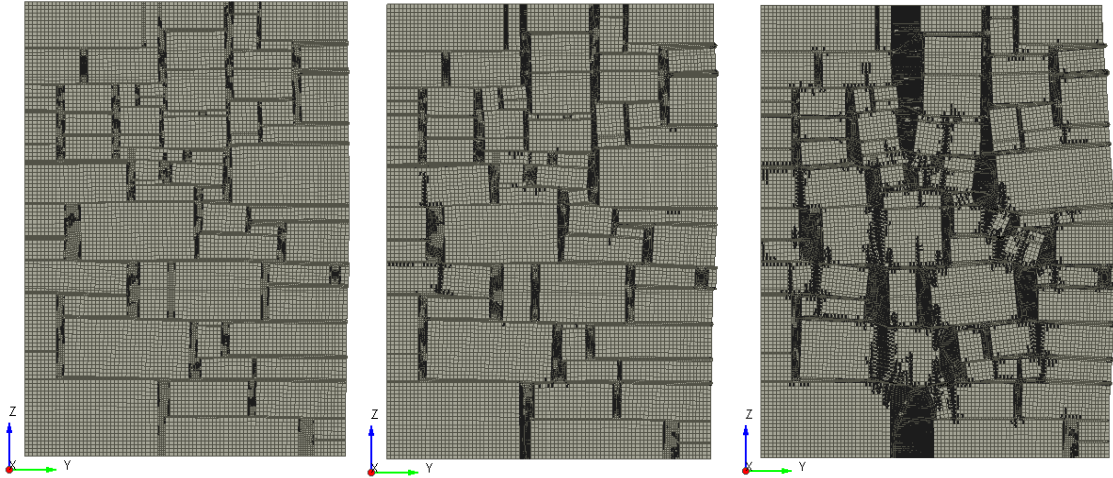


Figure 5-18: STONE, [A] Deformed-shape ($\epsilon = 0.000462$ mm/mm), [B] Deformed-shape ($\epsilon = 0.00138$ mm/mm), [C] Deformed-shape ($\epsilon = 0.00277$ mm/mm)

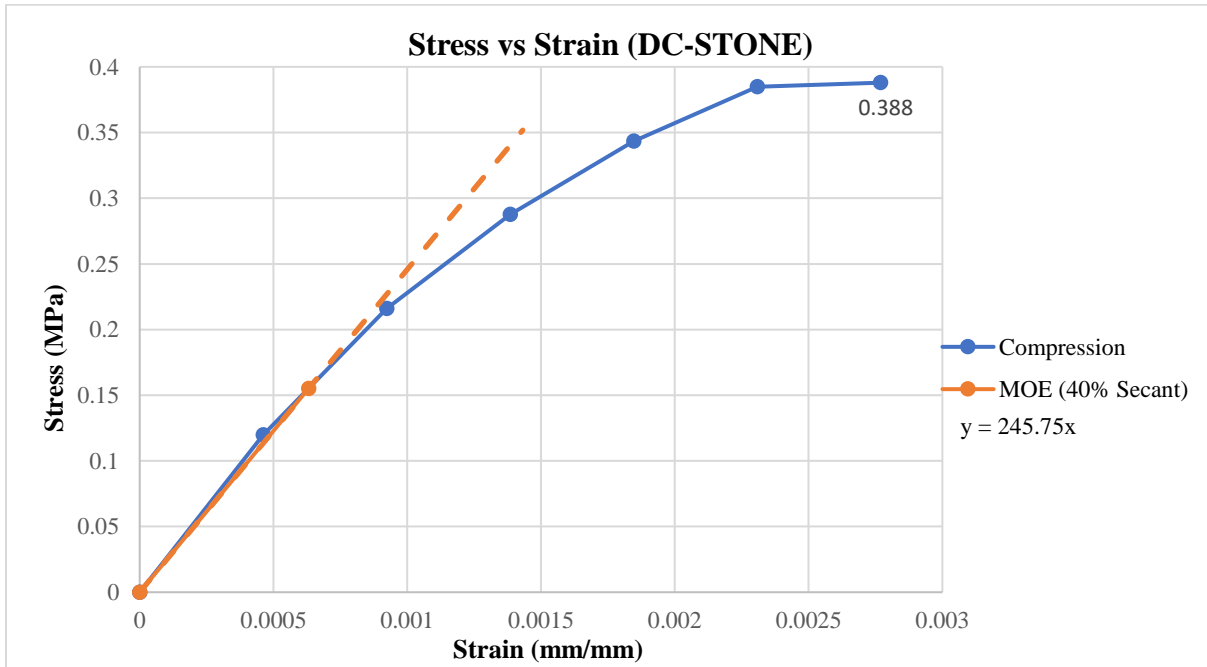


Figure 5-19: Stress - Strain diagram of STONE

During the early stages of the analysis, various head joints begin to crack and open causing the bricks with the specimen to translate shown by an axial strain of 0.000462 mm/mm in Figure 5-18 and the green marker in Figure 5-19. As the analysis progresses, the openings along the head joints continue to open and cause significant cracking and separation along the height of the specimen, specifically at along the center of the specimen commencing downwards from the top surface as shown at an axial strain of 0.00277 mm/mm in Figure 5-18. These openings cause significant damage and translation to the masonry bricks and cause the bulging effect observed

along the right edge at an axial strain of 0.00277 mm/mm. The damage caused by the head joints significantly reduced the strength of the specimen. At the peak represented by the red marker in Figure 5-19, the maximum displacement applied to the structure was 1.8 mm which equals a total load of 6.60 kN. The maximum load equals a 0.388 MPa compressive strength for the stone specimen which is significantly lower than the other three designs.

The MOE was also computed using the 40% and 5% to 33% secant methods for the stone specimen. The 40% method provided a MOE of 245.75 MPa, whereas the 5% to 33% method shown below in Figure 5-20 provided a MOE of 245.72 MPa.

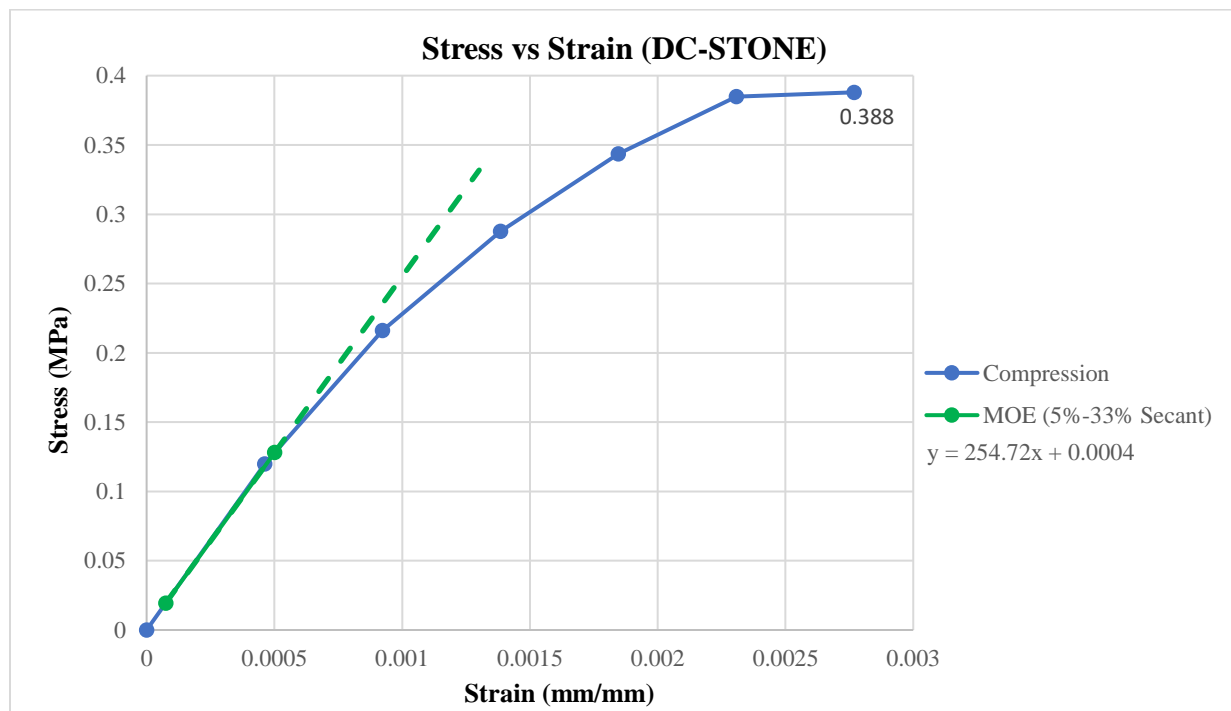


Figure 5-20: Stress - Strain diagram of STONE (5%-33% Secant Method)

The two MOE values were similar as the upper bound of both secants exceeded the elastic limit, however, the 40% method provided a lower MOE since its upper bound exceeded the elastic limit by 7% more than the 5% to 33% method therefore decreasing the slope of the secant.

5.7 Conclusions

After conducting all of the analyses on the 4 designs, it was determined that the designs with a set arrangement such as SYM and EQS performed better than the designs which replicated historic principles such as RAN and STONE. Figure 5-21 below compares the compressive behaviour of the 10 mm versions of each design.

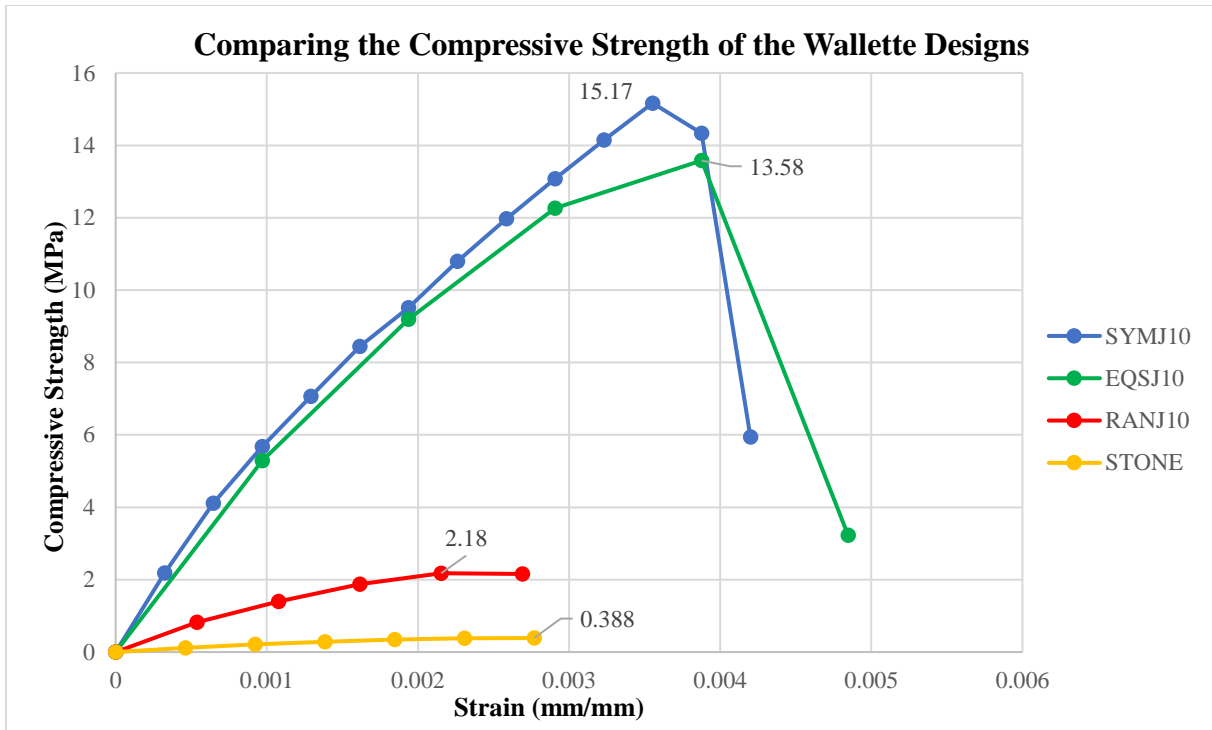


Figure 5-21: Comparing the compressive behaviour of each design.

Overall, the SYM design outperformed all the remaining designs with a compressive strength of 15.17 MPa, followed by EQSJ10 that had a strength of 13.58. The performance drop between the designs with assigned arrangements and the historic designs was 85.6% from EQSJ10 to RANJ10 which had a strength of 2.18 MPa. The strength further decreased by 82.2% to the STONE design which had a strength of 0.388 MPa. The data highlights the importance of the arrangement of head joints which is crucial to the performance of a wallette.

Chapter 6

Results of the Pushover Study on Wallette Specimens

6.0 Introduction

The second phase of the finite element modelling investigation involved analysing the 10 wallette specimens under increasing lateral displacement until failure. The following chapter will discuss the results obtained and the resulting resistance curves; these provide the basis for calculation of the effective elastic modulus for lateral deformation of the composite masonry. In the investigation a series of parametric studies on the effects of changes to the specimen design, including brick arrangement, mortar joint thickness and overbearing axial load were considered. Please note that Figures displaying the intermediate behaviour during each pushover analysis can be found in Appendix A.

6.1 Review of Loading Conditions

To push the specimen laterally, a total of 3 mm of prescribed deformation was applied as a point load at the center of the steel plate in the positive Y direction. The displacements were applied at a point to allow the displacement and reactions to be calculated from the monitoring point at the location of loading. The overbearing stress (OB) was applied as forces on the top surface corresponding to the normal compressive stress magnitudes shown in Table 6-1. Overall, eight different axial stress values were considered on each specimen as shown in Table 6-1 below.

Table 6-1: Summary of overbearing stress and values and suppressed conditions.

Test #	Overbearing Stress (MPa)	Suppressed Conditions
1	0.05	N/A
2	0.1	N/A
3	0.2	N/A
4	0.3	N/A
5	0.4	N/A
6	1.79	Sliding
7	4.47	Sliding
8	7.15	Sliding

It should be noted that the sliding mechanism of behavior was not suppressed for all eight OB values but only for Tests 6 through 8. This was done to see how axial precompression affects specifically the failure mechanism.

6.2 SYM Results

The SYM design contains on average the highest brick to mortar ratio among the designs which creates the expectation that SYM specimens would outperform the others under lateral loads. It is anticipated however, that the arrangement of the head joints will dominate failure with increasing lateral displacement, eventually separating the stacked masonry wall into independent and non-interacting columns.

6.2.1 SYMJ5

SYMJ5 is designed with a global joint thickness of 5 mm, meaning it has the highest percentage of bricks among the three SYM specimens. Therefore, it is expected that it would have the highest shear strength of the SYM specimens. The first set of analyses conducted were Tests 1 through 5 which involved OB values ranging from 0.05 MPa to 0.4 MPa. The final failure state of each of the 5 analyses is depicted in Figure 6-1 below.

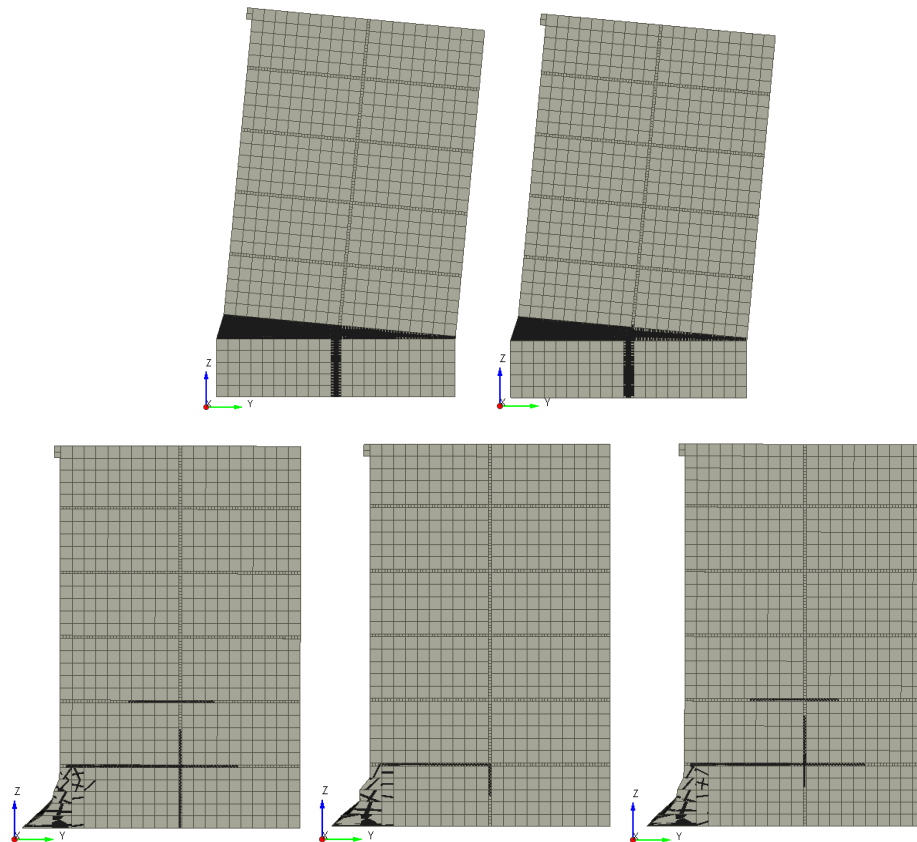


Figure 6-1: [A] Failure state SYMJ5 (0.05 MPa), [B] Failure state SYMJ5 (0.1 MPa), [C] Failure state SYMJ5 (0.2 MPa), [D] Failure state SYMJ5 (0.3 MPa), [E] Failure state SYMJ5 (0.4 MPa)

As shown in Figure 6-1 above, the failure patterns for the SYMJ5 specimens vary as the overbearing stress applied increases. Throughout the five tests two main failure patterns are observed. For Tests 1 and 2 with overbearing stresses of 0.05 MPa and 0.1 respectively, the damage is focused on the bed joint which connects the two courses of bricks at the bottom of the specimen as well as the head joint on the bottom course. The upper 5 courses are rotating about the rightmost edge of the cracked bed joint, with no other damage present to the bricks or mortar joints. As the applied overbearing stress increases from Tests 3 to 5, the failures are predominantly caused by shear deformation of the lower course bricks. The performance of the five tests varied and the results were dependent on the value of overbearing stress. The summary of pushover resistance curves is depicted in Figure 6-2 below.

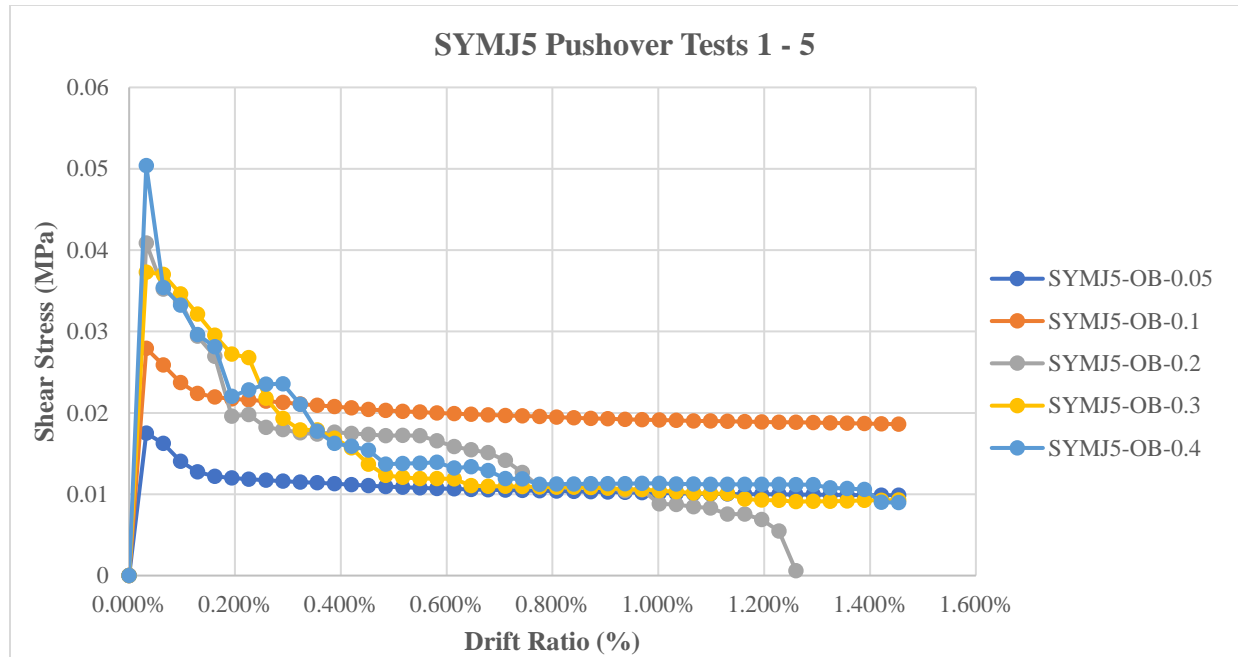


Figure 6-2: SYMJ5 Pushover Curves Tests 1-5

As shown in Figure 6-2 above, the tests which incorporated higher values of overbearing stress attained higher shear strengths during the pushover analyses. The highest shear stress observed was 0.0504 MPa and occurred at an overbearing stress of 0.4 MPa. The lowest lateral load observed was 0.0175 MPa and occurred at an overbearing stress of 0.05 MPa. Overall, the trend of the results indicate that the shear strength is directly proportional to the amount of overbearing stress applied to the specimen.

For the final three tests, labelled 6 to 8, the sliding action was suppressed by higher compressive stresses so as to ensure that the entirety of the specimen is engaged by eliminating tension stress cracking in the bed joints, and sliding does not dominate the behaviour. The failure states of Tests 6 through 8 of SYMJ5 are shown in Figure 6-3 below.

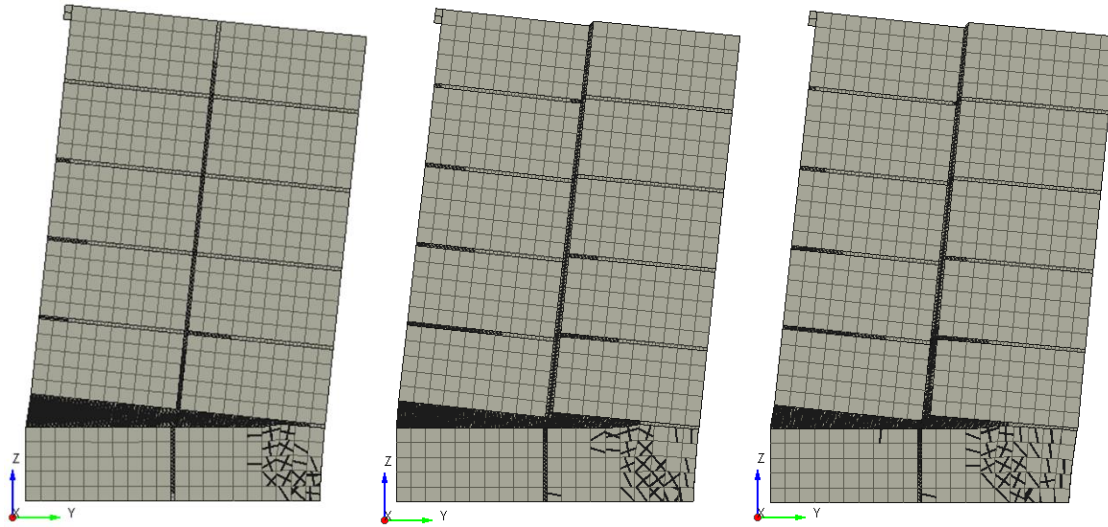


Figure 6-3: [A] Failure state SYMJ5 (1.79 MPa), [B] Failure state SYMJ5 (4.47 MPa), [C] Failure state SYMJ5 (7.15 MPa)

As shown in Figure 6-3, the failure states of Tests 6 through 8 differed greatly from Tests 1 through 5 due to the suppression of shear deformation in the lower course and sliding of the bed joint directly above. In Tests 6 through 8 toe crushing is the dominant mode of failure on account of the overturning action caused by the lateral forces. In addition to crushing, it can be observed that vertical sliding occurs along the head joint which spans the height of the specimen. The sliding increases as the applied overbearing stress increases. The sliding along the head joint occurs as the flexural resistance created by the applied overbearing stress limits the overturning action therefore causing internal dislocation in the specimen.

Overall, it was found that the performance and lateral capacity of the specimens increased as the overbearing stress increased as shown in Figure 6-4 below.

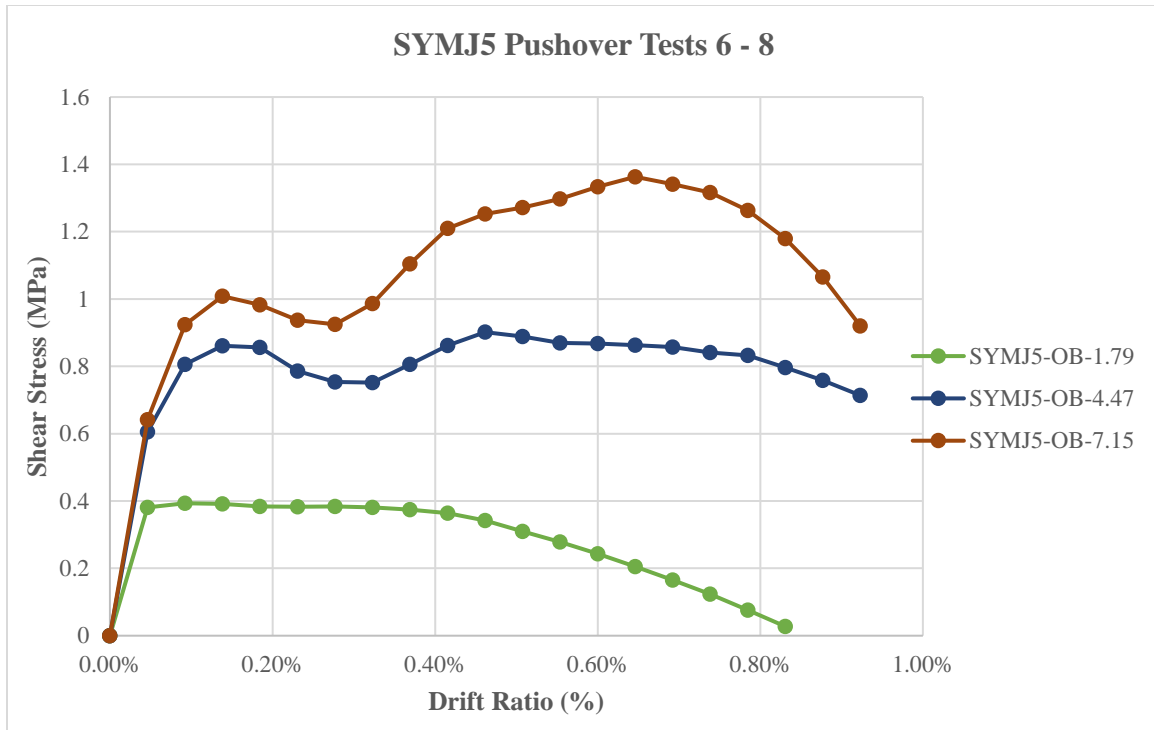


Figure 6-4: SYMJ5 Pushover Curves Tests 6-8

As described the overbearing stress plays an essential role in the lateral performance of an unreinforced wall. In Figure 6-4 above, the peak lateral capacity increased as the overbearing stress increased. Test 8 resulted in the highest shear strength of 1.01 MPa, followed by Test 7 with 0.862 MPa and lastly Test 6 with 0.393 MPa. Therefore, the results underscore the direct relationship between lateral capacity and overbearing strength.

6.2.2 SYMJ10

The second set of tests conducted was on the SYMJ10 specimen. This specimen utilizes 10 mm mortar joints throughout and has the second highest fraction of mortar joints among the SYM specimens. With the added mortar material which is an area of increased compliance, it is expected that SYMJ10 will have a lower lateral capacity at each of the 8 values of overbearing stress. The failure states of Tests 1 through 5 are shown in Figure 6-5 below.

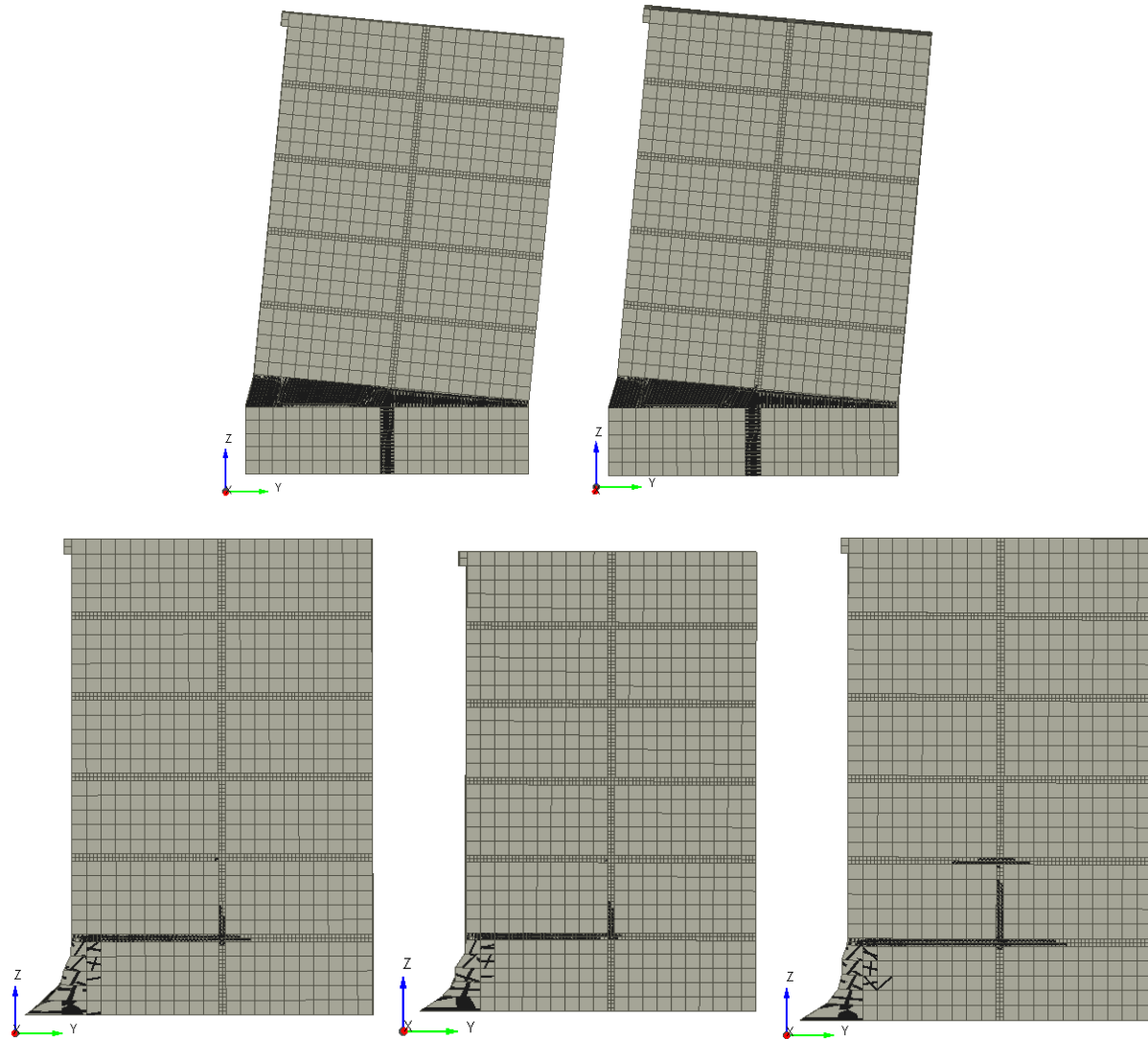


Figure 6-5: [A] Failure state SYMJ10 (0.05 MPa), [B] Failure state SYMJ10 (0.1 MPa), [C] Failure state SYMJ10 (0.2 MPa), [D] Failure state SYMJ10 (0.3 MPa), [E] Failure state SYMJ10 (0.4 MPa)

For Tests 1 and 2 a similar crack has opened along the bed joint which connects the bottom 2 courses as well as the head joint along the bottom course. The top 5 courses are overturning at the toe of the bed joint crack. For Tests 3 to 5, sliding is occurring with increasing cracking within the mortar joints as the overbearing stress increases. The lateral response for Tests 1 to 5 is shown in Figure 6-6 below.

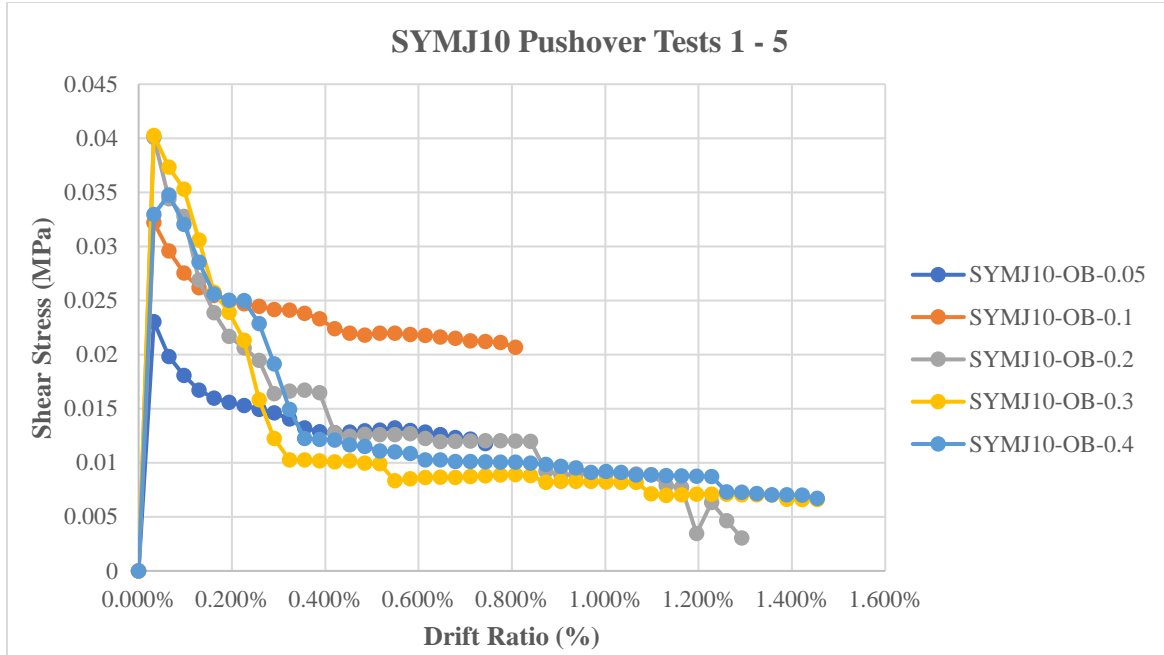


Figure 6-6: SYMJ10 Pushover Curves Tests 1-5

The lateral behaviour of SYMJ10 follows similar trends regarding the relationship between shear strength and overbearing stress. For Tests 1 to 5 as shown in Figure 6-6 above, the peak lateral capacity increases as the applied overbearing stress increases. The relationship holds true except for an applied overbearing stress of 0.4 MPa which reached a lower shear strength ($=0.0348$ MPa) as compared to the case with 0.3 MPa axial stress (shear strength = 0.0402 MPa). The reduction could be a result of the specimen surpassing its compressive strength limit under the proposed boundary conditions which allow for the sliding behaviour. The failure states of SYMJ10 Tests 5 to 8 are shown in Figure 6-7 below.

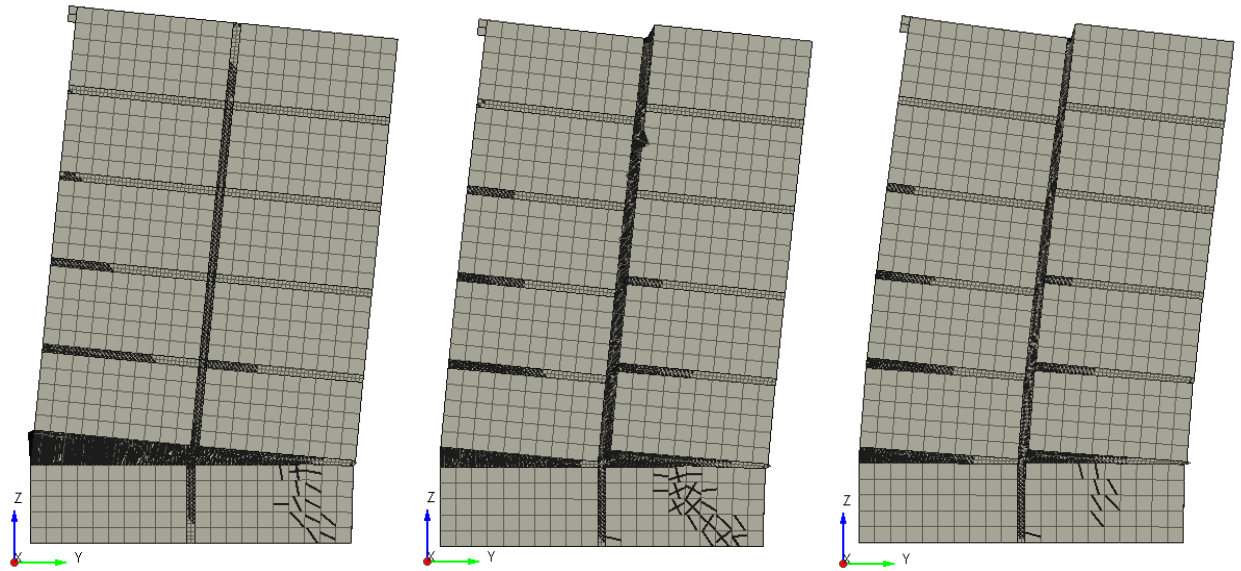


Figure 6-7: [A] Failure state SYMJ10 (1.79 MPa), [B] Failure state SYMJ10 (4.47 MPa), [C] Failure state SYMJ10 (7.15 MPa)

As shown above, crushing at the toe of the specimen is common to all three tests as the specimen is resisting overturning at the toe due to the applied lateral forces. Furthermore, the upper 5 courses of bricks are being pushed laterally, but as the overbearing stress increases, sliding begins to occur along the head joint which spans the height of the specimens. The severity of the sliding increases as the overbearing stress increases from Tests 6 to 8. The lateral resistance curves of the Tests 6-8 are shown in Figure 6-8 below.

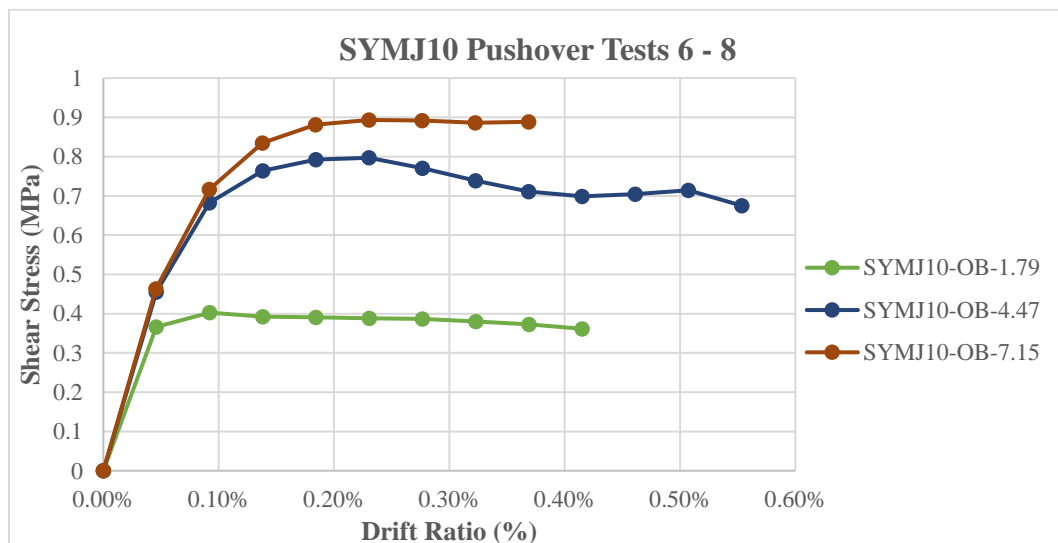


Figure 6-8: SYMJ10 Pushover Curves Tests 6-8

Figure 6-8 above presents the lateral pushover curves for Tests 5 through 8 of SYMJ10. The graph shows that the peak shear strength of the SYMJ10 specimen increases as the applied overbearing stress increases. The peak shear strength starts at a value of 0.402 MPa for an overbearing stress of 1.79 MPa. The strength then increases to 0.797 MPa for an overbearing stress of 4.47 MPa. The shear strength finally reaches its maximum value of 0.893 MPa for an overbearing stress of 7.15 MPa which was the highest value of overbearing stress considered.

6.2.3 SYMJ20

The final SYM specimen tested was SYMJ20 which contains a global mortar joint thickness of 20 mm. With the largest percentage of mortar among the three SYM specimens, it is expected that SYMJ20 will have the lowest shear strength after the concluding the collection of pushover analyses. The failure states and results of Tests 1-5 which allow for sliding to occur are shown in Figure 6-9 below.

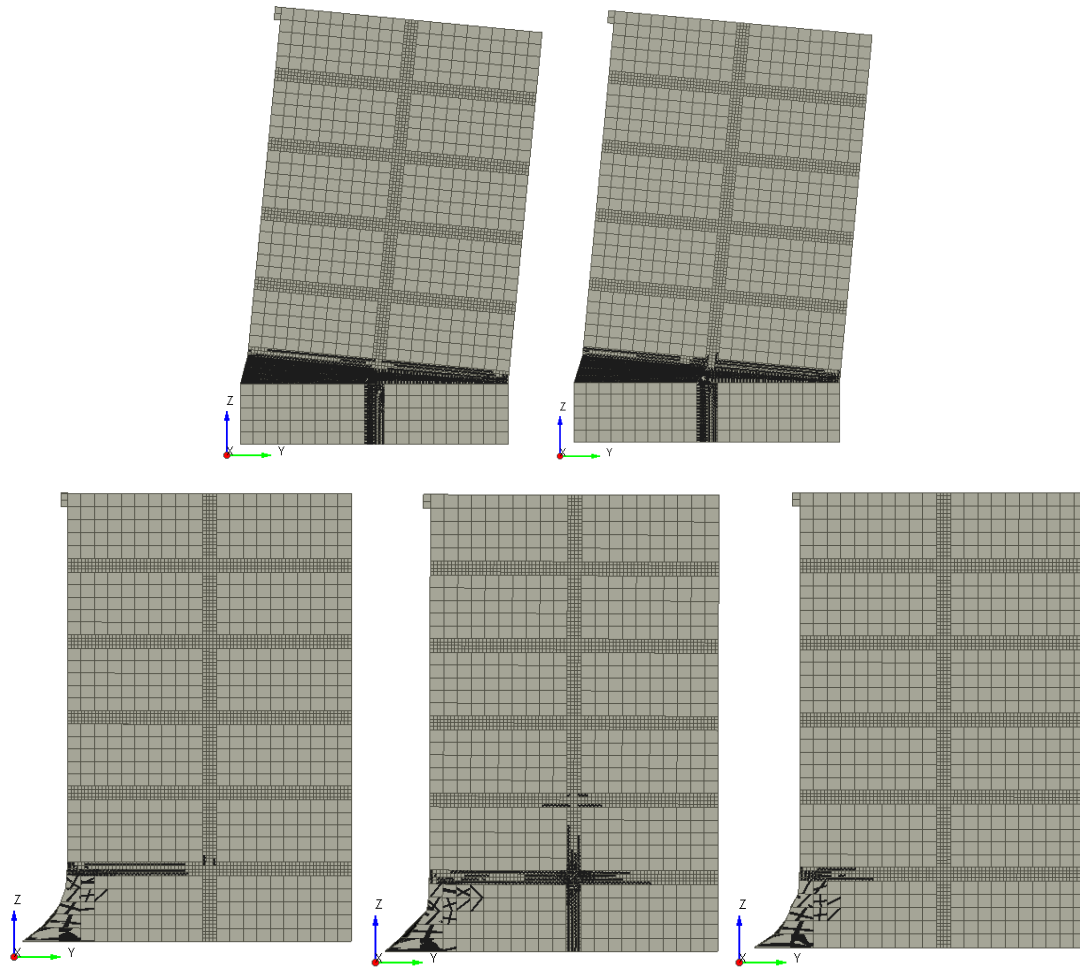


Figure 6-9: [A] Failure state SYMJ20 (0.05 MPa), [B] Failure state SYMJ20 (0.1 MPa), [C] Failure state SYMJ20 (0.2 MPa), [D] Failure state SYMJ20 (0.3 MPa), [E] Failure state SYMJ20 (0.4 MPa)

Throughout Tests 1 and 2 shown above in Figure 6-10, the failure state is primarily dominated a large crack along the bed joint between the lower 2 courses of bricks. The remainder of the specimen which lies above the bed joint is rotating about the toe of the joint leaving the upper portion of the specimen undamaged. Furthermore, the head joint between the bricks on the lowest course is opening as well. As the overbearing stress reaches the increased levels in Tests 3 through 5, the behaviour becomes dominated by sliding along the base of the specimen. This

failure mechanism is common to Tests 3 through 5 where sliding is occurring with increased levels of damage to the mortar joints common to the lower course of bricks. Figure 6-10 below presents the pushover curves for tests 1 through 5 of SYMJ20.

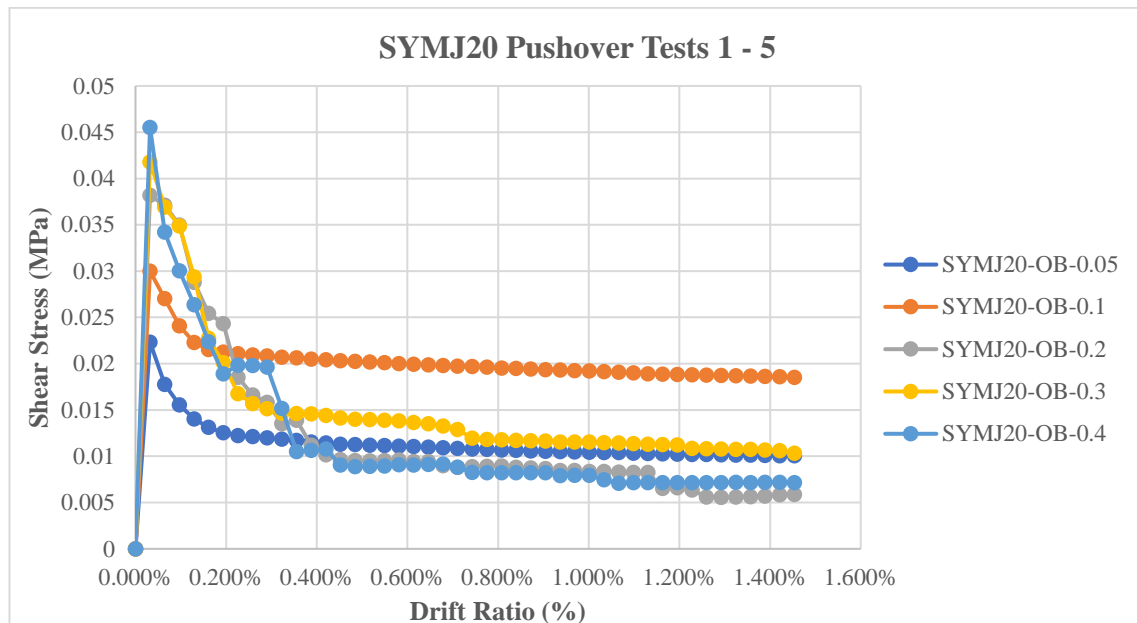


Figure 6-10: SYMJ20 Pushover Curves Tests 1-5

As shown in Figure 6-10 above, the peak lateral capacity computed for SYMJ20 increased as the applied axial overbearing stress increased. At an overbearing stress of 0.05 MPa the shear strength was 0.0223 MPa. The shear strength then increased to 0.03 MPa at an overbearing stress of 0.1 MPa. The capacity continued to increase to 0.0382 MPa and 0.0418 MPa under overbearing stresses of 0.2 MPa and 0.3 MPa respectively. The peak lateral capacity observed was 0.0455 MPa for an overbearing stress of 0.4 MPa. The results indicate a consistently increasing computed lateral capacity and shear strength for SYMJ20 as the overbearing stress increases.

The final three tests run on SYMJ20 present altered failure states as the sliding action was suppressed. The failure states for Tests 5 through 8 are shown in Figure 6-11 below; it is noted that damage is now entirely concentrated within the mortar joints, whereas the brick units rotate crushing the mortar sounding them without enduring any form of toe crushing.

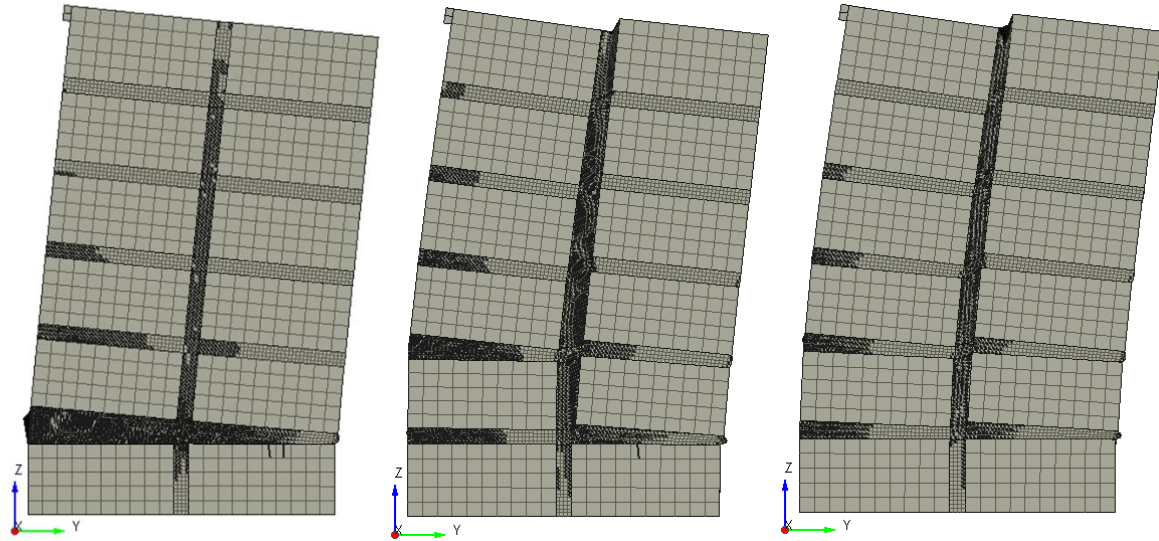


Figure 6-11: [A] Failure state SYMJ20 (1.79 MPa), [B] Failure state SYMJ20 (4.47 MPa), [C] Failure state SYMJ20 (7.15 MPa)

As shown in Figure 6-11, the behaviour of the specimens as they reach their failure point differs significantly from Tests 1 through 5. At failure, Test 6 which incorporates an overbearing stress of 1.79 MPa develops cracking along the head joint spanning the height of the specimen, and rotation along the bed joint between courses 1 and 2. As the overbearing stress increases in Tests 7 and 8, upper courses of the specimen are engaged, and sliding is occurring along the main head joint.

The lateral capacity computed for Tests 6 to 8 are shown in Figure 6-12 below.

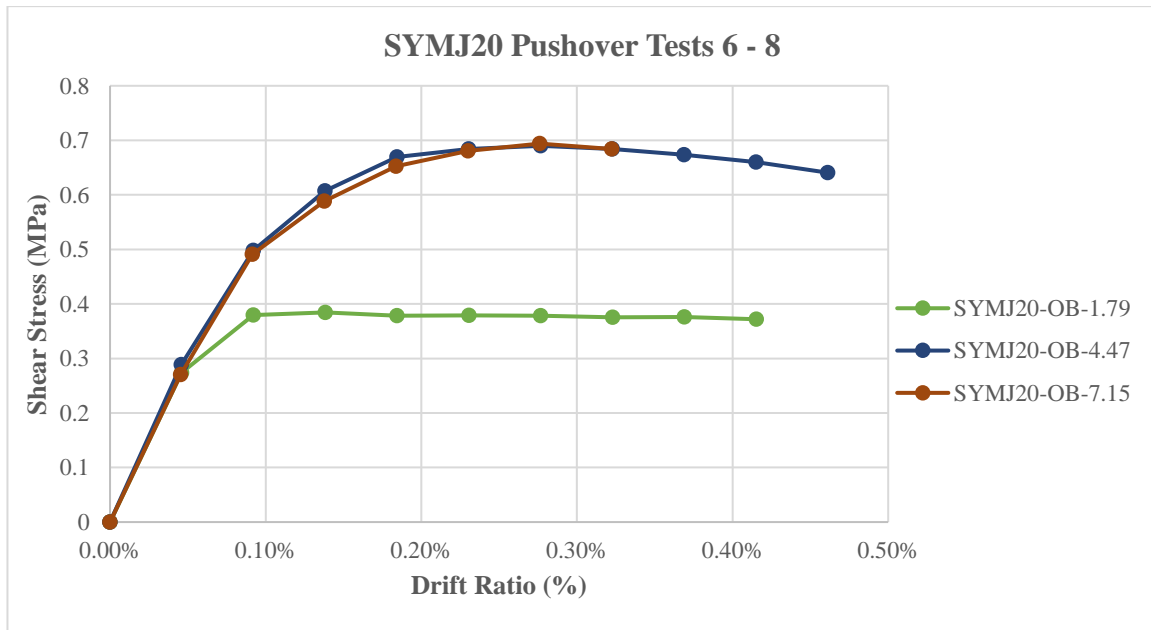


Figure 6-12: SYMJ20 Pushover Curves Tests 6-8

As shown in Figure 6-12 the capacity of the SYMJ20 specimen increases as the applied axial overbearing stress increases. At an overbearing stress of 1.79 MPa the computed shear strength was 0.384 MPa. When the overbearing stress was increased to 4.47 MPa the shear strength increased to 0.690 MPa. Finally, when the overbearing stress reached a peak value of 7.15 MPa, the shear strength further increased to 0.694 MPa. The computed results show that the shear strength is increasing consistently with the axial overbearing stress.

6.2.4 SYM Summary

Throughout the SYM pushover analyses, the two main objectives were to study the relationship between shear strength and overbearing stress, as well as to obtain the characteristic lateral load resistance curves for the wall elements. The effect of the relative fraction of mortar and brick units within the specimen on the computed shear strength was also of interest. Figure 6-13 below presents the interaction diagram of the three analyzed SYM specimens. Shear strength values were computed by dividing the peak lateral capacity for each of the analyses by the cross-sectional area of the XZ plane where the lateral load was applied which were then normalized with the peak compressive strength for each specimen.

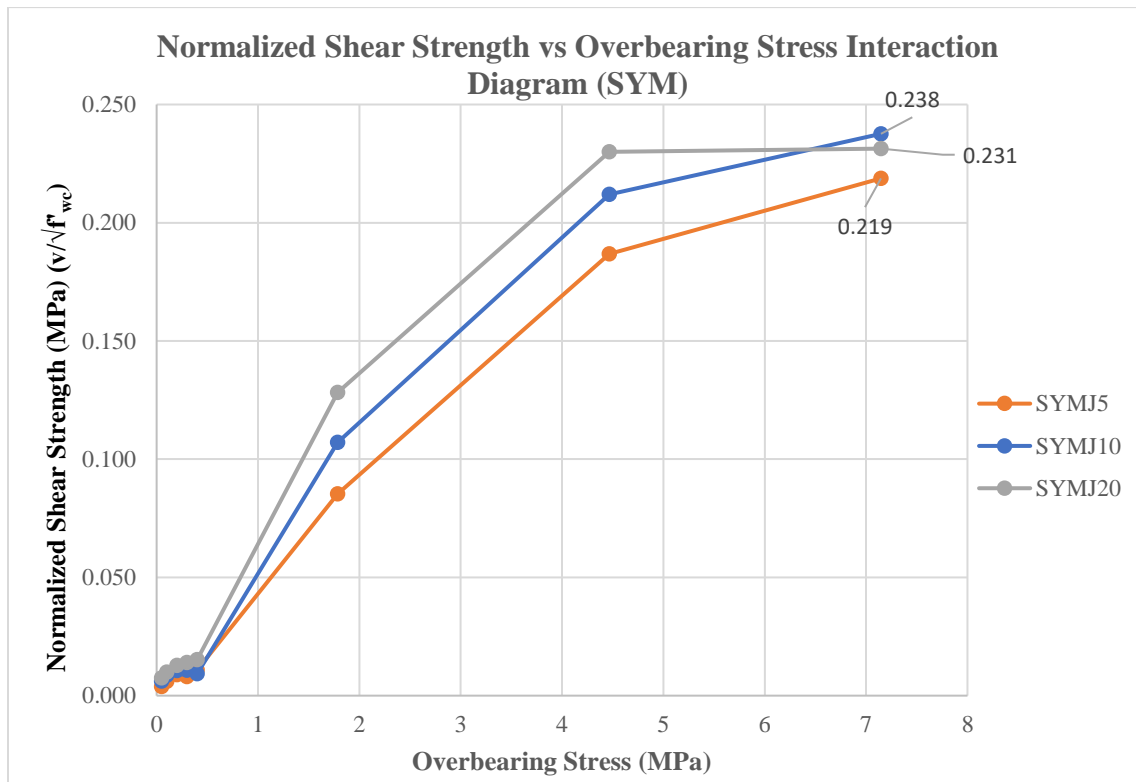


Figure 6-13: Summary of SYM Results (Pushover)

The interaction diagram illustrates there a nonlinear dependence of shear strength on overbearing stress: beyond a limit the material yields, and no further strength increase is possible. Decreasing the global mortar joint thickness increased the peak shear strength of the specimen. However, when normalized it was found that thicker mortar joints translated to higher normalized shear strength values. As shown in Figure 6-13, for a global joint thickness of 10 mm the peak normalized shear strength was 0.238 MPa. When the global joint thickness was decreased to 5 mm the peak normalized shear strength increased by 7.98% to 0.219 MPa. The results of the lateral investigation on the collection of SYM specimens illustrate that walls with a significant mortar ratio are primarily controlled by the weaker mechanical properties of the mortar joints.

6.3 EQS Results

The second set of lateral pushover analyses conducted was on the EQS specimens. Under compression, the EQS performed second best of the remaining three patterns in performance due to the lateral spacing of the head joints. Therefore, it is expected that the EQS specimens will perform well under lateral loading.

6.3.1 EQSJ5

The first set of EQS lateral analyses were conducted on the EQSJ5 specimen. This wallette utilizes a global mortar joint thickness of 5 mm, meaning EQSJ5 has the highest percent area of masonry bricks and the highest compressive strength from among the 3 EQS specimens. With the higher compressive strength, it is expected that EQSJ5 will have the highest lateral capacity and shear strength due to the higher levels of axial overbearing stress it can support.

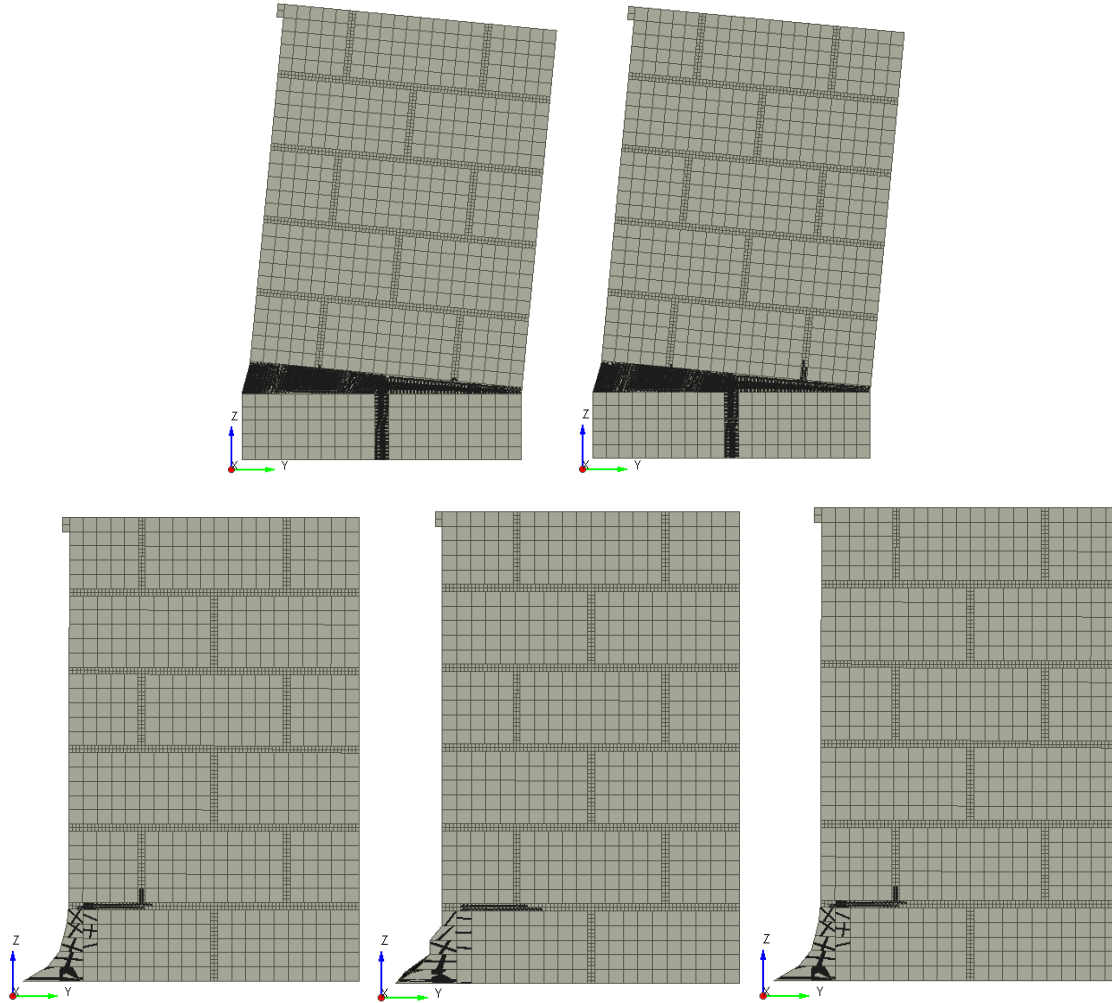


Figure 6-14: [A] Failure state EQSJ5 (0.05 MPa), [B] Failure state EQSJ5 (0.1 MPa), [C] Failure state EQSJ5 (0.2 MPa), [D] Failure state EQSJ5 (0.3 MPa), [E] Failure state EQSJ5 (0.4 MPa)

Figure 6-14 above presents the failure states of Tests 1 through 5 of EQSJ5. In Tests 1 and 2 where the overbearing stress reaches a maximum of 0.1 MPa, cracking is occurring on the bed joint between the lower two courses and the upper 5 courses are rotating about the toe of the cracked bed joint. As the overbearing stress increases in Tests 3 through 5, the main source of failure is sliding along the heel of the specimen.

The lateral responses of EQSJ5 shown in Figure 6-15 below, do not follow the trends observed for the SYM specimens where lateral strength increased continuously with the applied overbearing stress.

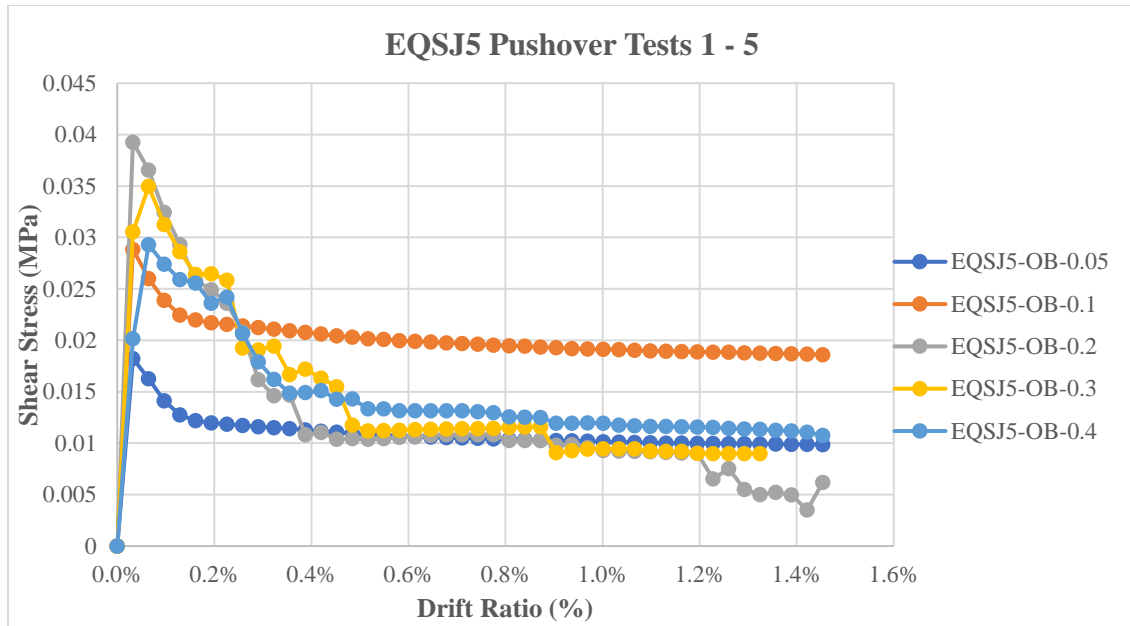


Figure 6-15: EQSJ5 Pushover Curves Tests 1-5

The collection of lateral pushover curves for EQSJ5 shown above in Figure 6-15 outline an alternate trend within the data. The lowest peak shear stress occurs at an overbearing stress of 0.05 MPa and equals 0.0182 MPa. At an overbearing stress of 0.1 MPa, the shear stress increases to 0.0288 MPa. The shear stress then reaches its peak of 0.0392 MPa at an overbearing stress of 0.2 MPa. The shear stress then decreases to values of 0.0350 MPa and 0.0293 MPa at overbearing stress of 0.3 MPa and 0.4 MPa respectively. As the overbearing stress reaches the increased values observed in Tests 6 through 8, different failure states are observed as shown in Figure 6-16 below.

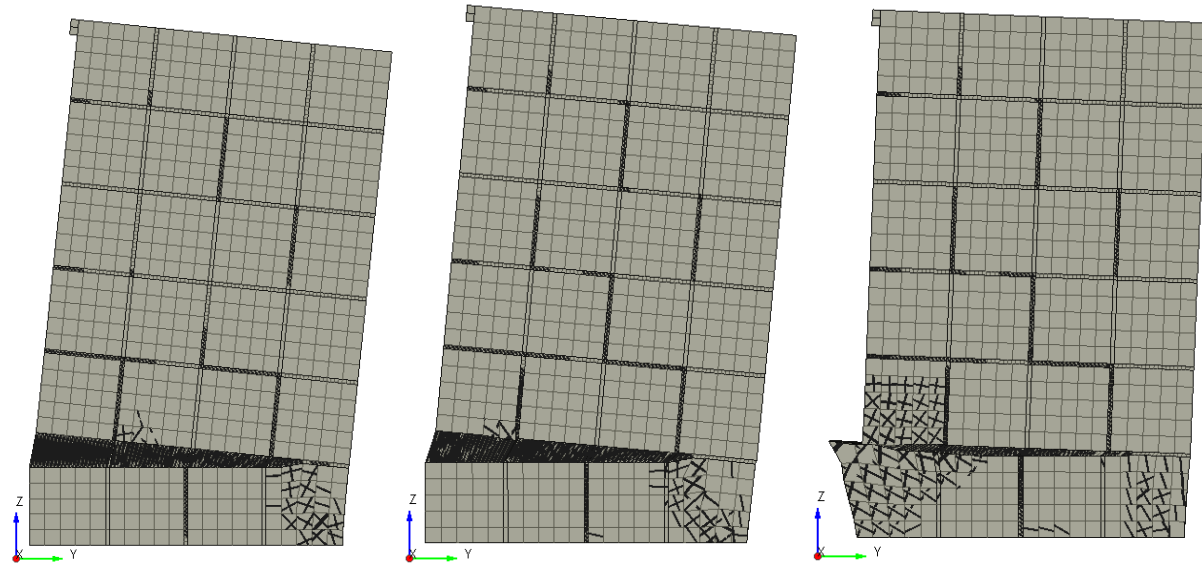


Figure 6-16: [A] Failure state EQSJ5 (1.79 MPa), [B] Failure state EQSJ5 (4.47 MPa), [C] Failure state EQSJ5 (7.15 MPa)

At failure, large cracks form at the toe of the specimen which increase in severity with the overbearing stress. Cracking and rotation occurs along the head joint between the lower two courses of masonry bricks. Finally, stair step cracking is observed with increased severity throughout the final three tests. Stair step cracking serves as an indicator that the entire specimen is engaging in the lateral action. The lateral responses show a consistent trend in the relationship between lateral capacity versus overbearing stress and is shown in Figure 6-17 below.

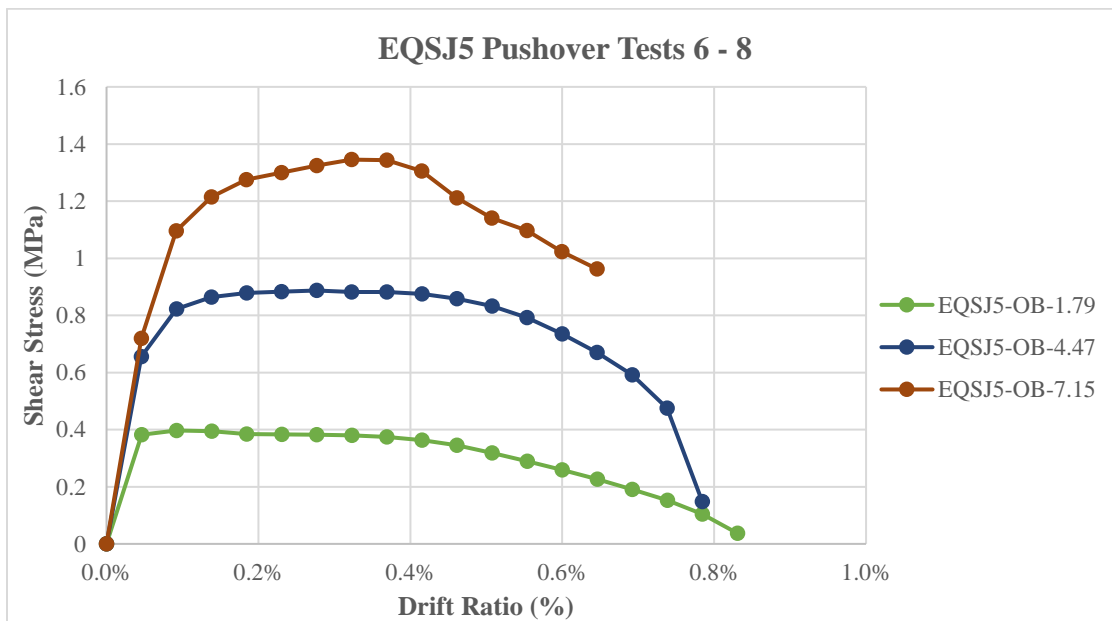


Figure 6-17: EQSJ5 Pushover Curves Tests 6-8

As shown above, lateral strength and therefore shear resistance varies depending on the quantity of overbearing stress applied to the specimen. The shear stress begins at a value of 0.397 MPa for an overbearing stress of 1.79 MPa; it increases to 0.887 MPa for an overbearing stress of 4.47 MPa and reaches its peak value of 1.345 MPa at an overbearing stress of 7.15 MPa.

6.3.2 EQSJ10

The second set of analyses were conducted on the EQSJ10 specimen. This specimen utilizes a global mortar joint thickness of 10 mm. With the additional mortar in the specimen, it is expected that the lateral capacity will decrease from the EQSJ5 results.

The failure states shown in Figure 6-18 is consistent with the observations from the previous set of EQS analyses.

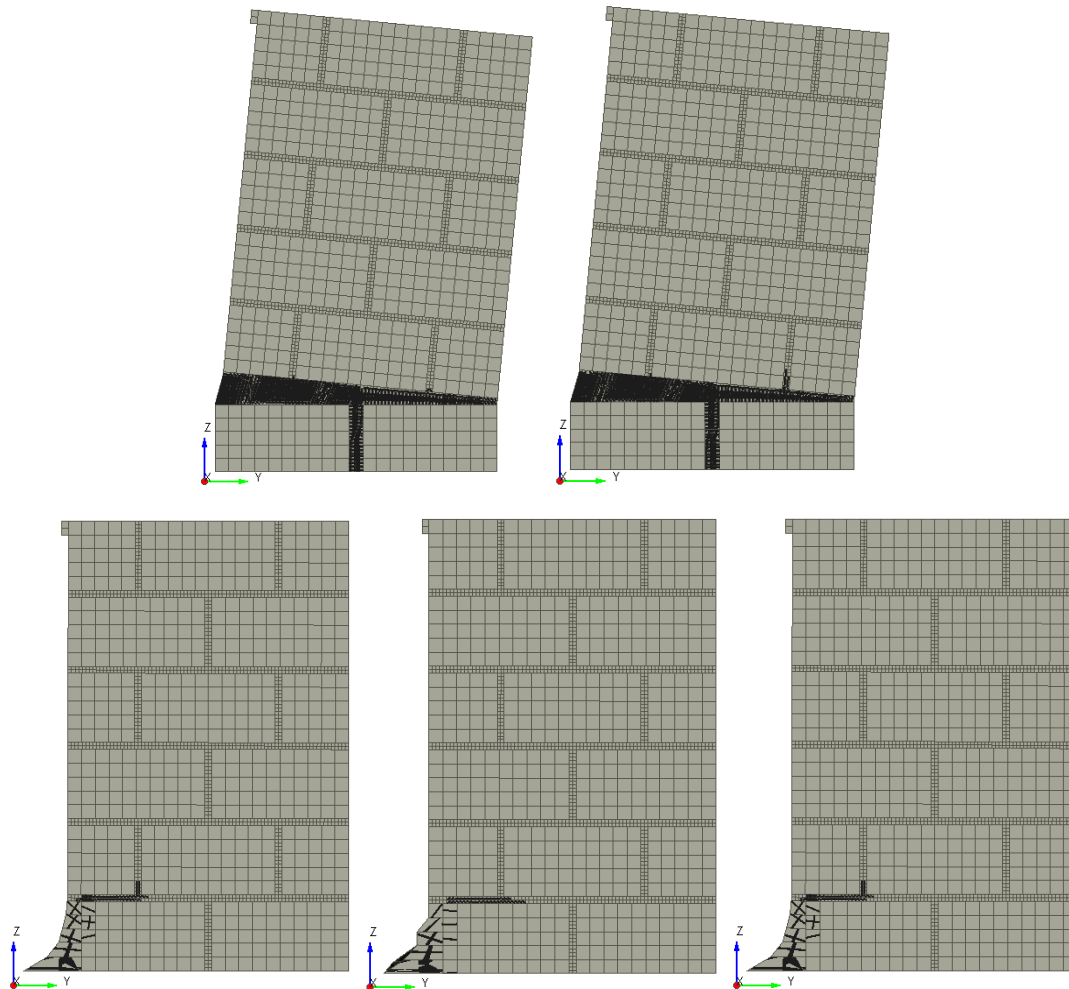


Figure 6-18: [A] Failure state EQSJ10 (0.05 MPa), [B] Failure state EQSJ10 (0.1 MPa), [C] Failure state EQSJ10 (0.2 MPa), [D] Failure state EQSJ10 (0.3 MPa), [E] Failure state EQSJ10 (0.4 MPa)

The failure states shown above closely resemble the results of Tests 1 through 5 of EQSJ5. Large cracking and rotation occurred along the bed joint between the lower two courses. As the overbearing stress values reach the increased levels of Tests 3 to 5 the main source of failure becomes sliding along the base of the specimen as was observed previously.

One main difference between the results of EQSJ10 and EQSJ5 is the trend of the peak lateral capacity. In previous analyses, the lateral capacity reached its peak at lower values of overbearing stress and decreased as the overbearing stress increased. In this set of analyses a more consistent trend is observed in the pushover curves shown in Figure 6-19 below.

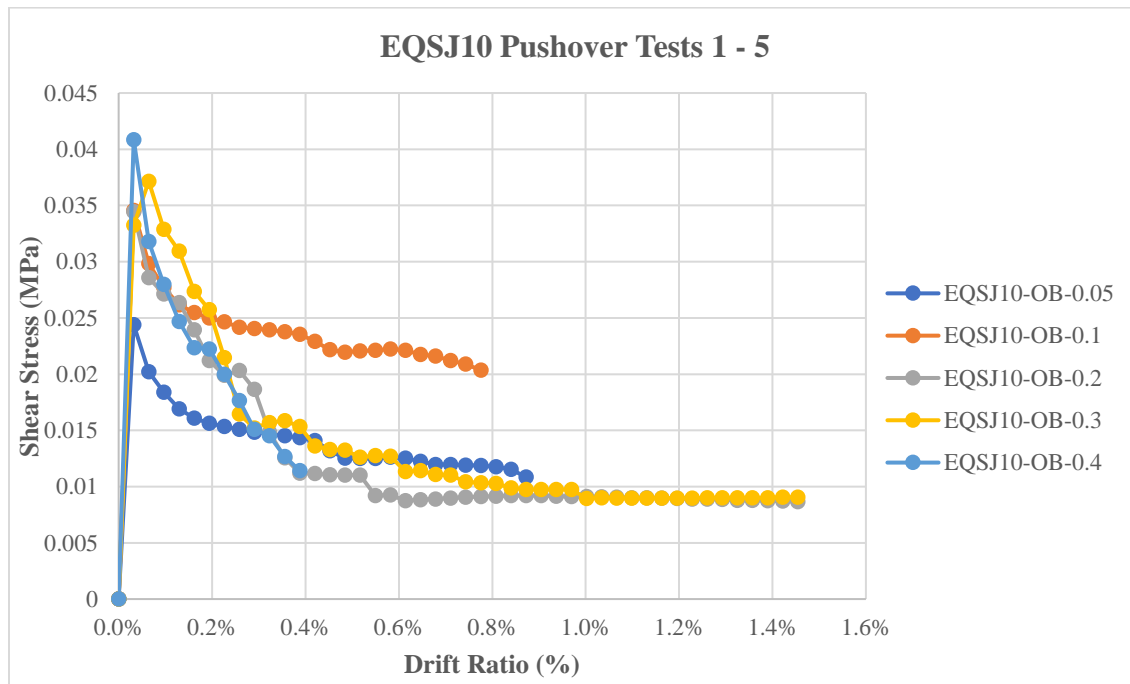


Figure 6-19: EQSJ10 Pushover Curves Tests 1-5

Lateral strength begins at an initial value of 0.0244 MPa at an overbearing stress of 0.05 MPa, increases to 0.0346 MPa at an overbearing stress of 0.1 MP whereas it reduces to 0.0344 MPa at an overbearing stress value of 0.2 MPa. The shear stress increases further to 0.0371 MPa at an overbearing stress value of 0.3 MPa reaching a peak value of 0.0408 MPa at an overbearing stress of 0.4 MPa. In this set of analyses a more consistent trend are shown within the first five tests between the lateral capacity and the overbearing stress.

As the overbearing stress increases to the levels analyzed in Tests 6 to 8, slightly different failure states are observed and shown below in Figure 6-20.

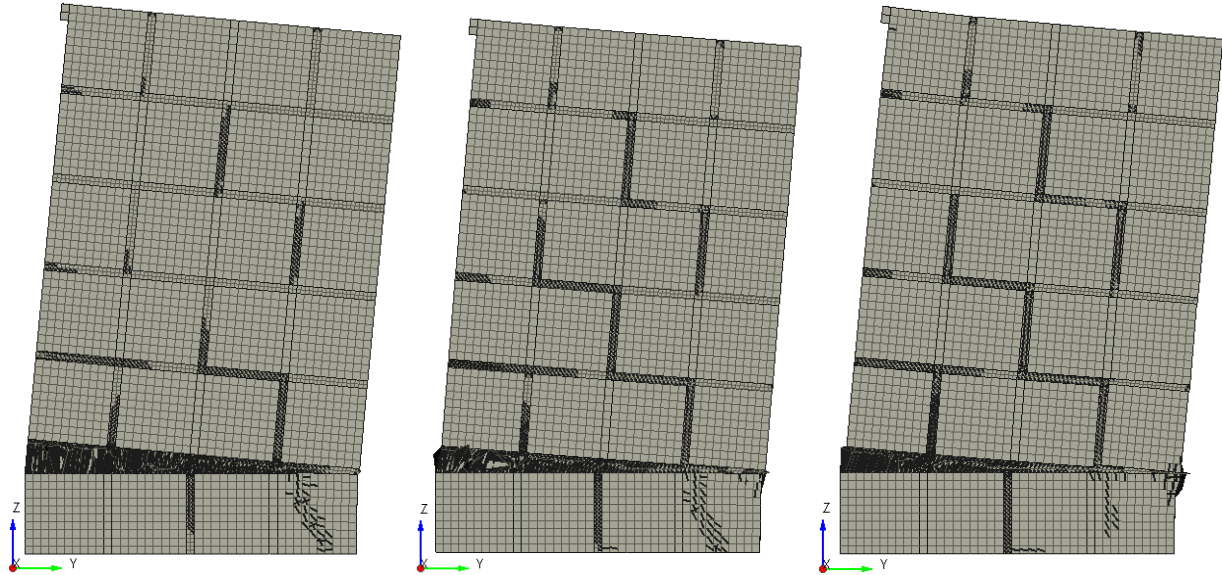


Figure 6-20: [A] Failure state EQSJ10 (1.79 MPa), [B] Failure state EQSJ10 (4.47 MPa), [C] Failure state EQSJ10 (7.15 MPa)

As shown in Figure 6-20, cracking and rotation is occurring along the bed joint between the lower 2 courses. However, as the overbearing stress increases, cracking is observed at the toe of the cracked bed joint where the bricks from the adjacent layers are meeting. Throughout Tests 6 to 8 stair step cracking of increased intensity is also observed. The lateral capacity computed for Tests 6 to 8 are shown in Figure 6-21 below.

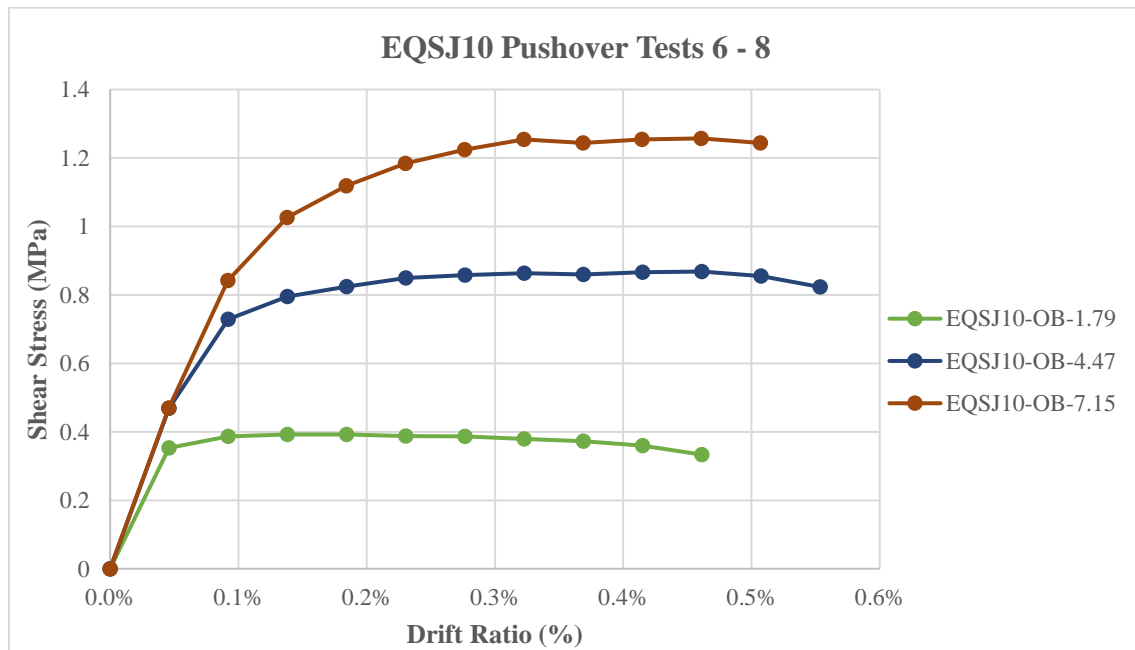


Figure 6-21: EQSJ10 Pushover Curves Tests 6-8

As shown in Figure 6-21 above, the peak lateral capacity is increased as the overbearing stress increases. To begin, at an overbearing stress value of 1.79 MPa, the observed shear stress is 0.392 MPa. When the applied overbearing stress is increased to 4.47 MPa the computed shear stress increases to 0.868 MPa. Finally, at a peak overbearing stress of 7.15 MPa, the computed shear stress increased to 1.257 MPa. The results further confirm the directly proportional relationship between the shear strength of a masonry wallette to the quantity of overbearing stress applied.

6.3.3 EQSJ20

The final set of EQS analyses were conducted on the EQSJ20 specimen. This specimen utilizes a global mortar joint thickness of 20 mm and therefore has the lowest percent area of masonry bricks of the EQS specimens. This creates an expectation that EQSJ20 will have the lowest shear strength throughout the 8 tests. The failure states of Tests 1 through 5 are shown in Figure 6-22 below.

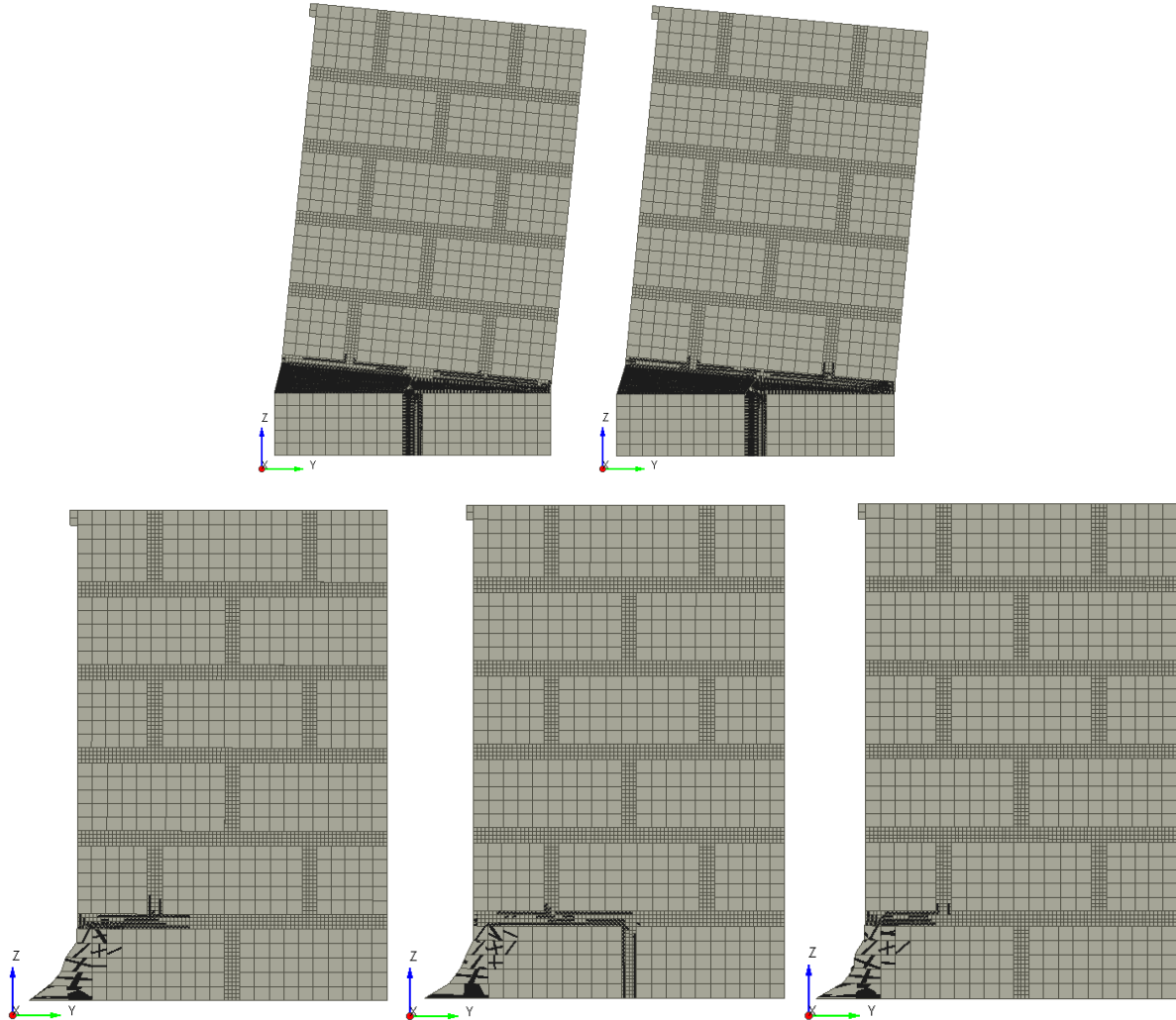


Figure 6-22: [A] Failure state EQSJ20 (0.05 MPa), [B] Failure state EQSJ20 (0.1 MPa), [C] Failure state EQSJ20 (0.2 MPa), [D] Failure state EQSJ20 (0.3 MPa), [E] Failure state EQSJ20 (0.4 MPa)

For this specimen, cracking is occurring along the bed joint connecting the lower 2 courses with the upper portion of the specimen rotating about the toe of that joint. As the overbearing stress increases to the values considered in Tests 3 to 5, sliding failure is occurring.

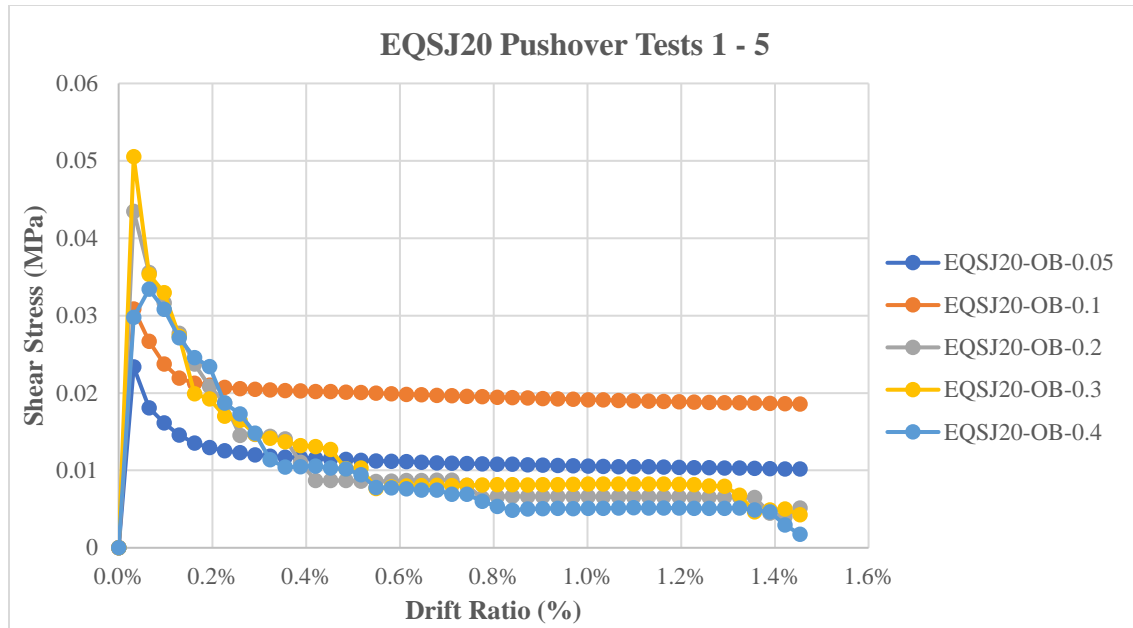


Figure 6-23: EQSJ20 Pushover Curves Tests 1-5

As shown in Figure 6-23 above, the lateral capacity does not increase consistently as the overbearing stress increases. For values of overbearing stress at 0.05 MPa and 0.1 MPa the shear stress increases from 0.0234 MPa to 0.0308 MPa. As the failure type changes to sliding failure observed in Tests 3 to 5 the trend of the data changes. From Tests 3 to 5 the shear stress does not consistently increase and in fact the peak shear stress of 0.0505 MPa occurs at an overbearing stress of 0.3 MPa.

For Tests 6 to 8, more consistency is observed within the results. As shown in Figure 6-24 below, there is no shift in the failure state, instead the source of failure remains constant with increased intensity as the overbearing stress increases.

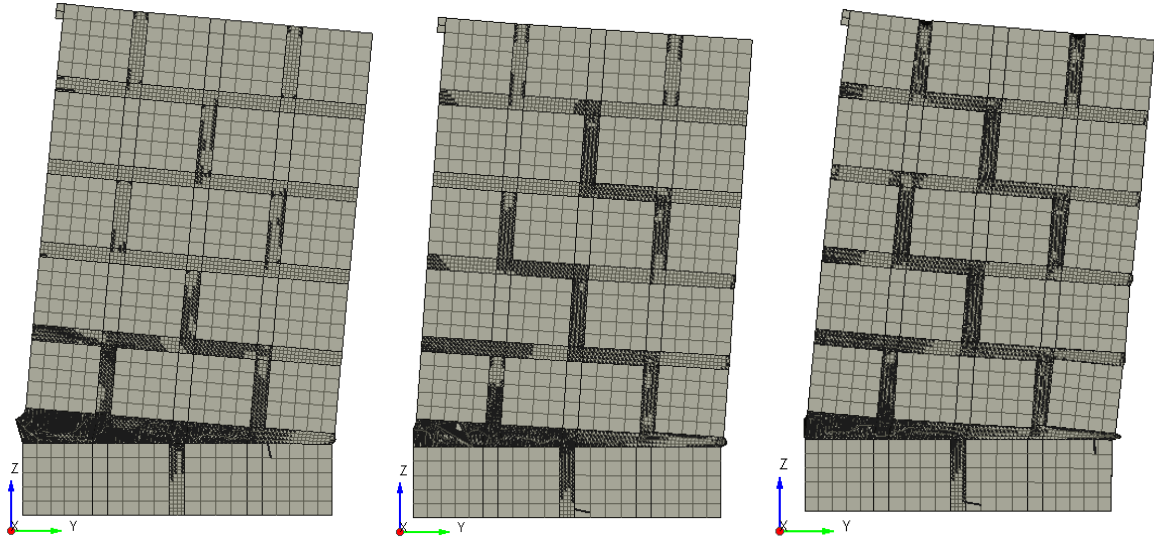


Figure 6-24: [A] Failure state EQSJ20 (1.79 MPa), [B] Failure state EQSJ20 (4.47 MPa), [C] Failure state EQSJ20 (7.15 MPa)

Throughout the final analyses similar damage types are occurring such as stair step cracking, cracking and rotation about the first bed joint, and cracking at the toe of the specimen. One observation is that the severity of the damage types is lower than the specimens with smaller mortar joints as those specimens such as EQSJ5 reach higher lateral capacities therefore inducing higher levels of damage onto the specimen. The lateral resistance curves for Tests 6-8 are shown below in Figure 6-25.

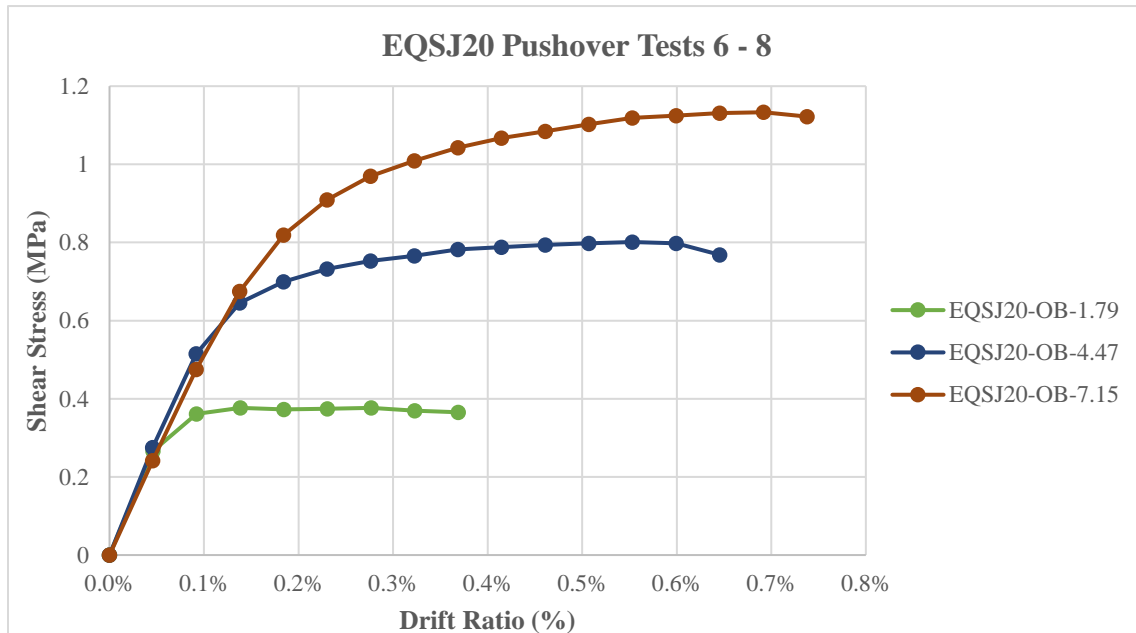


Figure 6-25: EQSJ20 Pushover Curves Tests 6-8

As shown in Figure 6-25 above, the shear stress of the EQSJ20 specimen increases as the applied overbearing stress increases. At an overbearing stress value of 1.79 MPa the computed capacity equals 0.377 MPa. The shear stress then increases to 0.801 MPa as the overbearing stress is increased to 4.47 MPa. Finally, the peak shear stress observed is 1.133 MPa at the peak overbearing stress considered being 7.15 MPa.

6.3.4 EQS Summary

The EQS lateral analyses aimed to assess the implications of altering the global mortar joint thickness and the applied overbearing stress on the specimen. Throughout the investigation the objective was to assess the implications the alterations had on the lateral capacity and therefore shear strength of the specimen and compare the trends in the EQS results and compare them with the results of the SYM analyses. From the SYM analyses it was found that a directly proportional relationship exists between shear strength and lateral capacity with overbearing stress. It was also found that there exists an inversely proportional relationship between shear strength and the global mortar joint thickness. Figure 6-26 below presents the final summary and normalized interaction diagrams for the EQS analyses which is used to validate the trends found in the results.

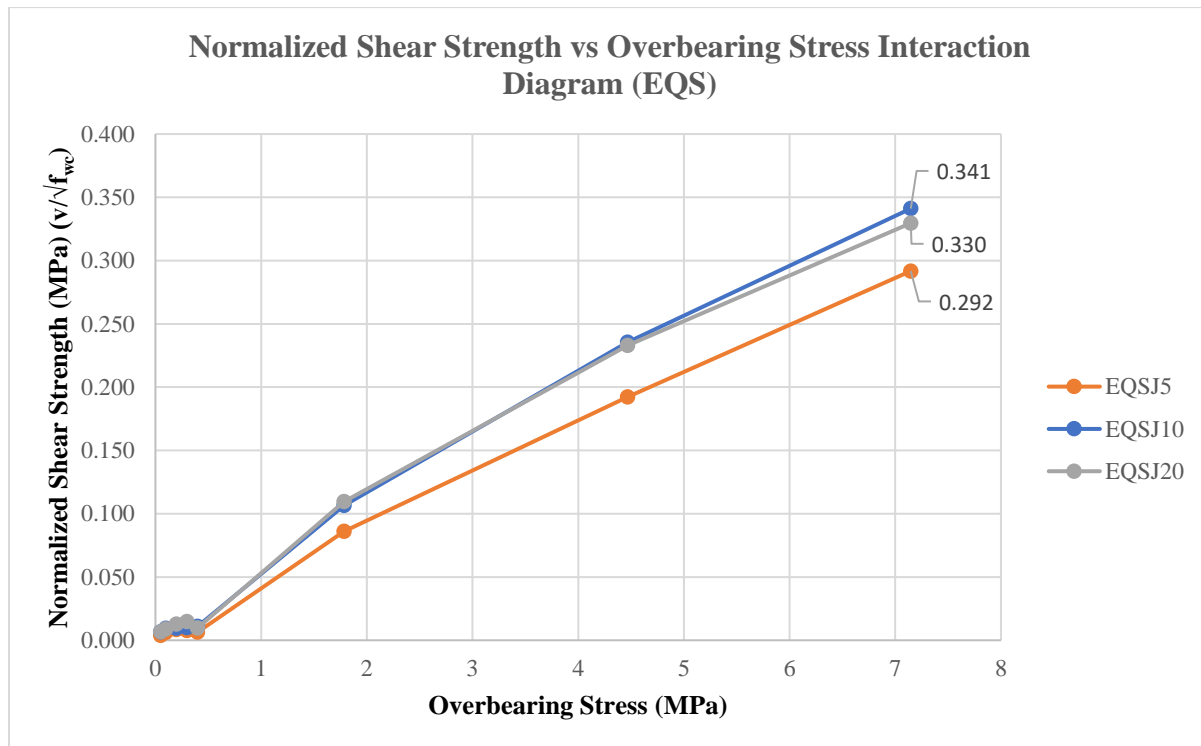


Figure 6-26: Summary of EQS Results (Pushover)

Throughout the individual EQS analyses it was discovered that as the overbearing stress increases the lateral capacity and therefore shear strength increases. However, when normalized with the peak compressive strength as shown in Figure 6-26 above, it can be observed that the thicker mortar joints translated to higher normalized shear strengths as was observed with the SYM specimens. Therefore, after concluding the EQS analyses, the same two trends initially found in the SYM results remain true throughout the EQS data.

6.4 RAN Results

The next portion of the lateral investigation was on the collection of RAN specimens. As previously discussed, the RAN design does not follow any patterns when organizing the arrangement of the bricks in each course. The bricks are placed at random however the heights of the bricks are constant in each course. The RAN design therefore encompasses the inconsistencies used in historic times. As observed in the compression results, the proximity of the head joints created large cracks along the height of the specimen which lowered its compressive strength and overall performance.

6.4.1 RANJ5

To begin the investigation, the first specimen analyzed was RANJ5. Like the other two wallette designs, the specimen with a global joint thickness of 5 mm typically has the highest performance due to the increased percentage of bricks within the area of the specimen. Therefore, it is expected that RANJ5 will have the highest lateral capacity and shear strength of the RAN specimens. Figure 6-27 below presents the failure states of Tests 1 to 5.

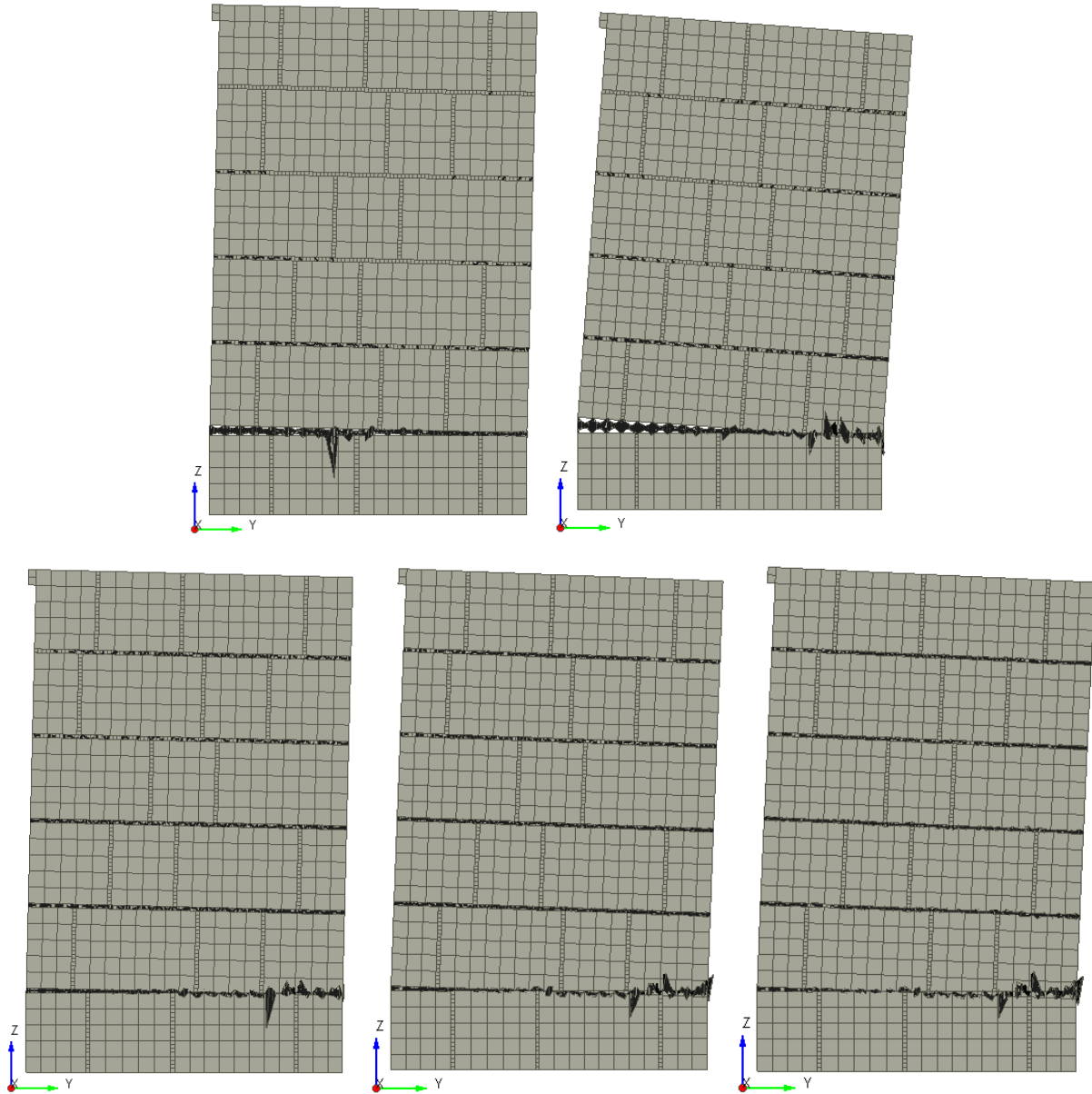


Figure 6-27: [A] Failure state RANJ5 (0.05 MPa), [B] Failure state RANJ5 (0.1 MPa), [C] Failure state RANJ5 (0.2 MPa), [D] Failure state RANJ5 (0.3 MPa), [E] Failure state RANJ5 (0.4 MPa)

As shown above, the failure states remained constant throughout the five tests. Unlike the previous results where a shift to sliding failure occurred, in this case the damage is localized along the lowest bed joint between the lower two courses of masonry.

The performance of the specimen throughout the first five tests shows similar trends to the previously discussed results. As shown below in Figure 6-28, the peak lateral capacity changed as the applied axial overbearing stress increased.

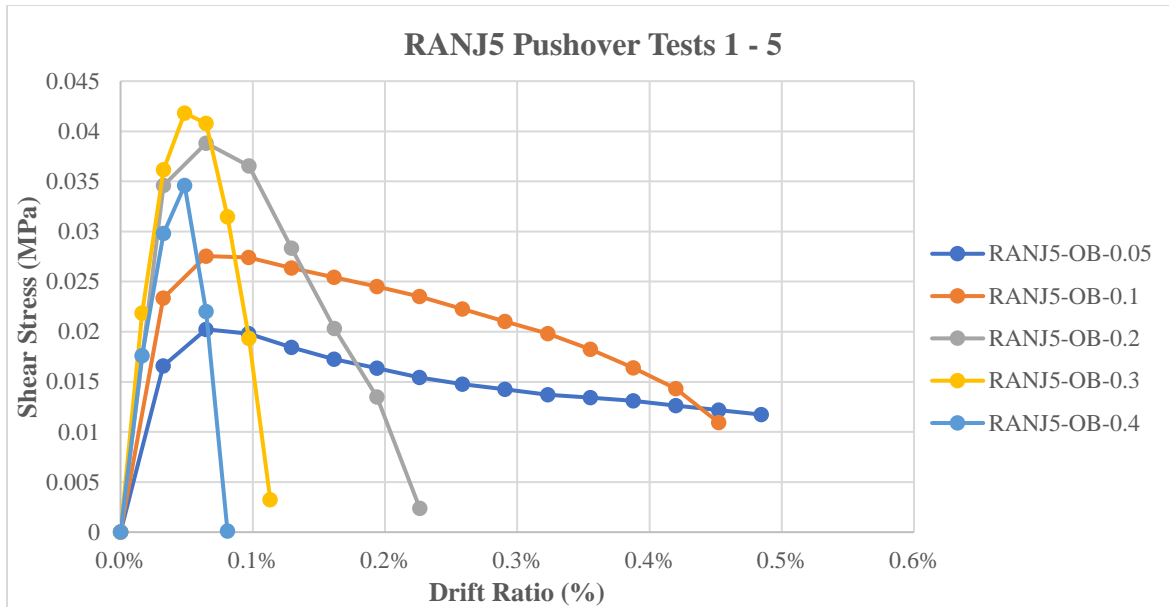


Figure 6-28: RANJ5 Pushover Curves Tests 1-5

Shown above, the peak lateral capacity was at its minimum value of 0.0202 MPa at an overbearing stress of 0.05 MPa. As the overbearing stress increased to 0.1 MPa the shear stress also increased to 0.0275 MPa. From Tests 3 to 5 the trend shifted. Although the failure states remained constant throughout, the peak shear stress increased to values of 0.0388 MPa and 0.0418 MPa at overbearing stress values of 0.2 MPa and 0.3 MPa respectively before decreasing to 0.0346 MPa at the peak overbearing stress of 0.4 MPa.

In Tests 6 to 8 where the sliding was suppressed, more distinguishable changes were observed throughout the failure states shown below in Figure 6-29.

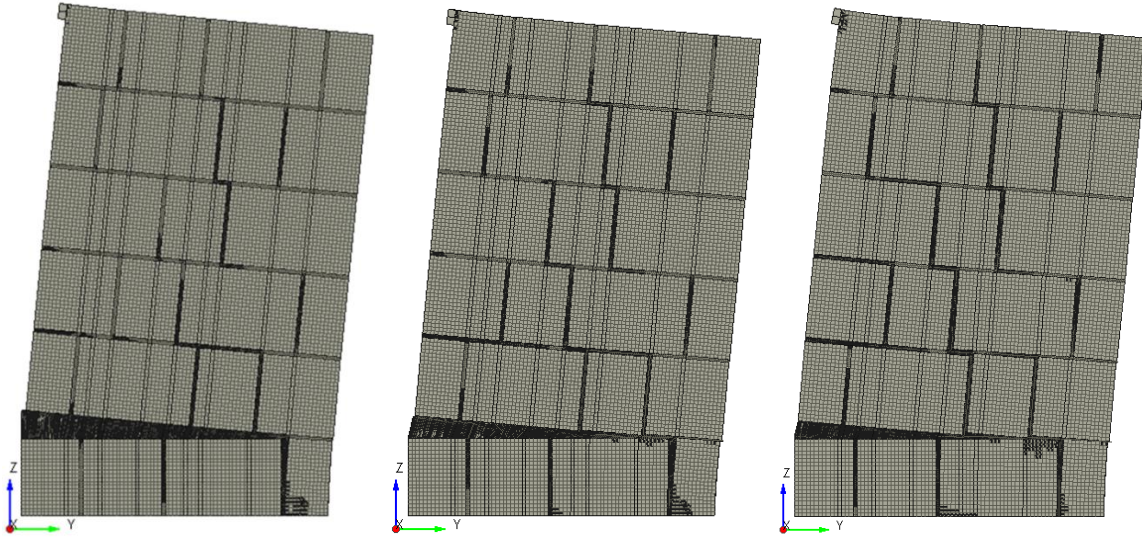


Figure 6-29: [A] Failure state RANJ5 (1.79 MPa), [B] Failure state RANJ5 (4.47 MPa), [C] Failure state RANJ5 (7.15 MPa)

Throughout Tests 6 to 8, the damage is mainly focused on the lowest bed joint between courses 1 and 2. Along that joint a large crack is opening, and the toe serves as the point of rotation for the upper 5 courses. In addition, as the overbearing stress increases throughout the three tests, the stair step cracking increases, and spreads throughout the specimen indicating the increased engagement as the overbearing stress increases. The lateral responses of Tests 6 to 8 are shown in Figure 6-30 below.

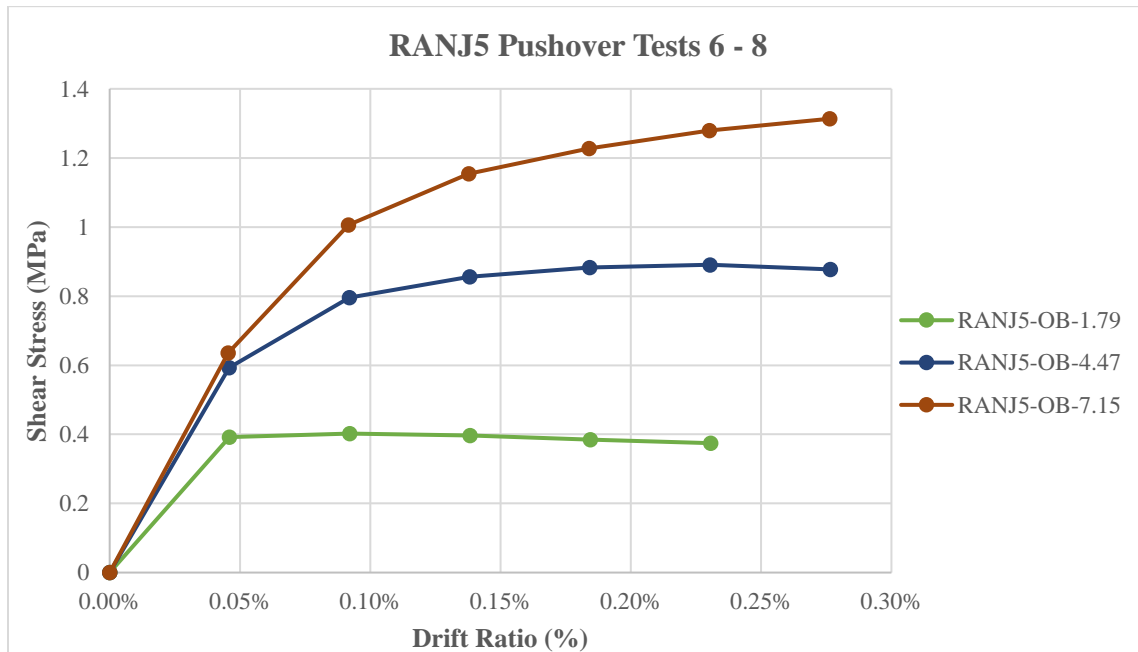


Figure 6-30: RANJ5 Pushover Curves Tests 6-8

As shown in Figure 6-30 above, the peak lateral capacity of the specimen increased as the applied overbearing stress increased. For an overbearing stress value of 1.79 MPa, the observed shear stress was 0.402 MPa. When the overbearing stress increased to 4.47 MPa the shear stress also increased to 0.891 MPa. Finally, at the highest value of overbearing stress 7.15 MPa, the shear stress reached its peak of 1.313 MPa.

6.4.2 RANJ10

The next specimen analyzed was RANJ10. This specimen utilizes a global mortar joint thickness of 10 mm and therefore contains a lower percent area of masonry bricks than the previously discussed RANJ5. Therefore, it is expected that the lateral capacity and shear strength of RANJ10 will be lower than what was observed with RANJ5. The failure states of Tests 1 to 5 are shown in Figure 6-31 below.

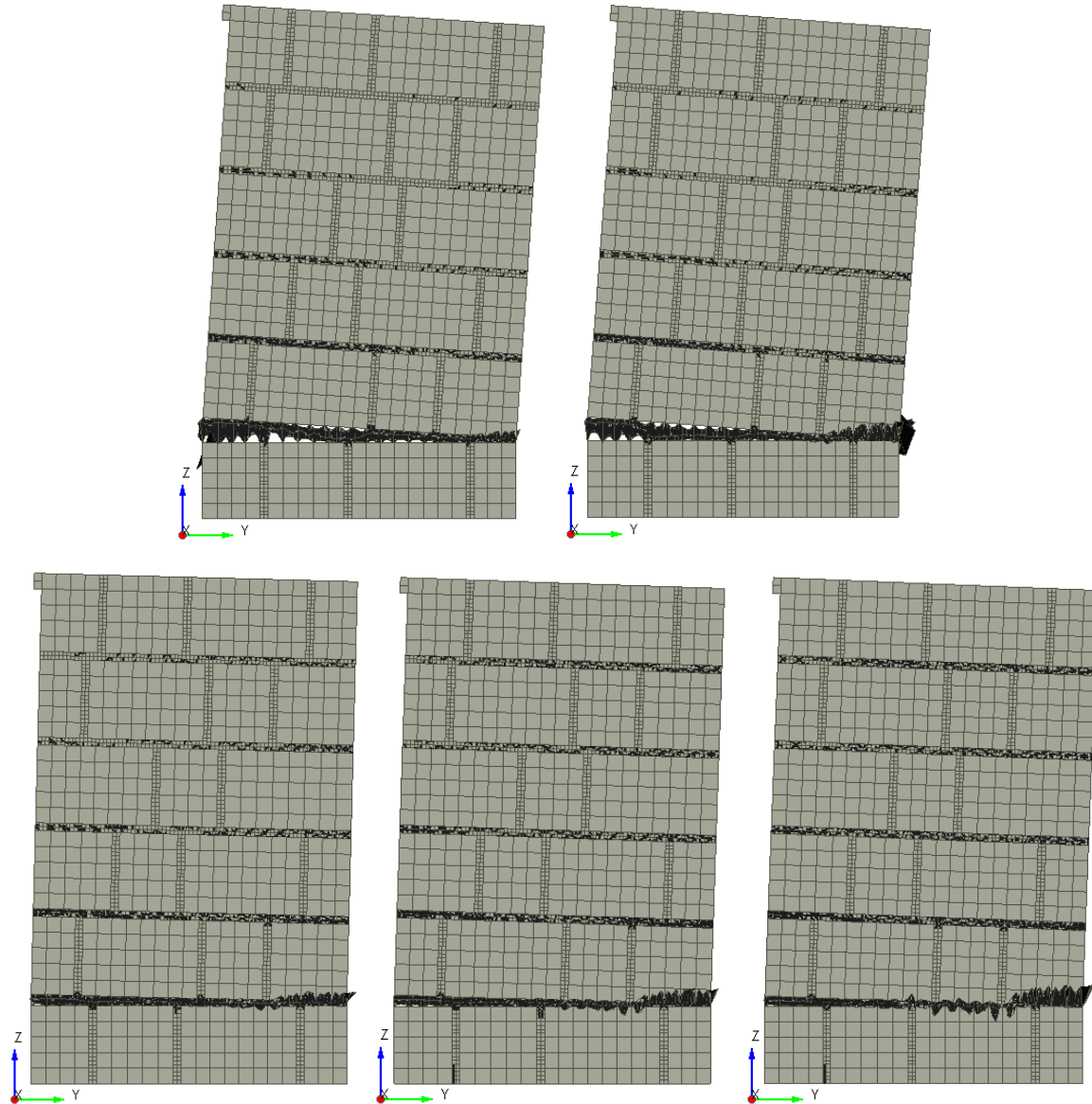


Figure 6-31: [A] Failure state RANJ10 (0.05 MPa), [B] Failure state RANJ10 (0.1 MPa), [C] Failure state RANJ10 (0.2 MPa), [D] Failure state RANJ10 (0.3 MPa), [E] Failure state RANJ10 (0.4 MPa)

As shown in Figure 6-31 above, the failure states throughout the first 5 Tests did not differ greatly, and the damage was mainly focused along the lowest bed joint between the lower two courses of masonry. For the RAN design no shift in failure source was found like the transition to sliding failure found in the EQS and SYM results.

The lateral capacity results were consistent with the directly proportional trends found throughout the finite element investigation. As shown below in Figure 6-32, the lateral capacity consistently increased as the applied axial overbearing stress increased.

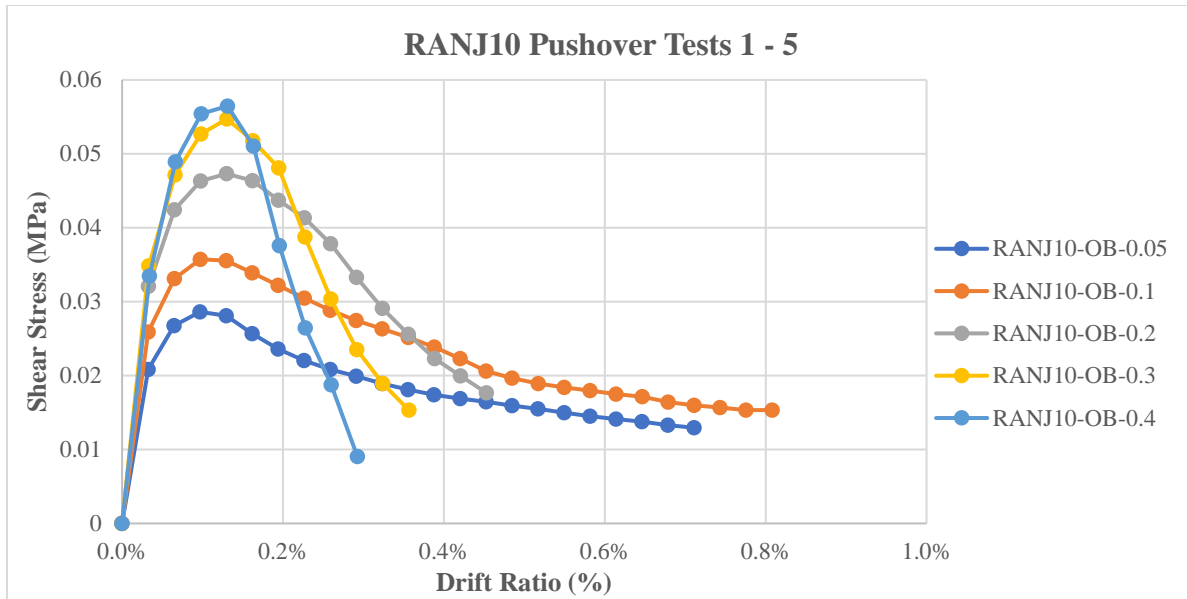


Figure 6-32: RANJ10 Pushover Curves Tests 1-5

From Test 1 which utilized an axial overbearing stress of 0.05 MPa, the peak lateral capacity of the specimen was found to be 0.0281 MPa. As the overbearing was increased to 0.1 MPa in Test 2, the peak shear stress increased to 0.0357 MPa. For the final three tests the shear stress continued to increase consistently as the overbearing stress was increased. For the final three tests the shear stress continued to increase to values of 0.0473 MPa, 0.0547 MPa, and 0.0565 MPa. Next, Tests 6 to 8 were conducted and the failure states from those analyses are shown in Figure 6-33 below.

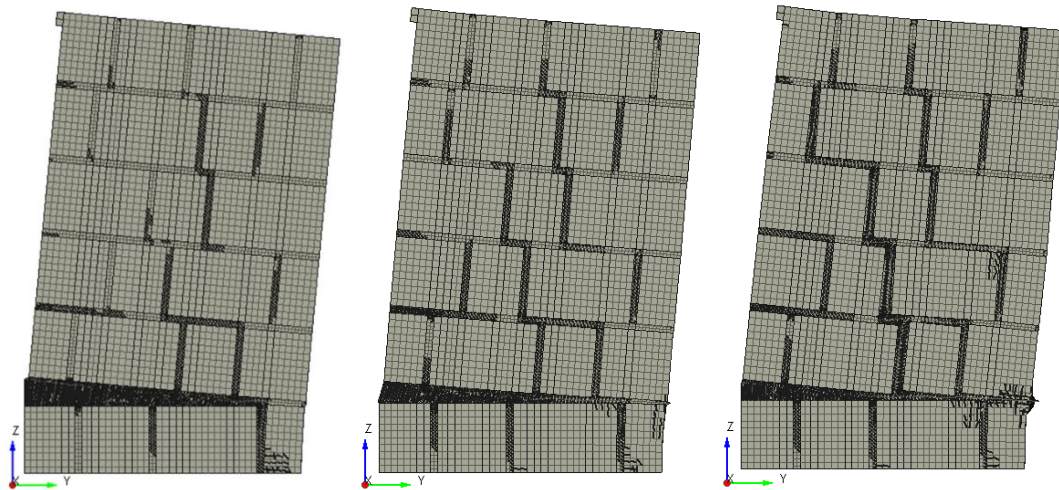


Figure 6-33: [A] Failure state RANJ10 (1.79 MPa), [B] Failure state RANJ10 (4.47 MPa), [C] Failure state RANJ10 (7.15 MPa)

For RANJ10 more damage was observed at the toe of the bed joint between the lower two courses of masonry, specifically in Test 8 where the overbearing stress was equal to 7.15 MPa. The lateral resistance curves for Tests 6-8 are shown in Figure 6-34 below.

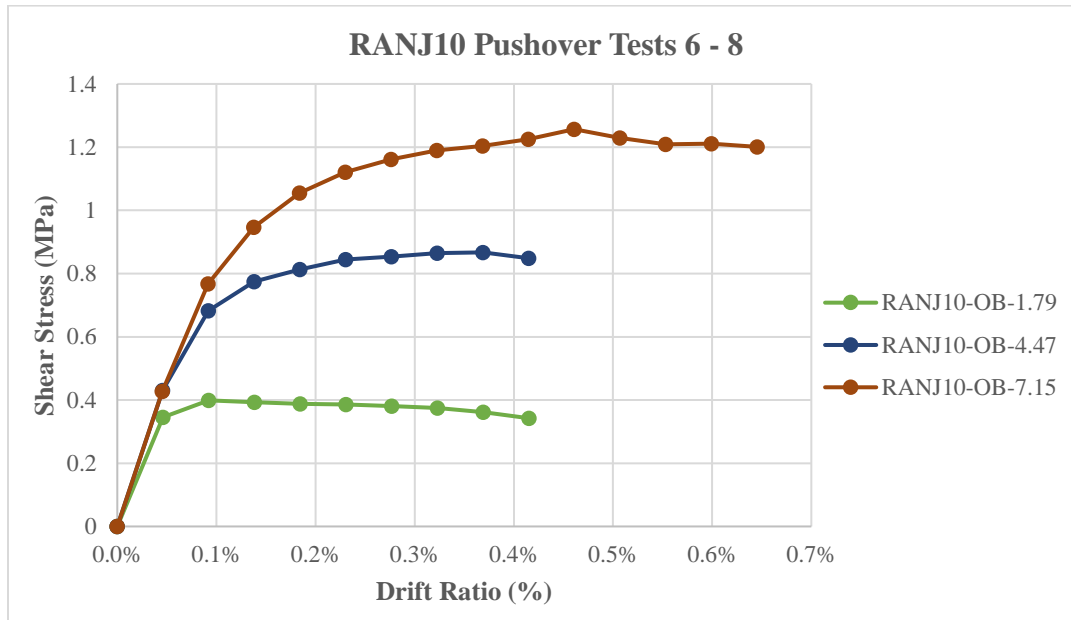


Figure 6-34: RANJ10 Pushover Curves Tests 6-8

As has been consistent throughout this investigation, Tests 6 to 8 while sliding failure is suppressed has resulted in a directly proportional trend between peak shear stress and overbearing stress. In the pushover curves for RANJ10 shown in Figure 6-34 above the same trend is present. At an overbearing stress value of 1.79 MPa, the peak shear stress is equal to 0.399 MPa. At increased overbearing stress values of 4.47 MPa and 7.15 MPa, the peak shear stress also increased to values of 0.867 MPa and 1.257 MPa respectively.

6.4.3 RANJ20

The final stage of the RAN investigation involved the RANJ20 specimen. This specimen utilized the largest global mortar joint thickness equal top 20 mm and therefore has the lowest percent area of masonry bricks amongst the 3 RAN specimens. The failure states of the first five tests are shown in Figure 6-35 below.

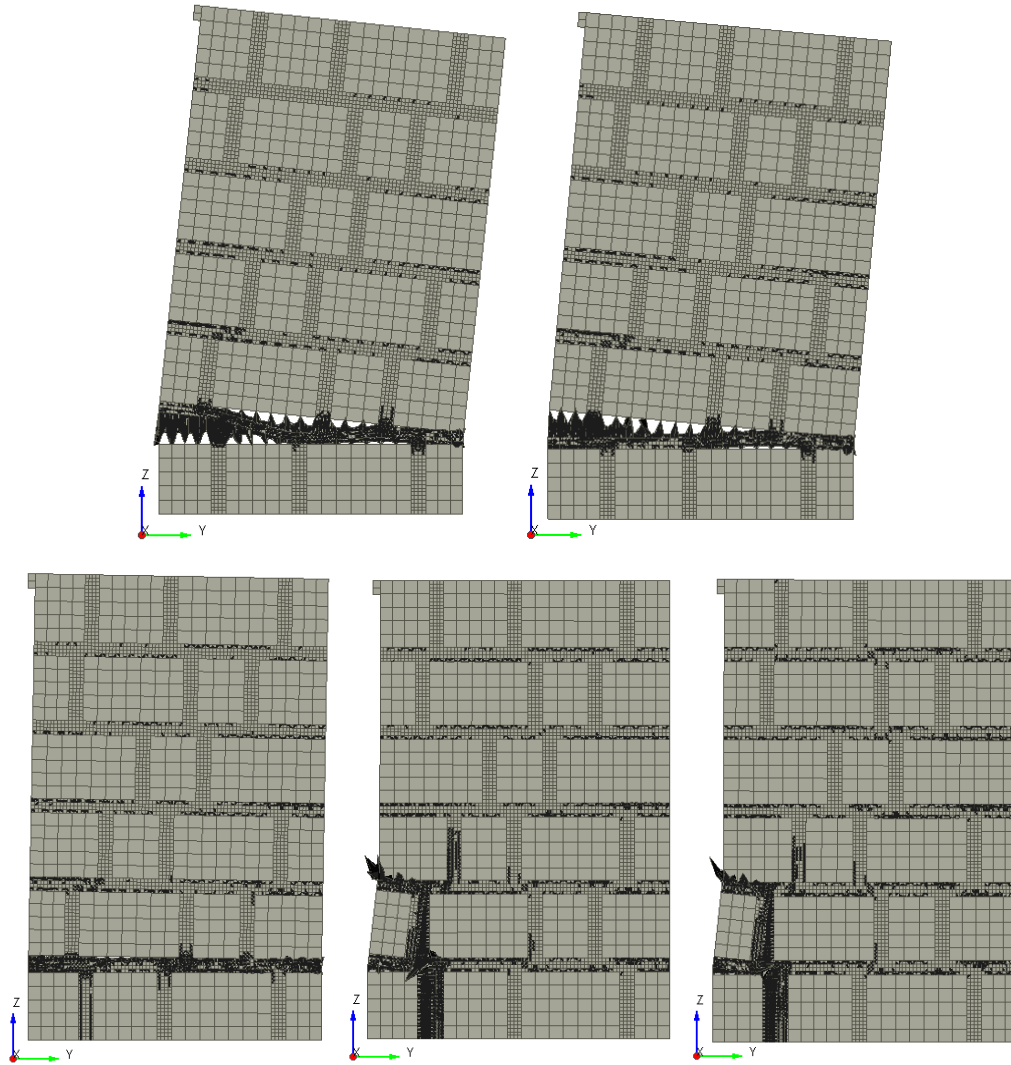


Figure 6-35: [A] Failure state RANJ20 (0.05 MPa), [B] Failure state RANJ20 (0.1 MPa), [C] Failure state RANJ20 (0.2 MPa), [D] Failure state RANJ20 (0.3 MPa), [E] Failure state RANJ20 (0.4 MPa)

For Tests 1 to 3 the damage is focused at the lowest bed joint between the lowest 2 courses of masonry. During Tests 4 and 5 the failure state changed, and the damage is focused at the heel of the specimen where large cracks and openings are occurring surrounding the leftmost brick on

the bottom two courses of the specimen. The differences observed throughout the failure states was also reflected in the pushover curves which are shown below in Figure 6-36.

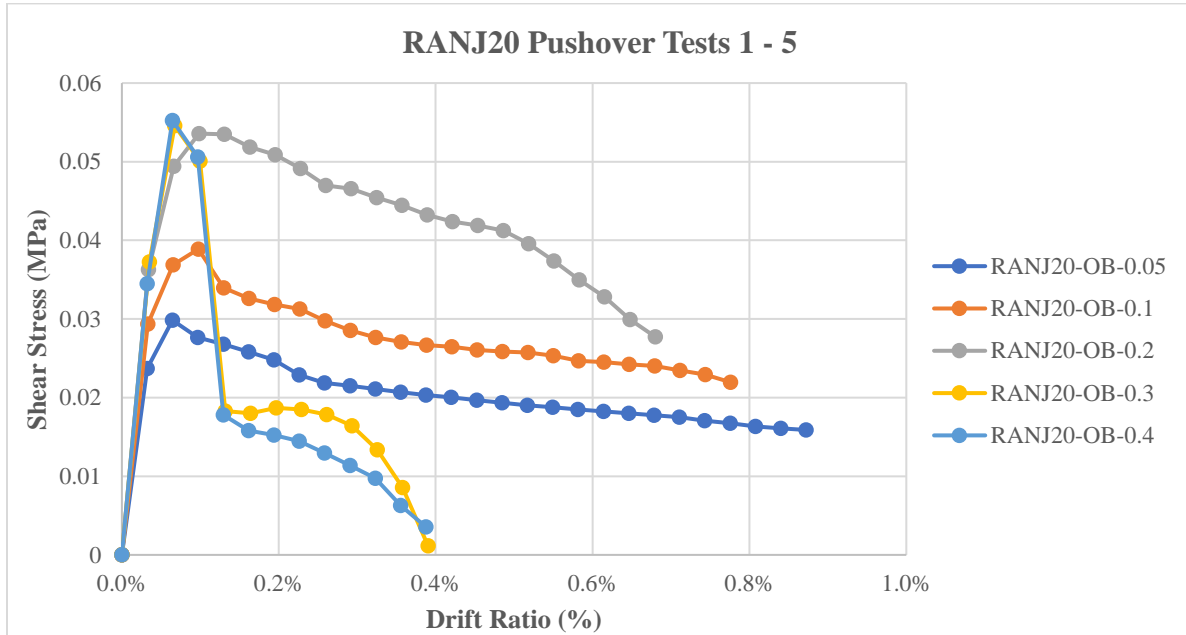


Figure 6-36: RANJ20 Pushover Curves Tests 1-5

At the initial overbearing stress value of 0.05 MPa, the initial peak shear stress is 0.0298 MPa. In Test 2 at an overbearing stress value of 0.1 MPa, the peak shear stress increases to 0.0389 MPa. For Tests 3 to 5 the peak shear stress does increase consistently but by small margins compared to previously discussed specimens. For the final three tests which utilized overbearing stresses of 0.2 MPa, 0.3 MPa, and 0.4 MPa, the recorded peak shear stresses were 0.0536 MPa, 0.0546 MPa, and 0.0552 MPa respectively. Therefore, while the directly proportional relationship between shear strength with overbearing stress was held true, the impact of increasing the overbearing stress was minimized which was likely caused by the change in failure states throughout Tests 3 to 5.

For the increased values of overbearing stress considered in Tests 6 to 8, the failure states were consistent and did not change as was observed in Tests 1 to 5. The failure states of Tests 6 to 8 are shown in Figure 6-37 below.

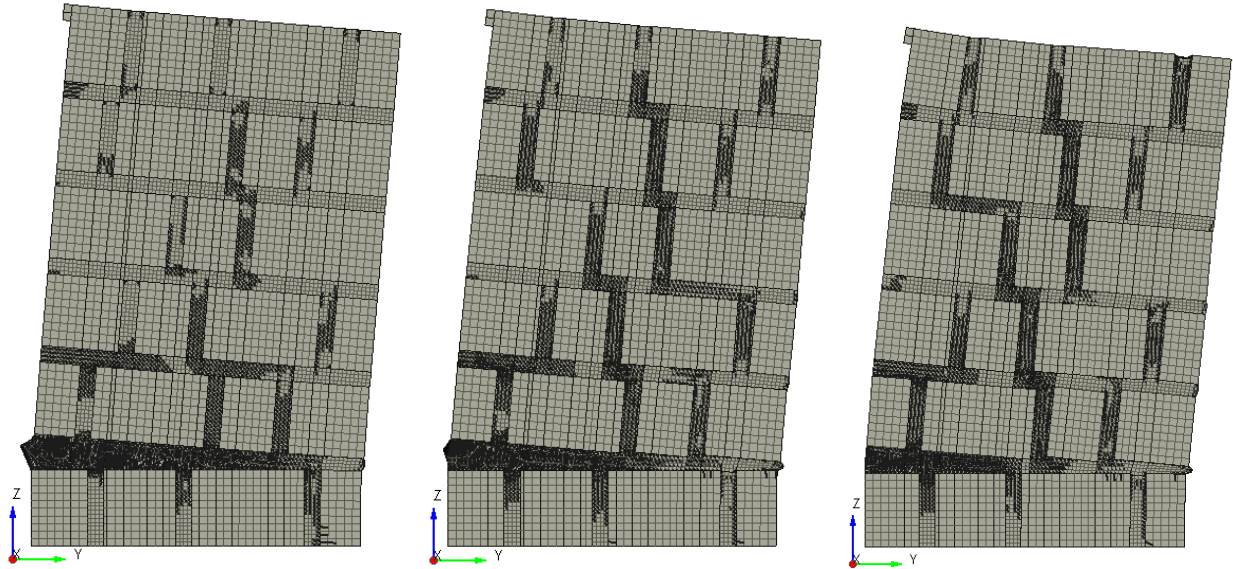


Figure 6-37: [A] Failure state RANJ20 (1.79 MPa), [B] Failure state RANJ20 (4.47 MPa), [C] Failure state RANJ20 (7.15 MPa)

Throughout each of the three failure states cracking is occurred along the bed joint between the lowest 2 courses and the upper courses of the specimen rotated about the toe of the joint. In addition, stair step cracking occurred throughout the upper portion of the specimen and the severity of the stair step cracks increased throughout Tests 6 to 8.

The lateral pushover curves presented in Figure 6-38 below further confirmed the data relationship discussed throughout this chapter.

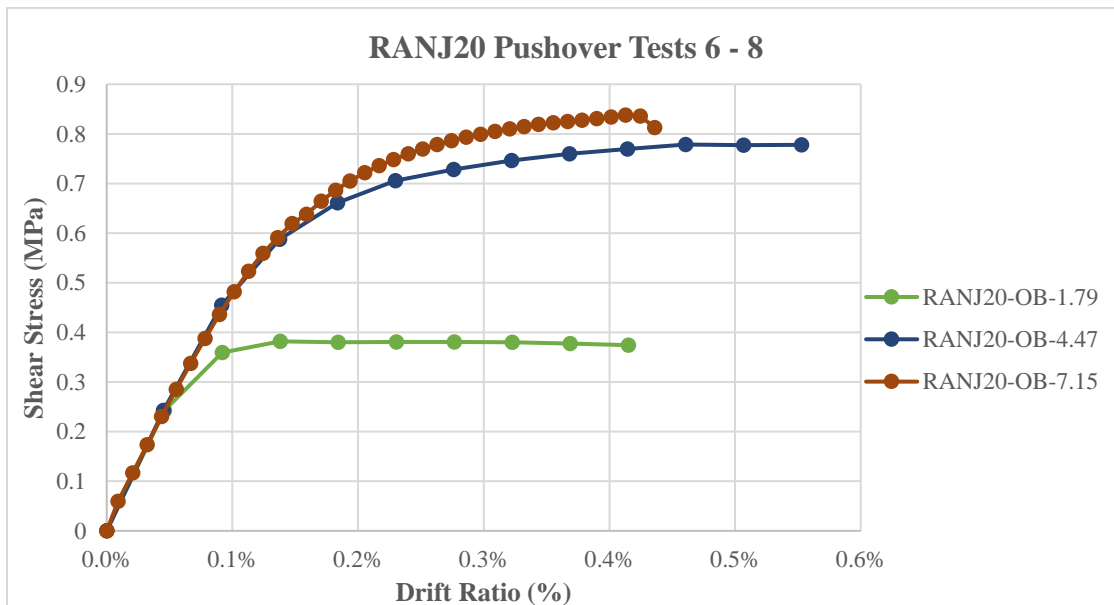


Figure 6-38: RANJ20 Pushover Curves Tests 6-8

The pushover curves presented in Figure 6-38 verify that the directly proportional relationship between shear stress with applied overbearing stress is true for RANJ20. At an initial overbearing stress value of 1.79 MPa the peak shear stress was found to be 0.382 MPa. In Test 7 where the overbearing stress was equal to 4.47 MPa, the peak shear stress was equal to 0.778 MPa. Finally, in Test 8 where the peak value of overbearing stress 7.15 MPa was applied to the specimen, the peak shear stress increased to 0.838 MPa.

6.4.4 RAN Summary

The RAN investigation was the final stage for the three initial designs which considered alternate global mortar joint thicknesses. Like the previous designs, it was found in the RAN results that the directly proportional relationship between shear strength and overbearing stress is true and can be verified in Figure 6-39 below.

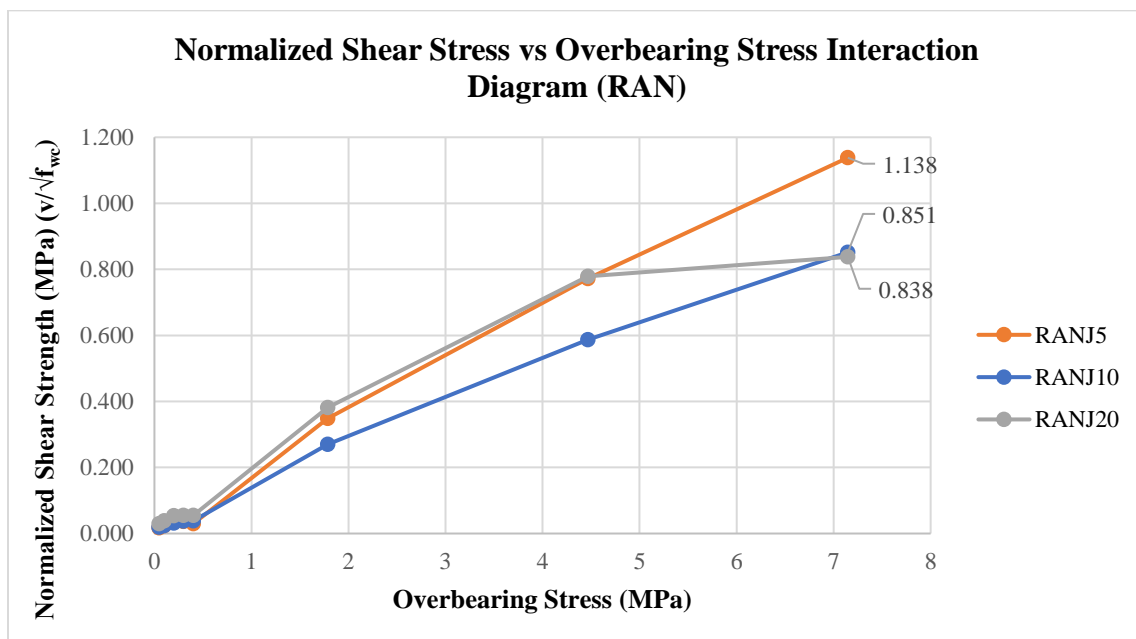


Figure 6-39: Summary of RAN Results (Pushover)

The interaction diagram shown in Figure 6-39 above presents the effects increasing the overbearing stress has on the shear strength for each of the RAN specimens. As shown above, for each of the three curves the shear strength increases as the overbearing stress applied to the specimens increases. For the normalized values of shear strength, it was found that the resultant normalized shear decreased as the mortar joints thickness increased. The results therefore verify

both the directly proportional relationship between shear strength and overbearing stress, and the inversely proportional relationship between shear strength and the global mortar joint thickness.

6.5 STONE Results

The final portion of the pushover investigation done in ATENA 3D was on the STONE design. As discussed in Chapter 3, the STONE design was created to reflect a historical stone masonry layout. The design involves stones with varying shapes and orientations, varying mortar joint thicknesses, and no axes of symmetry within the design. It must be noted that sliding was suppressed for all 8 tests for the STONE investigation whereas for the other 3 designs sliding was suppressed for only Tests 6 – 8. With complex arrangement of the bed and head joints, it is expected that the specimen will be well engaged under lateral loading especially at the higher levels of overbearing stress considered in the later tests. The failure states of Tests 1 – 5 are shown in Figure 6-40 below.

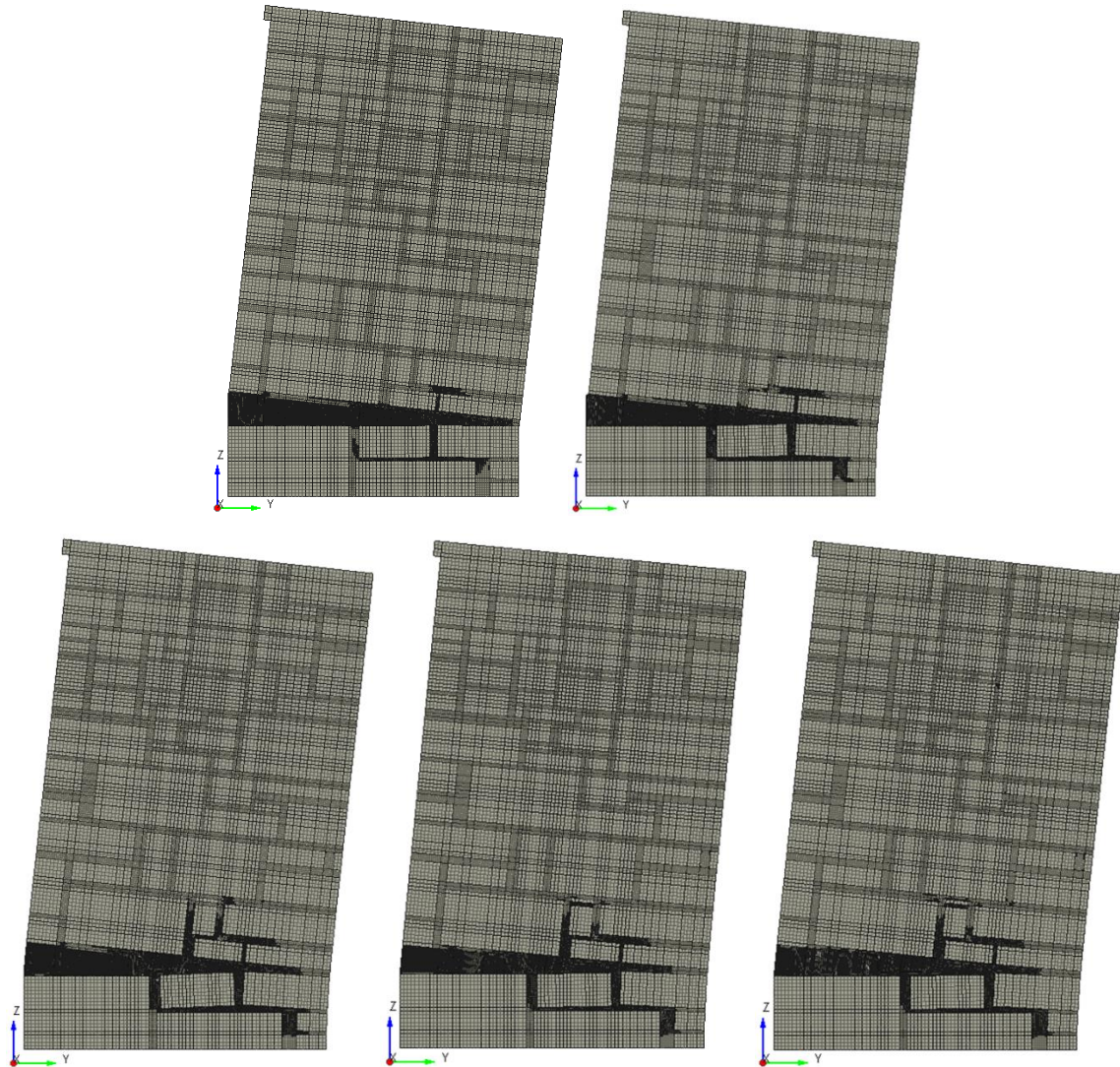


Figure 6-40: [A] Failure state STONE (0.05 MPa), [B] Failure state STONE (0.1 MPa), [C] Failure state STONE (0.2 MPa), [D] Failure state STONE (0.3 MPa), [E] Failure state STONE (0.4 MPa)

The failure states for Tests 1 – 5 show similar patterns to what was observed in the previous 3 designs. Throughout the five tests one bed joint is the main area where the damage is occurring with the upper portion of the specimen rotating about the toe of the bed joint. In this case the same observations are had, but as the overbearing stress increased the cracking began to spread upwards to the joints above the main bed joint. The results of the initial tests follow the same trends observed previously and are presented in Figure 6-41 below.

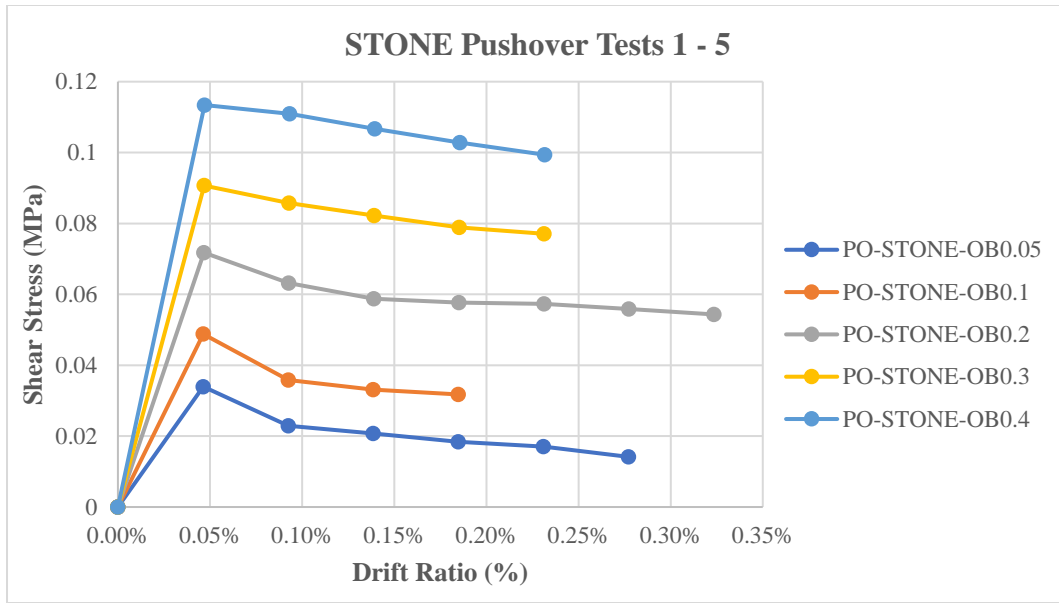


Figure 6-41: STONE Pushover Curves Tests 1-5

The pushover curves shown above display the lateral behaviour during the first five tests in the STONE investigation. One of the main focuses of the results is to verify if a directly proportional relationship is present between lateral capacity and overbearing stress. As shown in Figure 6-41 above, the relationship of interest is present and holds true. At the initial overbearing stress value of 0.05 MPa, the computed shear stress was equal to 0.034 MPa. The shear stress increased consistently as the overbearing stress increased until reaching the peak shear stress value of 0.113 MPa at an overbearing stress of 0.4 MPa. The failure states of the Tests 6 to 8 are shown in Figure 6-42 below.

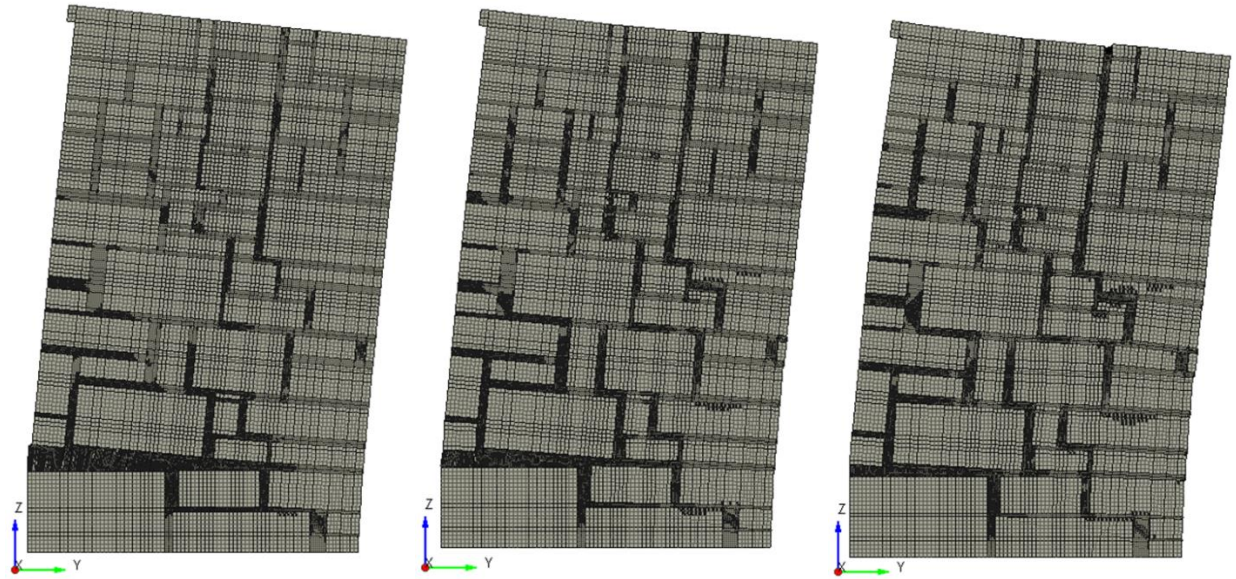


Figure 6-42: [A] Failure state STONE (1.79 MPa), [B] Failure state STONE (4.47 MPa), [C] Failure state STONE (7.15 MPa)

Throughout Tests 6 – 8 the failure states remained consistent with no change in failure mode, but rather an increase in severity as the overbearing stress increased. An important observation from the failure states is how majority of the specimens are engaged as the lateral loading was applied. In the previous designs, stair step cracking did occur. However, in the STONE analyses the stair step cracking occurred throughout the specimen especially when the overbearing stress reached the higher values considered in Tests 7 and 8.

The lateral pushover curves shown in Figure 6-43 below serve as the final indicator that the directly proportional relationship between lateral capacity and therefore shear strength with overbearing stress is true.

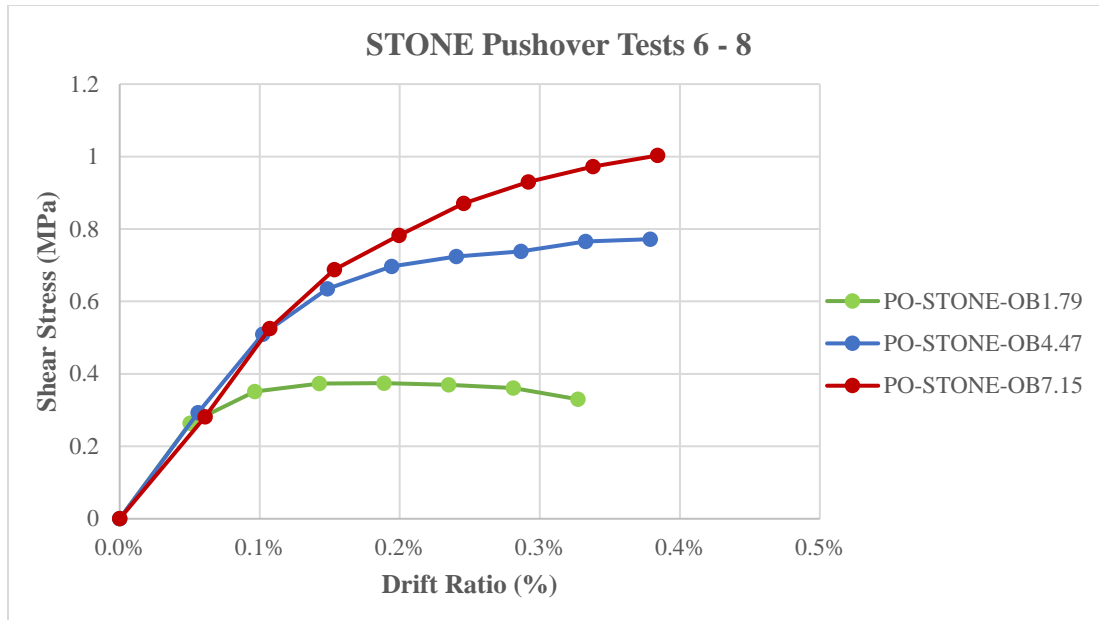


Figure 6-43: STONE Pushover Curves Tests 6-8

As presented above, the peak lateral capacity increased consistently as the overbearing stress increased. At the initial overbearing stress value of 1.79 MPa, the computed shear stress was equal to 0.374 MPa. Next when the overbearing stress was increased to 4.47 MPa, the shear stress also increased to 0.772 MPa. Finally, at the peak overbearing stress value of 7.15 MPa, the shear stress increased to its peak of 1.003 MPa. Therefore, since the shear stress continuously increased as the overbearing stress increased, the relationship previously discussed between shear strength and overbearing stress is true.

6.5.1 STONE Summary

The STONE investigation provided insight regarding the behaviour of historic masonry due to the design of the wallette. Regarding the results the main difference between the previous three designs is that the impact of altering the global mortar joint thickness was not considered since the design did not use a global thickness. The interaction diagram shown in Figure 6-44 below highlights the effects of increasing the overbearing stress on the shear strength of the specimen.

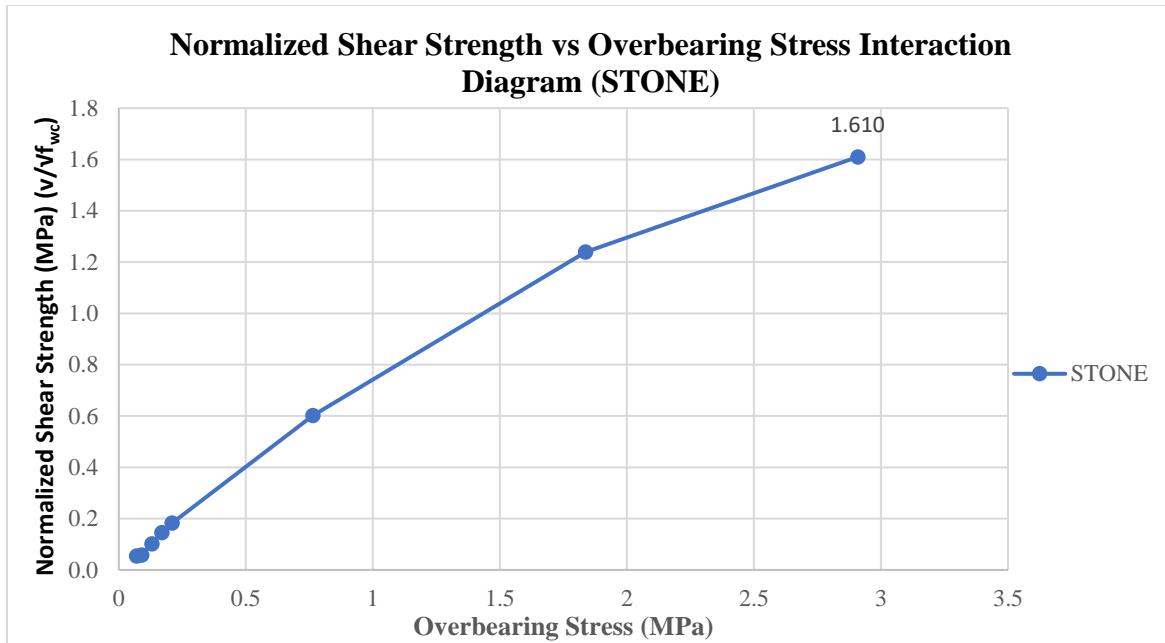


Figure 6-44: Summary of STONE Results (Pushover)

From the STONE interaction diagram, it can be observed that the directly proportional relationship between shear strength and overbearing stress is indeed present and is true. Throughout the 8 tests the shear strength increased as the overbearing stress increased until reaching its peak normalized shear strength value of 1.610 MPa at an overbearing stress of 7.15 MPa.

6.6 Conclusions

The lateral pushover investigation was conducted to define a method to determine the shear strength of a masonry wallette numerically using ATENA 3D. Using the four presented designs an extensive collection of numerical cases was created where each design was tested under varying loading conditions. In addition to assessing the numerical modelling capabilities for computing the shear strength of masonry, three main behavioural aspects were also studied. The first design aspect as discussed was the design and layout of the bricks and mortar joints. Secondly, the impact of changing the global mortar joint thickness was assessed. Finally, the effects of increasing the overbearing stress applied axially to a specimen has on the computed peak shear strength was assessed.

Throughout the discussed results, it was found that as the thickness of the mortar joints is increased, the peak shear strength of the specimen decreases. Throughout the EQS, SYM, and RAN discussions, it was found that the 5 mm version of each design provided the highest shear strength. This is caused by the increase in area of masonry bricks within the specimen. Since the masonry bricks modelled have a higher compressive and tensile strength than the mortar used, as the proportion of bricks increases so does the strength properties therefore increasing the specimen's performance as was observed throughout the pushover investigation.

Overbearing stress plays a crucial role in the lateral capabilities of unreinforced masonry. The stress which is applied axially to compress the specimen is needed to develop the flexural strength needed to resist the applied lateral loading. Throughout the investigation the importance of overbearing stress was tested by considering 8 different values to see if the peak shear strength increases. As was discussed above, the overbearing stress did play a crucial role in the lateral performance. For example, in the STONE investigation from Test 6 to 8 the peak shear strength increased by 168.2%. Therefore, it was determined that a directly proportional relationship exists between shear strength and overbearing stress.

The final aspect studied was the effect of changing the design of the masonry. In the compression it was found that the design plays a crucial role in the compressive strength of a wallette and the same was found in the lateral investigation. In Figure 6-45 below the interaction diagrams for the 10 mm specimens from the 3 main designs as well as the STONE interaction diagram is presented.

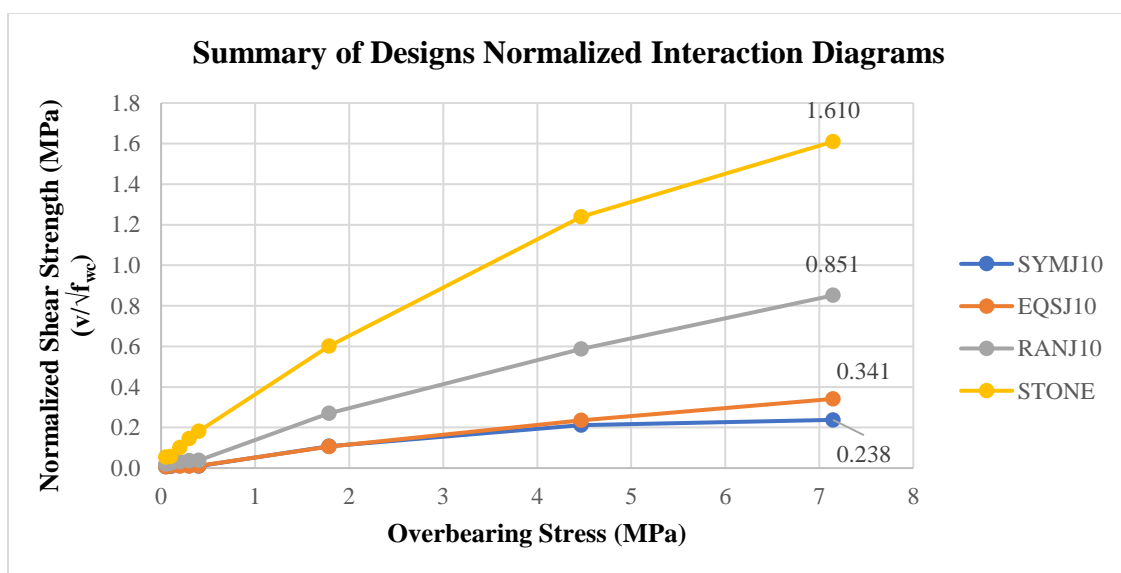


Figure 6-45: Collection of Interaction Diagrams (All Designs)

As shown above, the design of the wallette specimens did impact the lateral performance. The STONE specimen had the highest normalized shear strength with 1.610 MPa followed by the RAN specimen with 0.851 MPa. Next, the EQS specimen had a 59.9% reduction in performance and had a peak normalized shear strength of 0.341 MPa. Finally, the SYM design had a peak normalized shear strength of 0.238 MPa which was 30.2% lower than the EQS specimen. Overall, the design and layout of the masonry bricks and mortar joint is important to the performance. As shown in the results above, the significant reductions in normalized shear strength were observed as the design of the specimens was altered. Therefore, the design and layout of masonry should be considered as an essential factor when designing and analyzing any unreinforced masonry structure.

Chapter 7

Parametric Studies and Empirical Comparisons

7.0 Introduction

In designing or analyzing masonry, all the material and geometric variables affect the performance. In previous chapters some basic parameters such as the global mortar joint thickness and masonry brick layout were examined, and both were found to be crucial to the mechanical performance. Another important aspect is the contribution of strength from the participating materials within masonry. Throughout this chapter the strength and modulus of elasticity of masonry as a product of two participating materials will be examined, and the sensitivity of the estimated values will be examined based on the results obtained from the parametric studies on masonry panels conducted in the preceding chapters.

Empirical equations have been assembled based on a variety of experiments from the literature. Results obtained from these equations for the panel cases examined will be compared in this chapter with the objective to qualify their relevance in estimating homogenized values for the key variables that are used in seismic analysis of complete structures.

7.1 Empirical Equations

In this investigation, various codes and standards and literature have been studied and five empirical equations have been collected which will be used to correlate the results for the homogenized compressive strength of masonry with the values obtained from the parametric studies, as presented below.

- EC6-1-1, 3.6.1.2 (CEN, 2005)

$$f_k = K f_b^{0.7} f_m^{0.3}, \text{ (MPa)} \quad (7.1)$$

where,

f_k is the characteristic compressive strength of masonry [MPa],

f_b is the normalized mean compressive strength of a masonry unit [MPa],

f_m is the compressive strength of masonry mortar [MPa], and

K : is a calibrated constant, taken as 0.45 from Table 3.3 from Eurocode 6-3.6.1.2(6)

- KADET, 2017

$$f_{wc} = \xi \left(\left[\frac{2}{3} \sqrt{f_{bc}} - f_0 \right] + \lambda f_{mc} \right) \text{ (MPa)} \quad (7.2)$$

where,

f_{wc} is the compressive strength of masonry [MPa],

f_{bc} is the compressive strength of the masonry units [MPa],

f_{mc} is the uniaxial compressive strength of mortar bed joints [MPa],

f_0 is a coefficient, that accounts for stone dressing, taken as 1.5 [MPa], and ξ is a factor

which accounts for the thickness of the mortar joints: $\xi = 1/[1 + 3.5(k - k_0)] < 1$

$k_0 = 0.3$, $K = \frac{V_m}{V_w} \geq 0.30$, if $K \leq 0.30$ then $\xi = 1.0$ and,

V_m : is the volume of mortar in the composite masonry volume V_m

V_w : is the reference volume of masonry

- Tassios, 1992

$$f_{wc} = \frac{f_{bc}}{6} + \frac{\sqrt{f_{bc} f_{mc}}}{4} - \frac{f_{mc}}{20} + 1.40 \text{ [MPa]} \quad (7.3)$$

where,

f_{wc} is the compressive strength of the masonry composite [MPa]

f_{bc} is the uniaxial compressive strength of masonry units [MPa]

f_{mc} is the uniaxial compressive strength of mortar bed joints [MPa]

- Penelis & Penelis, 2020

$$f_{wc} = \left(\frac{2}{3} \sqrt{f_{bc}} - \alpha \right) + \beta f_{mc} \text{ [MPa]} \quad (7.4)$$

where,

f_{wc} is the compressive strength of a wall [MPa]

f_{bc} is the uniaxial compressive strength of masonry units [MPa]

f_{mc} is the uniaxial compressive strength of mortar bed joints [MPa]

α is a constant, taken as 2.50 for natural stonework

β is a constant, taken as 0.50 for stonework

- Brocker, 1961:

$$f_{wc} = 0.7 \sqrt{f_{bc}}^3 \sqrt{f_{mc}} \text{ [MPa]} \quad (7.5)$$

where,

f_{wc} is the compressive strength of a wall [MPa]

f_{bc} is the uniaxial compressive strength of masonry units [MPa]

f_{mc} is the uniaxial compressive strength of mortar bed joints [MPa]

In addition, two empirical equations were analyzed which are used to compute the effective modulus of elasticity of masonry. The two equations were compared with the modulus of elasticity values from the pushover analyses.

- Penelis & Penelis, 2020

$$E_w = E_b \frac{1+a}{aE_b/E_m} \text{ [MPa]} \quad (7.6)$$

where,

$$a = \frac{t_b}{t_m}$$

E_w is the composite modulus of elasticity of masonry [MPa]

t_b is equal to the thickness of the masonry bricks [mm]

t_m is equal to the thickness of the mortar joints [mm]

E_b is the modulus of elasticity of the masonry bricks [MPa]

E_m is the modulus of elasticity of the mortar [MPa]

- CSA S304.1-04, 6.5.2 (CSA, 2010)

$$E_m = 850 f'_m \text{ [MPa]} \quad (7.7)$$

where,

E_m is the modulus of elasticity of masonry [MPa]

f'_m is the compressive strength of masonry [MPa]

The above models were used to calculate the composite compressive strength of the masonry panels for each modelling case considered, and results were plotted against the Finite

Element Simulation Results. For the correlation to be successful, the estimations from the above models will need to meet the success criteria defined below:

1. The calculated values should not overestimate the simulation results.
2. The parametric sensitivities of the empirical formulae should agree with those obtained from the detailed simulation.

7.2 Review of Compressive Strength Panels

The correlation study included the 10 sub-cases obtained from four designs shown in Figure 7-1.

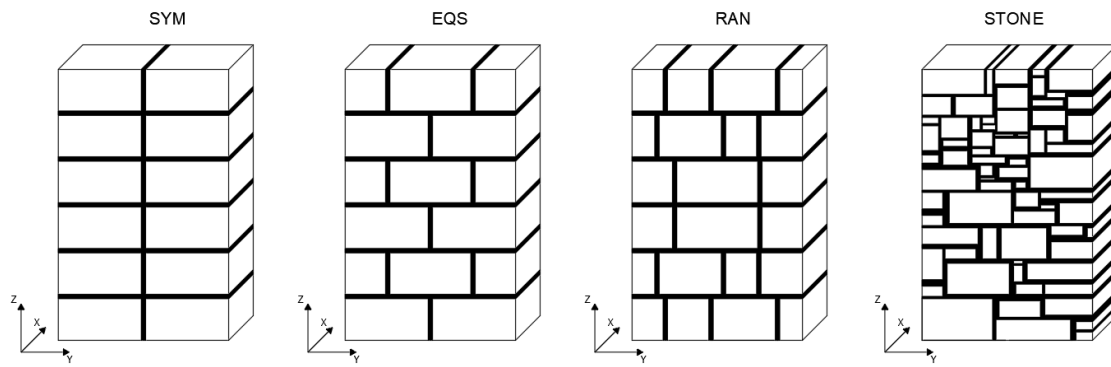


Figure 7-1: Wallette Panel Designs.

7.3 Material Strength Combinations

The simulation results were supplemented with the addition of four material strength combinations as shown in Table 1 below. Of those, apart from case A which was the original combination (Chapter 4), cases B to E were created to enrich the parametric study.

Table 7-1: Combinations of Material Strengths.

Case	Masonry Bricks		Mortar	
	Compressive Strength (MPa)	Tensile Strength (MPa)	Compressive Strength (MPa)	Tensile Strength (MPa)
A	100	10	4.6	0.46
B	50	5	4.6	0.46
C	30	3	4.6	0.46
D	100	10	2.3	0.23
E	100	10	1.0	0.1

Here the objective was to provide significantly different ratios of strength between mortar and the masonry bricks. As shown in the table, compressive strengths were a variable, whereas the tensile strengths were assumed to be 10% of the compressive strength.

7.4 SYM Results

The first of three specimens analyzed was the SYM specimen. The SYM design was found to have the second highest compressive strength of the 4 considered designs. Figures 7-2 to 7-13 present the calculated interaction diagrams and failure states for the parametric studies on bricks and mortar. The parameters of the investigation include analyzing each of the three SYM specimens under compression using each of the five strength combinations shown in Table 7-1 above. Following Figure 7-13 an overview of the findings will be discussed.

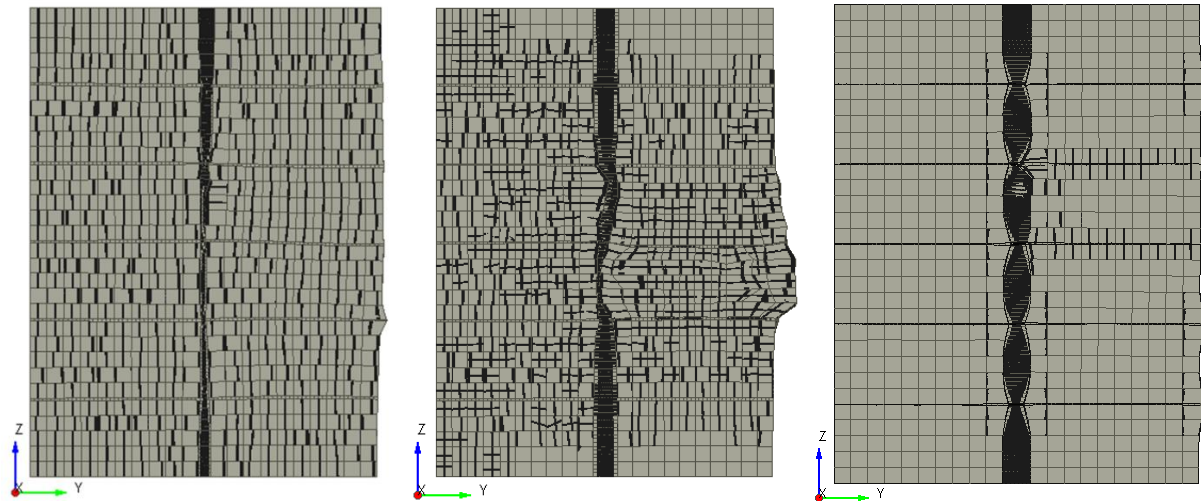


Figure 7-2: [LEFT] SYMJ5 $f_{bc} = 30 \text{ MPa}$, [MIDDLE] SYMJ5 $f_{bc} = 50 \text{ MPa}$, [RIGHT] SYMJ5 $f_{bc} = 100 \text{ MPa}$

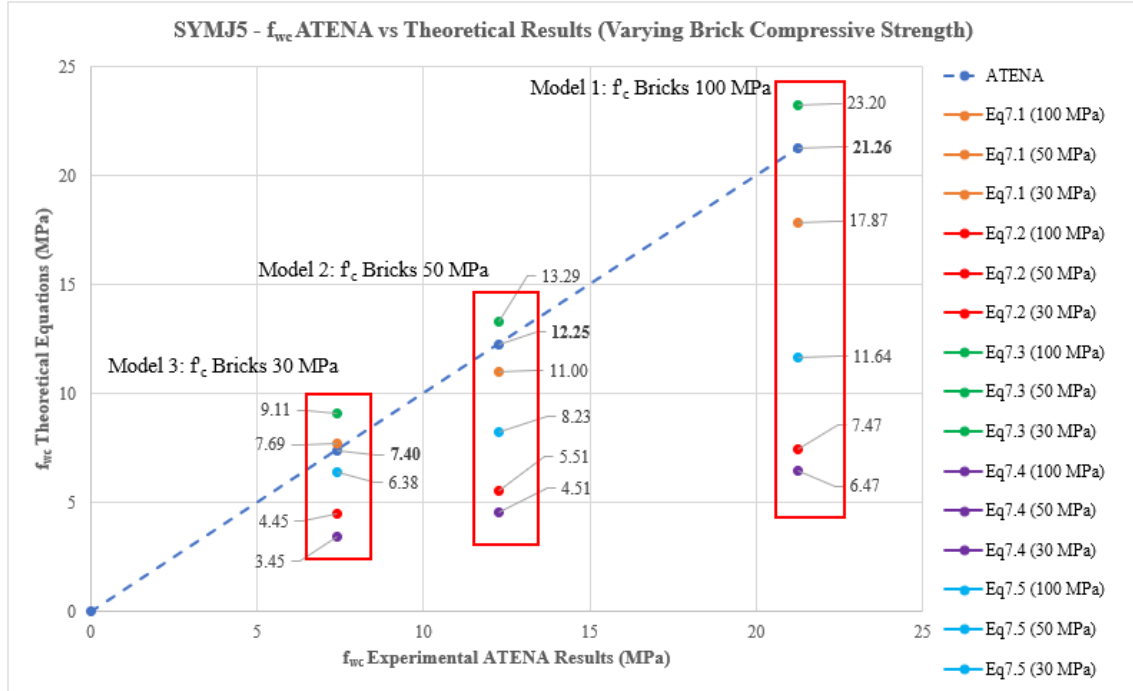


Figure 7-3: SYMJ5 ATENA vs Theoretical Equations (Varying Brick Compressive Strength)

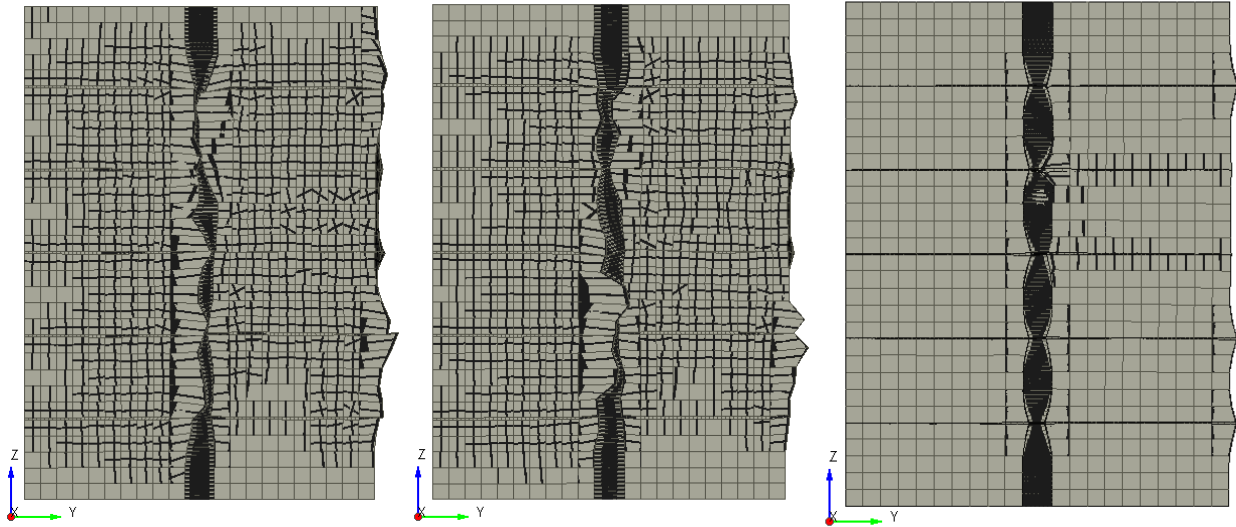


Figure 7-4: [LEFT] SYMJ5 $f_{mc} = 1.0$ MPa, [MIDDLE] SYMJ5 $f_{mc} = 2.3$ MPa, [RIGHT] SYMJ5 $f_{mc} = 4.6$ MPa

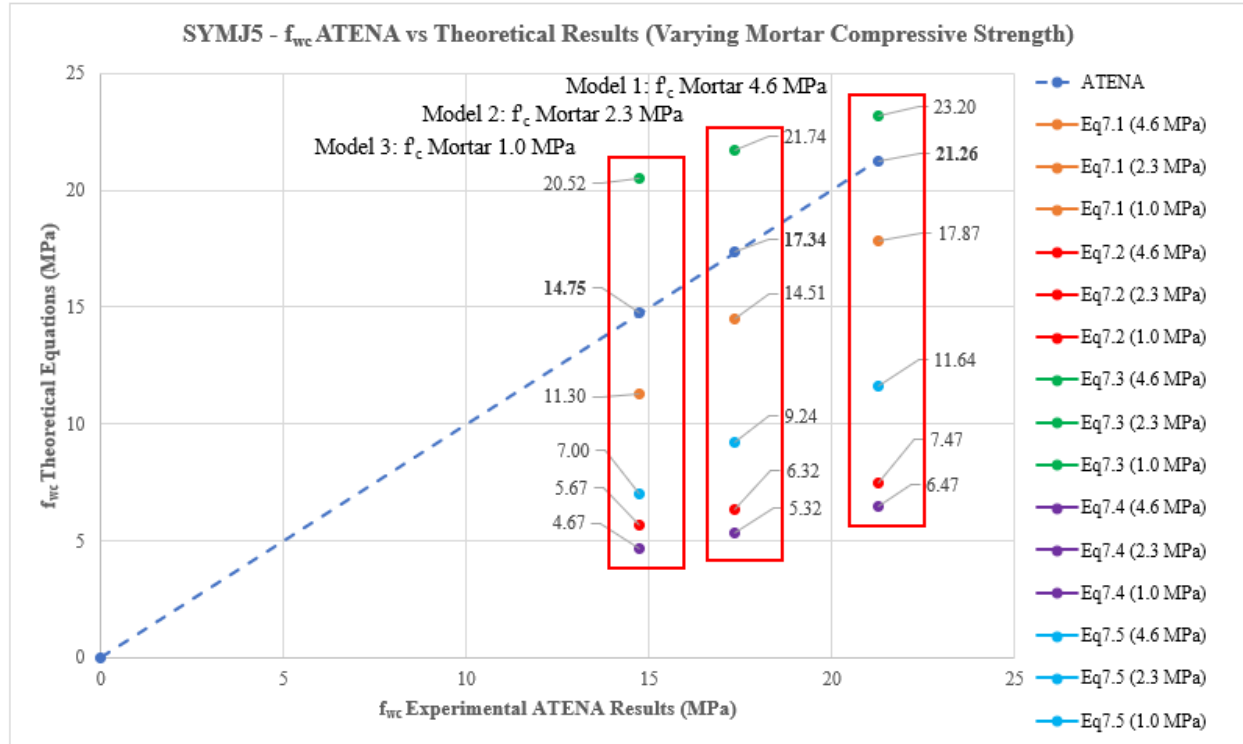


Figure 7-5: SYMJ5 ATENA vs Theoretical Equations (Varying Mortar Compressive Strength)

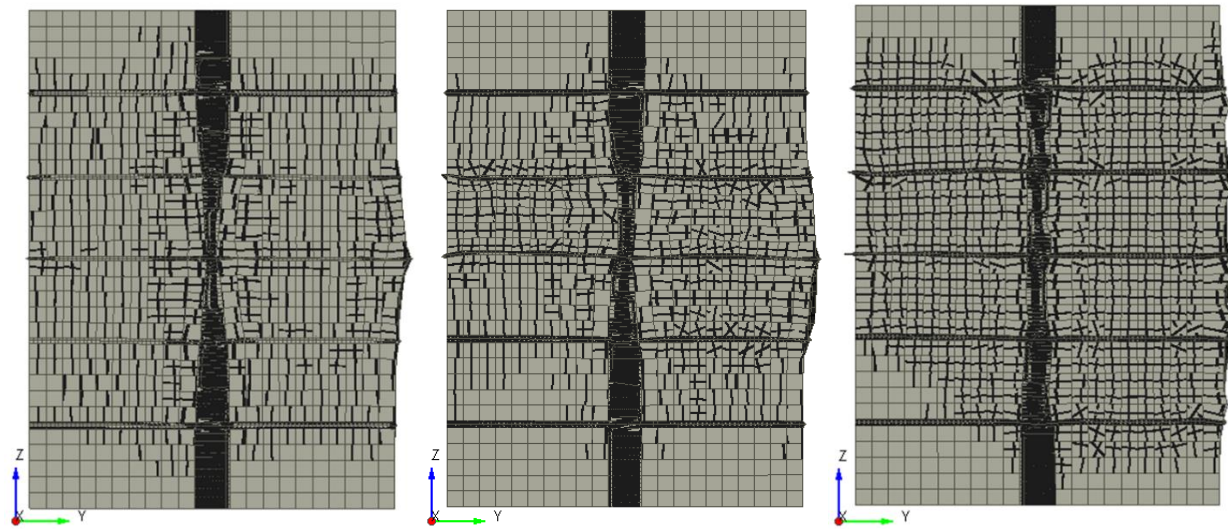


Figure 7-6: [LEFT] SYMJ10 $f_{bc} = 30$ MPa, [MIDDLE] SYMJ10 $f_{bc} = 50$ MPa, [RIGHT] SYMJ10 $f_{bc} = 100$ MPa

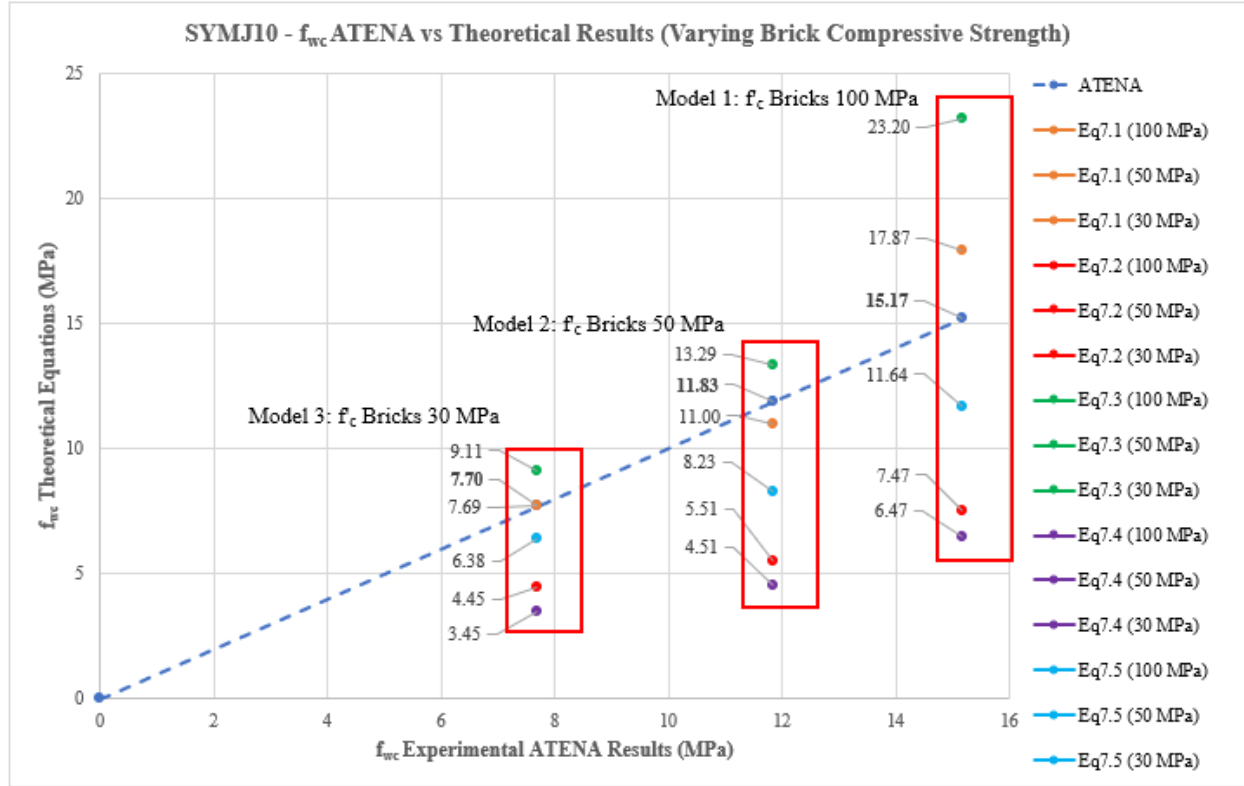


Figure 7-7: SYMJ10 ATENA vs Theoretical Equations (Varying Brick Compressive Strength)

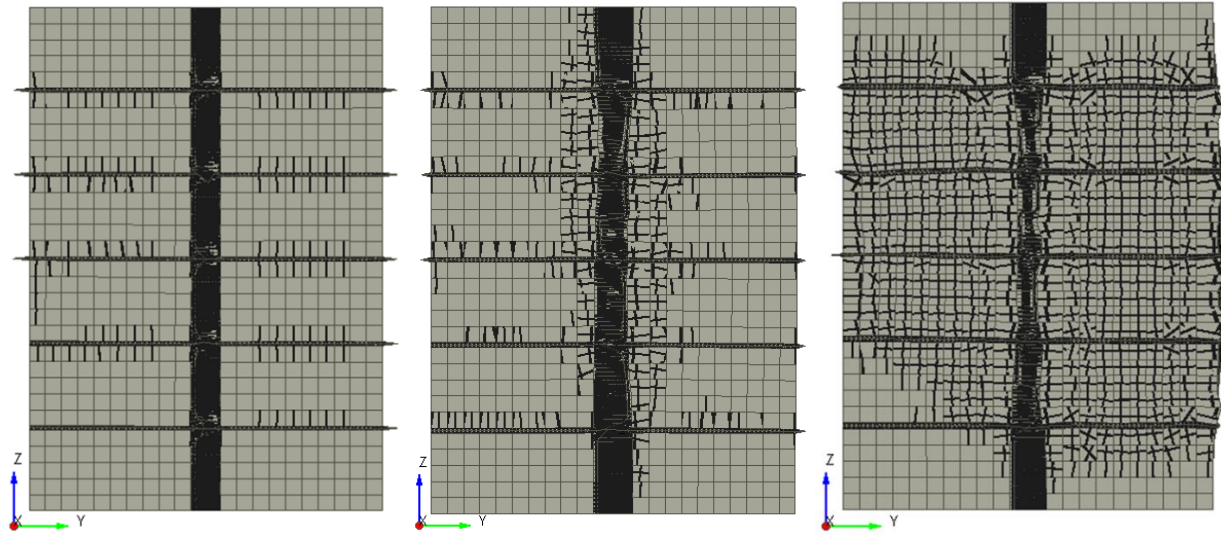


Figure 7-8: [LEFT] SYMJ10 $f_{mc} = 1.0$ MPa, [MIDDLE] SYMJ10 $f_{mc} = 2.3$ MPa, [RIGHT] SYMJ10 $f_{mc} = 4.6$ MPa

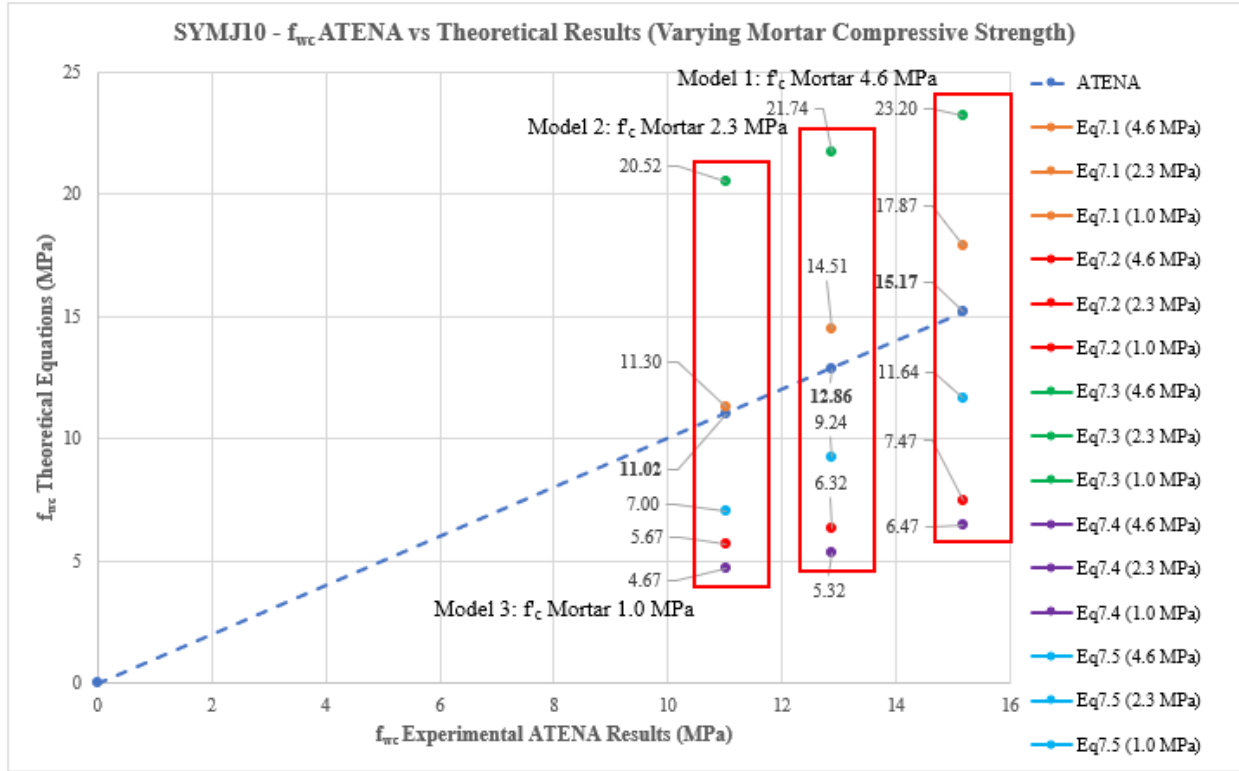


Figure 7-9: SYMJ10 ATENA vs Theoretical Equations (Varying Mortar Compressive Strength)

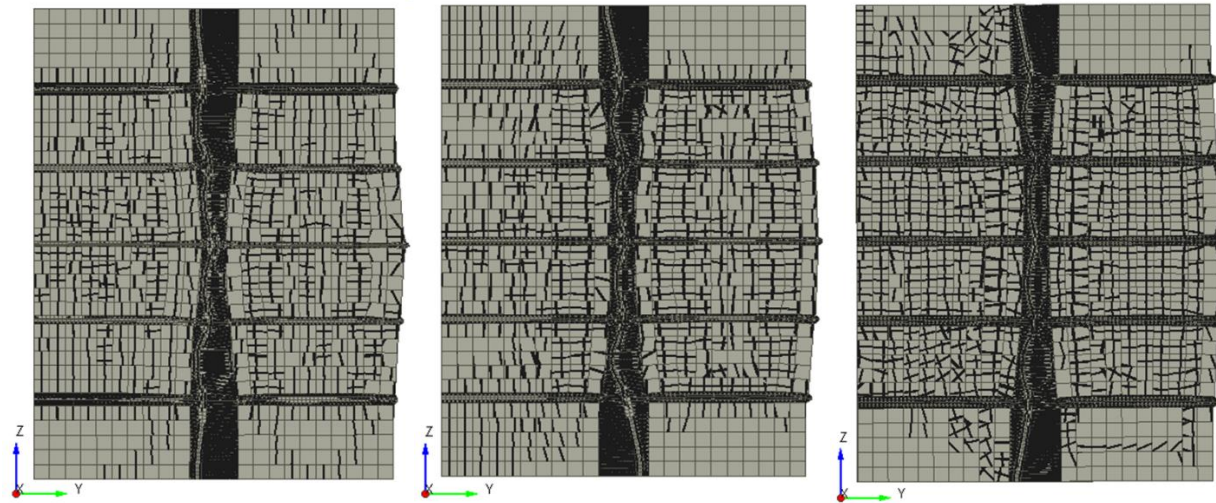


Figure 7-10: [LEFT] SYMJ20 $f_{bc} = 30$ MPa, [MIDDLE] SYMJ20 $f_{bc} = 50$ MPa, [RIGHT] SYMJ20 $f_{bc} = 100$ MPa

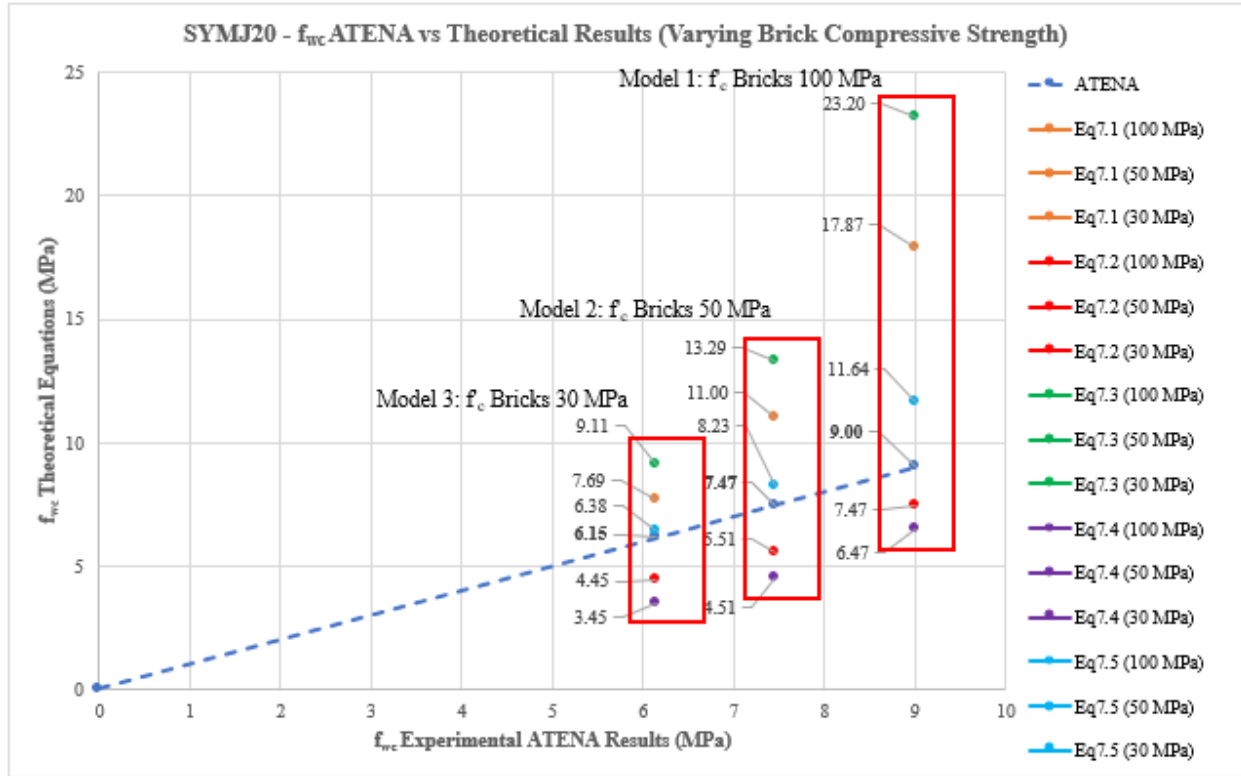


Figure 7-11: SYMJ20 ATENA vs Theoretical Equations (Varying Brick Compressive Strength)

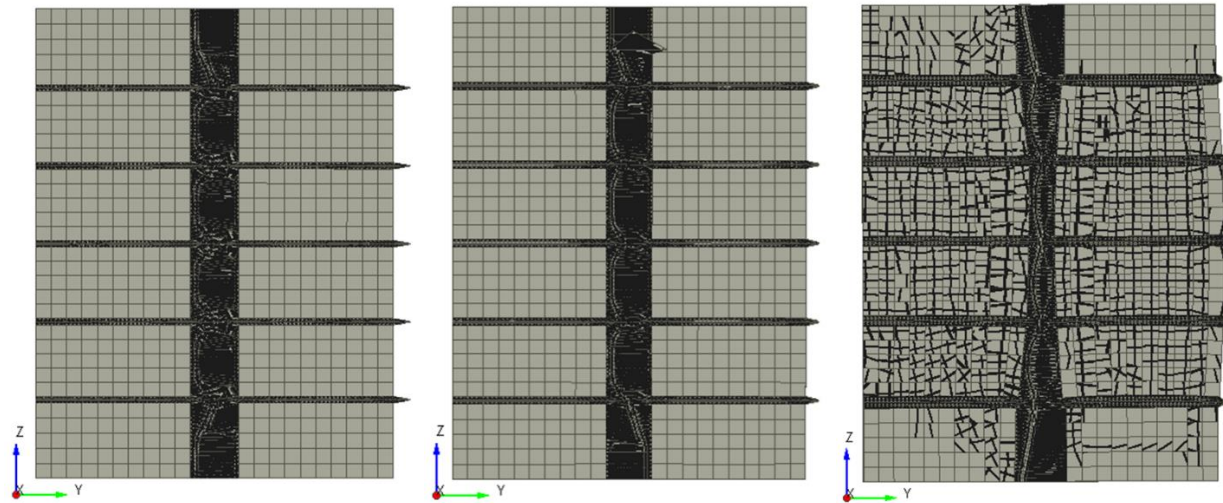


Figure 7-12: [LEFT] SYMJ20 $f_{mc} = 1.0$ MPa, [MIDDLE] SYMJ20 $f_{mc} = 2.3$ MPa, [RIGHT] SYMJ20 $f_{mc} = 4.6$ MPa

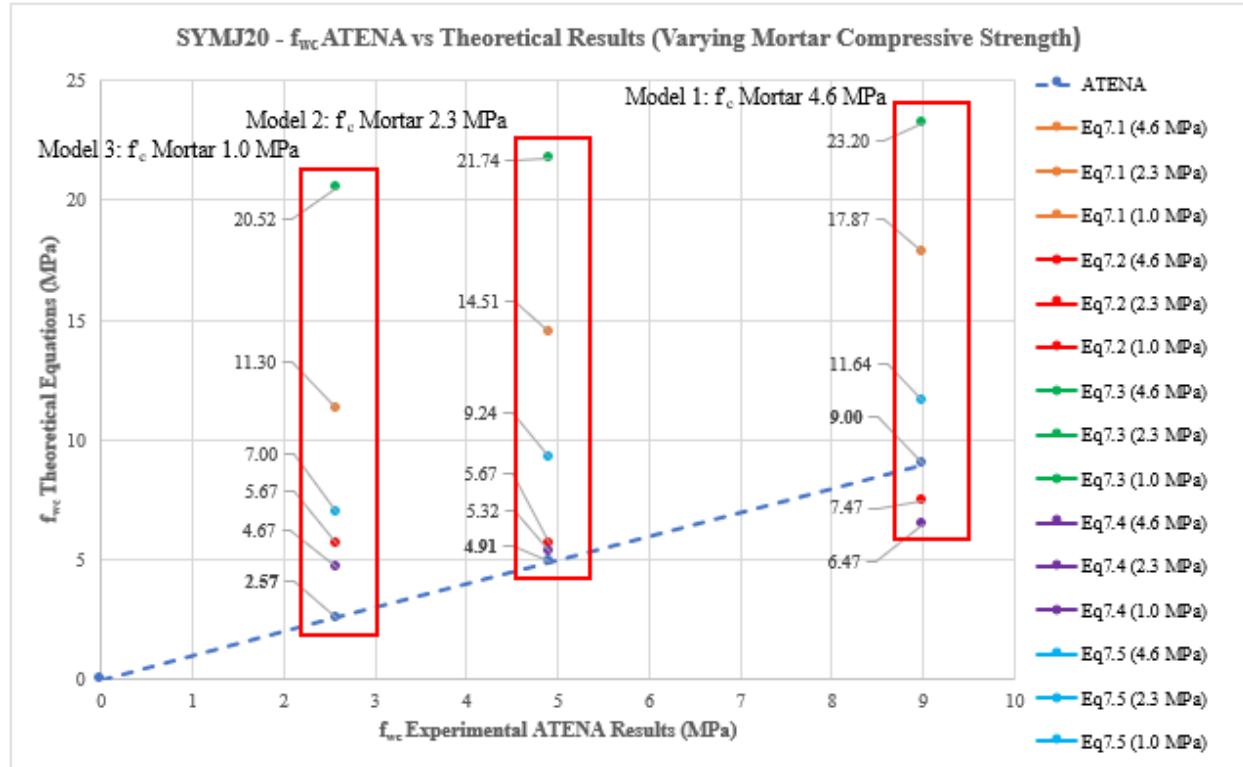


Figure 7-13: SYMJ20 ATENA vs Theoretical Equations (Varying Mortar Compressive Strength)

7.4.1 SYM Overview

Throughout the series of analyses involved in the parametric studies on the compressive strength of masonry bricks and mortar, the forms of damage remained relatively constant throughout. One of the common forms of damage in the SYM analyses was lateral dilation, which increased as the strength of the masonry bricks was increased from 30 MPa to 50 MPa, and finally 100 MPa. The increase in the bulging effect signifies that the specimen was able to reach higher lateral strains before failure.

Overall, it was observed that as the strength of the masonry bricks increased from 30 MPa to 50 MPa, and finally 100 MPa, the composite compressive strength of the specimens increased linearly. The same trend was observed when considering the compressive strength of mortar. As the strength increased, the composite compressive strength of the specimens also increased linearly. This observation is verified by the linear relationship found between the compressive strength of bricks and mortar with the compressive strength of the specimen shown in Figures 7-7, 7-7, and 7-9 above.

An additional factor which was assessed was the contribution of strength from the bricks and mortar to the composite strength of the wallette specimens. Overall, it was found that the effect

of the masonry bricks predominates over that of the mortar. In the case of SYMJ10, decreasing the compressive strength of masonry bricks by 50% led to 22.02% reduction in composite strength, whereas in the case of mortar, the effect was only 15.23%. Therefore, altering the strength of the masonry bricks had a larger impact on the composite material properties than altering the strength of mortar.

When comparing the numerical results from ATENA 3D with the results from the five empirical equations considered, it is observed that effectiveness of the empirical equations changed as the specifications of the considered specimen were altered including the material strengths and the mortar joints thickness. For 5 mm and 10 mm joints it was found that Equation 7.5 provides the most conservative estimate while meeting all of the defined success criteria. For 20 mm joints it was found that only Equation 7.2 provides a valid estimate and only when the compressive strength of the mortar was held constant at 4.6 MPa.

7.5 EQS Results

Under compression, EQS was one of the superior designs of the 4 presented. The horizontal placement of having each head joint end at the center of a masonry brick allowed for improved engagement of the bricks which increased the composite properties of the specimens. Figures 7-14 to 7-25 present the calculated interaction diagrams and failure states for the parametric studies on bricks and mortar. The parameters of the investigation include analyzing each of the three EQS specimens under compression using each of the five strength combinations shown in Table 7-1 above. Following Figure 7-25 an overview of the findings will be discussed.

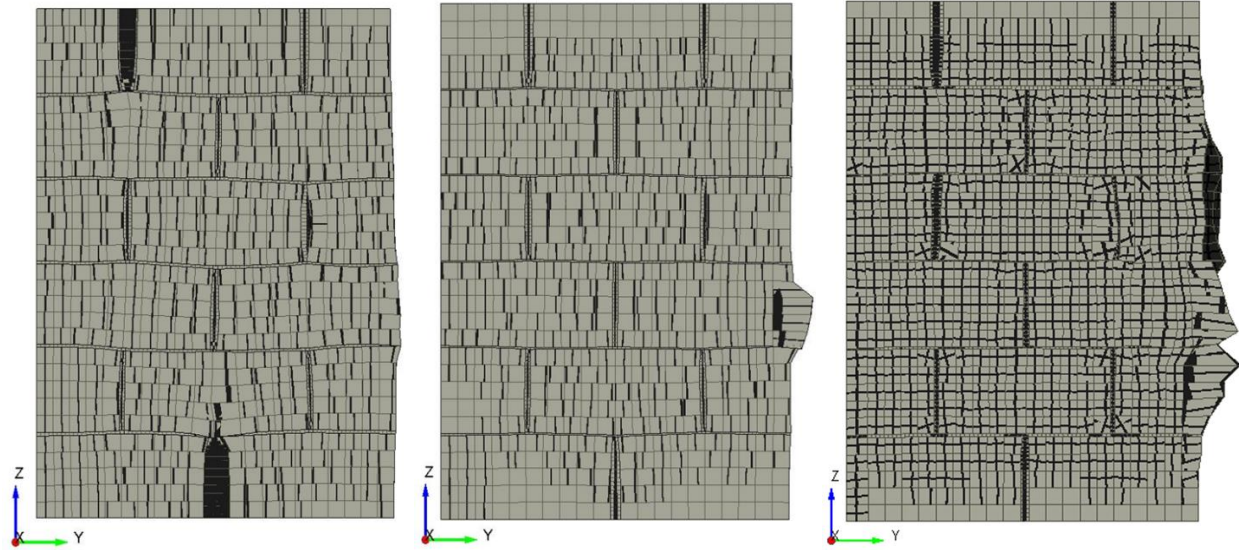


Figure 7-14: [LEFT] EQSJ5 $f_{bc} = 30$ MPa, [MIDDLE] EQSJ5 $f_{bc} = 50$ MPa, [RIGHT] EQSJ5 $f_{bc} = 100$ MPa

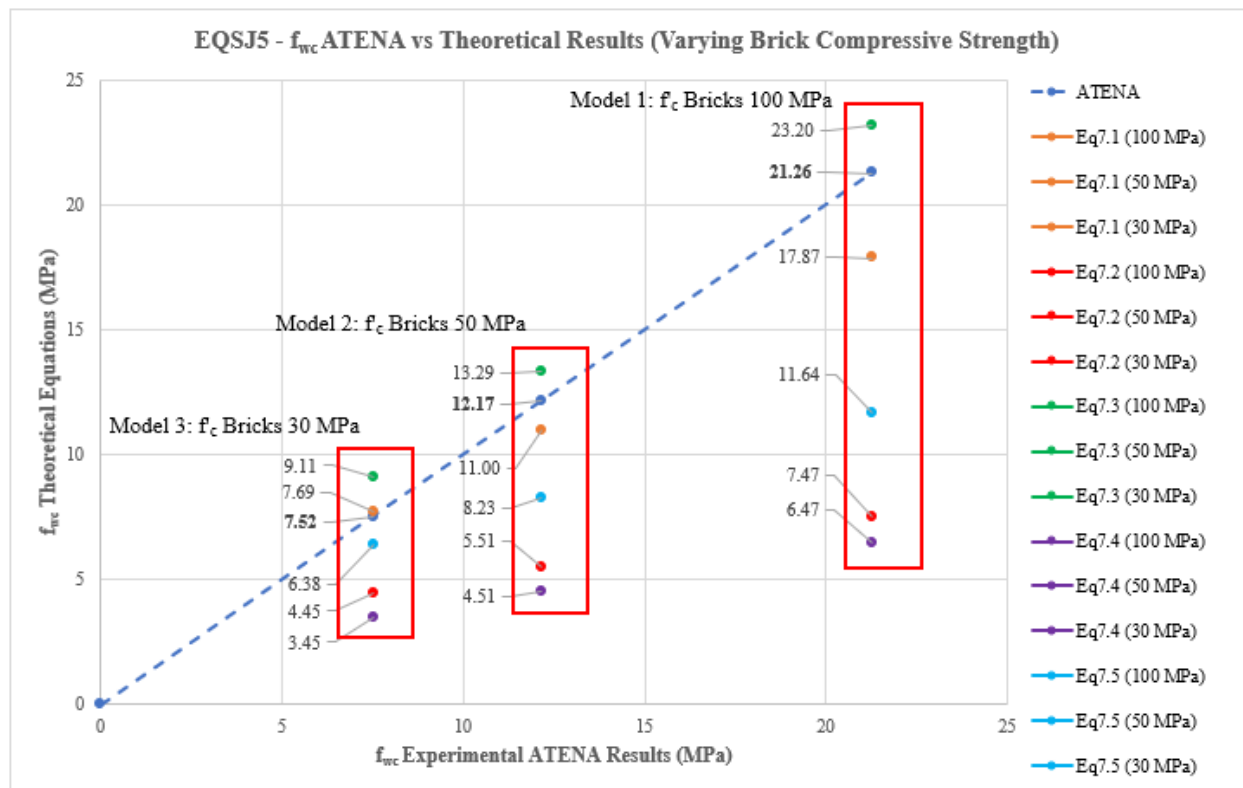


Figure 7-15: EQSJ5 ATENA vs Theoretical Equations (Varying Brick Compressive Strength)

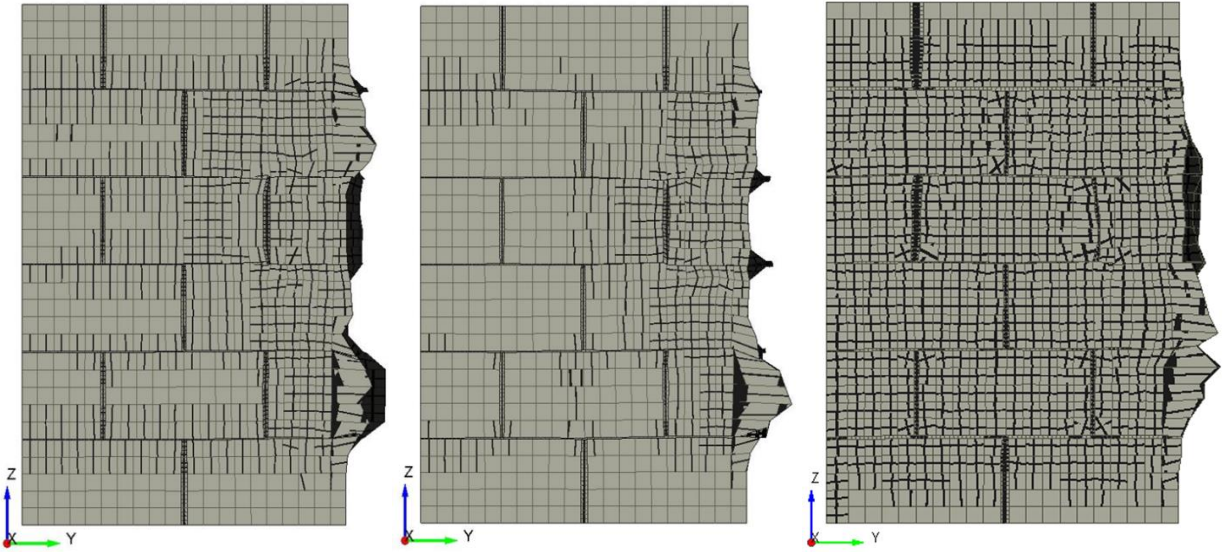


Figure 7-16: [LEFT] EQSJ5 $f_{mc} = 1.0$ MPa, [MIDDLE] EQSJ5 $f_{mc} = 2.3$ MPa, [RIGHT] EQSJ5 $f_{mc} = 4.6$ MPa

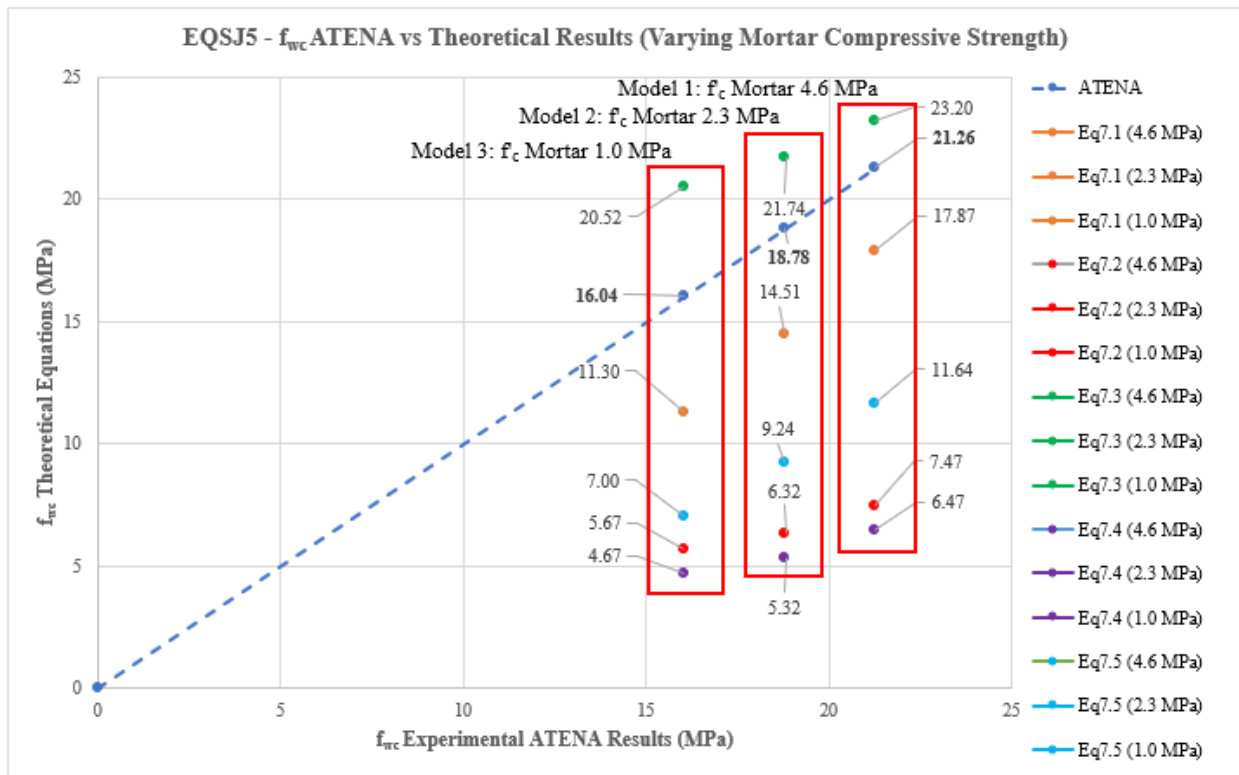


Figure 7-17: EQSJ5 ATENA vs Theoretical Equations (Varying Mortar Compressive Strength)

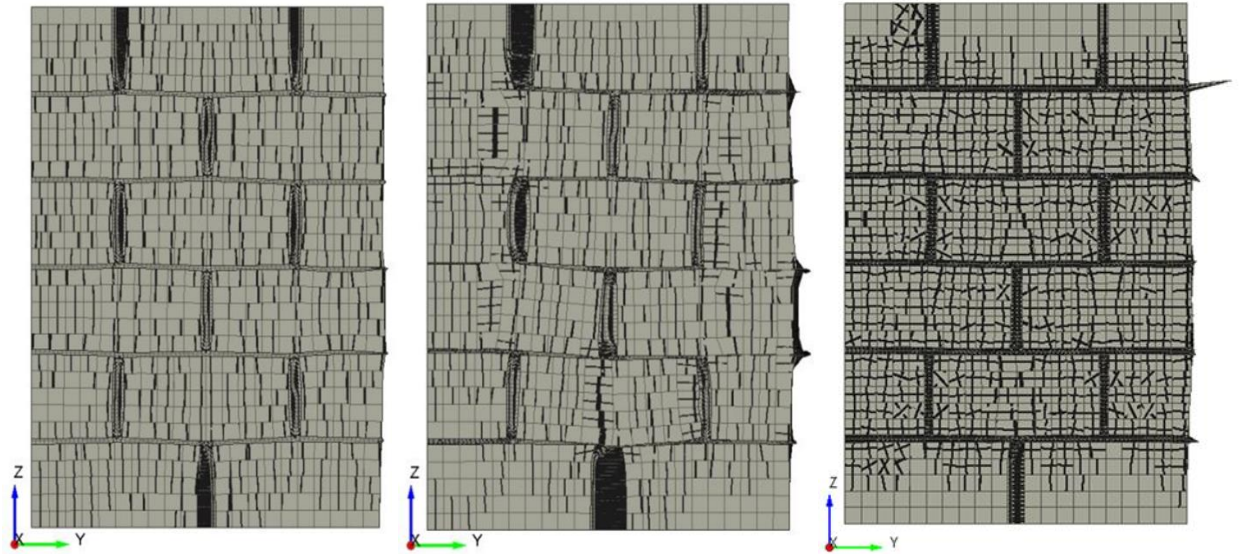


Figure 7-18: [LEFT] EQSJ10 $f_{bc} = 30$ MPa, [MIDDLE] EQSJ10 $f_{bc} = 50$ MPa, [RIGHT] EQSJ10 $f_{bc} = 100$ MPa

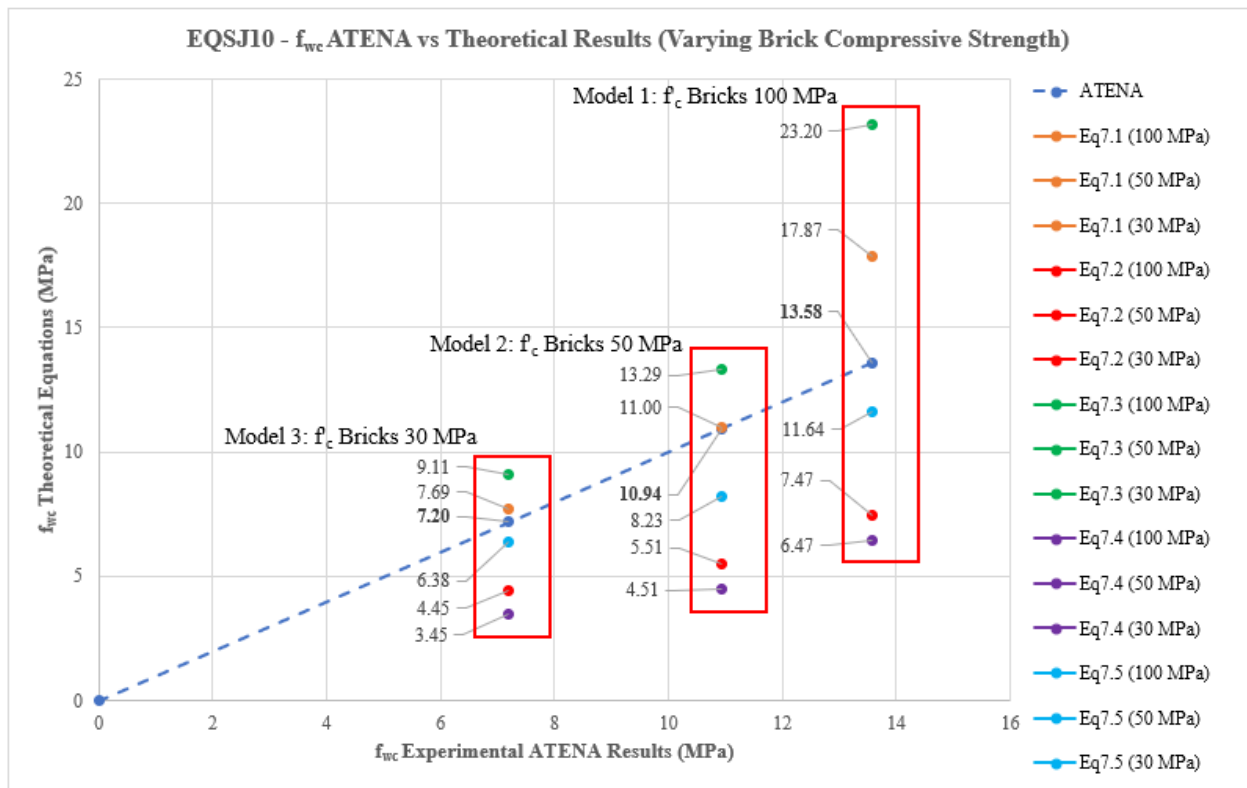


Figure 7-19: EQSJ10 ATENA vs Theoretical Equations (Varying Brick Compressive Strength)

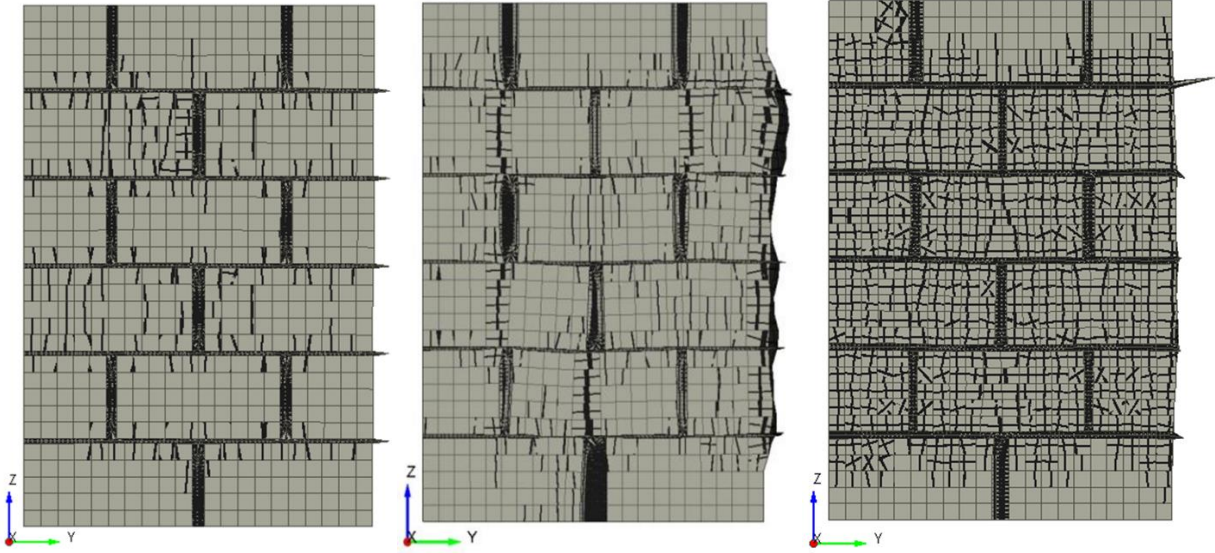


Figure 7-20: [LEFT] EQSJ10 $f_{mc} = 1.0$ MPa, [MIDDLE] EQSJ10 $f_{mc} = 2.3$ MPa, [RIGHT] EQSJ10 $f_{mc} = 4.6$ MPa

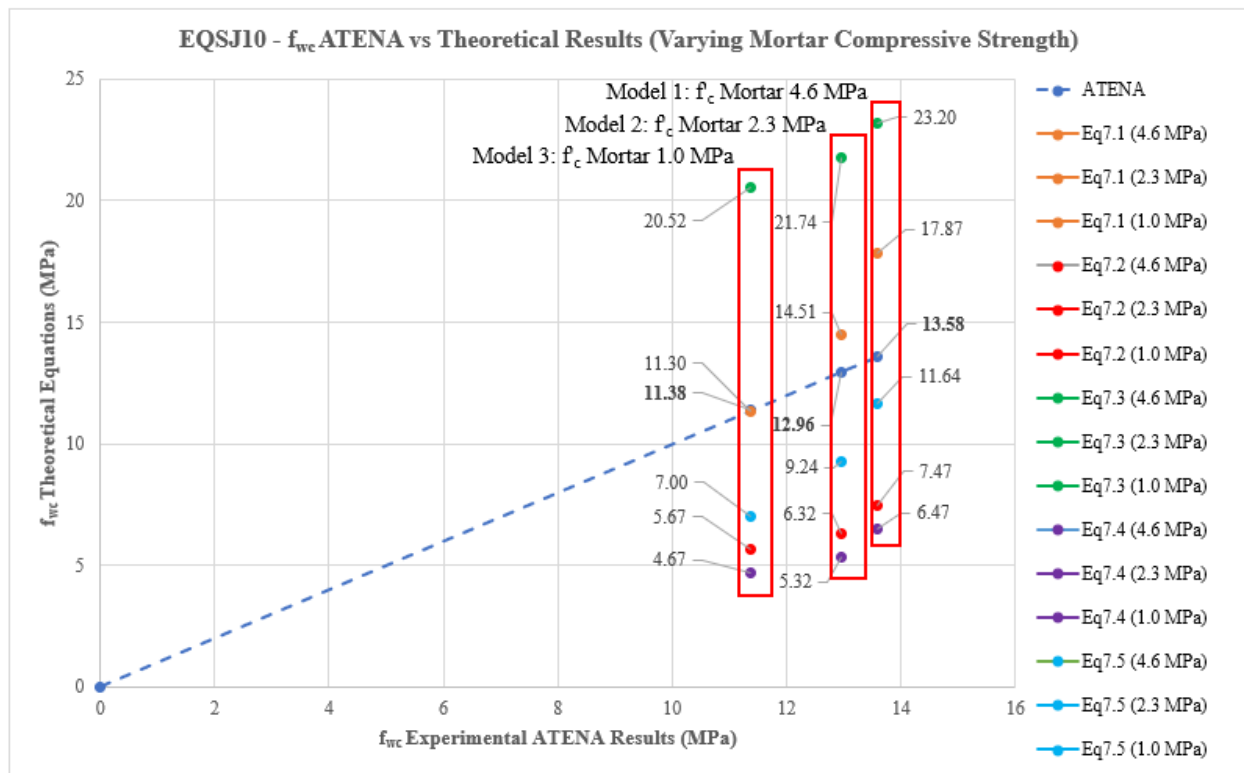


Figure 7-21: EQSJ10 ATENA vs Theoretical Equations (Varying Mortar Compressive Strength)

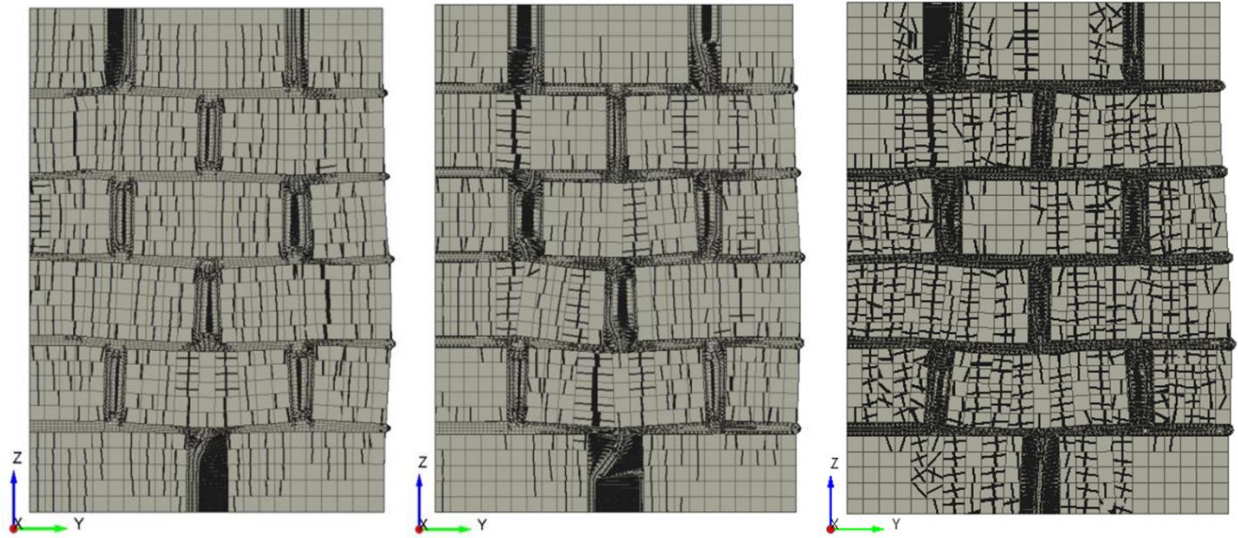


Figure 7-22: [LEFT] EQSJ20 $f_{bc} = 30$ MPa, [MIDDLE] EQSJ20 $f_{bc} = 50$ MPa, [RIGHT] EQSJ20 $f_{bc} = 100$ MPa

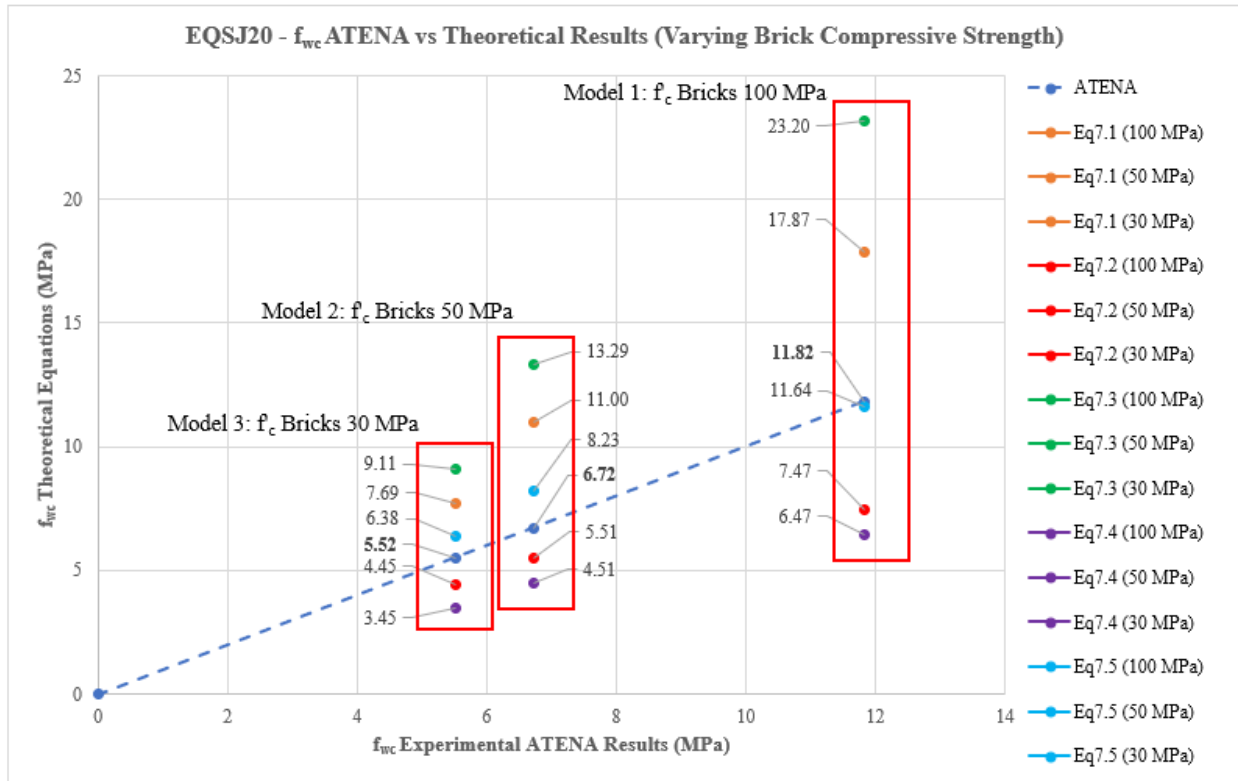


Figure 7-23: EQSJ20 ATENA vs Theoretical Equations (Varying Brick Compressive Strength)

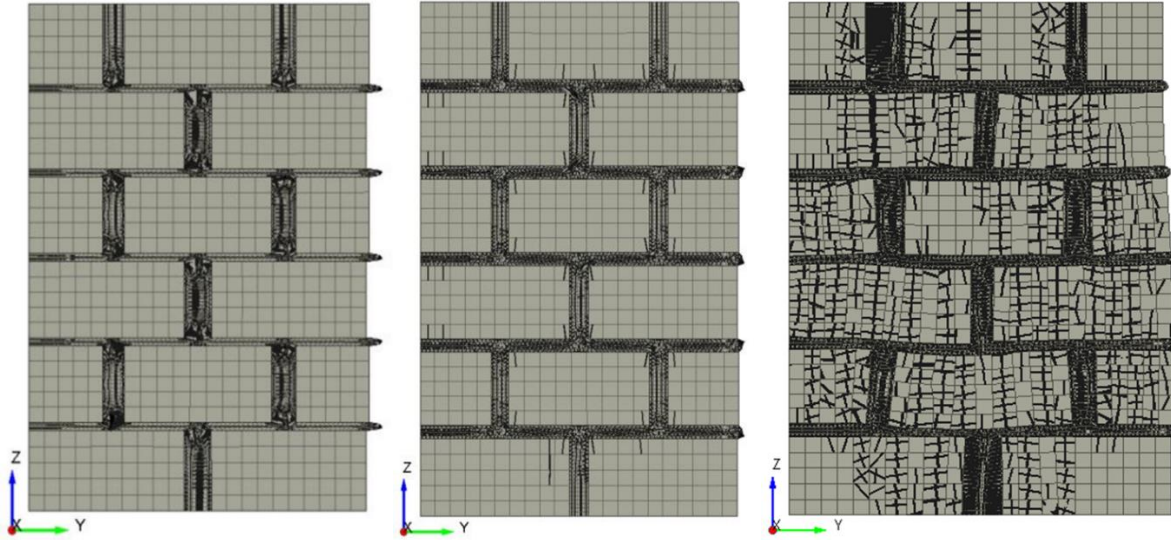


Figure 7-24: [LEFT] EQSJ20 $f_{mc} = 1.0$ MPa, [MIDDLE] EQSJ20 $f_{mc} = 2.3$ MPa, [RIGHT] EQSJ20 $f_{mc} = 4.6$ MPa

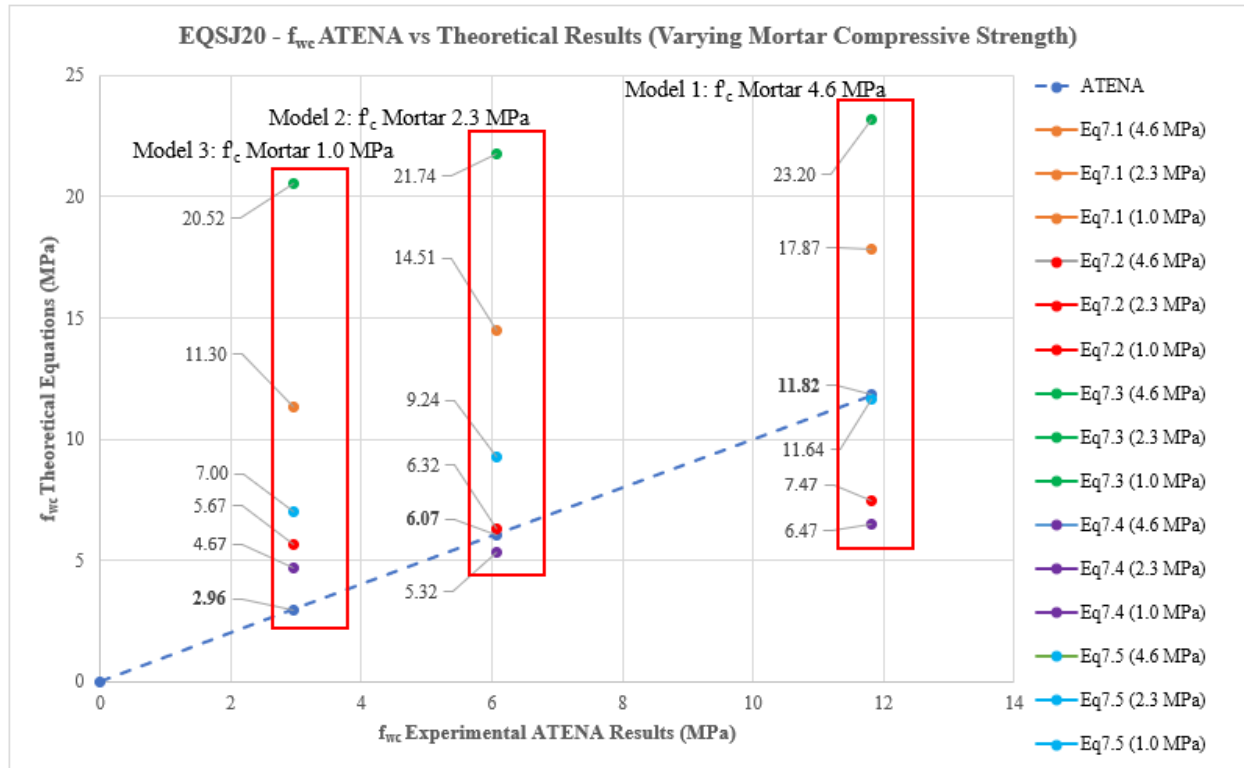


Figure 7-25: EQSJ20 ATENA vs Theoretical Equations (Varying Mortar Compressive Strength)

7.5.1 EQS Overview

Throughout the analyses the main source of damage observed was bulging along the right edge of the specimens. In addition, it was found that cracking and deformation occurred at the centre of the masonry bricks which had a head joint located above or below its center. This is due to increased deformations along the head joints due to the mortar's lower compressive strength in comparison to the masonry bricks. In some cases, such as EQSJ10, as the compressive strength of mortar was reduced, the masonry bricks lying above and below the head joints were completely severed at the center. As the compressive strength of the masonry bricks and mortar increased, the deformations and cracking along the center of the masonry bricks no longer occurred.

From the interaction diagrams above, a positive linear relationship was found between the compressive strength of masonry and mortar with the composite strength of the wallettes. As the compressive strength of the mortar increased from 1.0 MPa, to 2.3 MPa, and finally 4.6 MPa, the computed composite compressive strength of the specimen also increased. It was observed that the overall effects of decreasing the compressive strength of mortar was less than decreasing the compressive strength of the masonry bricks. In the case of EQSJ5, when the compressive strength of the masonry bricks was reduced by 50% from 100 MPa to 50 MPa, the compressive strength of the specimen reduced by 42.76%. When the compressive strength of the mortar was reduced by 50% from 4.6 MPa to 2.3 MPa, the compressive strength of the specimen was reduced by 11.66%. Therefore, the effects of altering the material properties of the masonry bricks were significantly greater than altering the material properties of mortar. This signifies that the masonry bricks have a large contribution on the composite properties and is more significant than mortar.

When correlating the results from the finite element analyses with the empirical equations, it was found that once again only Equation 7.5 provided a valid estimate of the composite compressive strength for global mortar joint thicknesses of 5 mm and 10 mm. For 20 mm joints it was found that Equation 7.2 provided a valid estimate but only when the compressive strength of mortar was held constant at 4.6 MPa.

7.6 RAN Results

The next design studied was the RAN design. The RAN specimens as discussed are modelled to reflect a form of masonry more typical of the historic times. As was observed in the compression and pushover investigations, the randomness of the brick and mortar joint layout led

to large crack patterns and openings at failure specifically under compression. This led to a severely reduced performance in comparison to the previously discussed designs. For the parametric investigations to be presented below, the two main points of interest are firstly if a positive linear relationship will be present throughout the results. Secondly, with the expected reduction in performance under compression, will the empirical equations provide valid estimations that meet the success criteria. Figures 7-26 to 7-37 present the calculated interaction diagrams and failure states for the parametric studies on bricks and mortar. The parameters of the investigation include analyzing each of the three RAN specimens under compression using each of the five strength combinations shown in Table 7-1 above. Following Figure 7-37 an overview of the findings will be discussed.

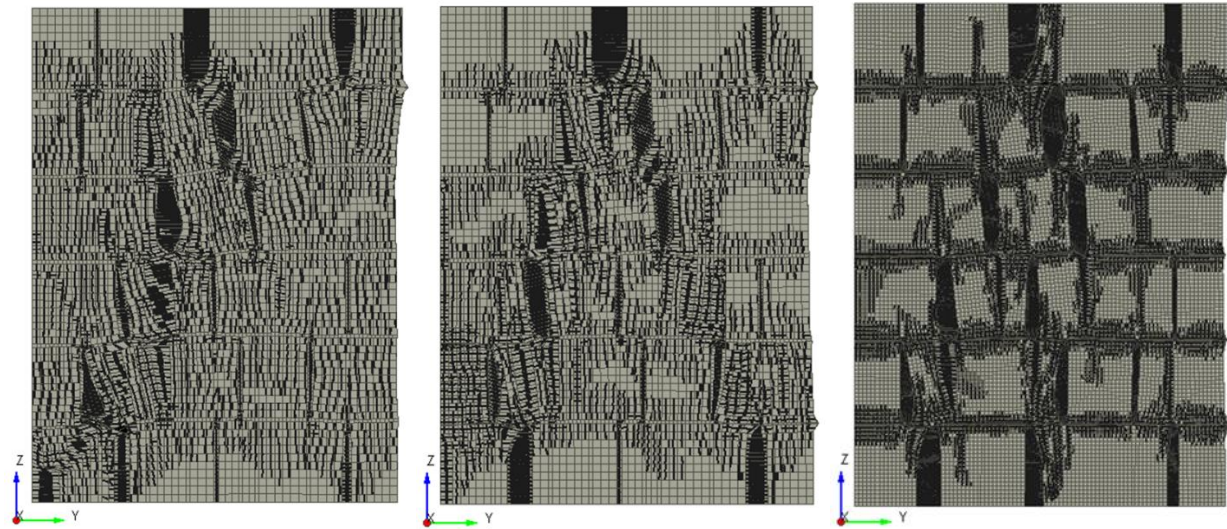


Figure 7-26: [LEFT] RANJ5 $f_{bc} = 30 \text{ MPa}$, [MIDDLE] RANJ5 $f_{bc} = 50 \text{ MPa}$, [RIGHT] RANJ5 $f_{bc} = 100 \text{ MPa}$

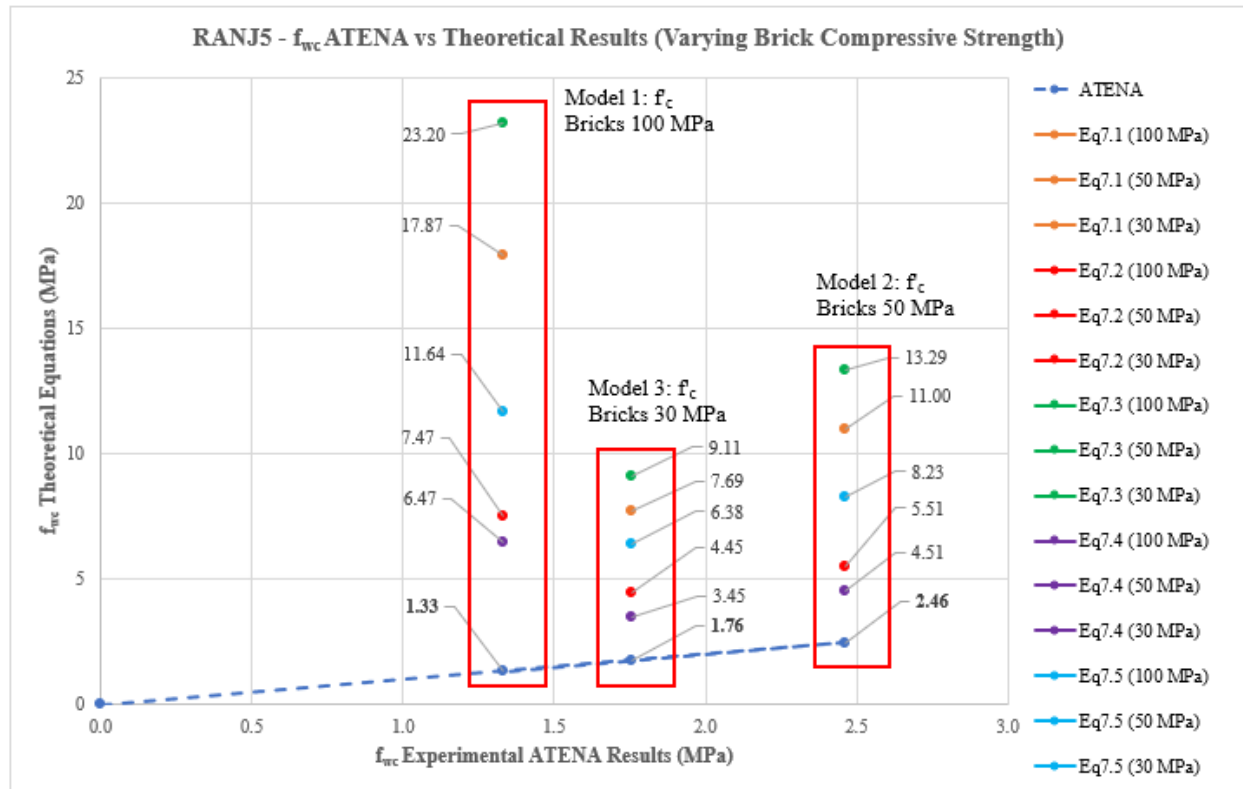


Figure 7-27: RANJ5 ATENA vs Theoretical Equations (Varying Brick Compressive Strength)

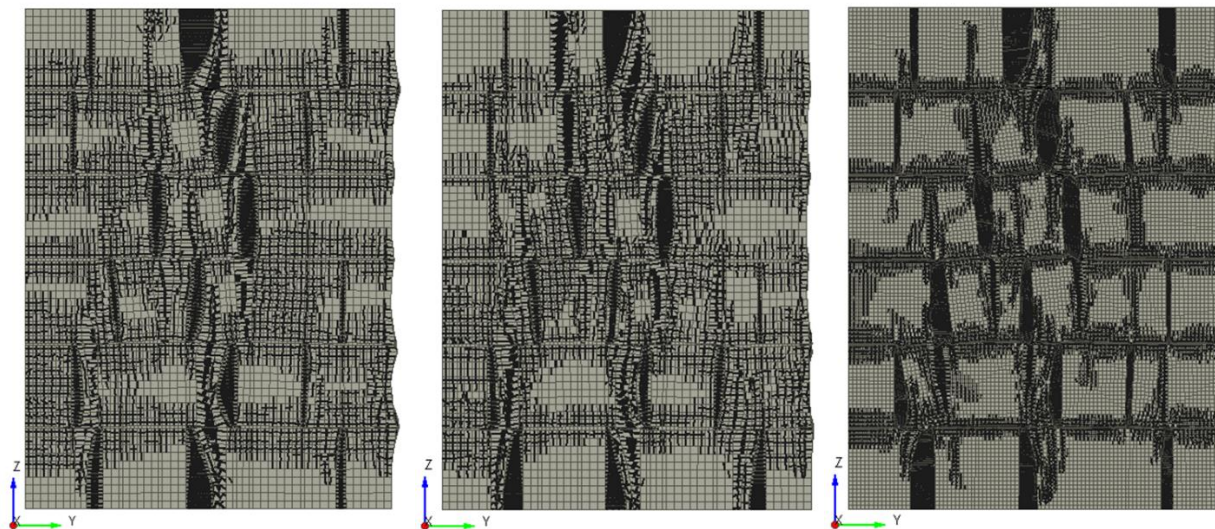


Figure 7-28: [LEFT] RANJ5 $f_{mc} = 1.0$ MPa, [MIDDLE] RANJ5 $f_{mc} = 2.3$ MPa, [RIGHT] RANJ5 $f_{mc} = 4.6$ MPa

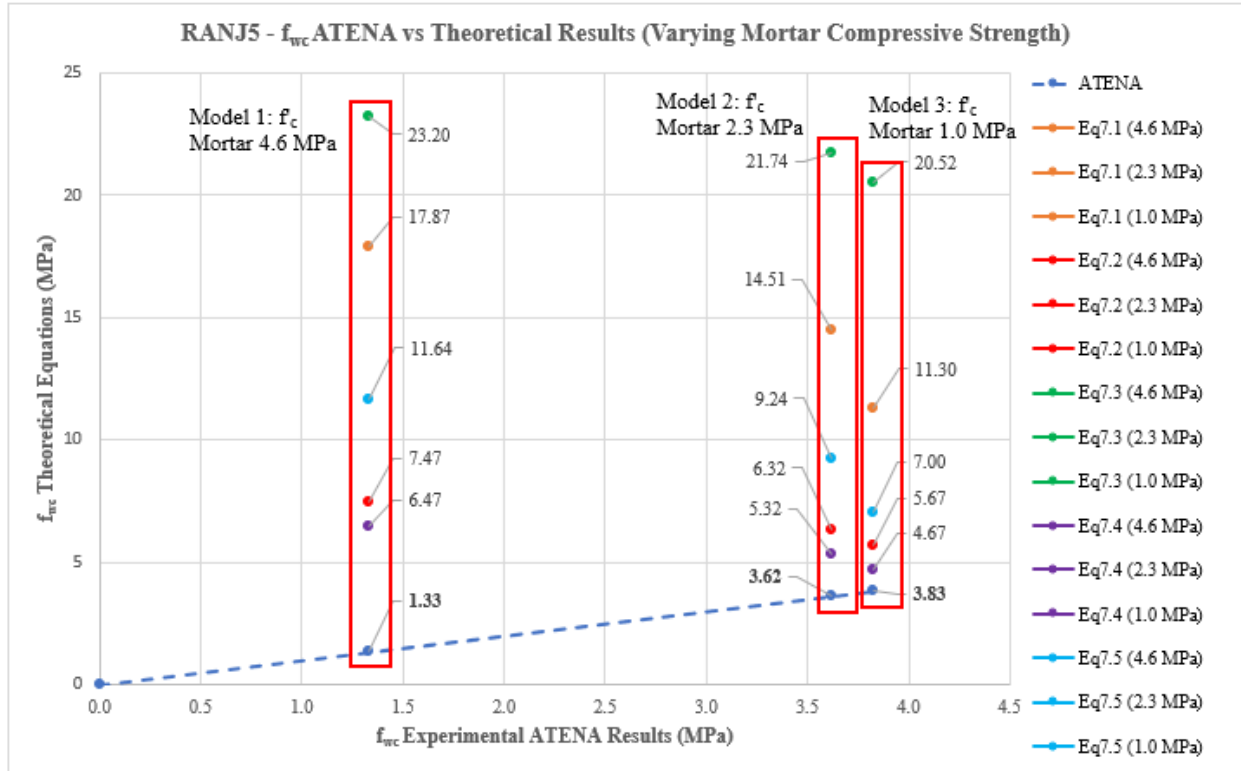


Figure 7-29: RANJ5 ATENA vs Theoretical Equations (Varying Mortar Compressive Strength)

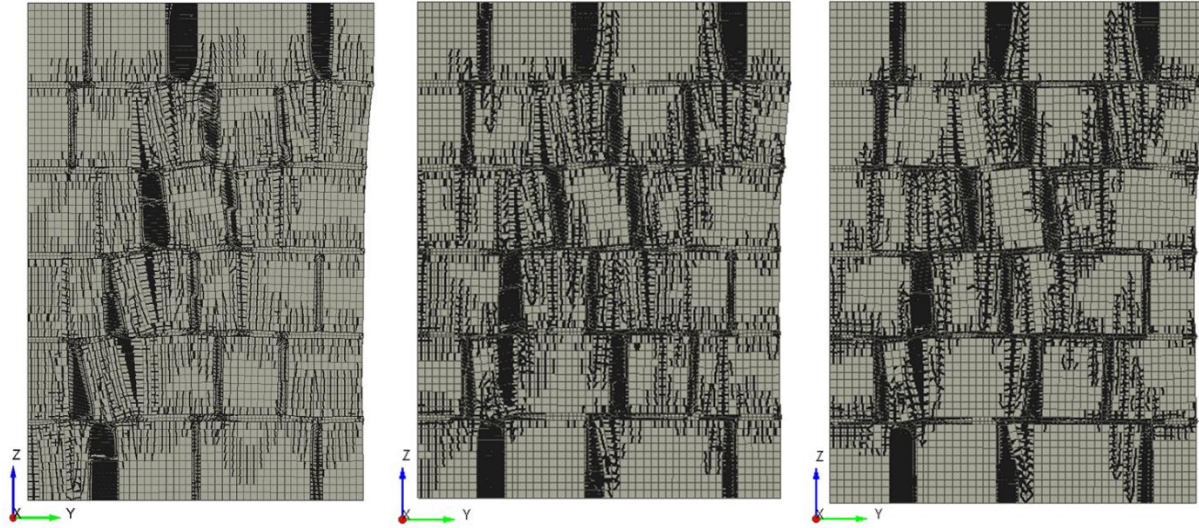


Figure 7-30: [LEFT] RANJ10 $f_{bc} = 30$ MPa, [MIDDLE] RANJ10 $f_{bc} = 50$ MPa, [RIGHT] RANJ10 $f_{bc} = 100$ MPa

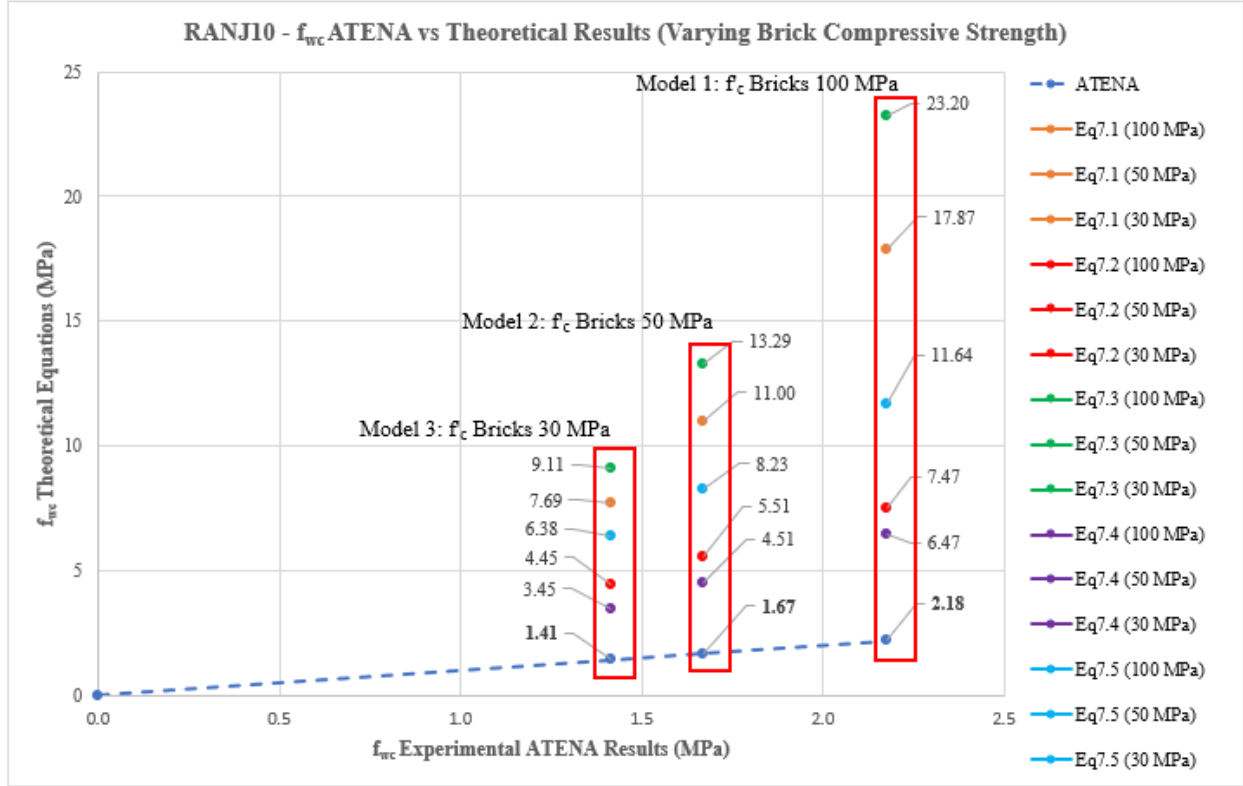


Figure 7-31: RANJ10 ATENA vs Theoretical Equations (Varying Brick Compressive Strength)

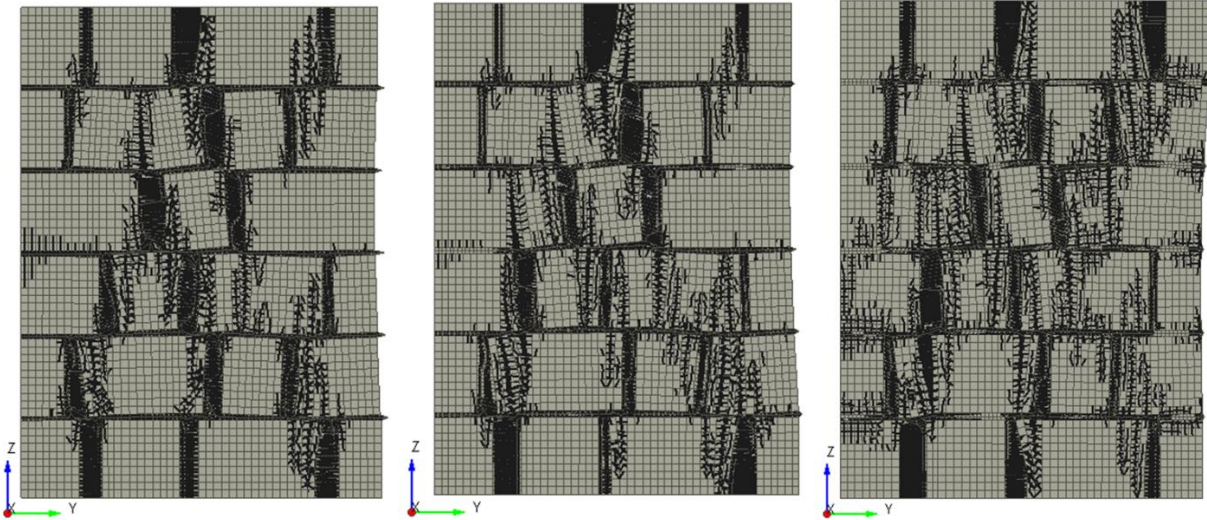


Figure 7-32: [LEFT] RANJ10 $f_{mc} = 1.0$ MPa, [MIDDLE] RANJ10 $f_{mc} = 2.3$ MPa, [RIGHT] RANJ10 $f_{mc} = 4.6$ MPa

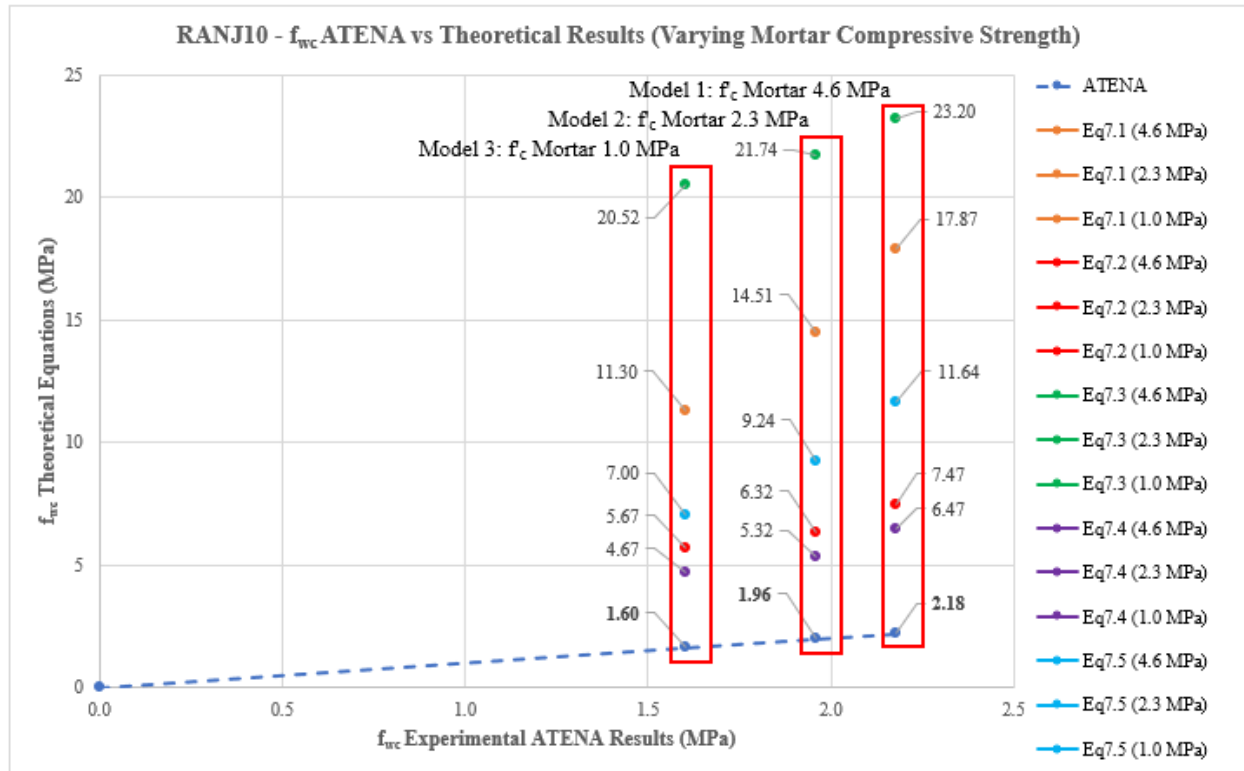


Figure 7-33: RANJ10 ATENA vs Theoretical Equations (Varying Mortar Compressive Strength)

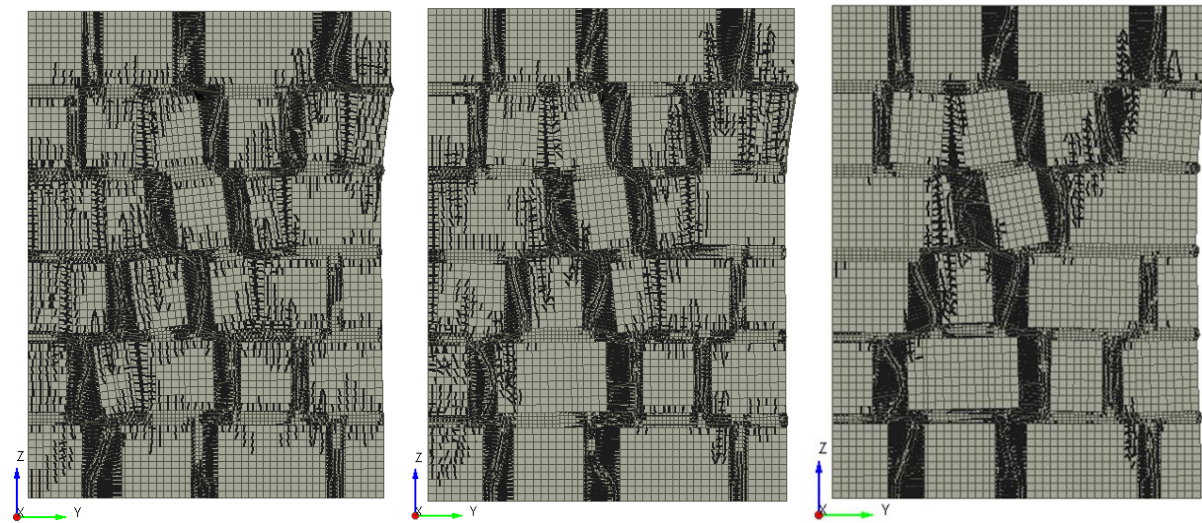


Figure 7-34: [LEFT] RANJ20 $f_{bc} = 30$ MPa, [MIDDLE] RANJ20 $f_{bc} = 50$ MPa, [RIGHT] RANJ20 $f_{bc} = 100$ MPa

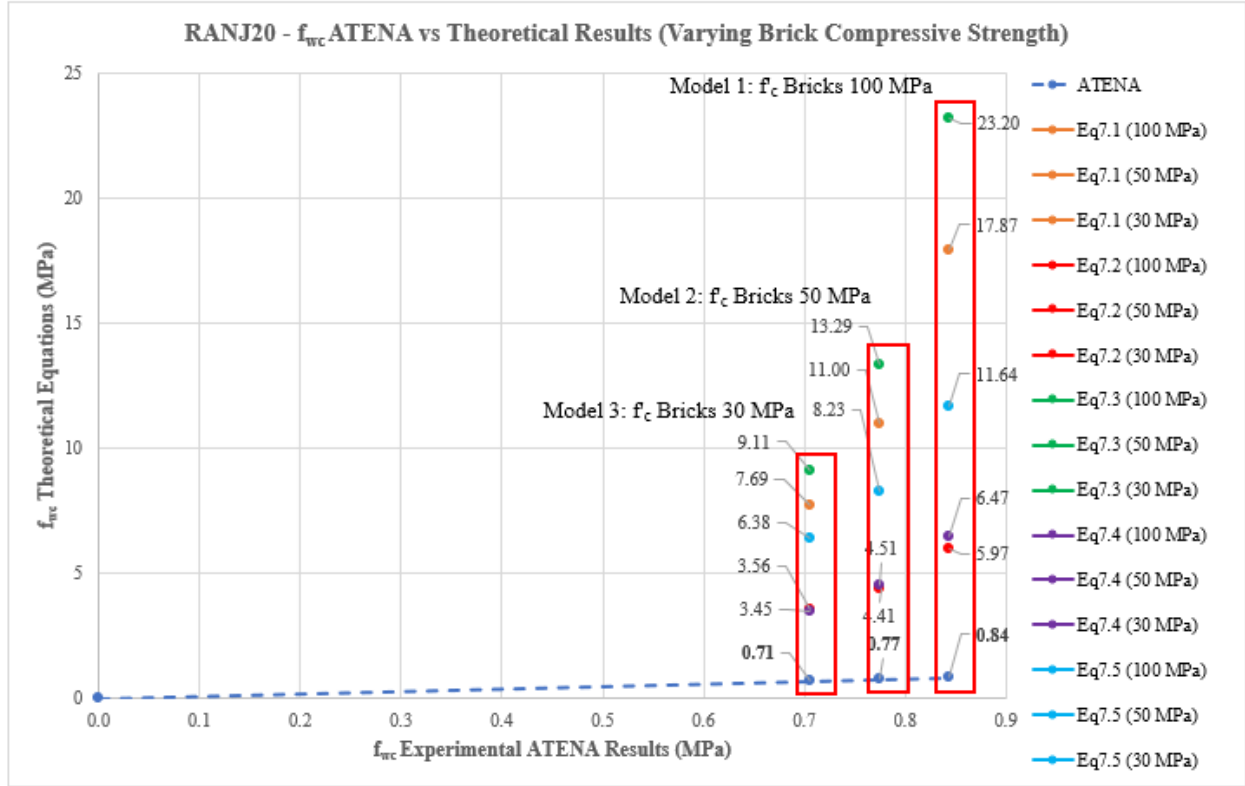


Figure 7-35: RANJ20 ATENA vs Theoretical Equations (Varying Brick Compressive Strength)

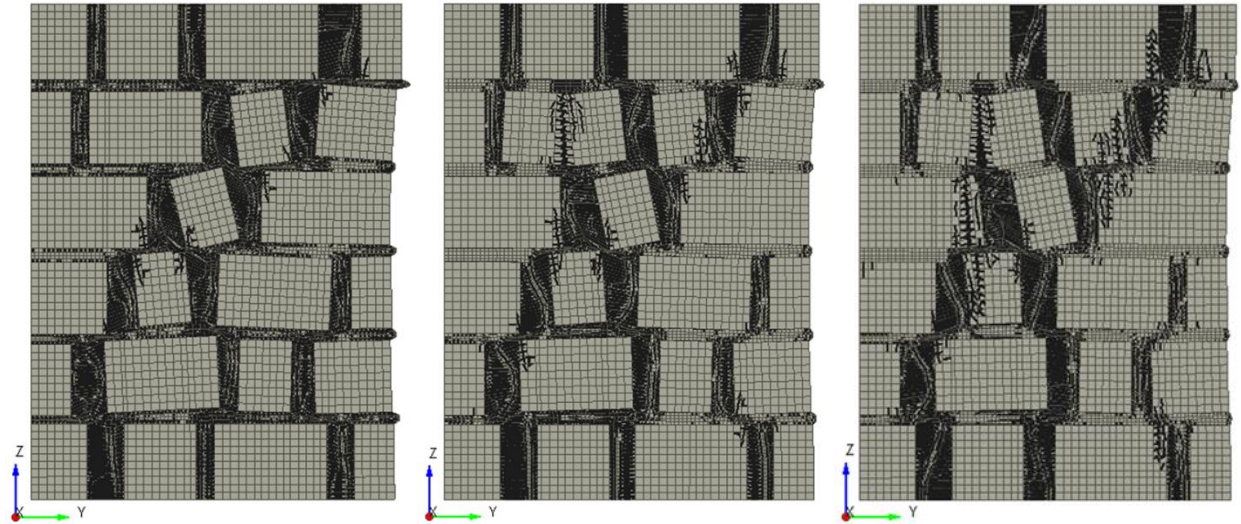


Figure 7-36: [LEFT] RANJ20 $f_{mc} = 1.0$ MPa, [MIDDLE] RANJ20 $f_{mc} = 2.3$ MPa, [RIGHT] RANJ20 $f_{mc} = 4.6$ MPa

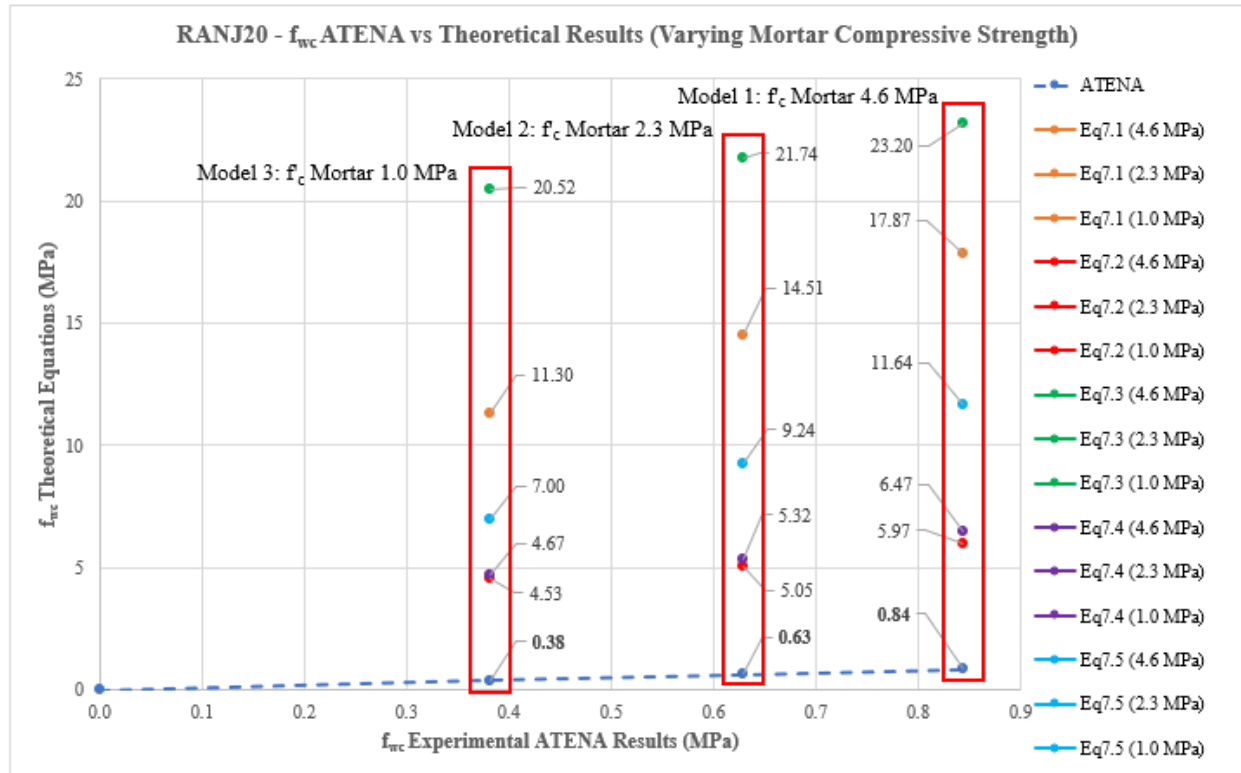


Figure 7-37: RANJ20 ATENA vs Theoretical Equations (Varying Mortar Compressive Strength)

7.6.1 RAN Overview

From the failure states above, the main observation is that as the compressive strength of the masonry bricks increased the damage transferred from the bricks to the mortar joints. In the earlier analyses which utilized weaker bricks ($f_{bc} = 30$ MPa, $f_{bc} = 50$ MPa), at failure many of the bricks had completely failed, whereas some of the bed joints suffered less cracking and damage. As the compressive strength of the bricks increased to their peak value of 100 MPa, the damage at failure was centralized on the mortar joints with limited cracking occurring in the masonry bricks. However, looking at RANJ5 and RANJ10 in comparison to RANJ20, the total damage suffered by the masonry bricks was lower in RANJ20 signifying that as the thickness of the mortar joints increased the properties of mortar became more crucial to the behaviour of the specimens. The decrease in cracking within the bricks as they increase in strength also signifies that the specimen is increasing in strength as a whole and the compression results reflected that.

From the results shown above, a positive linear relationship is present between the compressive strength of the masonry bricks and mortar with the composite compressive strength of the RAN specimens. It was also found that the impacts of altering the strength of mortar was larger than altering the strength of the bricks. In the case of the RANJ20 specimen reducing the

compressive strength of mortar by 50% to 2.3 MPa caused a 25% decrease in composite compressive strength, whereas, reducing the compressive strength of the masonry bricks by 50% caused an 8.33% decrease in composite compressive strength. From this it can be concluded that the contribution of strength is dependent on the percentage area of the material within the specimen. As the area of mortar increased, so did its impact on the composite strength of the wallette specimens.

When correlating the numerical results with the empirical equations, it was found that none of the five considered equations provided valid estimates according to the defined success criteria. As a result, it signifies that the considered equations must be used on conventional brick and mortar layouts like the EQS design. When used on historic masonry similar to the layout of the RAN design the empirical estimates are not successful.

7.7 STONE Results

To conclude the series of parametric studies, the final stage of the discussion will be on the STONE design. The STONE design utilizes various mortar joint thicknesses throughout the specimen which is uncommon of the previous three designs. This design models what was common of the historic times with stones of various lengths, thicknesses, and orientations. This makes the specimen very complex to analyze which is common of historic unreinforced masonry. Figures 7-38 to 7-41 present the calculated interaction diagrams and failure states for the parametric studies on bricks and mortar. The parameters of the investigation include analyzing the STONE specimen under compression using each of the five strength combinations shown in Table 7-1 above. Following Figure 7-41 an overview of the findings will be discussed.

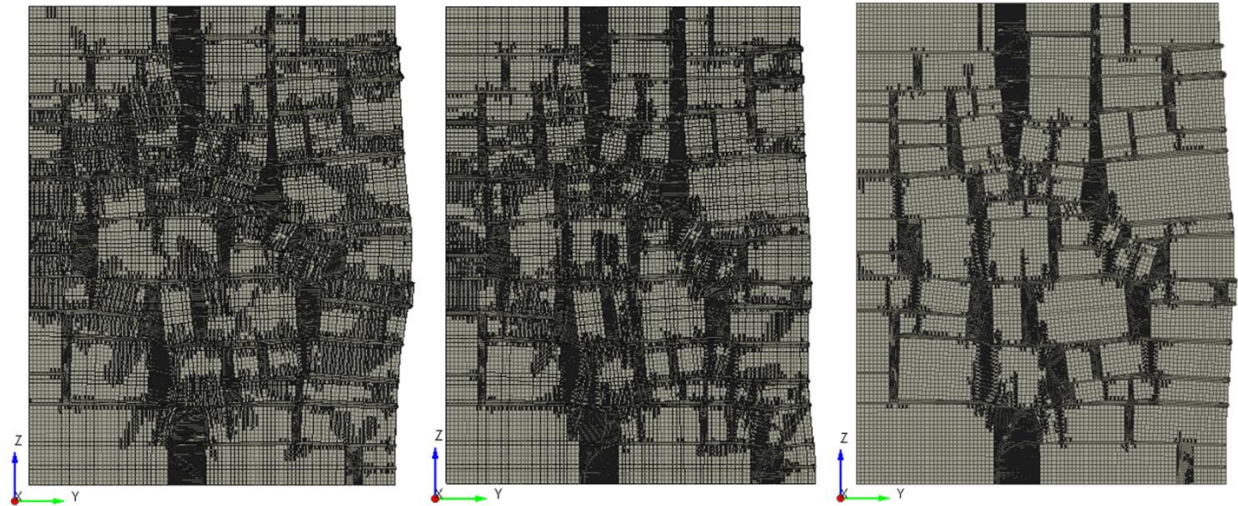


Figure 7-38: [LEFT] STONE $f_{bc} = 30$ MPa, [MIDDLE] STONE $f_{bc} = 50$ MPa, [RIGHT] STONE $f_{bc} = 100$ MPa

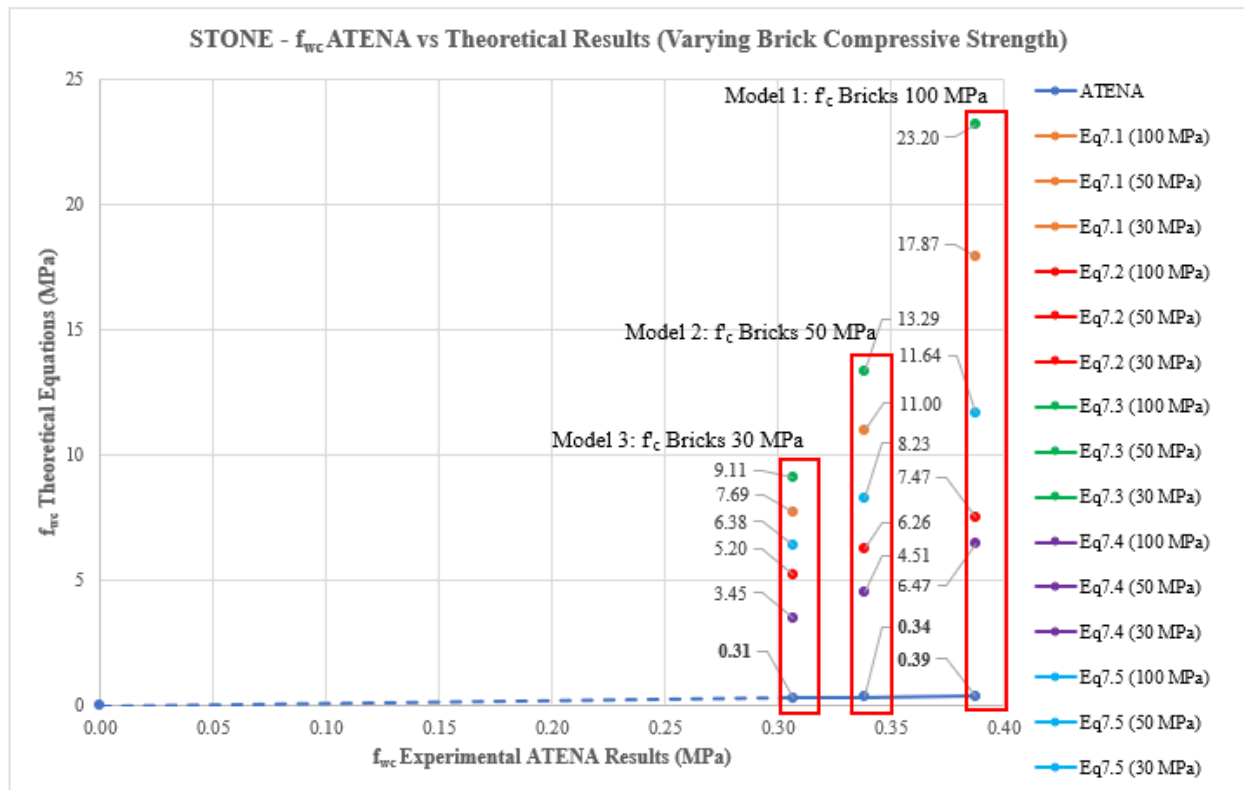


Figure 7-39: STONE ATENA vs Theoretical Equations (Varying Brick Compressive Strength)

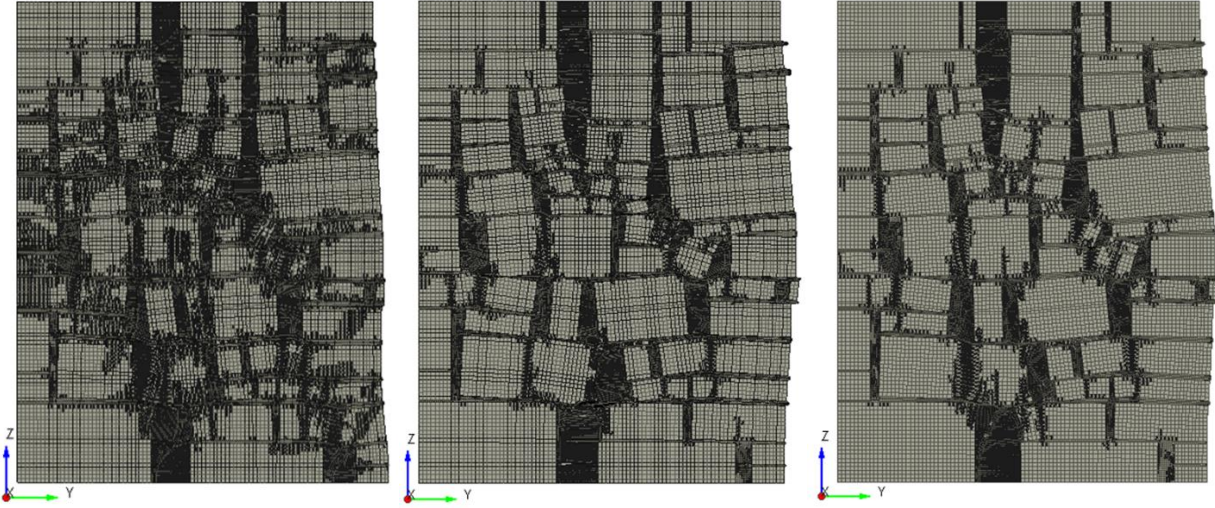


Figure 7-40: [LEFT] STONE $f_{mc} = 1.0$ MPa, [MIDDLE] STONE $f_{mc} = 2.3$ MPa, [RIGHT] STONE $f_{mc} = 4.6$ MPa

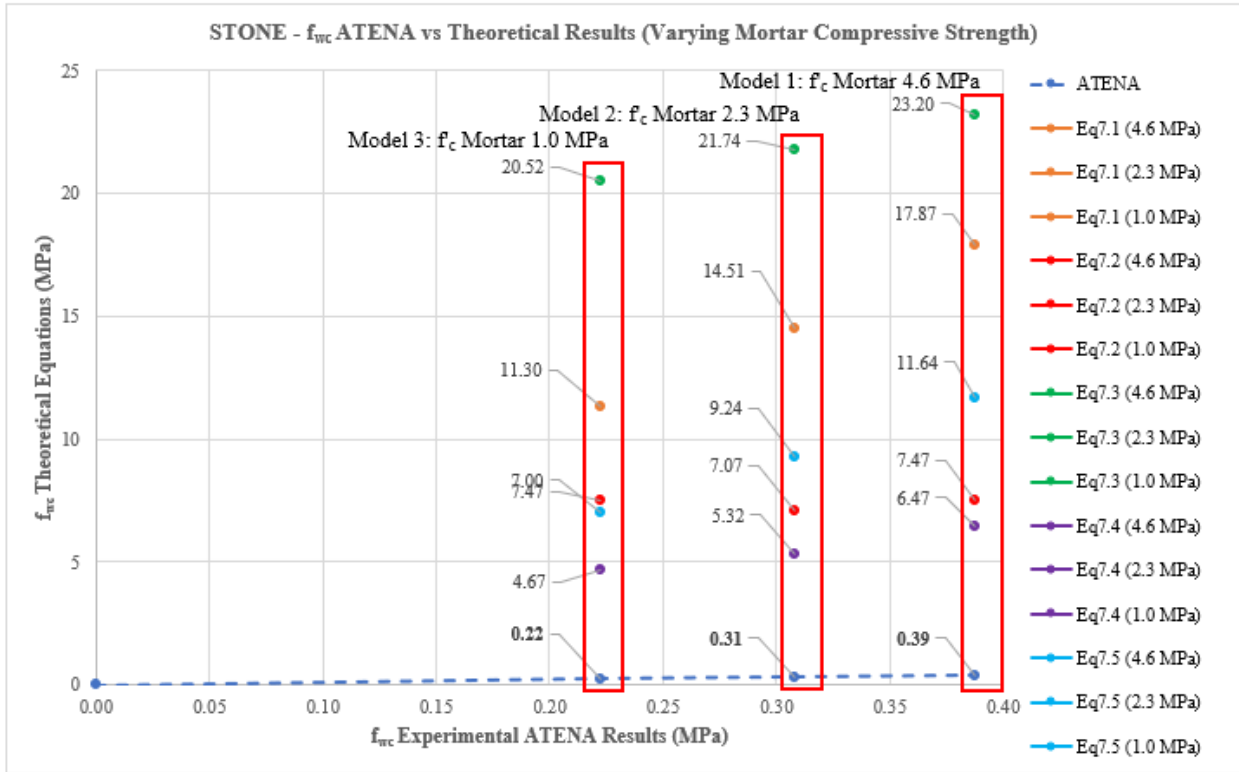


Figure 7-41: STONE ATENA vs Theoretical Equations (Varying Mortar Compressive Strength)

7.7.1 STONE Overview

Throughout the failure states shown above, the main observation as the masonry bricks increase in strength is the cracking occurring throughout the specimen decreases. The decrease in cracks occurs because the masonry bricks become stronger as their compressive strength increases, therefore, they can withstand increased loading before failure. This observation signifies that the specimen is increasing in composite compressive strength. Throughout the three analyses, with the compressive strength of the masonry bricks held constant at 100 MPa, minimal cracking occurs. However, as the compressive strength of the mortar is decreased from 4.6 MPa to lower values of 2.3 MPa, and 1.0 MPa, cracking does begin to occur as the mortar joints have completely failed and the masonry bricks begin to come into contact with each other causing cracking to begin.

As shown above, a positive linear relationship exists between the compressive strength of the masonry bricks and mortar with the composite compressive strength of the specimen. At a masonry brick compressive strength of 30 MPa, the computed composite compressive strength was equal to 0.31 MPa. When the compressive strength of the bricks increased to 50 MPa and 100 MPa, the composite strength of the specimen further increased to 0.34 MPa and 0.39 MPa respectively. Overall, reducing the brick compressive strength by 50% to 50 MPa had a small impact on the composite strength and was equal to 12.82%.

In addition, as the compressive strength of mortar increased, the composite compressive strength of the specimen increased in a positive and linear trend. Overall, reducing the compressive strength of mortar by 50% to 2.3 MPa caused a 20.51% decrease in composite compressive strength which was higher than the decrease observed from reducing the compressive strength of the masonry bricks by 50% which was 12.82%. This design had a number of large crack patterns due to the placement of the head joints therefore, it is valid that the mortar played a more significant role in developing the compressive strength of the specimen.

When correlating the results, it was found that none of the 5 considered equations provided valid estimations according to the defined criteria. All 5 equations provided estimations which exceeded the experimental results during each of the three analyses.

7.8 Lateral Stiffness and Effective Modulus of Elasticity

When creating a numerical model of a URM structure, it is crucial that the modulus of elasticity has been estimated correctly. The final portion of this chapter involved computing the lateral stiffness of the masonry wallettes using the results of the pushover analyses and computing the effective modulus of elasticity by calibrating the linear elastic portion of the finite element analysis with a shell type model built in SAP 2000. The additional wallette model created in SAP utilized the same material properties, loading conditions and boundary conditions as the SYM, EQS, RAN and STONE wallettes.

The first step of the methodology was to extract the key characteristics from the pushover results including V_{MAX} , Δ_y , Δ_u , and Δ_{MAX} where, V_{MAX} refers to the peak lateral capacity of the wallette specimen in kN, Δ_y refers to the peak lateral displacement assuming a linear elastic behaviour, and Δ_u refers to the ultimate displacement as shown in Figure 7-42 below.

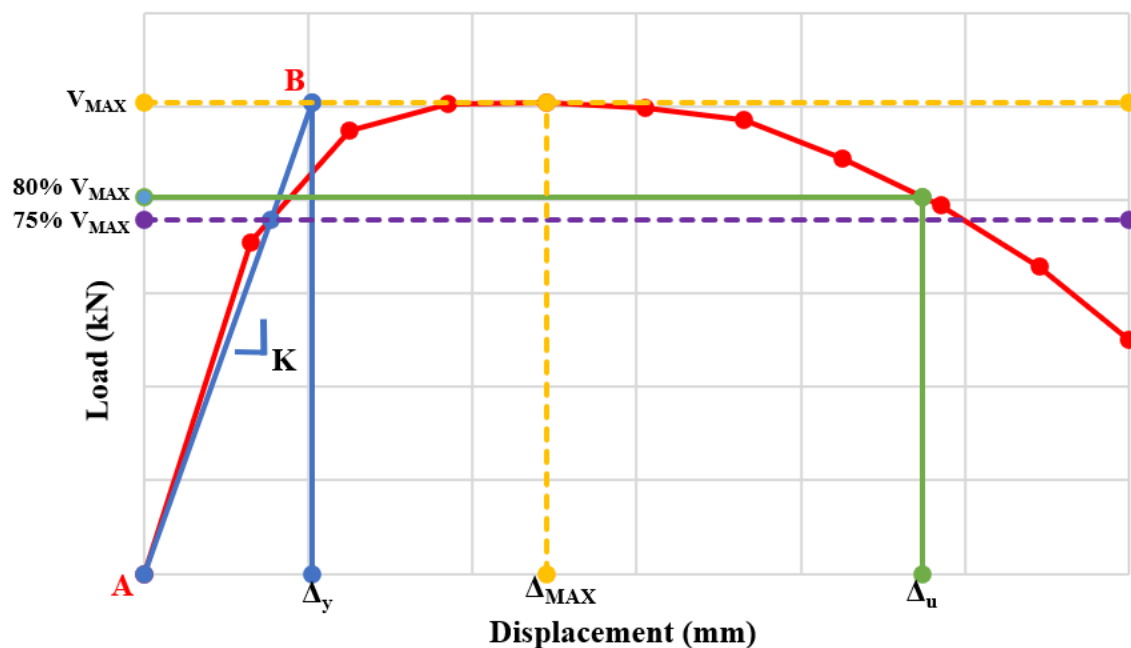


Figure 7-42: Characteristic Values from Lateral Pushover Curve

After collecting the key characteristics, the lateral stiffness was computed as the slope of the secant which spans from point A to B as shown in Figure 7-10 above. To compute the modulus of elasticity, a pushover analysis was conducted on the SAP model where the specimen was pushed laterally to a predefined displacement equal to Δ_y . The modulus of elasticity of the SAP model was adjusted until the pushover analysis in SAP provided a base force equal to V_{max} . The summary of the results can be seen in Table 7-2 below.

Table 7-2: Summary of Lateral Stiffness and Modulus of Elasticity Results

Stiffness and Effective Modulus of Elasticity Results from Pushover Analyses												
Design	Mortar Joint Thickness (mm)	Overbearing Stress (MPa)	V _{MAX} (kN)	Δ _{MAX} (m)	Δ _u (m)	Δ _y (m)	K _{ATENA} (kN/m)	E (MPa) Calibrated in SAP2000	E (MPa) from Eq. 7.6	E (MPa) from Eq. 7.7, f _{wc} from ATENA	E (MPa) from Eq. 7.7, f _{wc} from Eq. 7.2	E (MPa) from Eq. 7.7, f _{wc} from Eq. 7.5
SYM	5	1.79	10.6	0.0006	0.0033	0.000309	34300	3366.12	2445.8	18074.1	6346.7	9895.5
		4.47	24.3	0.0030	0.0060	*	0.000542	44874				
		7.15	36.8	0.0042	0.0056	0.000813	45248	4435.76				
SYM	10	1.79	10.9	0.0006	0.0027	*	0.000329	33043	2565.2	12892.0	6346.7	9895.5
		4.47	21.5	0.0015	0.0036	*	0.000648	33188				
		7.15	24.1	0.0015	0.0024	*	0.000722	33378				
SYM	20	1.79	10.4	0.0009	0.0027	*	0.000453	22889	2822.9	7649.3	6346.7	9895.5
		4.47	18.6	0.0018	0.0030	*	0.000869	21419				
		7.15	18.7	0.0018	0.0021	*	0.000915	20469				
EQS	5	1.79	10.7	0.0006	0.0033	0.000311	34482	3380.19	2445.8	18072.5	6346.7	9895.5
		4.47	23.9	0.0018	0.0040	0.000420	56946	5582.33				
		7.15	36.3	0.0021	0.0037	0.000703	51594	5057.74				
EQS	10	1.79	10.6	0.0009	0.0030	*	0.000332	31873	2565.2	11543.6	6346.7	9895.5
		4.47	23.4	0.0030	0.0036	*	0.000678	34553				
		7.15	33.9	0.0030	0.0033	*	0.001014	33449				
EQS	20	1.79	10.2	0.0009	0.0024	*	0.000466	21797	2850.2	10048.6	6346.7	9895.5
		4.47	21.6	0.0036	0.0042	*	0.001057	20447				
		7.15	30.6	0.0045	0.0048	*	0.001733	17645				
RAN	5	1.79	10.9	0.0006	0.0015	*	0.000307	35350	2445.8	1132.1	6346.7	9895.5
		4.47	24.0	0.0015	0.0018	*	0.000546	44014				
		7.15	35.4	0.0018	0.0018	*	0.000772	45897				
RAN	10	1.79	10.8	0.0006	0.0027	*	0.000345	31171	2565.2	1851.6	6346.7	9895.5
		4.47	23.4	0.0024	0.0027	*	0.000745	31379				
		7.15	33.9	0.0030	0.0042	*	0.001184	28623				
RAN	20	1.79	10.3	0.0009	0.0027	*	0.000547	18829	2850.2	716.8	6346.7	9895.5
		4.47	21.0	0.0030	0.0036	*	0.001181	17784				
		7.15	22.6	0.0027	0.0028	*	0.001327	17035				
STONE	-	1.79	10.1	0.0012	0.0021	*	0.000513	19682	-	329.8	6346.7	9895.5
		4.47	20.8	0.0025	0.0025	*	0.001107	18806				
		7.15	27.1	0.0025	0.0025	*	0.001599	16917				

*Δ_u value taken as failure displacement

From the results in Table 7-2 above, it is observed that the modulus of elasticity values computed from the SAP model differ greatly from the referenced empirical equations. The results from the empirical equations differ greatly from each other and do not follow any consistent trends. Therefore, it concludes that empirical equations are not effective for estimating the modulus of elasticity for masonry. Of the analyzed equations, Equation 7.6 provides the best estimate for the modulus of elasticity when analyzing conventional brick arrangements such as the EQS design. For arrangements which lack symmetry and consistent patterns such as RAN or STONE, Equation 7.7 provides the most conservative estimate but should not be combined with a empirical estimate for the compressive strength of masonry.

7.9 Conclusions

Throughout the series of parametric investigations, several observations and conclusions were found which were common to all four designs. The first conclusion was regarding the trend of the resulting data from each of the specimens. Overall, it was found that a linear and positive relationship was present between the individual compressive strength properties of the masonry bricks and mortar with the composite properties of the masonry wallettes.

The second area of observation and found conclusions was regarding the studied empirical equations. It was found that each of the 5 equations provided different estimations at each of the material strength combinations. However, not every equation provided estimates which met the defined success criteria. Also, as the conditions of the analyses changed, so did the effectiveness of each considered equation. Overall, it was found that the 5 considered equations only met the success criteria for the SYM and EQS designs. To better understand the outcome on the study of the empirical equations, Figure 7-43 below presents the percentage error of each estimate from the empirical equations plotted against the experimental results starting with the results of the SYM study.

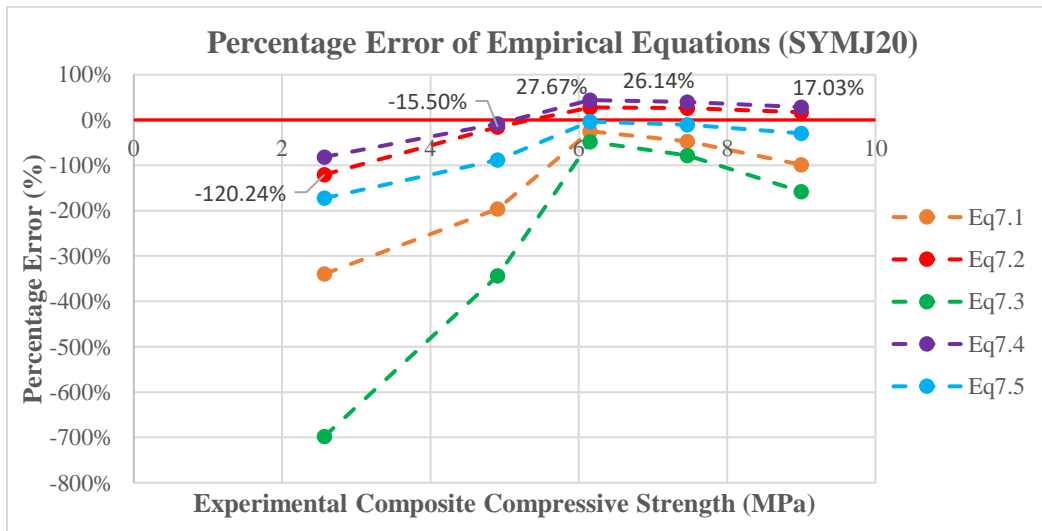
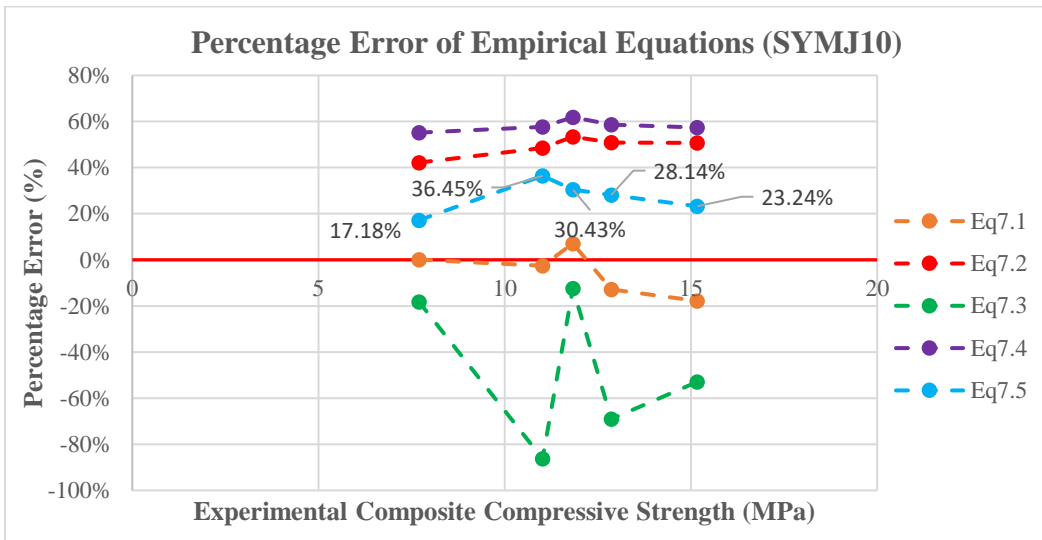
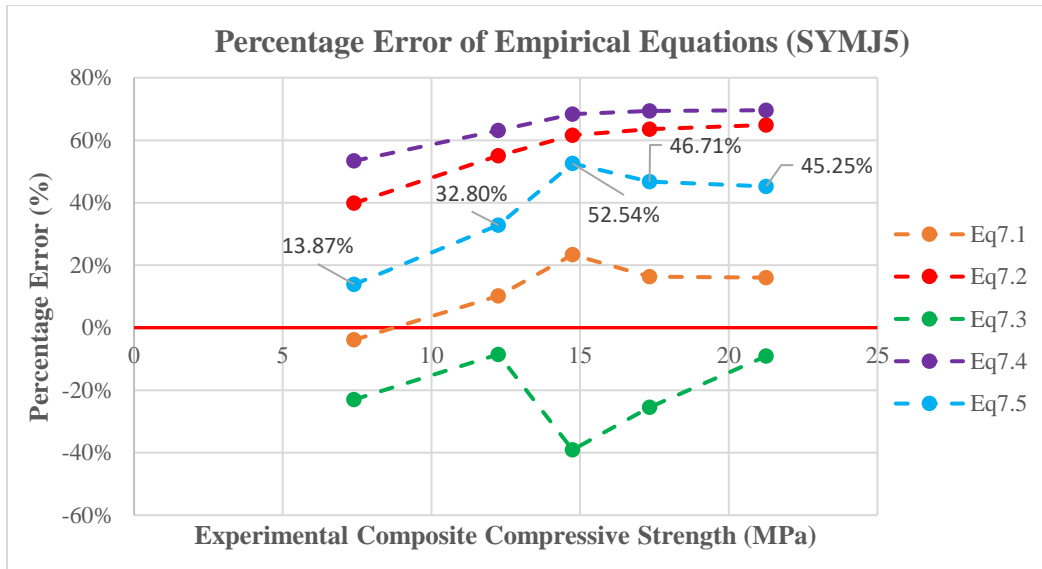


Figure 7-43: Percentage Error of Empirical Equations. [A] SYMJ5, [B] SYMJ10, [C] SYMJ20

From the 3 graphs presented in Figure 7-42 above, it can be observed that the accuracy of the 5 considered equations changed as the global mortar joint thickness was altered. For SYMJ5 and SYMJ10 Equation 7.5 provided the most accurate estimates which met the success criteria of the investigation. It is shown however, that the accuracy was improved when the mortar joints were 10 mm thick with the maximum percentage error decreasing from 52.54% to 36.43%. Then when observing the results of SYMJ20 none of the five equations met the success criteria throughout. Equation 7.2 provided the most accurate estimates when the mortar compressive strength was held constant at 4.6 MPa, but as shown in Figure 7-42, when the composite strength of the specimen decreased as the mortar became weaker, Equation 7.2 was no longer valid.

When observing the results of the EQS design, similar observations were found from the empirical estimates and are shown in Figure 7-44 below.

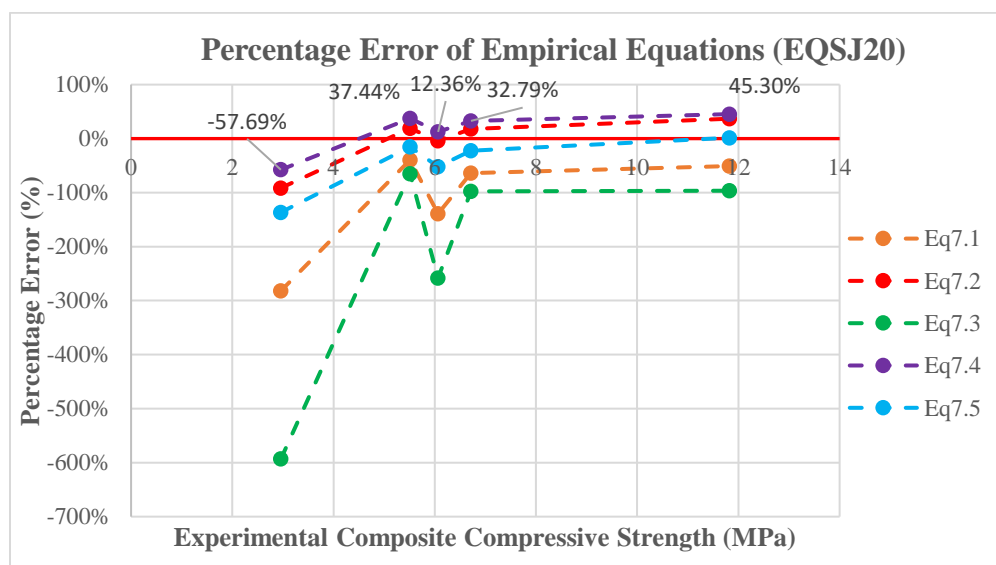
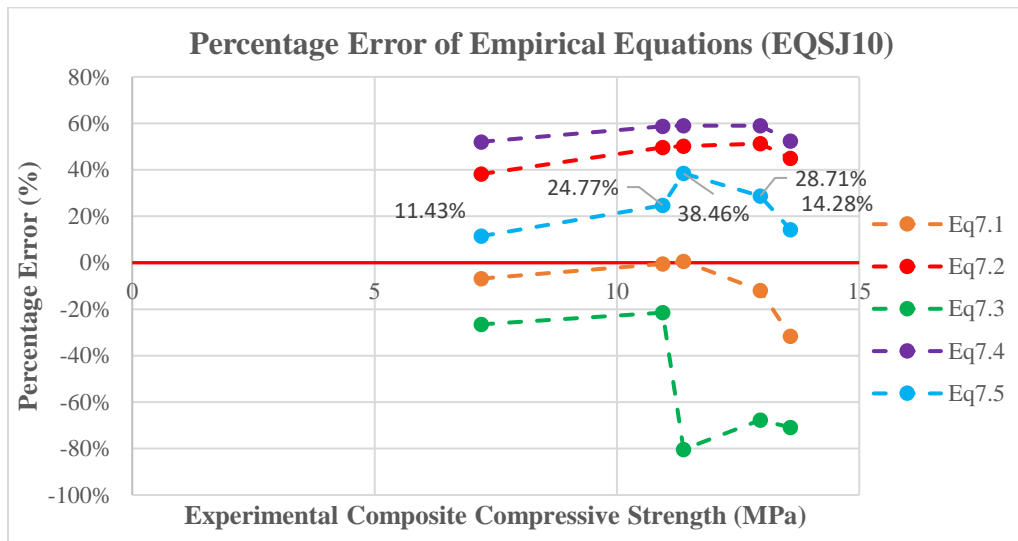
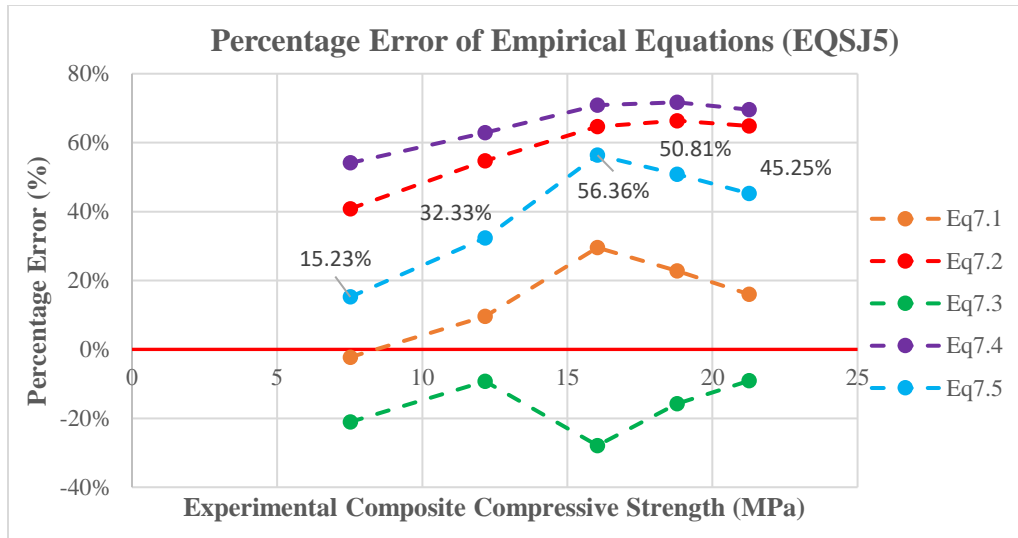


Figure 7-44: Percentage Error of Empirical Equations. [A] EQSJ5, [B] EQSJ10, [C] EQSJ20

Overall, from Figure 7-44 above, similar conclusions can be found for the EQS design such as Equation 7.5 being the most accurate for 5 mm and 10 mm joints with higher accuracy for 10 mm joints. Furthermore, for 20 mm joints Equation 7.4 provided valid estimates, however, when the compressive strength of the mortar was reduced Equation 7.4 was no longer valid.

From the investigation, it was concluded that Equation 7.5 is optimal for estimating the compressive strength of masonry. Equation 7.5 is considered valid when the global mortar joint thickness does not exceed 10 mm and the design of the specimen is conventional of modern masonry construction such as the EQS design. It was also concluded that the empirical equations are not effective for estimating the modulus of elasticity of masonry. It is recommended that Equation 7.6 is used when analyzing conventional masonry such as EQS and Equation 7.7 is used when analyzing complex arrangements such as RAN or STONE. However, Equation 7.7 should not be used with empirical estimations for the compressive strength of masonry.

Therefore, the empirical equations can be used as valid tools for providing preliminary estimates of the compressive strength of masonry. However, the equations are quite sensitive to the input variables and therefore for specimens with unconventional materials and designs such as the RAN and STONE specimens, the estimates should be followed up with an experimental analysis to ensure the value taken for the composite compressive strength of masonry is reasonable.

Chapter 8

SAP2000 Modelling of NIKER Project Specimen

8.0 Introduction

The following chapter discusses the series of analysis conducted on the finite element model of the NIKER specimen developed in SAP. Following the finite element modelling investigation on masonry wallettes, modifications were made to the SAP model to improve its behaviour and ensure the results are accurate in comparison to the NIKER results. After introducing the modifications, a series of linear and non-linear analyses were conducted and the results of which will be discussed below.

8.1 Model Modifications

Following the wallette investigation on the mechanical properties of masonry, two modifications were done to the SAP model prior to conducting the series of analyses. Firstly, the modulus of elasticity which was previously taken as 840 MPa was recomputed using the results of the wallette analyses. Secondly, springs were introduced at the base of the structure to represent the compliance between the base of the structure and the shake table. Further details on these adjustments will be discussed below.

8.1.1 Masonry Mechanical Properties

To ensure that the final results of this experiment are consistent with the results of the studied NIKER project, the masonry mechanical properties were improved and included a combination of properties from the literature and properties which were computed following the masonry wallette investigation. The summary of the modified material properties are shown in Table 8-1 below.

Table 8-1: Chosen material properties for Masonry (Karapitta et al., 2012)

Weight	18.63 kN/m ³
Modulus of Elasticity	429.5 MPa
Compressive Strength	2.18 MPa
Poisson's Ratio	0.2
Shear Modulus	178.96 MPa

From the material properties shown above, the modulus elasticity was computed from the results of the finite element modelling investigation. From the ATENA 3D results, the compressive strength was taken from the compression results of RANJ10. Furthermore, the modulus of elasticity was computed by calibrating a wallette built in SAP 2000 to provide a pushover curve equal to 80% of V_{max} shown below in Figure 8-1.

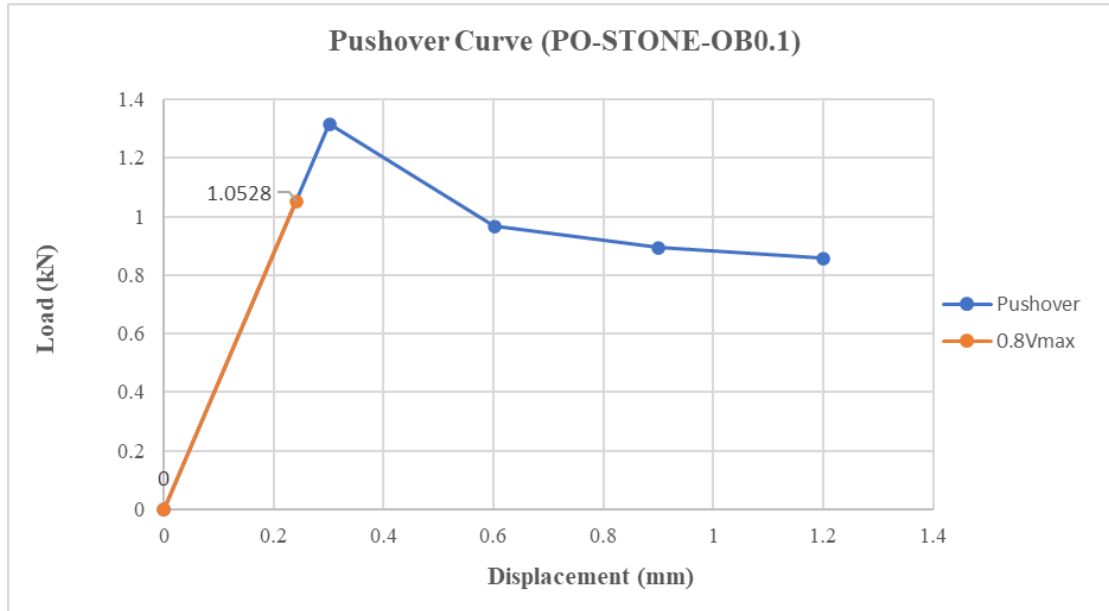


Figure 8-1: PO-STONE-OB0.1 Pushover Curve for SAP 2000 Calibration

The additional wallette model created in SAP utilized the same material properties, loading conditions and boundary conditions as the STONE wallette. To calibrate the SAP analysis with the ATENA 3D results, a pushover analysis was conducted where the specimen was pushed laterally to a predefined displacement of 0.241mm which was the value of displacement observed at 80% of V_{max} from ATENA 3D. The modulus of elasticity of the SAP model was adjusted until the pushover analysis in SAP provided a base force equal to 1.053 kN which is equal to 80% of V_{max} from the STONE finite element analysis. It was found that a modulus of elasticity of 429.5 MPa was needed to calibrate the two results and was therefore taken as the modulus of elasticity for the remainder of the SAP investigation. The computed value was then correlated with Equation 7.6.

Using Equation 7.6, the empirical estimate of the modulus of elasticity for RANJ10 was equal to 2565.2 MPa which is significantly greater than the computed experimental value of 429.5 MP. Thus, due to the deviation between the numerical and empirical results, it is critical to validate

any empirical estimations of the modulus of elasticity when intending to utilize the value in a numerical model.

For non-linear analyses, a second masonry material was created with a defined stress-strain relationship. This additional masonry material utilized all of the same properties discussed above but had a defined stress-strain relationship which was provided by the finite element compression results of the RANJ10 specimen. The compression values were taken directly from the RANJ10 compression results with the peak compressive strength of the masonry equal to 2.18 MPa. The peak tensile strength was computed as 10% of the peak compressive strength and was equal to 0.218 MPa. The peak tensile strain was computed by dividing the peak compressive strength by the modulus of elasticity and was equal to 5.07×10^{-4} mm/mm. The stress-strain curve inputted into SAP for the purpose of non-linear analyses is shown in Figure 8-2 below.

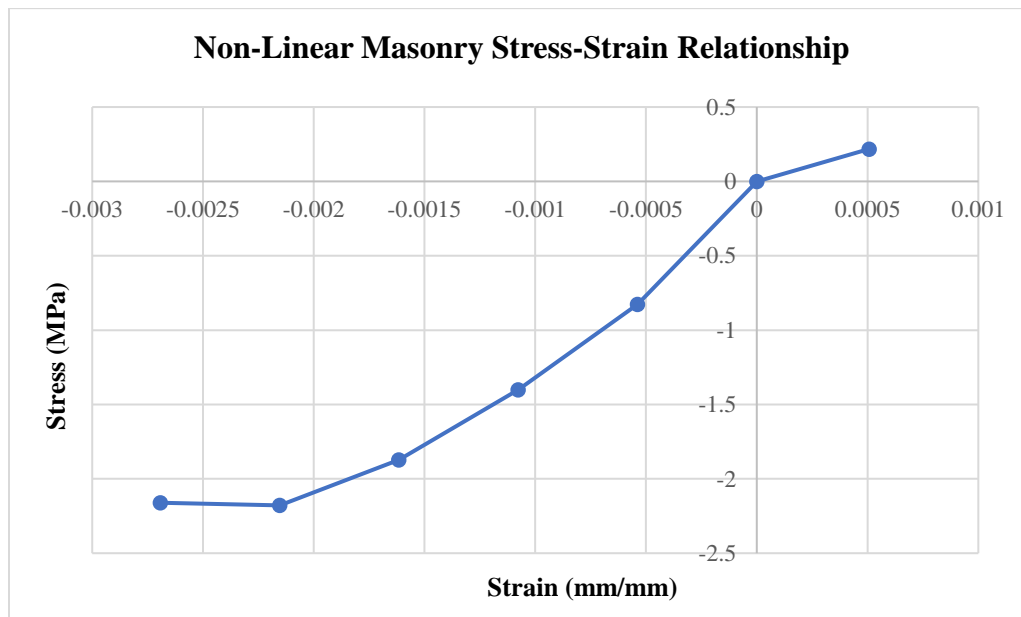


Figure 8-2: Non-Linear Stress-Strain Relationship of Utilized Masonry

The properties that were modified when defining the custom masonry material in SAP were only those which pertain to the type of analysis being conducted. For example, because the effects of temperature change are not of interest in this experiment, the coefficient of thermal expansion was not modified as it would not have any effect on the results.

8.1.2 Base Spring Connections

To ensure that this numerical model was consistent with previous numerical and physical models, appropriate joint restraints were required. The main purpose of joint restraints and why

they are required is to apply boundary conditions to the structure. The physical specimen which was previously tested was fixed to the shake table surface to ensure the structure deforms relative to its original position in reference to the shake table. Without doing so the structure would be at risk of sliding on the table, and the deflection results would not be accurate. However, even when fixed together, there is a small degree of compliance between the steel base and the shake table, therefore this was also considered. To account for such compliance, the base of the SAP model was restrained through two different one joint links with computed stiffness values. The first of the two links was a spring fixing the base of the structure in the Z direction. The Z spring was assigned a very large stiffness of 10^4 kN/m to ensure the structure was sufficiently restrained in the Z direction. The second link was used to allow for the discussed compliance in the X and Y directions and was calculated from the results of the pushover analysis on RANJ10-OB0.1 in Chapter 6. The computed stiffness which was applied in the X and Y directions was computed as shown below.

$$V_{\max} = 0.964 \text{ MPa (From Section 6.4.2)}$$

$$0.75V_{\max} = 0.723 \text{ MPa}$$

$$\Delta 0.75 = 0.238 \text{ mm}$$

$$K_0 = (0.723 \text{ kN}) * (1000) / (0.238 \text{ mm})$$

$$K_0 = 3037.82 \text{ kN/m}$$

$$K = K_0 * L_{\text{TRIB}} * t / L_{\text{wall}} * t_{\text{wall}}$$

$$K = (3038.82 \text{ kN/m}) * (0.1\text{m}) * (0.250\text{m}) / (0.41\text{m}) * (0.083\text{m})$$

$$K = 2231.72 \text{ kN/m}$$

Both discussed springs were applied as one-joint links to each node which is located along the XY plane at the base of the structure. One-joint links uses the original node location as a reference point and during the analyses the new location is linked to the reference point and restrained with the defined stiffness. With springs defined for both the floor elements as well as the base, the boundary conditions of the structure were complete and represented what is expected.

8.2 Results/Analysis

The developed SAP model of the NIKER specimen was analyzed through a series of analyses divided into two main categories, linear and non-linear. The linear analyses conducted involved a modal analysis, and a gravity analysis where the gravitational field was applied in the

X and Y directions. The non-linear analyses involved the series of records from the 1986 Kalamata Earthquake presented above, and a non-linear pushover analysis. All the analyses were conducted in the in-plane and out-of-plane directions.

8.2.1 Modal Analysis

Modal analysis is a typical procedure conducted to define the fundamental periods and shapes of a structure. When running a modal analysis, the software excites a portion of the total mass laterally. In the case of unreinforced masonry structures, modal analyses become quite complex due to the amount of degrees of freedom, therefore requiring a significant quantity of modes to be considered in order to excite an acceptable quantity of mass in the lateral directions (Pantazopoulou, 2013). The modal analyses were completed to define the fundamental modes and periods of the model and correlate the results to the referenced NIKER physical specimen. The physical specimen being modelled had fundamental periods of 0.238s in the out-of-plane direction (UY) and 0.165s in the in-plane direction UX which therefore are the reference values which were target in the numerical modal analyses (Vintzileou et al., 2015).

The results of the modal analyses provided fundamental periods and modes which were quite close to the referenced values discussed above. The first fundamental mode discovered was in the out-of-plane direction (UY) and excited 70.687% of the total mass of the structure and is shown in Figure 8-3 below.

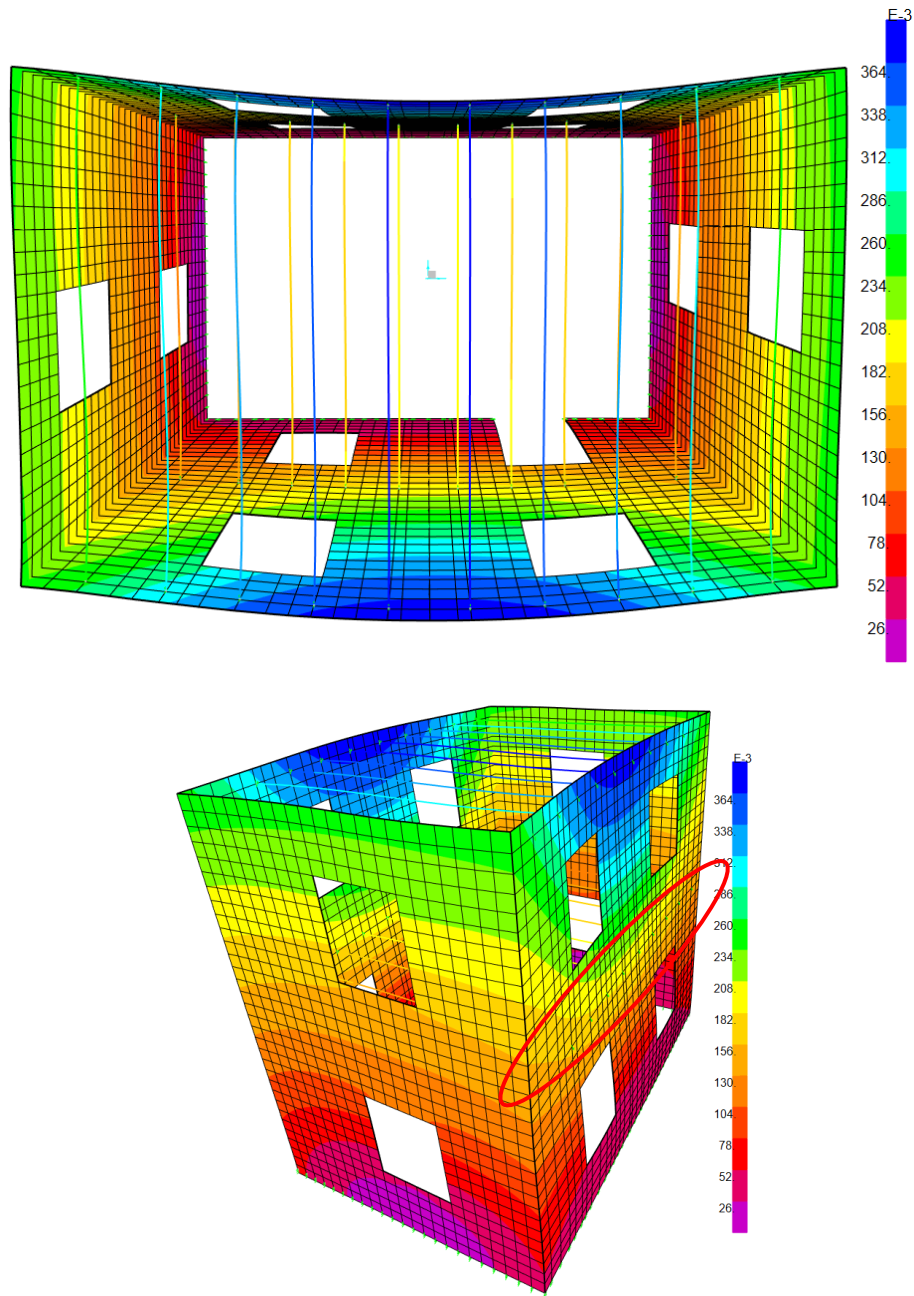


Figure 8-3: Mode 1 (UY)

The period of Mode 1 was equal to 0.214s which is close to the target value provided by the referenced literature. From the contours shown above, at the bottom floor location circled in red in Figure 8-3, the contours vary along the floor indicating that the unreinforced conditions desired are indeed present.

The second fundamental mode was in the in-plane direction (UX) and excited a total of 77.73% of the structures mass laterally and is shown in Figure 8- 4 below.

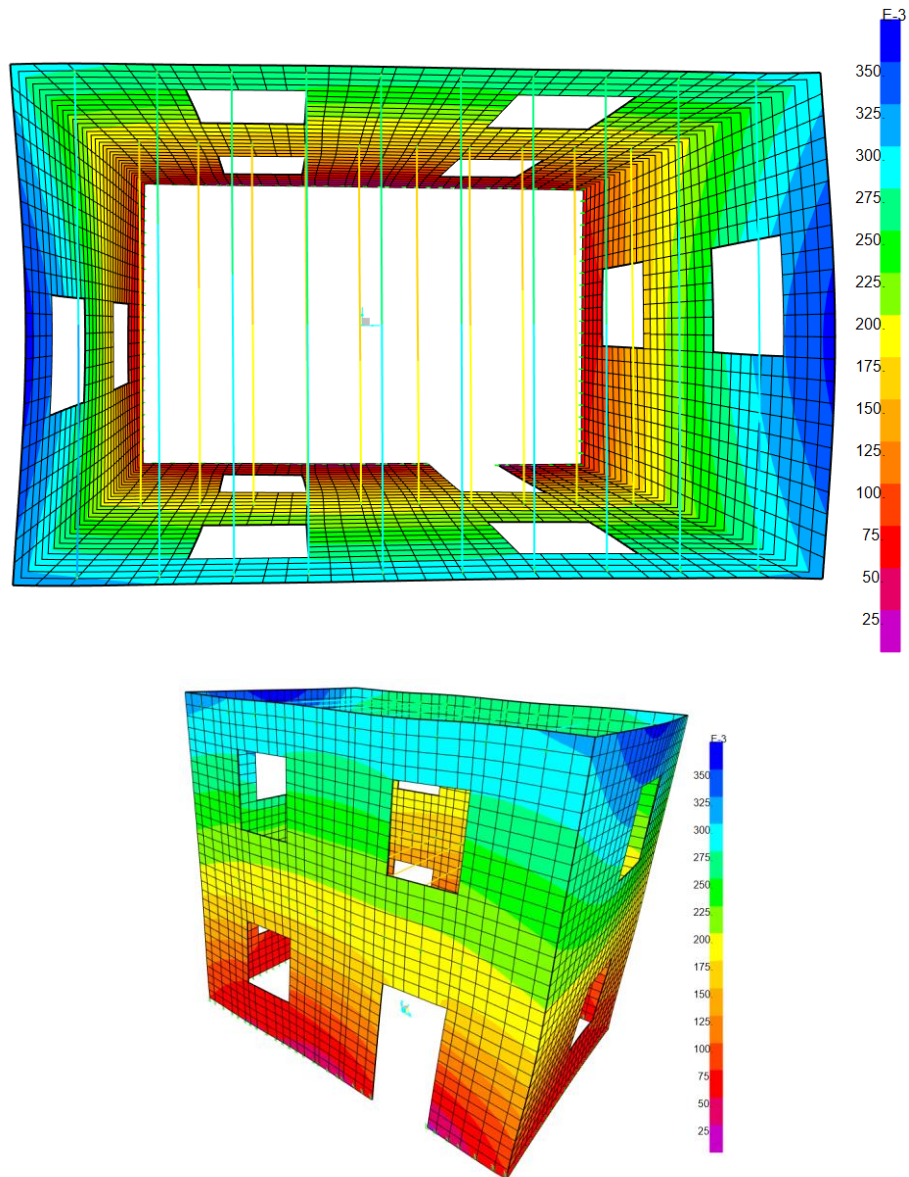


Figure 8-4: Mode 2 (UX)

The period of Mode 2 was equal to 0.167s which again is quite close to the target value of 0.165s from the referenced literature. Therefore, simply from comparing the 2 fundamental periods from the numerical analyses to the referenced physical experiment, it can be concluded that numerical practices can confidently estimate the fundamental properties of an existing physical structure.

As mentioned above, modal analyses on URM structures are quite complex and further investigation is required to confidently define the 2 modes discussed above as fundamental. The

graph shown below in Figure 8-5 displays the mass participation of 11 collected modes providing valid shapes such as in-plane or out-of-plane translations as well as torsion.

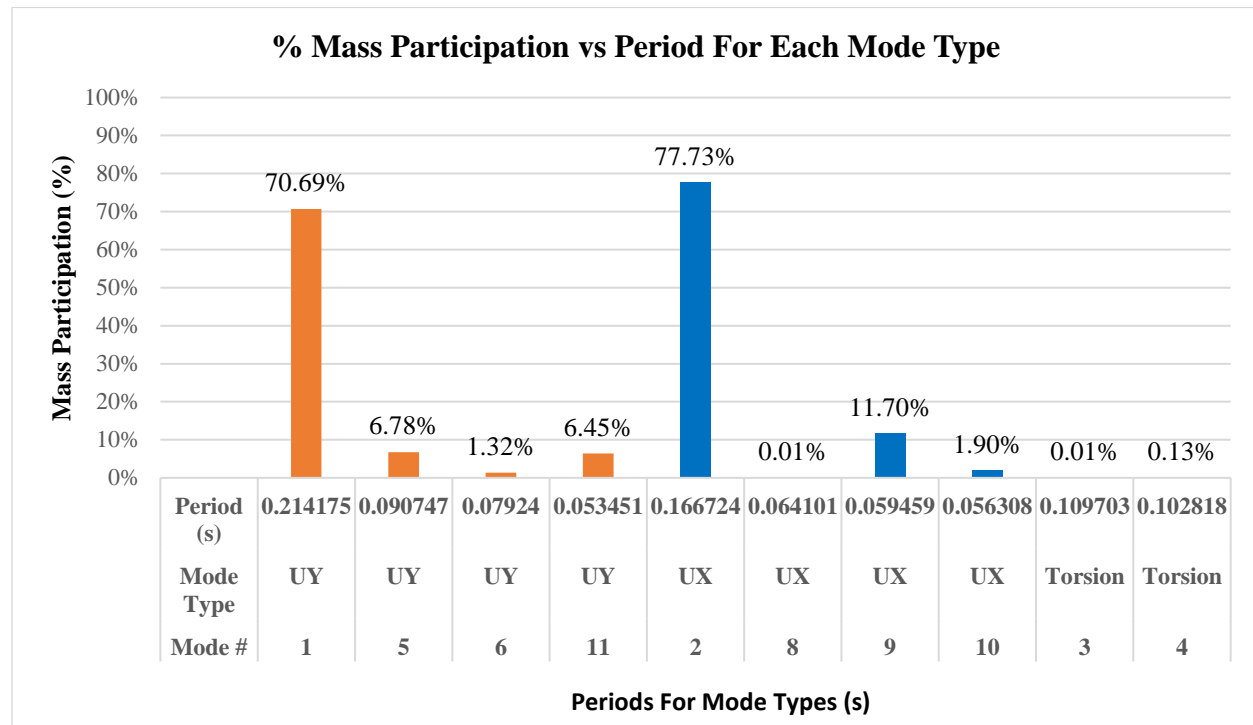


Figure 8-5: Mass participation vs mode type

As shown above the two modes which excite a significant portion of mass are Modes 1 and 2, all others have valid shapes but do not excite enough mass to be considered fundamental modes. Therefore, the fundamental modes from the numerical modal analysis are modes 1 and 2 and have periods of 0.0214s and 0.167s respectively.

When analyzing URM structures, a significant quantity of modes is required in order to excite close to 100% of the mass of the structure. Figure 8-6 below represents the increasing fraction of mass participation by increasing the number of modes considered.

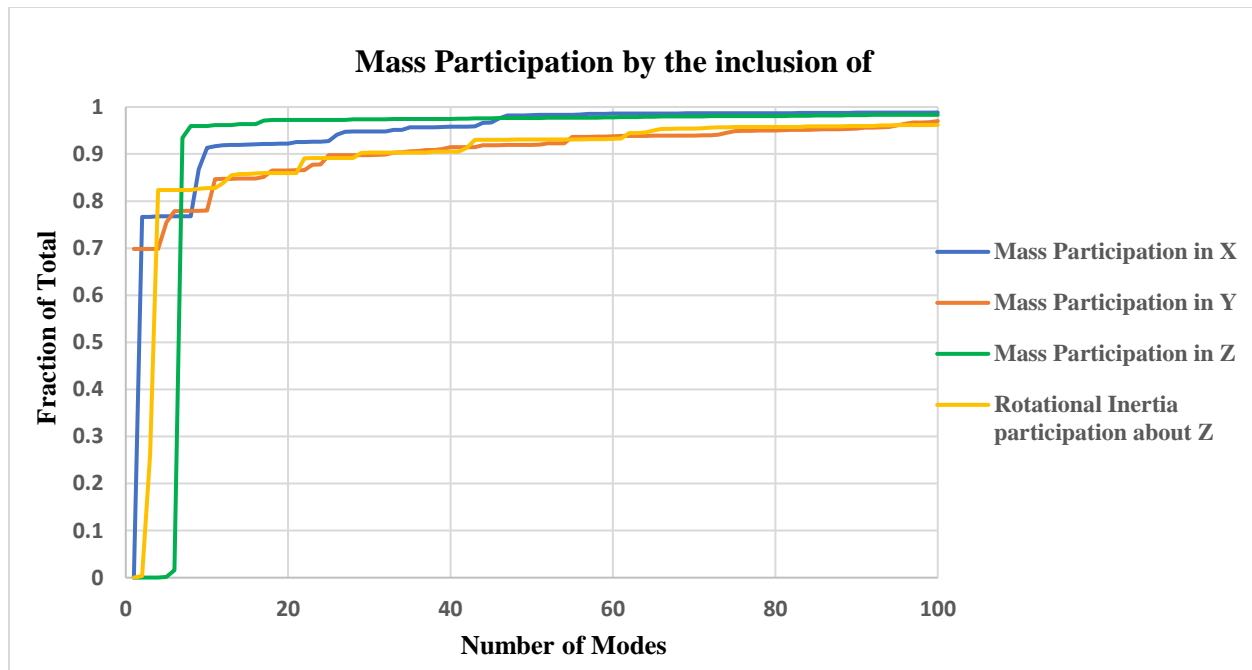


Figure 8-6: Mass participation by the inclusion of modes

As shown above, the cumulative sum of mass participated does not reach values close to 100% until the number of modes considered reaches 100. This highlights the complexities mentioned regarding modal analyses on URM structures and why deep investigation is required to define the fundamental modes of a URM structure.

8.2.2 Gravitational Analysis

The final linear elastic analysis conducted was a gravitational analysis. This analysis involved applying a gravitational field in the lateral directions to provide natural shapes of the structure. The gravitational analysis is comparable to the modal analysis however, gravitational analysis is a hypothetical scenario but can be used to validate the mode shapes provided by a modal analysis.

The results of the gravitational analysis provided contours in both the in-plane and out-of-plane direction which are comparable to the modal analysis. The gravitational field was applied by applying gravity forces to all of the shells within the structure. The gravitational loads were applied first in the in-plane direction using a factor of 1 in the UX direction and 0 in all others. The same was done for the out-of-plane direction but instead a factor of 1 was applied in the UY direction and 0 for all others. The resulting deformed shapes in both directions are shown in Figures 8-7 and 8-8 below.

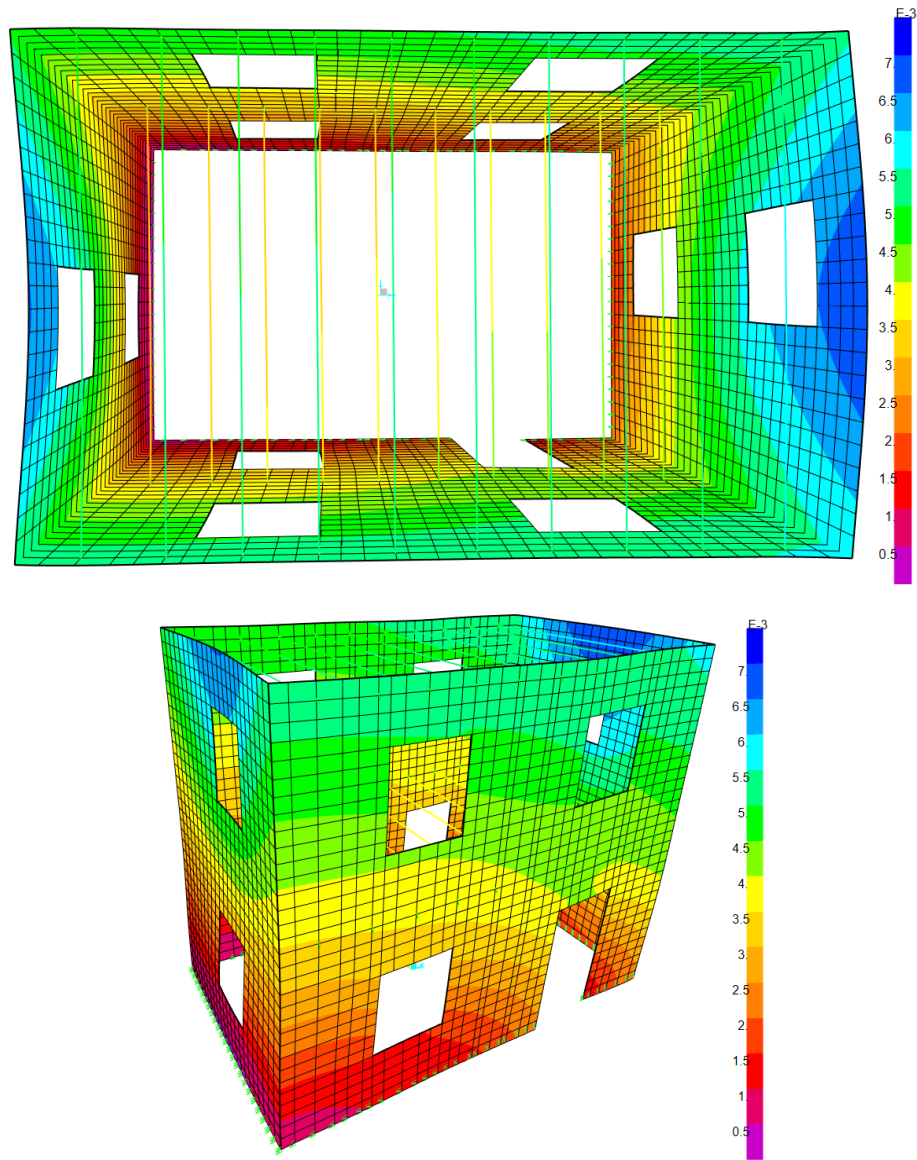


Figure 8-7: Gravitational Analysis (UX)

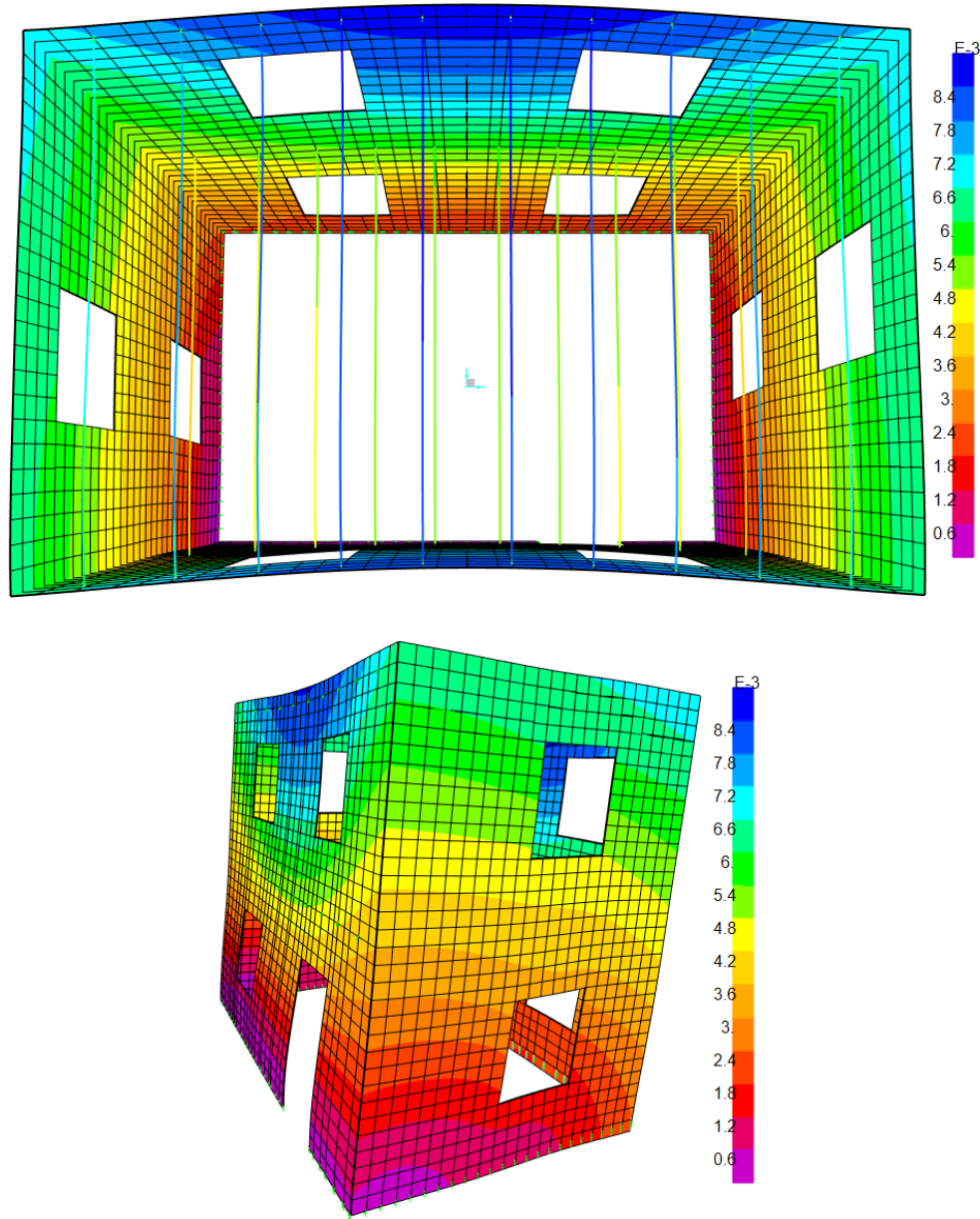


Figure 8-8: Gravitational Analysis (UY)

As shown above, the resulting contours and deformed shapes are approximately the same as the results of the modal analysis. This validates the resulting mode shapes from the modal analysis, however, the two results can be further compared by observing the collection of deformed cross-sections shown below in Figure 8-9.

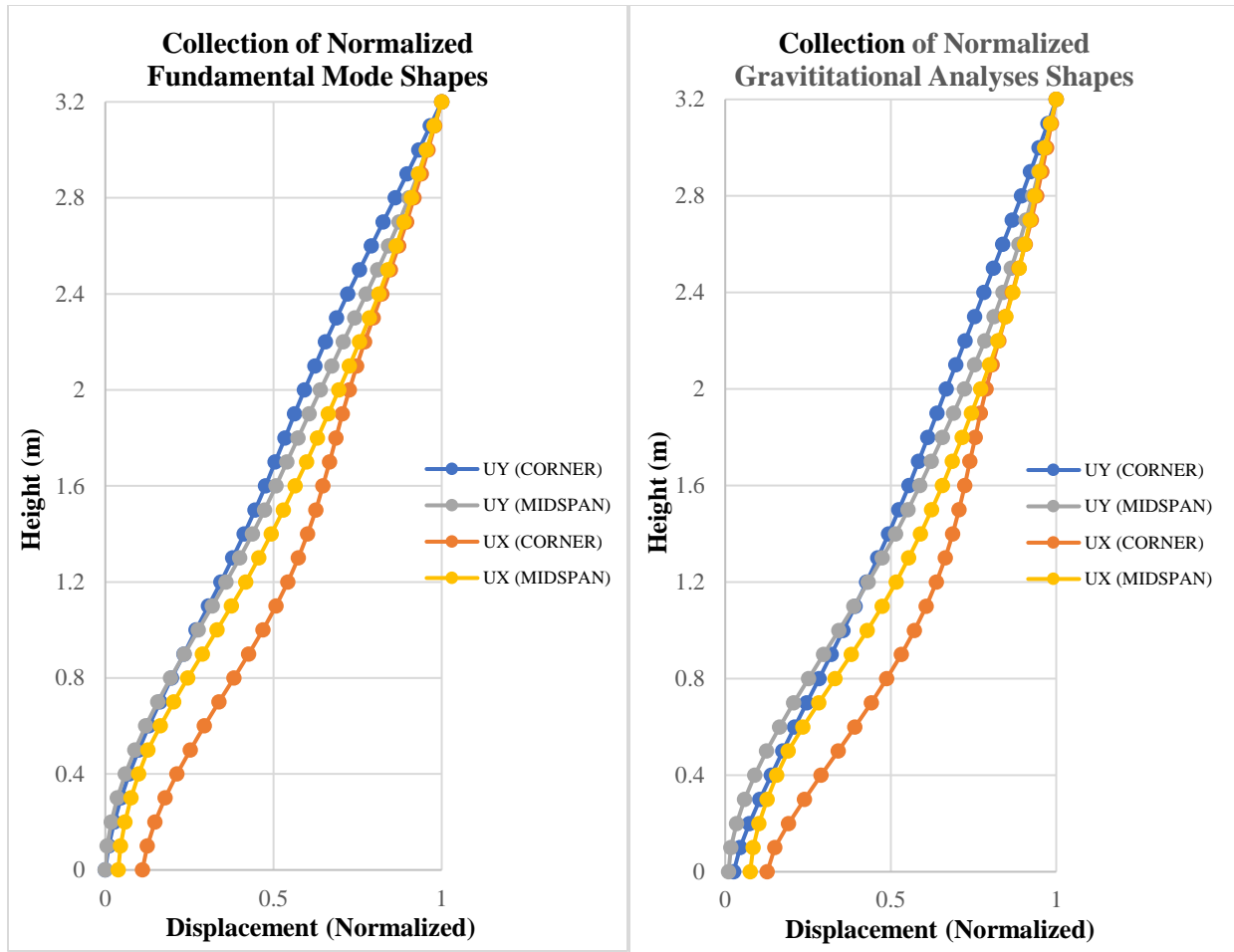


Figure 8-9: Normalized Mode Shapes vs Normalized Gravitational Shapes

As shown above in Figure 8-9, each of the 4 shapes consisting of the corner and midspan of both the long and short walls resemble each other closely validating the results of the modal analyses through the correlation of the gravitational analyses.

8.2.3 Time History Analysis

The first of the three non-linear analyses was a time history analysis where the earthquake record of the 1986 Kalamata earthquake was applied to the structure. The record applied was the 90% scaled record which is the same as what was applied in the physical experiment being referenced. The deformed shapes of the in-plane (UX) and out-of-plane (UY) analyses are shown in Figures 8-10 and 8-11 below.

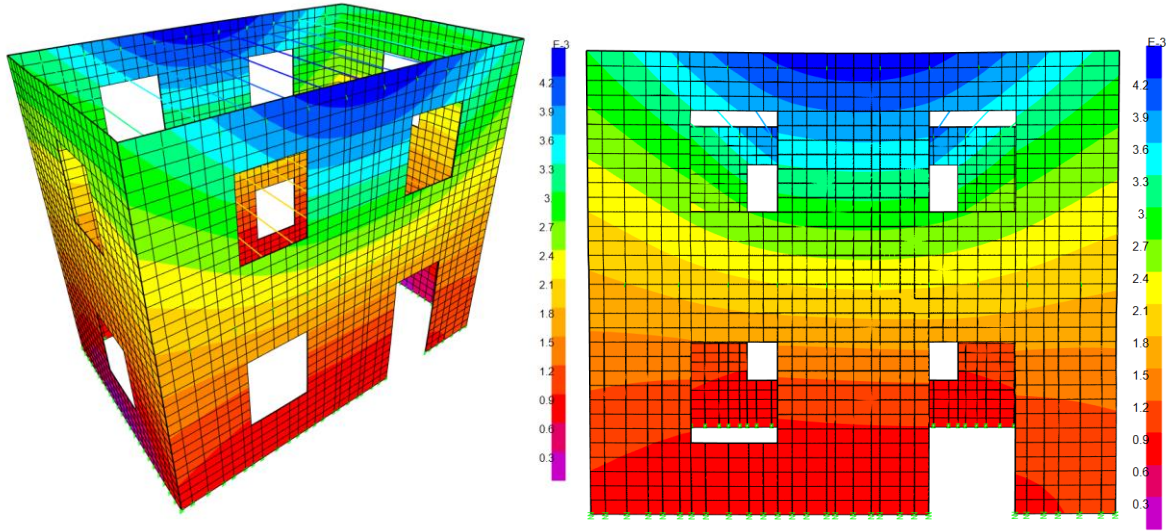


Figure 8-10: Deformed Shape 90% Kalamata UY

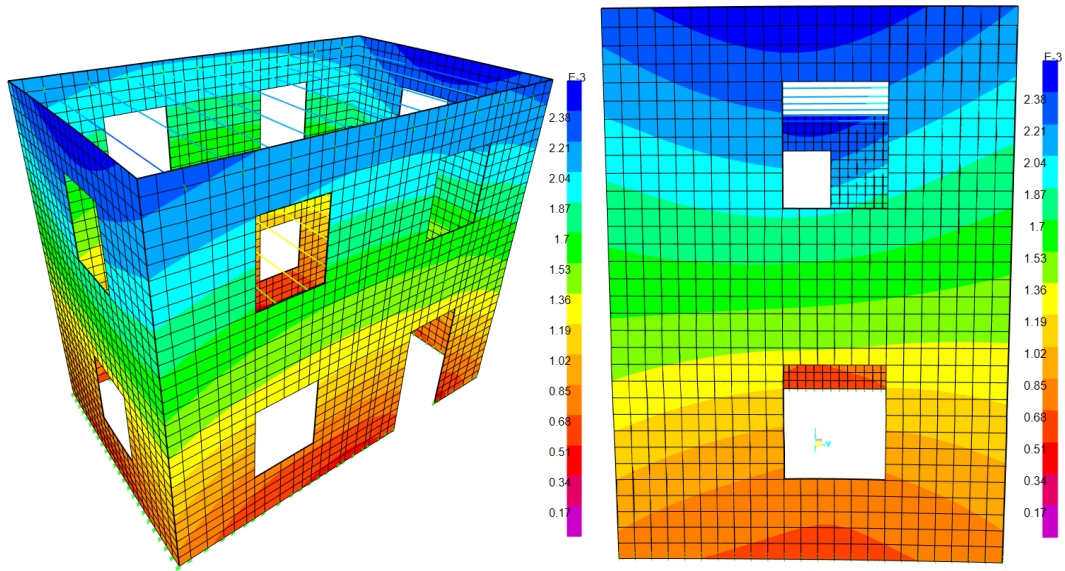


Figure 8-11: Deformed Shape 90% Kalamata UX

The deformed shapes from both the in-plane and out-of-plane analyses show continuous contours throughout the masonry walls confirming that unreinforced conditions were present. The outcome of the analyses saw a peak lateral displacement of 4.39 mm at the top of the midspan of the long wall which is equal to a drift of 0.14% in the UY direction. In the UX direction, a peak lateral displacement of 2.98 mm was measured at the top of the midspan of the short wall equalling a peak drift of 0.093%.

8.2.4 Spectral Analysis

The second analysis involving the records of the 1986 Kalamata earthquake was a spectral analysis using a scaled response spectrum. The scaled spectrums discussed above were applied respectively in the UX and UY directions. The deformed shapes from those analyses are displayed below in Figures 8-12 and 8-13.

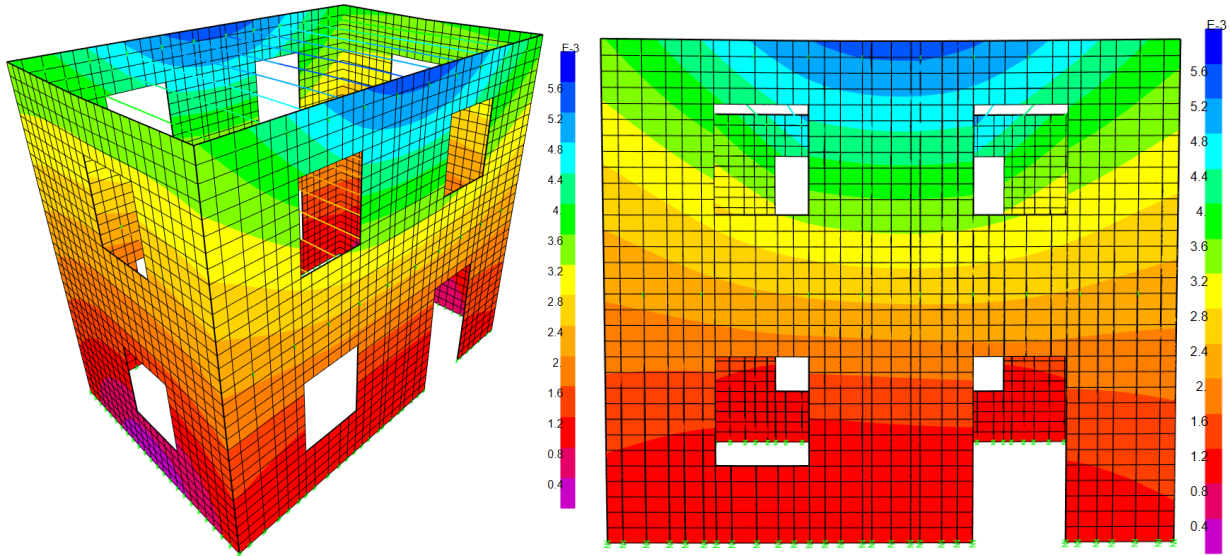


Figure 8-12: Deformed Shape 90% Response Spectrum UY

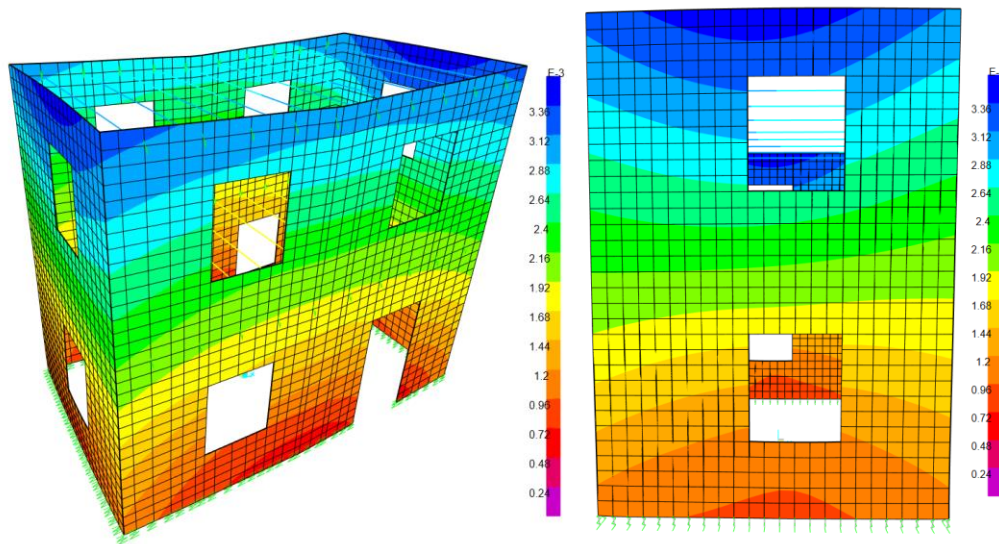


Figure 8-13: Deformed Shape 90% Response Spectrum UX

The deformed shape and contours from the spectral analysis were approximately the same as what was observed in the time history analyses. Considering both the UX and UY directions, varying displacements were observed at the floor levels therefore confirming that unreinforced

conditions are taking place. In the UY direction, the peak displacement observed at the top of the midspan of the long wall was 5.32 mm which equals a drift of 0.166%. In the UX direction a peak displacement of 3.33 mm was observed at the top of the midspan of the short wall equalling a drift of 0.104%. The drift values observed at failure were similar between the spectral and the time history. The similarity between the two types of analyses is expected as both come from the same earthquake record. The collections of normalized cross-sectional shapes shown in Figure 8-14 below confirm the close relation between the spectral and time history analyses.

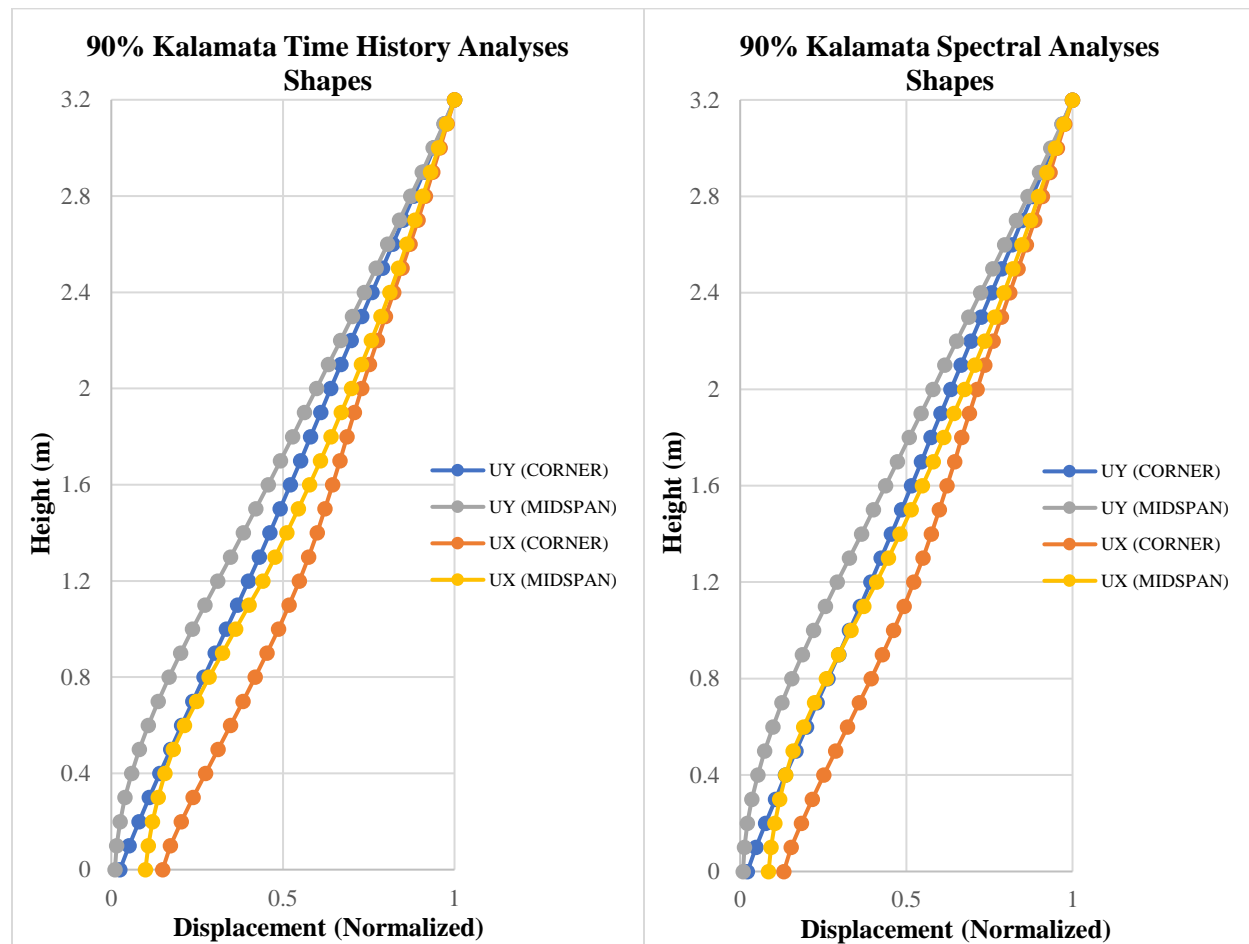


Figure 8-14: Normalized Mode Shapes vs Normalized Gravitational Shapes

As shown above, the deformed shapes from each of the 4 locations within the structure are the same in both the time history and spectral analyses. This validates both analyses as they provide the same results using two unique methods of analysis.

8.2.5 Pushover Analysis

The final analysis conducted on the SAP model was a non-linear pushover analysis. In order to consider non-linearities during the analysis, a novel approach was developed. The pushover analysis was conducted manually using staged loading. First, the non-linear dead load case was run which accounts for the self-weight of the structure and the additional loads applied for scaling reasons. Once the non-linear dead load case had concluded, a lateral acceleration equal to 3.3 m/s^2 ($0.34g$) was applied to the structure in the X direction and the Y direction independently. This novel method ensured that the overbearing stress caused by the self-weight of the structure was applied accordingly.

To capture the plastic behaviour of the structure during the pushover analyses, a few adjustments were made to the model. These adjustments were primarily focussed on the material properties and the definition of the masonry walls. Firstly, the masonry material was redefined as concrete in SAP using all of the same material properties listed in Table 8-1. Next, the Darwin-Pecknold concrete model was introduced to the material which is needed to link the non-linear properties to the non-linear layered shells. The Darwin-Pecknold model is a two-dimensional material model which accounts for bending and shear interactions within a structure and attempts to model the coupling of the two behaviours (Computers & Structures, 2015). Using the predefined material properties, the model computes an effective uniaxial stress-strain curve as shown in Figure 8-15 below.

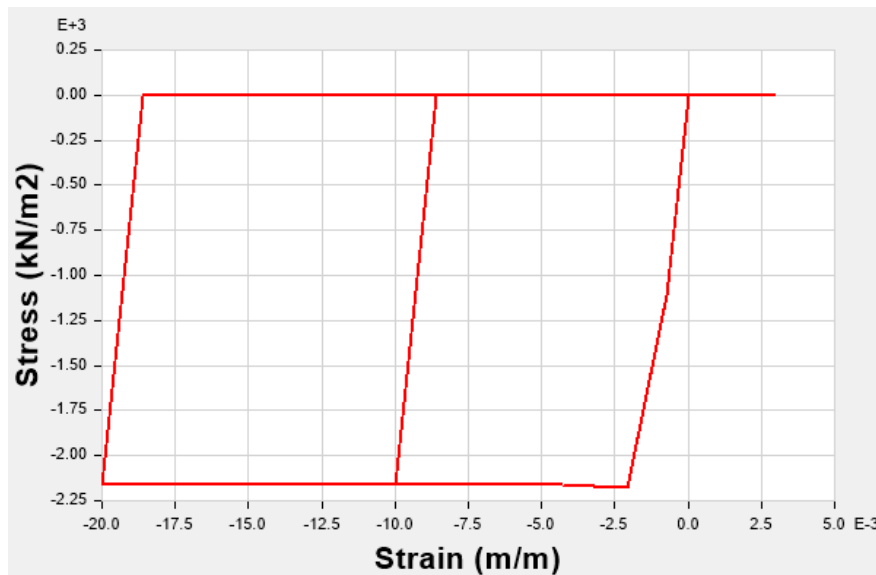


Figure 8-15: Darwin-Pecknold effective uniaxial stress-strain curve

The final adjustment involved the shell elements which represented the masonry walls. The non-linear shells were altered from 10 layers of equal thickness to 1 layer to improve convergence during the analyses. Finally, the layer type was set to coupled to include the non-linearities from the Darwin-Pecknold model.

To collect the results, the lateral displacements were monitored at the top of the midspan of both the long and short walls and plotted against the base shear observed throughout each step of the analyses. The results of the pushover analysis in the out-of-plane direction (Y) are shown in Figures 8-16 and 8-17 below.

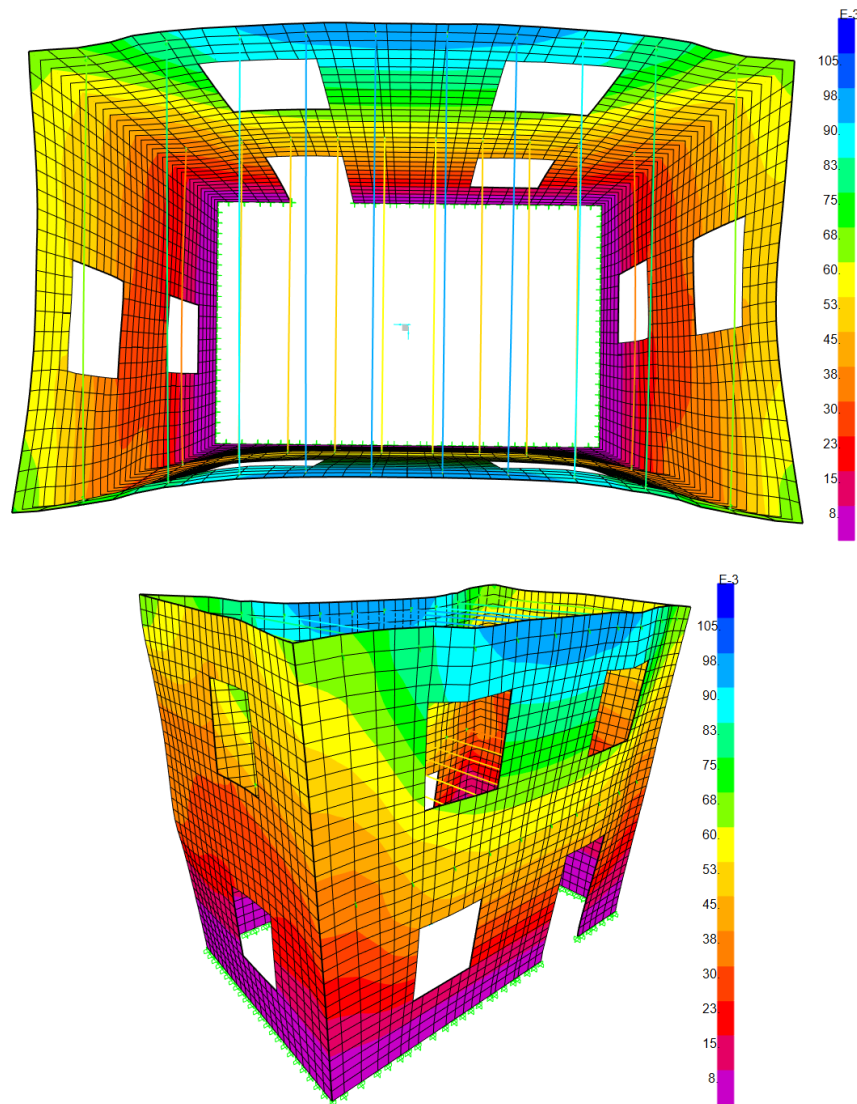


Figure 8-16: Deformed Shape Pushover UY

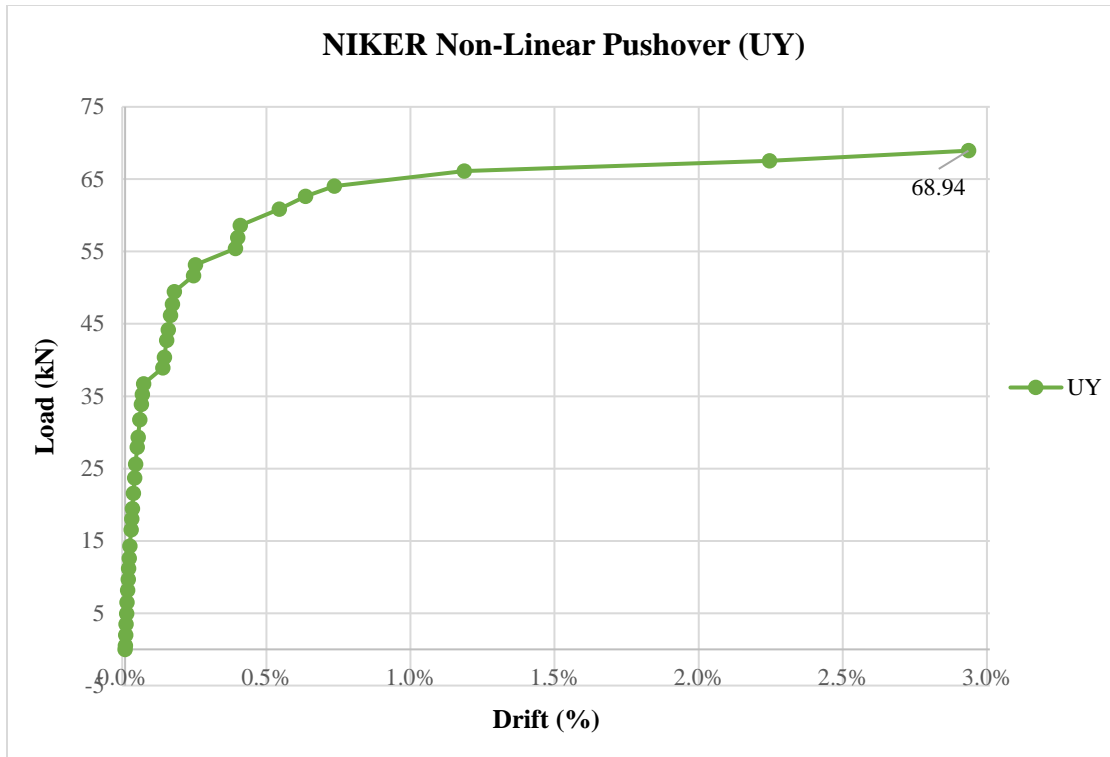


Figure 8-17: Pushover Curve UY

The deformed shape and contours shown in Figure 8-15 above present a common pattern that has been observed through all the analyses conducted both linear and non-linear. This common pattern is defined by varying contours at the floor levels, signifying that unreinforced conditions are present. The results of the pushover analysis showed a peak base shear of 68.94 kN and a peak displacement of 93.63 mm at failure which corresponds to a drift ratio of 2.93%.

The results of the pushover analysis conducted in the in-plane direction is shown in Figures 8-18 and 8-19 below.

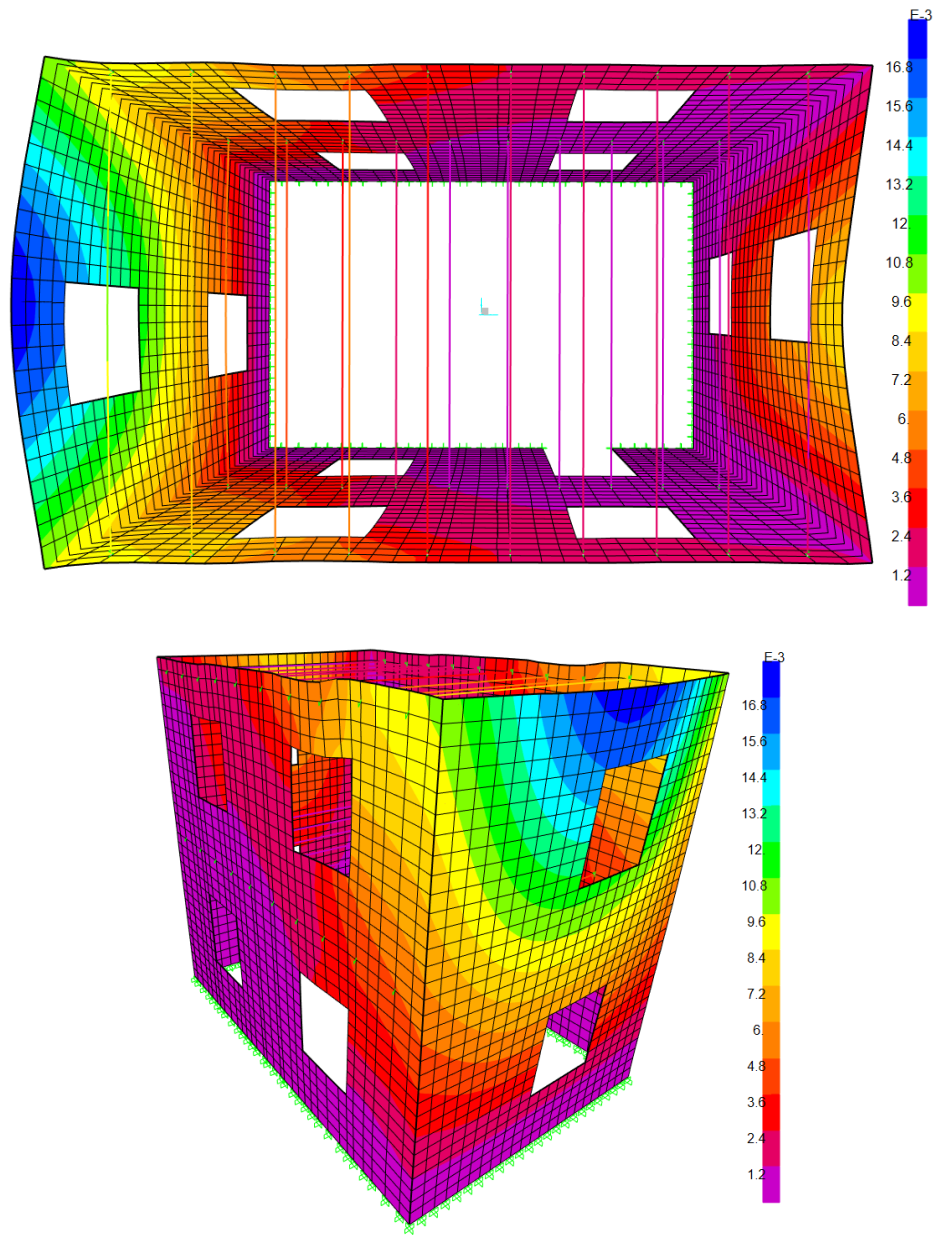


Figure 8-18: Deformed Shape Pushover UX

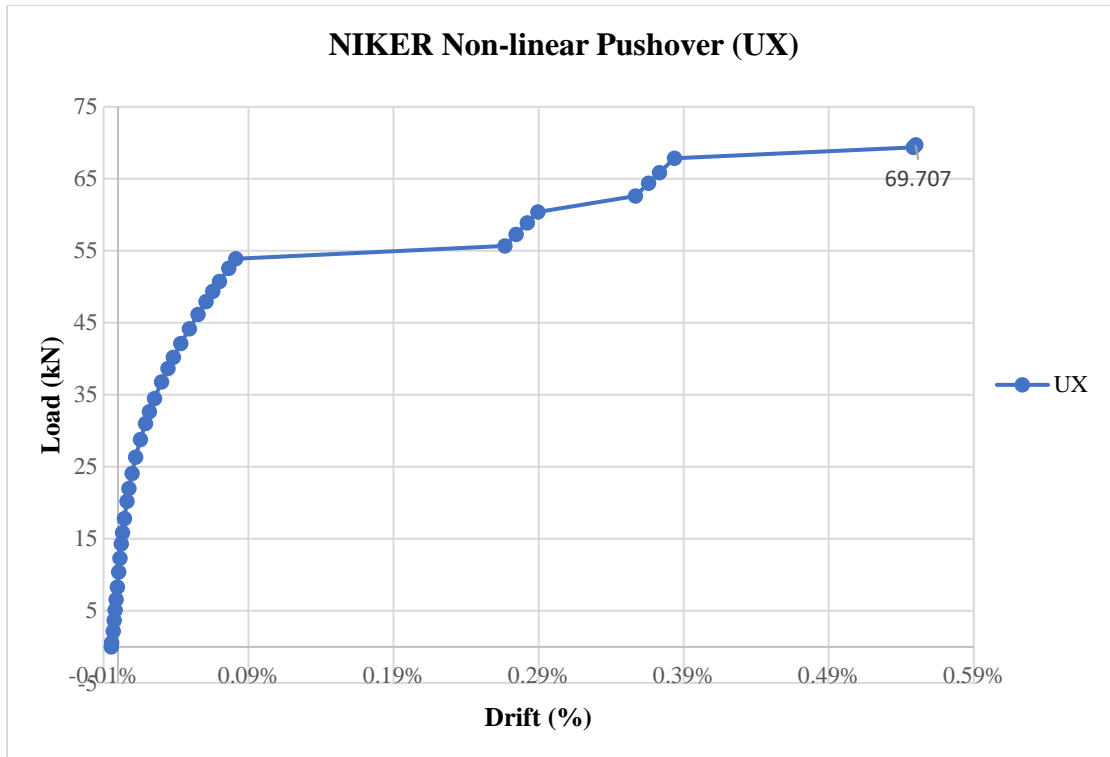


Figure 8-19: Pushover Curve UX

By observing the deformed shape shown above, it can be concluded that the unreinforced conditions are once again present; confirming that the spring connections between the floors and masonry walls is functional in both linear and non-linear analyses. The pushover curve for the in-plane analysis shows an equal base shear of 69.707 kN which is what was observed for the out-of-plane analysis. The peak drift ratio at failure was equal to 17.60 mm which equates to a drift ratio of 0.55%. Therefore, the pushover analyses indicates that the structure can support higher levels of lateral drift in the out-of-plane direction as the peak drift ratio exceeds the in-plane peak drift ratio by 2.38% of the height of the structure.

8.3 Conclusion

The analyses conducted in SAP 2000 served as a final step in the investigation on the NIKER project. Using the outcomes of the finite element modelling investigation on the NIKER material properties, the SAP model was able to fully represent the physical specimen through its geometry and also its mechanical behaviour. After completing the series of linear and non-linear analyses, it was concluded that numerical tools such as SAP can successfully model and estimate the fundamental properties of an existing URM structure like the natural periods. This was

observed through the correlation of the numerical results to the physical results from the referenced literature. Secondly, it was observed throughout the non-linear analyses that the structure had a higher shear strength in the out-of-plane direction versus the in-plane direction. This is highlighted in the pushover analyses where the specimen was able to reach higher lateral drift ratios at the failure while reaching the same base shear as what was observed in the in-plane analysis.

The results of these numerical analyses provide validation that numerical modelling techniques can successfully estimate the capacity of an existing structure. More importantly, the result of these analyses is a methodology which can be used to develop additional models of unreinforced masonry structures in the future. These models serve as a powerful tool for Engineers in areas of the world which are vulnerable to seismic activity. Using a similar methodology as presented in this chapter, estimations can be made on the behaviour of historic unreinforced masonry structures which will then provide an insight on whether the structure is at risk or not. Using these techniques, Engineers will be able to maintain and save iconic and valuable structures without losing the historical characteristics. This will both maintain the sentimental value of many structures of this kind, but also ensure that the public is safe to occupy them for generations to come.

Chapter 9

Conclusion

This thesis consisted of a series of investigations on the mechanical behaviour of masonry and URM structures. This included finite element models on masonry wallettes which were analyzed in order to compute essential, homogenized mechanical properties of masonry. To this end, a series of parametric studies were conducted on the critical factors involved with masonry composition such as brick and mortar joint arrangement, global mortar joint thickness and strength contribution. In addition, parametric studies were conducted involving several strength combinations between the masonry bricks and mortar. The results of the study were correlated with several empirical equations collected from various governing codes and background literature. Three-dimensional finite element modelling was also done in SAP 2000 to model a physical specimen which was tested as part of the past NIKER project. The 3D finite element modelling included various analyses including linear elastic and non-linear analyses.

9.0 Findings

Throughout this thesis, a number of critical conclusions were drawn regarding the mechanical behaviour of masonry and numerical modelling techniques which can be applied to model masonry and URM structures. A summary of the conclusions is as follows:

- The arrangement of masonry bricks and mortar joints plays a crucial role in the resulting compressive and shear strength of a masonry specimen. From the compression and pushover results it was observed that the equally staggered (EQS) brick pattern provides one of the highest compressive and shear strengths due to the optimal load paths created.
- The mortar joint thickness is an essential parameter that affects the mechanical properties of masonry. It was observed that as the global mortar joint thickness is increased, the mechanical properties of masonry such as the compressive and tensile strength values decrease. The mechanical properties from each of the four brick and joint patterns reached their maximum value when using a minimum mortar joint thickness.
- From the pushover analysis it was found that overbearing stress is the primary source of lateral load strength in masonry. The results concluded that the shear strength of the specimen increased as the overbearing stress is increased. It was also observed that the overbearing stress has an impact on the observed failure pattern. For low values of overbearing stress, insufficient lateral resistance was observed and sliding shear failure

resulted. As the overbearing stress increased, the failure modes shifted to diagonal shear and toe crushing failures.

- Empirical equations serve as a valuable tool for preliminary estimations of various parameters. From the parametric studies it was found that the empirical equations considered are effective at estimating the compressive strength of masonry when used with conventional brick and mortar joint patterns and when the global mortar joint thickness does not exceed 10 mm.
- When computing the modulus of elasticity from the pushover analyses conducted on the wallette specimens, it was found that the results are significantly lower than many of the referenced empirical equation provided. Overall, discrepancies exist between the results of the models and the empirical equations. Therefore, the equations showing be used for preliminary estimates only. Overall, it was found that empirical equations are not very effective at computing the modulus of elasticity of masonry. It is recommended that Equation 7.6 be used on conventional brick arrangements such as EQS. For historic arrangements it is recommended that Equation 7.7 be used, however, it is not to be used with an empirical estimation for the compressive strength of masonry.
- Using shell type elements for masonry walls, three-dimensional finite element modelling of URM structures can be conducted and can successfully reproduce the key dynamic characteristics of the structural system such as the fundamental periods and mode shapes.
- When conducting three-dimensional finite element modelling, special consideration should be given to the boundary conditions of the model. Spring connections should be considered for implementing flexible diaphragms and for accounting for the compliance between the base of a structure and a shake table which occurs in a physical experiment.
- In detailed finite element modelling of masonry that account explicitly for bricks and mortar arrangements, attention should be given to the contacts between the macro-elements especially when conducting micro-modelling. Full contacts should be achieved throughout the specimen. However, as the number of contacts and macro-elements increases the magnitude of the analyses and computational power required significantly increases.
- When conducted the shell-type analyses on the URM structure in SAP 2000, it was found that the structure experiences significant deformation in the out-of-plane direction specifically in the longitudinal walls. This signifies that the longitudinal walls are potential

locations for damage to occur particularly when subjected to lateral loads in the transverse direction. To prevent major damage or total collapse during an earthquake, it is recommended that the retrofitting techniques are utilized to create fixed diaphragms at the floor and roof levels. An example is the use of steel ties along the perimeter of the floor and roof levels to fully fix the walls and diaphragms together.

- A novel pushover analyses method has been analyzed. This method utilizes the self-weight of the structure along with a gravitational field which acts laterally. From this it was found that the specimen is most vulnerable when the longitudinal walls are loaded in the out-of-plane direction.

The thesis has presented numerical modelling techniques to successfully analyze and assess URM structures and can serve as a guide. Overall, the greatest contribution from this project is the methodology and steps taken to successfully model and reproduce the dynamic properties of the NIKER project in SAP 2000. These models can increase the efficiency the field of seismic assessment by eliminating the need of physical experiments to compute key dynamic properties of URM structures. Following the steps and methods utilized in this project, any URM structure in question can be modelled with a high degree of accuracy.

9.1 Next Steps

After concluding this thesis several areas within the topic of heritage URM structures were identified to be explored further. Additional modelling of URM structures particularly those with complex conditions such as pitched roofs should be completed. By modelling more specimens with unique conditions, the methodology for modelling URM structures will become broader and more detailed and will be able to be applied on a variety of structures. Additional three-dimensional finite element models should be completed to calibrate further empirical equations for the mechanical properties. Practical but more realistic estimates of material properties are critical for a dependable seismic assessment of URM structures. Overall, this thesis has explored and revealed the capabilities of numerical modelling and their uses for the analysis and assessment of URM structures. Further exploration and implementation of the methods discussed will help ensure the safe and non-invasive restoration of heritage URM structures, and ensure they survive future seismic events with minimal loss.

References

- Adami, C.-E., Vintzileou, E., Mouzakis, C., & Karapitta, L. (2012). *Dynamic Tests On Timber-Laced Three-Leaf Stone Masonry Model*.
- Benedetti, D., Benedetti, D., Carydis, P., & Pezzoli, P. (1996). Shaking table tests on 24 simple masonry buildings. In *Earthquake Engineering and Structural Dynamics* (Vol. 27). John Wiley & Sons.
- Bilous, J. (n.d.). *The University College Building at sunset, at the University of Toronto, in Toronto, Ontario* [Photograph]. Toronto, Ontario. <https://www.shutterstock.com/image-photo/university-college-building-sunset-toronto-ontario-450746794>
- Bothara, J. K., Dhakal, R. P., & Mander, J. B. (2010). Seismic performance of an unreinforced masonry building: An experimental investigation. *Earthquake Engineering and Structural Dynamics*, 39(1), 45–68. <https://doi.org/10.1002/eqe.932>
- Brocker, O. (1961). Stein Festigkeit und Wand Festigkeit. In *Ziegelindustrie* (Vol. 2, pp. 19–21).
- Bruneau, M. (1994). Seismic evaluation of unreinforced masonry buildings — a state-of-the-art report. *Can. J. Civ. Eng.*, 21, 512–539. <https://doi.org/10.1139/194-054>
- Campbell, J. W. P. (2003). *Brick: A World History* (illustrate). Thames & Hudson.
- Canadian Standards Association. (2010). *Design of masonry structures (S304.1-04)* (Issue Reaffirmed). Canadian Standards Association.
- Cervenka, V., & Cervenka, J. (2017). *ATENA Program Documentation Part 2-2 User 's Manual for ATENA 3D*. Prague, Czech Republic, 1-144.
- Computers & Structures, Inc. (2017). *CSi Analysis Reference Manual*. Computers & Structures, Inc.
- Computers & Structures, Inc. (2015). *Technical Note Modified Darwin-Pecknold 2-D Reinforced Concrete Material Note*. Computers & Structures, Inc.
- Crespi, P., Giordano, N., & Frascaro, G. (2019). Seismic loss estimation for an old masonry building in Italy. *13th International Conference on Applications of Statistics and Probability in Civil Engineering, ICASP 2019*.
- Engineering ToolBox, (2004). *Density of Various Wood Species*. [online] Available at: https://www.engineeringtoolbox.com/wood-density-d_40.html [Accessed 15 December 2019].

- European Committee for Standardization. (2005). EN 1996-1-1 Eurocode 6: Design of Masonry Structures - Part 1-1: General Rules for Reinforced and Unreinforced Masonry Structures. In *Civil Engineering*. European Committee for Standardization.
<https://doi.org/10.1680/cien.144.6.44.40610>
- Institute of Engineering Seismology & Earthquake Engineering. (2021). *GID Hellenic Accelerograms Database - GHEAD v1.0*. <http://ghead.itsak.gr/>
- Esposito, R., Messali, F., Ravenshorst, G. J. P., Schipper, H. R., & Rots, J. G. (2019). Seismic assessment of a lab-tested two-storey unreinforced masonry Dutch terraced house. *Bulletin of Earthquake Engineering*, 17(8), 4601–4623. <https://doi.org/10.1007/s10518-019-00572-w>
- Giordano, A., Mele, E., & De Luca, A. (2002). Modelling of historical masonry structures: Comparison of different approaches through a case study. *Engineering Structures*, 24(8), 1057–1069. [https://doi.org/10.1016/S0141-0296\(02\)00033-0](https://doi.org/10.1016/S0141-0296(02)00033-0)
- Hartill, A., & Hartill, M. (n.d.). *City of Pompeii (Founded circa 5th century BCE)* [Photograph, Architecture]. Pompeii, Italy. https://library-artstor-org.ezproxy.library.yorku.ca/asset/HARTILL_12311762
- Hendry, A. W., Sinha, B. P., & Davies, S. R. (2004). *Design of Masonry Structures* (Third). E & FN Spon.
- KADET. (2017) Code for assessment and structural interventions in masonry buildings. Athens: Earthquake Planning and Protection Organization (EPPO).
- Karantoni, F. V., Papadopoulos, M. L., & Pantazopoulou, S. J. (2016). Simple Seismic Assessment of Traditional Unreinforced Masonry Buildings. *International Journal of Architectural Heritage*, 10(8), 1055–1077. <https://doi.org/10.1080/15583058.2016.1183062>
- Karapitta, L., Mouzakis, C., Adami, C.-E., & Vintzileou, E. (2012). *Non Linear Seismic Response of Three-Leaf Masonry Structures*.
- Karatzetzou, A., Iliou, K., Pitilakis, D., Lagomarsino, S., Cattari, S., Vintzileou, E., & Adamis, C.-E. (2014). *Numerical Investigation On The Seismic Response Of Historical Masonry Structures: Linear and Non-Linear Modelling of Shaking Table Tests on a Building of URM Before Strengthening*.
- Krawczyk, B. (n.d.). *Beardmore Building* [Photograph]. Toronto, Ontario.
https://acotoronto.ca/show_building.php?BuildingID=2823

- Lagomarsino, S., Penna, A., Galasco, A., & Cattari, S. (2013). TREMURI program: An equivalent frame model for the nonlinear seismic analysis of masonry buildings. *Engineering Structures*, 56, 1787–1799. <https://doi.org/10.1016/j.engstruct.2013.08.002>
- Laube, J. (1987). *Kalamata Earthquake, 1986: Psychological reactions and roles for health care workers*.
http://scholarcommons.usf.edu/fmhi_pubhttp://scholarcommons.usf.edu/fmhi_pub/40
- Lourenco, P. B. (2015). Masonry Structures: Overview. *Encyclopedia of Earthquake Engineering*, 1–10. <https://doi.org/https://doi.org/10.1007/978-3-642-35344-4>
- Magenes, G., Penna, A., Galasco, A., Magenes, G., Penna, A., & Galasco, A. (2010). *A full-scale shaking table test on a two-storey stone masonry building*.
<https://www.researchgate.net/publication/257333070>
- Magenes, G., Penna, A., Senaldi, I. E., Rota, M., & Galasco, A. (2014). Shaking table test of a strengthened full-scale stone masonry building with flexible diaphragms. *International Journal of Architectural Heritage*, 8(3), 349–375.
<https://doi.org/10.1080/15583058.2013.826299>
- Mazzon, N., Valluzzi, M. R., Aoki, T., Garbin, E., De Canio, G., Ranieri, N., & Modena, C. (2009). *Shaking table tests on two multi-leaf stone masonry buildings*.
- Mendes, N., & Lourenco, P. B. (2010). Seismic assessment of masonry Gaioleiro buildings in Lisbon, Portugal. *Journal of Earthquake Engineering*, 14(1), 80–101.
<https://doi.org/10.1080/13632460902977474>
- Mouzakis, C., Vintzileou, E., Adami, C. E., & Karapitta, L. (2012). *Dynamic Tests on Three Leaf Stone Masonry Building Model Before and After Interventions*.
- Pantazopoulou, S. J. (2013). *State of the art report for the analysis methods for unreinforced masonry heritage structures and monuments*.
www.diocesilaquila.it/laquila/allegati/24504/Maria%2520Paganica.jpg
- Pardalopoulos, S. I., Karantoni, F. V., & Pantazopoulou, S. J. (2019). Practical assessment of the seismic behavior of a confined masonry system. *Soil Dynamics and Earthquake Engineering*, 127(January). <https://doi.org/10.1016/j.soildyn.2019.105831>
- Pardalopoulos, S. I., & Pantazopoulou, S. J. (2017). Methodology for practical seismic assessment of unreinforced masonry buildings with historical value. *Earthquake Engineering and Structural Dynamics*, 46(15), 2793–2810. <https://doi.org/10.1002/eqe.2931>

- Penelis, G. G., & Penelis, G. G. (2020). *Structural Restoration of Masonry Monuments*. Taylor & Francis Group, LLC.
- Pulviser, S. (2005). *The First Toronto Post Office* [Photograph]. Toronto, Ontario.
https://en.wikipedia.org/wiki/First_Toronto_Post_Office#/media/File:First_Toronto_Post_Office.JPG
- Reitherman, R., & Perry, S. C. (2009). *FEMA P-774: Unreinforced Masonry Buildings and Earthquakes Developing Successful Risk Reduction Programs*.
- Schiavi, A., Cellai, G., Secchi, S., Brocchi, F., Grazzini, A., Prato, A., & Mazzoleni, F. (2019). Stone masonry buildings: Analysis of structural acoustic and energy performance within the seismic safety criteria. *Construction and Building Materials*, 220, 29–42.
<https://doi.org/10.1016/j.conbuildmat.2019.05.192>
- Simões, A., Bento, R., Lagomarsino, S., & Cattari, S. (2013). *Seismic Pushover Analysis of “Gaioleiro” Buildings in Lisbon*.
- Tassios, T. (1992). *Masonry mechanics*. In Greek. Athanassopoulos-Papadonis Ltd.
- Tomazevic, M. (1999). *Earthquake-Resistant Design of Masonry Buildings*. Imperial College Press.
- UN Educational, Scientific and Cultural Organization (UNESCO). (1977). Convention for the protection of the world cultural and natural heritage. *United Nations Educational, Scientific and Cultural Organization*, 1037(15511), 151–211. <https://doi.org/10.1163/ilwo-vb4>
- Vintzileou, E., Mouzakis, C., Adami, C. E., & Karapitta, L. (2015). Seismic behavior of three-leaf stone masonry buildings before and after interventions: Shaking table tests on a two-storey masonry model. *Bulletin of Earthquake Engineering*, 13(10), 3107–3133.
<https://doi.org/10.1007/s10518-015-9746-x>
- Vlachakis, G., Vlachaki, E., & Lourenço, P. B. (2020). Learning from failure: Damage and failure of masonry structures, after the 2017 Lesvos earthquake (Greece). *Engineering Failure Analysis*, 117(August). <https://doi.org/10.1016/j.engfailanal.2020.104803>

Appendices

Appendix A – Lateral response of masonry wallettes

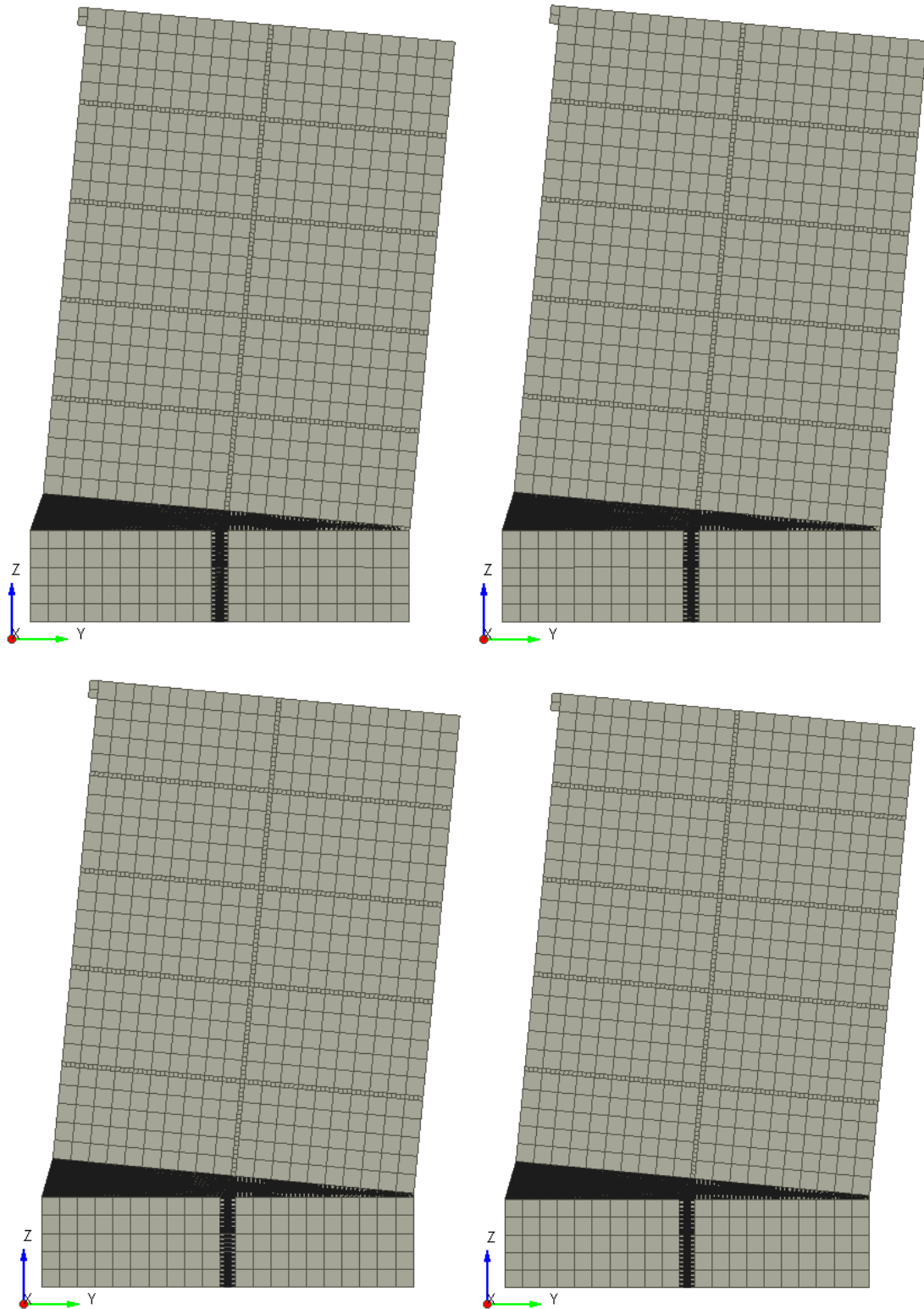


Figure A-1: PO-SYMJ5-OB0.05 Response [A] 0.1% Drift, [B] 0.2% Drift, [C] 0.5% Drift, [D] 1% Drift

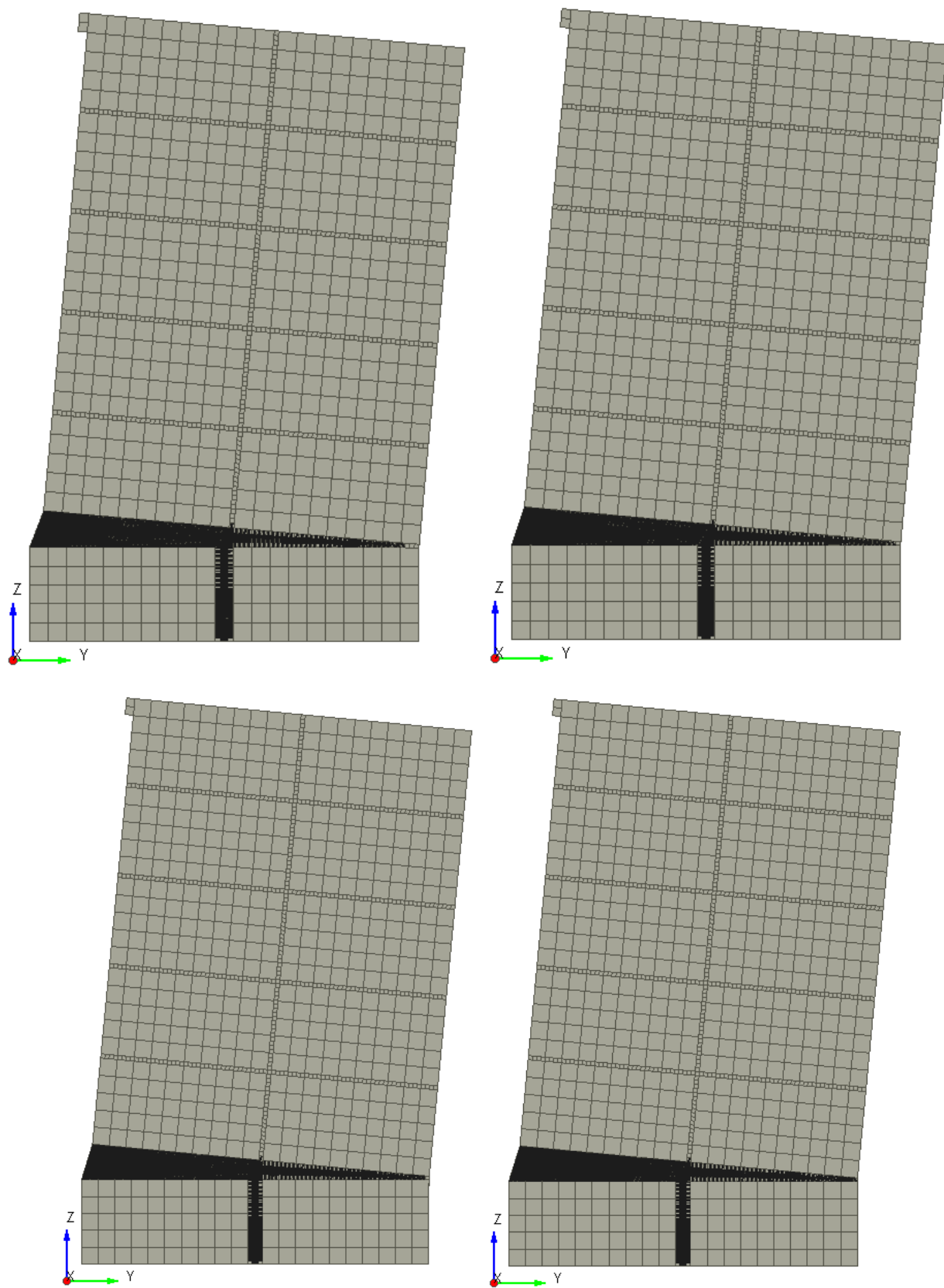


Figure A-2: PO-SYMJ5-OB0.1 Response [A] 0.1% Drift, [B] 0.2% Drift, [C] 0.5% Drift, [D] 1% Drift

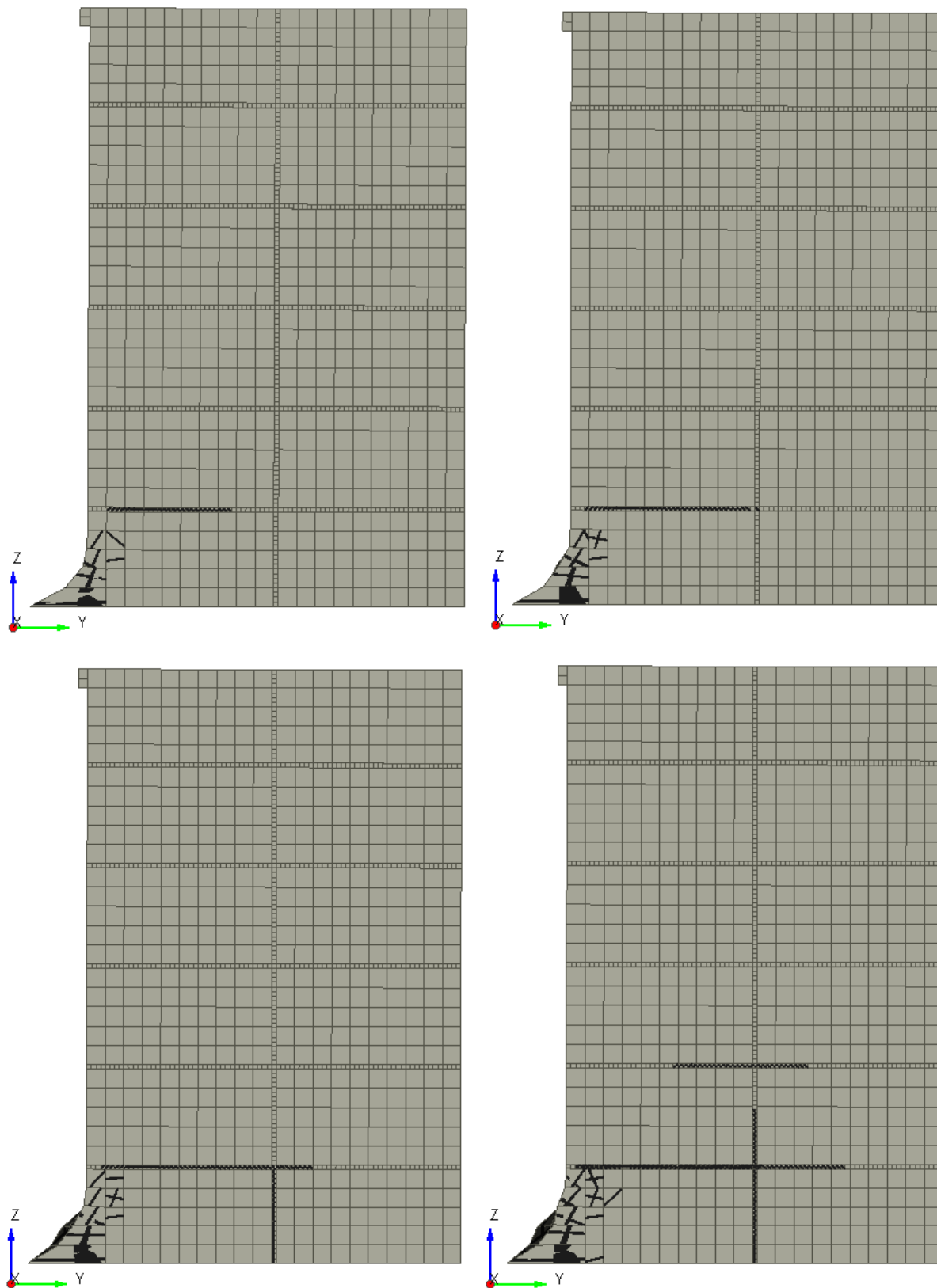


Figure A-3: PO-SYMJ5-OB0.2 Response [A] 0.1% Drift, [B] 0.2% Drift, [C] 0.5% Drift, [D] 1% Drift

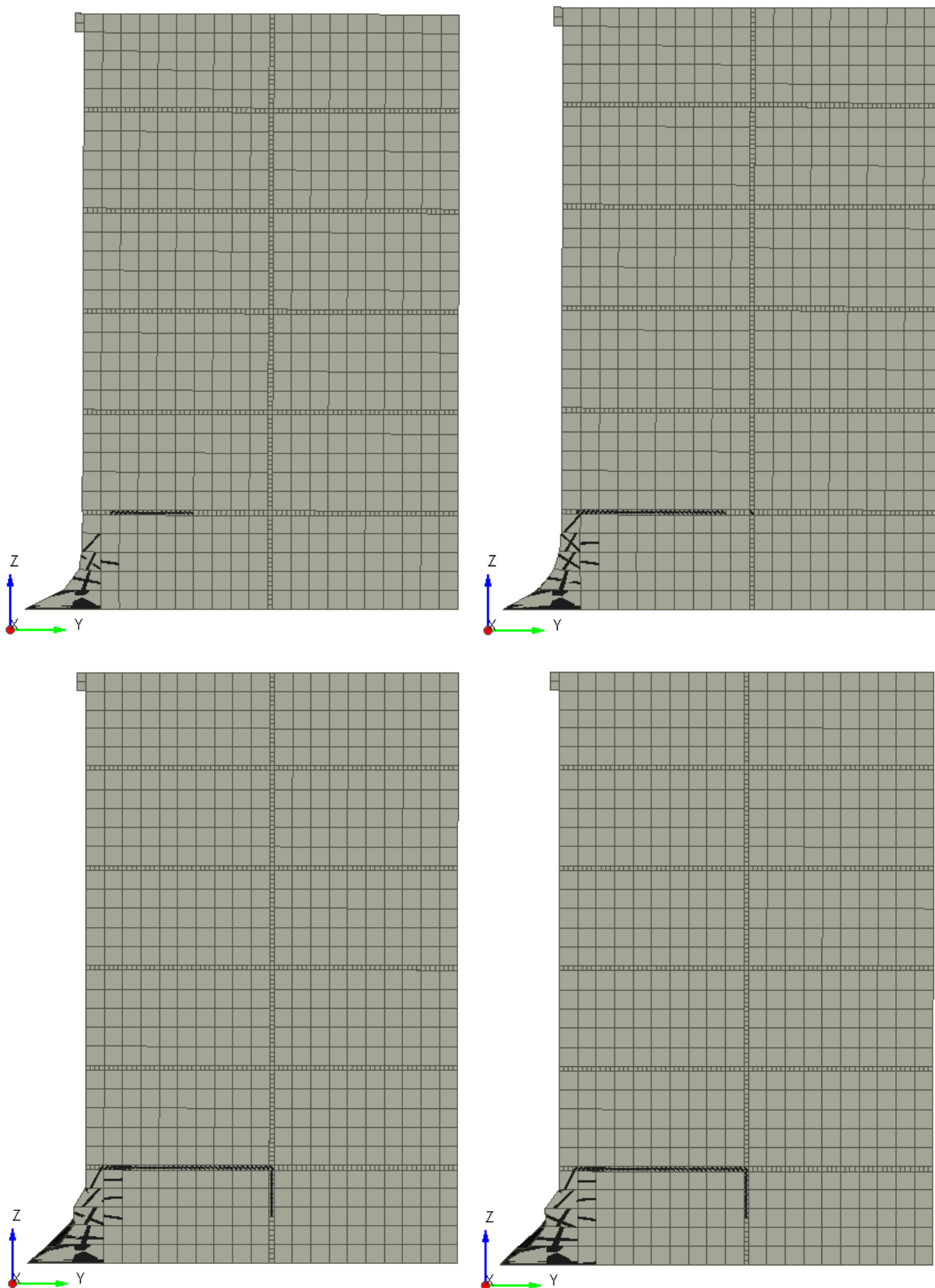


Figure A-4: PO-SYMJ5-OB0.3 Response [A] 0.1% Drift, [B] 0.2% Drift, [C] 0.5% Drift, [D] 1% Drift

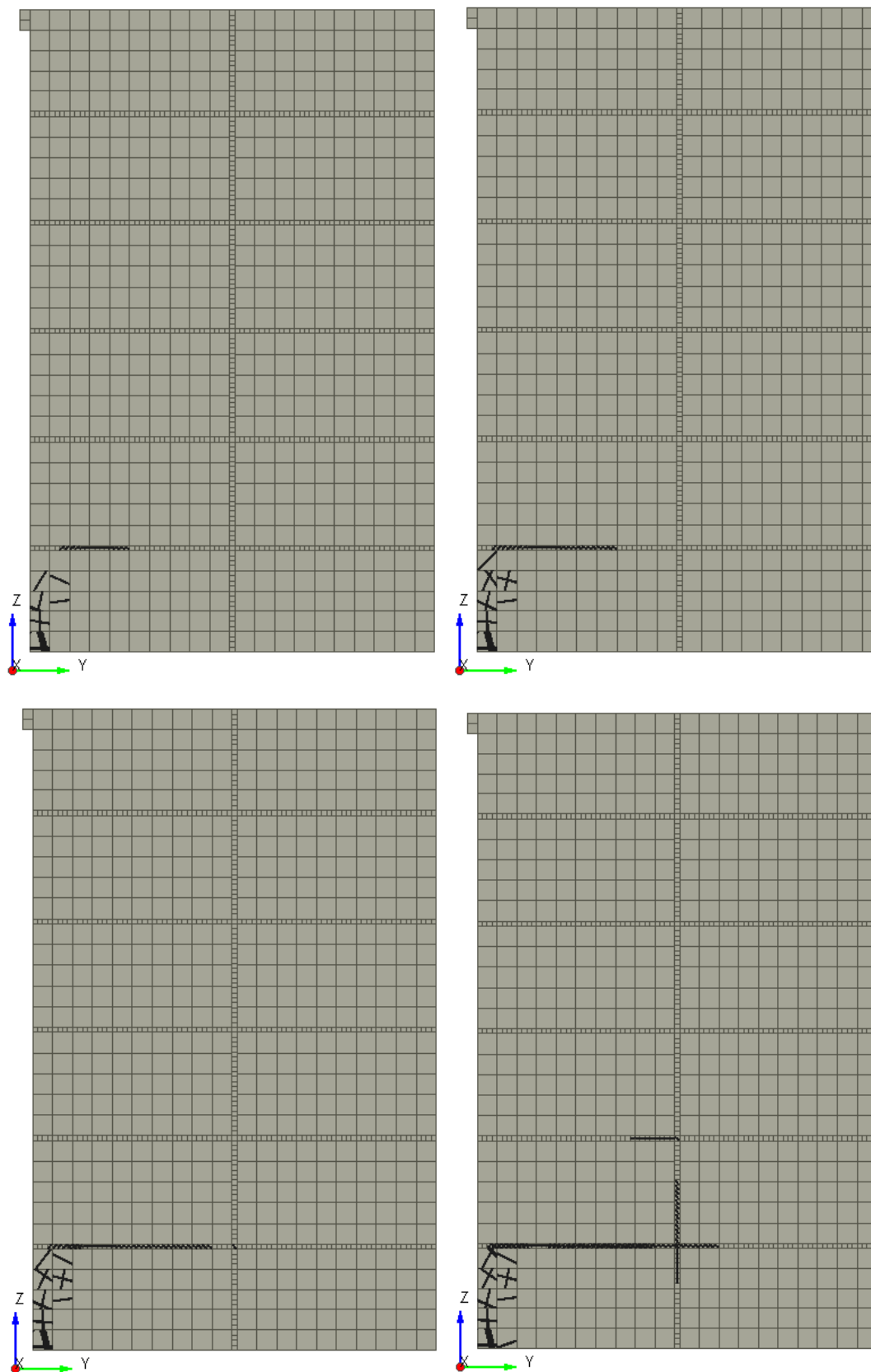


Figure A-5: PO-SYMJ5-OB0.4 Response [A] 0.1% Drift, [B] 0.2% Drift, [C] 0.5% Drift, [D] 1% Drift

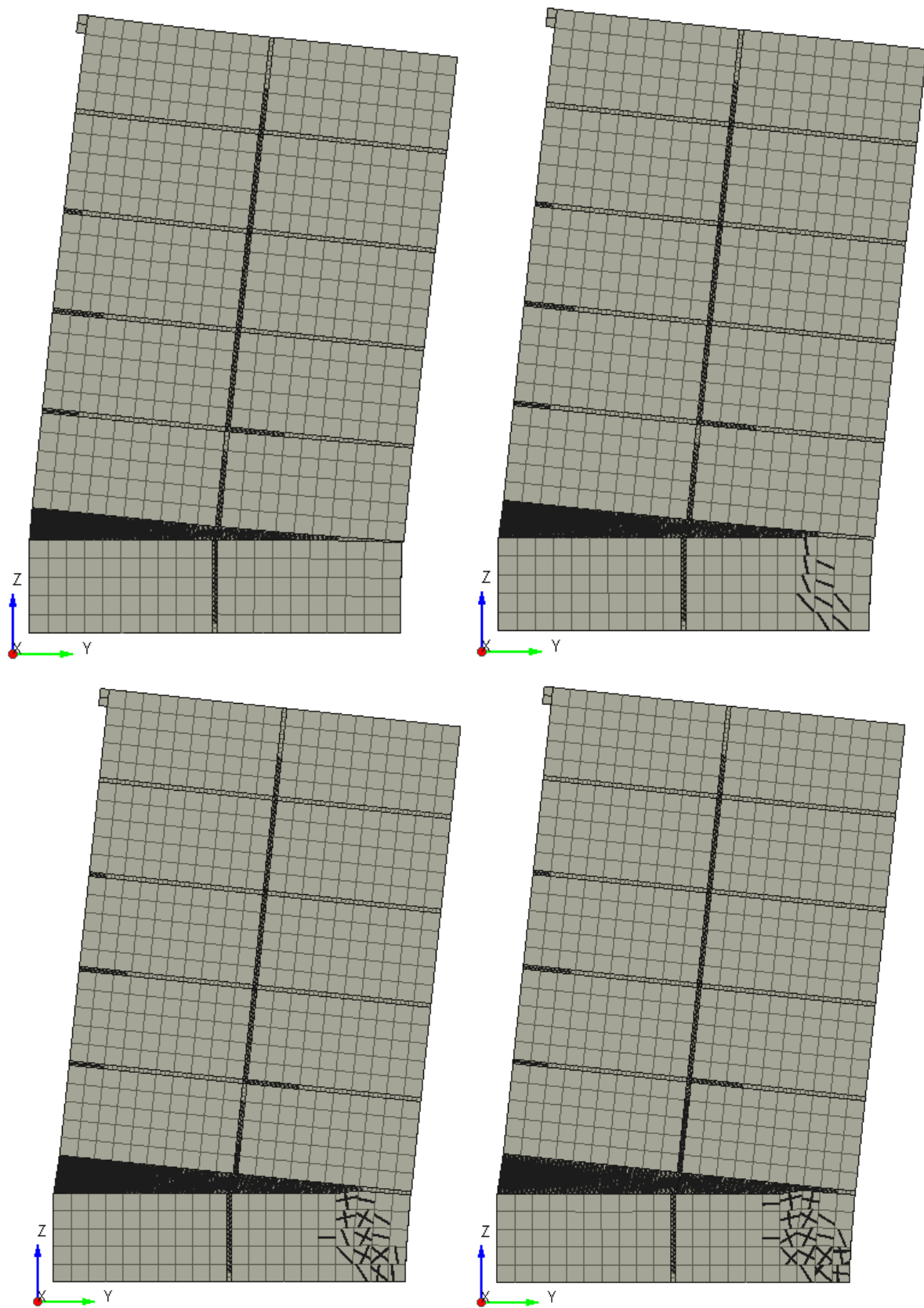


Figure A-6: PO-SYMJ5-OB1.79 Response [A] 0.092% Drift, [B] 0.23% Drift, [C] 0.51% Drift, [D] 0.83% Drift

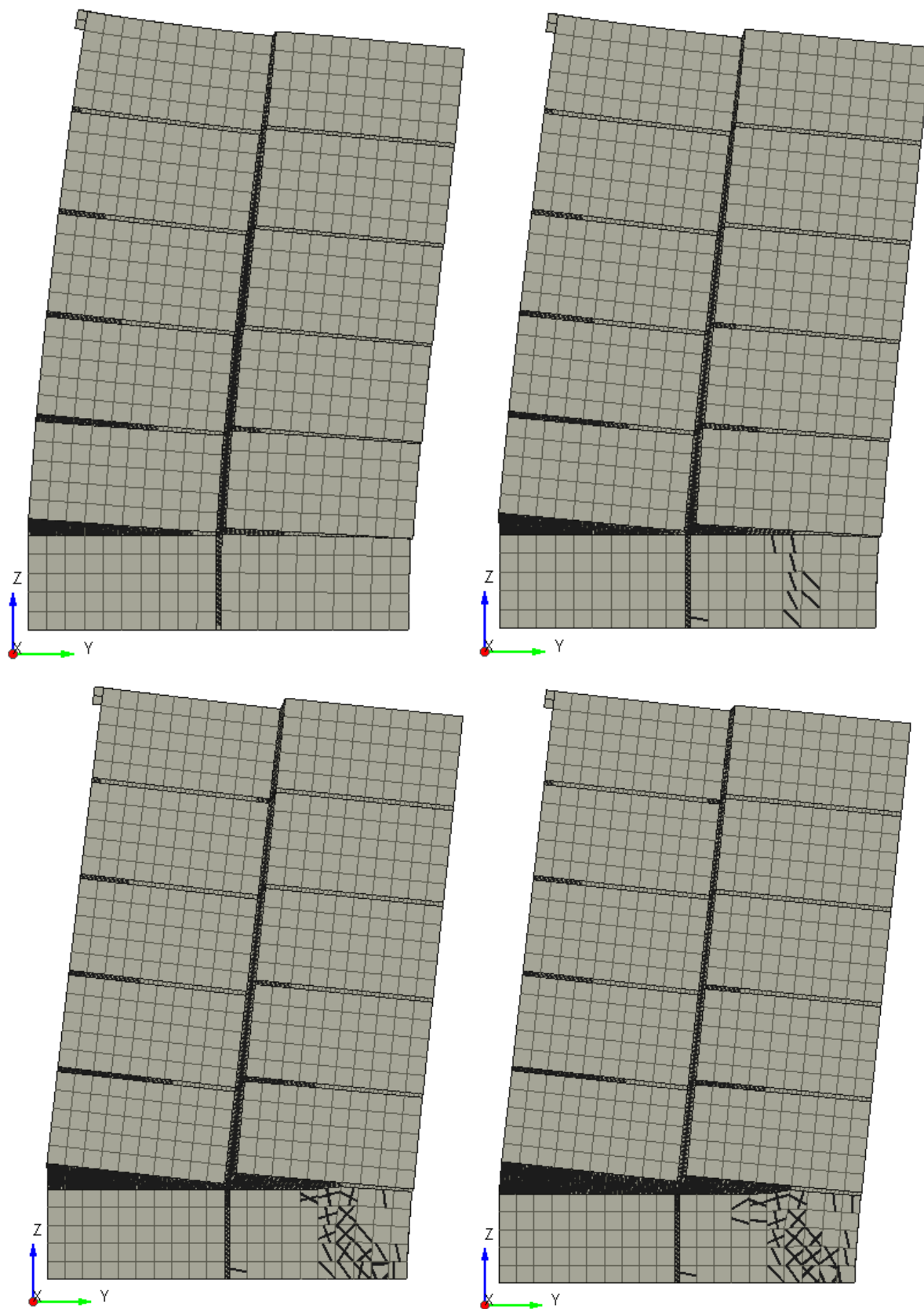


Figure A-7: PO-SYMJ5-OB4.47 Response [A] 0.092% Drift, [B] 0.18% Drift, [C] 0.51% Drift, [D] 0.92% Drift

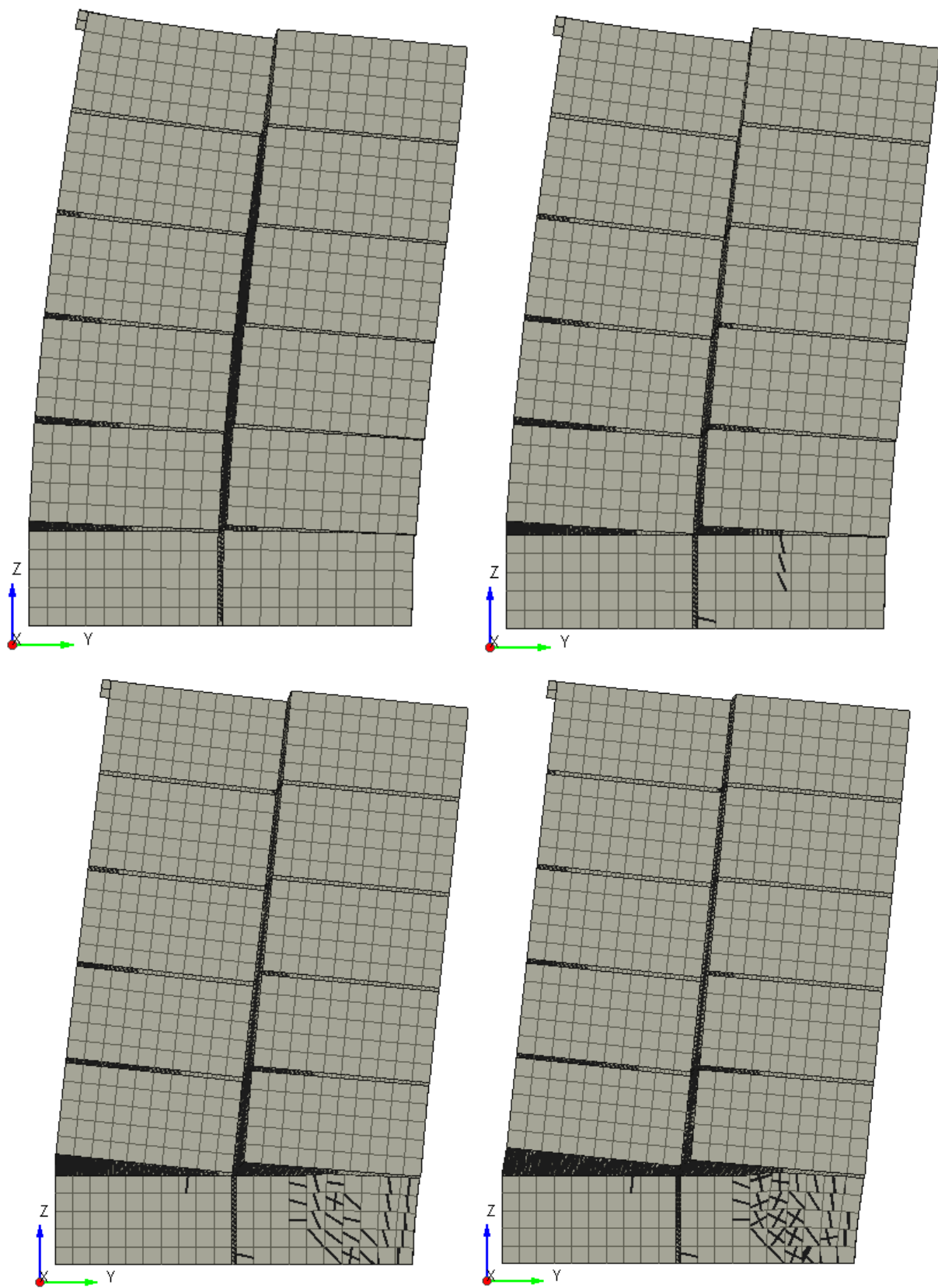


Figure A-8: PO-SYMJ5-OB7.15 Response [A] 0.092% Drift, [B] 0.18% Drift, [C] 0.51% Drift, [D] 0.92% Drift

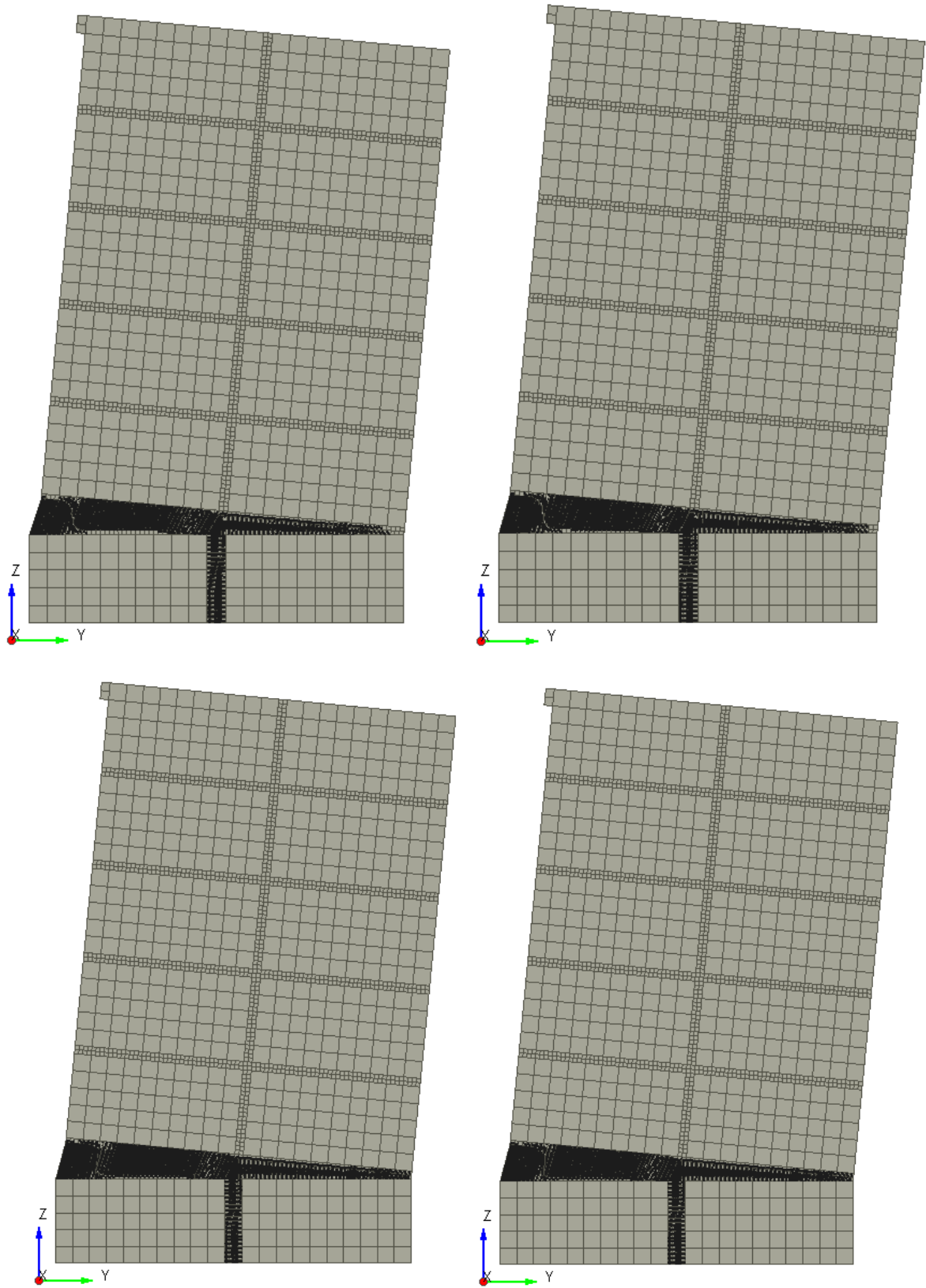


Figure A-9: PO-SYMJ10-OB0.05 Response [A] 0.1% Drift, [B] 0.2% Drift, [C] 0.5% Drift, [D] 0.74% Drift

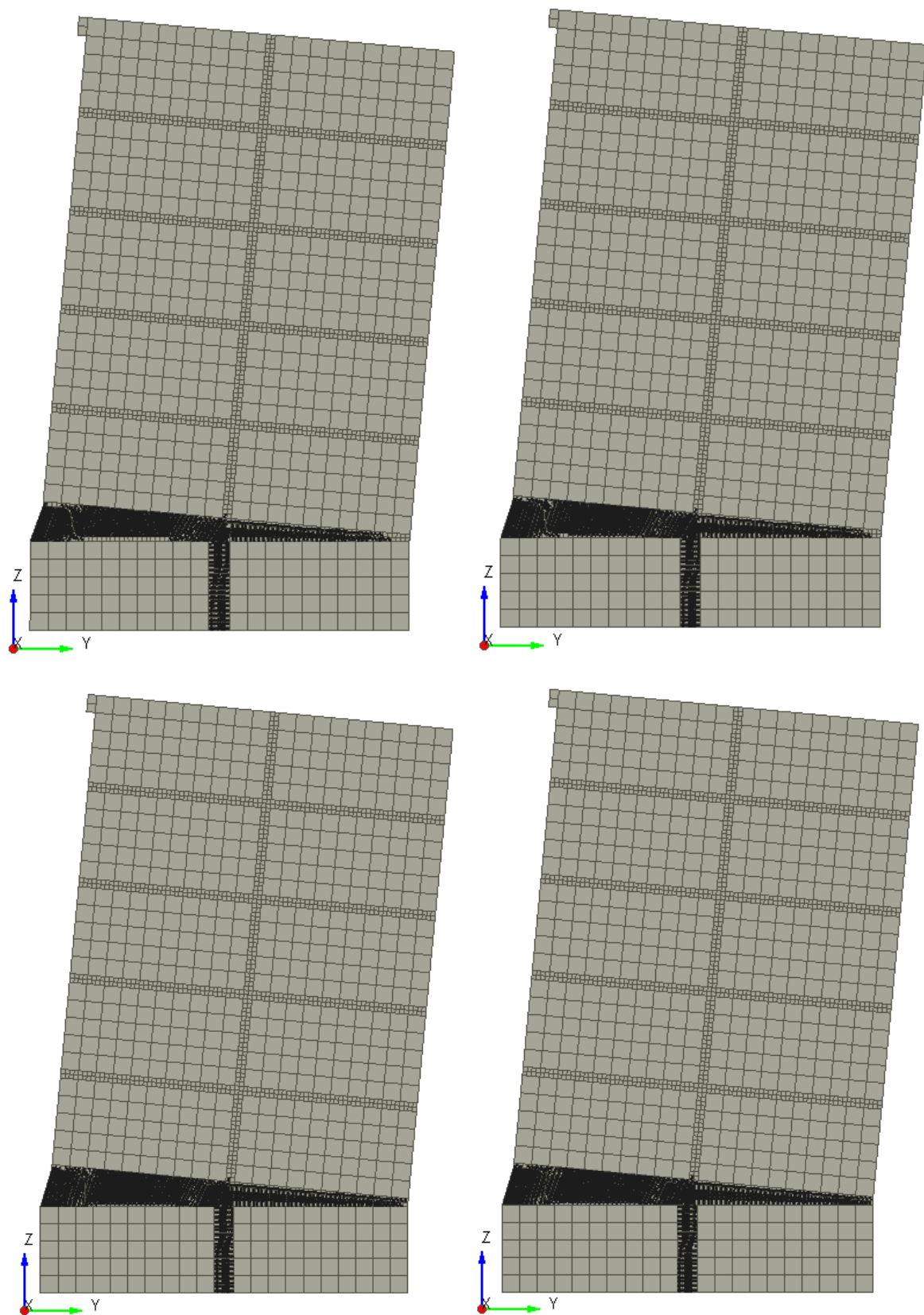


Figure A-10: PO-SYMJ10-OB0.1 Response [A] 0.1% Drift, [B] 0.2% Drift, [C] 0.5% Drift, [D] 0.81% Drift

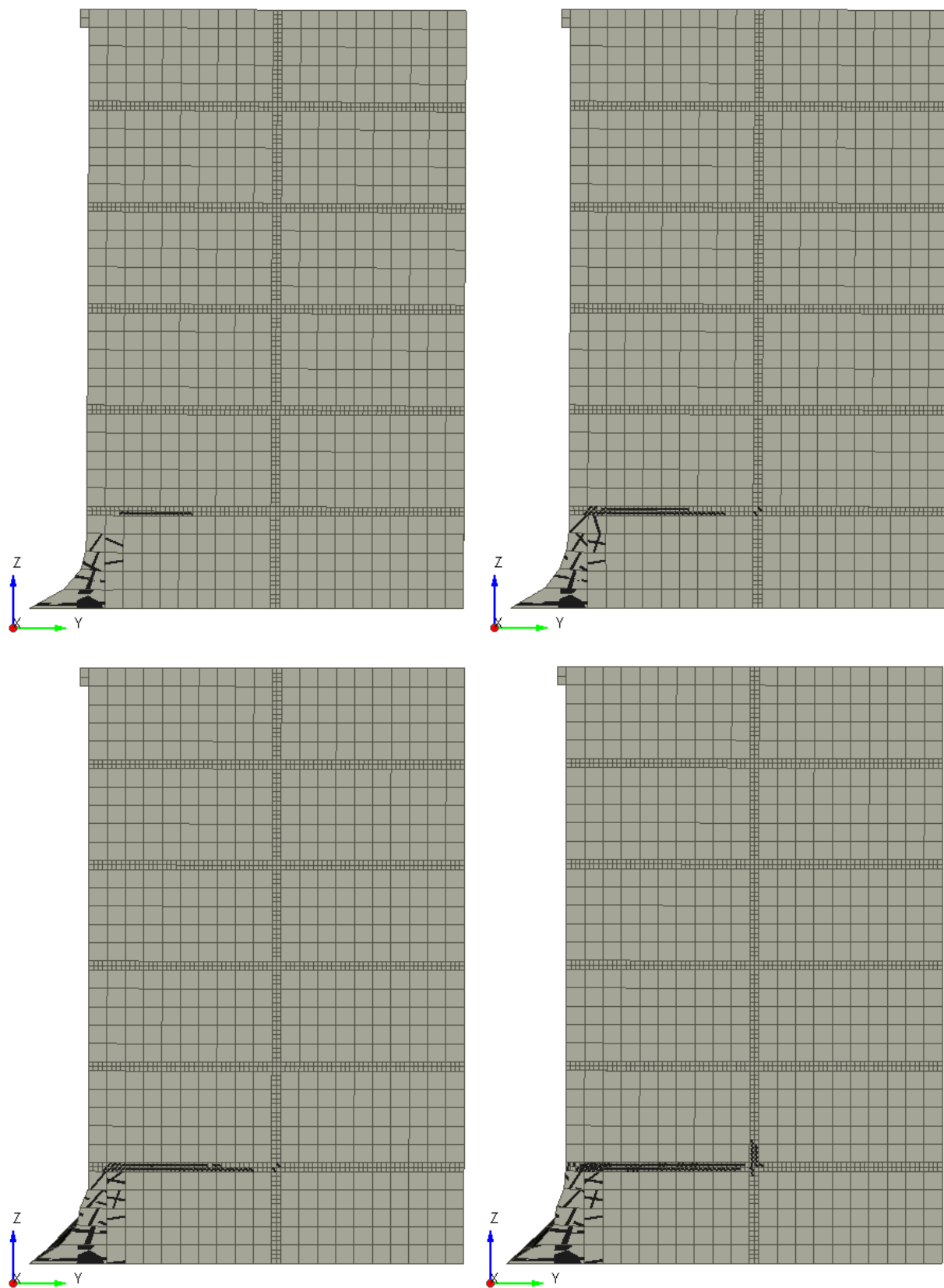


Figure A-11: PO-SYMJ10-OB0.2 Response [A] 0.1% Drift, [B] 0.2% Drift, [C] 0.5% Drift, [D] 0.94% Drift

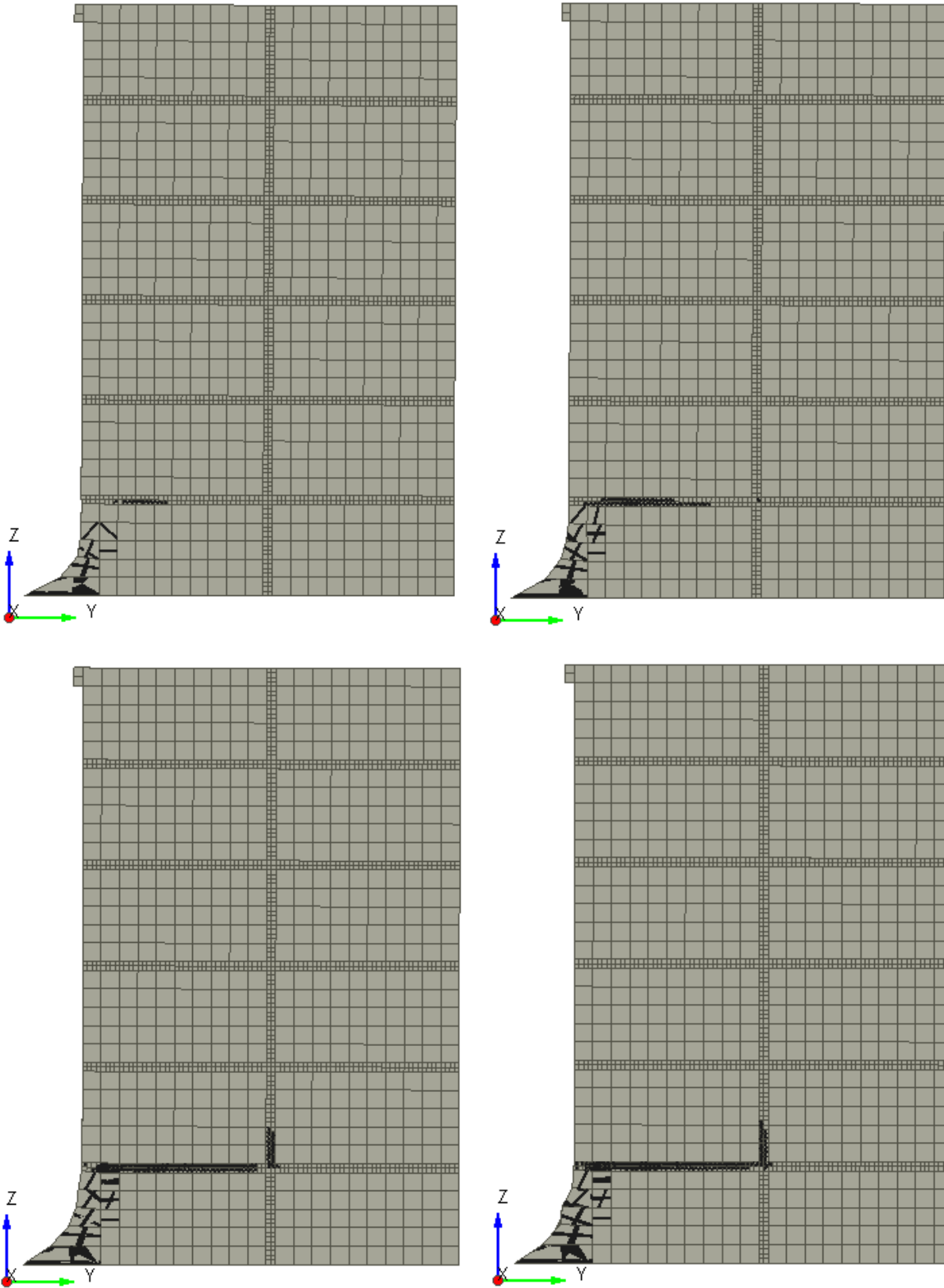


Figure A-12: PO-SYMJ10-OB0.3 Response [A] 0.1% Drift, [B] 0.2% Drift, [C] 0.5% Drift, [D] 1% Drift

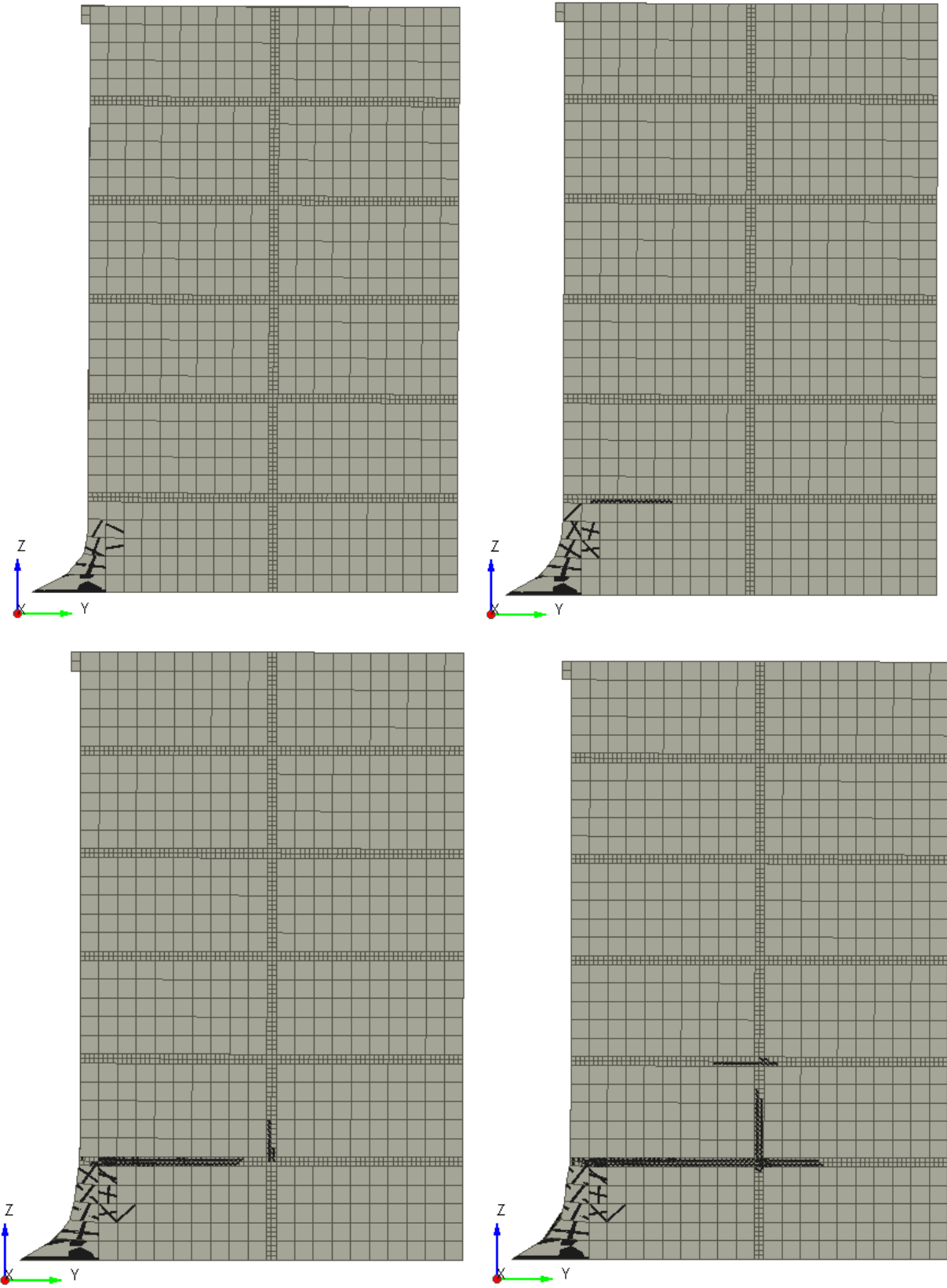


Figure A-13: PO-SYMJ10-OB0.4 Response [A] 0.1% Drift, [B] 0.2% Drift, [C] 0.5% Drift, [D] 1% Drift

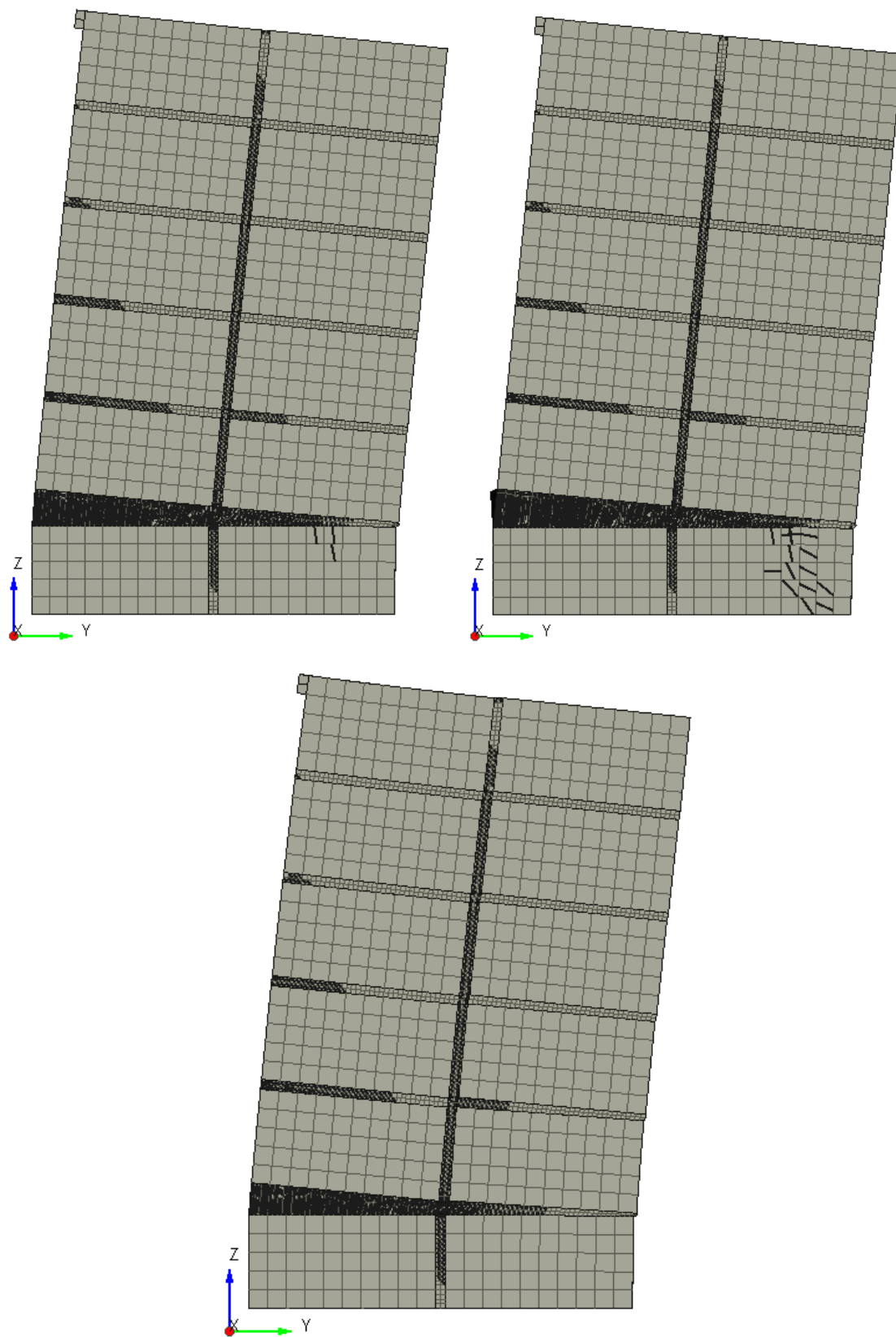


Figure A-14: PO-SYMJ10-OB1.79 Response [A] 0.231% Drift, [B] 0.415% Drift, [C] 0.922% Drift

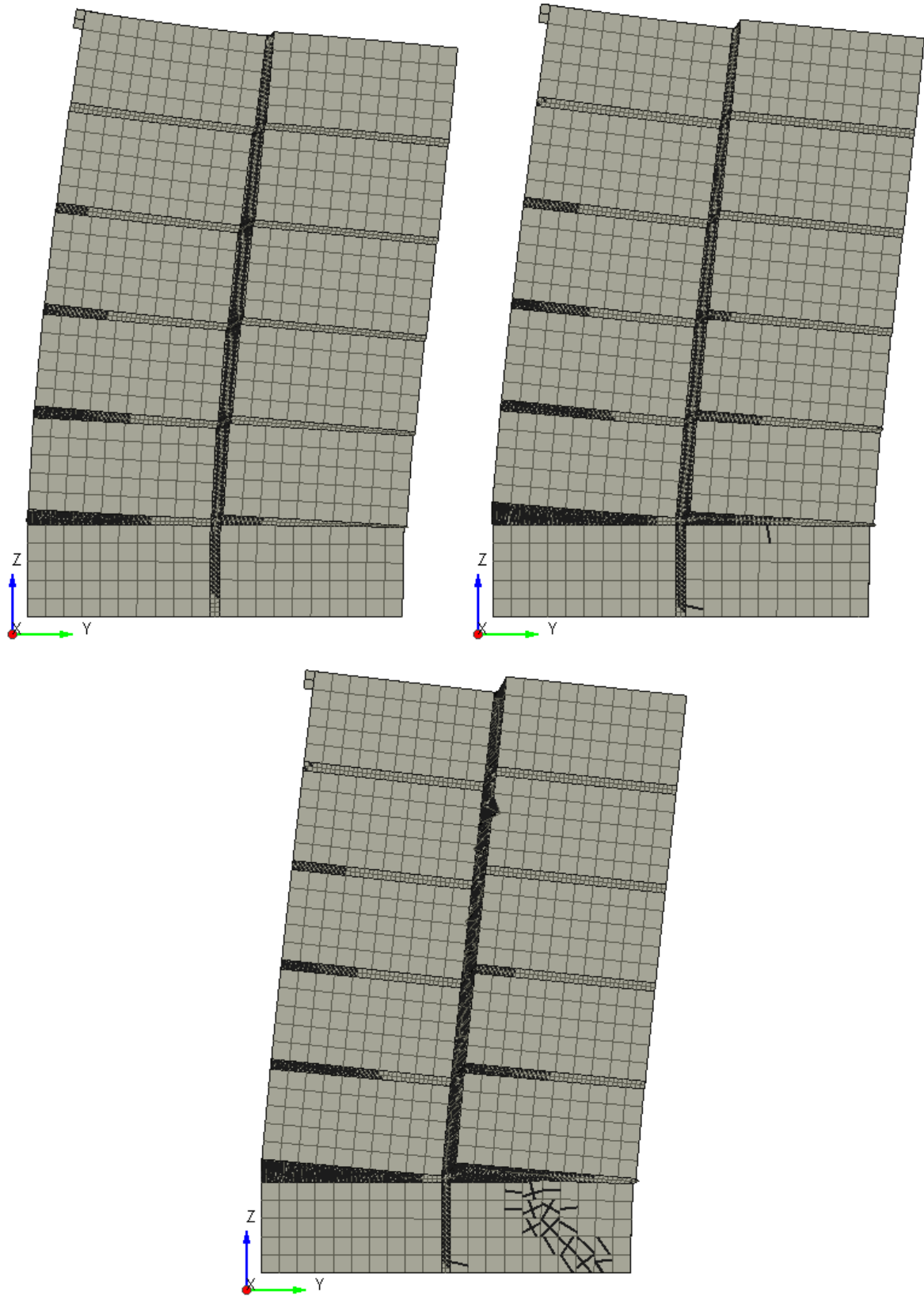


Figure A-15: PO-SYMJ10-OB4.47 Response [A] 0.092% Drift, [B] 0.23% Drift, [C] 0.55% Drift

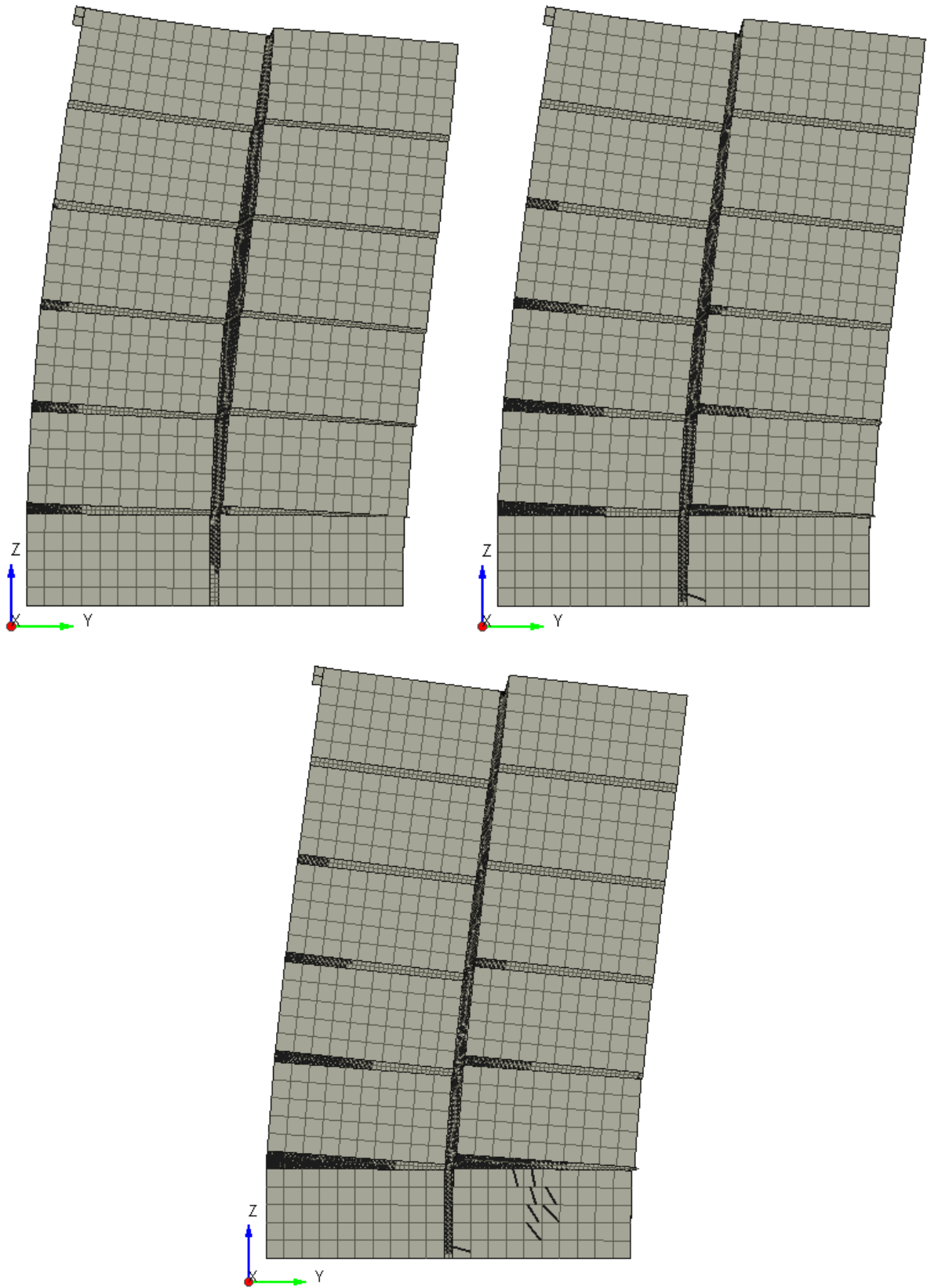


Figure A-16: PO-SYMJ10-OB7.15 Response [A] 0.092% Drift, [B] 0.23% Drift, [C] 0.369% Drift

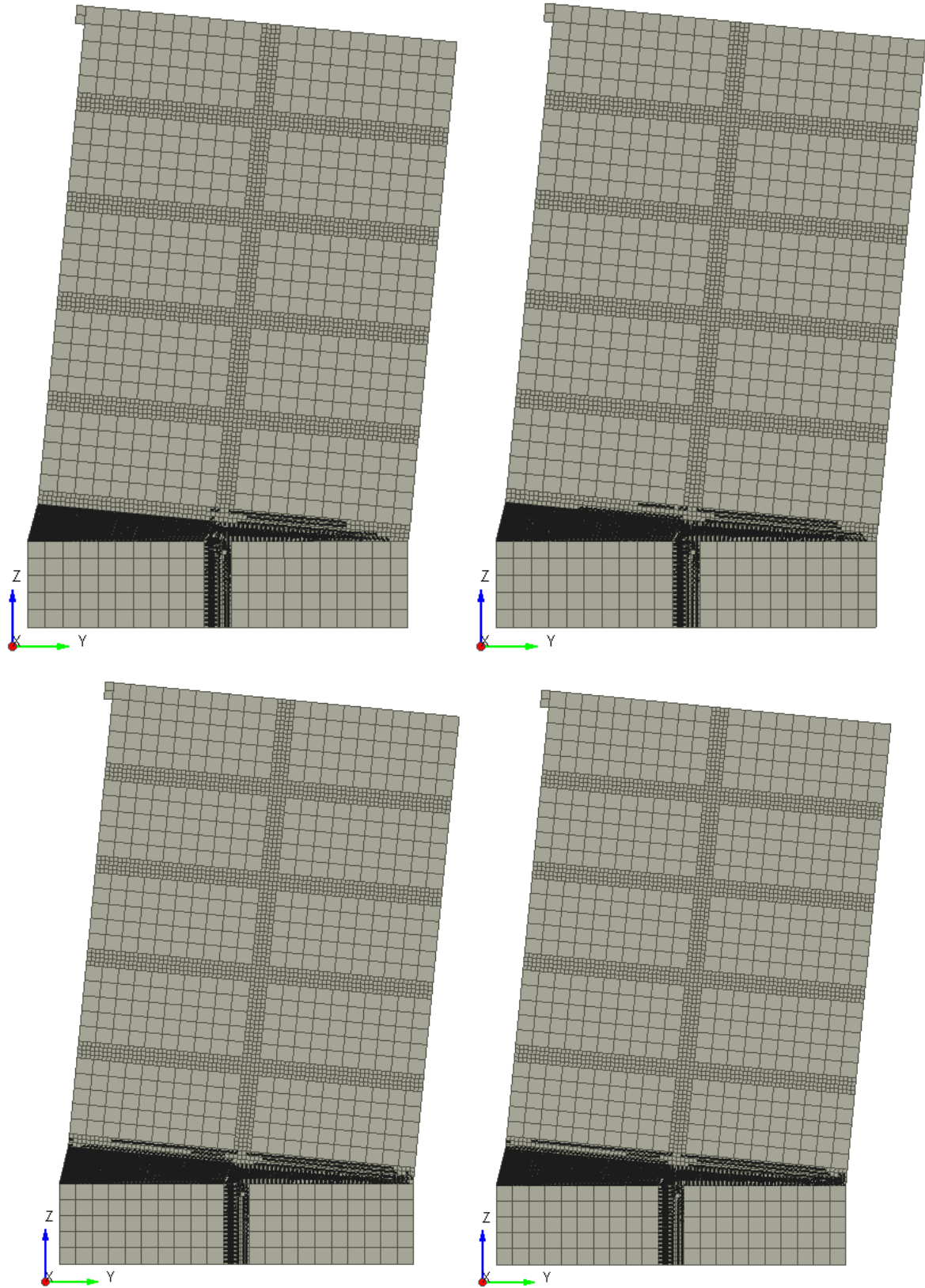


Figure A-17: PO-SYMJ20-OB0.05 Response [A] 0.1% Drift, [B] 0.2% Drift, [C] 0.5% Drift, [D] 1% Drift

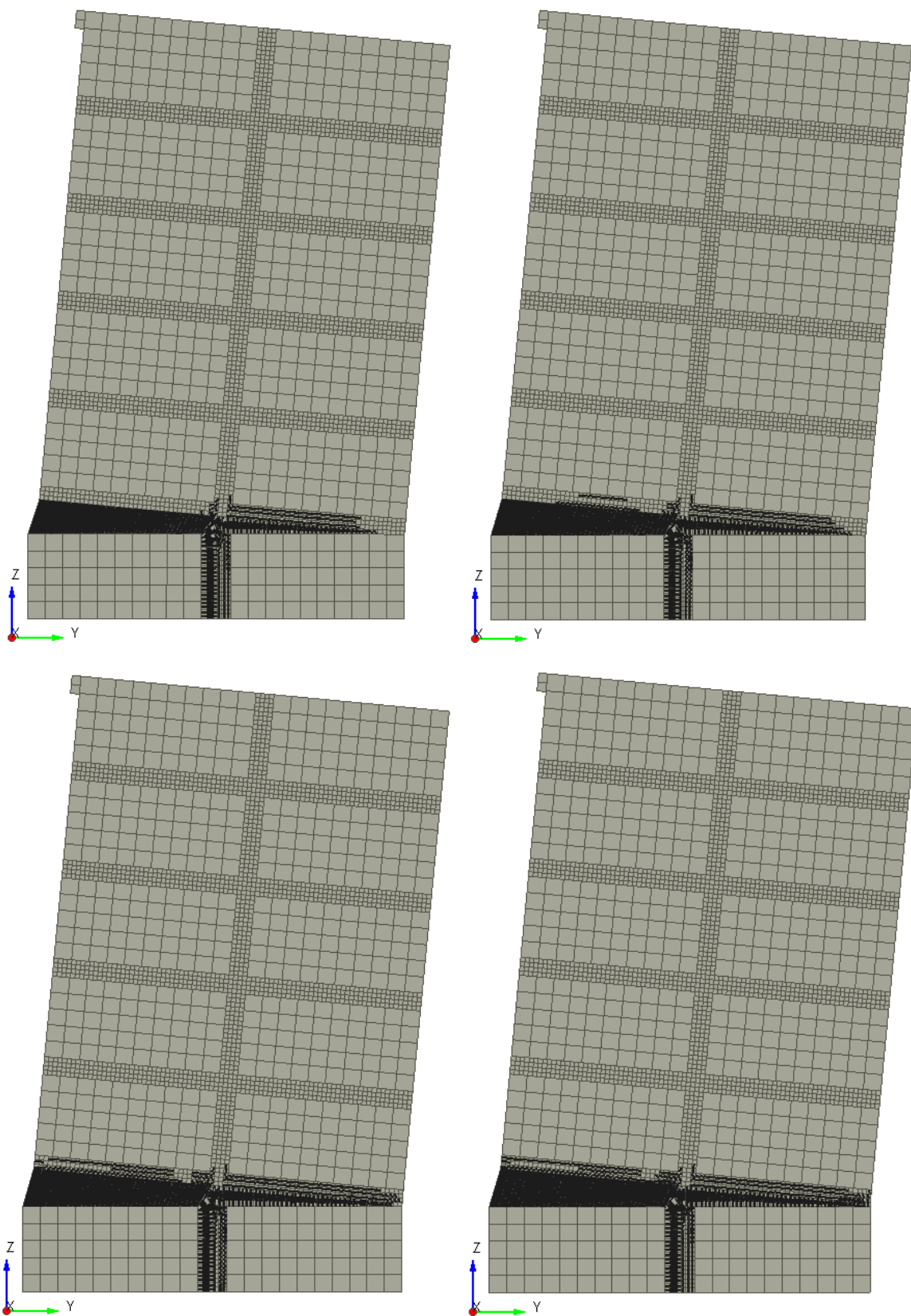


Figure A-18: PO-SYMJ20-OB0.1 Response [A] 0.1% Drift, [B] 0.2% Drift, [C] 0.5% Drift, [D] 1% Drift

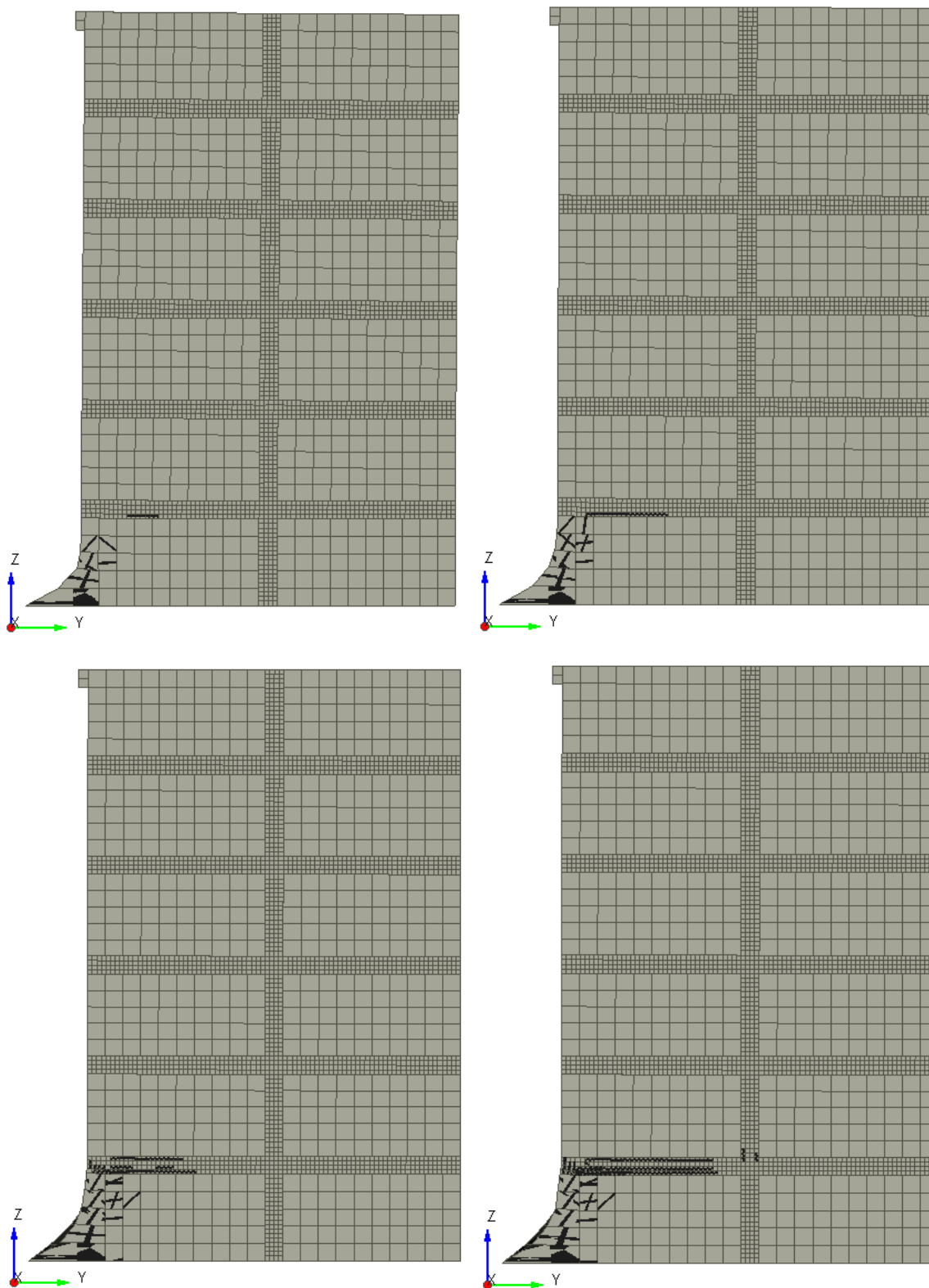


Figure A-19: PO-SYMJ20-OB0.2 Response [A] 0.1% Drift, [B] 0.2% Drift, [C] 0.5% Drift, [D] 1% Drift

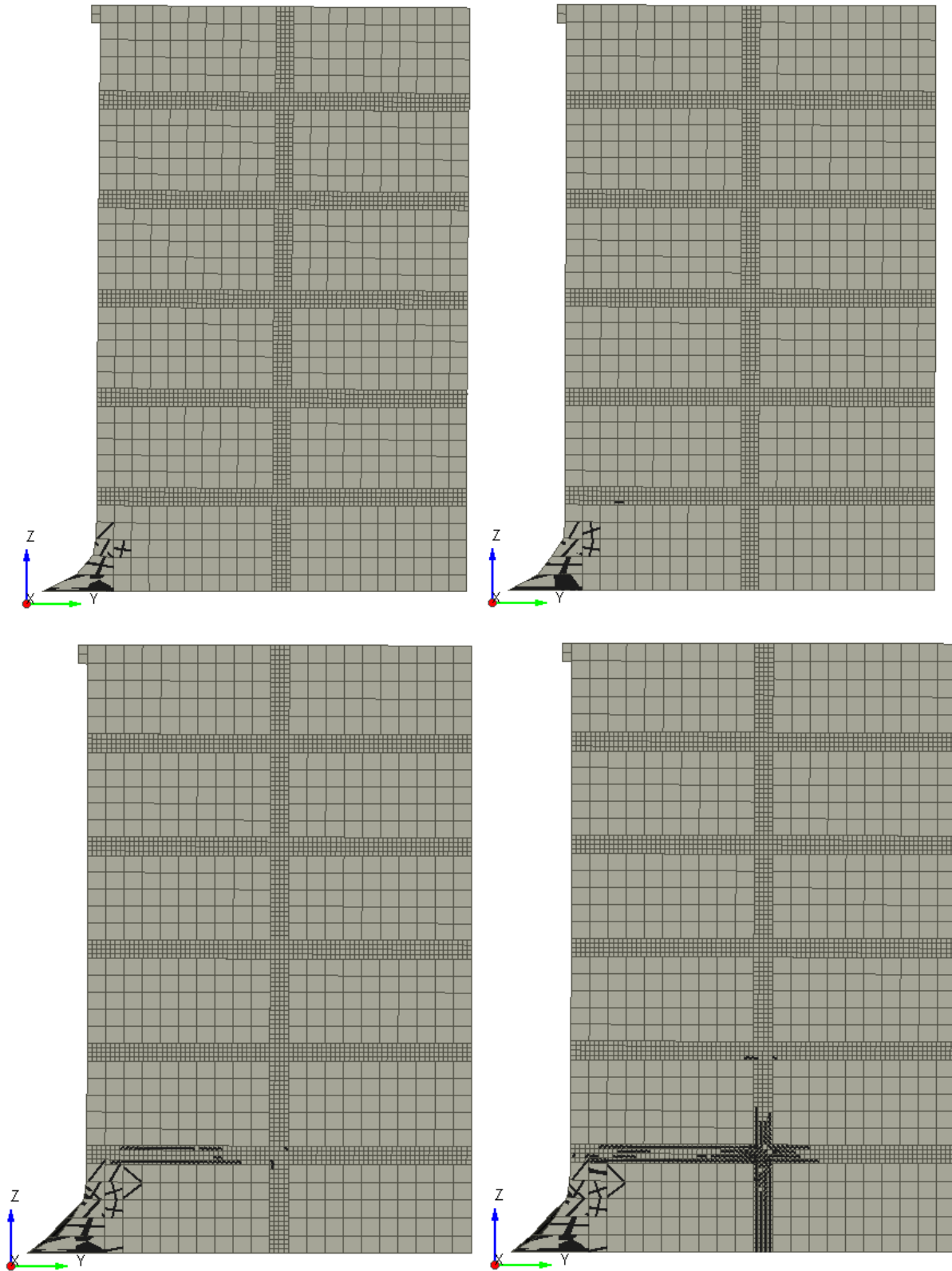


Figure A-20: PO-SYMJ20-OB0.3 Response [A] 0.1% Drift, [B] 0.2% Drift, [C] 0.5% Drift, [D] 1% Drift

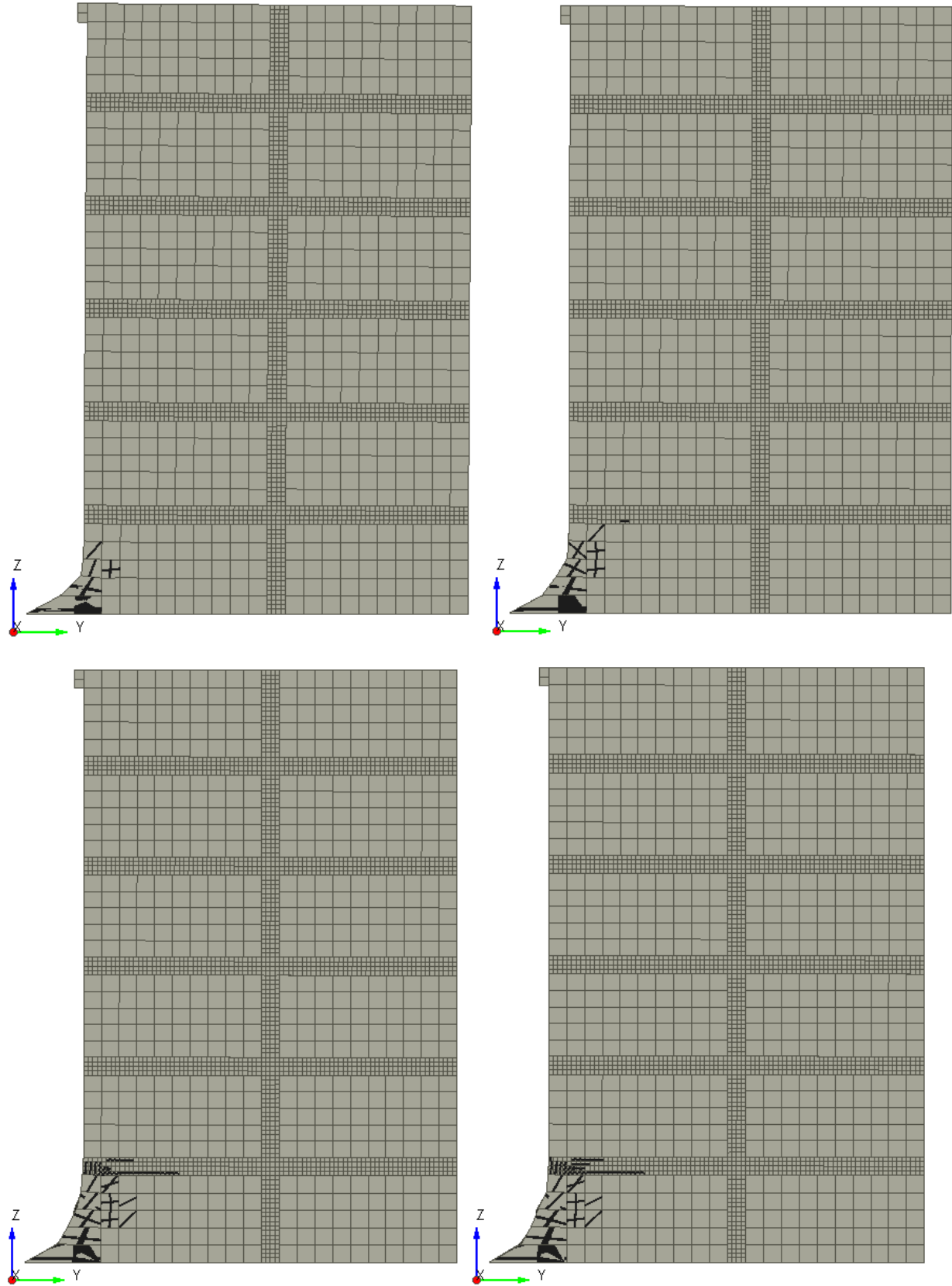


Figure A-21: PO-SYMJ20-OB0.4 Response [A] 0.1% Drift, [B] 0.2% Drift, [C] 0.5% Drift, [D] 1% Drift

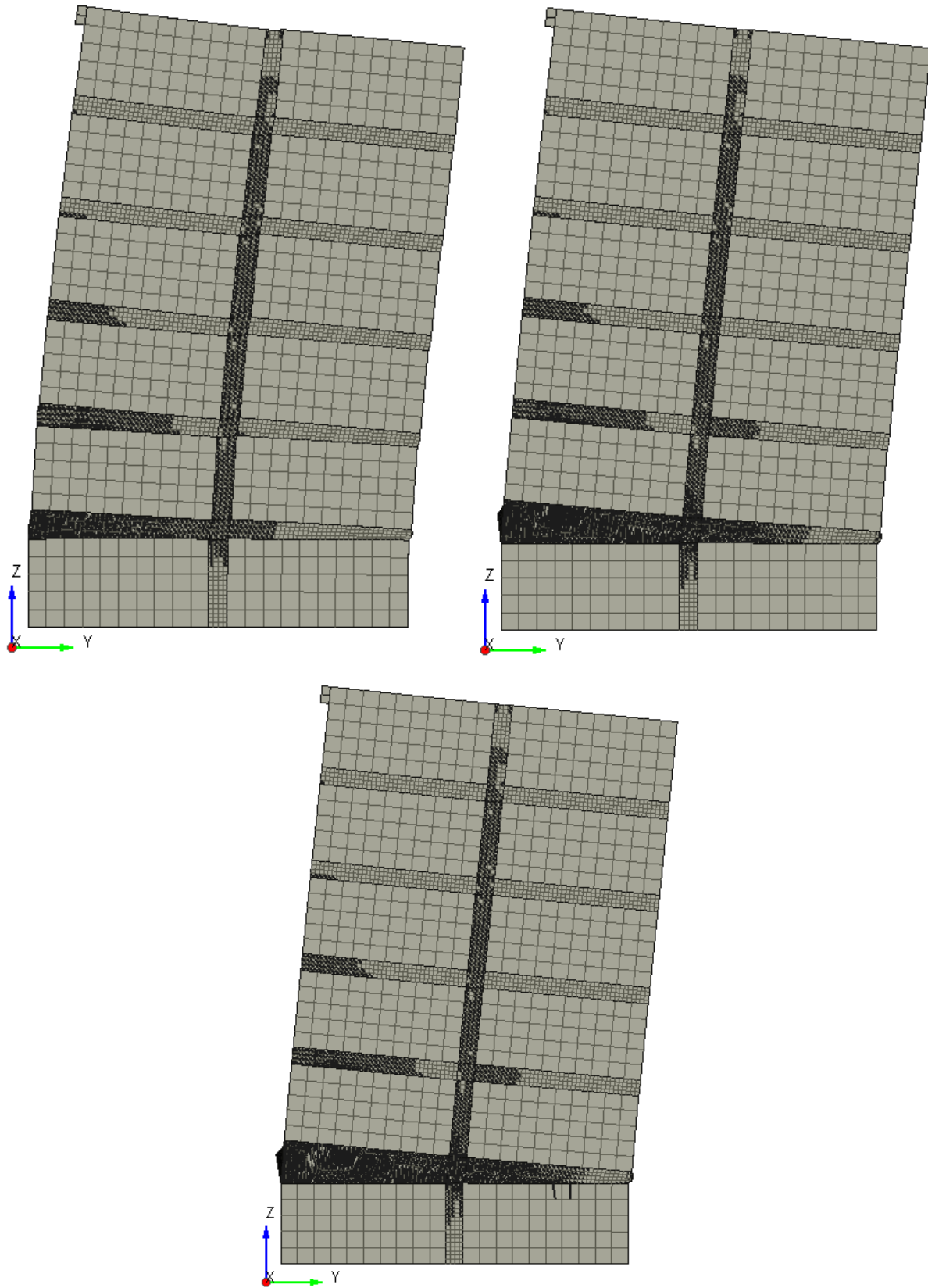


Figure A-22: PO-SYMJ20-OB1.79 Response [A] 0.092% Drift, [B] 0.23% Drift, [C] 0.415% Drift

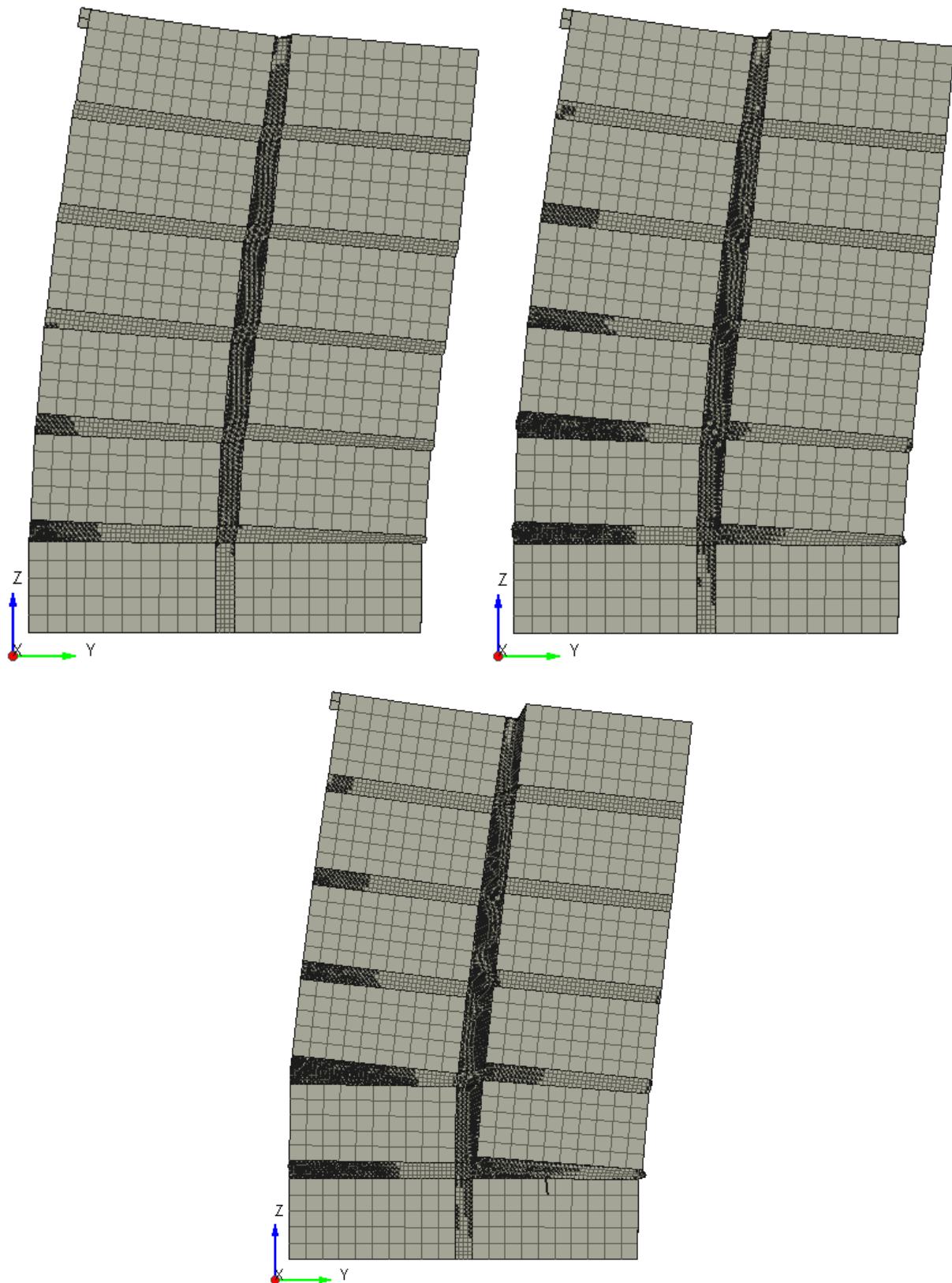


Figure A-23: PO-SYMJ20-OB4.47 Response [A] 0.092% Drift, [B] 0.231% Drift, [C] 0.431% Drift

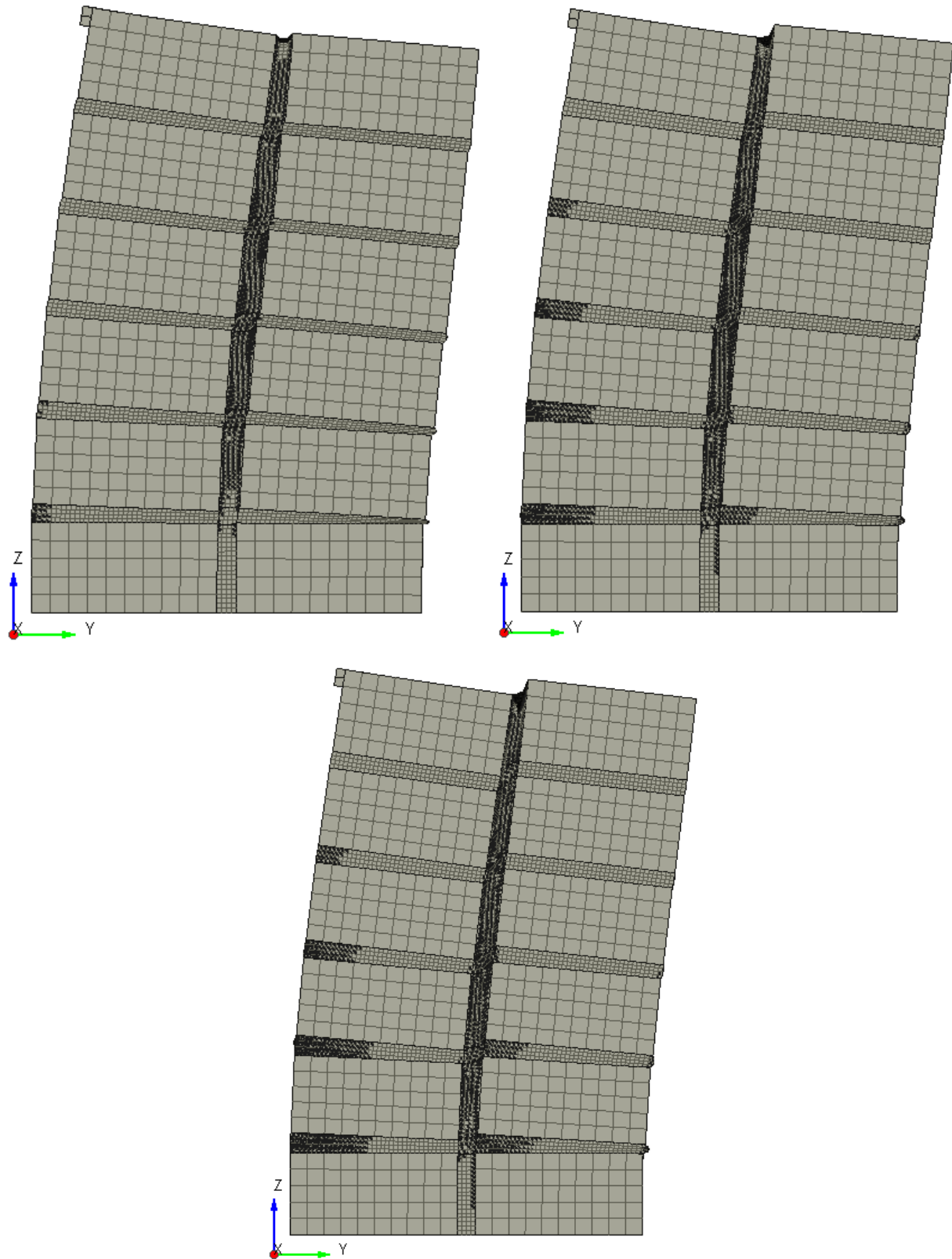


Figure A-24: PO-SYMJ20-OB7.15 Response [A] 0.092% Drift, [B] 0.23% Drift, [C] 0.322% Drift

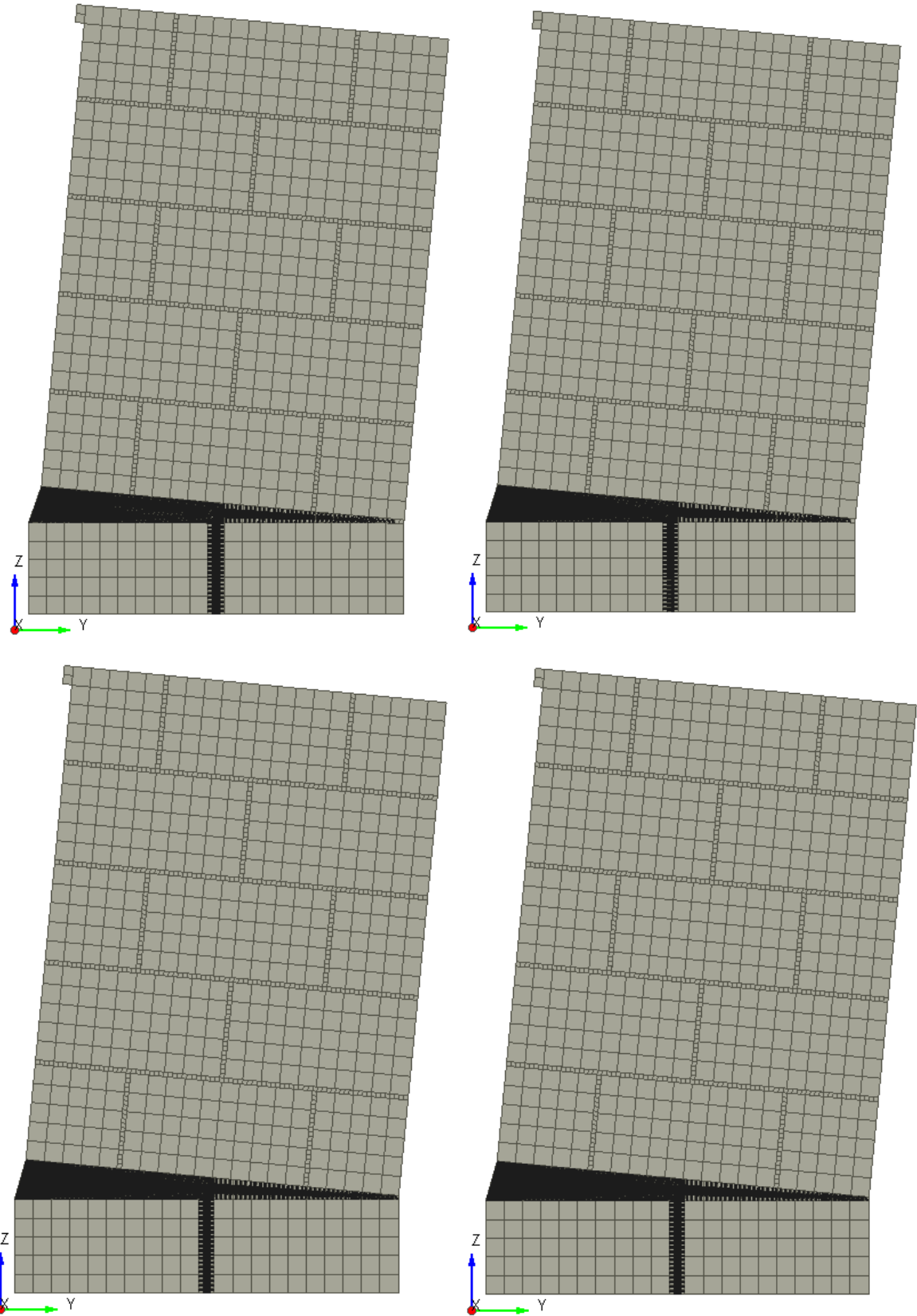


Figure A-25: PO-EQSJ5-OB0.05 Response [A] 0.1% Drift, [B] 0.2% Drift, [C] 0.5% Drift, [D] 1% Drift

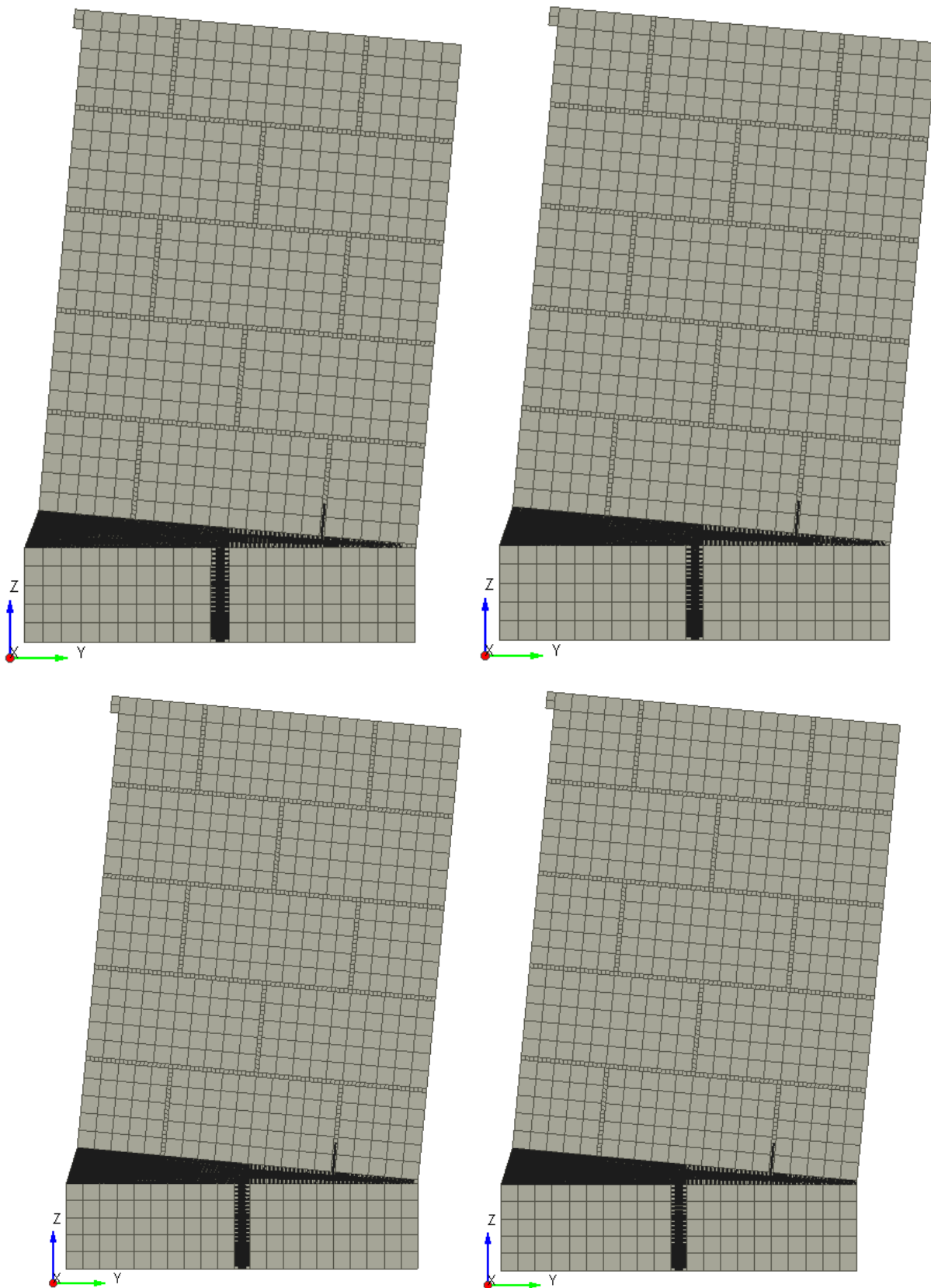


Figure A-26: PO-EQSJ5-OB0.1 Response [A] 0.1% Drift, [B] 0.2% Drift, [C] 0.5% Drift, [D] 1% Drift

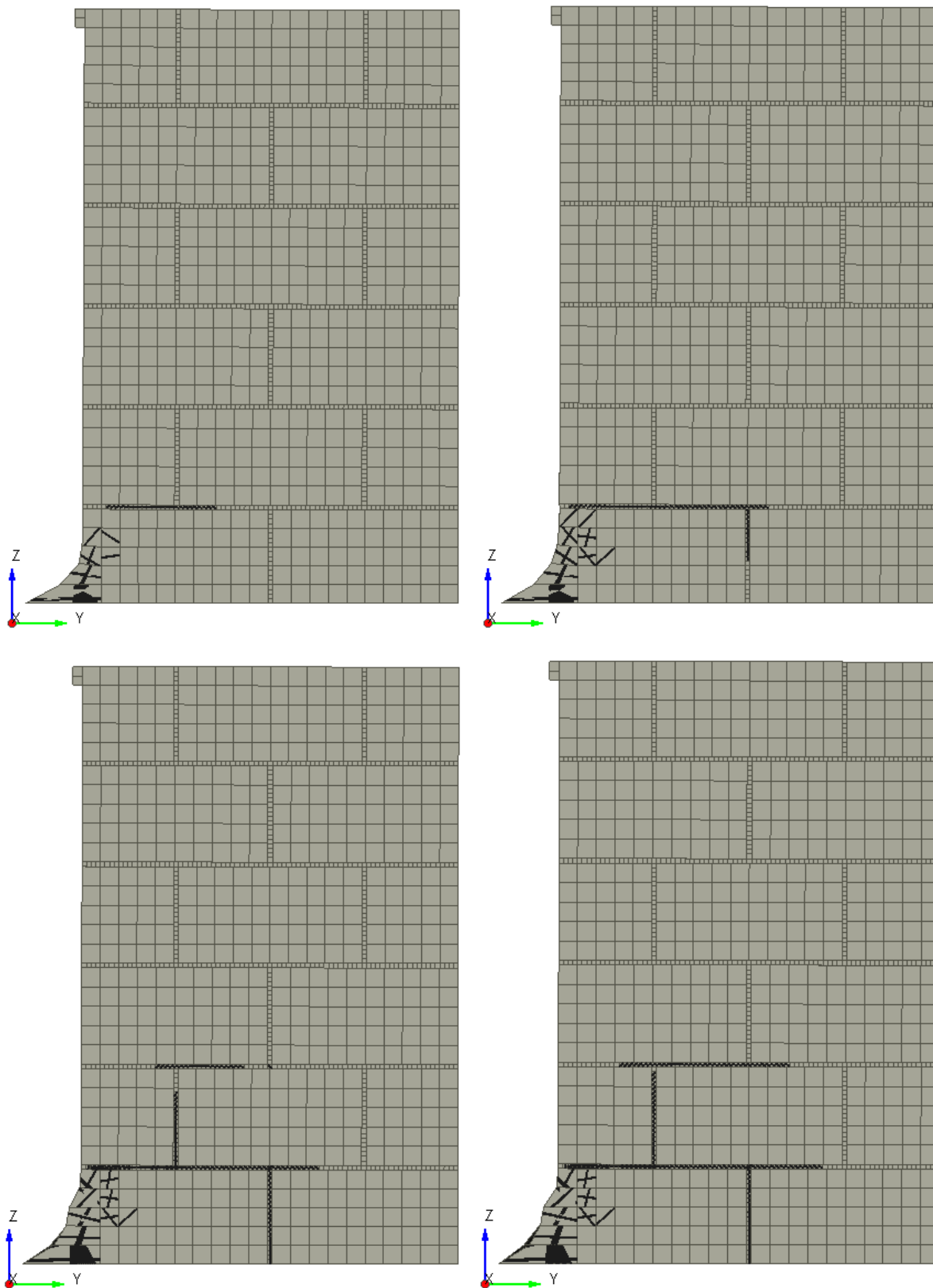


Figure A-27: PO-EQSJ5-OB0.2 Response [A] 0.1% Drift, [B] 0.2% Drift, [C] 0.5% Drift, [D] 1% Drift

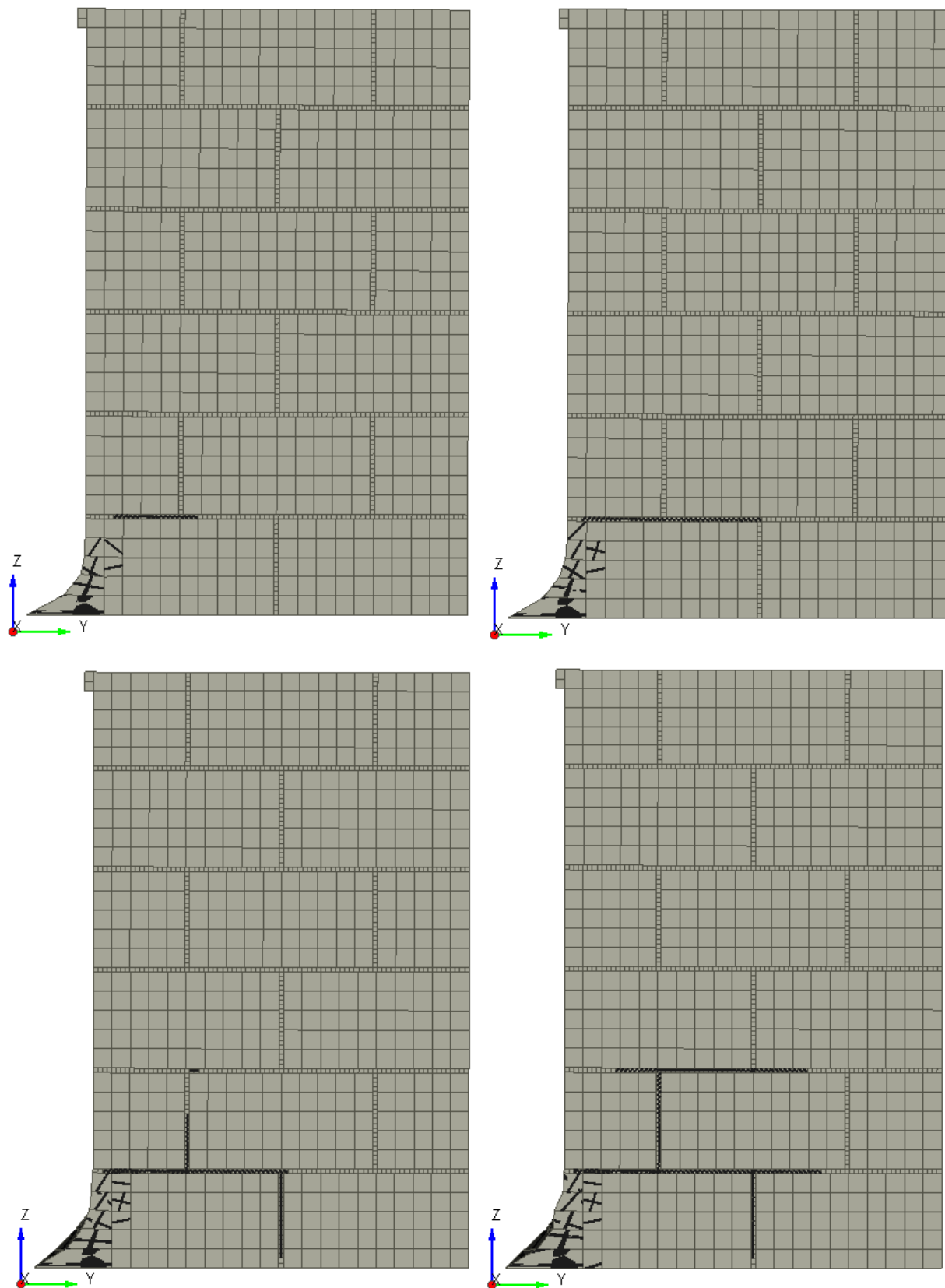


Figure A-28: PO-EQSJ5-OB0.3 Response [A] 0.1% Drift, [B] 0.2% Drift, [C] 0.5% Drift, [D] 1% Drift

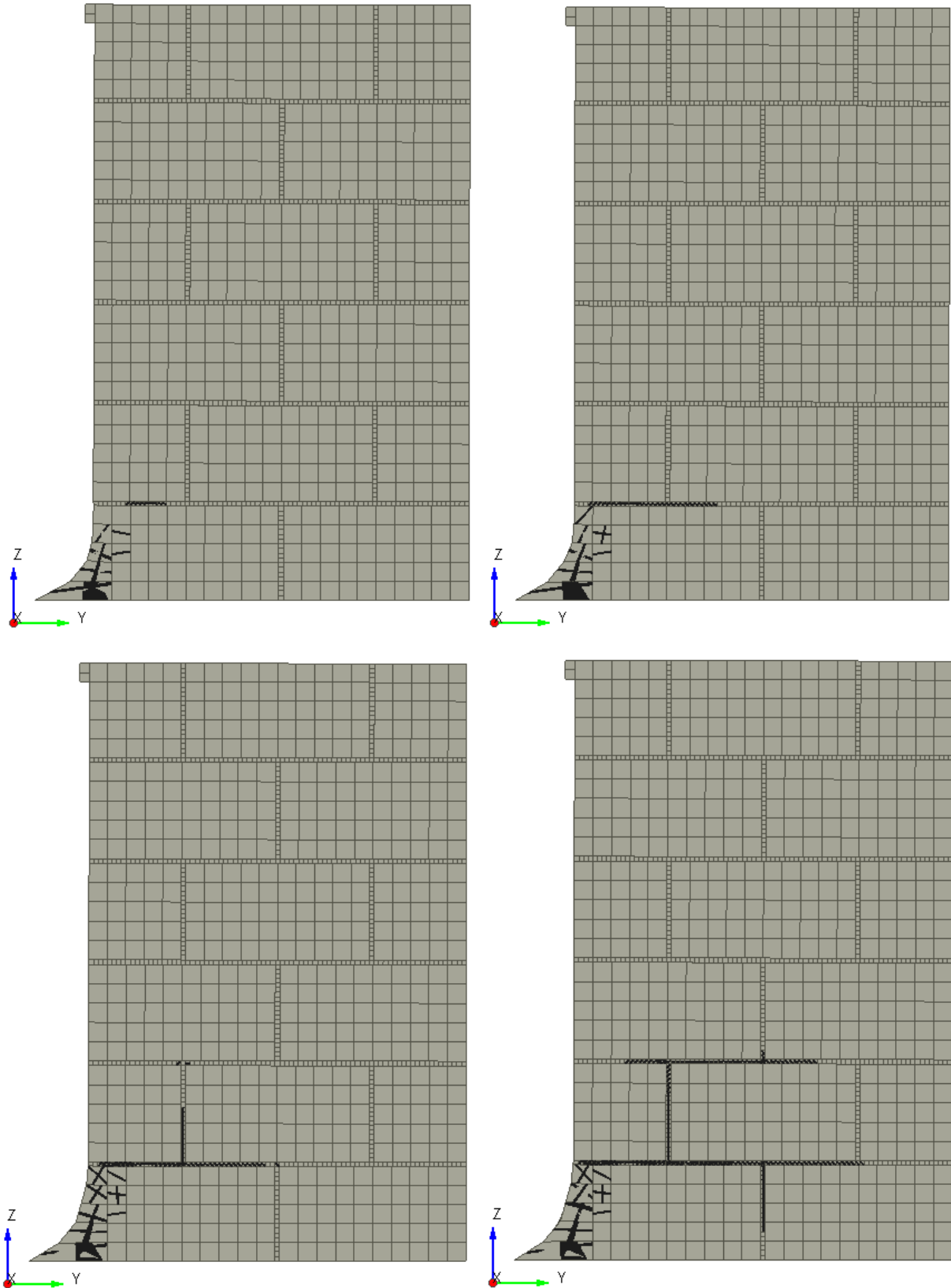


Figure A-29: PO-EQSJ5-OB0.4 Response [A] 0.1% Drift, [B] 0.2% Drift, [C] 0.5% Drift, [D] 1% Drift

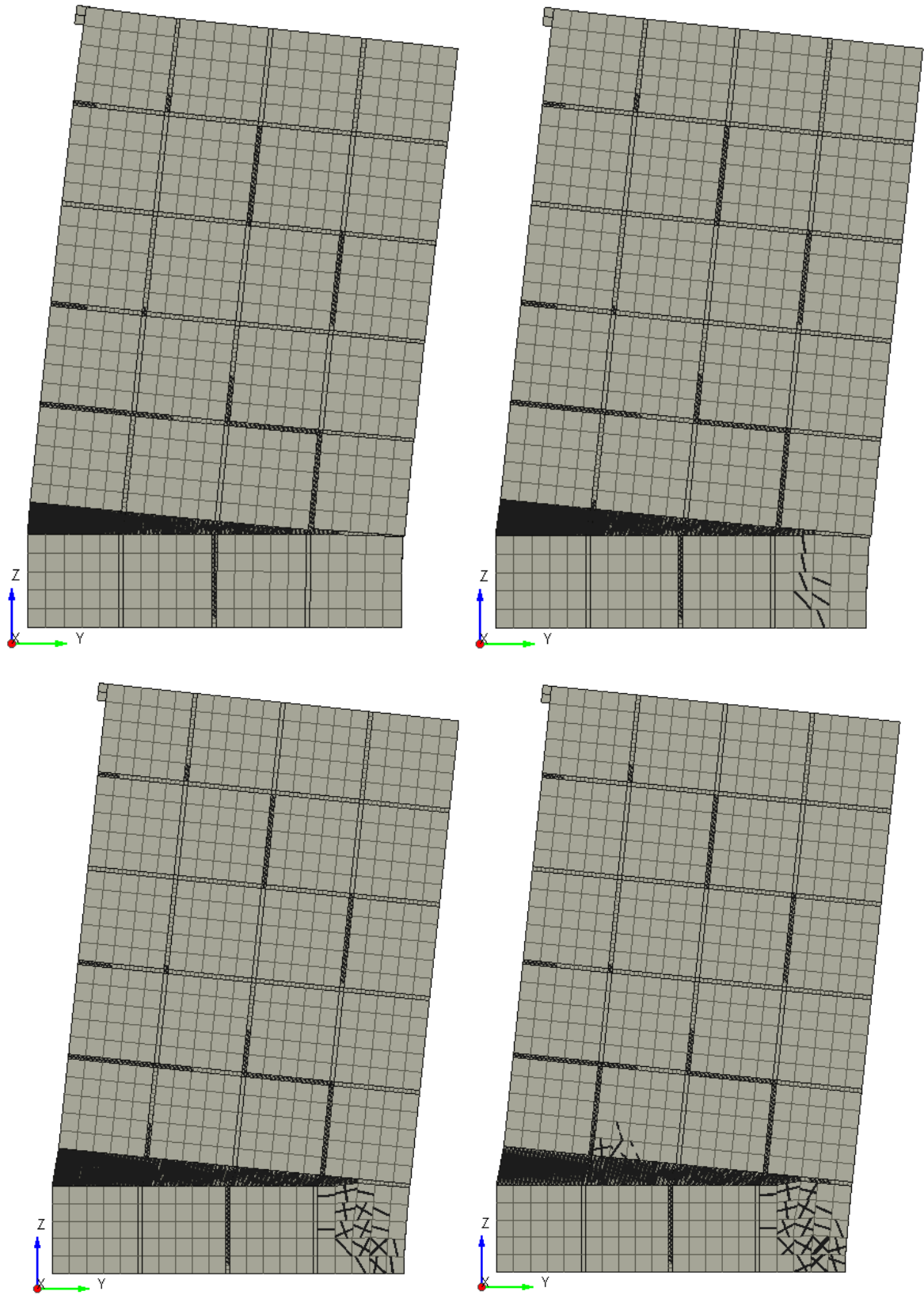


Figure A-30: PO-EQSJ5-OB1.79 Response [A] 0.092% Drift, [B] 0.184% Drift, [C] 0.508% Drift, [D] 0.831% Drift

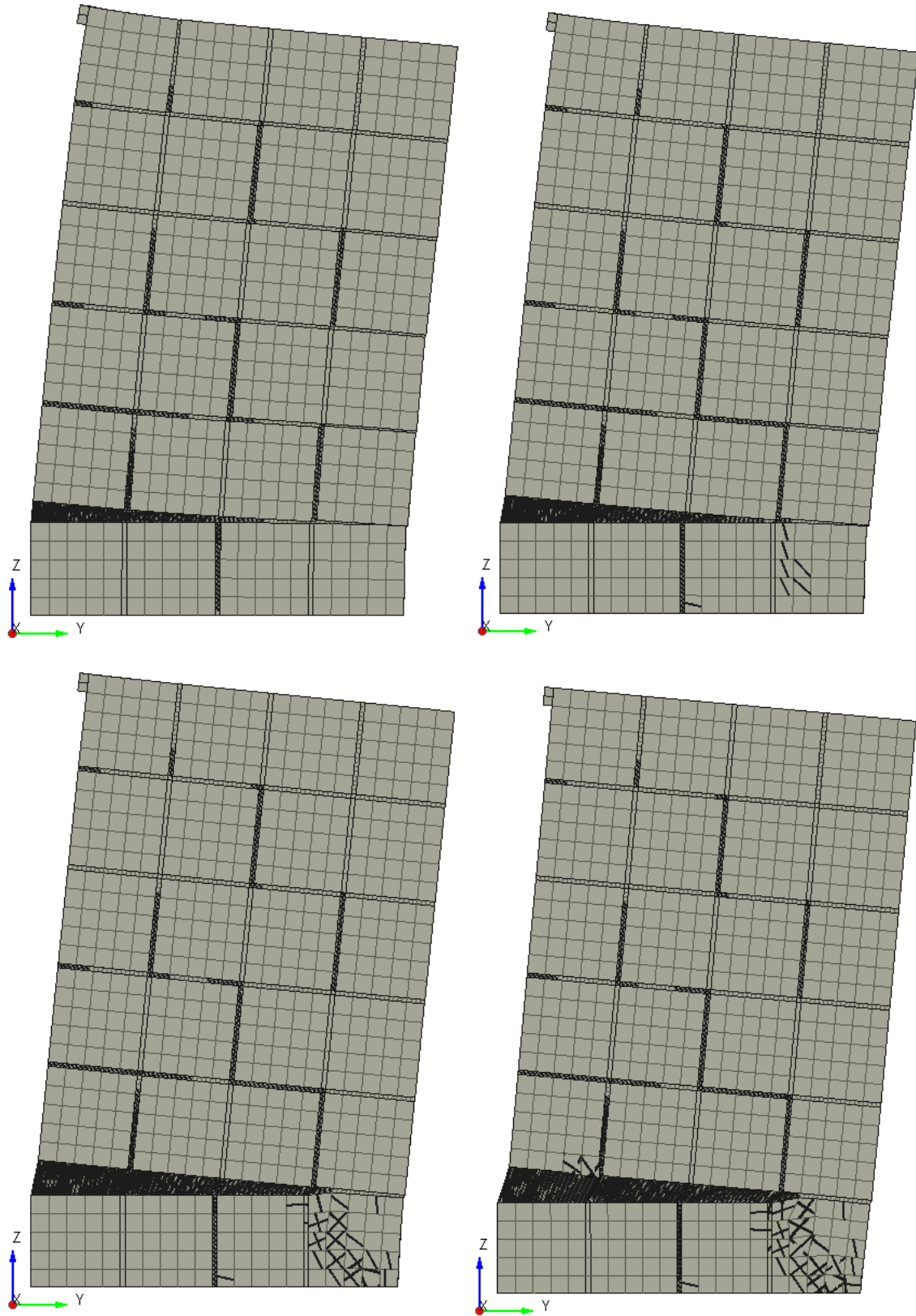


Figure A-31: PO-EQSJ5-OB4.47 Response [A] 0.092% Drift, [B] 0.184% Drift, [C] 0.507% Drift, [D] 0.784% Drift

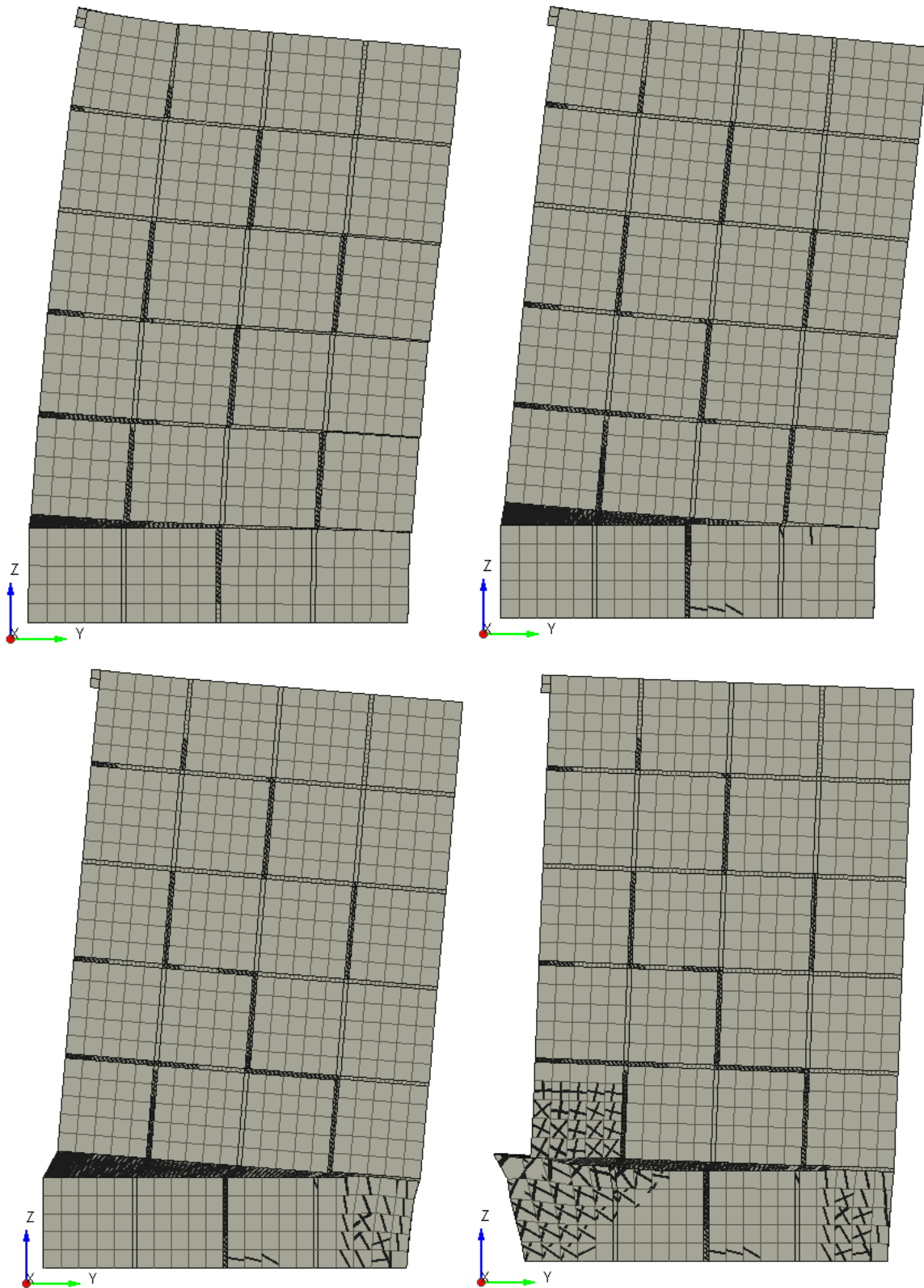


Figure A-32: PO-EQSJ5-OB7.15 Response [A] 0.092% Drift, [B] 0.184% Drift, [C] 0.507% Drift, [D] 0.646% Drift

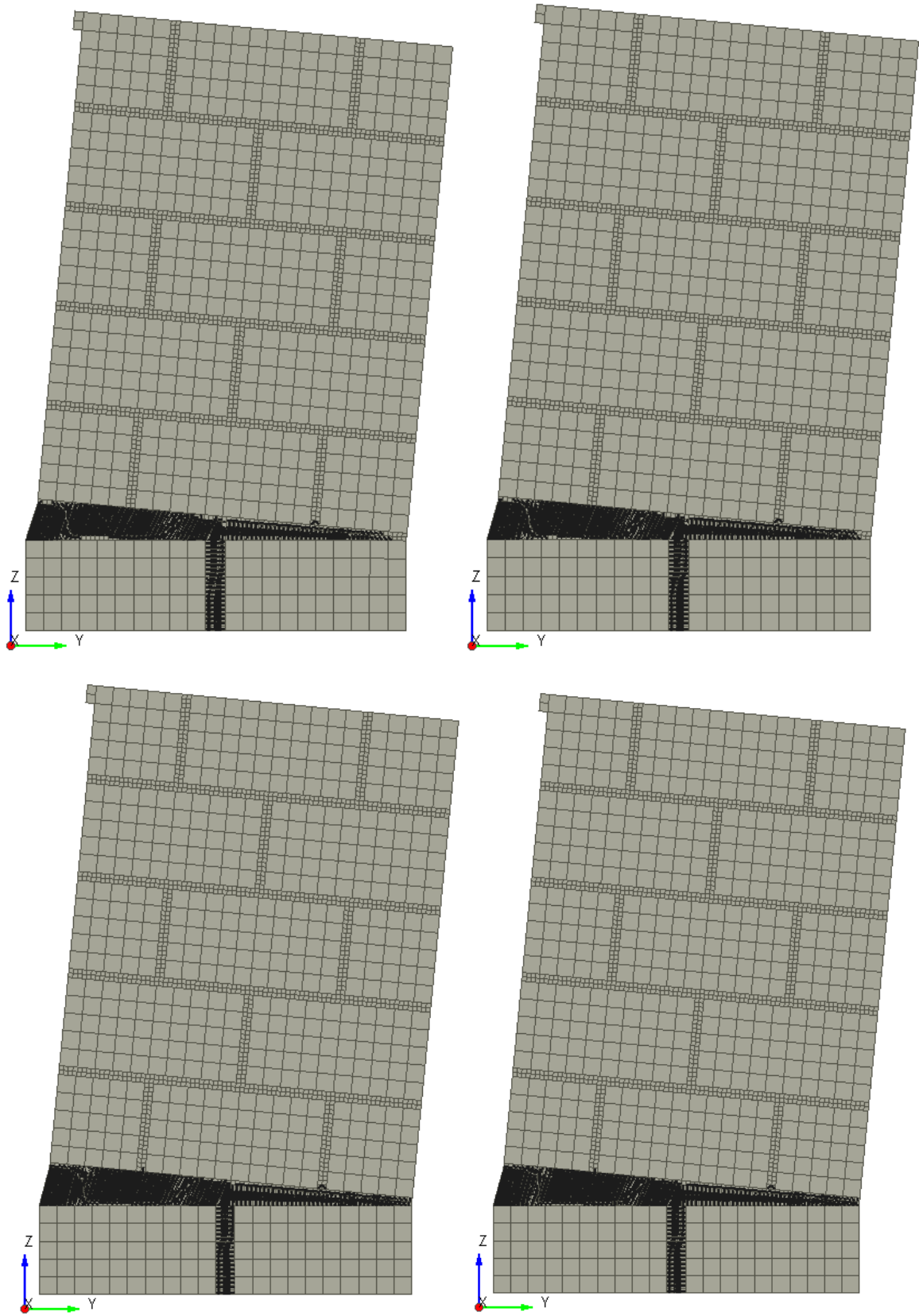


Figure A-33: PO-EQSJ10-OB0.05 Response [A] 0.1% Drift, [B] 0.2% Drift, [C] 0.5% Drift, [D] 0.87% Drift

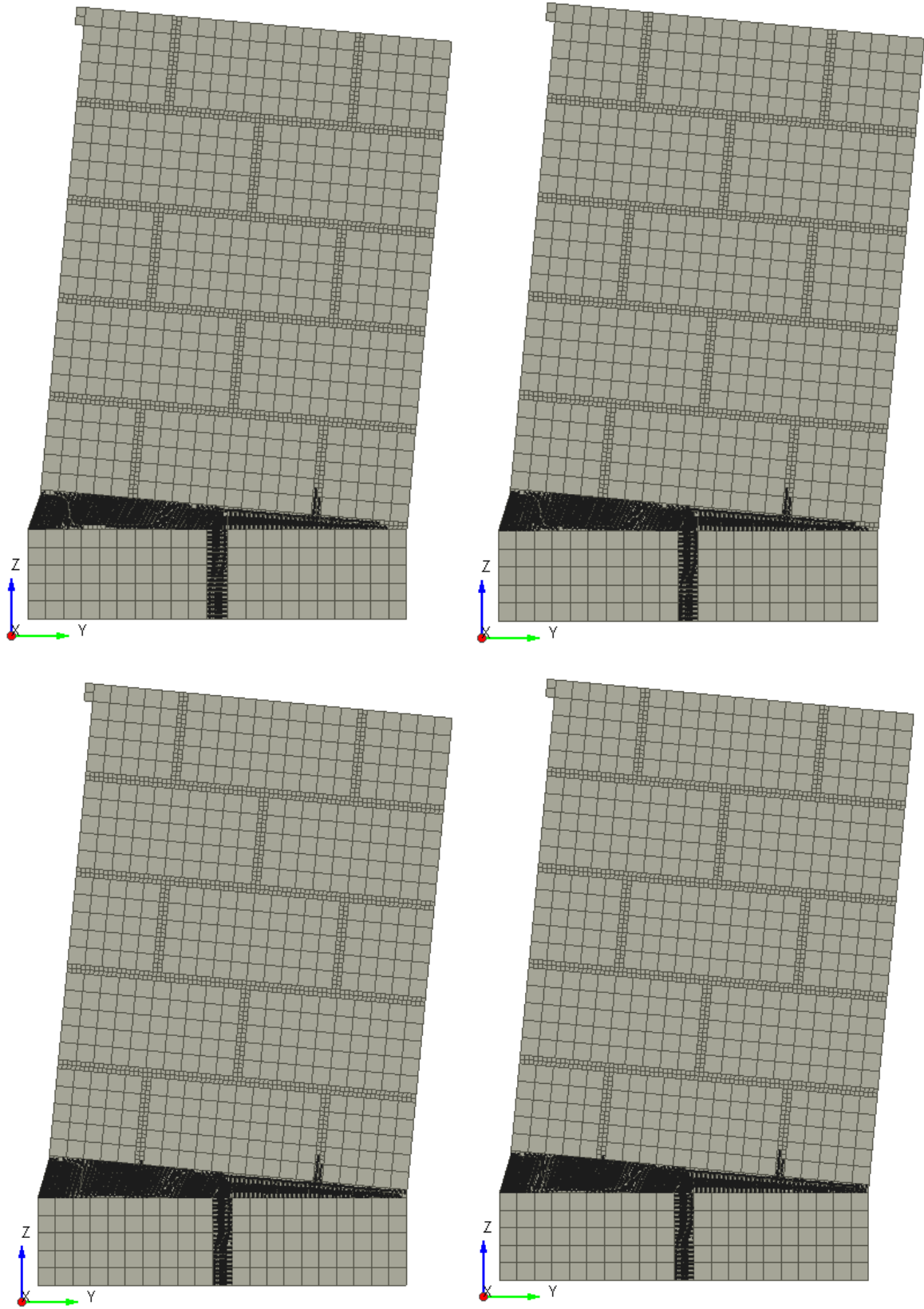


Figure A-34: PO-EQSJ10-OB0.1 Response [A] 0.1% Drift, [B] 0.2% Drift, [C] 0.5% Drift, [D] 0.78% Drift

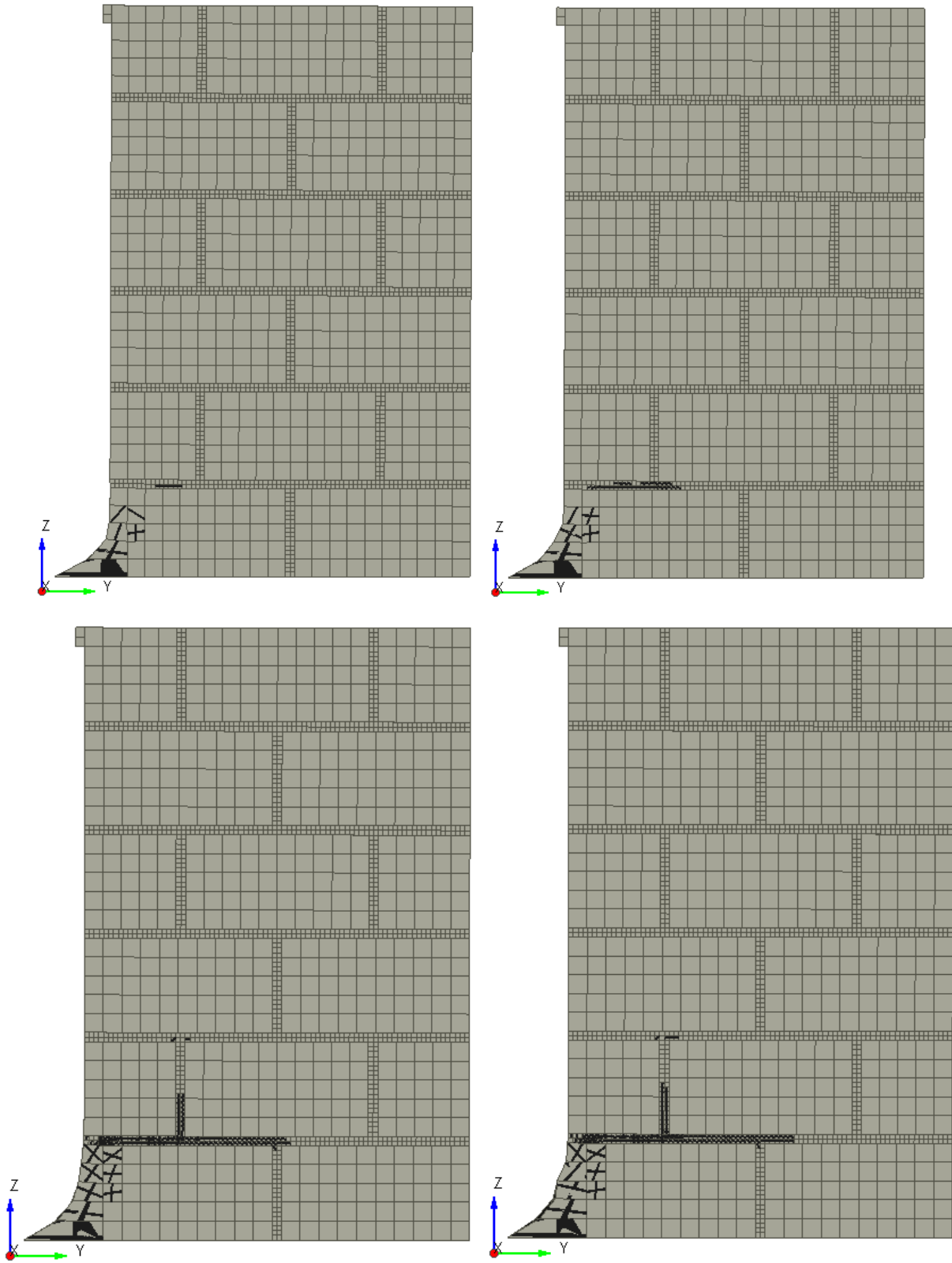


Figure A-35: PO-EQSJ10-OB0.2 Response [A] 0.1% Drift, [B] 0.2% Drift, [C] 0.5% Drift, [D] 1% Drift

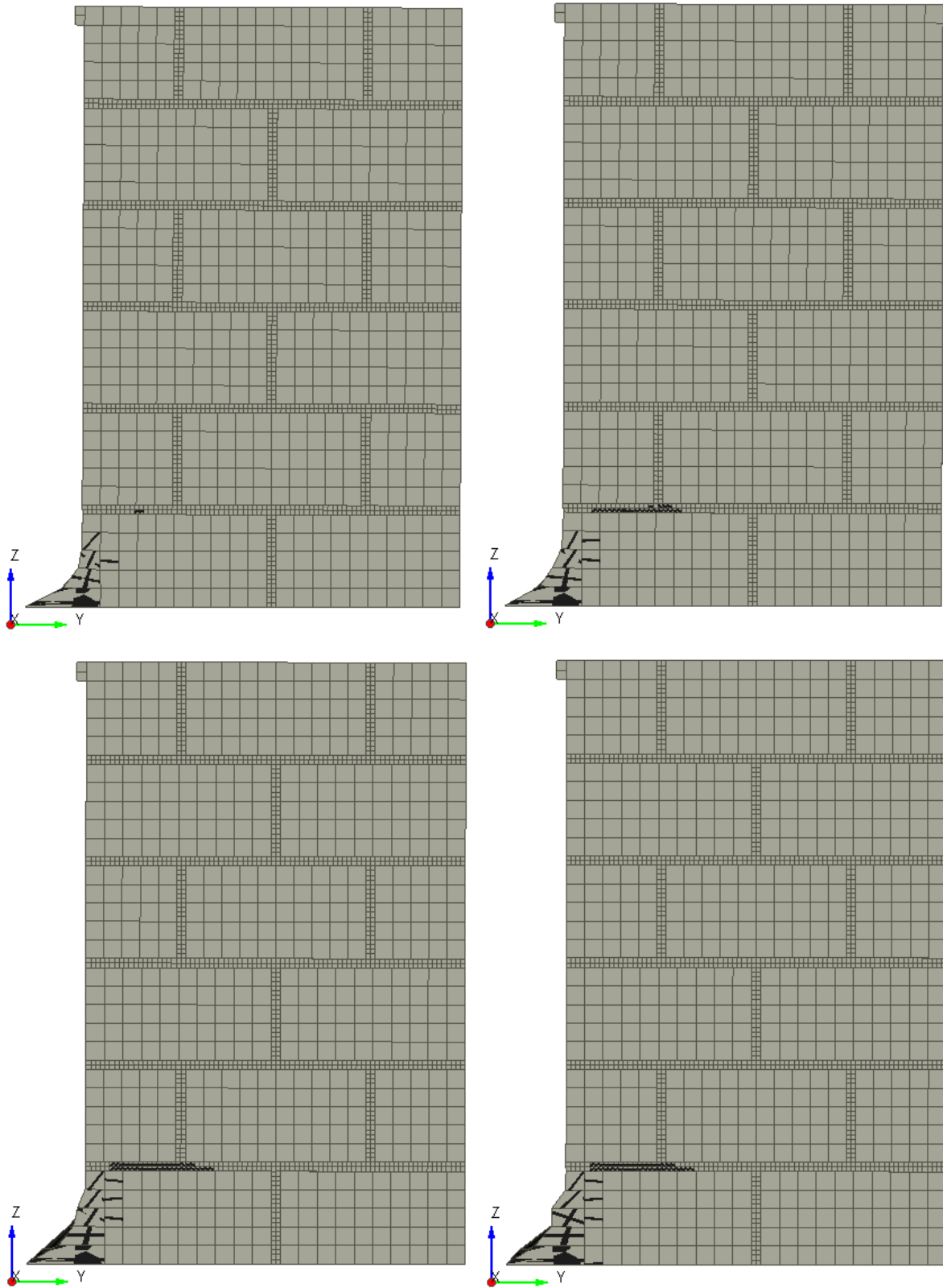


Figure A-36: PO-EQSJ10-OB0.3 Response [A] 0.1% Drift, [B] 0.2% Drift, [C] 0.5% Drift, [D] 1% Drift

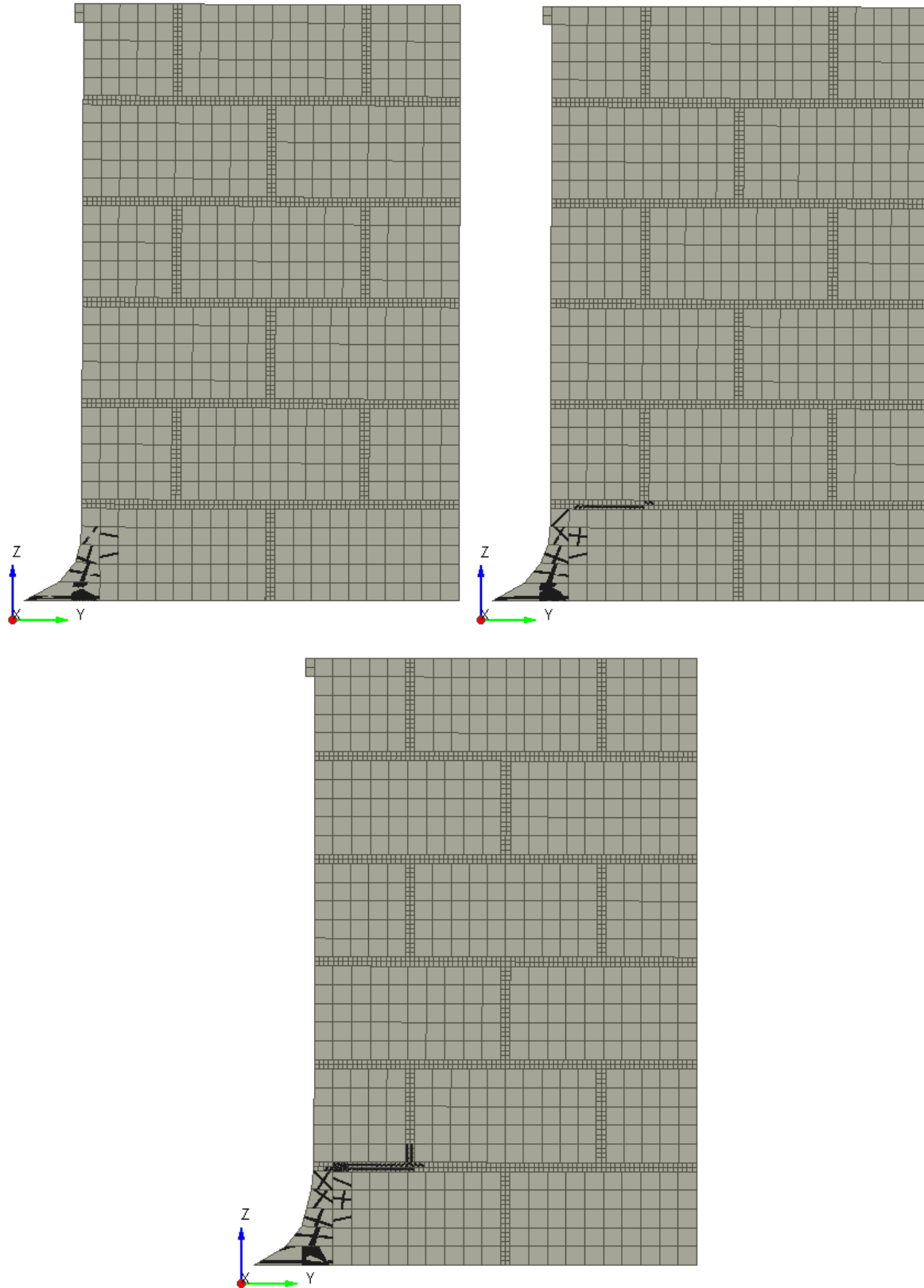


Figure A-37: PO-EQSJ10-OB0.4 Response [A] 0.1% Drift, [B] 0.2% Drift, [C] 0.39% Drift

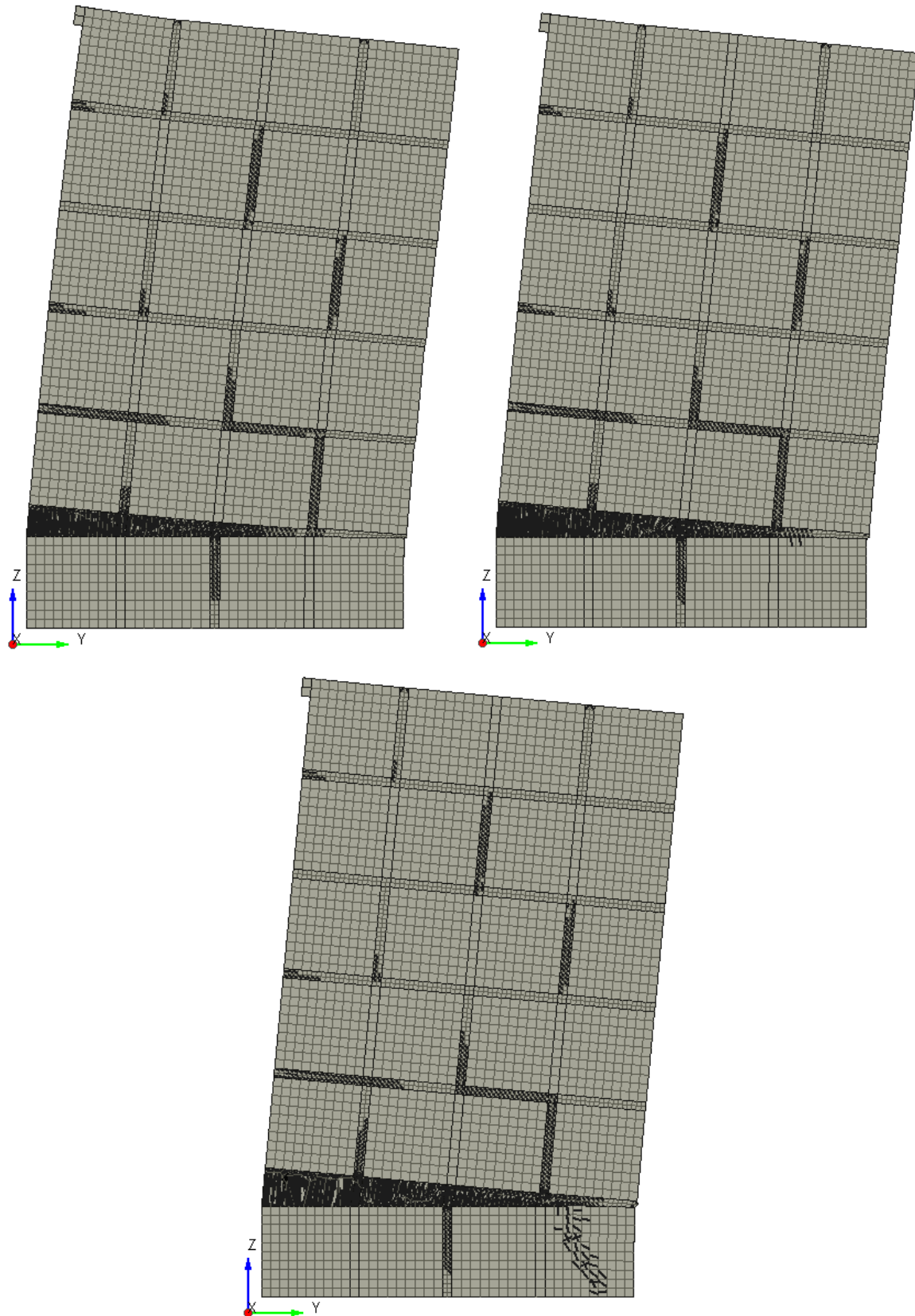


Figure A-38: PO-EQSJ10-OB1.79 Response [A] 0.092% Drift, [B] 0.184% Drift, [C] 0.461% Drift

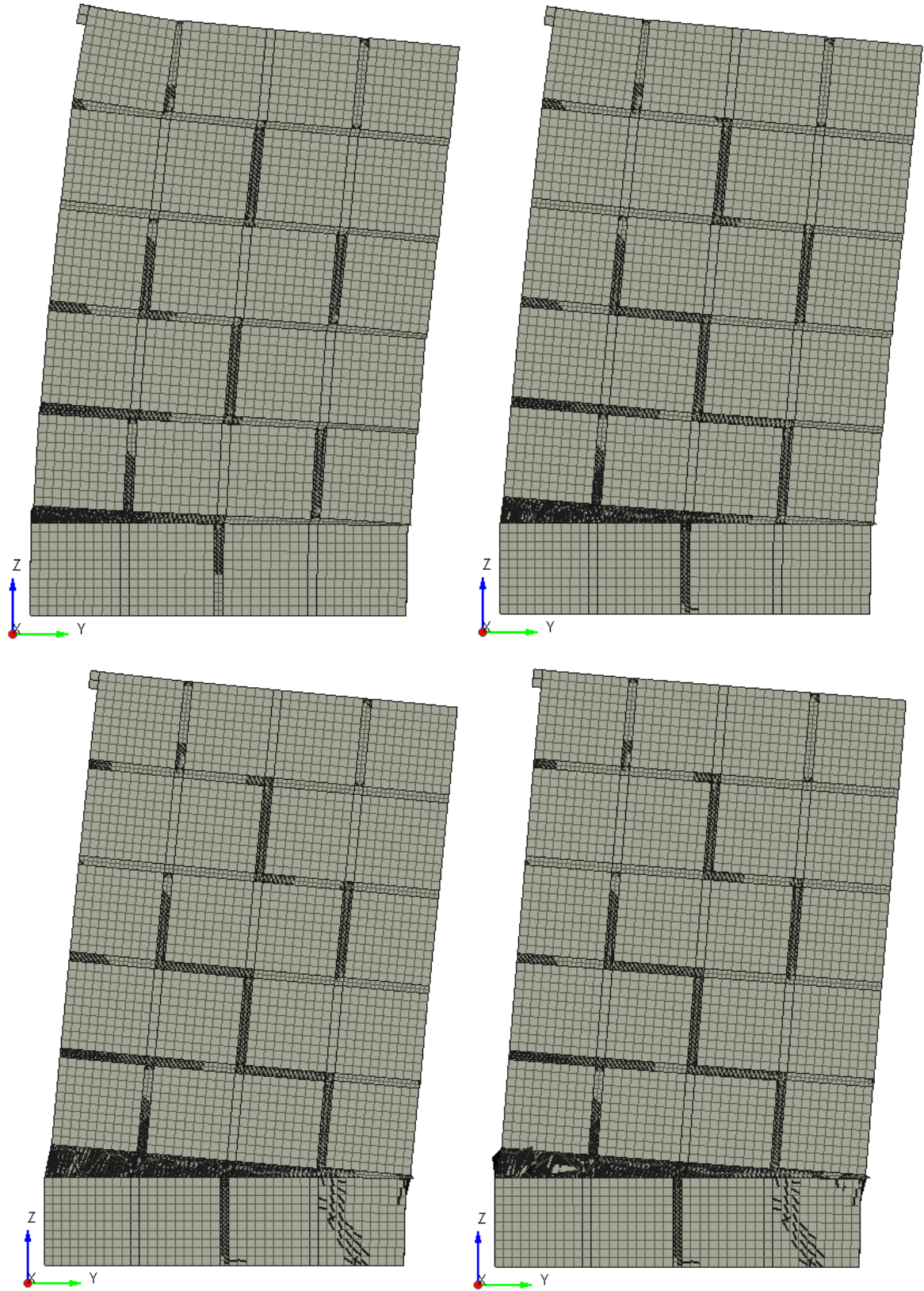


Figure A-39: PO-EQSJ10-OB4.47 Response [A] 0.092% Drift, [B] 0.184% Drift, [C] 0.507% Drift, [D] 0.554% Drift

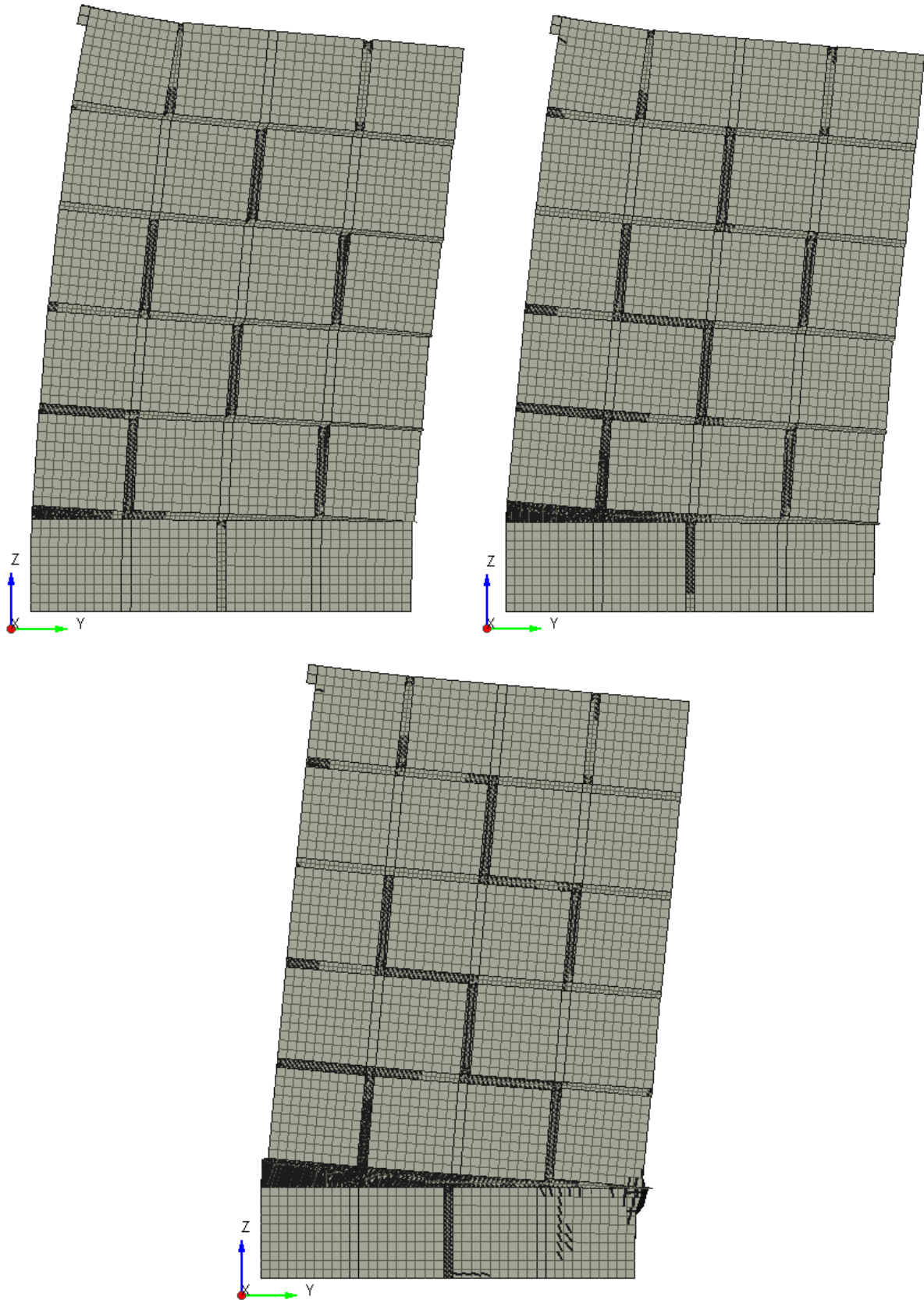


Figure A-40: PO-EQSJ10-OB7.15 Response [A] 0.092% Drift, [B] 0.184% Drift, [C] 0.507% Drift

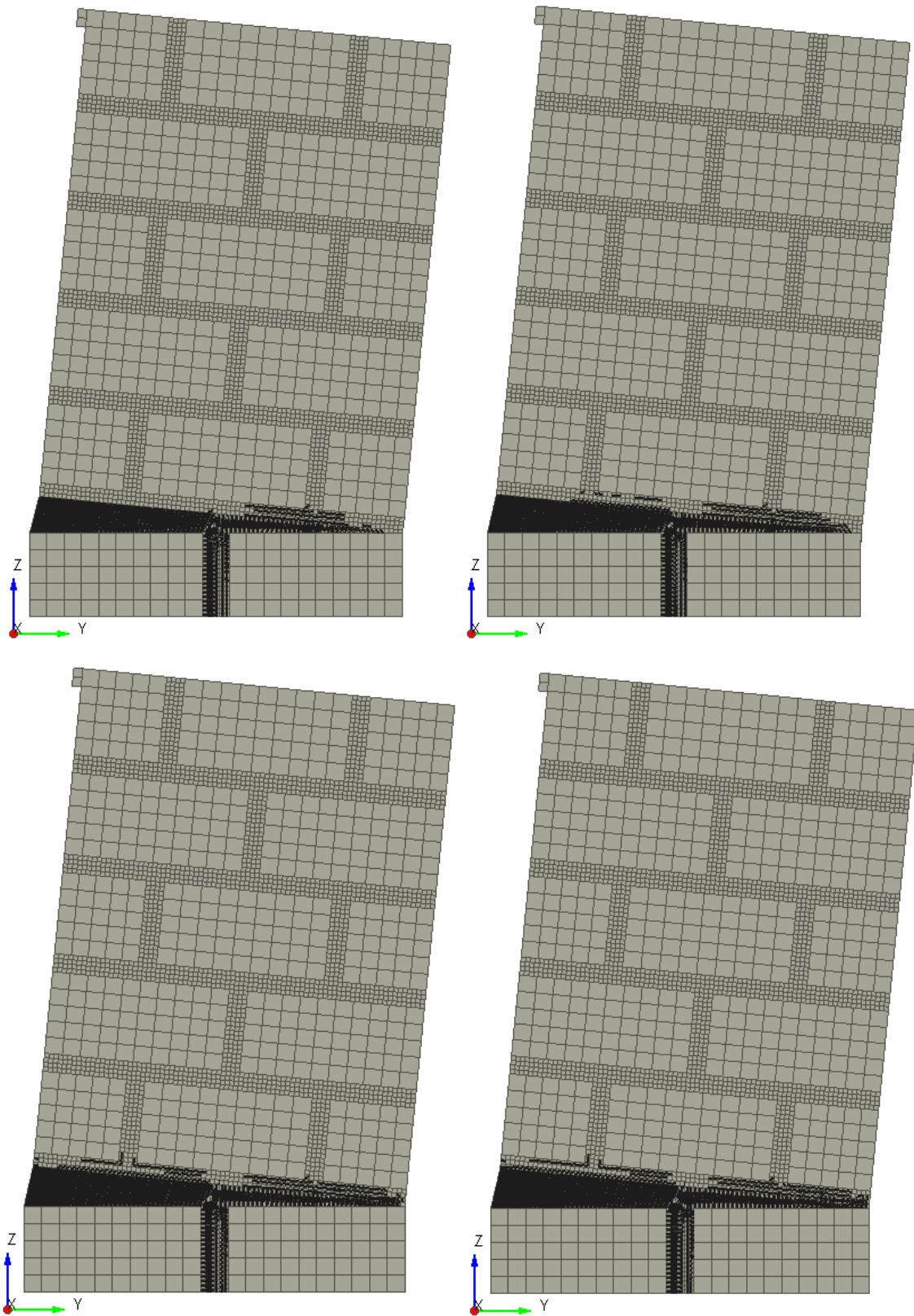


Figure A-41: PO-EQSJ20-OB0.05 Response [A] 0.1% Drift, [B] 0.2% Drift, [C] 0.5% Drift, [D] 1% Drift

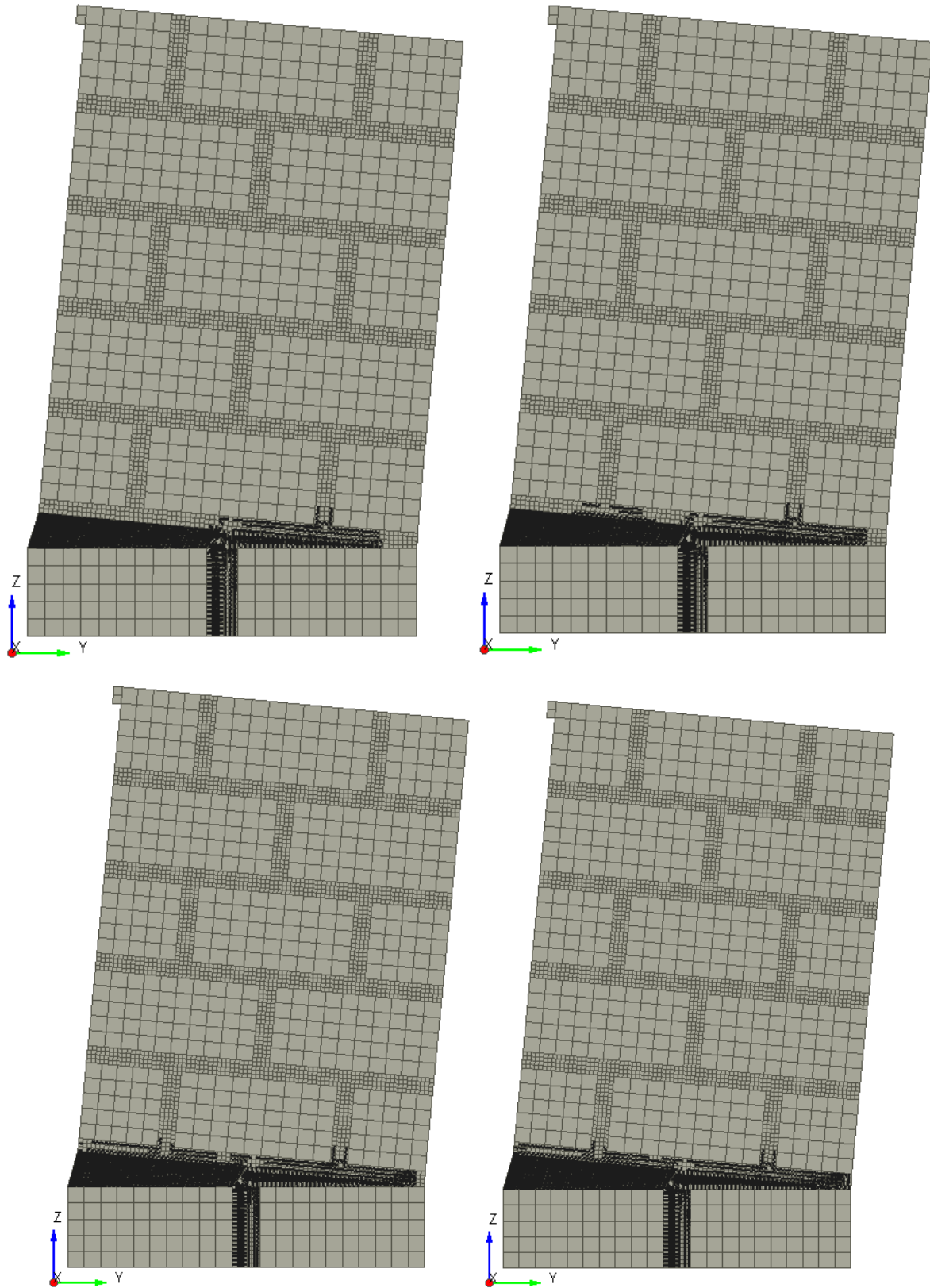


Figure A-42: PO-EQSJ20-OB0.1 Response [A] 0.1% Drift, [B] 0.2% Drift, [C] 0.5% Drift, [D] 1% Drift

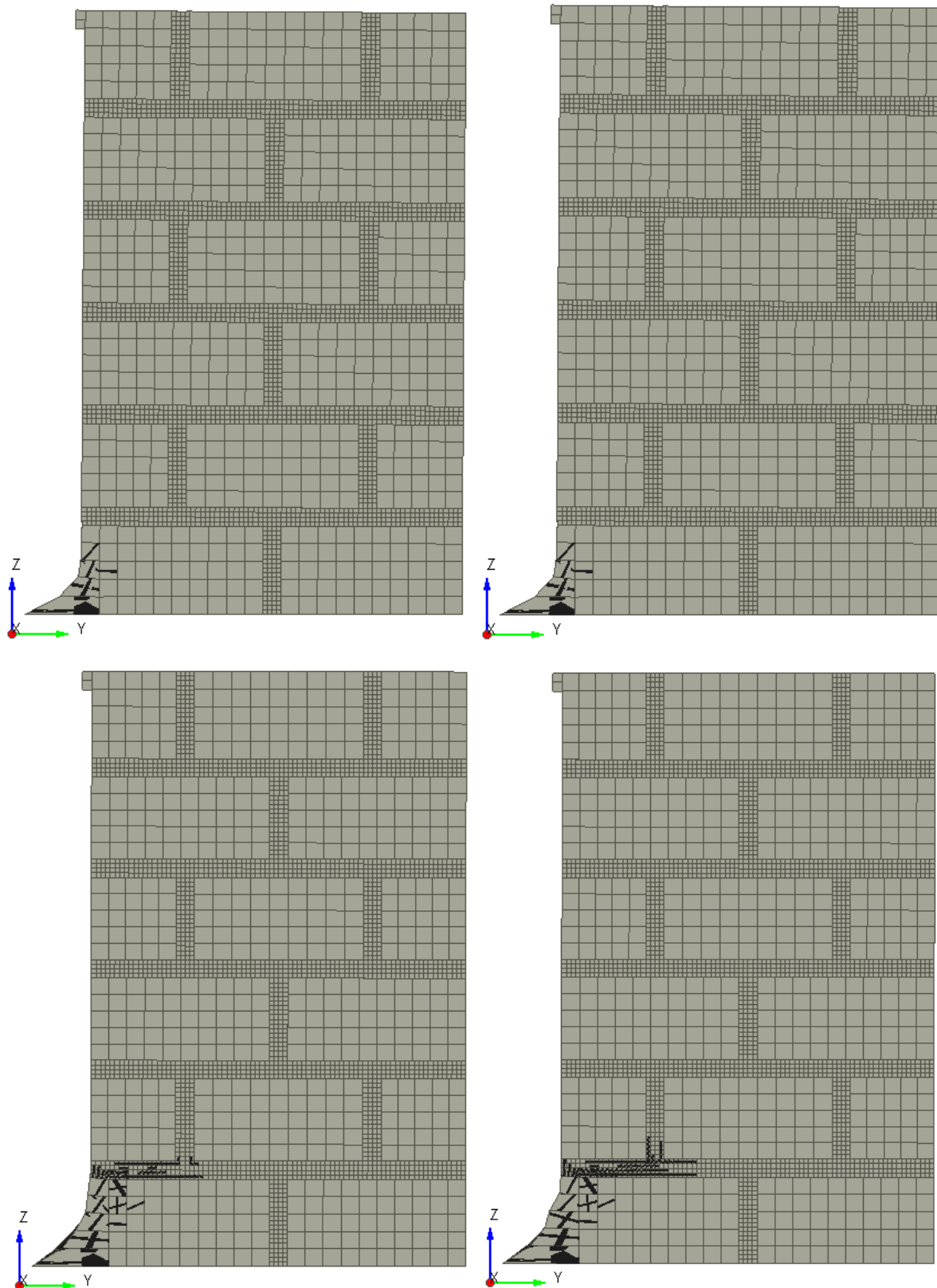


Figure A-43: PO-EQSJ20-OB0.2 Response [A] 0.1% Drift, [B] 0.2% Drift, [C] 0.5% Drift, [D] 1% Drift

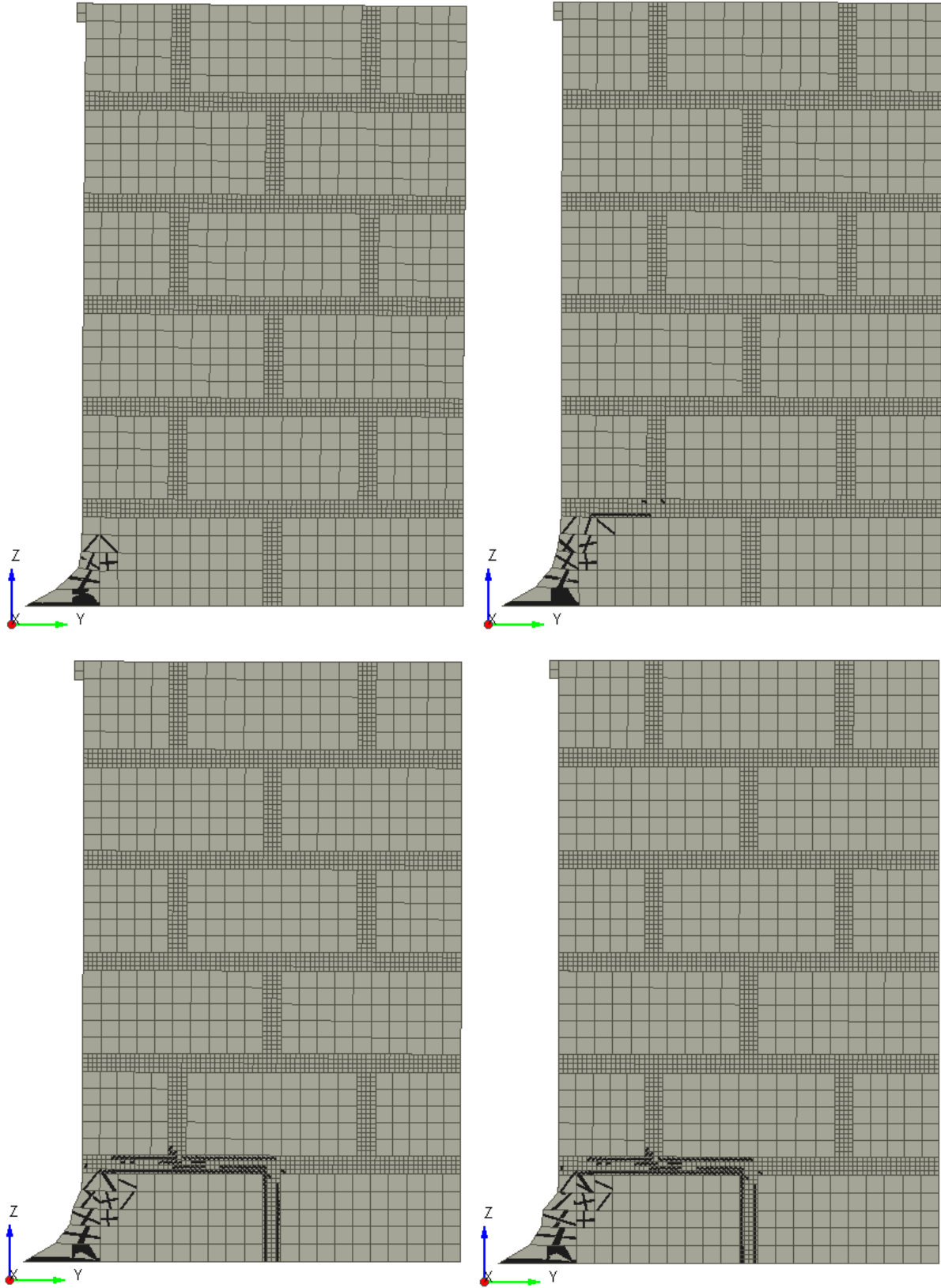


Figure A-44: PO-EQSJ20-OB0.3 Response [A] 0.1% Drift, [B] 0.2% Drift, [C] 0.5% Drift, [D] 1% Drift

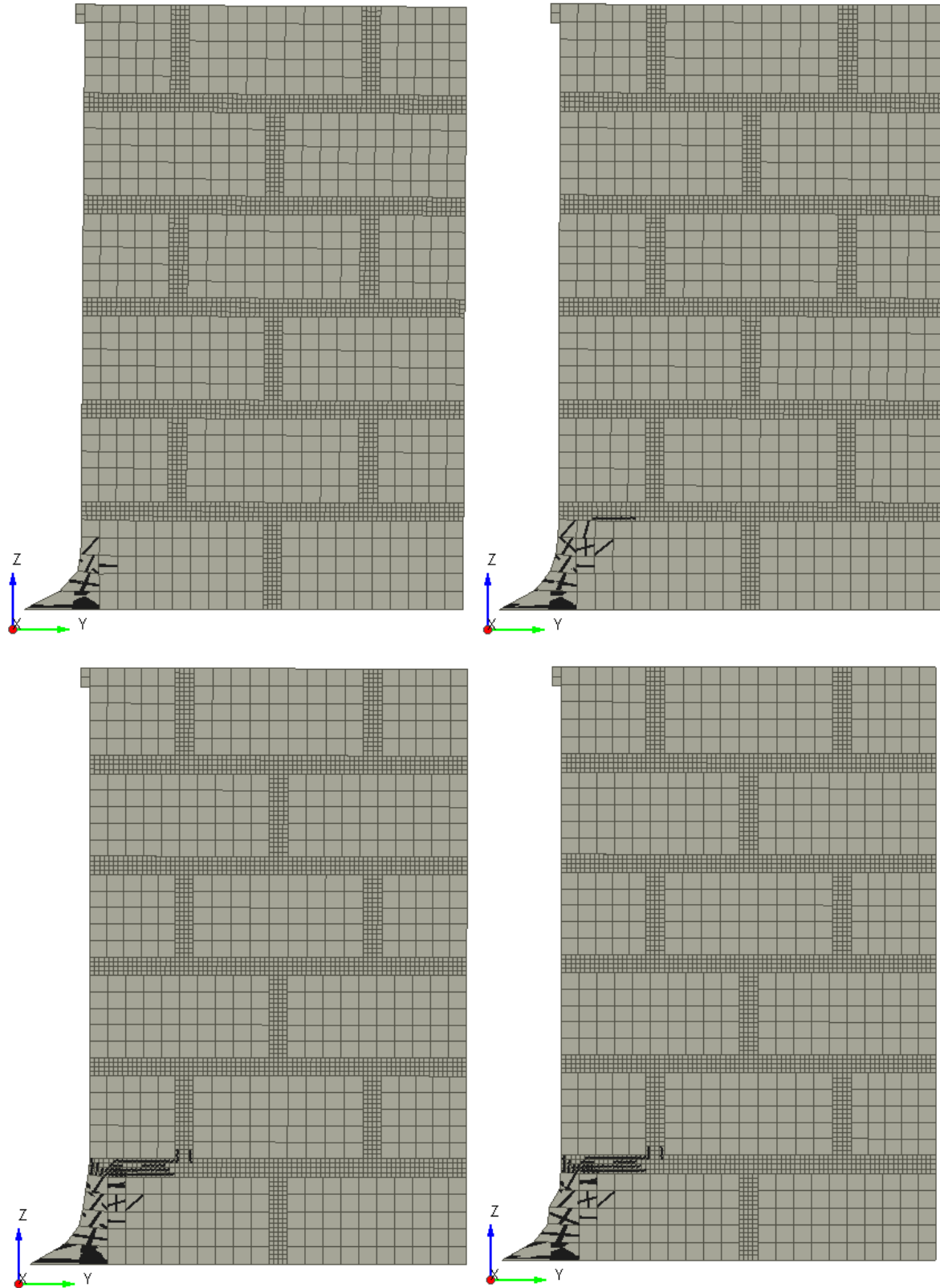


Figure A-45: PO-EQSJ20-OB0.4 Response [A] 0.1% Drift, [B] 0.2% Drift, [C] 0.5% Drift, [D] 1% Drift

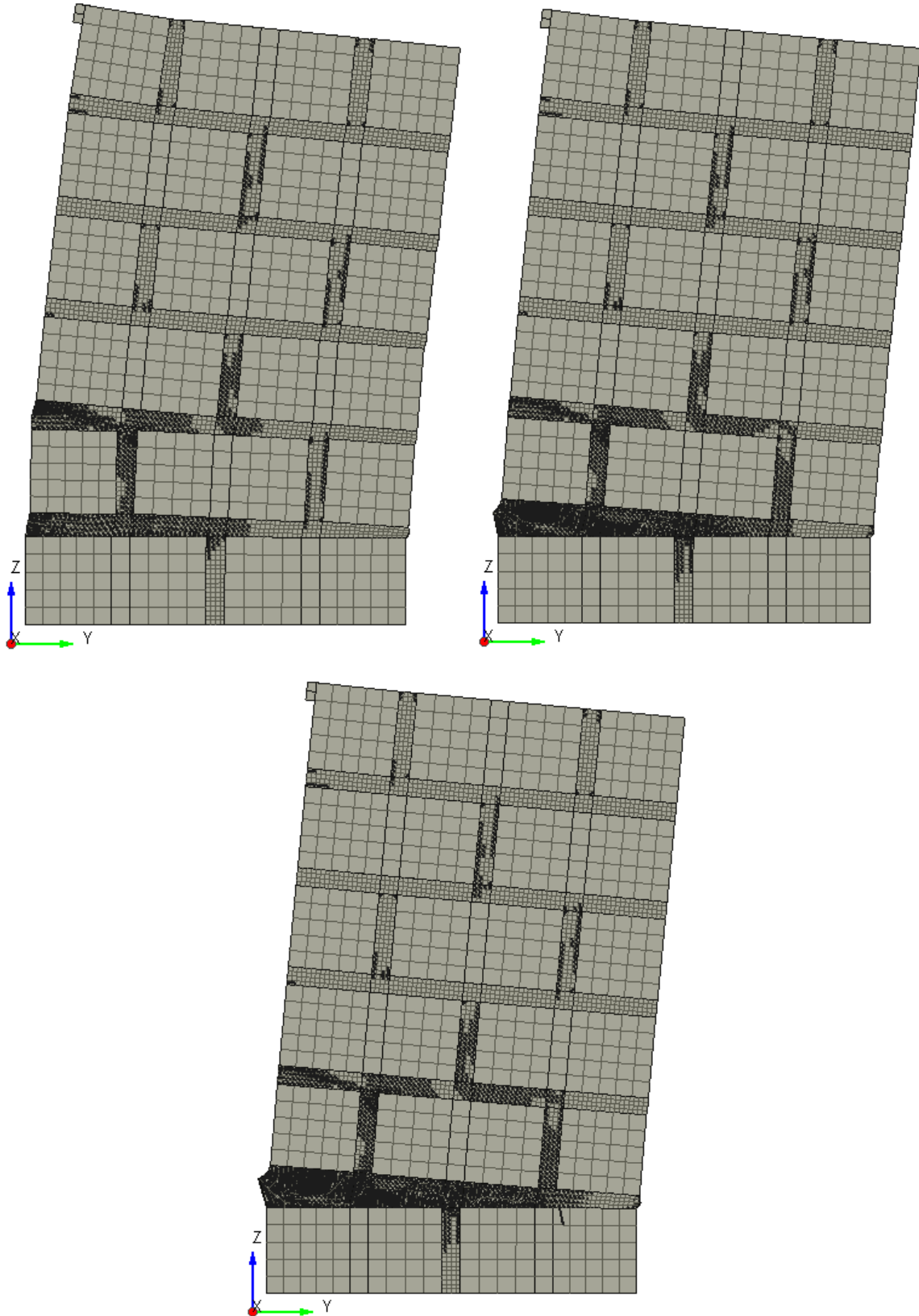


Figure A-46: PO-EQSJ20-OB1.79 Response [A] 0.092% Drift, [B] 0.184% Drift, [C] 0.369% Drift

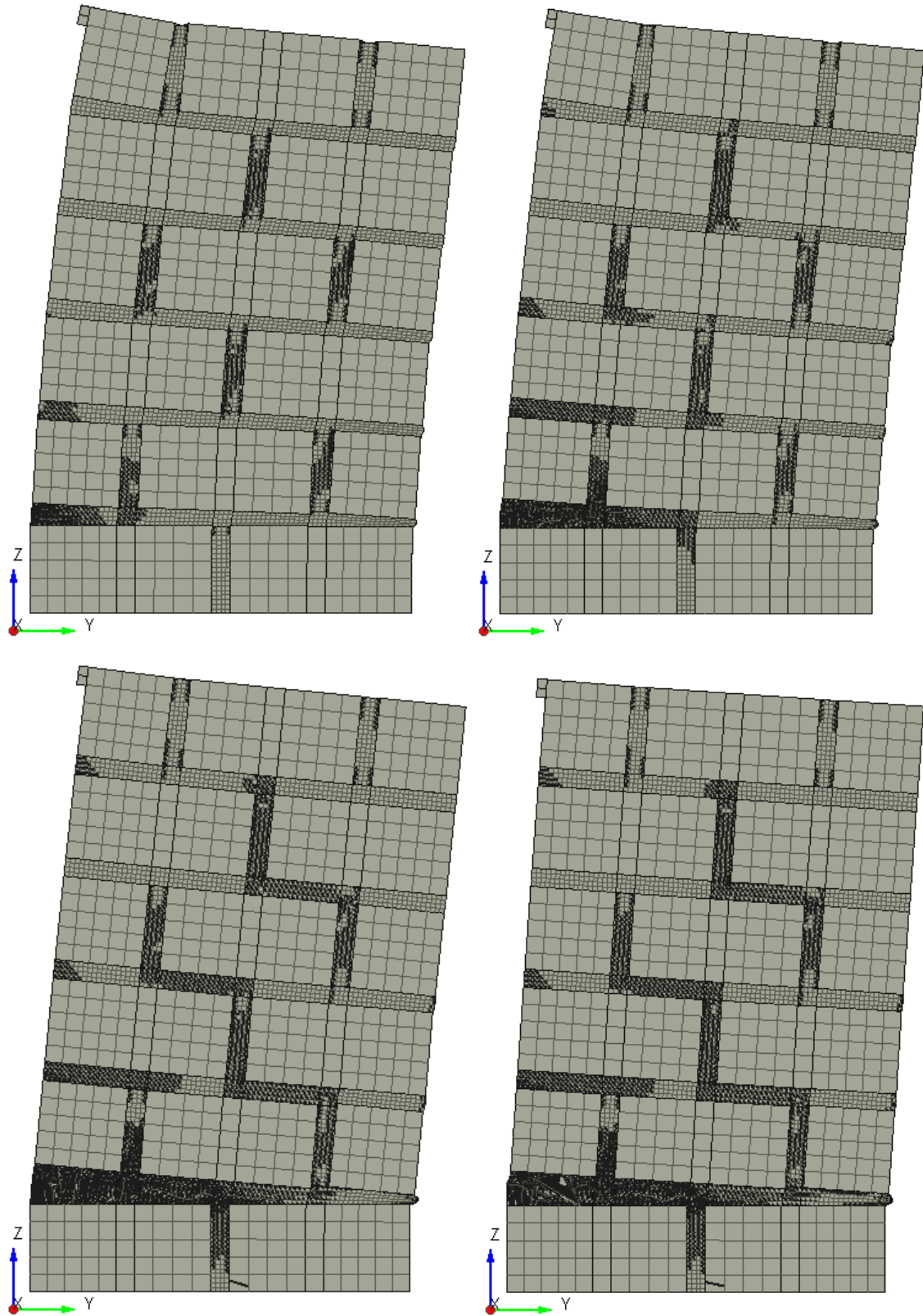


Figure A-47: PO-EQSJ20-OB4.47 Response [A] 0.092% Drift, [B] 0.184% Drift, [C] 0.507% Drift, [D] 0.646% Drift

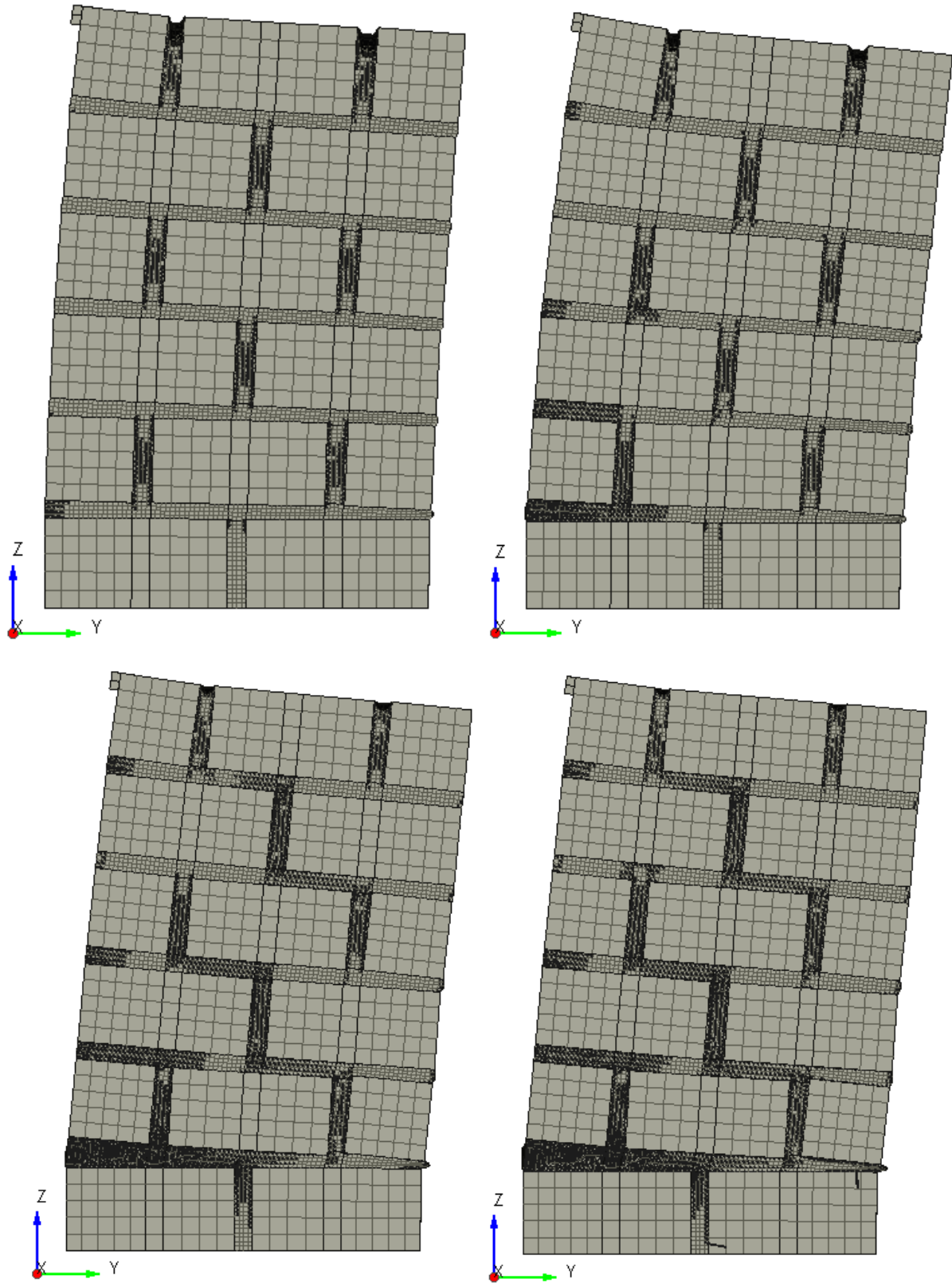


Figure A-48: PO-EQSJ20-OB7.15 Response [A] 0.092% Drift, [B] 0.184% Drift, [C] 0.507% Drift, [D] 0.738% Drift

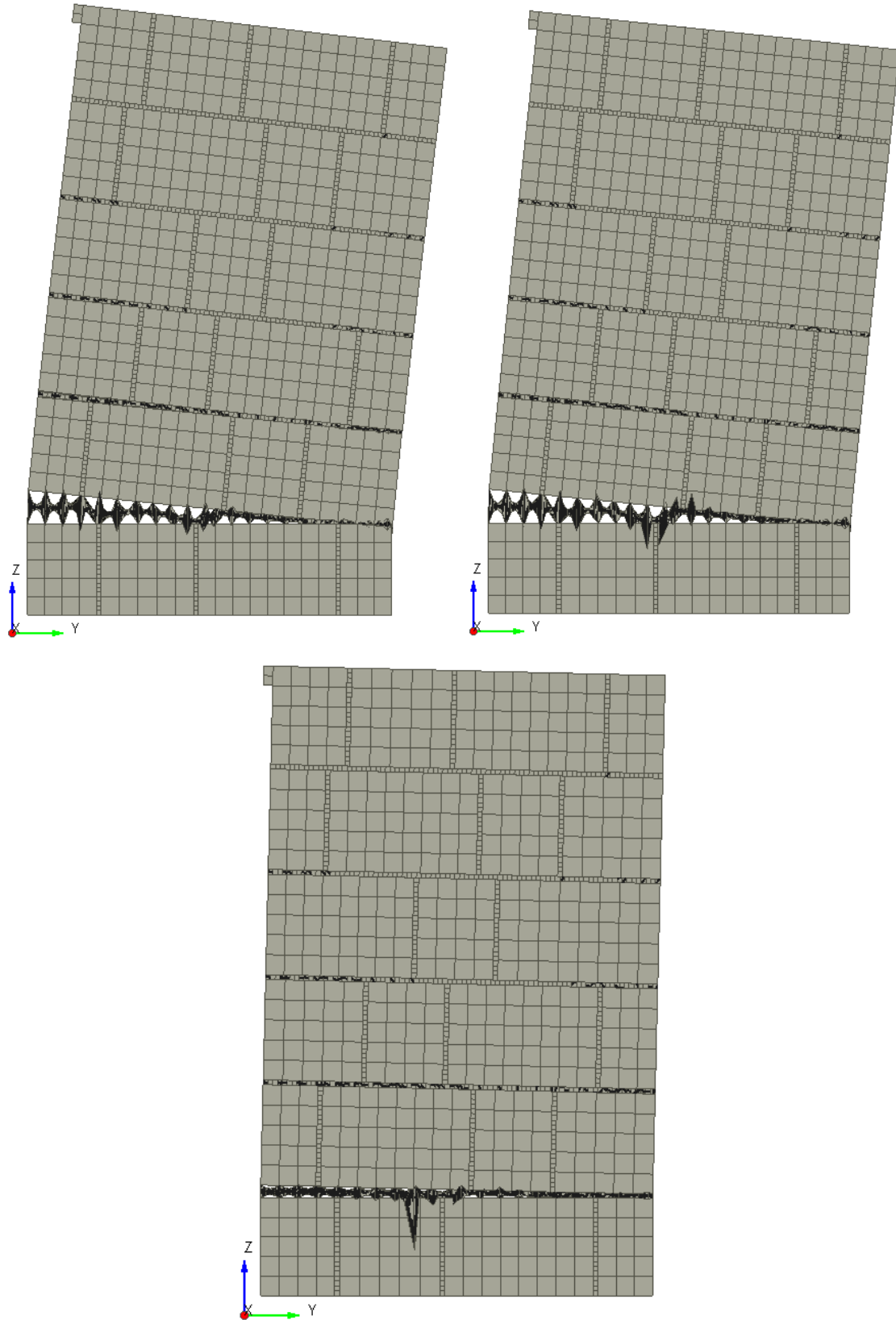


Figure A-49: PO-RANJ5-OB0.05 Response [A] 0.1% Drift, [B] 0.2% Drift, [C] 0.48% Drift

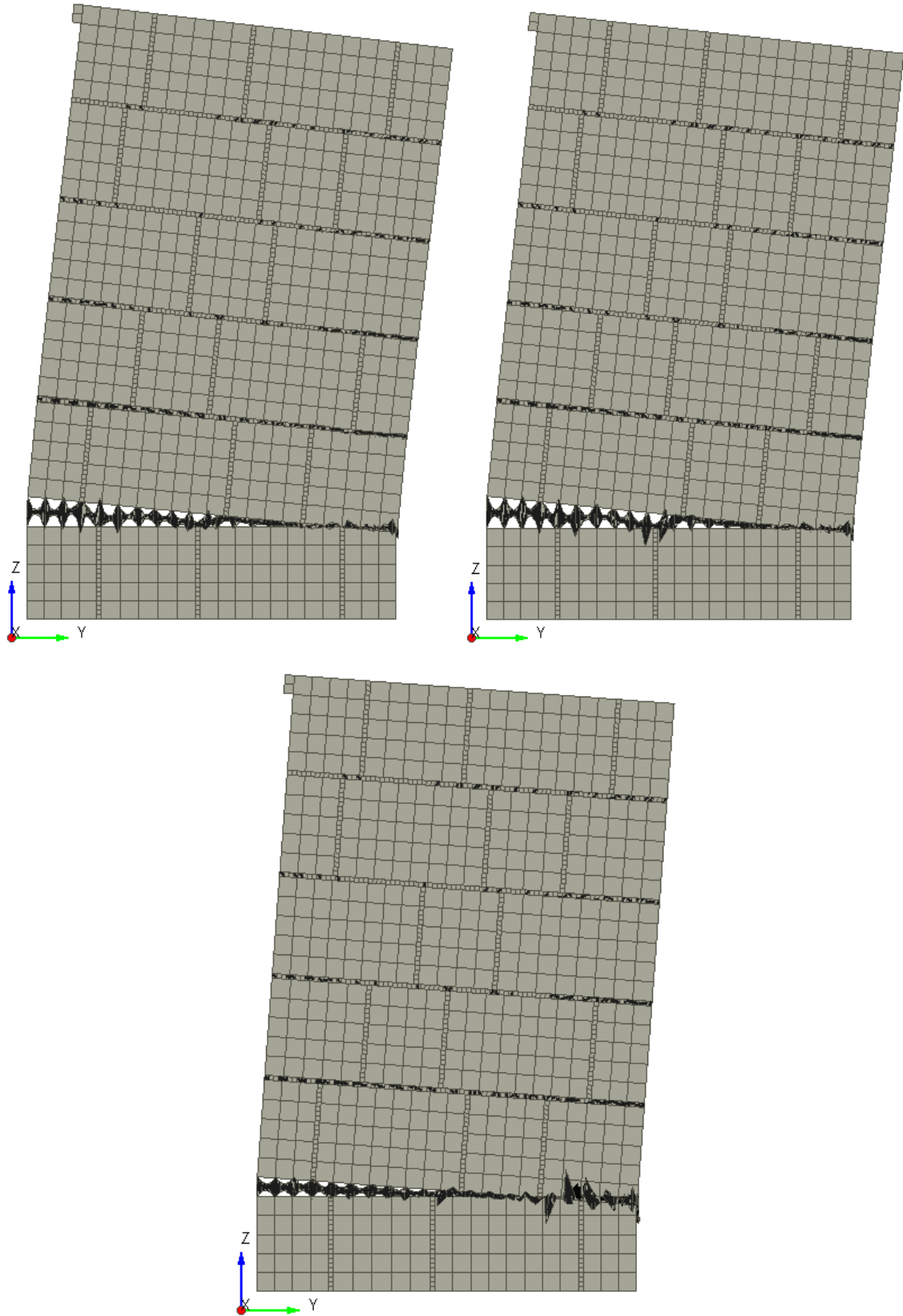


Figure A-50: PO-RANJ5-OB0.1 Response [A] 0.1% Drift, [B] 0.2% Drift, [C] 0.45% Drift

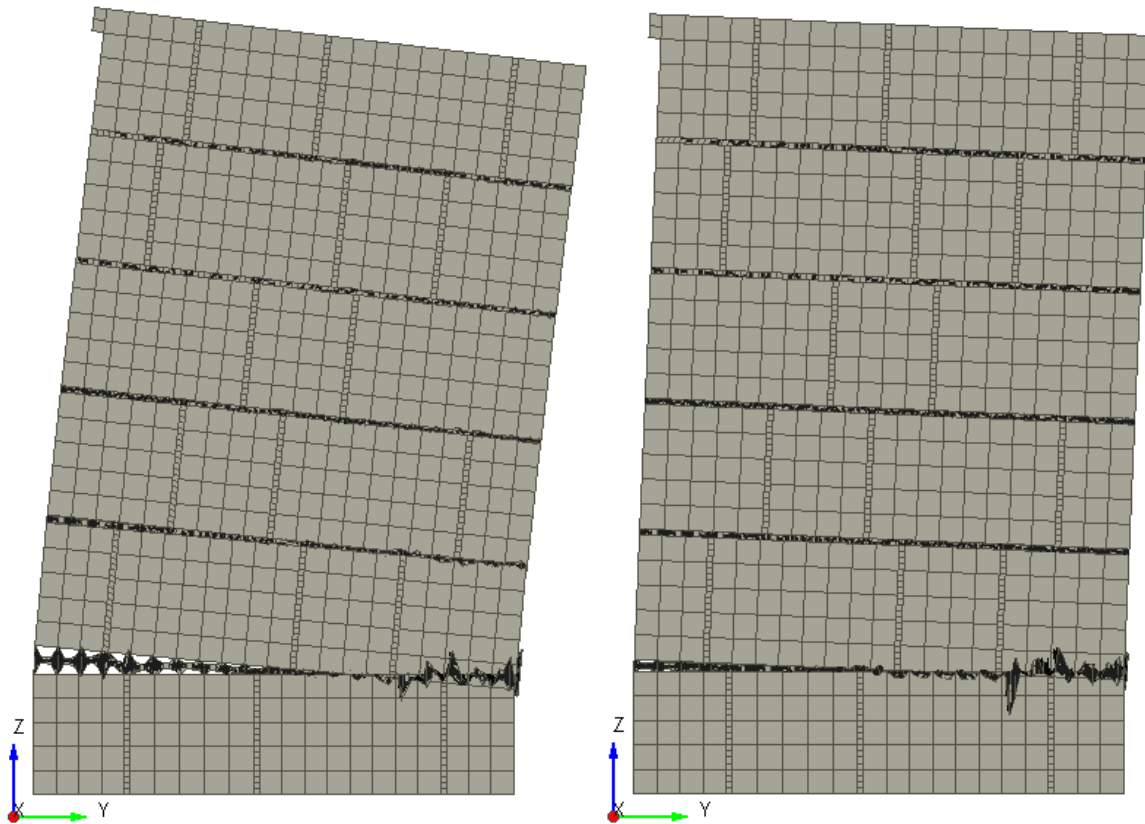


Figure A-51: PO-RANJ5-OB0.2 Response [A] 0.1% Drift, [B] 0.2% Drift

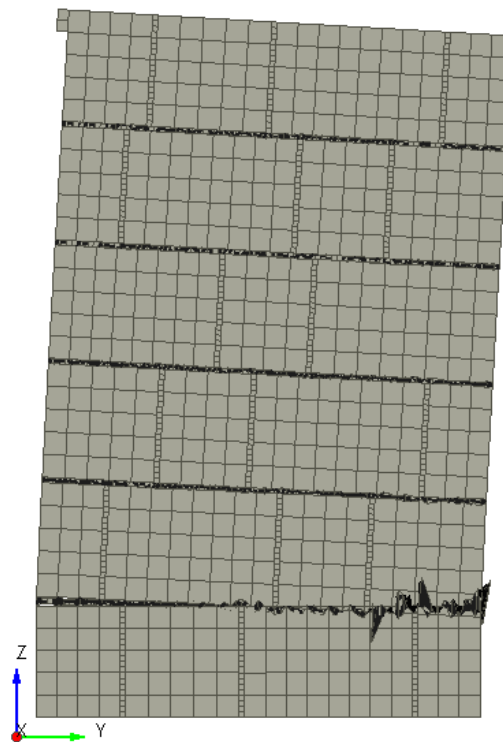


Figure A-52: PO-RANJ5-OB0.3 Response [A] 0.1% Drift

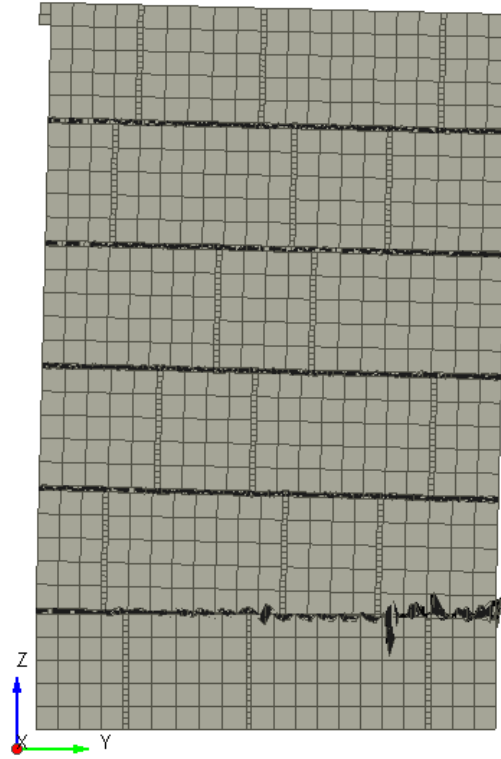


Figure A-53: PO-RANJ5-OB0.4 Response [A] 0.1% Drift

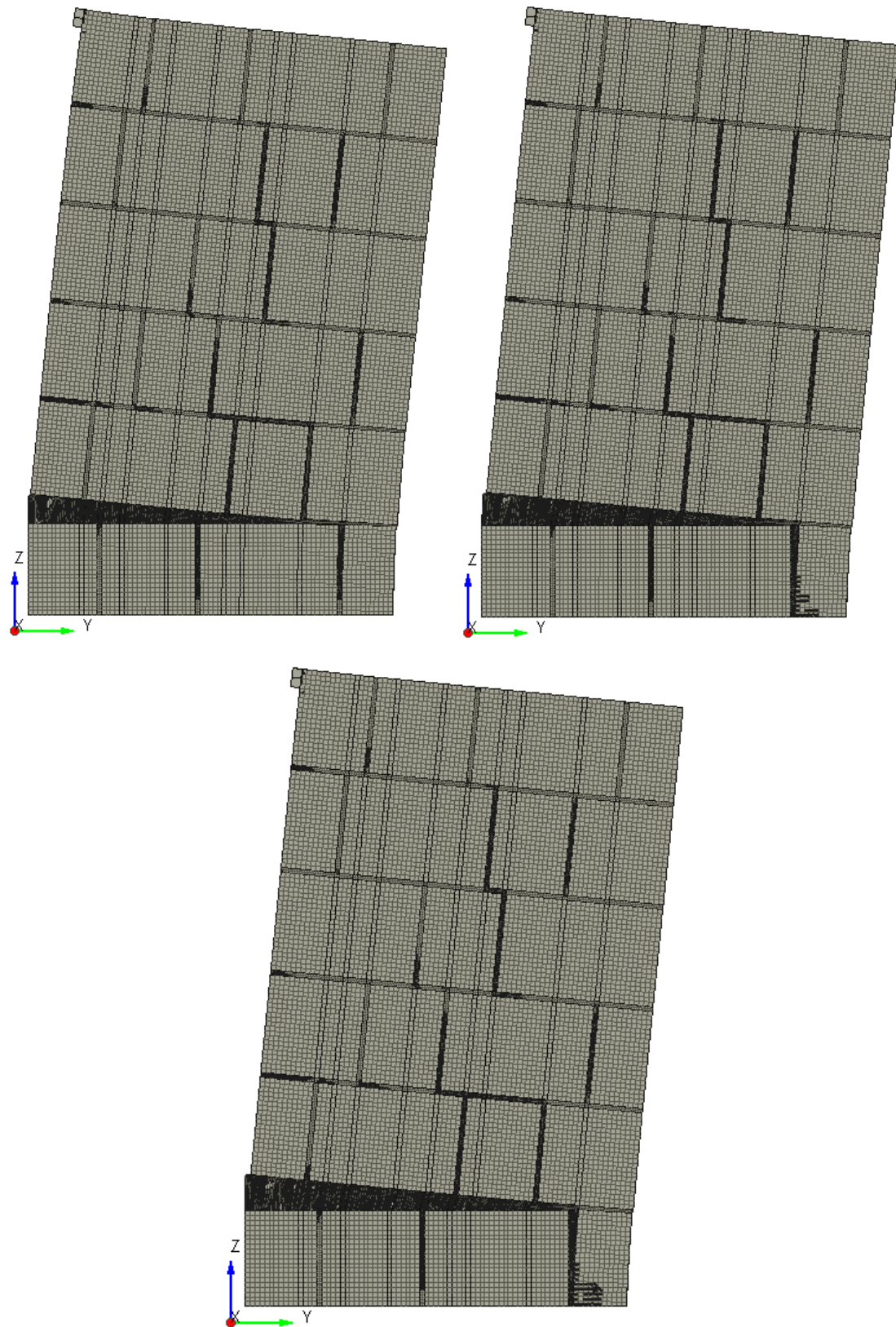


Figure A-54: PO-RANJ5-OB1.79 Response [A] 0.092% Drift, [B] 0.184% Drift, [C] 0.231% Drift

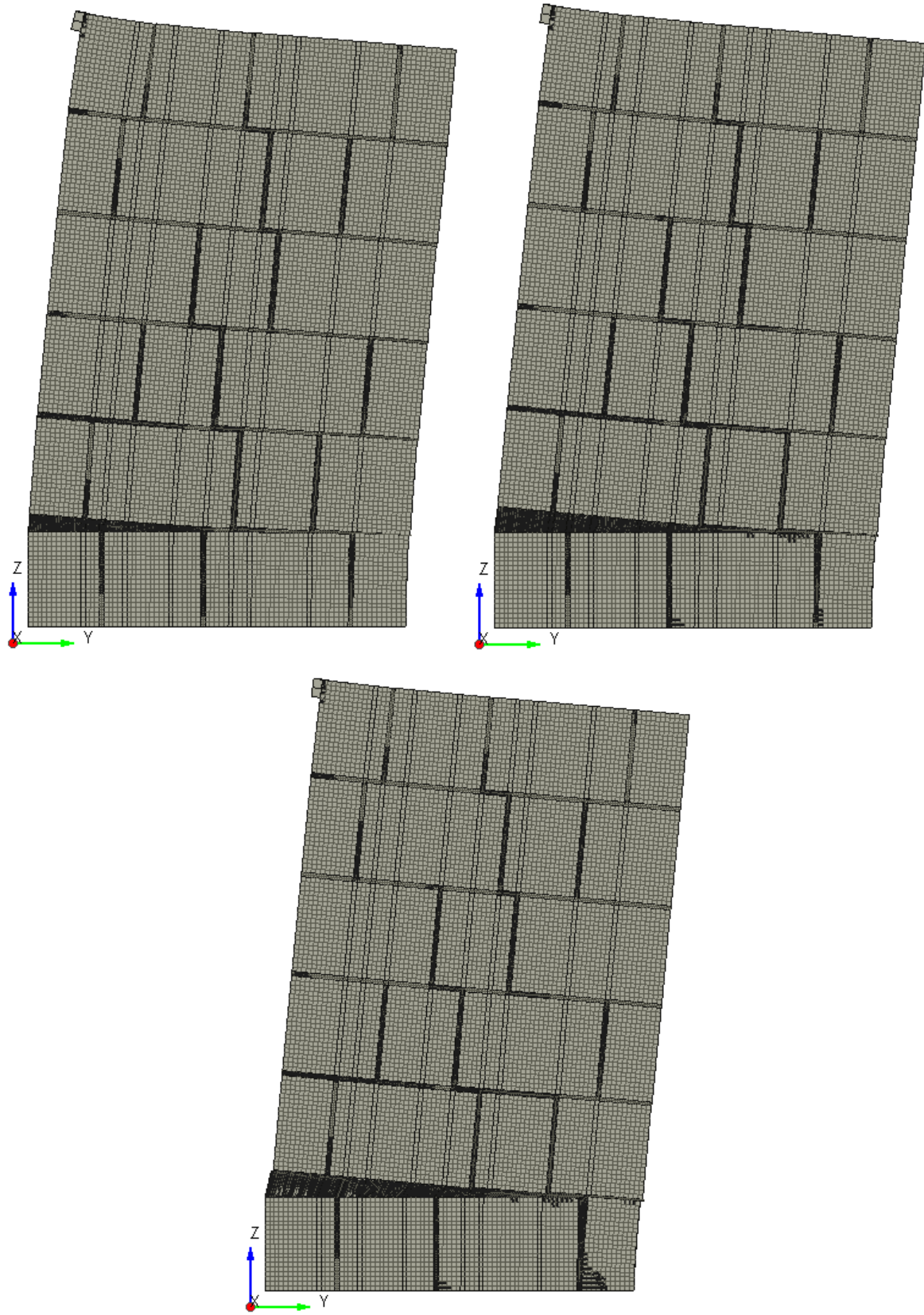


Figure A-55: PO-RANJ5-OB4.47 Response [A] 0.092% Drift, [B] 0.184% Drift, [C] 0.277% Drift

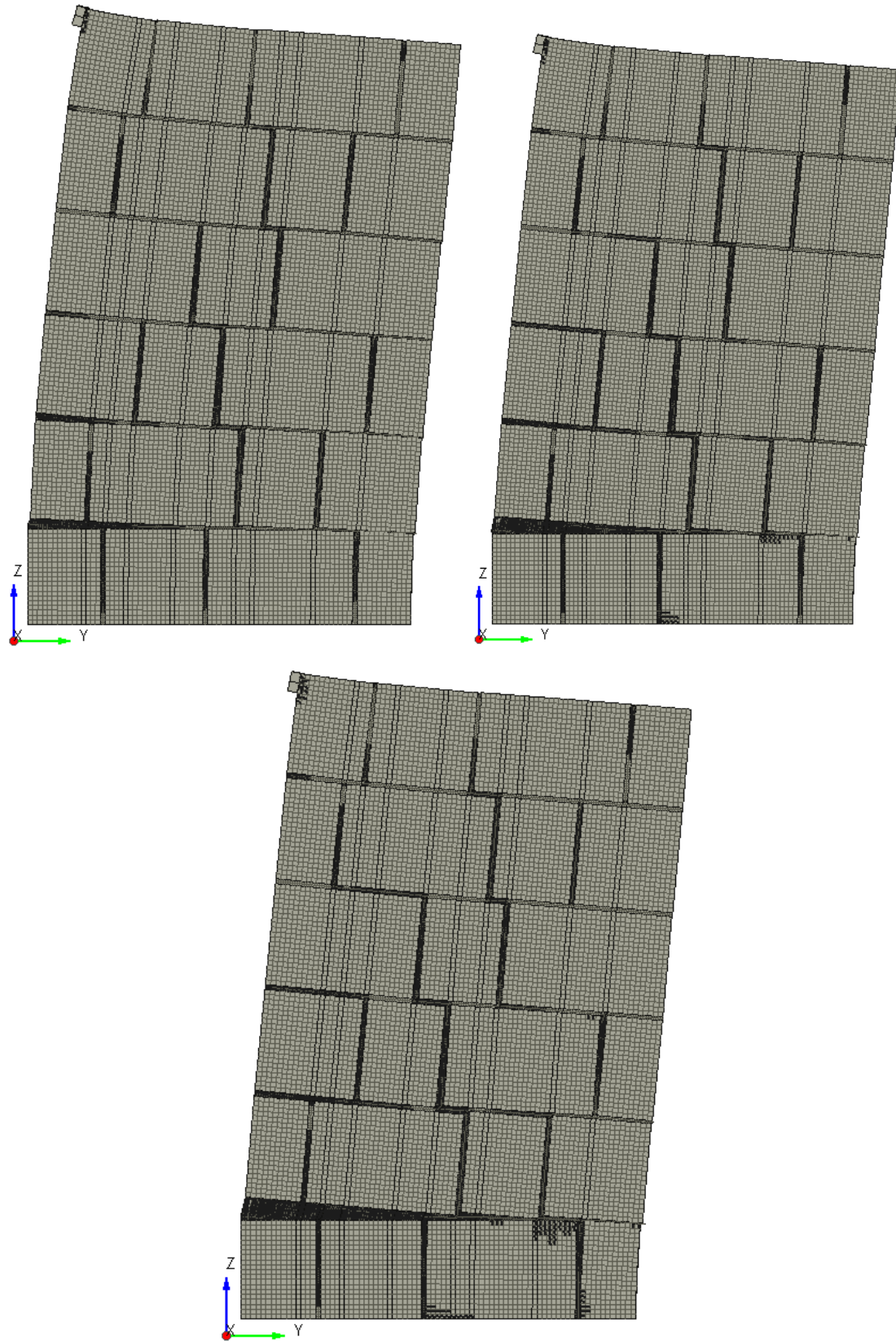


Figure A-56: PO-RANJ5-OB7.15 Response [A] 0.092% Drift, [B] 0.184% Drift, [C] 0.276% Drift

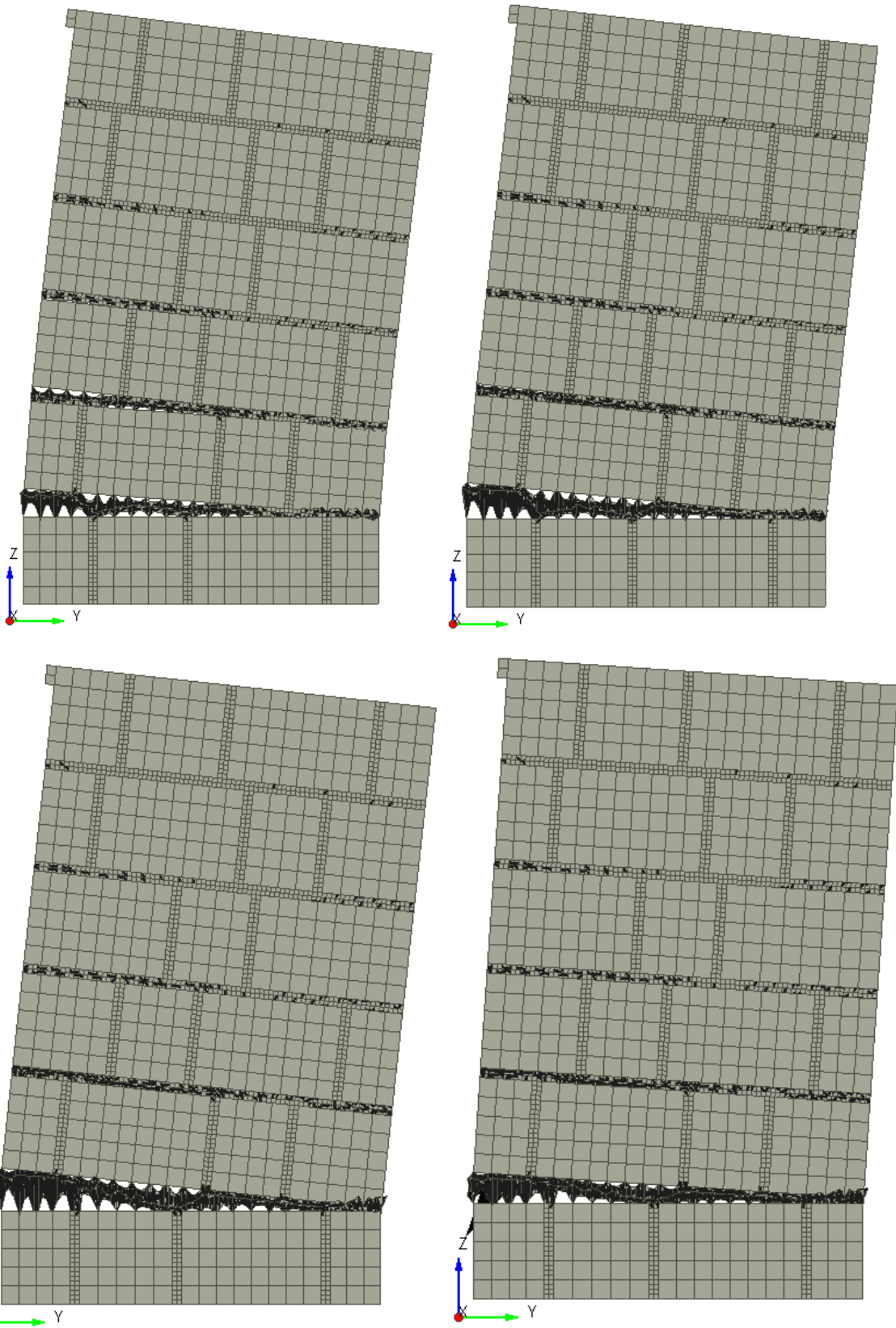


Figure A-57: PO-RANJ10-OB0.05 Response [A] 0.1% Drift, [B] 0.2% Drift, [C] 0.5% Drift, [D] 0.71% Drift

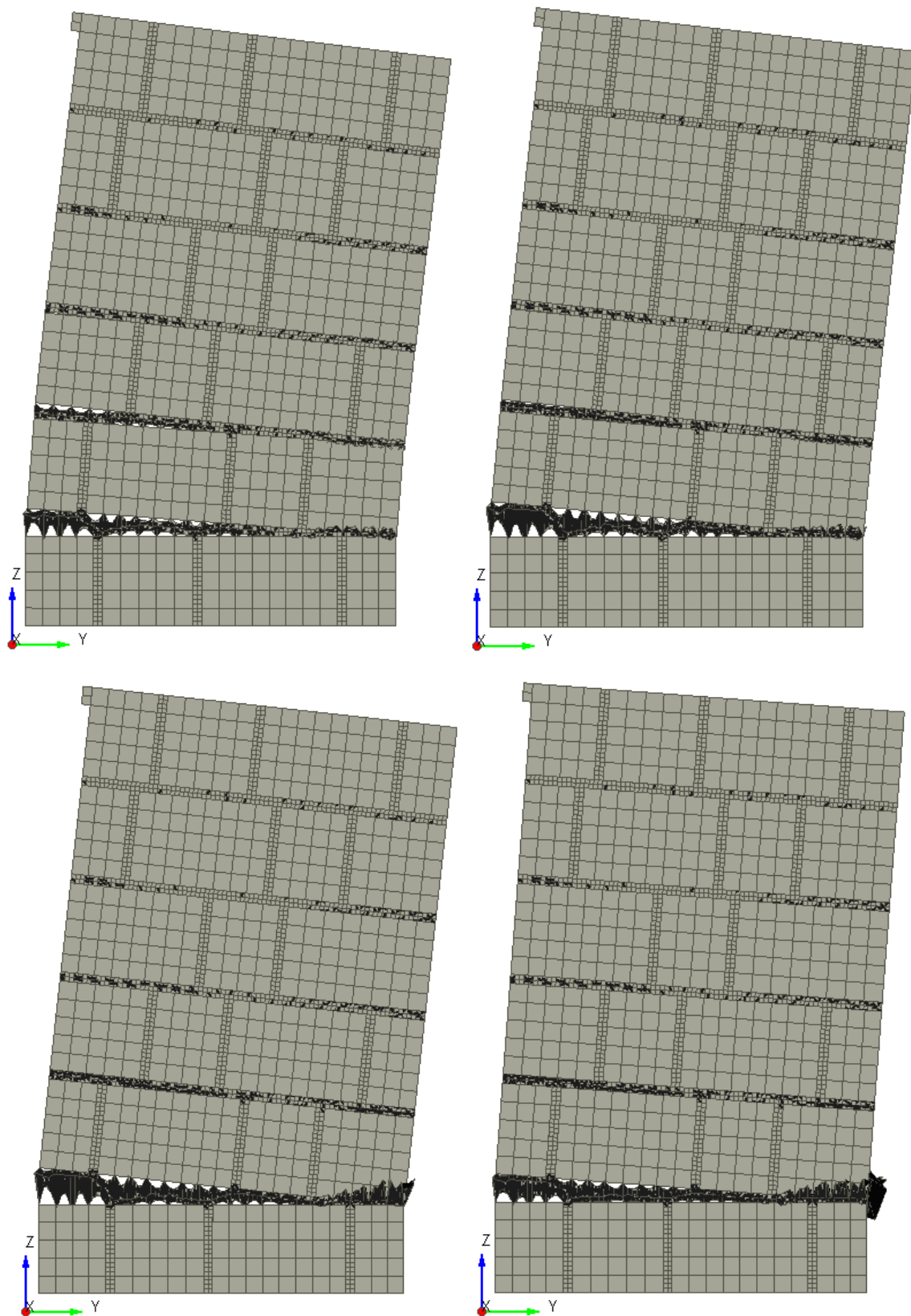


Figure A-58: PO-RANJ10-OB0.1 Response [A] 0.1% Drift, [B] 0.2% Drift, [C] 0.5% Drift, [D] 0.81% Drift

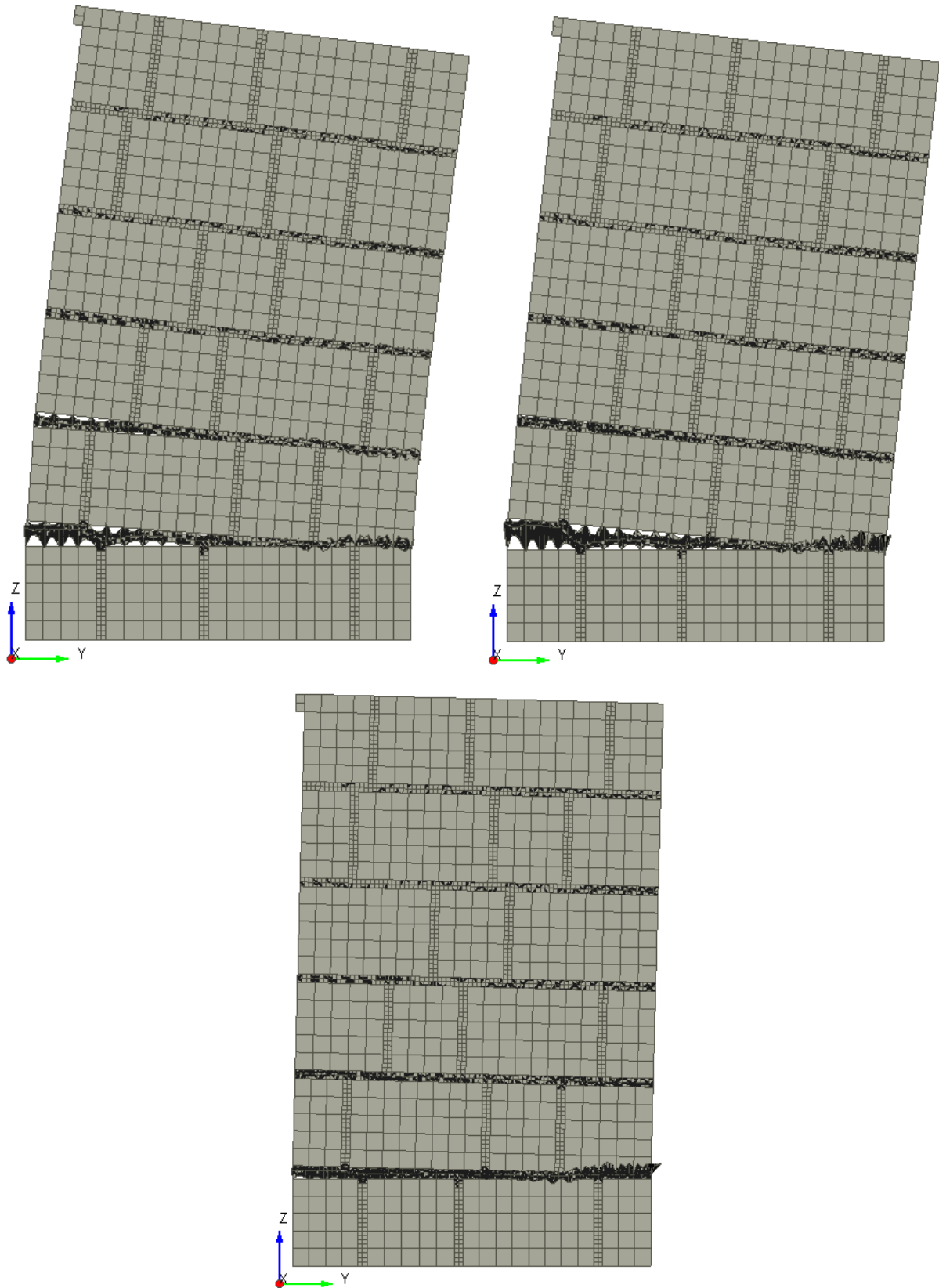


Figure A-59: PO-RANJ10-OB0.2 Response [A] 0.1% Drift, [B] 0.2% Drift, [C] 0.45% Drift

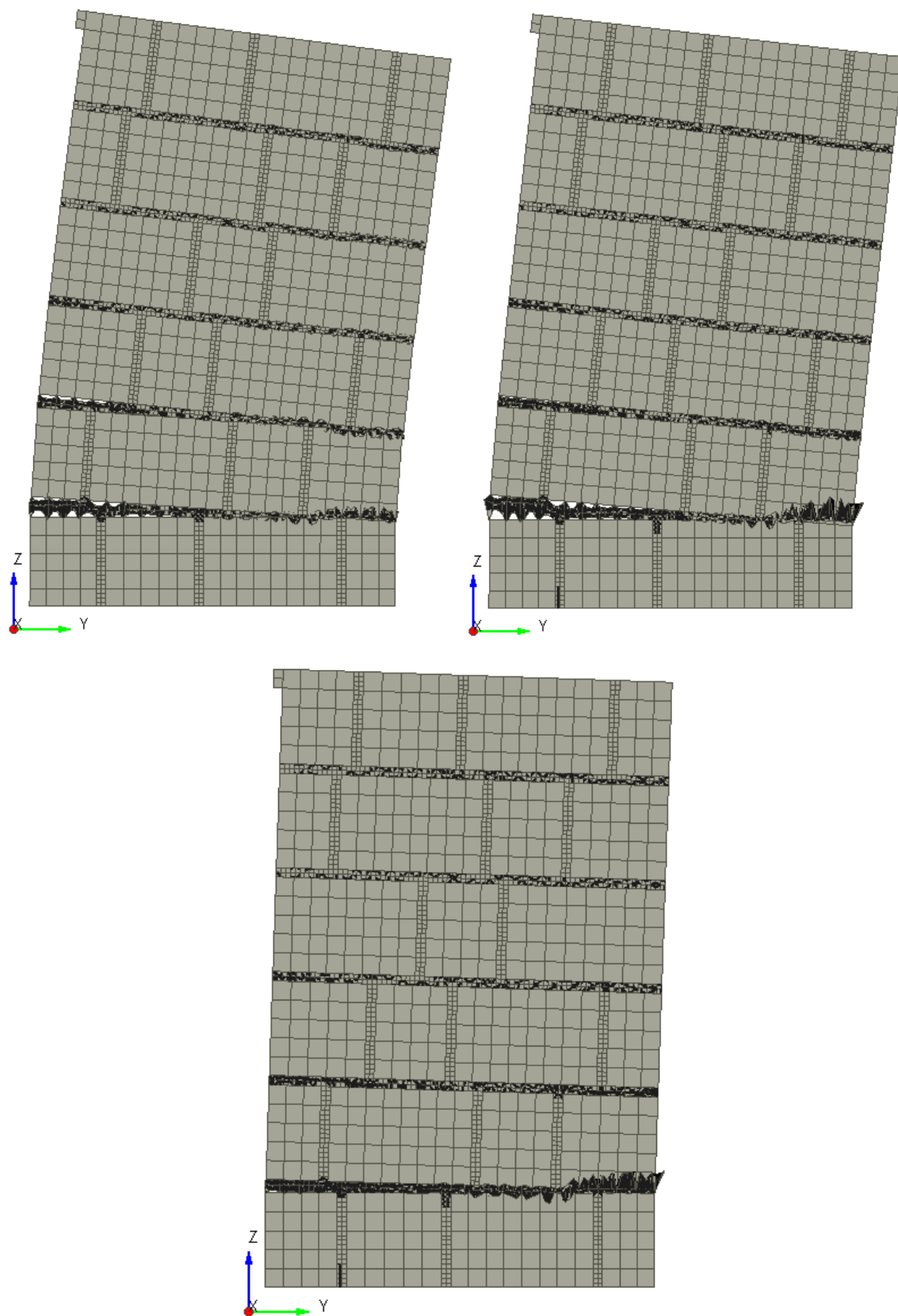


Figure A-60: PO-RANJ10-OB0.3 Response [A] 0.1% Drift, [B] 0.2% Drift, [C] 0.35% Drift

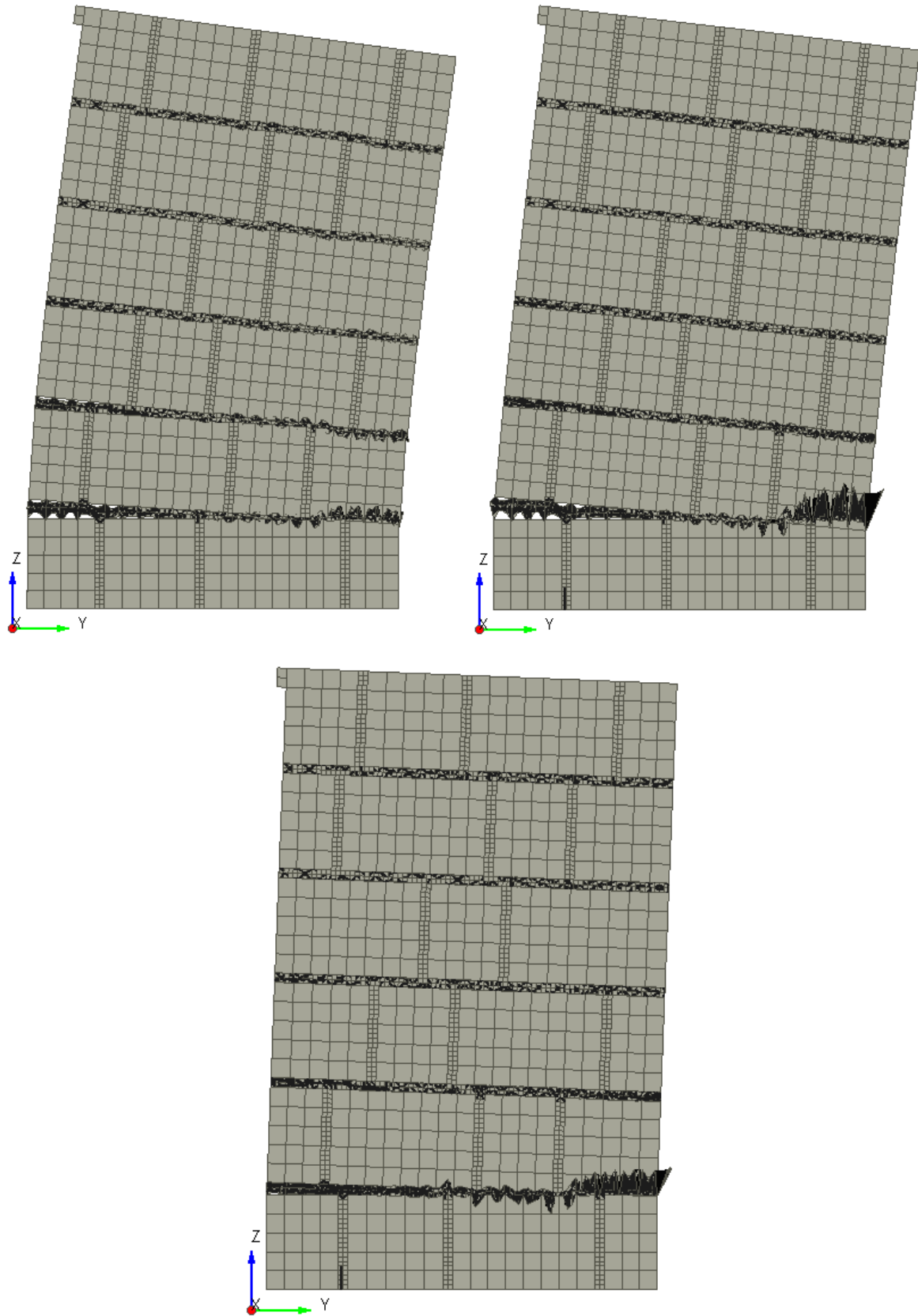


Figure A-61: PO-RANJ10-OB0.4 Response [A] 0.1% Drift, [B] 0.2% Drift, [C] 0.29% Drift

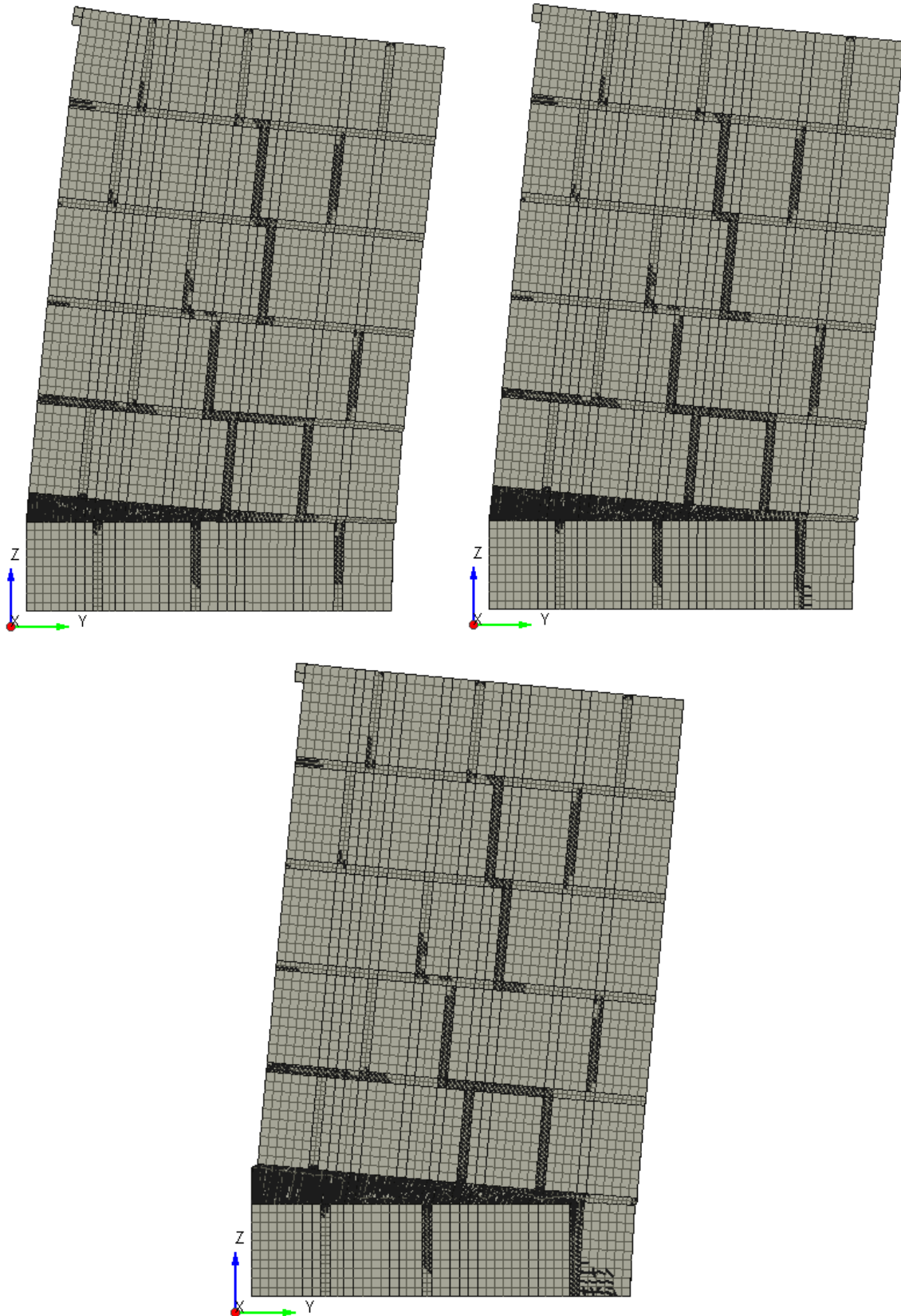


Figure A-62: PO-RANJ10-OB1.79 Response [A] 0.092% Drift, [B] 0.184% Drift, [C] 0.415% Drift

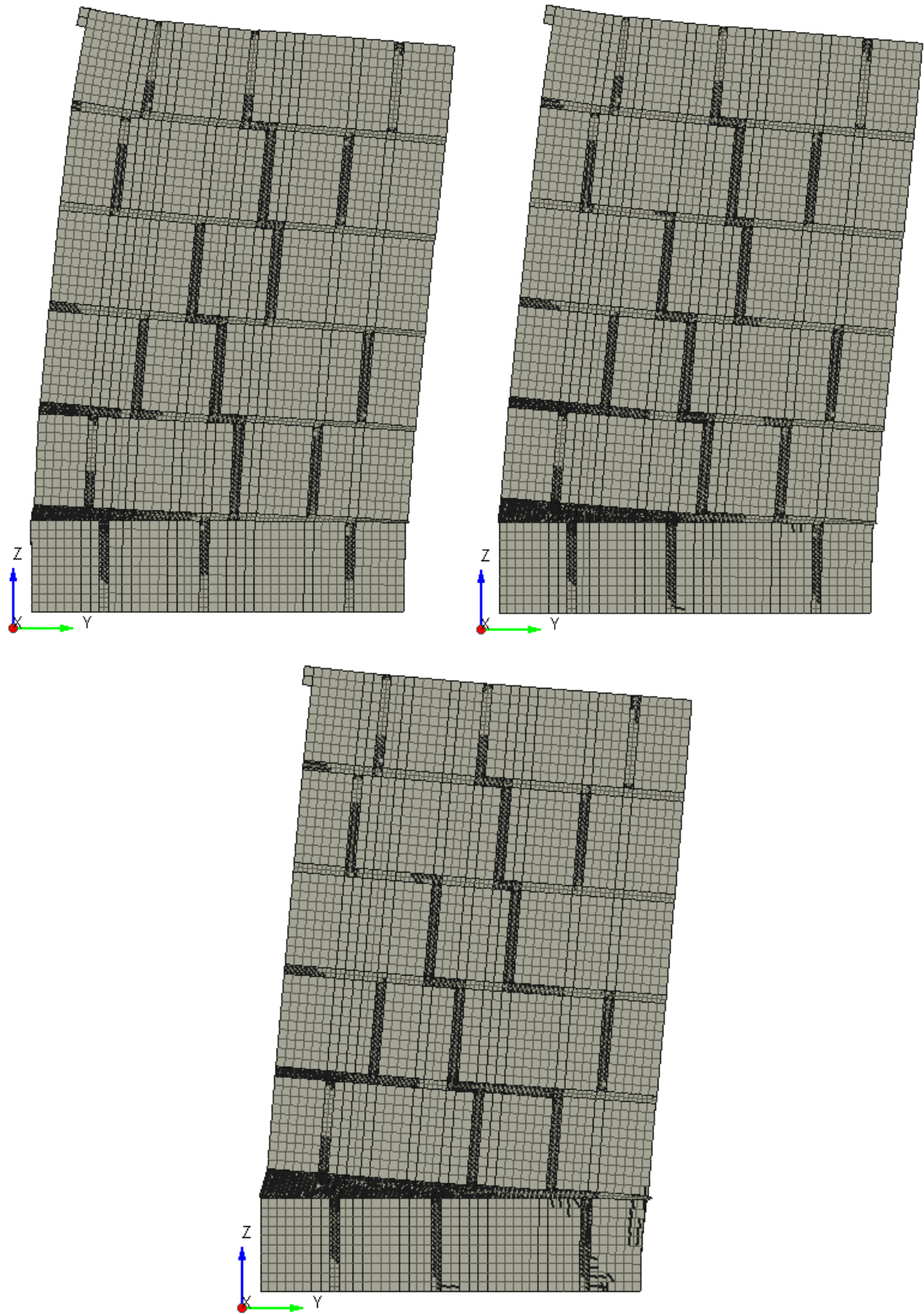


Figure A-63: PO-RANJ10-OB4.47 Response [A] 0.092% Drift, [B] 0.184% Drift, [C] 0.415% Drift

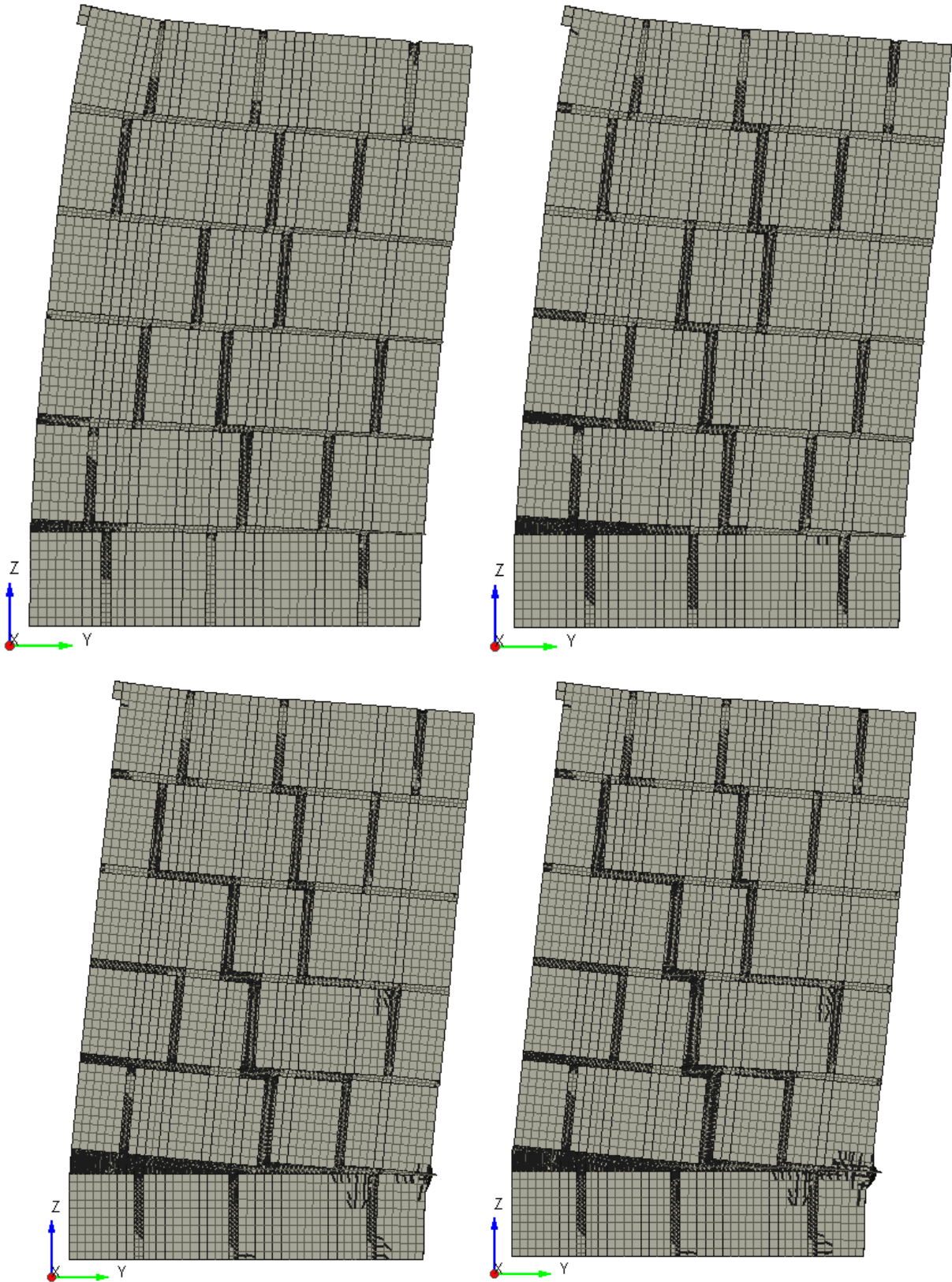


Figure A-64: PO-RANJ10-OB7.15 Response [A] 00921% Drift, [B] 0.184% Drift, [C] 0.507% Drift, [D] 0.646% Drift

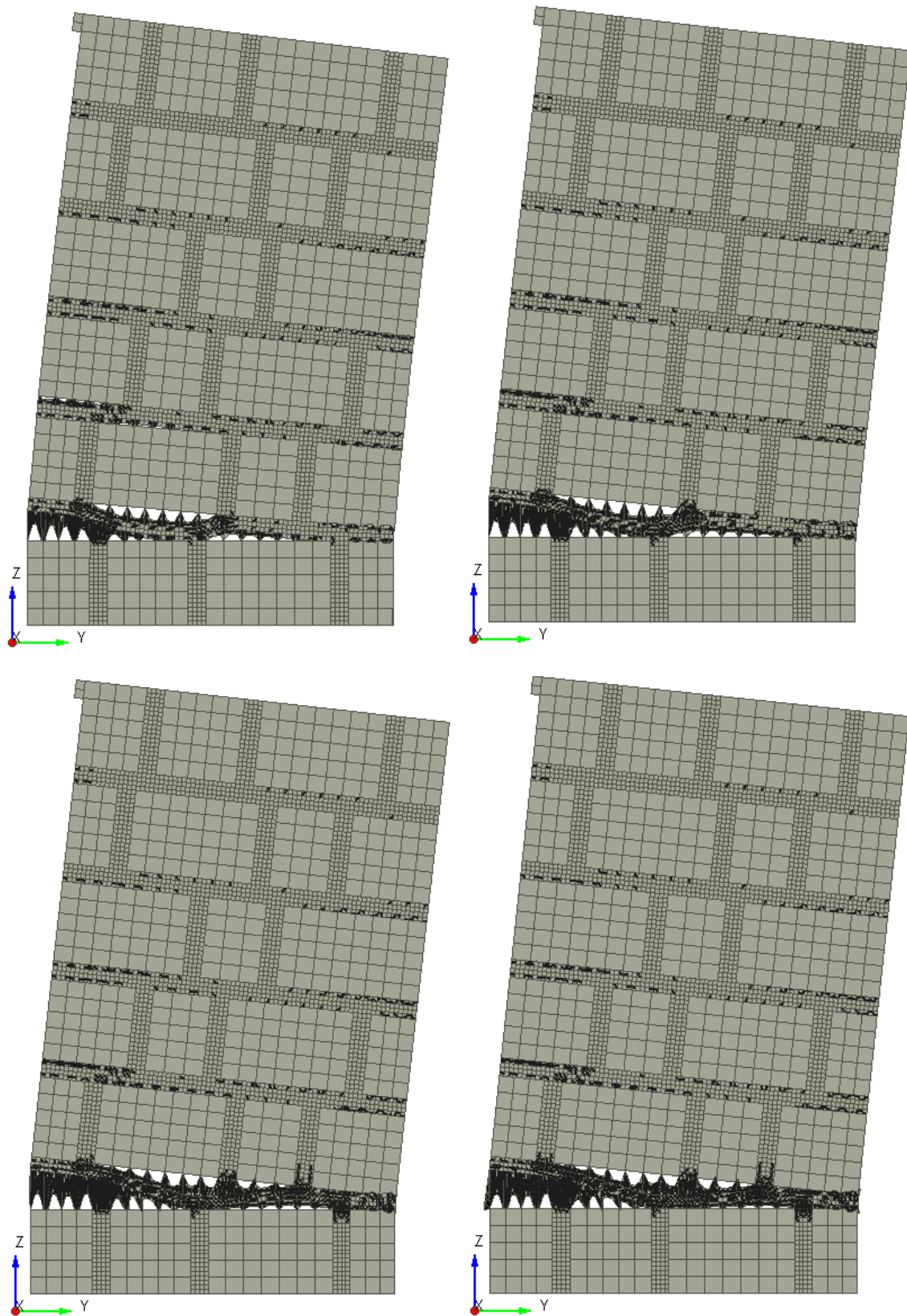


Figure A-65: PO-RANJ20-OB0.05 Response [A] 0.1% Drift, [B] 0.2% Drift, [C] 0.5% Drift, [D] 0.87% Drift

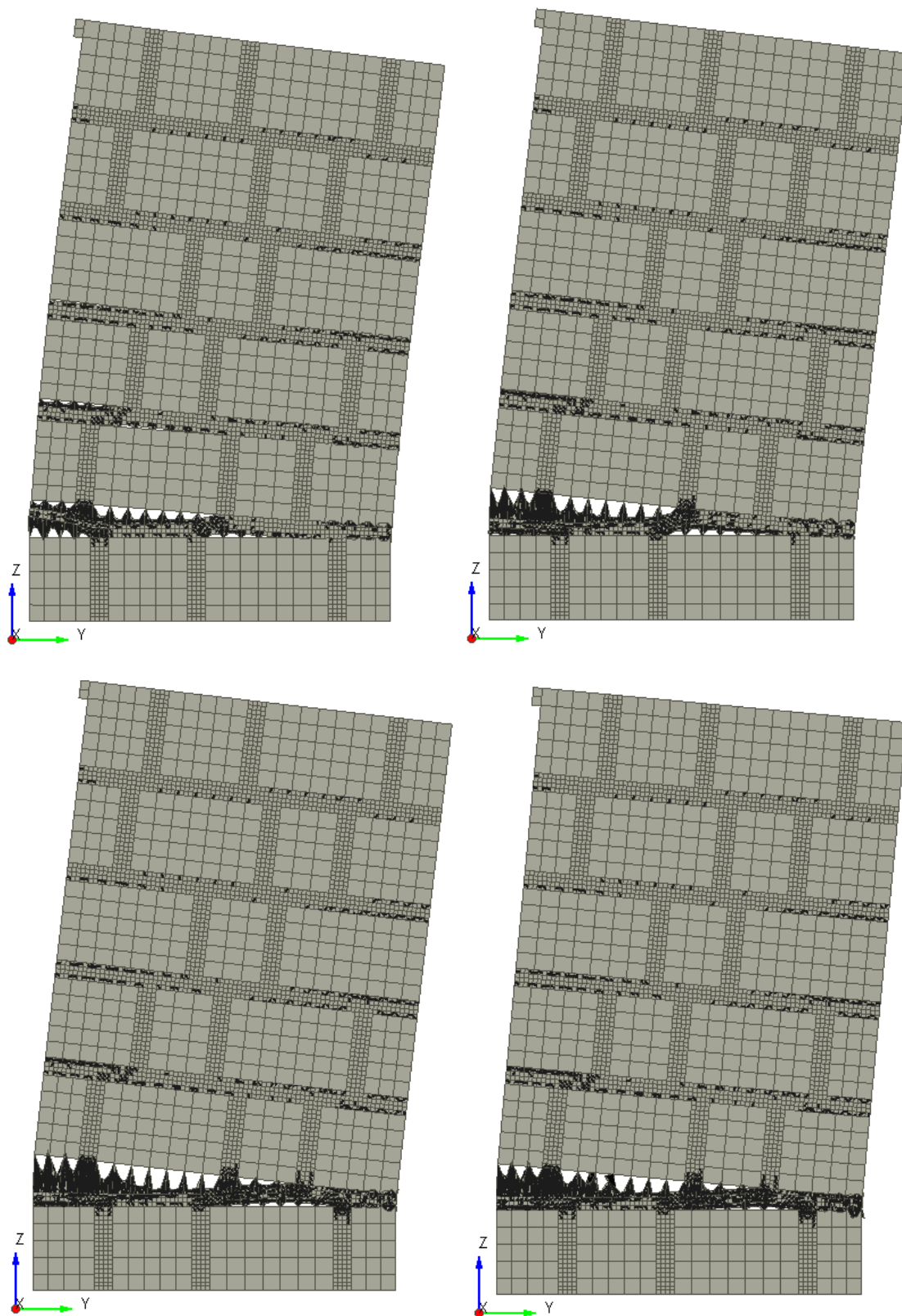


Figure A-66: PO-RANJ20-OB0.1 Response [A] 0.1% Drift, [B] 0.2% Drift, [C] 0.5% Drift, [D] 0.78% Drift

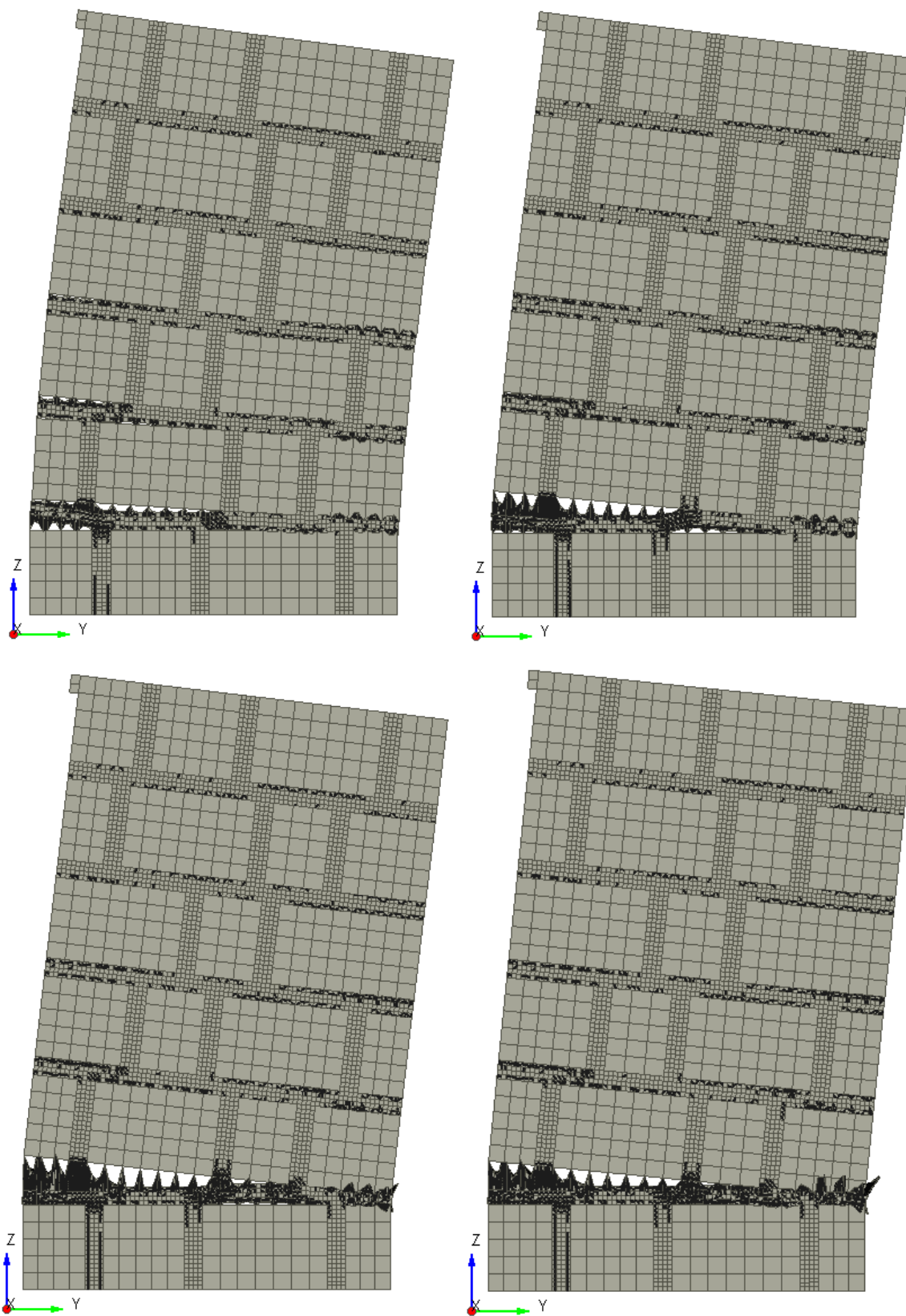


Figure A-67: PO-RANJ20-OB0.2 Response [A] 0.1% Drift, [B] 0.2% Drift, [C] 0.5% Drift, [D] 0.65% Drift

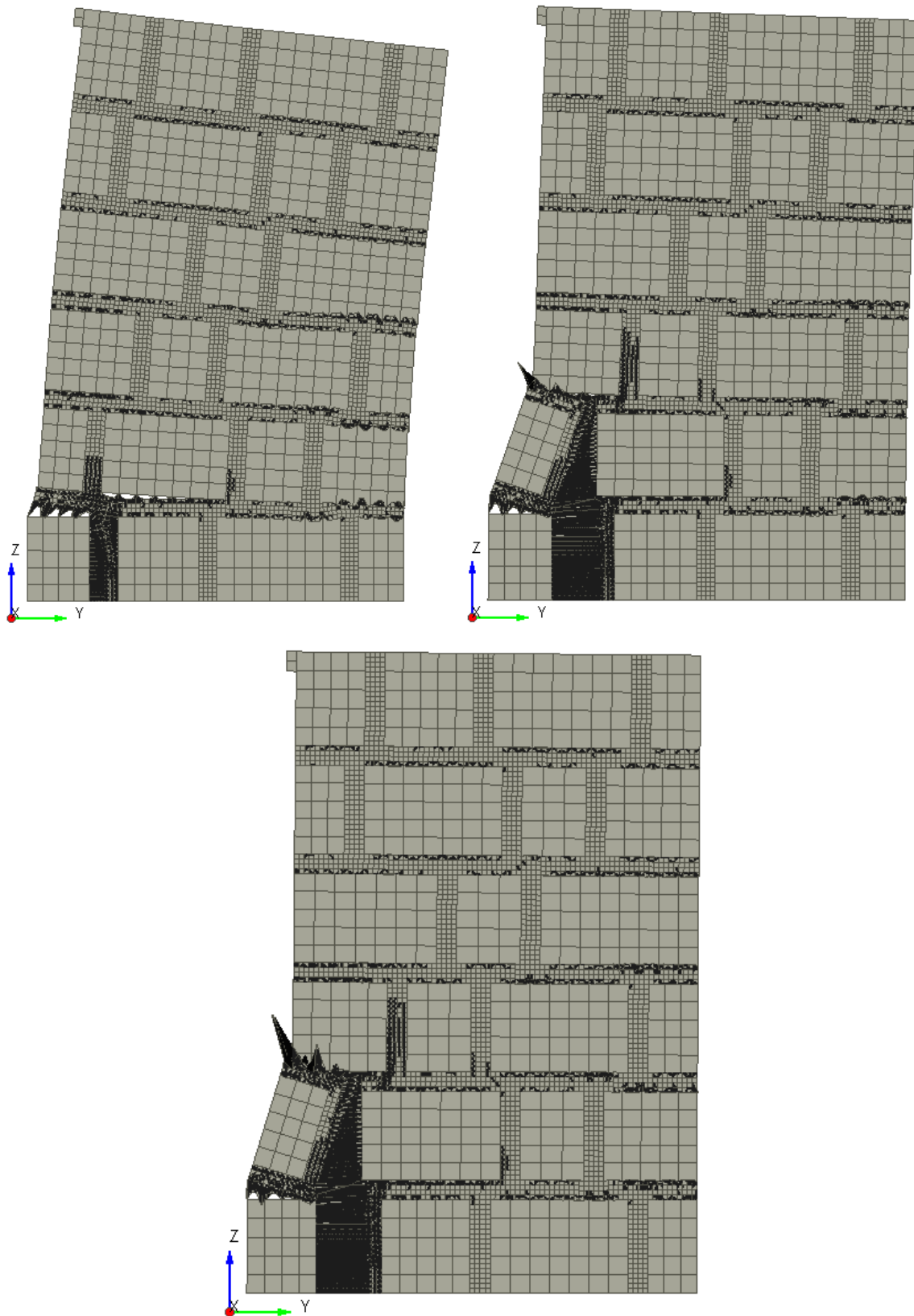


Figure A-68: PO-RANJ20-OB0.3 Response [A] 0.1% Drift, [B] 0.2% Drift, [C] 0.36% Drift

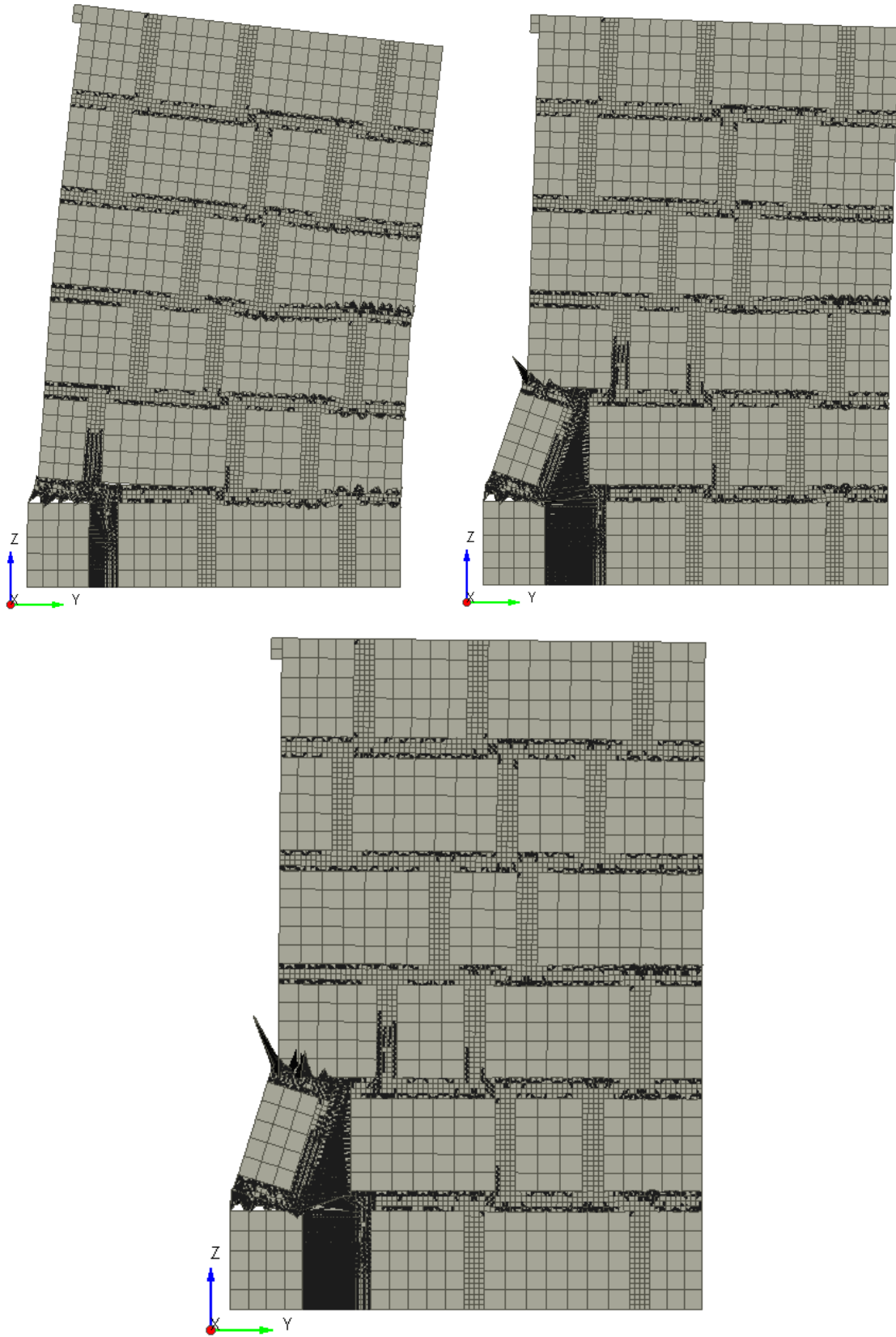


Figure A-69: PO-RANJ20-OB0.4 Response [A] 0.1% Drift, [B] 0.2% Drift, [C] 0.36% Drift

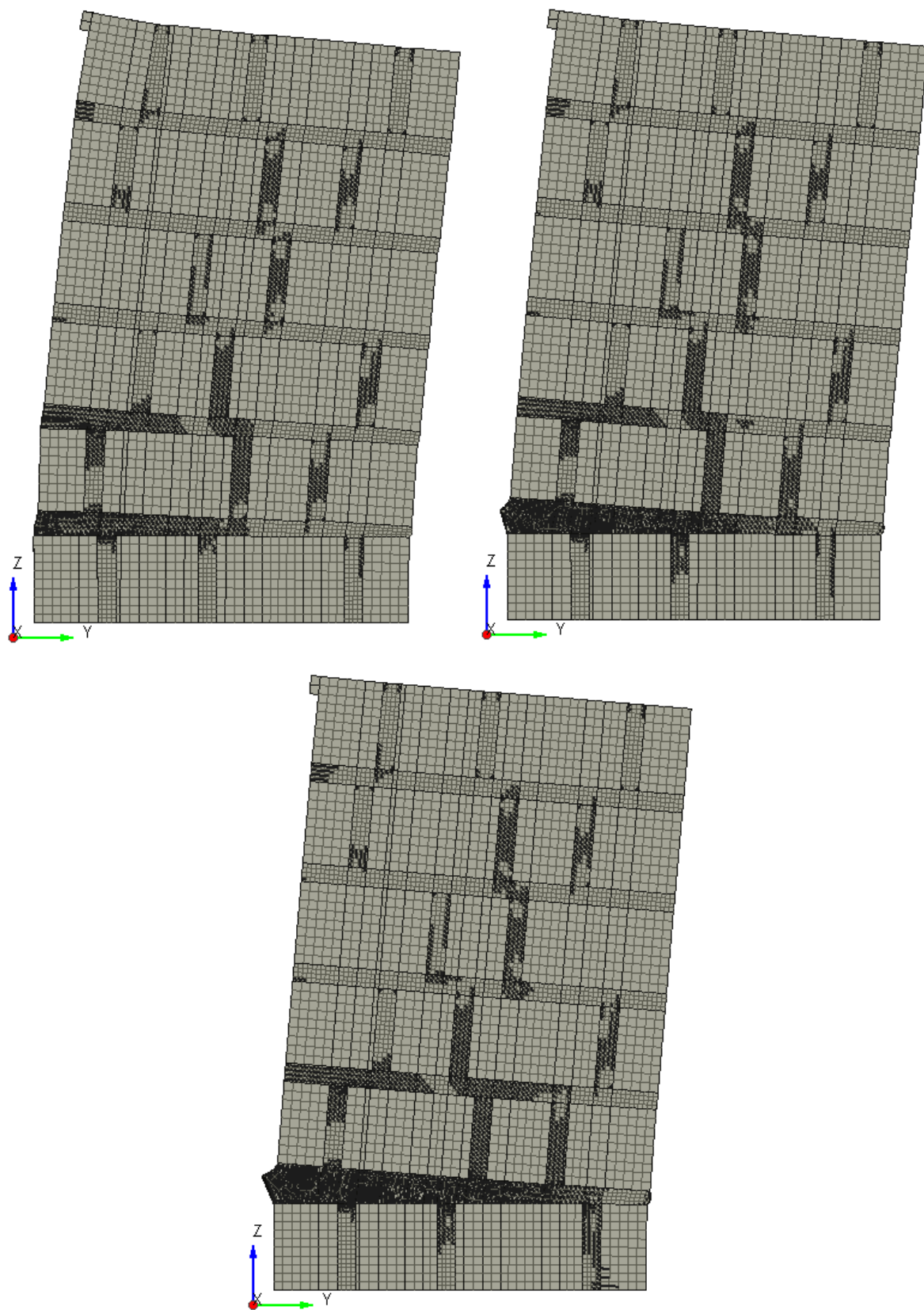


Figure A-70: PO-RANJ20-OB1.79 Response [A] 0.092% Drift, [B] 0.184% Drift, [C] 0.415% Drift

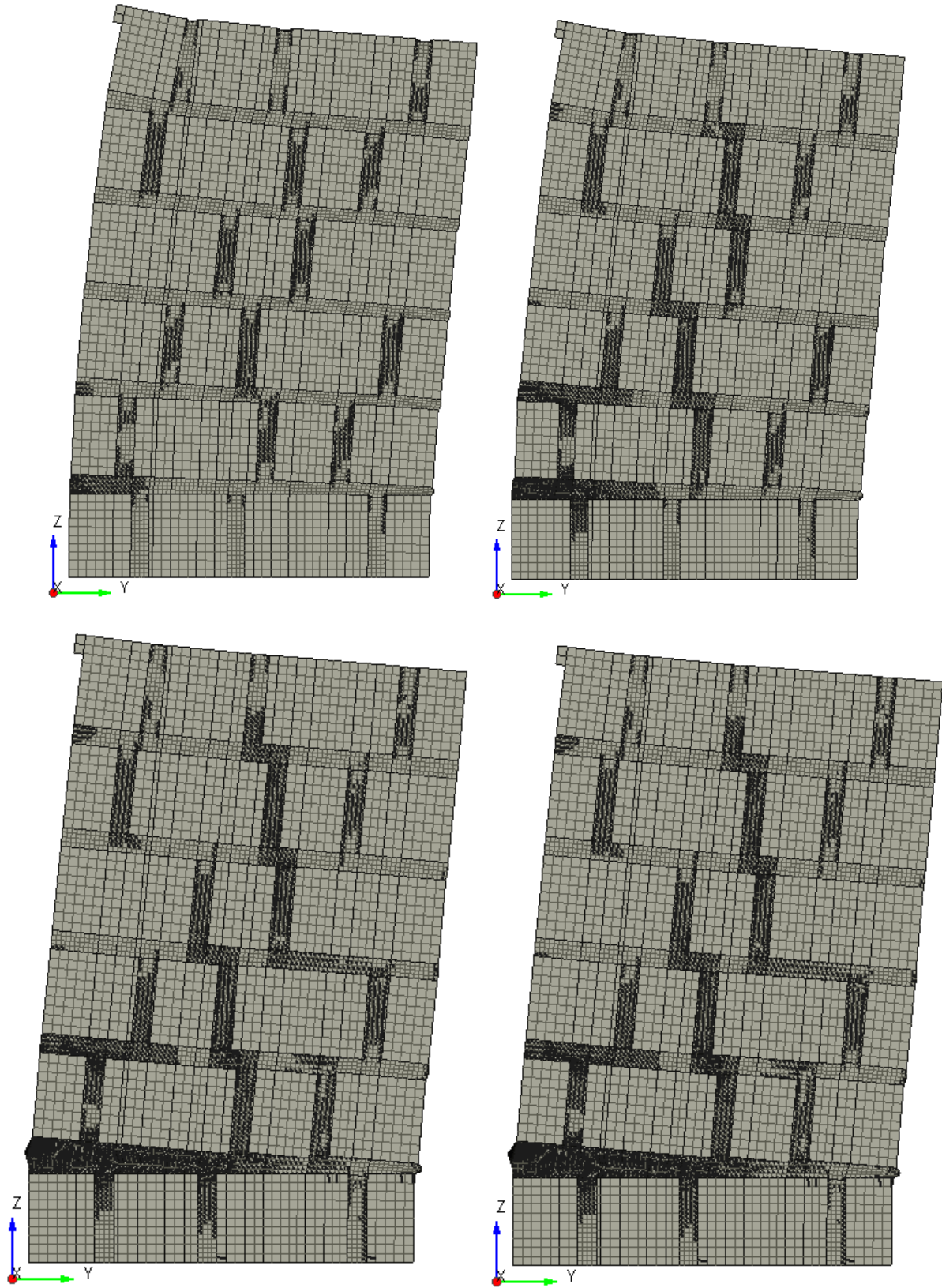


Figure A-71: PO-RANJ20-OB4.47 Response [A] 0.091% Drift, [B] 0.184% Drift, [C] 0.507% Drift, [D] 0.553% Drift

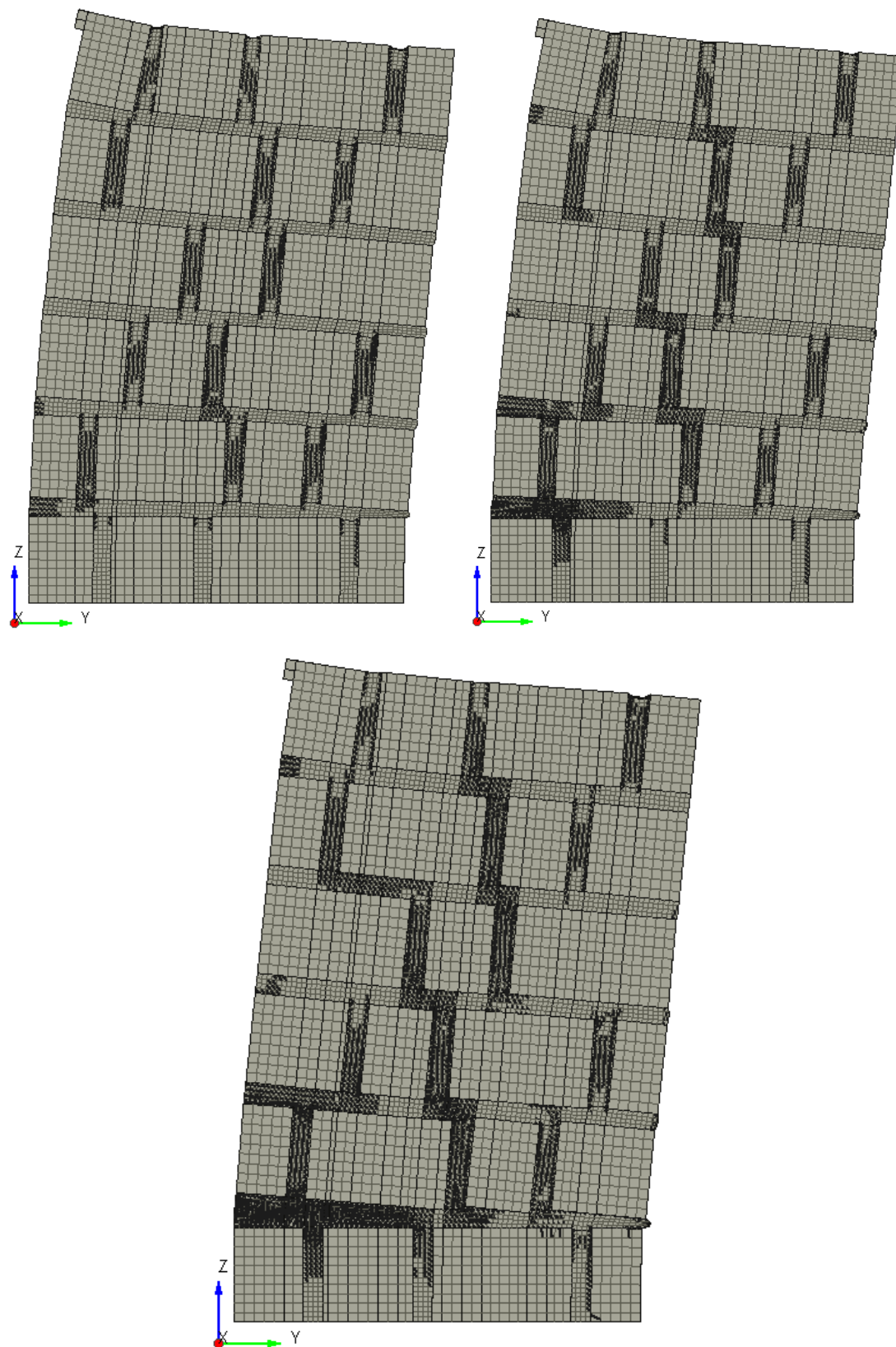


Figure A-72: PO-RANJ20-OB7.15 Response [A] 0.101% Drift, [B] 0.205% Drift, [C] 0.436% Drift

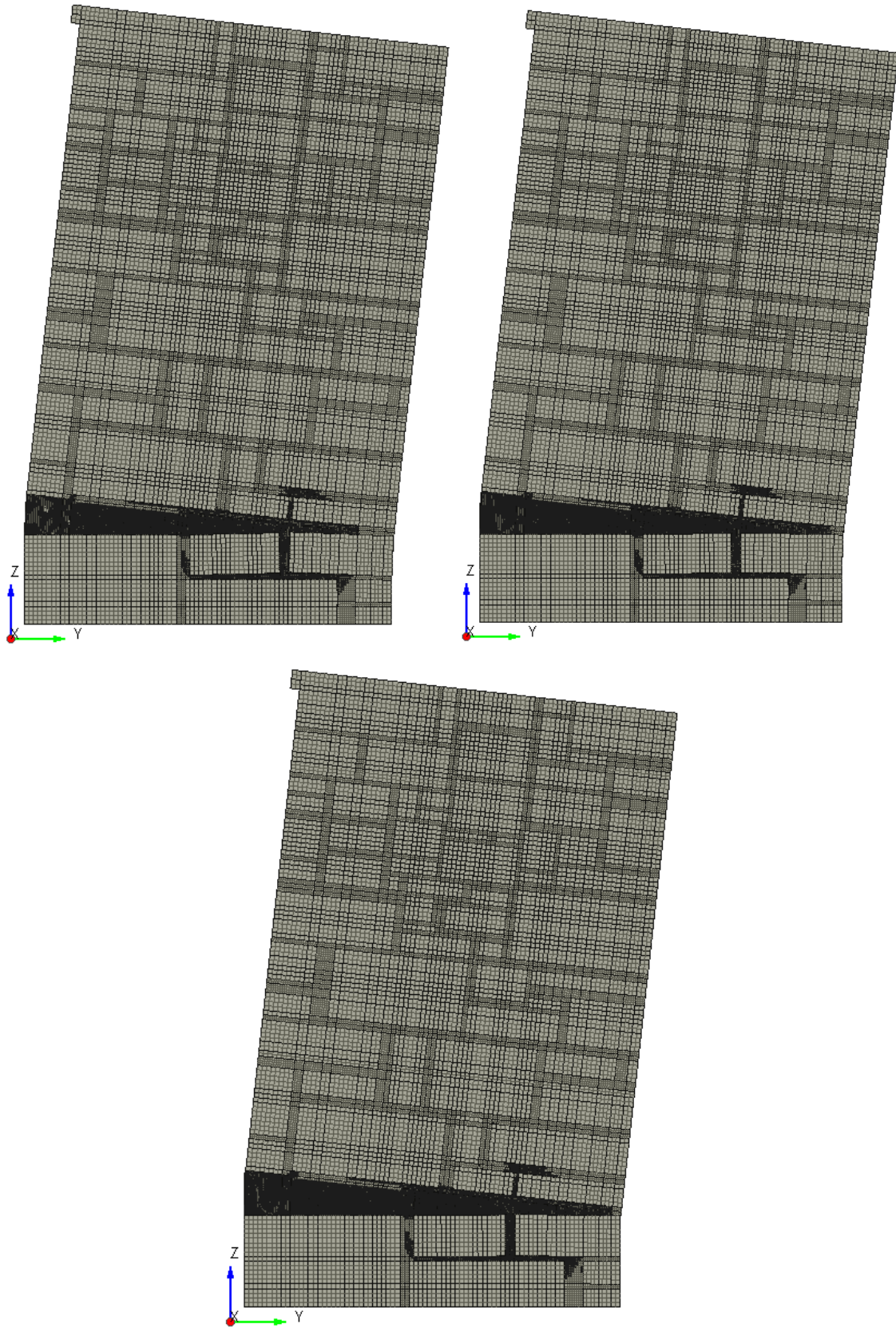


Figure A-73: PO-STONE-OB0.05 Response [A] 0.0925% Drift, [B] 0.185% Drift, [C] 0.277% Drift

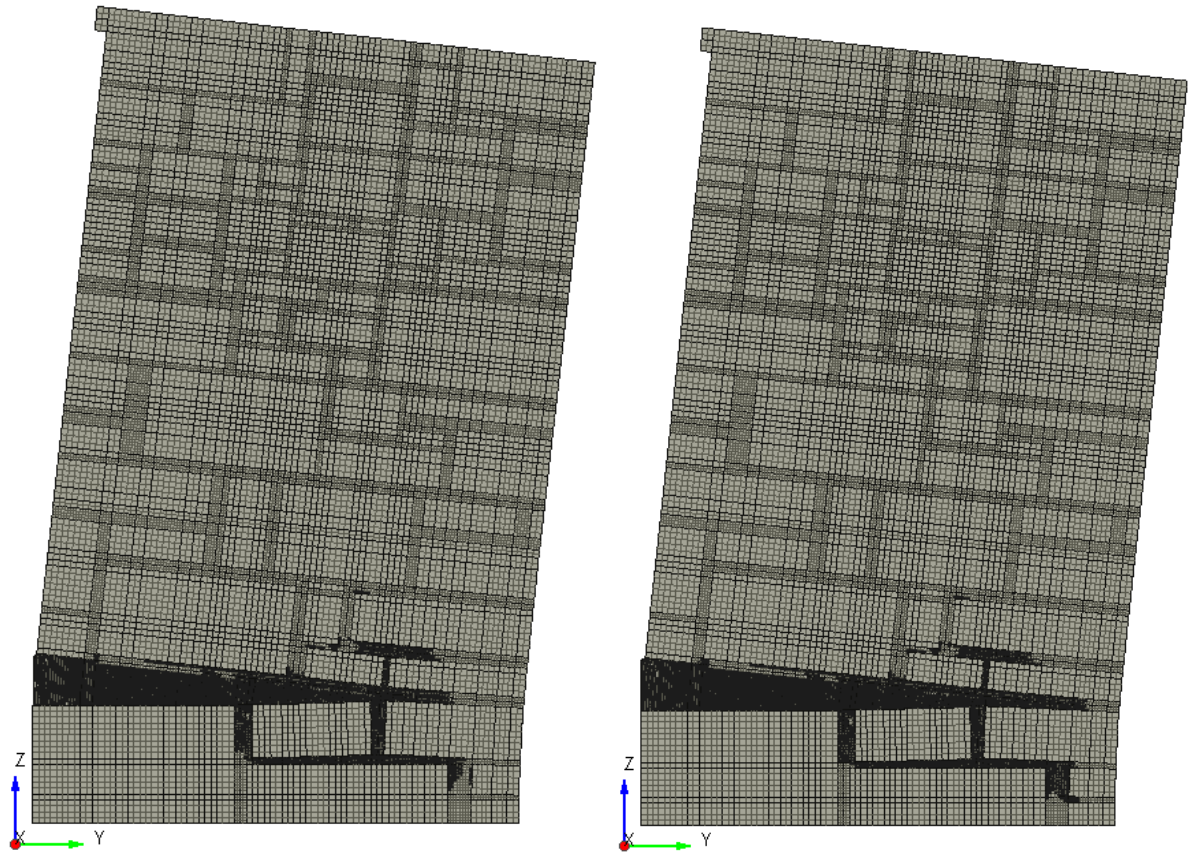


Figure A-74: PO-STONE-OB0.1 Response [A] 0.0925% Drift, [B] 0.185% Drift

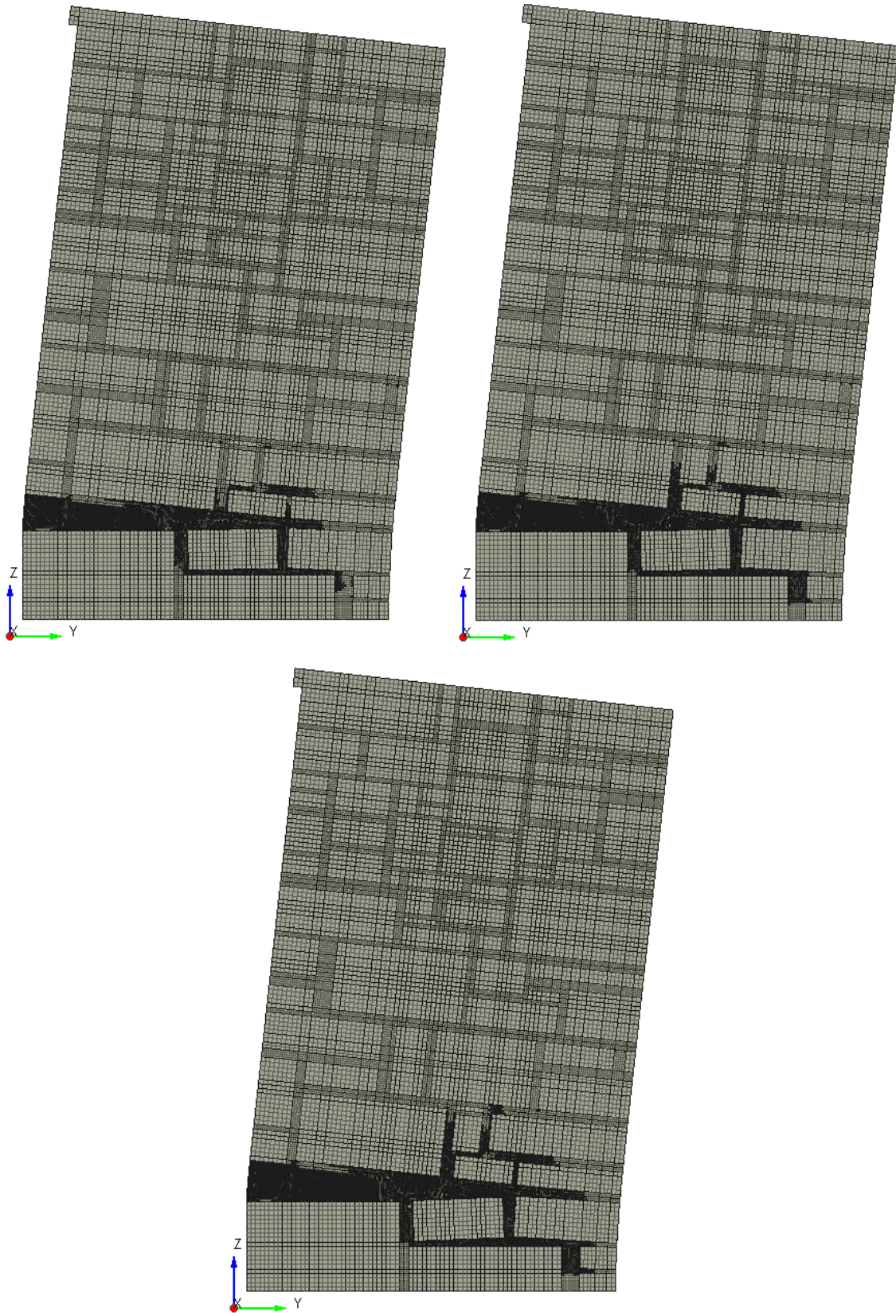


Figure A-75: PO-STONE-OB0.2 Response [A] 0.0928% Drift, [B] 0.185% Drift, [C] 0.324% Drift

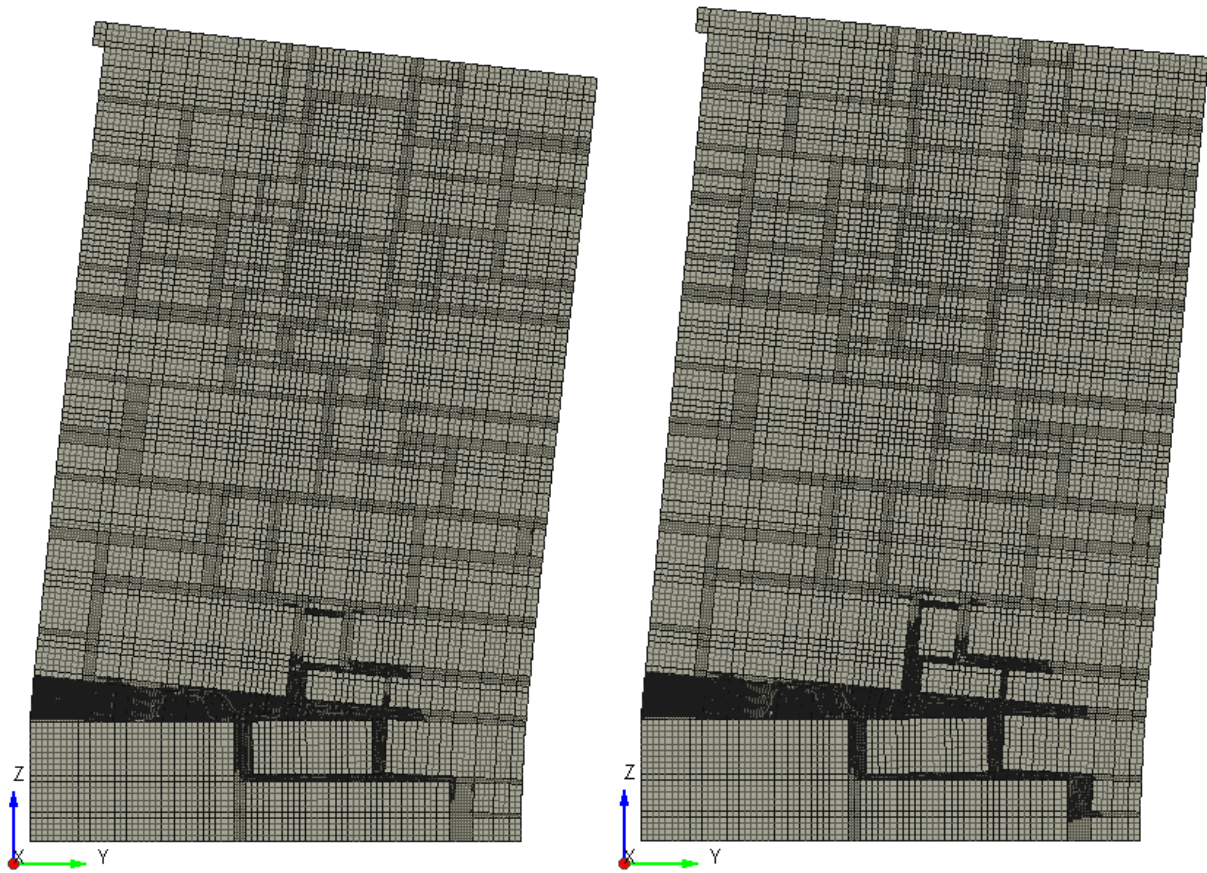


Figure A-76: PO-STONE-OB0.3 Response [A] 0.0929% Drift, [B] 0.231% Drift

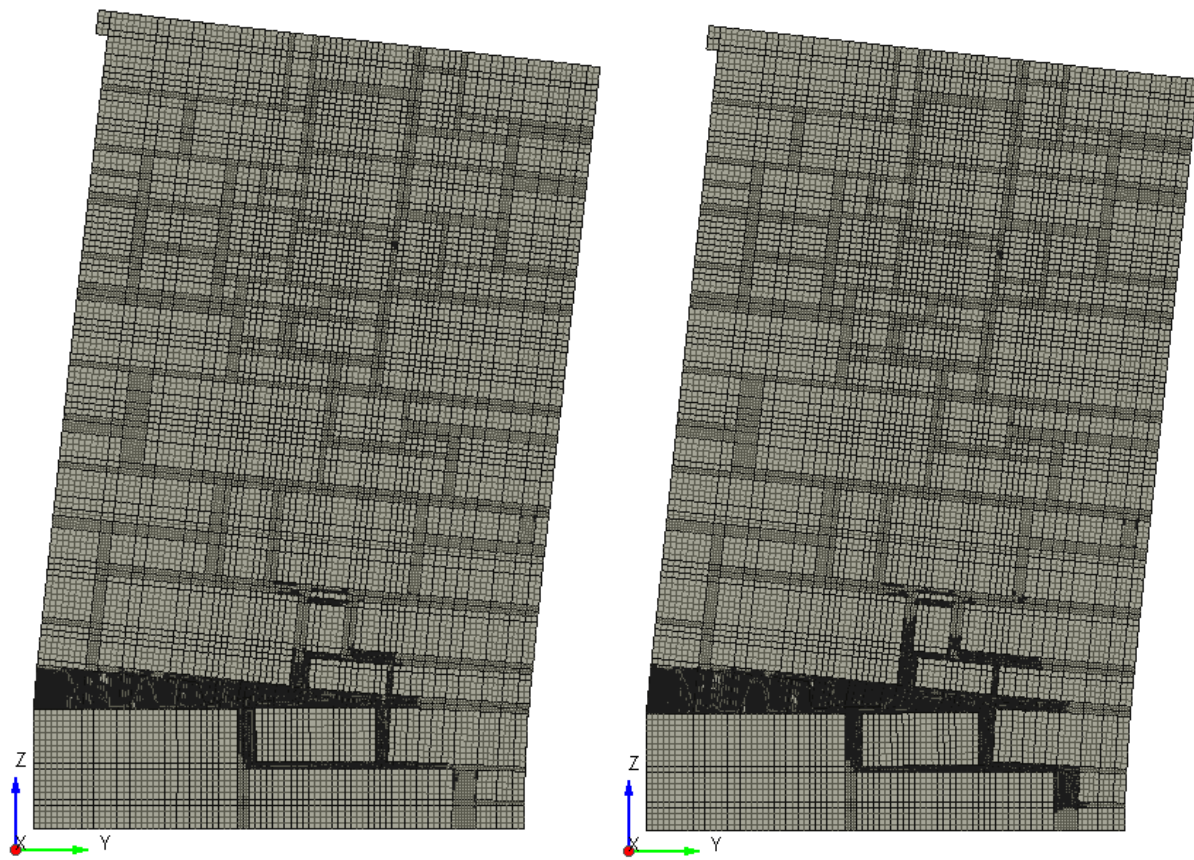


Figure A-77: PO-STONE-OB0.4 Response [A] 0.0932% Drift, [B] 0.232% Drift

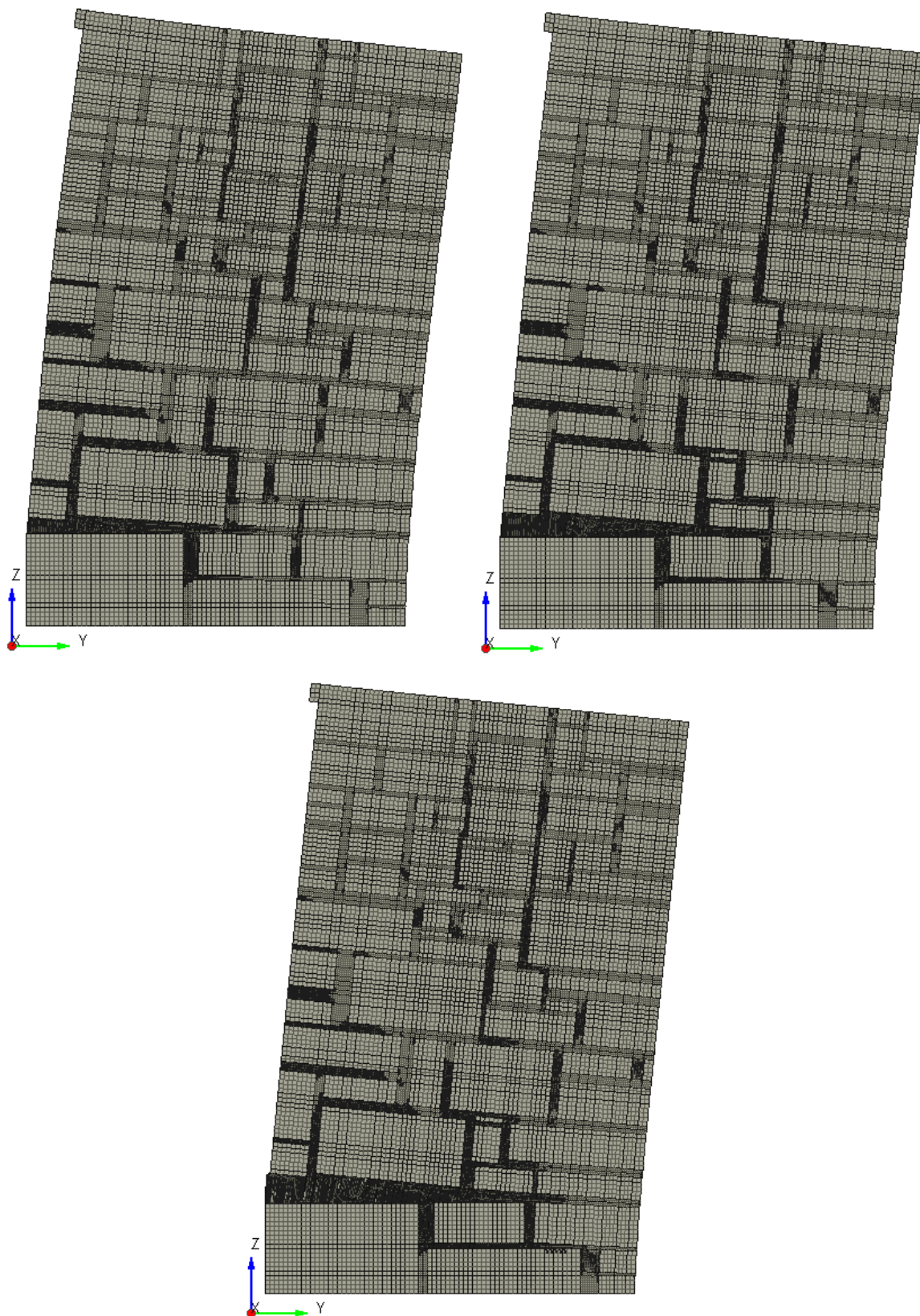


Figure A-78: PO-STONE-OB1.79 Response [A] 0.096% Drift, [B] 0.189% Drift, [C] 0.327% Drift

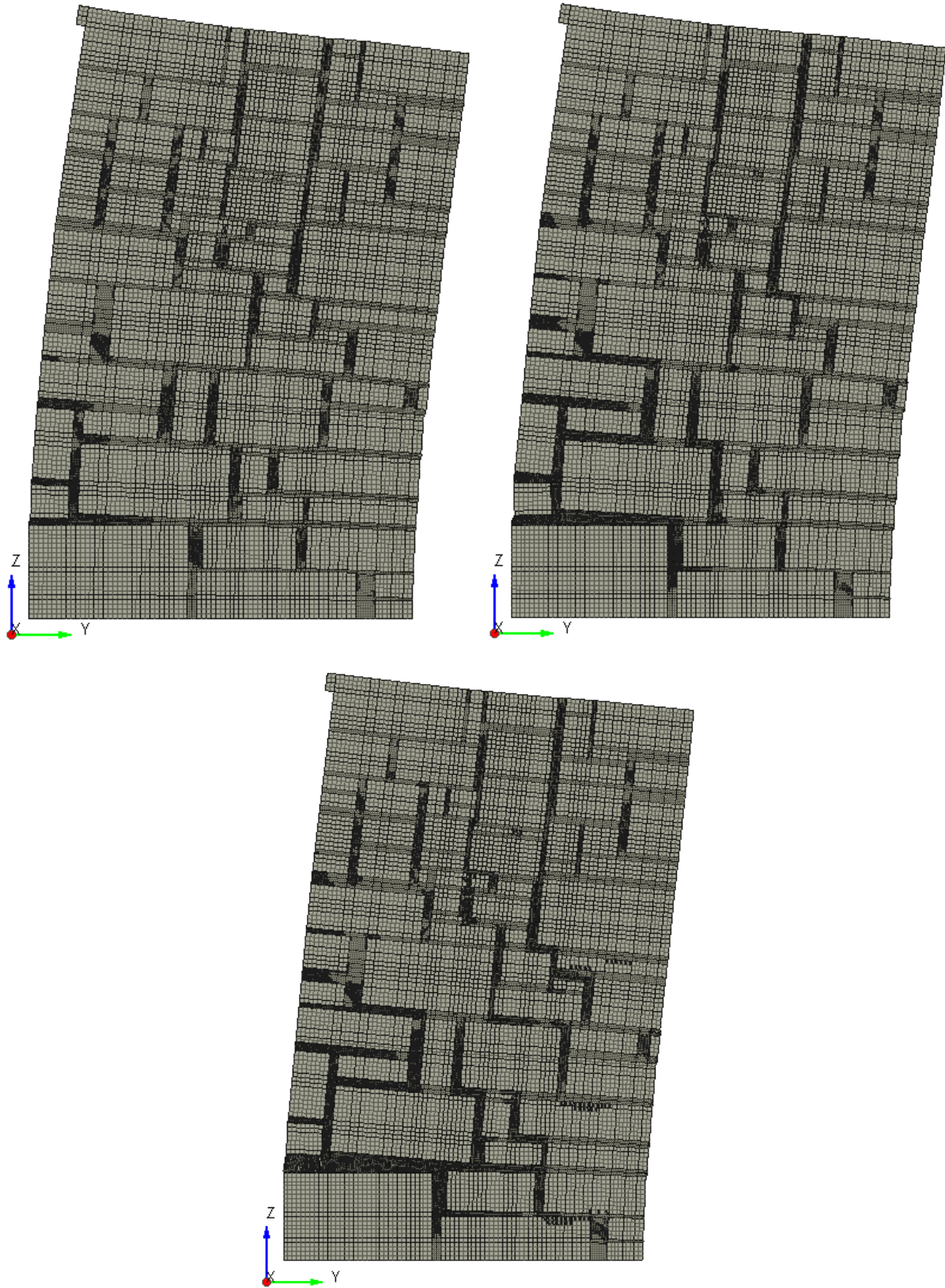


Figure A-79: PO-STONE-OB4.47 Response [A] 0.102% Drift, [B] 0.194% Drift, [C] 0.379% Drift

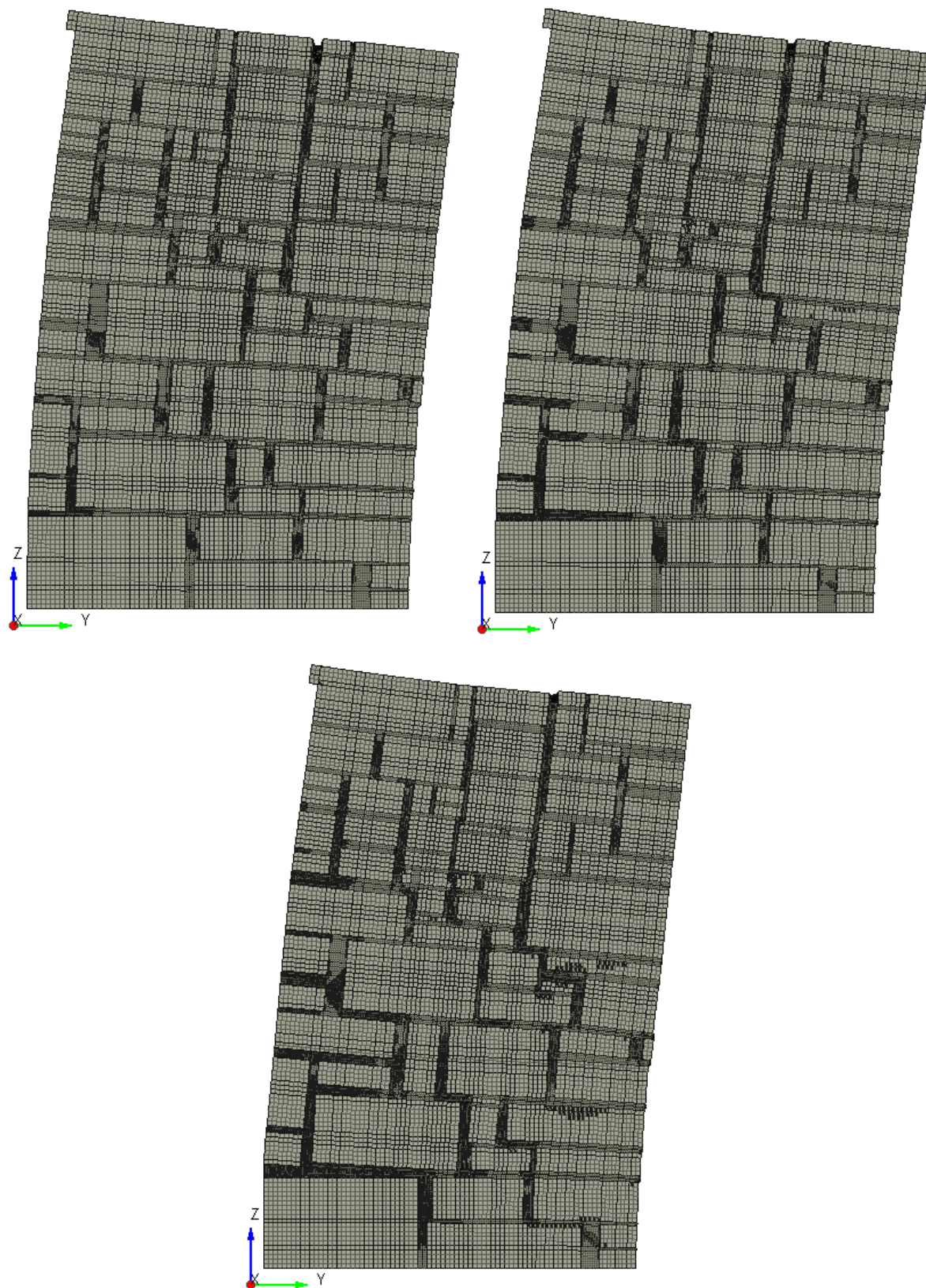


Figure A-80: PO-STONE-OB7.15 Response [A] 0.107% Drift, [B] 0.199% Drift, [C] 0.384% Drift

Appendix B – Axial response of masonry wallettes

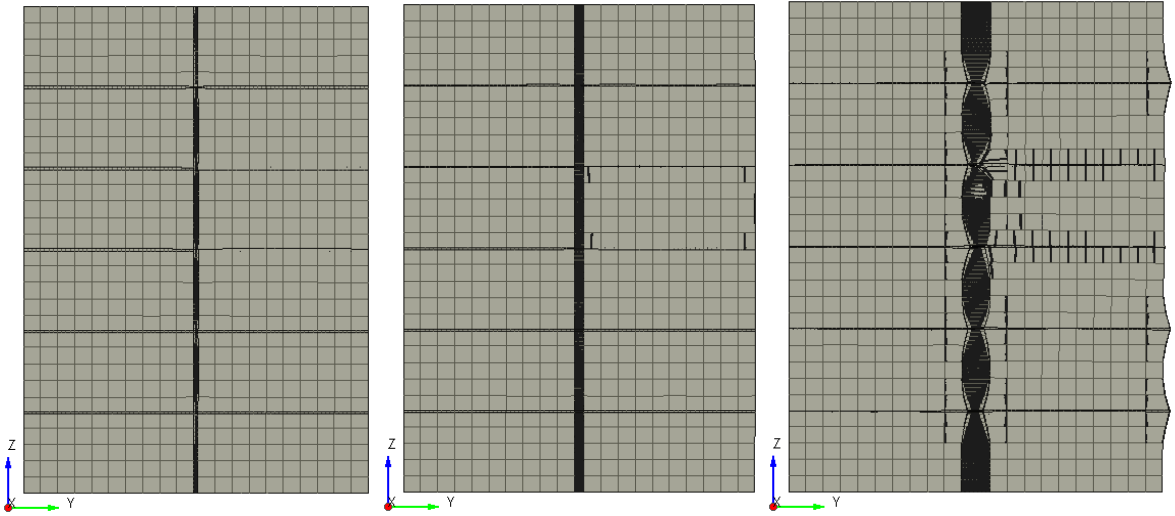


Figure B-1: SYMJ5, [A] Deformed Shape & Cracks ($\epsilon = 0.00124$ mm/mm), [B] Deformed Shape & Cracks ($\epsilon = 0.00248$ mm/mm), [C] Deformed Shape & Cracks ($\epsilon = 0.00372$ mm/mm)

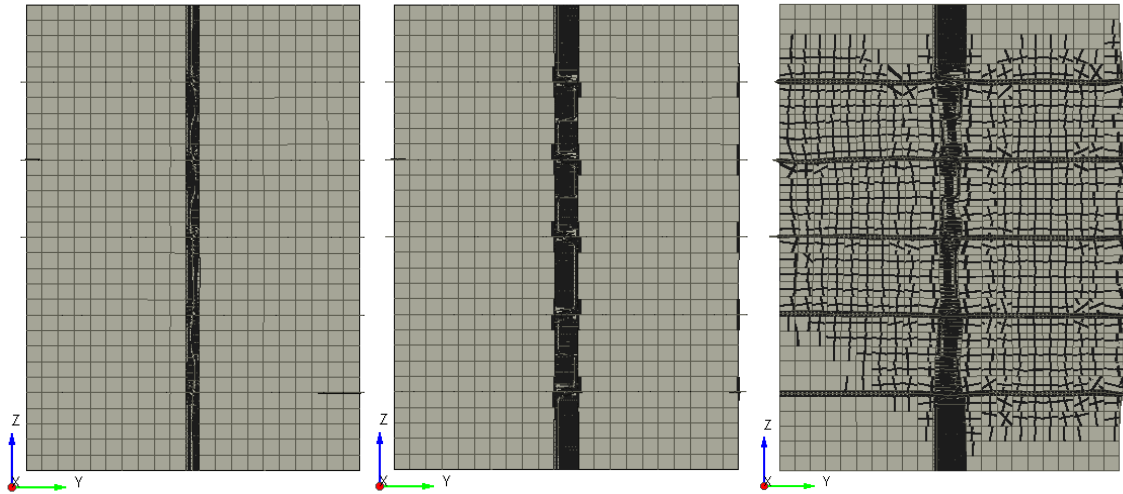


Figure B-2: SYMJ10, [A] Deformed-shape ($\epsilon = 0.00162$ mm/mm), [B] Deformed-shape ($\epsilon = 0.00355$ mm/mm), [C] Deformed-shape ($\epsilon = 0.0042$ mm/mm)

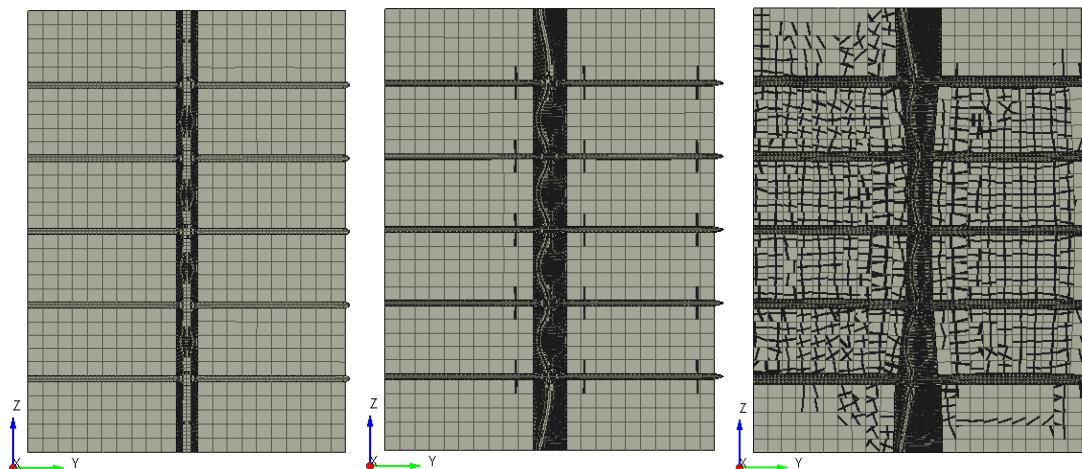


Figure B-3: SYMJ20, [A] Deformed-shape ($\varepsilon = 0.00124$ mm/mm), [B] Deformed-shape ($\varepsilon = 0.00495$ mm/mm), [C] Deformed-shape ($\varepsilon = 0.00743$ mm/mm)

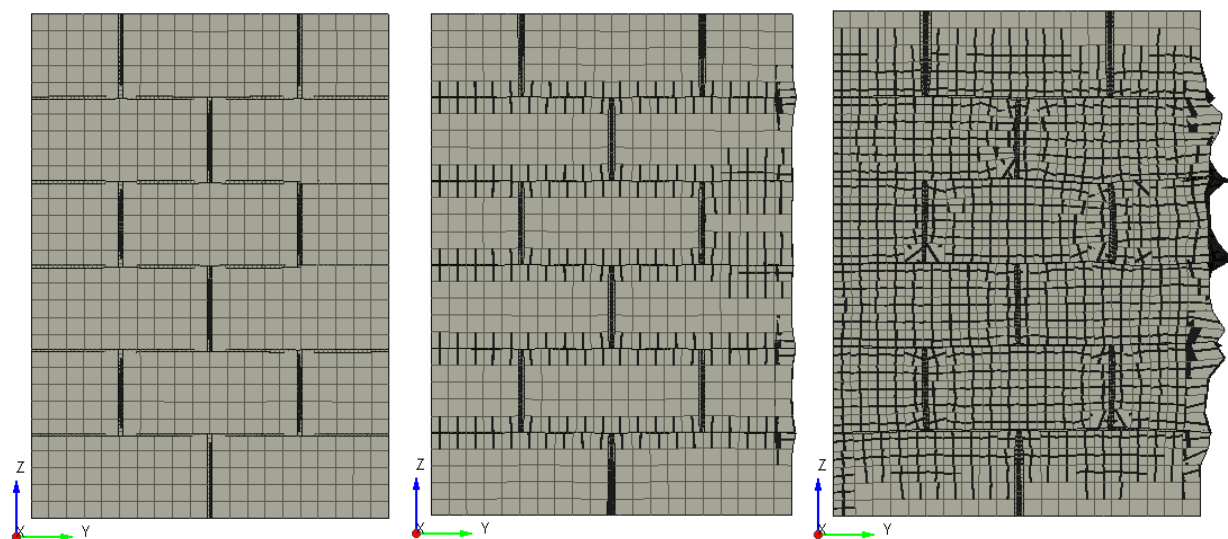


Figure B-4: EQSJ5, [A] Deformed-shape ($\varepsilon = 0.000969$ mm/mm), [B] Deformed-shape ($\varepsilon = 0.00388$ mm/mm), [C] Deformed-shape ($\varepsilon = 0.00485$ mm/mm)

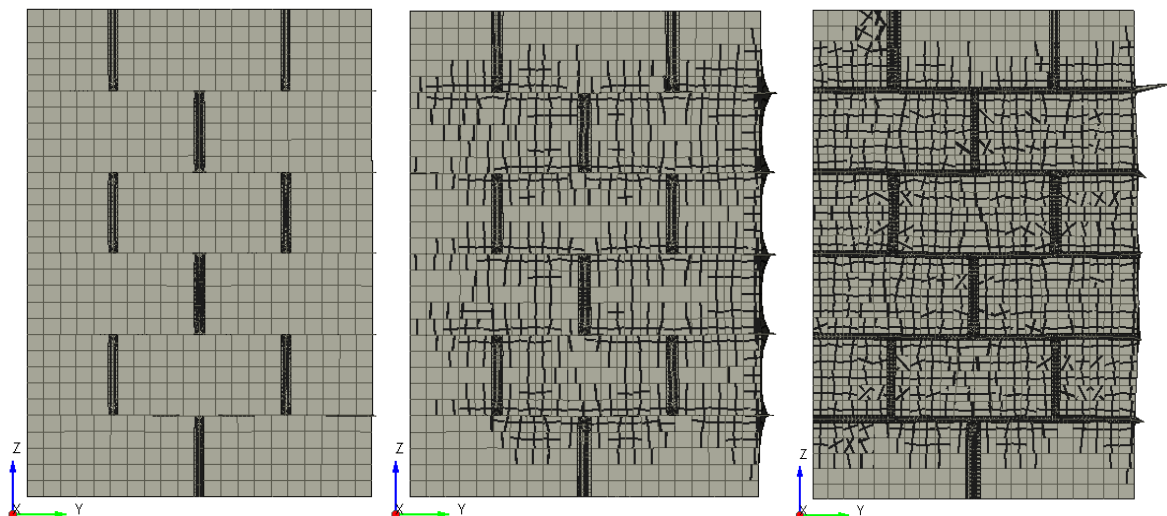


Figure B-5: EQSJ10, [A] Deformed-shape ($\varepsilon = 0.000969$ mm/mm), [B] Deformed-shape ($\varepsilon = 0.00388$ mm/mm), [C] Deformed-shape ($\varepsilon = 0.00485$ mm/mm)

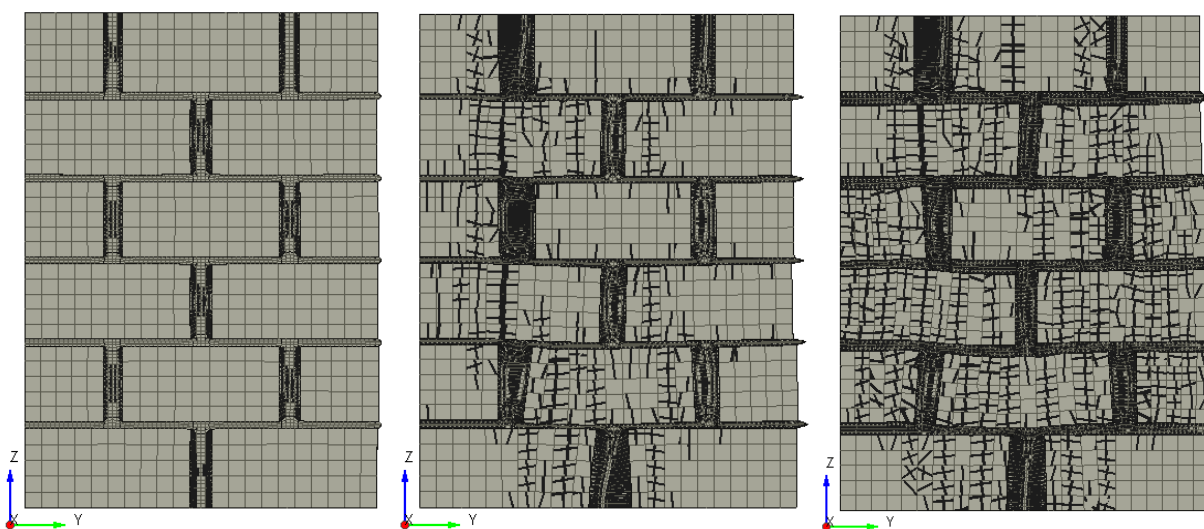


Figure B-6: EQSJ20, [A] Deformed-shape ($\varepsilon = 0.000969$ mm/mm), [B] Deformed-shape ($\varepsilon = 0.00485$ mm/mm), [C] Deformed-shape ($\varepsilon = 0.00582$ mm/mm)

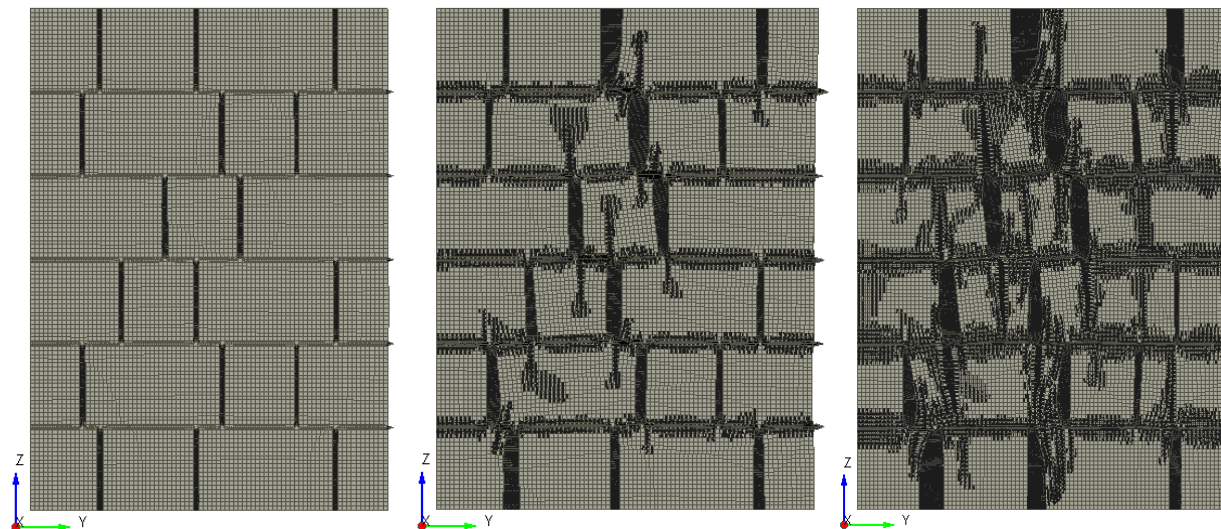


Figure B-7: RANJ5, [A] Deformed-shape ($\varepsilon = 0.000808$ mm/mm), [B] Deformed-shape ($\varepsilon = 0.00242$ mm/mm), [C] Deformed-shape ($\varepsilon = 0.00323$ mm/mm)

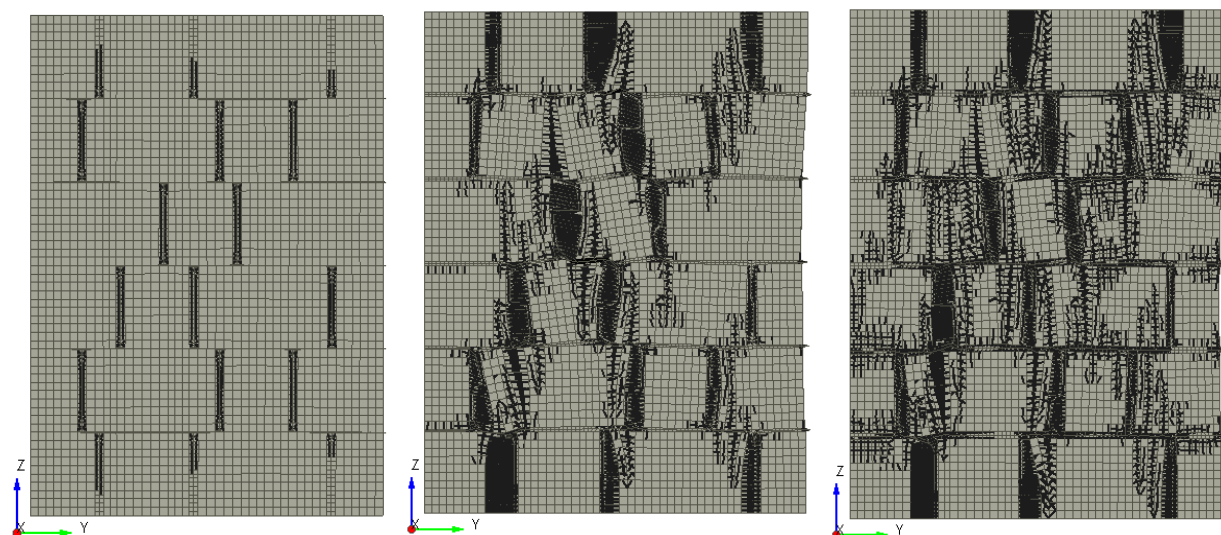


Figure B-8: RANJ10, [A] Deformed-shape ($\varepsilon = 0.000538$ mm/mm), [B] Deformed-shape ($\varepsilon = 0.00215$ mm/mm), [C] Deformed-shape ($\varepsilon = 0.00269$ mm/mm)

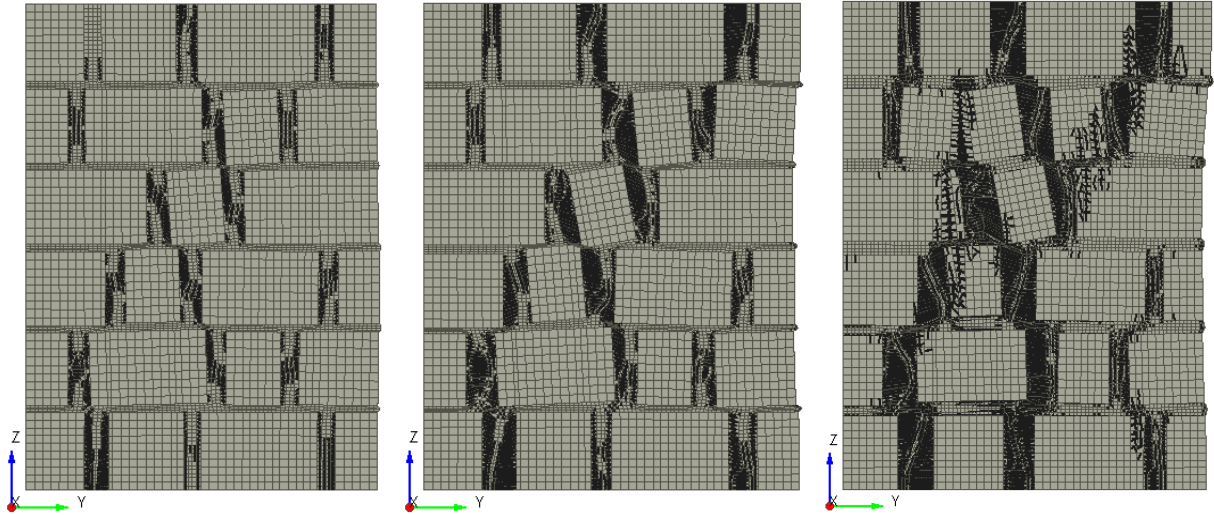


Figure B-9: RANJ20, [A] Deformed-shape ($\varepsilon = 0.000538$ mm/mm), [B] Deformed-shape ($\varepsilon = 0.00108$ mm/mm), [C] Deformed-shape ($\varepsilon = 0.00269$ mm/mm)

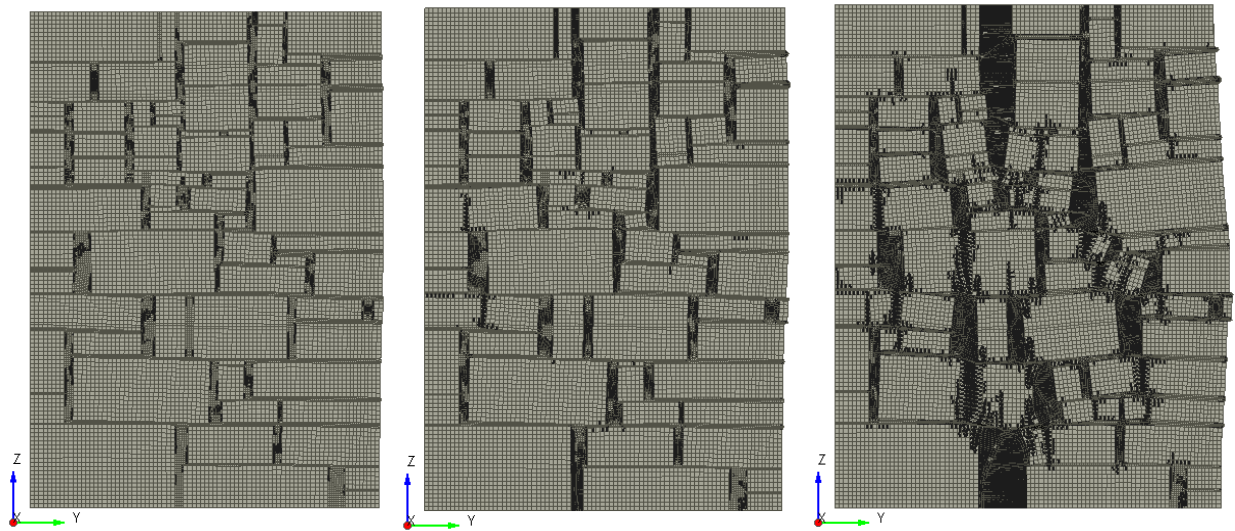


Figure B-10: STONE, [A] Deformed-shape ($\varepsilon = 0.000462$ mm/mm), [B] Deformed-shape ($\varepsilon = 0.00138$ mm/mm), [C] Deformed-shape ($\varepsilon = 0.00277$ mm/mm)